Year : 2020

nteractions between tectonics, climate and erosion : a case study of the central Andes using low-temperature thermochronology

Stalder Nadja F

Faculté des géosciences et de l'environnement

Institut des dynamiques de la surface terrestre

INTERACTIONS BETWEEN TECTONICS, CLIMATE AND EROSION

A CASE STUDY OF THE CENTRAL ANDES USING

LOW-TEMPERATURE THERMOCHRONOLOGY

THÈSE DE DOCTORAT

présentée à la Faculté des géosciences et de l'environnement de l'Université de Lausanne pour

l'obtention du grade de Docteur en sciences de la Terre par

NADJA F. STALDER

Master en Sciences de la Terre, ETH Zürich, Zürich

Jury

Prof. Dr. Frédéric Herman	Université de Lausanne	Directeur de thèse
Prof. Dr. Lukas Baumgartner	Université de Lausanne	Expert interne
Prof. Dr. Manfred Strecker	University of Potsdam	Expert externe
Prof. Dr. Peter W. Reiners	University of Arizona	Expert externe
Dr. Maria Giuditta Fellin	ETH Zürich	Experte externe
Prof. Dr. Christian Kull	Université de Lausanne	Président du jury

LAUSANNE, 2020

IMPRIMATUR

Vu le rapport présenté par le jury d'examen, composé de

Président de la séance publique :	M. le Professeur Christian Kull
Président du colloque :	M. le Professeur Christian Kull
Directeur de thèse :	M. le Professeur Frédéric Herman
Expert interne :	M. le Professeur Lukas Baumgartner
Expert externe :	M. le Professeur Manfred Strecker
Expert externe :	M. le Professeur Peter Reiners
Experte externe :	Mme la Docteure Maria Giuditta Fellin

Le Doyen de la Faculté des géosciences et de l'environnement autorise l'impression de la thèse de

Madame Nadja STALDER

Titulaire d'un
Master en sciences de la Terre
de l'ETHZ

intitulée

INTERACTIONS BETWEEN TECTONICS, CLIMATE AND EROSION
A CASE STUDY OF THE CENTRAL ANDES USING
LOW-TEMPERATURE THERMOCHRONOLOGY

Lausanne, le 10 septembre 2020

Pour le Doyen de la Faculté des géosciences et de l'environnement

Professeur Christian Kull

INTERACTIONS BETWEEN TECTONICS, CLIMATE AND EROSION

A CASE STUDY OF THE CENTRAL ANDES USING

LOW-TEMPERATURE THERMOCHRONOLOGY

THÈSE DE DOCTORAT

présentée à la Faculté des géosciences et de l'environnement de l'Université de Lausanne pour

l'obtention du grade de Docteur en sciences de la Terre par

NADJA F. STALDER

Master en Sciences de la Terre, ETH Zürich, Zürich

LAUSANNE, 2020

Science makes people reach selflessly for truth and objectivity;
it teaches people to accept reality, with wonder and admiration,
not to mention the deep awe and joy that the natural
order of things brings to the true scientist.

Lise Meitner

Logic will get you from A to B. Imagination will take you everywhere

Albert Einstein

Acknowledgments

<div align="right">Lausanne, September 2020</div>

Synopsis

La topographie de la Terre est déterminée par les forces tectoniques et les processus d'érosion. La tectonique des plaques contrôle la distribution et les positions des continents et crée les montagnes, les océans et les îles. Comme elle régit l'activité volcanique et la vitesse d'expansion des fonds océaniques, elle est aussi le contributeur principal de l'émission de CO_2 dans l'atmosphère, ce qui détermine la température et donc le climat. De plus, la création des montagnes altère la circulation atmosphérique: le relief agit comme une barrière qui empêche le transport d'humidité d'un versant à l'autre. Le climat, en revanche, contrôle l'érosion et la sédimentation et peut donc changer le bilan de masse dans les chaînes de montagnes. Bien que prédites par des modèles numériques, ces interactions sont très rarement observées sur le terrain. Cette étude présente l'utilisation de la thermochronologie pour mieux comprendre les relations entre le climat, la tectonique et l'érosion.

Les Andes d'Amérique du Sud s'étendent sur plus de 7000 km le long de la marge de subduction chilienne, traversent plusieurs zones climatiques, du désert d'Atacama à l'Antarctique, et présentent des altitudes moyennes supérieures à 4000 m.s.m. Dans ce travail, j'utilise les Andes centrales (latitude 18-36° S) pour étudier les influences respectives du climat et de la tectonique sur l'érosion à différentes échelles spatiales (quelques km à l'étendue d'une chaîne) et temporelles (milliers à millions d'années). Les taux d'érosion sont quantifiés par la modélisation des données thermochronologiques et comparés aux histoires climatiques et tectoniques issues des observations sédimentaires.

Tout d'abord, je présente 238 nouveaux âges thermochronologiques qui sont ajoutés à 744 âges issus de la littérature. Ces âges permettent de quantifier les taux d'érosion des Andes centrales au cours des 80 derniers millions d'années. L'étude des corrélations entre l'évolution des taux d'érosion et les changements tectoniques et climatiques révèle que l'activité tectonique soutient un taux d'érosion de base qui est fortement impacté par le climat. Les taux d'érosion dans la partie Nord-Ouest des Andes centrales sont petits (<0.2 mm/an) à cause des précipitations réduites et de la faible activité tectonique. Au contraire, les taux d'érosion dans la partie Est reflètent le début et la propagation de la déformation vers l'Est et sont augmentés par l'établissement du système de mousson sud-américaine il y a environ 10 millions d'années. Les taux d'érosion les plus élevés sont observés pendant les deux derniers millions d'années. Ils proviennent des régions qui sont tectoniquement actives et qui reçoivent des précipitations abondantes et/ou qui étaient autrefois glaciaires.

Dans la deuxième partie, je concentre mes recherches sur une zone d'étude plus petite (33-35° S). Elle présente un fort gradient Nord-Sud de précipitations dans un cadre tectonique déjà bien étudié. Suite à une expansion vers le Nord de l'influence des vents d'Ouest, les précipitations dans cette région ont augmenté pendant les périodes glaciales, ce qui a entraîné l'avancement des glaciers. Ici, j'applique un nouveau thermochronomètre, basé sur la thermoluminescence, qui permet d'obtenir des séries temporelles des taux d'érosion sur les dernières 100'000 années. Je constate que les taux d'érosion étaient élevés (40-60 mm/an) il y a plus de 40'000 ans et sont plus faibles (~4 mm/an) dans des périodes plus récentes. La diminution des taux d'érosion correspond à la fin de la dernière période glaciaire, lorsque les glaciers ont recouvert une grande partie de la Terre. Les taux d'érosion élevés pendant cette période sont alors expliqués par l'apparition d'érosion glaciaire et l'augmentation des précipitations. Cependant, la région étudiée est et a été tectoniquement active. Donc, on ne peut pas exclure que le soulèvement des roches, induit par la tectonique, soit le facteur principal contrôlant les taux d'érosion élevés observés au cours des deux derniers millions d'années. Pour vérifier si les âges thermochronologiques observés dans cette région peuvent être expliqués par l'activité tectonique, j'utilise un modèle pour prédire les âges attendus par cette activité. Le résultat montre un décalage important entre les âges observés et les âges prévus. Cela indique que l'activité tectonique ne peut pas être la raison principale des taux d'érosion élevés.

Cette étude conforte l'idée que le refroidissement global et le début des glaciations ont eu un impact prononcé sur l'ampleur de l'érosion pendant les deux derniers millions d'années dans les régions montagneuses.

Contents

List of Figures

List of Tables

Abstract

The Earth's topography reflects a dynamic equilibrium between tectonics and climate-modulated surface processes through erosion. In the nineties, numerical models and analogue experiments have set the stage for our understanding of how these processes control the morphology and the dynamic evolution of mountain belts. However, field evidence of the interactions between climate, tectonics and erosion remains sparse. This is in part due to the complexity of feedback loops, and partly due to the uncertainties when reconstructing tectonic, climatic and erosional histories. Furthermore, several studies that have associated increased Late Cenozoic erosion rates to global cooling have been contested by studies questioning the techniques used to quantify erosion rates and how erosion rate measurements can be compared across timescales.

In this work, I use the Central Andes (18-36° S) as a natural laboratory to study the respective influences of climate and tectonics on erosion on different spatial (km to mountain-belt) and temporal (kyr to Myr) scales. Erosion rates are quantified by inverse modelling of thermochronological data and compared to the past and present climatic and tectonic settings extracted from the sedimentary record.

First, I provide 238 new thermochronological ages (apatite and zircon (U-Th)/He (AHe, ZHe) and apatite fission-track (AFT) dating) from Chile that are combined with 744 ages (AHe, ZHe, AFT, and zircon fission-track (ZFT)) from the literature to constrain the exhumation history of the Central Andes (18-36° S) during the last 80 Ma. The comparison of exhumation rates with changes in the tectonic and climatic conditions reveals that tectonic activity sustains a background exhumation rate which is strongly modified by the climate. Exhumation rates in the north-western part of the Central Andes are low (<0.2 km/Myr) due to low precipitation and low tectonic activity. Exhumation rates in the eastern part likely reflect the onset and east-ward propagation of deformation. Here, the rates increase in the late Miocene probably due to the establishment of the South American Monsoon system. Highest erosion rates are observed during the Plio-Pleistocene in tectonically active regions that receive abundant precipitation and/or that were formerly glaciated.

Second, I focus my research on a smaller study area (33-35° S) that combines a strong N-S precipitation gradient with a well-constrained tectonic setting. Precipitation in this region increased during glacial periods due to a northward shift of the mid-latitude storm tracks, leading to pronounced glaciations. I apply a recently developed thermochronometer (thermoluminescence thermochronometry, TLT) to granitic bedrock samples from Chile to extract time series of erosion rates over the Quaternary. I find that erosion rates were high (40-60 mm/yr) during the last glacial maximum (~20 ka) and slowed down to ~4 mm/yr in more recent times. This result suggests a significant impact of glaciation and enhanced precipitation on erosion rates, despite tectonic convergence.

Finally, to test if observed thermochronological ages (AHe, ZHe, AFT, ZFT) in this region can be explained by tectonic-induced rock uplift, I use a thermo-kinematic model to predict thermochronological ages expected from the geologically constrained fault kinematics. The result shows a significant mismatch between observed and predicted ages and implies that the tectonic activity alone cannot explain the high Plio-Pleistocene erosion rates. This reinforces the findings from above and strengthens the idea that Late Cenozoic cooling and the onset of glaciations may have had a pronounced impact on erosion rates in mountain ranges.

Résumé

La topographie de la Terre représente l'équilibre entre les processus tectoniques et climatiques, qui sont liés par l'érosion. Dans les années 1990, les modèles numériques et les expériences analogiques ont ouvert la voie à notre compréhension de comment ces processus contrôlent la morphologie et le régime des contraintes internes des chaînes de montagnes. Cependant, les observations des interactions entre le climat, la tectonique et l'érosion dans le terrain sont rares. Cela est en partie dû à la complexité de ces rétroactions et en partie aux incertitudes liées aux reconstructions du climat, de l'activité tectonique et de l'érosion. En outre, l'hypothèse que l'augmentation des taux d'érosion du Cénozoïque tardif est causée par le refroidissement global reste débattue. En effet, plusieurs études ont mis en question les techniques utilisées pour quantifier les taux d'érosion et la manière dont les mesures de ces taux peuvent être comparées entre les différentes échelles de temps.

Dans ce travail, j'utilise les Andes centrales (18-36° S) comme laboratoire naturel pour étudier les influences respectives du climat et de la tectonique sur l'exhumation, sur différentes échelles spatiales (10 à >1000 km) et temporelles (ka à Ma). Les taux d'érosion sont quantifiés par la modélisation inverse des données thermochronologiques et comparés aux histoires climatiques et tectoniques issues des observations sédimentaires.

Premièrement, je présente 238 nouveaux âges thermochronologiques (apatite et zircon (U-Th)/He (AHe, ZHe) et apatite fission-track (AFT)) du Chili qui sont ajoutés à 744 âges (AHe, ZHe, AFT, et zircon fission-track (ZFT)) issus de la littérature. Ces âges permettent de quantifier les taux d'érosion des Andes centrales au cours des derniers 80 Ma. L'étude des corrélations entre l'évolution des taux d'érosion et les changements tectoniques et climatiques révèle que l'activité tectonique soutient un taux d'érosion de base qui est fortement modifié par le climat. Les taux d'érosion dans la partie Nord-Ouest des Andes centrales sont petits (<0.2 mm/an) à cause des précipitations réduites et de la faible activité tectonique. Au contraire, les taux d'érosion dans la partie Est reflètent le début et la propagation de la déformation vers l'Est et sont augmentés par l'établissement du système de mousson sud-américain il y a environ 10 Ma. Les taux d'érosion les plus élevés sont observés au cours du Plio-Pléistocène dans les régions tectoniquement actives et qui reçoivent des précipitations abondantes et/ou qui étaient autrefois glaciaires.

Dans la deuxième partie, je concentre mes recherches sur une zone d'étude plus petite (33-35° S) qui présente un fort gradient Nord-Sud de précipitations dans un cadre tectonique bien étudié. Suite à une expansion vers le Nord de l'influence des vents d'Ouest, les précipitations dans cette région ont augmenté pendant les périodes glaciales, ce qui a entraîné l'avancement des glaciers. Ici, j'applique un nouveau thermochronomètre, la "thermoluminescence thermochronometry" (TLT), aux échantillons granitiques du Chili. Cela permet d'obtenir des séries temporelles des taux d'érosion durant le Quaternaire. Je constate que les taux d'érosion étaient élevés (40-60 mm/an) pendant le dernier maximum glaciaire (~20 ka) et sont plus faibles (~4 mm/an) dans des périodes plus récentes. Cela indique un impact significatif de la glaciation et des précipitations accrues sur les taux d'érosion.

Finalement, pour vérifier si les âges thermochronologiques observés (AHe, ZHe, AFT, ZFT) dans cette région peuvent être expliqués par l'activité tectonique, j'utilise un modèle thermo-cinématique pour prédire les âges attendus par la cinématique des failles géologiquement contraintes. Le résultat montre un décalage important entre les âges observés et prédits et indique que le soulèvement des roches induit par la tectonique ne peut pas être la raison principale des taux d'érosion élevés du Plio-Pléistocène. Cela renforce les conclusions obtenues précédemment. Cette étude conforte l'idée que le refroidissement global et le début des glaciations ont probablement eu un impact prononcé sur l'ampleur de l'érosion dans des chaînes de montagnes.

Introduction

The Earth's topography reflects the balance between tectonic and climatic processes, which are linked by erosion and coupled through a system of complex feedback mechanisms (e.g., Molnar and England, 1990; Raymo and Ruddiman, 1992; Reiners et al., 2003; Molnar, 2009; Whipple, 2009; Champagnac et al., 2012). On a global scale, plate tectonic processes set the long-term climate by controlling atmospheric greenhouse gases through volcanism and sea floor spreading, the distribution and topography of landmass, and the opening and closure of oceanic gateways (e.g., Berner et al., 1983; Raymo and Ruddiman, 1992; Hay, 1996). More regionally, tectonic activity accelerates chemical and physical erosion by sustaining high relief and steep slopes through rock-uplift and by fracturing the bedrock. In turn, climate-modulated erosion and (re-)deposition change the mass balance and lithospheric stress regime of a mountain belt, influencing its internal deformation and shape (Dahlen and Suppe, 1988; Koons, 1990; Molnar and England, 1990; Beaumont et al., 1992; Willett, 1999) (Fig. 1.1A). Erosional unloading also leads to isostatic rock uplift (Molnar and England, 1990, Fig. 1.1B). Climate may ultimately control topographic height and width of mountain ranges (e.g., Brozović et al., 1997; Montgomery et al., 2001; Egholm et al., 2009).

Theoretical concepts and numerical models developed in the early nineties set the stage for our understanding of the possible links between tectonic evolution of mountain belts and climate-modulated erosion (Dahlen and Suppe, 1988; Jamieson and Beaumont, 1988; Beaumont et al., 1992; Willett et al., 1993; Willett, 1999). In these studies, mountain belts are considered as tapering wedges controlled by an internal state of stress close to Coulomb failure (Dahlen and Suppe, 1988) (Fig. 1.2). In the absence of erosion, the width and height of such a tapering wedge grows self-similarly (i.e., maintaining its critical taper) with little deformation as new material is being accreted. An eroding wedge instead continually deforms to maintain its critical taper and attains, when accretionary influx is balanced by erosion, a steady-state width controlled by the
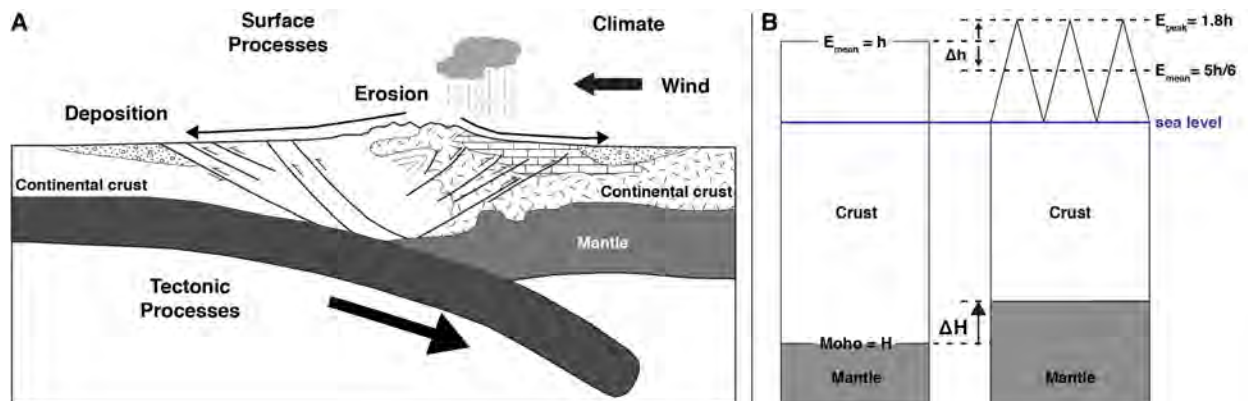
Figure 1.1: A Conceptual view of the interactions between tectonics, climate and surface processes in orogenesis. Tectonic convergence leads to crustal thickening and isostatic uplift. The resulting topography acts as orographic barrier perturbing moisture transport, increasing precipitation and erosion on the windward side of the orogen. Surface processes change the internal stress regime by redistributing mass through erosion and sediment deposition. Figure redrawn from Willett (1999). **B)** Isostatic effect of erosion and crustal thickening on elevation, rock uplift and the crustal–mantle boundary (Moho). Valley incision to sea level results in a drop of the mean elevation h to $h = \frac{5}{6}h$ and in crustal thinning ΔH. In response, isostasy causes the uplift of rocks and the Moho, rising mountain peaks to $1.8h$. Figure modified from Molnar and England (1990).

magnitude of the erosion rate (Dahlen and Suppe, 1988). Erosion also influences the spatial extent of exhumation and its position relative to topography as well as the metamorphic histories of rocks incorporated into the mountain belt (Dahlen and Suppe, 1988; Jamieson and Beaumont, 1988; Koons, 1990; Beaumont et al., 1992; Willett, 1999). Such critical wedge models also apply to large-scale orogenic belts (Jamieson and Beaumont, 1988; Willett et al., 1993; Willett, 1999; Reiners et al., 2015) (Fig. 1.2 C,D). These early concepts of how erosion affects deformation were tested in a number of analogue experiments that show that surface processes not only modify the timing, location and amplitude of rock displacements in accretionary wedges but can also influence the number of active thrusts or promote out-of-sequence reactivation of faults (e.g., Persson and Sokoutis, 2002; Konstantinovskaia and Malavieille, 2005; Hoth et al., 2006; see Graveleau et al., 2012, for a review).

However, validation of these ideas through field studies remains challenging because evidence of feedbacks, rather than mere coincidences, is difficult to observe in nature (Whipple, 2009, 2014). Especially observations of tectonic responses to climate change have rarely been documented (e.g., in the St. Elias Range, Alaska (Berger et al., 2008) or in Patagonia (Thomson et al., 2010)), because it requires detailed knowledge about the temporal and spatial histories of individual faults, foreland basin sedimentation and erosion rates, which are difficult to constrain with confidence (Whipple, 2009). On the other hand, late Cenozoic cooling and the onset of wide-spread glaciations have been attributed to plate-tectonic processes that control the atmospheric CO_2 concentration and distribution of landmass (e.g., Raymo and Ruddiman, 1992; Zachos et al., 2001),

A

Retro-wedge   Pro-wedge

U_r U_p

W_r W_p

F_A

B

U^*, F_E^*, W^*, R^*

dimensionless time

2 K
0.5 K

U^*
F_E^*
W^*, R^*

C

West   East

Wind

Exhumation

Topographic divide

strain rate

Fixed plate   Subducting plate

D

U_{tot}

Elevation [km]

Alpine fault

Exhumation   Elevation

High-grade schists and gneiss

Greenschist-Zeolite facies

Australian plate   zone of intermediate depth seismicity   Pacific plate   20 km

Total uplift [km]

Figure 1.2: see next page for figure caption.

Figure 1.2: A) Critical tapered wedge model. For a constant accretionary flux F_A, a climate-induced increase in erosional efficiency leads to a reduction in the size of the wedge (blue lines) and an increase in the steady-state rock uplift rates. U_p and U_r are near-surface rock uplift rates on the pro- and retro-sides of the wedge with widths W_p and W_r, respectively. Uplift rates are proportional to the length of the arrows. Figure redrawn from Whipple (2009). **B)** Response of mountain belt characteristics to a two-fold increase (2K) or decrease (0.5K) in erosional efficiency. Uplift U and erosional flux F_E are almost doubled under increased precipitation rates, whereas the half-width W and relief R decrease. All quantities are normalized by their initial steady-state values; time is normalized by the response time of the system. Modified from Whipple (2009). **C)** Numerical model for viscous-plastic deformation and erosion during convergence, using tectonic and climatic parameters that match conditions in the Southern Alps of New Zealand. Total exhumation is given by the extension of the Lagrangian mesh (grey) above the topography (black line). Precipitation arrives from the western side, resulting in high exhumation above an active thrust fault (orange band, indicating high strain rate). The results match the topography, total uplift and exhumation (grey area) observed in the Southern Alps of New Zealand shown in **D)**. Fig. C) from Willett (1999), Fig. D) from Koons (1990); both redrawn from Whipple (2009).

but here again cause and effect are difficult to unravel due to the complexities of the system and due to uncertainties in the exact timing of specific events. The link between climate and erosion seems to be somewhat better established. $\delta^{18}O$ isotopes from marine sediment cores show that the world's climate gradually cooled since 50 Ma, leading to continental ice growth in the Southern hemisphere at the Eocene-Oligocene boundary and to the onset of glaciations in the Northern hemisphere during the Plio-Pleistocene transition (e.g., Zachos et al., 2001; Lisiecki and Raymo, 2005, 2007). This long-term cooling trend is overlined by short-term oscillations dictated by the Milankovitch cycles, which describe variations in the Earth's orbital parameters (axial precession (23 kyr), obliquity (41 kyr), and eccentricity (400 and 100 kyr)) and control the spatial and seasonal distribution of incoming solar radiation and thus the expansion and retreat of continental ice sheets (Shackleton et al., 1984). Because the size of glacial accumulation area is affected by changes in the snowline as a direct function of landscape hypsometry, lowering of the snowline during glacial cycles might double or quadruple the area covered by ice relative to interglacial cycles (Brozović et al., 1997). In this context, increased Plio-Pleistocene erosion rates derived from global terrigenous sedimentation rates (England and Molnar, 1990; Zhang et al., 2001; Molnar, 2004) and low-temperature thermochronological data (Herman et al., 2013) have been explained by the late Cenozoic cooling, enhanced climate variability and widespread glaciations. Glaciers have shaped some of the most spectacular landscapes on Earth, such as deep fjords in Norway, rugged alpine terrains with hanging valleys, horns and arêtes in Alpine environments, or broad, U-shaped valleys in polar regions, and many studies have documented the profound impact of glaciations on the topographic evolution, relief, valley shape and erosion rates in mountainous landscapes, as for instance in the northwestern Himalayas (Brozović et al., 1997), the southern Coast Mountains of British Colombia, Canada (Shuster et al., 2005), Fiordland, New Zealand (Shuster et al., 2011) or the Patagonian Andes (Thomson et al., 2010).

However, whether Late Cenozoic global cooling is the main driver of increased erosion rates remains debated, and several studies have questioned the techniques used to quantify erosion rates and how erosion rate measurements can be compared across timescales (Gardner et al., 1987;

Schumer and Jerolmack, 2009; Willenbring and von Blanckenburg, 2010; Ganti et al., 2016). In fact, due the stochastic nature of erosional processes (Finnegan et al., 2014; Ganti et al., 2016) and the incompleteness of the sedimentary record (Barrell, 1917; Sadler, 1981), erosion rates may scale with the time interval they are averaged with, thus producing higher erosion rates towards the present. For instance, sedimentation rates derived from continental sediment records are not only biased by a better preservation of young sediments relative to old deposits, but also suffer from large uncertainties when estimating the accumulated sediment volume and depositional age (Sadler, 1981; Molnar, 2004; Schumer and Jerolmack, 2009; Willenbring and von Blanckenburg, 2010). Hence, quantification of past erosion rates remains problematic due to the loss of information when going back in time, and insights into the interactions between tectonics, climate and erosion derived from studies measuring erosion rates might be biased due to comparison of rates across different time scales (Gardner et al., 1987). Furthermore, over large (>Ma) temporal scales, erosion is limited by the mass balance of uplifted material. As any increase in erosion rate caused by climate change is transient, global rates of landscape denudation may not vary over the late Cenozoic despite major mountain building events and global climate change (Willenbring and von Blanckenburg, 2010; Willenbring and Jerolmack, 2016). Attributing cause and effect to a highly complex system such as the interactions of tectonics, climate and erosion is difficult (Molnar, 2009), also because uncertainties when measuring erosion rates and reconstructing climate and tectonic histories are high.

This PhD contributes to this debate by using the Central Andes (18-36° S) as a natural laboratory to investigate the relation between erosion, climate and tectonics on different spatial (km to mountain-belt) and temporal scales (kyr to Myr). In Chapter 2, I use sedimentary archives to review the tectonic and climatic histories of the Central Andes and compare them to changes in erosion rates quantified by inverse modelling of traditional low-temperature thermochronological data from literature and own data, specifically apatite and zircon U-Th/He (AHe, ZHe) and fission-track (AFT, ZFT) dating. In Chapter 3, thermoluminescence thermochronometry is applied on a formerly glaciated area in the Chilean Andes (33-36° S). This new thermochronometer allows to extract time series of erosion rates over the last ~100 ka (Biswas et al., 2018) that do not suffer from the time scale bias mentioned above and enables me to investigate the role of glaciations on erosion in more detail. The region between 33 and 36° S covers a climatic transition from semi-arid in the north to humid in the south and is especially susceptible to climatic variations. The tectonic setting of this region has recently been analyzed in detail by Riesner et al. (2017, 2018), and a thermo-kinematic fault model has been developed that predicts thermochronological ages according to the constrained fault activity (Riesner, 2017). In Chapter 4, I modify and apply this fault model to new and published thermochronological data to study the influence of tectonics and climate on erosion in a well-constrained setting.

1.1 Deciphering erosion rates using thermochronology

Exhumation describes the vertical distance covered by rocks on the way to the Earth's surface (England and Molnar, 1990) and is caused by erosional processes and tectonic activities such as normal faulting and ductile thinning (e.g., Ring et al., 1999). Erosion is the removal of mass on the Earth's surface by mechanical and chemical processes and is equivalent to exhumation in simple, monotonically exhuming settings (Ring et al., 1999). Because it represents the dynamic link between tectonic uplift and surface processes modulated by climatic conditions, quantifying erosion rates is key to understand the influence of climate and tectonics on mountain belts.

There are several means to quantify erosion rates on various time scales, for example sediment load in rivers (1-10 year), catchment averaged cosmogenic nuclides like ^{10}Be (10^3-10^4 years) or thermochronology (10^5-10^7 years). Because tectonic, climatic and erosional processes interact on Ma-timescales and affect several kilometers of the upper crust, thermochronology is the most suitable method to investigate the relation between these processes. Thermochronology uses the temperature-dependent retention behavior of decay-products to measure the timing and rates at which rocks cool while approaching the surface. At high temperatures, daughter products from the radioactive decay are lost by diffusion. Cooling through exhumation causes diffusion processes to slow down and daughter products to accumulated. In its simplest approximation, a thermochrono-metric age represents the time since a rock with steady, monotonous cooling passed its closure temperature T_c (Dodson, 1973). Yet, thermochronometric systems actually close over a tempera-ture range, the partial retention zone, which separates full loss and full retention. This zone spans several tens of degrees and depends on various factors like crystal composition, grain size, ra-diation damage or the residence time of the rock in this zone (Ketcham et al., 1999; Reiners and Brandon, 2006). The closure temperature also strongly depends on the cooling rate (Dod-son, 1973). Because the closure temperature is individual for each thermochronometric system and its associated mineral (Fig. 1.3), combinations of different thermochronometers can provide erosion rates with higher resolution than using single thermochronometers only. In this thesis, I am using the traditional techniques (U-Th)/He and fission-track dating on apatite and zircon, with closure temperatures between 70 and 240 °C (Brandon and Vance, 1992; Ketcham et al., 1999; Farley, 2000; Reiners et al., 2002, 2004), and the recently developed thermoluminescence ther-mochronology on feldspars (TLT), with closure temperature between 30 and 80 °C (Biswas et al., 2018), to estimate erosion rates in the Central Andes (Fig. 1.3).

1.1.1 Fission-track dating

Fission-track dating of apatite and zircon is based on the spontaneous decay of ^{238}U into two atomic fragments under the release of ionization energy. The two newly formed, highly charged
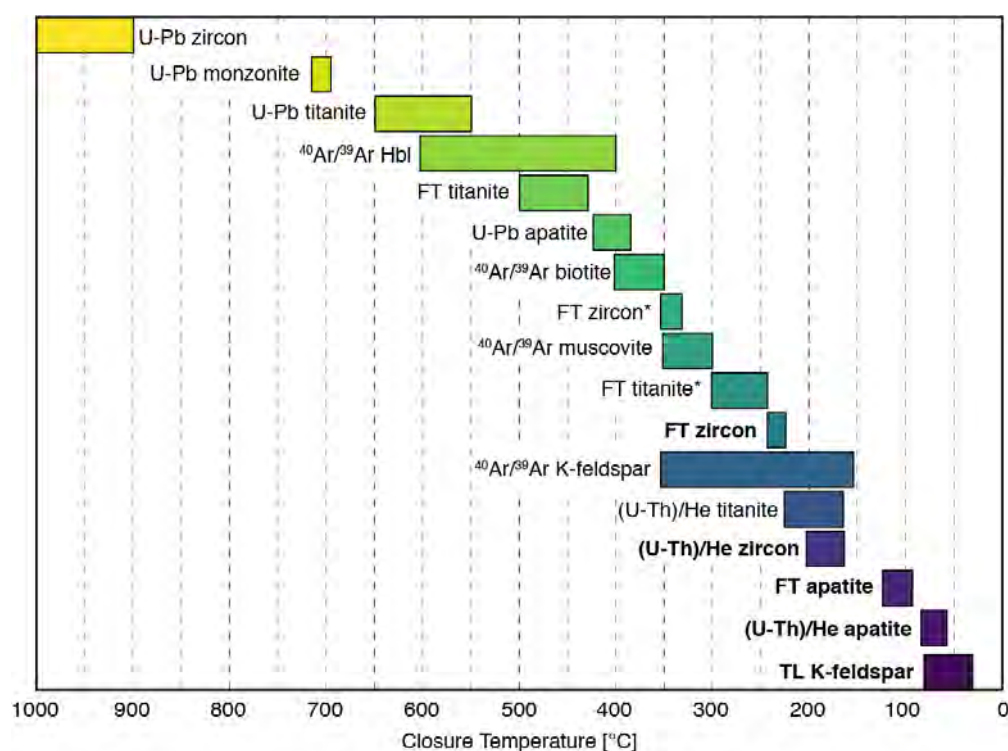
Figure 1.3: Closure temperatures of common thermochronometers (data from Tab. 1 in Reiners and Ehlers (2018)). Systems used in this work are highlighted in bold. * = closure temperature for zero-damage crystals, as opposed to natural crystals.

nuclei repel each other and travel in opposite directions, leaving linear trails of ionization damage behind (Fleischer et al., 1975). The tracks are annealed under thermally activated diffusion and are only preserved at temperatures below ~240 °C for zircons (Brandon and Vance, 1992) and ~116 °C for apatites (Ketcham et al., 1999). The closure temperature depends on the chemical composition (for apatites), the cooling rate, and the activation energy for annealing (Ketcham et al., 1999). To calculate a cooling age, tracks are counted under the microscope after mounting, polishing and chemical etching of the crystals, and the ^{238}U concentration is determined by neutron irradiation in a nuclear reactor.

1.1.2 (U-Th)/He dating

(U-Th)/He dating uses the concentration of ^{4}He produced by the alpha-decay of ^{238}U, ^{232}Th, ^{147}Sm. ^{4}He accumulation becomes important below ~180 °C (Reiners et al., 2002, 2004) and ~70 °C (Farley, 2000) for zircons and apatites, respectively. The closure temperature depends on the chemical composition (for apatites), the activation energy, the cooling rate as well as the size and geometry of the grain.

1.1.3 TLT

Thermoluminescence thermochronology (TLT) is part of the trapped-charge dating techniques used to constrain Quaternary erosion rates (King et al., 2016; Herman and King, 2018) and has recently been applied as low-temperature thermochronometer (Brown et al., 2017; Biswas et al., 2018). Radioactive energy ionizes the atoms, leading to excited, freed electrons that are eventually trapped in the proximities of positively-charged impurities and defects situated in the crystal lattice (Aitken, 1985). Stimulation with heat in the laboratory causes the detrapping of these electrons and their recombination with luminescence centers under the emission of light (luminescence), which is measured. The amount of light released (i.e., the amount of photons) is proportional to the number of trapped electrons, which are in turn proportional to the amount of nuclear radiation to which the crystal has been exposed (Aitken, 1985). The amount of trapped electrons depends on the amount of irradiation and the electron's residence time in such a trapping center. A trapped electron is freed by either athermal fading (Wintle, 1973) or when thermal lattice vibrations provide sufficient energy for the electron to escape (thermal fading). Thus, the natural thermoluminescence reflects a dynamic equilibrium level maintained by radiation-induced growth and thermal and athermal decay. When a rock cools from high to low temperature during exhumation, the thermal decay decreases and the amount of trapped electrons increases. Because different trapping depths exist in feldspars (Pagonis et al., 2014), which are characterized by different activation energies needed for an electron to escape, the measured thermoluminescence signal can be exploited as a multi-thermochronometer that allows to constrain thermal histories between ~30 and ~80 °C (Biswas et al., 2018). Using inverse modelling, this enables us to extract time series of erosion rates that span the last glacial-interglacial cycle.

However, the conversion of cooling ages to erosion rates is not straightforward. Problems arise from the dependence of the closure temperature on the cooling rate (Dodson, 1973) and from the strong connection between the erosion rate and the geothermal gradient. Higher erosion rates increase the geothermal gradient because heat is more efficiently transported to the surface, while higher geothermal gradients lead to shallower closure depths and thus to lower rates. Furthermore, topography disturbs the shallow geothermal field which affects primarily the lower temperature systems AHe and AFT (Stüwe et al., 1994; Mancktelow and Grasemann, 1997; Braun, 2002a,b). The magnitude of the disturbance also depends on the rate of relief production or destruction (Braun, 2002b). Finally, comparison of thermochronometric ages might be affected by the time scale bias outlined above, and estimated erosion rates are only as good as the data used. Combining multiple thermochronometric systems and using thermal models, which solve the heat transport equation for diffusion and advection and account for topography, partially extenuate these problems. Furthermore, a careful selection and analysis of the acquired data is substantial to achieve thrust-worthy results.

1.2 The Andes

Formed by the active subduction of the Nazca plate below the South American plate (Barazangi and Isacks, 1976; Cahill and Isacks, 1992), the Andes are the most prominent mountain belt in the Southern hemisphere and a major topographic feature on Earth. They strike north-south along the west coast of South America from approximately 10° N in Colombia to 53° S in Patagonia and have a mean maximum elevation in excess of 4000 m. The Andes cross all latitudinal climate zones from the Equator to the southern Pole and represent a major barrier for moisture transport across the orogen. The climatic differences between the Atacama Desert in Northern Chile, one of the world's driest places, and the tropical rain forest on the eastern side in Argentina are an impressive example of this gradient. South of 30° S, the climatic pattern reverses and the Westerlies bring abundant precipitation to the western side, while the Argentinian side is depleted in rainfall. This climatic gradient is also reflected in the geomorphology (Fig. 1.4) and in the position of modern and Pleistocene snow lines that show a steep decrease in elevation south of ca. 30° S (Schwerdtfeger, 1976) (Fig. 1.5A).

Tectonostratigraphic and magmatic records indicate that the Andean orogeny started in the Late Cretaceous (e.g., Charrier et al., 2007; Horton, 2018a,b). Tectonic deformation in the Andes was widespread but strongly variable in space and time. Deformation in the northern part of the Andes initiated on the western side and moved eastwards to the Eastern Cordillera during the late Eocene and to the Inter- and Subandean zones during the Miocene (e.g., McQuarrie et al., 2005). Most deformation was accommodated in the eastern part of the orogen. In the south, compressional deformation was disturbed by a period of late Eocene-to-Oligocene extension and then accommodated in an east- (Giambiagi et al., 2015) or doubly-vergent (Riesner et al., 2018) wedge that is still active today.

The particular climatic and tectonic setting of the Andes has inspired many researchers to investigate different aspects of the interactions between climate, tectonics and erosion in this mountain belt. In 1999, Horton applied concepts of the critical wedge theory to tectonic and morphologic observations in the Subandean zone. Out-of-sequence thrusting and the narrow width of the Andes north of 18° S were attributed to high erosion rates, whereas the progressive eastward migration of the thrust front and overall widening of the orogen south of 18° S were explained by low erosion rates. Montgomery et al. (2001) investigated the role of climate on Andean morphology on the whole mountain range. Using geomorphological observations such as fluvial discharge, regional slope, cross-range asymmetry and hypsometry, the authors observed a significant first-order correlation between climate-modulated erosion and the width and height of the orogen (Fig. 1.5). In particular, they noted that fluvial erosion in the north correlates with a narrow orogen, whereas tectonic wedge propagation causes crustal thickening, plateau growth and widening of the mountain

Figure 1.4: see next page for figure caption

Figure 1.4: A,B) The Atacama Desert is one of the driest places on earth. The landscape is characterized by smooth hills, occasionally dissected by deep canyons. The picture in (B) has been taken on top of the northern-most age elevation profile sampled in this study. **C,D)** Pictures of the semi-arid conditions at 32° S, showing an increase in vegetation and a fluvial relief. Age-elevation profiles Clin10 and Clin16 were sampled along the ridges in the centers of the figures. **E,F,G)** The slope and relief get much steeper south of 33° S, and the landscape is characterized by U-shaped and hanging valleys, cirques and steep valley flanks indicating glacial overprinting. C-G: Photo courtesy B. Lehmann.

belt in the central part where precipitation is limited. In the south, maximum elevation and relief are lowered due to glacial erosion. However, Montgomery et al. (2001) emphasize the complexity of the coupling between tectonics and climate by stating that changes in tectonic parameters like the angle of the subducting slab could also explain the observed changes in topography and mass distribution. Another influence of climate on the Andean orogen was proposed by Lamb and Davis (2003), who suggested that climatically controlled sediment availability in the subduction trench might control elevation by setting the shear stress along the subducting plate interface. On the other hand, Hilley and Coutand (2010) concluded that the subduction zone geometry and crustal heterogeneities resulting from paleogeographic features and inherited structures exert a first-order control on the Andean morphology, while erosional processes may play an important role on the regional scale. Finally, the Neogene growth of the Andean belt has likely altered the South American climate from the past to present. Modelling results from Ehlers and Poulsen (2009) and Insel et al. (2010) show that the emergence of the Andes above half of their present height resulted in increased precipitation along the eastern flanks and the central plateau, while hyper-arid conditions were established in the Atacama Desert. The growing Andes blocked the easterly, moisture-laden wind from the Atlantic and led to the establishment of the low-level jet, which transports moist air from the tropical Amazon basin to the subtropics along the Eastern Andes (e.g., Strecker et al., 2007). The studies outlined above demonstrate the numerous expressions of the relations between climate, erosion and tectonics, but also attest that our understanding of these processes is still hindered by several factors. One of these factors are the uncertainties that arise when reconstructing the tectonic, climatic and erosional histories in time and space. For instance, many studies use the modern climate as an analogue of past conditions, yet it has been shown that the uplift of the Andean mountain belt has significantly altered atmospheric circulation patterns. Moreover, tectonic activities on the western side of the Andes have often been neglected since deformation markers there and in the Altiplano are obscured by both volcanic deposits and little to non-incised intramontane basins. Erosion rates, although representing the crucial link between climate and tectonics, have not yet been quantified on the orogen-scale and independently from climate (Montgomery et al., 2001).
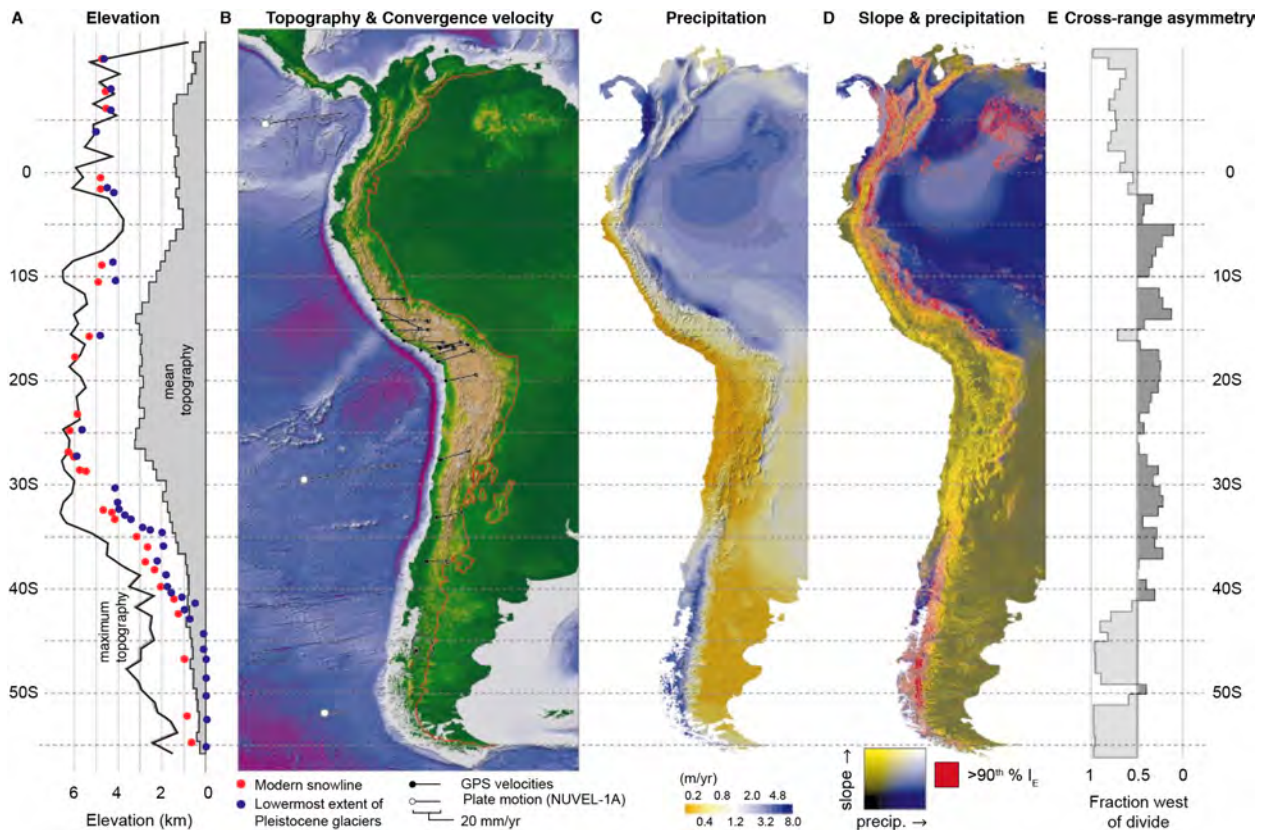
Figure 1.5: Figure 1 from Montgomery et al. (2001), who was one of the first studies to investigate the influence of climate on Andean morphology and observed a significant first-order correlation between climate-modulated erosion and the width and height of the orogen.

1.3 Contribution of this thesis

In this thesis, I exploit thermochronological data from the Central Andes to study the influence of climate and tectonics on erosion rates on different spatial and temporal scales using an integrative approach that combines field and laboratory work, inverse modelling and literature reviews.

In Chapter 2, I constrain the temporal-spatial exhumation history of the Andean mountain belt (18-36°S) to study possible feedback mechanism between climate, erosion and tectonics on large spatial (10^2-10^3 km) and temporal (Ma) scales. To quantify erosion rates, low-temperature thermochronometers from literature (AHe, AFT, ZHe, ZFT; 744 ages) are compiled and complemented by own data (AHe, AFT, ZHe; 238 ages) sampled along the precipitation gradient on the western side of the Andes where data is sparse. A total of 211 samples have been collected between 22° and 35°S during three field campaigns in collaboration with Germán Aguilar, First Quantum Minerals Ltd. (FQM) and Thibault Simon-Labric. The first campaign was conducted by Thibault Simon-Labric and FQM (95 samples) and Germán Aguilar (27 samples) in June 2014 and cov-

ered the area between 28° and 30° S. The two following campaigns in 2016 (44 samples) and 2017 (45 samples) covered the area between 31.5° and 35° S and 22° and 26.5° S, respectively. These campaigns were led by me with the help of FQM for the third one. Out of these 211 samples, 146 were analysed for AHe, AFT and/or ZHe. Thermochronological ages were converted to an erosion rate history using the inverse model developed by Fox et al. (2014) and modified by Herman and Brandon (2015). Past and present-day climates were synthesized using modern rainfall data and paleo-climate reconstructions from sediment archives. The tectonic history is summarized from syntectonic sediments and shortening rate reconstructions. Moreover, crustal thickening and the magmatic history of the Central Andes are briefly reviewed to account for exhumation signals induced by surface uplift associated with the crustal evolution. The following questions are addressed:

- **How does exhumation in the Central Andes vary in time and space?**

- **How do climate and tectonics influence the onset and magnitude of exhumation?**

- **What is the contribution of magmatism and crustal thickening to exhumation?**

This study has been published in Earth-Science Reviews (Stalder et al., 2020):

Stalder, N.F., Herman, F., Fellin, M.G., Coutand, I., Aguilar, G., Reiners, P.W., and Fox, M. (2020). The relationships between tectonics, climate and exhumation in the Central Andes (18-36° S): evidence from low-temperature thermochronology. *Earth-Science Reviews*, 210, 1–37.

   The results from Chapter 2 show that the style of deformation (i.e., thin- or thick-skinned), which is largely set by inherited structures and the presence of sediments in the foreland, has a significant impact on the magnitude of exhumation rates, as does glacial erosion and increased precipitation in active tectonic settings. Highest exhumation rates have been documented during the Plio-Pleistocene in the Chilean Andes between 33 and 36° S, where an an active tectonic setting is combined with a strong N-S precipitation gradient. Yet, the resolution of the tectonic and climatic histories as well as of the thermochronological data only allows to draw a first-order picture about the erosional response to tectonic and climatic changes. In this sense, Chapter 2 can be regarded as a framework synthesizing the tectonic, climatic and erosional histories of the Central Andes, where local particularities are partially neglected. To address this issue and to better understand the high Plio-Pleistocene exhumation rates observed between 33 and 36° S, the erosional signal resulting from climate (Chap. 3) and/or active tectonics (Chap. 4) have been investigated in more detail in the southern Central Andes.

Precipitation in Chile is almost entirely controlled by the westerly wind belt that is responsible for an extreme north-south gradient linking the arid climate in the northern Atacama Desert with the year-round southern humid part of Patagonia. The transition between the two climate regimes occurs between 32° and 36° S, where rainfall strongly increases from 400 mm/yr in the north to 800 mm/yr in the south. This climatic transition is directly represented by geomorphological changes from fluvial to glacial landscapes (Fig. 1.4). In Chapter 2, the region between 33° and 36° S has been identified as a zone of particularly high Plio-Pleistocene exhumation rates that might be explained by the onset of glaciation and increased climatic variability. However, ^{10}Be-derived millennial erosion rates from the same region (Carretier et al., 2013) are an order of magnitude lower than the rates observed with the thermochronological data. To allow a comparison of these rates that act on different time scales and to avoid the potential time scale bias discussed above (Ganti et al., 2016), time series of erosion rates need to be considered. To do so, I apply a recently developed multi-thermochronometer, TLT, to quantify erosion rates over the last 100 ka in Chapter 3. TLT is based on the luminescence signal emitted from K-feldspar and shows multiple closure temperatures between 30 and 80 °C (Biswas et al., 2018), thus allowing to constrain time series of erosion rates. The following questions are addressed in Chapter 3:

- **Is the mismatch between Ma- and ka-scale erosion rates the expression of a time scale bias?**

- **What is the cause of the Pleistocene high erosion rates and the following decrease between 32° and 35° S?**

The results from Chapter 3 show that erosion rates were systematically higher during the last glacial maximum than today. These findings imply that glacial erosion is probably more efficient than fluvial erosion and that erosion has remained transient during the Quaternary. This study is being prepared for submission to Nature Geoscience:

Stalder, N.F., Herman, F., and Biswas, R. (in prep.). Maximized erosion at the last glacial maximum revealed by luminescence thermochronometry. *Nature Geoscience*.

Finally, the high Plio-Pleistocene erosion rates might also be explained by tectonic-induced rock uplift, which is addressed in Chapter 4. The tectonic activity and fault geometry in the Chilean Andes around 33.5° S have recently be studied in detail by Riesner et al. (2017) and Riesner et al. (2018) and a thermo-kinematic model has been developed that predicts thermochronological ages according to any provided fault activity. By adapting this model to represent the fault kinematics and shortening rates observed in the study area during the last 23 Ma, thermochronological ages are predicted and compared to observed new and literature data compiled in Chapter 2 to address the following question:

- **Can tectonic-induced rock uplift alone explain the high Plio-Pleistocene erosion rates observed from thermochronometric data?**

I show in Chapter 4 that the thermochronological data imply a significant increase in erosion rates in the mid-Pleistocene that cannot be explained by tectonically-driven rock uplift only. I infer that increased precipitation and important glacial growth related to the northward migration of the Westerlies during glacial periods (e.g., Lamy et al., 2010) are the main factors in setting the magnitude of the observed Pleistocene erosion rates, while active tectonic shortening kept sustaining rock-uplift. Together, Chapters 3&4 demonstrate a strong impact of Pleistocene glaciations even in tectonically active areas expressed by high, but transient erosion rates.

Bibliography

Aitken, M.J. (1985). *Thermoluminescence dating*. Academic Press, London.

Barazangi, M. and Isacks, B.L. (1976). Spatial distribution of earthquakes and subduction of the Nazca plate beneath South America. *Geology*, 4(11):686–692.

Barrell, J. (1917). Rhythms and the measurements of geologic time. *Geol. Soc. Am. Bull.*, 28(1):745–904.

Beaumont, C., Fullsack, P., and Hamilton, J. (1992). Erosional control of active compressional orogens. In *Thrust tectonics*, pages 1–18. Springer.

Berger, A.L., Gulick, S.P.S., Spotila, J.A., Upton, P., Jaeger, J.M., Chapman, J.B., Worthington, L.A., Pavlis, T.L., Ridgway, K.D., Willems, B.A., and McAleer, R.J. (2008). Quaternary tectonic response to intensified glacial erosion in an orogenic wedge. *Nat. Geosci.*, 1(11):793–799.

Berner, R.A., Lasaga, A.C., and Garrels, R.M. (1983). The carbonate-silicate geochemical cycle and its effect on atmospheric carbon dioxide over the past 100 million years. *Am. J. Sci.*, 283:641–683.

Biswas, R.H., Herman, F., King, G.E., and Braun, J. (2018). Thermoluminescence of feldspar as a multi-thermochronometer to constrain the temporal variation of rock exhumation in the recent past. *Earth Planet. Sci. Lett.*, 495:56–68.

Brandon, M.T. and Vance, J.A. (1992). Tectonic evolution of the Cenozoic Olympic subduction complex, Washington State, as deduced from fission track ages for detrital zircons. *Am. J. Sci.*, 292:565–565.

Braun, J. (2002a). Estimating exhumation rate and relief evolution by spectral analysis of age–elevation datasets. *Terra Nova*, 14(3):210–214.

Braun, J. (2002b). Quantifying the effect of recent relief changes on age-elevation relationships. *Earth Planet. Sci. Lett.*, 200(3-4):331–343.

Brown, N.D., Rhodes, E.J., and Harrison, T.M. (2017). Using thermoluminescence signals from feldspars for low-temperature thermochronology. *Quat. Geochronol.*, 42:31–41.

Brozović, N., Burbank, D.W., and Meigs, A.J. (1997). Climatic limits on landscape development in the northwestern Himalaya. *Science*, 276(5312):571–574.

Cahill, T. and Isacks, B.L. (1992). Seismicity and shape of the subducted Nazca plate. *J. Geophys. Res.: Solid Earth*, 97(B12):17503–17529.

Carretier, S., Regard, V., Vassallo, R., Aguilar, G., Martinod, J., Riquelme, R., Pepin, E., Charrier, R., Hérail, G., Farías, M., et al. (2013). Slope and climate variability control of erosion in the Andes of central Chile. *Geology*, 41(2):195–198.

Champagnac, J.D., Molnar, P., Sue, C., and Herman, F. (2012). Tectonics, climate, and mountain topography. *J. Geophys. Res.: Solid Earth*, 117.

Charrier, R., Pinto, L., and Rodríguez, M.P. (2007). Tectonostratigraphic evolution of the Andean Orogen in Chile. In *The Geology of Chile*. Geol. Soc. Spec. Pub.

Dahlen, F.A. and Suppe, J. (1988). Mechanics, growth, and erosion of mountain belts. *Geol. Soc. Am. Spec. Pap.*, 218:161–178.

Dodson, M.H. (1973). Closure temperature in cooling geochronological and petrological systems. *Contrib. Mineral. Petrol.*, 40(3):259–274.

Egholm, D.L., Nielsen, S.B., Pedersen, V.K., and Lesemann, J.E. (2009). Glacial effects limiting mountain height. *Nature*, 460(7257):884–887.

Ehlers, T.A. and Poulsen, C.J. (2009). Influence of Andean uplift on climate and paleoaltimetry estimates. *Earth Planet. Sci. Lett.*, 281(3):238–248.

England, P. and Molnar, P. (1990). Surface uplift, uplift of rocks, and exhumation of rocks. *Geology*, 18:1173–1177.

Farley, K.A. (2000). Helium diffusion from apatite: General behavior as illustrated by Durango fluorapatite. *J. Geophys. Res.*, 105(B2):2903–2914.

Finnegan, N.J., Schumer, R., and Finnegan, S. (2014). A signature of transience in bedrock river incision rates over timescales of 10^4–10^7 years. *Nature*, 505(7483):391–394.

Fleischer, R.L., Price, P.B., and Walker, R.M. (1975). *Nuclear tracks in solids: principles and applications*. Univ of California Press.

Fox, M., Herman, F., Willett, S.D., and May, D.A. (2014). A linear inversion method to infer exhumation rates in space and time from thermochronometric data. *Earth Surf. Dyn.*, 2(1):47.

Ganti, V., von Hagke, C., Scherler, D., Lamb, M.P., Fischer, W.W., and Avouac, J.P. (2016). Time scale bias in erosion rates of glaciated landscapes. *Sci. Adv.*, 2(e1600204).

Gardner, T.W., Jorgensen, D.W., Shuman, C., and Lemieux, C.R. (1987). Geomorphic and tectonic process rates: Effects of measured time interval. *Geology*, 15(3):259–261.

Giambiagi, L., Tassara, A., Mescua, J., Tunik, M., Alvarez, P.P., Godoy, E., Hoke, G., Pinto, L., Spagnotto, S., Porras, H., Tapia, F., Jara, P., Bechis, F., Garcìa, V.H., Suriano, J., Moreiras, S.M., and Pagano, S.D. (2015). Evolution of shallow and deep structures along the maipo–tunuyán transect (33° 40' S): from the Pacific coast to the Andean foreland. *Geol. Soc. London. Spec. Pub.*, 399(1):63–82.

Graveleau, F., Malavieille, J., and Dominguez, S. (2012). Experimental modelling of orogenic wedges: A review. *Tectonophysics*, 538:1–66.

Hay, W.W. (1996). Tectonics and climate. *Geol. Rundsch.*, 85(3):409–437.

Herman, F. and Brandon, M. (2015). Mid-latitude glacial erosion hotspot related to equatorial shifts in southern Westerlies. *Geology*, 43(11):987–990.

Herman, F. and King, G.E. (2018). Luminescence thermochronometry: Investigating the link between mountain erosion, tectonics and climate. *Elements*, 14(1):33–38.

Herman, F., Seward, D., Valla, P.G., Carter, A., Kohn, B., Willett, S.D., and Ehlers, T.A. (2013). Worldwide acceleration of mountain erosion under a cooling climate. *Nature*, 504(7480):423–426.

Hilley, G.E. and Coutand, I. (2010). Links between topography, erosion, rheological heterogeneity, and deformation in contractional settings: Insights from the central Andes. *Tectonophysics*, 495(1-2):78–92.

Horton, B.K. (1999). Erosional control on the geometry and kinematics of thrust belt development in the central Andes. *Tectonics*, 18:1292–1304.

Horton, B.K. (2018a). Sedimentary record of Andean mountain building. *Earth Sci. Rev.*, 178:279–309.

Horton, B.K. (2018b). Tectonic regimes of the central and southern Andes: Responses to variations in plate coupling during subduction. *Tectonics*, 37(2):402–429.

Hoth, S., Adam, J., Kukowski, N., and Oncken, O. (2006). Influence of erosion on the kinematics of bivergent orogens: results from scaled sandbox simulations. In Willett, S.D., Hovius, N., Brandon, M., and Fisher, D.M., editors, *Tectonics, Climate and Lanndscape Evolution*, volume 398, page 201. Geological Society of America.

Insel, N., Poulsen, C.J., and Ehlers, T.A. (2010). Influence of the Andes Mountains on South American moisture transport, convection, and precipitation. *Climate Dyn.*, 35(7-8):1477–1492.

Jamieson, R.A. and Beaumont, C. (1988). Orogeny and metamorphism: A model for deformation and pressure-temperature-time paths with applications to the central and southern Appalachians. *Tectonics*, 7(3):417–445.

Ketcham, R.A., Donelick, R.A., and Carlson, W.D. (1999). Variability of apatite fission-track annealing kinetics: III. Extrapolation to geological time scales. *Am. Mineral.*, 84(9):1235–1255.

King, G.E., Guralnik, B., Valla, P.G., and Herman, F. (2016). Trapped-charge thermochronometry and thermometry: A status review. *Chem. Geol.*, 446:3–17.

Konstantinovskaia, E. and Malavieille, J. (2005). Erosion and exhumation in accretionary orogens: Experimental and geological approaches. *Geochem. Geophys. Geosyst.*, 6(2).

Koons, P.O. (1990). Two-sided orogen: Collision and erosion from the sandbox to the Southern Alps, New Zealand. *Geology*, 18(8):679–682.

Lamb, S. and Davis, P. (2003). Cenozoic climate change as a possible cause for the rise of the Andes. *Nature*, 425(6960):792–797.

Lamy, F., Kilian, R., Arz, H.W., Francois, J.P., Kaiser, J., Prange, M., and Steinke, T. (2010). Holocene changes in the position and intensity of the southern westerly wind belt. *Nat. Geosci.*, 3(10):695–699.

Lisiecki, L.E. and Raymo, M.E. (2005). A Pliocene-Pleistocene stack of 57 globally distributed benthic δ ^{18}O records. *Paleoceanography*, 20(1).

Lisiecki, L.E. and Raymo, M.E. (2007). Plio-Pleistocene climate evolution: trends and transitions in glacial cycle dynamics. *Quat. Sci. Rev.*, 26(1-2):56–69.

Mancktelow, N.S. and Grasemann, B. (1997). Time-dependent effects of heat advection and topography on cooling histories during erosion. *Tectonophysics*, 270(3):167–195.

McQuarrie, N., Horton, B.K., Zandt, G., Beck, S., and DeCelles, P.G. (2005). Lithospheric evolution of the Andean fold–thrust belt, Bolivia, and the origin of the central Andean plateau. *Tectonophysics*, 399(1-4):15–37.

Molnar, P. (2004). Late cenozoic increase in accumulation rates of terrestrial sediment: How might climate change have affected erosion rates? *Annu. Rev. Earth Planet. Sci.*, 32:67–89.

Molnar, P. (2009). The state of interactions among tectonics, erosion, and climate: A polemic. *GSA Today*, 19(7):44–45.

Molnar, P. and England, P. (1990). Late Cenozoic Uplift of Mountain-Ranges and Global Climate Change – Chicken or Egg. *Nature*, 346(6279):29–34.

Montgomery, D.R., Balco, G., and Willett, S.D. (2001). Climate, tectonics, and the morphology of the Andes. *Geology*, 29(7):579–582.

Pagonis, V., Morthekai, P., and Kitis, G. (2014). Kinetic analysis of thermoluminescence glow curves in feldspar: evidence for a continuous distribution of energies. *Geochronometria*, 41(2):168–177.

Persson, K.S. and Sokoutis, D. (2002). Analogue models of orogenic wedges controlled by erosion. *Tectonophysics*, 356(4):323–336.

Raymo, M.E. and Ruddiman, W.F. (1992). Tectonic Forcing of Late Cenozoic Climate. *Nature*, 359(6391):117–122.

Reiners, P.W. and Brandon, M.T. (2006). Using thermochronology to understand orogenic erosion. *Annu. Rev. Earth Planet. Sci.*, 34:419–466.

Reiners, P.W. and Ehlers, T.A. (2018). *Low-Temperature Thermochronology: Techniques, Interpretations, and Applications*, volume 58. Walter de Gruyter GmbH & Co KG.

Reiners, P.W., Ehlers, T.A., Mitchell, S.G., and Montgomery, D.R. (2003). Coupled spatial variations in precipitation and long-term erosion rates across the Washington Cascades. *Nature*, 426(6967):645–647.

Reiners, P.W., Farley, K.A., and Hickes, H.J. (2002). He diffusion and (U–Th)/He thermochronometry of zircon: initial results from Fish Canyon Tuff and Gold Butte. *Tectonophysics*, 349(1-4):297–308.

Reiners, P.W., Spell, T.L., Nicolescu, S., and Zanetti, K.A. (2004). Zircon (U–Th)/He thermochronometry: He diffusion and comparisons with ^{40}Ar/^{39}Ar–dating. *Geochim. Cosmochim. Acta*, 68(8):1857–1887.

Reiners, P.W., Thomson, S.N., Vernon, A., Willett, S.D., Zattin, M., Einhorn, J., Gehrels, G., Quade, J., Pearson, D., and Murray, K.E. (2015). Low-temperature thermochronologic trends across the central andes, 21°S-28°S. *Geol. Soc. Am. Mem.*,

212:215–249.

Riesner, M. (2017). *Évolution tectonique des Andes centrales (33°S): implications sur la mécanique des chaînes de subduction.* PhD thesis, Institut de Physique du Globe de Paris (IPGP).

Riesner, M., Lacassin, R., Simoes, M., Armijo, R., Rauld, R., and Vargas, G. (2017). Kinematics of the active west Andean fold-and-thrust belt (Central Chile): Structure and long-term shortening rate. *Tectonics*, 36(2):287–303.

Riesner, M., Lacassin, R., Simoes, M., Carrizo, D., and Armijo, R. (2018). Revisiting the crustal structure and kinematics of the central Andes at 33.5°S: Implications for the Mechanics of Andean Mountain Building. *Tectonics*, 37:1347–1375.

Ring, U., Brandon, M.T., Willett, S.D., and Lister, G.S. (1999). Exhumation processes. *Geol. Soc. London. Spec. Pub.*, 154(1):1–27.

Sadler, P.M. (1981). Sediment accumulation rates and the completeness of stratigraphic sections. *J. Geol.*, pages 569–584.

Schumer, R. and Jerolmack, D.J. (2009). Real and apparent changes in sediment deposition rates through time. *J. Geophys. Res.: Earth Surf.*, 114(F3).

Schwerdtfeger, W. (1976). *World survey of climatology volume 12: Climates of Central and South America*, volume 12. Elsevier Sci. Pub., Amsterdam.

Shackleton, N.J., Backman, J., Zimmerman, H., Kent, D.V., Hall, M.A., Roberts, D.G., Schnitker, D., Baldauf, J.G., Desprairies, A., Homrighausen, R., and et al. (1984). Oxygen isotope calibration of the onset of ice-rafting and history of glaciation in the North Atlantic region. *Nature*, 307:620–623.

Shuster, D.L., Cuffey, K.M., Sanders, J.W., and Balco, G. (2011). Thermochronometry reveals headward propagation of erosion in an alpine landscape. *Science*, 332(6025):84–88.

Shuster, D.L., Ehlers, T.A., Rusmoren, M.E., and Farley, K.A. (2005). Rapid glacial erosion at 1.8 Ma revealed by ^{4}He/^{3}He thermochronometry. *Science*, 310(5754):1668–1670.

Stalder, N.F., Herman, F., Fellin, M.G., Coutand, I., Aguilar, G., Reiners, P.W., and Fox, M. (2020). The relationships between tectonics, climate and exhumation in the Central Andes (18-36°S): evidence from low-temperature thermochronology. *Earth-Science Reviews*, 210:1–37.

Strecker, M.R., Alonso, R.N., Bookhagen, B., Carrapa, B., Hilley, G.E., Sobel, E.R., and Trauth, M.H. (2007). Tectonics and Climate of the Southern Central Andes. *Annu. Rev. Earth Planet. Sci.*, 35:747–787.

Stüwe, K., White, L., and Brown, R. (1994). The influence of eroding topography on steady-state isotherms. Application to fission track analysis. *Earth Planet. Sci. Lett.*, 124(1-4):63–74.

Thomson, S.N., Brandon, M.T., Tomkin, J.H., Reiners, P.W., Vásquez, C., and Wilson, N.J. (2010). Glaciation as a destructive and constructive control on mountain building. *Nature*, 467(7313):313–317.

Whipple, K.X. (2009). The influence of climate on the tectonic evolution of mountain belts. *Nat. Geosci.*, 2(2):97–104.

Whipple, K.X. (2014). Can erosion drive tectonics? *Science*, 346(6212):918–919.

Willenbring, J.K. and Jerolmack, D.J. (2016). The null hypothesis: globally steady rates of erosion, weathering fluxes and shelf sediment accumulation during Late Cenozoic mountain uplift and glaciation. *Terra Nova*, 28(1):11–18.

Willenbring, J.K. and von Blanckenburg, F. (2010). Long–term stability of global erosion rates and weathering during late–Cenozoic cooling. *Nature*, 465(7295):211–214.

Willett, S.D. (1999). Orogeny and orography: The effects of erosion on the structure of mountain belts. *J. Geophys. Res.*, 104((B12)):28957–28981.

Willett, S.D., Beaumont, C., and Fullsack, P. (1993). Mechanical model for the tectonics of doubly vergent compressional orogens. *Geology*, 21(4):371–374.

Wintle, A.G. (1973). Anomalous fading of thermoluminescence in mineral samples. *Nature*, 245:143–144.

Zachos, J., Pagani, M., Sloan, L., Thomas, E., and Billups, K. (2001). Trends, Rhythms, and Aberrations in Global Climate 65 Ma to present. *Science*, 292(5517):686–693.

Zhang, P.Z., Molnar, P., and Downs, W.R. (2001). Increased sedimentation rates and grain sizes 2-4 Myr ago due to the influence of climate change on erosion rates. *Nature*, 410(6831):891–897.

CHAPTER 2 ▮

The relationships between tectonics, climate and exhumation in the Central Andes (18-36°S): evidence from low-temperature thermochronology

Nadja F. Stalder[1], Frédéric Herman[1], Maria Giuditta Fellin[2], Isabelle Coutand[3], German Aguilar[4], Peter W. Reiners[5], Matthew Fox[6]

[1]Institute of Earth Surface Dynamics, University of Lausanne, Switzerland
[2]Department of Earth Sciences, ETH Zurich, Switzerland
[3]Department of Earth Sciences, Dalhousie University, Canada
[4]Advanced Mining Technology Center, University of Chile, Chile
[5]Department of Geosciences, University of Arizona, U.S.A
[6]Department of Earth Sciences, University College London, U. K.

Abstract

The Central Andes between 18 and 36°S latitude strike north-south for 2000 km along the Chilean subduction margin, cross several climate zones from hyperarid to humid and exhibit mean elevations in excess of 4000 m.a.s.l. Here, we investigate the relationships between tectonics, climate and exhumation by inverting low-temperature thermochronological data compiled from the literature (824 ages from 549 samples) and new data (238 ages from 146 samples) to quantify the exhumation rate history of the Central Andes since 80 Ma. Our inferred exhumation rates west of the drainage divide and between 18 and 32°S did not exceed 0.25 km/Ma. Such low exhumation rates are consistent with low shortening rates and arid conditions in these regions. Local pulses of exhumation occurred only during the Eocene as response to active deformation and during the Miocene, probably as response to uplift of the western Andean slope. East of the drainage divide between 18 and 28°S, the observed exhumation pattern reflects the onset and eastward propagation of deformation. Here, exhumation occurred locally since the middle-to-late Eocene in the Eastern Cordillera and the Altiplano-Puna and subsequently affected larger parts of these regions and the north-western Sierra Pampeanas during the Oligocene. In the early Miocene (~20 Ma), the Interandean zone started exhuming and at 12-10 Ma exhumation propagated into the Subandean zone. Enhanced shortening rates and intensified precipitation along the eastern deformation front associated with the onset of the South American Monsoon led to increased exhumation rates in the eastern Interandean and the Subandean zones in the Plio-Pleistocene (0.6 km/Ma). Higher Pleistocene exhumation rates are also observed in the northern Sierra Pampeanas (1.5 km/Ma) that can be related to rock uplift along steep reverse faults coupled with high precipitation. South of 32°S on the western side, exhumation rates in the Principal Cordillera increase from ca. 0.25 km/Ma in the Miocene to rates locally exceeding 2 km/Ma in the Pleistocene. Whereas the tectonic regime in the southern Principal Cordillera remained unchanged since the late Miocene, these higher rates are likely associated with enhanced erosion resulting from intensified Pleistocene precipitation and glacial growth in this region, reinforced by isostatic rock uplift and active tectonics. Our study shows that the onset of exhumation correlates mainly with the initiation of horizontal shortening and crustal thickening, whereas the magnitude of exhumation is largely set by the amount of precipitation and glacial erosion and by the style of deformation, which is controlled by inherited structures and the amount of sediments in the foreland.

2.1 Introduction

The topographic, kinematic, and exhumational evolution of mountain belts reflects interactions between tectonic, climatic, and surface processes whose relative roles in forcing and modulating various features of orogens are widely debated (*e.g.*, England and Molnar, 1990; Molnar and England, 1990; Raymo and Ruddiman, 1992; Reiners et al., 2003; Molnar, 2009; Whipple, 2009; Champagnac et al., 2012; Herman et al., 2013). At convergent margins, tectonic forcing creates horizontal shortening that induces spatial gradients in crustal thickness, which drive both contractional deformation and surface uplift and initiate erosion. Erosion and sedimentation, in turn, have the potential to strongly influence the shape of the orogen by setting the orogenic mass balance and lithospheric stress regime that control internal deformation and isostatic uplift of mountain belts (Dahlen and Suppe, 1988; Koons, 1990; Molnar and England, 1990; Beaumont et al., 1992; Willett, 1999). The climatic factors that modulate these surface processes may also be influenced by the size, form and height of the orogen itself, further complicating efforts to resolve or distinguish the respective role of tectonics and climate in shaping mountain ranges.

Numerical (Beaumont et al., 1988; Koons, 1989; Beaumont et al., 1992; Willett et al., 1993; Batt and Braun, 1997; Willett, 1999) and analogue models (Davis et al., 1983; Dahlen and Suppe, 1988; Malavieille, 1984; Koons, 1990; Konstantinovskaia and Malavieille, 2005) suggest that along-strike variations in orogen height and width may be caused by either differences in tectonically-controlled variations in horizontal shortening rate (*e.g.*, Isacks, 1988; Gephart, 1994; Kley and Monaldi, 2002; Giambiagi et al., 2012), or climatically-forced variations in erosion rate (*e.g.*, Masek et al., 1994; Horton, 1999; Montgomery et al., 2001). Similarly, in an orogen with steady form, localized regions of high rock uplift and erosion rates, or cross-orogen differences in these rates, could be driven by either kinematic or climatic factors, or both. In both cases, positive feedbacks will complicate the discrimination between tectonic and climatic effects on the kinematics, erosion, and topography of orogens (*e.g.*, Molnar, 2009). Nevertheless, it is reasonable to expect that independent, far-field-driven changes in either tectonic or climatic processes affect orogens in ways that would allow us to examine their responses in size, form, internal kinematics, and erosion rates, as well as the response of the coupled forcing (climate or tectonics).

For example, a change in the convergence rates between plates may change the amount and rate of shortening. Shortening, together with other processes either contributing to crustal thickening, as for instance magmatism (*e.g.*, Francis and Hawkesworth, 1994; de Silva and Kay, 2018), or to surface uplift, as for instance dynamic uplift related to mantle processes (*e.g.*, Dávila and Lithgow-Bertelloni, 2015), construct topography that sustains higher exhumation rates. The amount and rate of shortening might also be influenced by the amount of sediments and the presence of décollement layers and inherited structures in the foreland that control the structural

mode of deformation (*i.e.*, thick- versus thin-skinned) and the fault geometry (*e.g.*, Allmendinger et al., 1983; Allmendinger and Gubbels, 1996). If the topographic growth is sufficient to build orographic barriers, the precipitation pattern changes and may alter the distribution and magnitude of exhumation rates. Increased precipitation should be observable in the sedimentary record of the orogen by a change in the sedimentary facies (*e.g.*, Strecker et al., 2007). Focused precipitation at the range front may also promote out-of-sequence thrusting related to enhanced erosion (Horton, 1999), whereas on the lee side of the orographic barrier the crust thickens in the absence of erosion and a high-elevation plateau in the orogen interior might form (Willett, 1999). Finally, the drop of the equilibrium line altitude (ELA) during the Late Cenozoic cooling resulted in wide-spread glaciations and might has led to increased erosion rates in mountainous regions (*e.g.*, Herman et al., 2013). Yet evidence of feedbacks that are not only circumstantial are challenging to observe in field studies (Whipple, 2009, 2014), which are complicated by uncertainties in the reconstruction of tectonic, climate and erosion rate histories (*e.g.*, Montgomery et al., 2001; Zhang et al., 2001; Molnar, 2004; Champagnac et al., 2012; Herman et al., 2013; Herman and Champagnac, 2016; Willenbring and Jerolmack, 2016; Carretier et al., 2018).

In this study, we use the Central Andes (18-36° S) as a natural laboratory to investigate how the exhumation rate varied through time with the evolution of the mountain belt and across different tectonic and climatic gradients. The Andes are formed by the active subduction of the Nazca plate below the South American plate and stretch for approximately 7000 km along the west coast of South America. They cross several climatic zones from the tropics to the polar regions, which results in strong precipitation gradients both across and along the strike of the orogen (*e.g.*, Schwerdtfeger, 1976; Garreaud, 2009; Garreaud et al., 2009). A large number of studies attributed the variable Andean rock uplift, erosion and morphology to different tectonic and geodynamic processes (*e.g.*, Barnes et al., 2006; Gillis et al., 2006; Spikings et al., 2008; Strecker et al., 2009; Hilley and Coutand, 2010; Carrapa and DeCelles, 2015; Reiners et al., 2015) and climatic conditions (*e.g.*, Masek et al., 1994; Horton, 1999; Montgomery et al., 2001; Lamb and Davis, 2003; Thomson et al., 2010; Barnes et al., 2012). To shed new light on the outstanding questions about the influence of climate through erosion on the dynamical evolution of mountain ranges, we integrate a wide range of stratigraphic, geochronologic and thermochronologic data sets at the scale of an orogen. We use the central and southern Central Andes (18-36° S) as a natural laboratory. To our knowledge, this has not been tempted at such spatial and temporal scales and in such detail.

In the following, we present new low-temperature thermochronological data (238 ages) that we complement with literature data (824 ages) to constrain the exhumation rate history of the Andean mountain belt at large temporal (Ma) and spatial scales (18 to 36° S). We focus on apatite and zircon fission track (AFT and ZFT, respectively) and apatite and zircon (U-Th)/He (AHe and ZHe)

data. Our study area is located in the central and southern part of the Central Andes (Gansser, 1973; Ramos, 1999) and is informally divided into a northern (18-28°S), a central (28-32°S), and a southern (32-35°S) segment based on the different morphotectonic structures observed in the study area (*e.g.*, Charrier et al., 2007). First, we review the deformation and climatic histories of the Central Andes and briefly discuss the geothermal field and magmatic activity that can influence the interpretation of thermochronological data. Based on the low-temperature thermochronological data, we then model thermal histories and interpret them in terms of the exhumation rate history of the Central Andes since 80 Ma using an inverse approach. The changes in exhumation rates are compared to changes in the tectonic and climatic records to investigate the role of tectonic and climatic processes on exhumation. We find that in the western part of the northern segment, where the climate is dry and shortening rates are low, Cenozoic exhumation rates vary little through time and are lower than 0.2 km/Ma. East of the drainage divide in the northern segment, exhumation locally starts in the middle-to-late Eocene in the Eastern Cordillera and Altiplano-Puna plateau and expands into larger parts of these regions during the Oligocene. During the Miocene, exhumation subsequently spreads into the eastern part of the southern Eastern Cordillera and the Interandean- and Subandean zones with rates between ca. 0.1 and 0.25 km/Ma. This reflects the onset and eastward propagation of compressional deformation. Compared to the west, these higher rates can be explained by higher shortening rates and higher precipitation in this region. Highest exhumation rates are observed in the Pleistocene in the southern segment in the Principal Cordillera west of the Andean range crest ($\geq$2 km/Ma), that coincide with Pleistocene glacial growth, and in the northern Sierra Pampeanas (1.5 km/Ma) and the Subandean belt (0.6 km/Ma) east of the crest that relate to tectonic activity and enhanced precipitation in these regions. We conclude that the onset of exhumation is mostly consistent with the beginning of compressional tectonics and crustal thickening, whereas the climate significantly influences the magnitude of the observed exhumation rates.

2.2 Deformation history of the Central Andes

The Andean mountain belt is a type-example of a non-collisional orogen in an ocean-continent subduction setting (Dewey and Bird, 1970), formed by the ongoing eastward subduction of the Nazca Plate below the South American Plate (*e.g.*, Barazangi and Isacks, 1976; Cahill and Isacks, 1992). The present-day geometry of the subduction zone in the study area shows a flat slab segment between 28 and 32°S latitude (Barazangi and Isacks, 1976; Cahill and Isacks, 1992) that initiated in the Miocene (Kay and Mpodozis, 2002) (Fig. 2.1). Based on the tectonostratigraphic and magmatic records, the Andean orogeny started in the Late Cretaceous at about 100 Ma, when the prevailing extensive regime of back-arc spreading and rift basins changed into a convergent arc setting (*e.g.*, Mpodozis and Ramos, 1989; Charrier et al., 2007; Horton, 2018a,b).
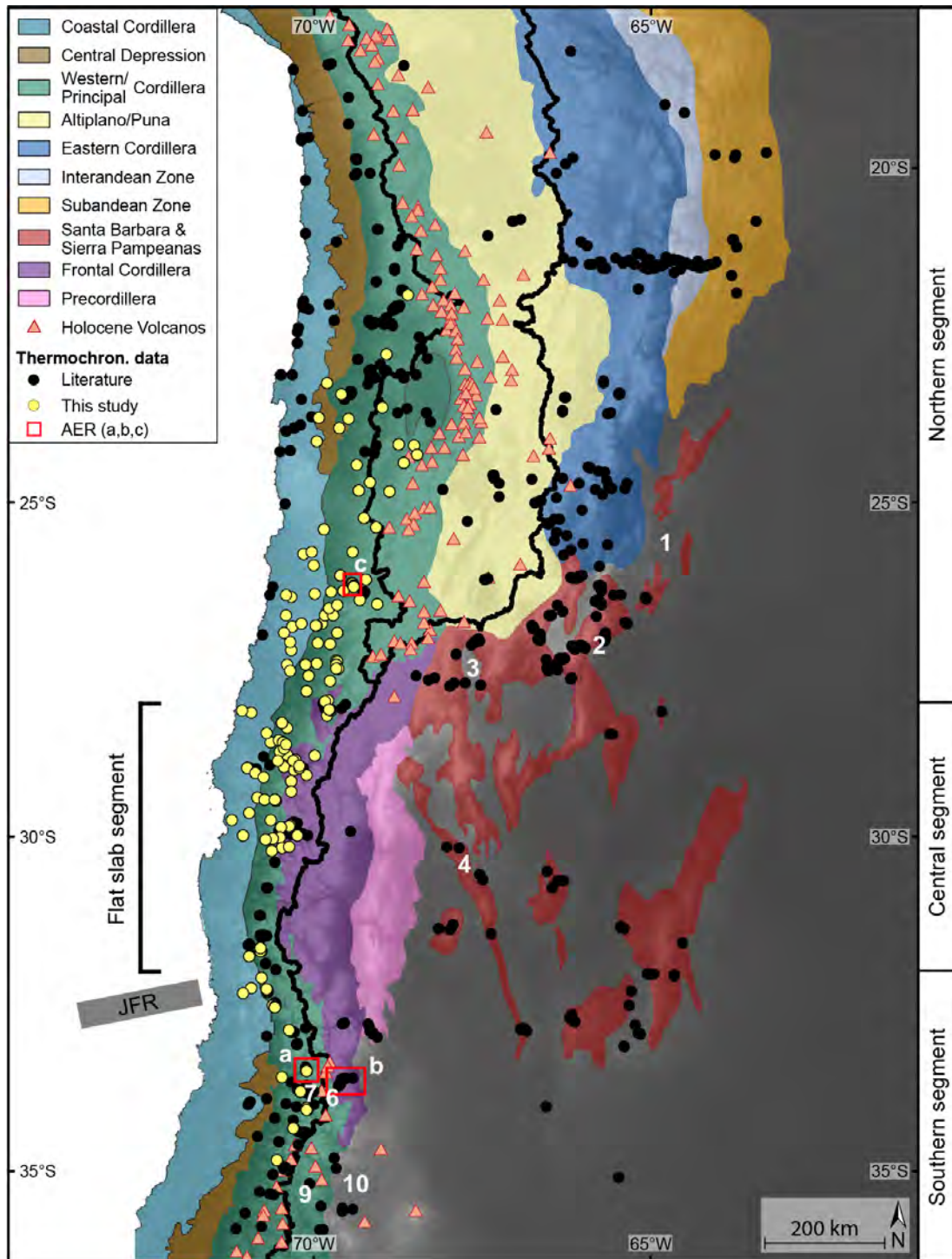
Figure 2.1: Tectonomorphic units of the Central Andes modified from Müller et al. (2002); Mpodozis et al. (2005); Hilley and Coutand (2010); Carrapa et al. (2014); Armijo et al. (2015) and Riesner et al. (2018) and based on geological maps from SegemAR (1997) and SERNAGEOMIN (2003). JFR = Juan Fernandez ridge, AER = locations of age-elevation relationships shown in Fig. 2.14 (AER-a,b) and in supplementary Fig. S3 (AER-c). Numbers represent specific locations referred to in the text: 1 = Santa Barbara system, 2 = Sierra Aconquíja, 3 = Fiambalá Basin, 4 = Sierra de Valle Fértil, 5 = Cuyo foreland basin, 6 = Aconcagua fold-and-thrust belt, 7 = West Andean fold-and-thrust belt, 8 = Laguna de Tagua Tagua, 9 = Malargüe fold-and-thrust belt, 10 = Malargüe foreland basin. S = Santiago de Chile (CL), M = Mendoza (AR), P = Potosi (BO). Underlying topography from GMTED2010, 7.5 arc-s (Danielson and Gesch, 2011).
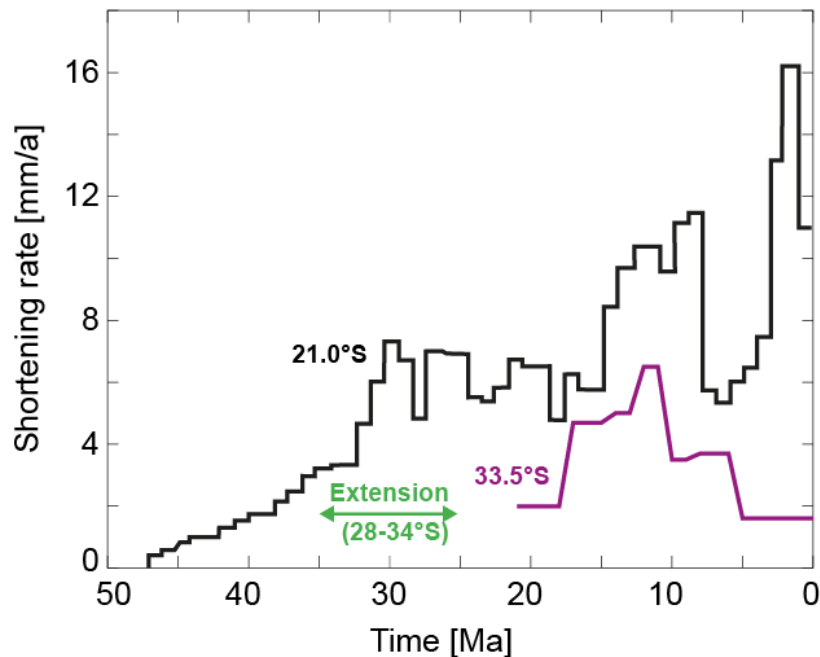
Figure 2.2: Average orogenic shortening rates for the northern (21° S, black line (Oncken et al., 2012)) and southern (33.5° S, purple line (Giambiagi et al., 2015b)) segments of the Central Andes. Green arrow indicates the period of Oligocene extension in the central and southern segments (see text for discussion).

Compilations of shortening estimates suggest a significant decrease of the total amount of crustal shortening with latitude, from 270-420 km at 21° S to 31-71 km at 33.5° S (*e.g.*, Kley and Monaldi, 1998; Oncken et al., 2006; Faccenna et al., 2017; Schepers et al., 2017, and references therein). Similarly, reconstructed average crustal shortening rates have consistently been higher in the North than in the South and varied between 1.2 mm/a and 16 mm/a in the north and between 1.2 and 6.5 mm/a in the south during the last 45 Ma (Oncken et al., 2006; Giambiagi et al., 2015b; Riesner et al., 2018) (Fig. 2.2). Due to structural inheritances and thickness variations in the pre-existing sedimentary cover, compressional deformation in the Central Andes can be described by three different deformational styles (*e.g.*, Allmendinger et al., 1983; Allmendinger and Gubbels, 1996; Kley et al., 1999; McQuarrie and DeCelles, 2001; McQuarrie, 2002; Giambiagi et al., 2003; Elger et al., 2005; Anderson et al., 2017). i) Thin-skinned deformation in a typical foreland basin system as observed in the Subandean fold-and-thrust belt and adjacent Chaco foreland basin in the Bolivian Andes. Here, the fold-and-thrust belt developed in a thick Paleozoic to Mesozoic sedimentary sequence, where shortening has been accommodated by intra-sedimentary deformation along primarily east-vergent, flat-ramp thrust systems and by displacement on the basal décollement (*e.g.*, Allmendinger et al., 1983; Baby et al., 1992; Dunn et al., 1995; Kley, 1996; Horton and DeCelles, 1997; Anderson et al., 2017). ii) Basement-core uplift as observed in the Sierra Pampeanas, where almost no sediment cover existed before the onset of contractional deforma-

tion (Allmendinger et al., 1983). Here, tectonic shortening is accommodated by spatially disparate, diachronous uplift of Proterozoic-to-Paleozoic basement blocks that are bound by high-angle reverse faults formed along inherited structures associated with earlier deformation (Jordan and Allmendinger, 1986; Strecker et al., 1989; Grier et al., 1991; Hilley et al., 2005). The newly formed Neogene contractional basins are passively transported in the hanging-wall of these basement ranges. iii) A combination of these two deformational styles, where both the basement and the sedimentary cover are deformed in a mix of flat-ramp thrusts and steep structures rooting in the deeper basement as for instance in the Eastern Cordillera (*e.g.*, McQuarrie and DeCelles, 2001; McQuarrie, 2002; Müller et al., 2002; Pearson et al., 2013; Anderson et al., 2017), the Interandean zone (*e.g.*, Kley, 1996; Anderson et al., 2017), the Altiplano-Puna (*e.g.*, Kraemer et al., 1999; Coutand et al., 2001), the Santa Barbara range (*e.g.*, Kley and Monaldi, 2002) and the Principal and Frontal Cordilleras (*e.g.*, Giambiagi et al., 2003; Riesner et al., 2018).

Below, we review the Andean deformation history by extracting the occurrence of syntectonic sediments and other structural and sedimentological observations from the literature in three segments (northern, central and southern) that show different tectonic and climatic conditions (Fig. 2.3 and Appendix, Table A6). Note that we exclude studies that use thermochronology to infer onset and magnitude of deformation or shortening rates to avoid circular reasoning when comparing it to the modelled exhumation rates derived by our approach. Our review aims at constraining shortening rates to provide a first-order constraint on crustal thickening processes. However, the amount of shortening and estimated shortening rate reconstructions summarized here and depicted in Figure 2 should be interpreted with care. Shortening estimates on the western side of the Andes and in large parts of the Altiplano are poorly resolved because deformation markers are obscured by both volcanic deposits and little to non-incised intramontane basins. Detailed reconstructions are thus restricted to the Eastern Cordillera and the Inter- and Subandean zones. Also, all estimates should be regarded as minimum values due to erosional removal of hanging-wall cut-offs and the incompleteness of the sedimentary record. Furthermore, shortening estimates are very variable among different studies as they rely largely on balanced cross-section, as for instance between 270 km (Oncken et al., 2006) and 420 km (Schepers et al., 2017) at 21° S. Such differences are due to the fact that balanced cross-sections are commonly built from surface observations with sparse control of the geometry and kinematics of deep structures and on the constant-area assumption that is generally valid at shallow crustal levels only, leaving shortening at depth largely unknown. Differences also arise from inherent subjectivity of the applied techniques and from the lack of unified structural evaluation, since most shortening estimates focus only on specific tectonomorphic units and transects across the entire Andes are rare. Yet, despite the fact that shortening estimates have clear limitations, they provide fundamental insight into the deformation history, which we summarize below.

2.2.1 Northern segment (18 – 28° S)

The northern part of this segment (18-23.5° S) is a wide mountain belt that comprises, from west to east, the Coastal Cordillera, the Central Depression, the Western Cordillera, the Altiplano-Puna plateau, the Eastern Cordillera and the Interandean and Subandean zones (Fig. 2.1). South of 23.5° S, the Subandean zone is replaced by the Santa Barbara system and the southern Eastern Cordillera, which sit over the transition zone from a steeply subducting Nazca Plate to a flat slab geometry. These units end at around 26° S and the Sierra Pampeanas appear. We first describe the deformation history in the region between 18 and 23.5° S and then briefly review the tectonic setting in the southern part between 23.5 and 28° S. Our main focus is on the eastern flank of the orogen since little is known about deformation on the western side.

At 21° S, the Central Andes are 720 km wide from the coast to the present mountain front in the Subandean zone and record more than 270-420 km of total shortening (*e.g.*, Kley and Monaldi, 1998; McQuarrie et al., 2005; Oncken et al., 2006; Eichelberger et al., 2013; Anderson et al., 2017; Faccenna et al., 2017; Schepers et al., 2017). This shortening is thought to have been accommodated mainly by the Eastern Cordillera and Interandean zone (190±46 km), the Subandean belt (82±21 km) and the Altiplano (65 km) over the last 40-50 Ma, whereas shortening in the Central Depression and Western Cordillera seems to be less important (Anderson et al., 2017). However, detailed structural shortening estimates are restricted to the Eastern Cordillera and the Inter- and Subandean zones because the deformation markers on the western flank and in the Altiplano are obscured by both volcanic deposits and little to non-incised intramontane basins.

Mountain building has possibly started in the Late Cretaceous (90 Ma) in the Central Depression and Western Cordillera as suggested by compressional growth structures and angular unconformities in Late Cretaceous to late Eocene sediments (Mpodozis et al., 2005; Arriagada et al., 2006; Amilibia et al., 2008; Herrera et al., 2017) and by the early foreland basin depositional history preserved in the Altiplano basin (Horton and DeCelles, 1997; Sempere et al., 1997; Horton et al., 2001; Elger et al., 2005; McQuarrie et al., 2005; DeCelles et al., 2011; Horton, 2018a) (Fig. 2.3A). This is also corroborated by increasing proportions of granitic clasts with western provenance observed in Late Cretaceous sediments of the Salar de Atacama Basin, which indicate unroofing of the Western Cordillera or "*Cordillera Domeyko*" during that time (Bascuñán et al., 2016). This initial period of shortening was followed by a complex deformation history with contractional, strike-slip and extensional phases from the Oligocene to the earliest Miocene in the Western Cordillera (Pananont et al., 2004; Arriagada et al., 2006; Jordan et al., 2007; Bascuñán et al., 2019). Since then, the area underwent west-vergent thrusting, tilting and local extension (Muñoz and Charrier, 1996; Victor et al., 2004; Farías et al., 2005). Shortening rates west of the Altiplano did not exceed 1.2 mm/a and were always lower than in the east of the Altiplano (Oncken et al., 2006). Highest

rates were observed during the Eocene that are commonly associated with enhanced mountain building in the Western Cordillera or *"Cordillera Domeyko"* (*e.g.*, Charrier et al., 2007). At about 40 Ma, shortening rates in the west slowed down to <0.25 mm/a (Victor et al., 2004; Oncken et al., 2006) and the thrust front moved into the Eastern Cordillera that shows tectonic activity until the late Miocene (McQuarrie and DeCelles, 2001; Müller et al., 2002; McQuarrie et al., 2005). By the early Oligocene, deformation affected most parts of the orogen including the Altiplano and expanded as far as 26° S south into the Puna (Coutand et al., 2001; DeCelles and Horton, 2003; Elger et al., 2005; McQuarrie et al., 2005; Oncken et al., 2006; DeCelles et al., 2011) (Fig. 2.3A). Shortening rates in the Altiplano show high local and temporal variability in the range of 0.1 and 3 mm/a, with a period of quiescence in the early Miocene (Elger et al., 2005). In the Eastern Cordillera, shortening rate estimates based on stratigraphy and fault kinematics suggest that shortening culminated in the Oligocene to early Miocene with rates of 5-10 mm/a (Müller et al., 2002; Elger et al., 2005). In the early Miocene (25-21 Ma), shortening in most parts of the Eastern Cordillera ceased except for some out-of-sequence thrusting in its central part (Müller et al., 2002; Horton, 2005; Anderson et al., 2017) and the deformation front migrated eastward across the Interandean zone, where the majority of the shortening between 25 and 10 Ma (70 km) took place (Horton, 2005; Elger et al., 2005; Anderson et al., 2017; Calle et al., 2018). At 12-10 Ma, deformation in these parts of the Andes finally terminated (Gubbels et al., 1993; McQuarrie et al., 2005; Calle et al., 2018) and moved into the Subandean fold-and-thrust belt, where east-vergent thrust systems subsequently incorporated sediments previously deposited in the early foreland basins and accommodated up to 82 km of shortening (Baby et al., 1992; Kley, 1996; Dunn et al., 1995; DeCelles and Horton, 2003; Echavarria et al., 2003; Uba et al., 2005, 2006, 2009; Calle et al., 2018). Shortening rate estimates in the Subandean zone suggest that shortening rates either (i) steadily increased since 9 Ma to a maximum of 11 mm/a at 3 Ma and a present-day rate of 8 mm/a or (ii) that shortening occurred in two discrete pulses from 9-7 Ma and 2-0 Ma with maximal rates of 13 mm/a, which were separated by a period of modest shortening (0-5 mm/a) (Echavarria et al., 2003).

At around 24.5° S, the Central Depression on the western side of the Central Andes narrows and finally disappears at 28° S. Similarly, the Subandean fold-and-thrust belt on the eastern side disappears around 23.5° S and is replaced by the southern Eastern Cordillera and the Santa Barbara system and, south of 26° S, the Sierra Pampeanas (Fig. 2.1). These structural changes in the foreland may be linked to the transition from a steep to a flat subduction geometry (*e.g.*, Jordan et al., 1983) as well as to inherited paleogeography and associated thickness variations of pre-Cenozoic strata (*e.g.*, Allmendinger et al., 1983; Allmendinger and Gubbels, 1996; Pearson et al., 2013; del Papa et al., 2013). Compared to the thin-skinned Sub-Andean fold-and-thrust belt that formed in a zone of thick Paleozoic and Mesozoic sedimentary cover, the preexisting sedimentary accu-
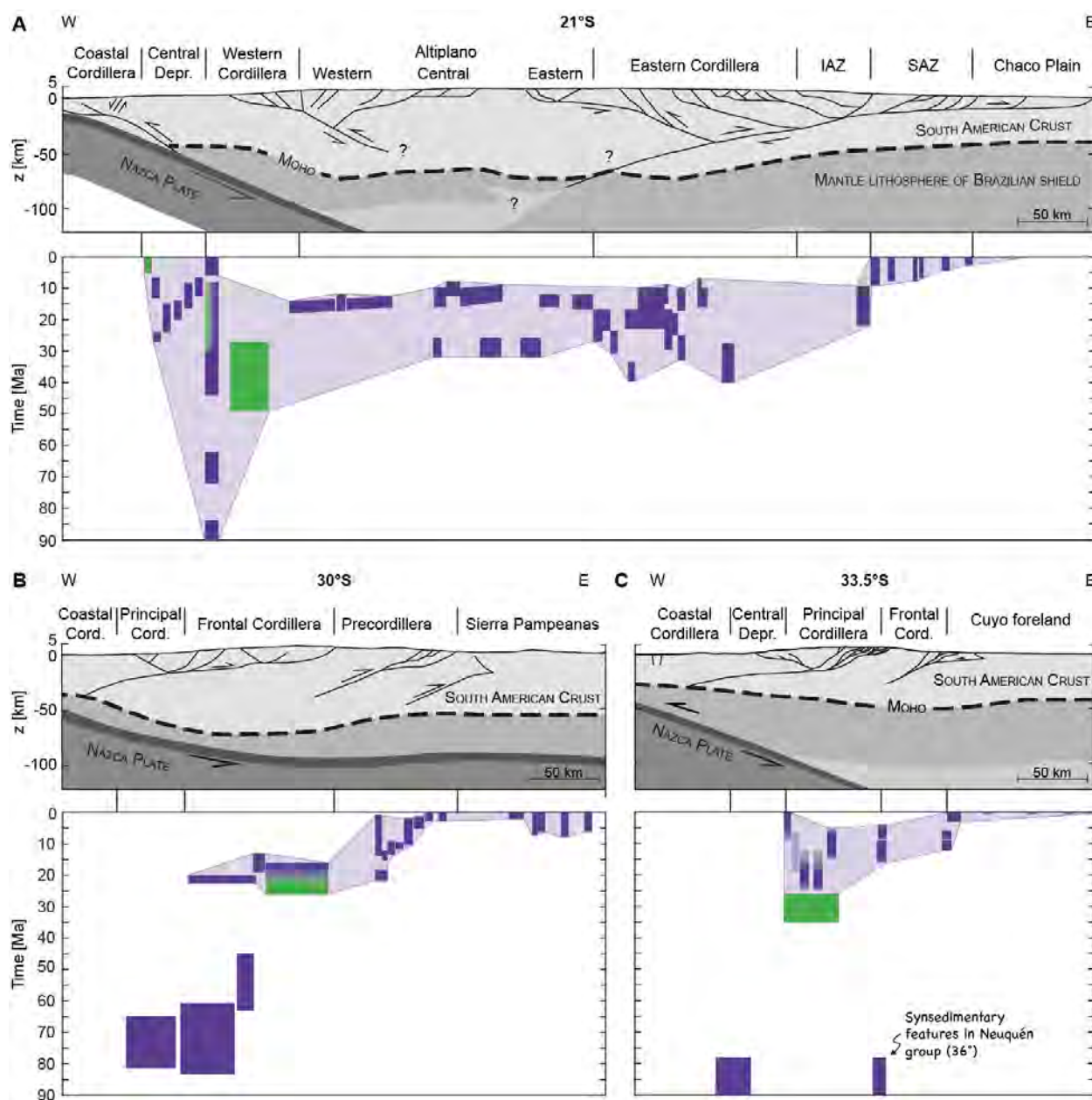
Figure 2.3: Lithospheric-scale cross-sections and approximate onset and duration of deformation in the Central Andes as observed in syntectonic sediments. Dark purple boxes represent compression, green boxes extension. Light purple envelope outlines the inferred timespan of compression, *i.e.* delimiting the onset and cessation of tectonic activity in the respective tectonic unit. See Appendix, Table A6 for data compilation and references. **A)** The northern segment comprises data between 19 and 24° S that was projected on a cross-section at 21° S within the respective tectonic units. Geological cross-section and crustal thickness modified from Armijo et al. (2015). Question marks indicate high uncertainty. IAZ = Interandean zone, SAZ = Subandean zone. **B)** The middle segment shows data between 28 and 31° S projected on a cross-section at 30° S within the respective tectonic units. Geological cross-section and crustal thickness modified from Lossada et al. (2017) and Gans et al. (2011), respectively. **C)** Data for the southern segment include studies between 32.5 and 34° S projected on a cross-section at 33.5° S within the respective tectonic units. Geological cross-section and crustal thickness modified from Giambiagi et al. (2015b) and Gans et al. (2011), respectively. Please note that Riesner et al. (2018) recently proposed a bi-vergent structural model for this section.

mulations are thinner in the Santa Barbara system and almost absent in the thick-skinned Sierra Pampeanas (Allmendinger et al., 1983). The total amount of shortening at 24-25° S is ca. 142 km and thus significantly less than at 21° S (Pearson et al., 2013). Deformation across the Puna, the southern Eastern Cordillera and the Santa Barbara system was spatially disparate and predominantly along reactivated extensional structures associated to the Cretaceous-to-Paleogene Salta rift system (Grier et al., 1991; Kley and Monaldi, 2002). This resulted in a Paleogene broken foreland where Cenozoic sediments were deposited in intermontane basins separated by uplifted ranges of Proterozoic and Paleozoic basement, similar to the present-day broken foreland of the Sierra Pampeanas (*e.g.,* Hongn et al., 2007; del Papa et al., 2013; Montero-López et al., 2016). Growth strata in these intermontane basins indicate that tectonic activity started in the middle Eocene at the Puna margin in the southern Eastern Cordillera (*e.g.,* Hongn et al., 2007; Montero-López et al., 2016) and in the late Eocene to Oligocene in the Puna plateau interior (Kraemer et al., 1999; Coutand et al., 2001; Carrapa and DeCelles, 2008). In the Puna, shortening was largest in the middle Miocene and continued until the Pliocene (Kraemer et al., 1999; Coutand et al., 2001). To the east, the exhuming Puna margin shed detritus into a formerly unrestricted foreland that became compartmentalized in the middle to late Miocene, when ensuing shortening led to the uplift of Paleozoic basement in the western and central parts of the Eastern Cordillera (Hilley and Strecker, 2005; Coutand et al., 2006; Deeken et al., 2006; Carrera and Muñoz, 2008; Hain et al., 2011). Concurrent range uplift at the Eastern Cordillera-Santa Barbara boundary documents the disparate nature of deformation (Hain et al., 2011). Tectonic activity continued during the Plio-Pleistocene across the entire foreland by promoting further basement uplift in its eastern part and by maintaining synsedimentary deformation in the intermontane basins of the Eastern Cordillera (Hilley and Strecker, 2005; Coutand et al., 2006; Carrera and Muñoz, 2008; Hain et al., 2011). Deformation in the northern Sierra Pampeanas started during the late Miocene by fragmentation of the former continous foreland basin (Strecker et al., 1989; Bossi et al., 2001; Carrapa et al., 2008; Zapata et al., 2019), although some topography may have already existed before in its eastern part (Strecker et al., 1989; Zapata et al., 2019). Major relief development and range uplift occurred after 6 Ma along reverse fault-bounded basement blocks akin to the structures in the Eastern Cordillera and the Santa Barbara system (Strecker et al., 1989; Bossi et al., 2001; Carrapa et al., 2008; Zapata et al., 2019). Folded and overthrusted Quaternary units in the eastern part document that deformation in this region continued during the Plio-Pleistocene (Strecker et al., 1989).

In summary, and as depicted in Figure 2.3A, the sedimentary record between 18 and 23.5° S shows different deformation histories for the western and the eastern sides of the Central Andes. The western side of the Andes shortened relatively continuously since the Late Cretaceous to the present-day, with deformation reaching its climax in the Eocene (*e.g.,* Charrier et al., 2007). At this

time, compressional deformation initiated in the Eastern Cordillera (*e.g.*, Müller et al., 2002; Elger et al., 2005). From the Oligocene until 10 Ma, the whole Andes except for the Subandean zone experienced major tectonic deformation (Fig. 2.3A). Since 12-10 Ma (*e.g.*, Gubbels et al., 1993), deformation north of 23.5° S has mainly been accommodated in the thin-skinned fold-and-thrust belt forming the Subandean zone, where shortening rates may have reached up to 13 mm/a in the Pliocene (Echavarria et al., 2003). South of 23.5° S, the Subandean belt disappears and the dominant deformation mode is thick-skinned. Here, deformation started in the Eocene in the Puna and the westernmost southern Eastern Cordillera (*e.g.*, Montero-López et al., 2016). In the middle to late Miocene, the continuous foreland was dissected into several intermontane basins that are separated by basement blocks uplifted along steep reverse faults related to inherited extensional structures (*e.g.*, Strecker et al., 1989; Coutand et al., 2006). Deformation continued during the Plio- and Pleistocene (*e.g.*, Strecker et al., 1989; Carrera and Muñoz, 2008).

2.2.2 Central segment (28 – 32° S)

The central segment of our study area (28-32° S) is located above the contemporary Pampean flat slab segment of the Nazca subduction zone. It comprises from west to east the Coastal, Principal and Frontal Cordilleras, the Precordillera, the Santa Barbara system and the Sierra Pampeanas (Fig. 2.1).

Syntectonic sediments from the Principal and Frontal Cordilleras indicate that a first pulse of compressional deformation may have taken place during the Late Cretaceous to the Paleocene, between 82 and 45 Ma (Martínez et al., 2016; Rossel et al., 2016; Martínez et al., 2018) (Fig. 2.3B). Such an early onset of mountain building and topographic growth is also corroborated by the onset of incipient retroarc foredeep sedimentation with provenance from the Frontal Cordillera and magmatic arc by at least the late Eocene (Fosdick et al., 2017). During the Oligocene, extensional structures in the Doña Ana Group are related to an intra-arc and retro-arc setting in the Frontal Cordillera (Winocur et al., 2015). Compression in the Frontal Cordillera resumed in the early Miocene and led to the inversion of the previously formed basins (Winocur et al., 2015; Martínez et al., 2016; Rossel et al., 2016; Martínez et al., 2018). Shortening now also affected the western part of the Precordillera, as evidenced by early Miocene (~20 Ma) syntectonic growth strata and onlap structures identified on seismic data (Allmendinger et al., 1990; Jordan et al., 1993) (Fig. 2.3B) and by the oxygen isotope record of pedogenic carbonates that indicate that this part of the Precordillera has attained present-day elevations before 9 Ma (Hoke et al., 2014). This early phase of deformation was followed by 3 to 4 Myr of tectonic quiescence. At 15 Ma, shortening resumed and peaked around 9-12 Ma with rates of 20-25 mm/a, followed by decreasing rates >10 mm/a (Jordan et al., 2001b; Allmendinger and Judge, 2014). Deformation then subse-

quently propagated to the east where it affected the eastern part of the Precordillera and the Sierra Pampeanas since 5-7 Ma (Strecker et al., 1989; Jordan et al., 1993, 2001b) (Fig. 2.3B).

2.2.3 Southern segment (32 - 36° S)

The southern segment of our study area (32-36° S) includes the transition from the shallowly dipping segment of the Nazca subduction zone to a moderately (30°) dipping segment south of 33° S. Here, the Central Andes comprise the Coastal Cordillera, the Central Depression, the Principal Cordillera, the Frontal Cordillera and the eastern Malargüe fold-and-thrust belt and foreland basin (Fig. 2.1).

Thrust-related growth strata and evidence of basin inversion in the Coastal Cordillera/Central Depression and in the Malargüe fold-and-thrust belt also suggest a late Cretaceous (~100 Ma) onset of shortening in this part of the Andes (Horton, 2018b, and references therein) (Fig. 2.3C). However, the formation of several basins filled by volcano-sedimentary deposits in the late Eocene to the Oligocene (~37-23 Ma) document large-scale extension and crustal thinning in this region, similar to the setting at 30° S (Jordan et al., 2001a; Charrier et al., 2002; Ramos and Folguera, 2005; Burns et al., 2006; Folguera et al., 2010; Rojas Vera et al., 2010; Horton et al., 2016; Horton, 2018b). Shortening finally resumed in the latest Oligocene by tectonic inversion of the former extensional basins (Godoy et al., 1999; Charrier et al., 2002). Neogene compressional syntectonic strata at 33-34° S are observed in the inverted Abanico basin in the western Principal Cordillera, in the Alto Tunuyán basin separating the Principal and Frontal Cordilleras, and in the foreland (Giambiagi et al., 2001, 2003; Porras et al., 2016; Riesner et al., 2017, 2018) (Fig. 2.3C).

Deformation in the southern segment was accommodated by two fold-and-thrust belts of opposite vergence located in the Principal Cordillera. Two contrasting views about the onset, the intensity and the partitioning of deformation have been proposed based on either an east-vergent structural model (*e.g.*, Giambiagi and Ramos, 2002; Farías et al., 2010; Giambiagi et al., 2012, 2015b) or a bi-vergent model (Armijo et al., 2010; Riesner et al., 2017, 2018, 2019). In the east-vergent model, most of the orogenic shortening has been accommodated by east-vergent thrusts in the hybrid thick- and thin-skinned Aconcagua fold-and-thrust belt, which is located in the eastern Principal Cordillera and separates the modern volcanic arc and the basement culmination of the Frontal Cordillera (Giambiagi et al., 2015b, and references therein). According to this model, compressional deformation started around 22 Ma in the western and central Principal Cordillera by inversion of the Abanico basin (Godoy et al., 1999; Charrier et al., 2002; Fock et al., 2006), which resulted in 7-16 km of shortening during the early Miocene (Farías et al., 2010; Giambiagi et al., 2015b). Shortening in the Aconcagua fold-and-thrust belt initiated around 18-15 Ma and was active until the early Pliocene (~5 Ma) as revealed by syntectonic sediments deposited in

the Alto Tunuyán wedge-top basin adjacent to the east (Giambiagi et al., 2001; Giambiagi and Ramos, 2002; Giambiagi et al., 2003, 2015b; Porras et al., 2016). East of the Principal Cordillera, shifts in the sedimentary provenances in the foreland basin at 16 Ma and in the Alto Tunuyán Basin at 11-9 Ma indicate important uplift of the Frontal Cordillera during that time that continued through the Pliocene (Irigoyen et al., 2000; Giambiagi et al., 2003; Porras et al., 2016; Buelow et al., 2018). This is also corroborated by the oxygen isotope record of pedogenic carbonates from the Alto Tunuyán Basin that indicates that 2 ± 0.5 km of surface uplift occurred during the Mio-Pliocene (Hoke et al., 2014). In the Pliocene (~4 Ma), compressional deformation in the eastern Principal Cordillera finally stopped and propagated to the eastern Frontal Cordillera and the Cuyo foreland (Irigoyen et al., 2000; Giambiagi et al., 2003; García and Casa, 2014; Giambiagi et al., 2015a). In this model, the Coastal Cordillera and the western Principal Cordillera were uplifted passively due to the tectonic activity of the Aconcagua fold-and-thrust belt (Giambiagi et al., 2015b), with main surface uplift occurring during the late Miocene (10.5 Ma) to the Pliocene (4.6 Ma) based on geomorphologic evidence (Farías et al., 2008). However, recent detailed analyses of syntectonic deposits in Oligocene-to-Miocene sedimentary rocks of the western Principal Cordillera indicate the activity of a series of west-vergent thrusts since 25 Myr, which form the West-Andean fault-and-thrust belt (Riesner et al., 2017). These faults inverted and folded the former Oligocene-to-Miocene Abanico basin with an average shortening rate of 0.1-0.5 mm/a. Its westernmost fault delineates the current western mountain front of the Principal Cordillera, where deformation is still active today as testified by shallow seismic activity and at least two paleo-earthquakes in the past 20 ka (Barrientos et al., 2004; Vargas et al., 2014). To the east, a series of out-of-sequence thrusts deformed Jurassic to Miocene sediments in west-vergent folds between 15 Ma to 5 Ma that link the West-Andean thrust belt with the east-vergent Aconcagua fold-and-thrust belt (Riesner et al., 2018). These new insights indicate that the western part of the Andean mountain belt has accommodated more shortening and deformation than previously thought (Armijo et al., 2010; Riesner et al., 2017, 2018). Therefore, shortening in the Principal Cordillera and uplift of the Frontal Cordillera is proposed to be accommodated by a bi-vergent orogen with continuous, primary westward deformation since 25-20 Ma. The Aconcagua fold-and-thrust belt is considered as a secondary structural feature which passively accommodated Andean deformation along thin-skinned thrusts (Riesner et al., 2018), instead of being the principal structure as suggested by Giambiagi et al. (2015b). These two contrasting models also lead to different shortening rate reconstructions across the Andes (Fig. 2.2). According to Riesner et al. (2018), the long-term average shortening rate is 1.2 - 2.2 mm/a. In the reconstruction of Giambiagi et al. (2015b), shortening peaks between 17-11 Ma with rates of 4.7-6.5 mm/a and is lower before 17 Ma (2 mm/a) and during the Pliocene (1.6 mm/a). The total amount of shortening decreases from 31-71 km at 33.5° S (Giambiagi and Ramos, 2002; Giambiagi et al., 2012, 2015b; Riesner et al., 2018) to 10-13 km at 36° S. The Frontal Cordillera disappears south of 34.5° S (Giambiagi et al., 2012)

and the Aconcagua fold-and-thrust belt gives way to the thick-skinned Malargüe fold-and-thrust belt and its corresponding foreland basin (Ramos et al., 1996), which are both characterised by syntectonic sediments younging to the east (*e.g.*, Horton, 2018b, and references therein).

2.2.4 Summary of the deformation history of the Central Andes

As outlined above, the magnitude and onset of deformation in the Central Andes varies considerably with latitude (Fig. 2.2, Fig. 2.3). The total amount of shortening is highest in the northern segment of the study area and was accommodated mostly in the eastern part of the orogen (Fig. 2.3A). Shortening amounts decrease substantially towards the south. The compressional regime in the central and southern segments was interrupted by a period of foreland quiescence and hinterland extension in the late Eocene to the late Oligocene (*e.g.*, Litvak et al., 2007; Winocur et al., 2015; Horton et al., 2016; Horton, 2018b), while the north experienced a major phase of deformation (*e.g.*, Elger et al., 2005; McQuarrie et al., 2005) (Fig. 2.3). Deformation resumed at about 25 Ma and was accommodated by either an east-vergent fold-and-thrust belt in the eastern Principal Cordillera or by a doubly-vergent wedge with mainly westward deformation located in the western Principal Cordillera (Giambiagi et al., 2015b; Riesner et al., 2018).

2.3 Crustal thickening, magmatism and the geothermal field of the Central Andes

The primary control on surface elevation is isostasy (*e.g.*, Molnar and England, 1990). Erosion, magmatism, and tectonic shortening set the crustal thickness that in turn controls elevation (*e.g.*, Allmendinger et al., 1997; Kley and Monaldi, 1998; Giese et al., 1999). Additionally, mantle dynamics especially above subduction zones or crustal flow also influence topography, exhumation, and the shape of a mountain belt (*e.g.*, Jordan et al., 1983; Braun, 2010; Martinod et al., 2010; Dávila and Lithgow-Bertelloni, 2015; Flament et al., 2015; Siravo et al., 2019). In particular, and as for instance observed for the modern Pampean flat slab segment (28-32° S), flattening of the subducting slab may generate dynamic uplift (Dávila and Lithgow-Bertelloni, 2015; Flament et al., 2015) and induce shortening in the upper plate's interior far away from the trench, which leads to the widening of the mountain belt (Martinod et al., 2010). On the contrary, steep and retreating subduction slabs can lead to dynamic subsidence and to a topography that is lower than expected from crustal thickening (Mitrovica et al., 1989; Royden, 1993). Based on the magmatic arc activity and on periods of deformation and crustal thickening, several past flat slab segments might have formed during the Cenozoic in the Central Andes (Ramos and Folguera, 2009, and references therein). These were located from 14 to 20° S between 45-35 Ma and 25 Ma, from 20 to 24° S between 18 and 12 Ma, and from 34.5 to 37.75° S between 15 and 5 Ma (Ramos and Folguera,

2009). However, our compilation of igneous activity in the Central Andes (Fig. 2.4, supplementary Table A7 provided in electronic form only) does not show the expected cessation of magmatism for the latest two periods of the proposed flat slab subduction in the respective locations of the Western and Principal Cordilleras. Hence, uncertainties about the past geometry of the subduction zone remain.

The magmatic contribution to crustal evolution and surface uplift in the Andes relative to crustal thickening due to tectonic shortening is difficult to constrain because of the uncertainty on the amount of igneous material added to the crust. This is commonly calculated from the volume of volcanic rocks by assuming a plutonic-to-volcanic ratio that can vary from 3:1 to 35:1 (*e.g.*, de Silva and Kay, 2018) and assuming a mantle contribution to the melt of roughly 50% (*e.g.*, Kay et al., 2010). Early estimates of magmatic addition are 13 km^2/Ma over the last 10 Ma at 21-22°S (Francis and Hawkesworth, 1994), but more recent estimates in the same region are much higher, up to 33-107 km^2/Ma over the last 11 Ma (de Silva and Kay, 2018). Assuming an average shortening rate of 9-10 mm/a (Fig. 2.2) and an average crustal thickness of 50 km, these estimates of magmatic addition indicate that the contribution of magmatic activity to crustal thickness relative to the contribution from tectonic shortening can vary between 2-3% and 6-24%. However, crustal thickening by shortening and magmatism is compensated in some places by crustal thinning resulting from processes like crustal delamination and forearc subduction erosion. For instance, the Altiplano-Puna plateau was rather a site of crustal loss than addition according to de Silva and Kay (2018). These processes of lithospheric removal and magmatic contribution may have resulted in ~1 km of Airy isostatic surface uplift in the Altiplano-Puna plateau over the last 11 Ma (Perkins et al., 2016). Although the highest estimates of magmatic contribution to crustal thickening do not exceed 25% relative to the amount of crustal thickening driven by tectonic shortening, these values indicate that magmatic addition is a non-negligible contribution to crustal growth. Therefore, we briefly review the current knowledge about crustal thickening and magmatic activity in the Central Andes.

2.3.1 Present-day crustal thickness

Continental-scale data analysis from satellite gravimetry, seismic refraction, receiver functions and surface wave tomography show that the thickest crust of South America (>70 km) is located below the central Andean Plateau (~10 to 28°S) (*e.g.*, Beck et al., 1996; Giese et al., 1999; Assumpção et al., 2013; Chulick et al., 2013; van der Meijde et al., 2013). The crustal thickness then gradually decreases southwards to ca. 45 km at 35°S (Assumpção et al., 2013; Chulick et al., 2013; van der Meijde et al., 2013). Thinner crust is also observed in the South-American craton east of the Andes (30-40 km) and along the range in the Andean foreland, where the average thickness is below 35 km (Assumpção et al., 2013). Hence, the Central Andes show variable crustal thicknesses that

correlate with topography at the orogen scale, suggesting a first-order local Airy-type isostatic compensation (*e.g.*, Molnar and England, 1990; Beck et al., 1996; Ryan et al., 2016).

2.3.1.1 Crustal thickening and magmatic arc evolution

The evolution of crustal thickening through time can be constrained by the geochemical composition of volcanic and magmatic arc products (*e.g.*, Leeman, 1983; Plank and Langmuir, 1988).

Several lines of evidence suggest that the Andean subduction and related magmatism along the Chilean continental margin were relatively continuous since the early Carboniferous, although variations in the global geodynamic processes and crustal thickness produced noticeable modifications of magmatism through time (*e.g.*, Scheuber et al., 1994; Mamani et al., 2010b; Charrier et al., 2015; Hervé et al., 2014; Del Rey et al., 2016; Oliveros et al., 2018). Since the late Paleozoic until the Late Cretaceous (91 Ma), the subduction margin underwent tectonic stretching that resulted in crustal thinning (Mamani et al., 2010b). A magmatic arc slightly oblique to the present-day coastline and a (mainly) marine back-arc basin to its east were formed (Charrier et al., 2007; Mamani et al., 2010b; Charrier et al., 2015; Oliveros et al., 2018). Several pulses of magmatism occurred during this time and initiated the creation of the Coastal Batholith and associated volcanoclastic deposits in the Coastal Cordillera (Oliveros et al., 2007; Mamani et al., 2010b; Oliveros et al., 2018) (Fig. 2.4, supplementary Table A7). In the Late Cretaceous to the middle Oligocene, a relatively wide forearc basin formed to the west of the magmatic arc and the marine back-arc basin evolved into a terrestrial foreland basin filled by volcanoclastic products and continental deposits (*e.g.*, Lamb et al., 1997; Mpodozis et al., 2005; Charrier et al., 2007; Mamani et al., 2010b; Wotzlaw et al., 2011; Di Giulio et al., 2012; Charrier et al., 2013, 2015; Bascuñán et al., 2016). The magmatic arc subsequently migrated to the east into the Western/Principal Cordillera where it is located today, with the exception of an amagmatic zone delineating the current Pampean flat slab segment between 28 and 32° S that initiated in the Miocene (*e.g.*, Kay and Mpodozis, 2002) (Fig. 2.4).

In the northern segment of the Central Andes, between 13 and 26° S, geochemical observations from magmatic and volcanic arc composition indicate incipient crustal thickening during the late Cretaceous (91 Ma) to the middle Oligocene (30 Ma) and major thickening since then (Kay et al., 1994; Mamani et al., 2010b; Profeta et al., 2015). Several observations suggest that the Western Cordillera and its slope reached a substantial part of its current elevation before or during the Miocene and that uplift in this region was a rather continuous process since at least the Neogene (Jordan et al., 2010; Evenstar et al., 2015; Scott et al., 2018). The uplift history of the Eastern Cordillera and the Altiplano is less clear (*e.g.*, Barnes and Ehlers, 2009). Studies using paleo-elevation and -temperature proxies from the Altiplano and Eastern Cordillera at 19-22° S suggest
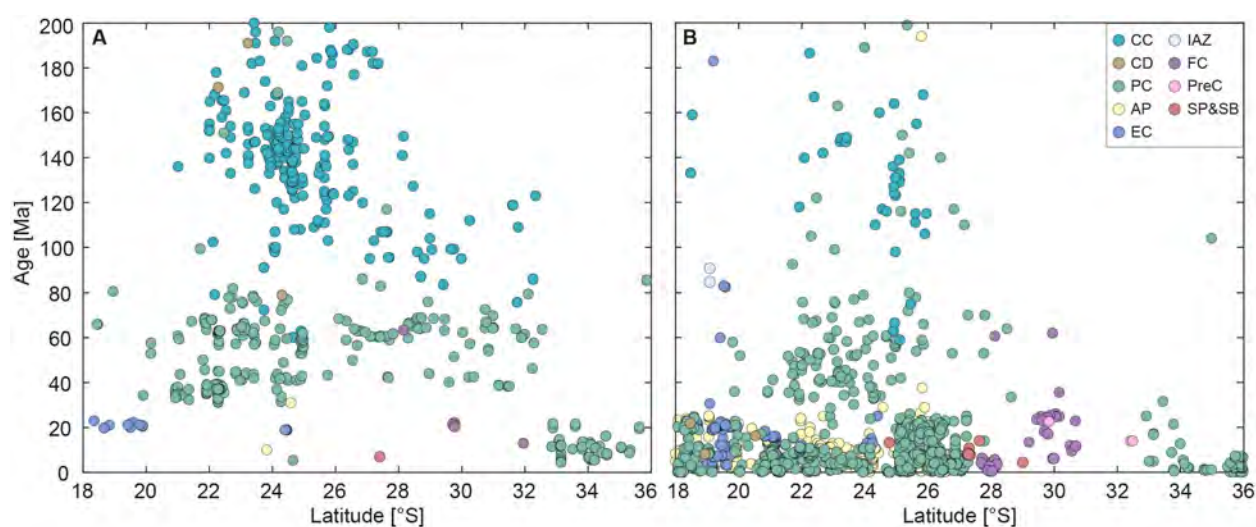
Figure 2.4: A) Magmatic and **B)** volcanic activity during the last 200 Ma along the strike of the Andes. Colors represent tectonomorphic units from Fig. 2.1 (see caption Fig. 2.9 fro abbreviations). Data compilation from Mamani et al. (2010a) with additional data from McNutt et al. (1975); Kurtz et al. (1997); Scheuber (1998); Mutschler et al. (2001); Farías et al. (2008); Singer et al. (1998); Hervé et al. (2014); Jones et al. (2015); Muir et al. (2015); Naranjo et al. (2018). Data are provided in supplementary Table A7.

that these regions reached their modern elevations between 16 and 9 Ma after a pulse of surface uplift of ca. 2.6 km between 16 and 13 Ma that is attributed to an isostatic response to crustal thickening and lower lithosphere delamination (Garzione et al., 2017, and references therein). However, the use of such proxies to infer paleo-altitudes remains debated mainly because they may reflect changes in climate rather than in elevation (*e.g.*, Molnar and England, 1990; Hartley et al., 2007; Ehlers and Poulsen, 2009) and other studies favour either an early, pre-Oligocene uplift history (*e.g.*, Canavan et al., 2014) or continuous growth since the Oligocene (*e.g.*, Fiorella et al., 2015) of the Eastern Cordillera and Altiplano-Puna plateau.

In the flat subduction segment and its margins, the late Oligocene to early Miocene volcanism is characterized by basaltic to andesitic composition erupted through a crust of normal thickness (30-35 km) in an extensional setting (*e.g.*, Kay and Mpodozis, 2002; Litvak et al., 2007). Incipient slab shallowing between 28 and 32° S in the latest early Miocene (~18 Ma) resulted in the broadening of the magmatic arc and in the eastward migration of the arc front into the Precordillera and Sierra Pampeanas (Kay et al., 1991; Kay and Mpodozis, 2002) (Fig. 2.4). Crustal thickening began in the middle to late Miocene. With the peak of slab shallowing in the latest Miocene, igneous activity in the Principal Cordillera ceased by 8 to 5 Ma and shut down completely by 2 Ma in the Precordillera and Sierra Pampeanas, indicating full emplacement of the flat slab segment by the Pliocene (Kay and Mpodozis, 2002) (Fig. 2.4).

To the south of the flat slab segment between 33 and 36° S, the late Oligocene to early Miocene magmatic activity was concentrated at the western border of the Principal Cordillera in a relatively thin crust of 30-35 km (Nyström et al., 2003; Kay et al., 2005) (Fig. 2.4). Geochemical changes in the composition of the magmatic arc products indicate that crustal thickening in this part of the Andes began in the latest early Miocene (Kay et al., 2005). The magmatic arc front migrated 35 km towards the east from 19 to 16 Ma and additional 50 km from ca. 7 to 3 Ma to its current position at the Argentinian-Chilean border, where it has stayed during the last 3 Ma (Kay et al., 2005). By this time, the crust reached its present-day thickness of about 45-50 km (Kay et al., 2005).

2.3.1.2 Heat flow and geothermal gradients in the Central Andes

Exhumation rates derived from thermochronological data strongly depend on the assumed geothermal field. Whereas modern and past geothermal gradients set the depth of the closure isotherms of thermochronometers, the geothermal field is influenced by erosion due to its control on how fast heat is advected to the surface. Furthermore, magma bodies emplaced in the lower crust also influence thermochronometric ages in their surroundings and can lead to a misinterpretation of the observed cooling ages and exhumation rate history (*e.g.*, Calk and Naeser, 1973; Murray et al., 2018). Geothermal gradients in the Central Andes are expected to be different in distinct regions due to variable distances from the subduction trench, locations of the magmatic arc and crustal thicknesses. Unfortunately, heat flow density measurements in the Central Andes are very sparse (Springer and Förster, 1998). Between 15 and 30° S, heat-flow density data from 74 boreholes reveal large across strike variations (Springer and Förster, 1998). The Coastal Cordillera shows low values (20 mW/m^2) that increase to about 60 mW/m^2 at the western flank of the Western/Principal Cordillera. In the active magmatic arc (Western/Principal Cordillera) and the Altiplano, heat flow density values range from 50 to 180 mW/m^2 but are extremely sparse (Springer and Förster, 1998). The higher heat flow values in these parts may be related to isolated magma reservoirs in the shallow crust. Relatively high heat flow (80 mW/m^2) is further observed in the Eastern Cordillera, whereas the Subandean zone shows lower values of about 40 mW/m^2. Assuming an upper crustal thermal conductivity of 2.6 W/m/K (*e.g.*, Čermák and Rybach, 1982), these heat flow measurements translate to the following geothermal gradients: 8 °C/km in the Coastal Cordillera, 23 °C/km in the western flank of the Western/Principal Cordillera, 19-69 °C/km in the magmatic arc and Altiplano, 31 °C/km in the Eastern Cordillera and 15 °C/km in the Subandean zone and Andean foreland. At around 33° S in the Principal Cordillera, a geothermal gradient of 30-35 °C/km was measured (Höfer-Öllinger and Millen, 2010). Estimates of the Oligocene geothermal gradients in the Altiplano, Eastern Cordillera and Inter- and Subandean zones at 21° S range from 19 °C/km to 32 °C/km (Ege et al., 2007) and are thus similar to the present-day values.

We expect that geothermal gradients change through time due to changes in exhumation rates which control the advection of heat, due to evolving spatial patterns of magmatic activity and due to changes in slab geometry which likely change the temperature at the base of the crust from ambient mantle temperature within the mantle wedge to relatively chilled oceanic lithosphere. Our modeling accounts for the advection of heat driven by exhumation and we expect that the effects of magmatic activity can be mitigated by analyzing samples that are unlikely to be influenced by this activity. However, we do not account for changes in the slab geometry. Based on a crustal thickness of 50 km and a thermal diffusivity of 20 km^2/Ma, we expect that the temperature of the shallow crust (1-6 km) will respond to temperature changes at depth over a time scale of 125 Ma. Therefore, these thermal effects are not as important as changes in exhumation rates. However, our prescribed geothermal gradient in the inversion will significantly influence the magnitude of exhumation rates derived from thermochronological data. In particular, higher geothermal gradients will result in lower exhumation rates due to more efficient heat advection and shallower depths of closure of the thermochronologic systems. Therefore, exhumation rates will likely be underestimated in regions where the true geothermal gradient is lower than the modelled gradient and overestimated in places where it is higher.

2.4 Present-day and Cenozoic climate

2.4.1 Present-day climate of the Central Andes

The Central Andes cross several climate zones from arid and tropical conditions in the north to temperate and semi-arid conditions in the south (Schwerdtfeger, 1976). This first-order global atmospheric circulation pattern was established at least since the early Cenozoic (Parrish et al., 1982) or the Mesozoic (Hartley et al., 1992) but was altered by the uplift of the Central Andes (*e.g.*, Campetella and Vera, 2002; Insel et al., 2010).

The present-day climate along and across the Andes exhibits strong climatic gradients and seasonality due to the combined effects of latitudinal position, continentality, rain shadow and cold oceanic upwelling (Schwerdtfeger, 1976; Lenters and Cook, 1995; Houston and Hartley, 2003) (Fig. 2.5). The interference of the Andes with the prevailing wind systems creates the Arid Diagonal (de Martonne, 1925; Gourou and Papy, 1966) that separates the northern and central Andes, which receive high precipitation on the eastern flank due to the South American Monsoon in austral summer, from the southern Andes, which are characterized by winter precipitation associated with the mid-latitude storm tracks or Westerlies (Schwerdtfeger, 1976; Lenters and Cook, 1995; Garreaud, 2007).
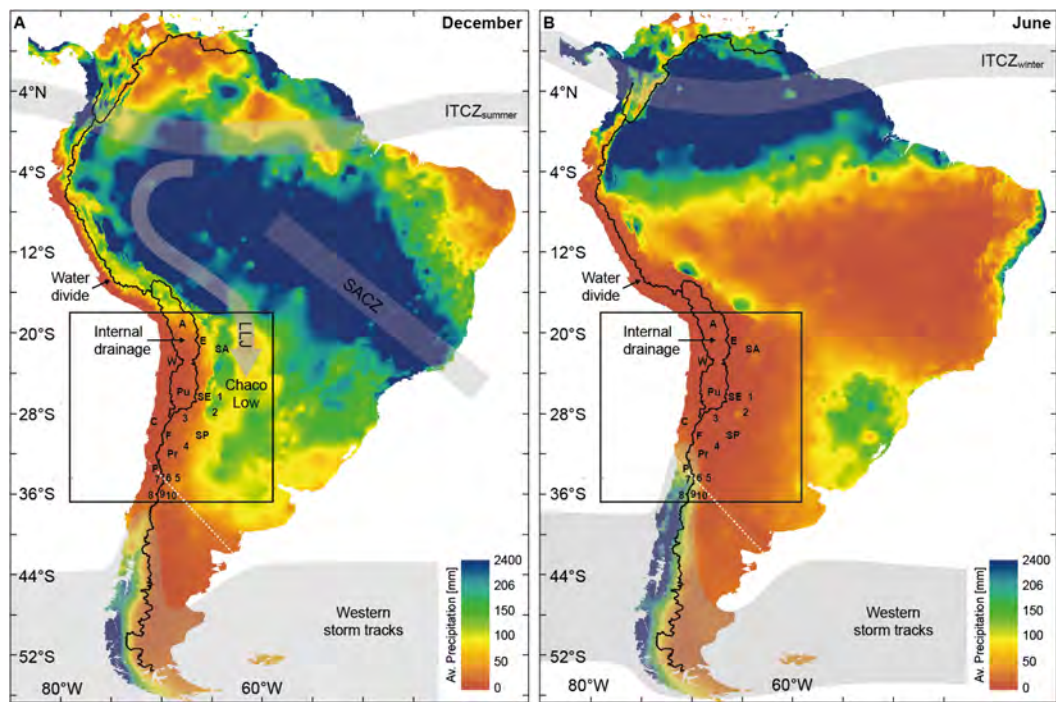
Figure 2.5: Precipitation pattern of South America averaged over 1960-1990, with 2.5 arc-minutes resolution (Hijmans et al., 2005). Black line represents the main drainage divide (Lehner and Grill, 2013), white stippled line the Arid Diagonal. Grey arrows indicate positions of main climatic features (after Nogués-Paegle et al., 2002; Vera et al., 2006; Garreaud, 2009): ITCZ = Intertropical Convergence Zone; SACZ = South Atlantic Convergence Zone; LLJ = low-level jet. 1 = Santa Barbara system, 2 = Sierra Aconquíja, 3 = Fiambalá Basin, 4 = Sierra de Valle Fértil, 5 = Cuyo foreland basin, 6 = Aconcagua fold-and-thrust belt, 7 = West Andean fold-and-thrust belt, 8 = Laguna de Tagua Tagua, 9 = Malargüe fold-and-thrust belt, 10 = Malargüe foreland basin. Letters correspond to tectonomorphic units: A = Altiplano, C = Coastal Cordillera, E = Eastern Cordillera, F = Frontal Cordillera, P = Principal Cordillera, Pr = Precordillera, Pu = Puna, SA = Subandean zone, SE = southern Eastern Cordillera, SP = Sierra Pampeanas, W = Western Cordillera. **A)** During austral summer, the LLJ brings moisture from the Atlantic to the eastern flank of the Andes. The SACZ is an additional source of moisture. The influence of the western storm tracks is restricted to areas south of 38° S. **B)** In austral winter, almost no precipitation reaches the eastern flank and plateau, whereas the area affected by westerly precipitation expands up to 30° S.

The South American Monsoon system is a major feature of the South American climate and forms in response to seasonal changes in the thermal contrast between the South American continent and the adjacent Atlantic Ocean (*e.g.*, Zhou and Lau, 1998; Nogués-Paegle et al., 2002; Vera et al., 2006; Marengo et al., 2012). In austral summer, the South American Monsoon system is characterized in the upper levels by the "Bolivian high", centered at 15° S, 65° W, and the "Nordeste through" over northeast Brazil (Lenters and Cook, 1997, 1999). The South Atlantic Convergence Zone (SACZ) delineates a zone of cloudiness and precipitation that extents from the southern Amazon towards southeast Brazil and the adjacent Atlantic Ocean (Kodama, 1992; Lenters and Cook, 1999; Carvalho et al., 2004) (Fig. 2.5A). At low level, the easterly trade-winds transport high amounts of moisture from the tropical Atlantic Ocean and the Amazon Basin to the west. When encountering the Andes, the moisture-bearing winds are deflected southward into the

Chaco Low via the South American low-level jet (Saulo et al., 2000; Nogués-Paegle et al., 2002; Marengo et al., 2004), which locally results in more than 1000 mm/yr of precipitation at the eastern flank of the Central Andes during austral summer (Fig. 2.5A). In austral winter, the zone of high precipitation migrates northwestward towards the equator (Vera et al., 2006). Precipitation on the eastern flank of the Andes is scarce and mainly related to northward incursions of the Westerlies (Vuille and Ammann, 1997) (Fig. 2.5B). In contrast, the Atacama Desert located between 5 and 27° S west of the Andes exhibits hyperarid conditions with mean annual precipitation <20 mm. Precipitation in the arid Altiplano-Puna plateau and intermontane basins to the east of the Puna is less than 200 mm/a and strongly variable throughout the year (Hijmans et al., 2005) (Fig. 2.5). South of 35° S, the mean annual rainfall is controlled by the mid-latitude storm-tracks that bring moisture from the Pacific to the western side of the Andes, whereas the eastern side of the Andes receives only little rain due to the orographic barrier effect (*e.g.*, Schwerdtfeger, 1976; Lenters and Cook, 1995). Because the latitudinal band of maximum precipitation associated with the Westerlies shifts from 45-55° S in summer to 35-45° S in winter (Garreaud, 2009), the region between 27 and 37° S shows strong seasonal variations and defines a transitional zone from a semi-arid climate with average rainfall of around 30 mm/a in the north to a Mediterranean climate with average rainfall of around 1000 mm/a in the south (Fig. 2.5).

2.4.2 Paleoclimate of the Central Andes

Modelling results from Ehlers and Poulsen (2009) and Insel et al. (2010) suggest that the emergence of the Andes above half of their present height may have resulted in increased precipitation along the eastern flanks and the central plateau, whereas hyperarid conditions replaced the semi-arid to arid conditions that prevailed since the Mesozoic in the Atacama Desert (Hartley et al., 1992; Dunai et al., 2005; Hartley et al., 2005; Le Roux, 2012; Oerter et al., 2016). The onset of Antarctic Bottom Water formation, the growth of the East Antarctic Ice Sheet and the resulting intensification of cold water upwelling along the Pacific Coast during the middle Miocene possibly contributed to the increasing aridity on the western side of the Andes (Houston and Hartley, 2003, and references therein). Sedimentologic, geomorphologic, pedogenic and isotopic data suggest that this change to hyperaridity occurred in the middle Miocene at about 12 Ma (Riquelme et al., 2007; Nalpas et al., 2008; Evenstar et al., 2009; Rech et al., 2010; Jordan et al., 2014; Rech et al., 2019) and was interrupted by several arid and semi-arid stages in the higher elevated regions of the western Andean margin (Sáez et al., 2012; Jordan et al., 2014). The middle Miocene also marks the onset of deep canyon incision on the western Andean slope in northern Chile that are either linked to these climatic changes (*e.g.*, García et al., 2011; Cooper et al., 2016) or to surface uplift related to westward tilting in the forearc (Farías et al., 2005; Garcia and Hérail, 2005; Hoke et al., 2007).

Starting in the Eocene to the Oligocene and throughout the Miocene, widespread, diachronous uplift of individual ranges in the Puna started to disconnect fluvial systems from the foreland and led to the establishment of internally drained basins in a semi-arid environment (see Strecker et al., 2007, for a review). Arid conditions were finally established in the late Miocene, when the Eastern Cordillera had built sufficient topography to block moisture transport towards the Puna plateau (Coutand et al., 2006). To the east, structurally similar basins in the Eastern Cordillera, Santa Barbara province and Sierra Pampeanas alternated between internal drainage conditions and open drainage to the foreland (Hilley and Strecker, 2005; Strecker et al., 2007). In the late Miocene (~9 Ma, Coutand et al., 2006), the sedimentary deposits in these intermontane basins mark a drastic shift from a (semi-)arid climate to fluvial conditions characterized by floodplains, lakes and swamps supporting an important flora and fauna (Starck and Anzótegui, 2001). Higher moisture availability during the late Miocene is also indicated by the appearance of authigenic clays in paleosols in the intermontane Santa María valley (Sierra Pampeanas) (Kleinert and Strecker, 2001), and from stable isotope data in pedogenic carbonates, leaf wax and volcanic class in the intermontane Angastaco Basin (Eastern Cordillera) (Rohrmann et al., 2016). Contemporaneously, a change from (semi-)arid to more humid conditions is also observed in the Subandean zone from sedimentary facies analyses (Uba et al., 2005, 2007) and from a fourfold increase in the sedimentation rate in the foreland stratigraphy (Uba et al., 2007); although the latter can also be associated to tectonic processes. These widespread climatic changes observed in late Miocene sediments are commonly attributed to the establishment of efficient orographic barriers due to the uplift of the Altiplano-Puna plateau, Eastern Cordillera and basement blocks in the Sierra Pampeanas (*e.g.*, Starck and Anzótegui, 2001; Coutand et al., 2006; Strecker et al., 2007). At present-day, the main source of moisture along the eastern side of the Andes is the LLJ which is a direct consequence of the interaction between the easterly trade-winds and the Andean mountain belt (Lenters and Cook, 1995; Campetella and Vera, 2002; Insel et al., 2010). It is thus likely that the topographic uplift resulted in the initiation or amplification of the South American monsoon and associated LLJ at around 10-7 Ma (*e.g.*, Strecker et al., 2007; Mulch et al., 2010; Rohrmann et al., 2016). The onset of fluvial megafan deposits in the Subandean zone in the late Miocene (Horton and DeCelles, 2001; Uba et al., 2005), which can be attributed to a monsoonal climate (Leier et al., 2005), corroborates this interpretation. Finally, the eastward migration of deformation in the Pliocene resulted in the subsequent uplift of individual ranges that acted as local orographic barriers, which led to focused precipitation on their eastern flank and renewed aridification in the adjacent intermontane basins located to the west (*e.g.*, Strecker et al., 1989; Kleinert and Strecker, 2001; Sobel and Strecker, 2003; Coutand et al., 2006).

In the southern part of the study area and west of the drainage divide, Cenozoic continental deposits between 27-37° S are sparse and paleoclimate reconstructions rely mainly on paleoflora

studies with poor data coverage (Villagrán et al., 2004; Gayó et al., 2005; Hinojosa, 2005). These reconstructions rely on the assumption that the paleoclimatic conditions can be inferred from the present-day environment of the closest living relative and are thus subject to high uncertainty. The paleobotanic analyses indicate a shift from a Paleocene-to-Eocene (sub-)tropical climate towards drier and colder conditions from the end of the Eocene to the early Miocene (Villagrán et al., 2004; Gayó et al., 2005; Hinojosa, 2005). The re-appearance of sub-topical flora (Hinojosa, 2005) and subtropical sea surface temperatures revealed by strontium isotopes of marine fossils (Nielsen and Glodny, 2009) suggest a warmer and more humid climate during the Mid-Miocene Climatic Optimum. On the eastern side of the Andes at these latitude, paleoclimatic evidence comes mainly from the basin stratigraphy of the foreland. Here, upper Cretaceous to Paleocene fluvial and lacustrine sediments were replaced by semi-arid conditions with ephemeral rivers and playa lake deposits in the Paleocene-Eocene (Fosdick et al., 2017). In the Oligocene to the early Miocene, arid conditions led to the establishment of extensive eolian dune fields that covered large parts of the foreland (Jordan et al., 2001b; Tripaldi and Limarino, 2005; Fosdick et al., 2017; Buelow et al., 2018). Clay mineralogy and isotope analyses of paleosoils from an intermontane basin adjacent to the Frontal Cordillera (Ruskin and Jordan, 2007) and the onset of fluvial and lacustrine deposits in the middle Miocene (Jordan et al., 2001b; Ciccioli et al., 2014; Buelow et al., 2018) finally record a shift to renewed semi-arid conditions with seasonal precipitation.

In general, the paleo-climate of the northern and central segments of our study area is strongly influenced by the rise of the Andean mountain belt that led to the establishment or intensification of the South American Monsoon on its eastern flank and to aridification on its western side (*e.g.*, Strecker et al., 2007). The onset of glaciations in West Antarctica and the formation of the cold Humboldt current in the middle Miocene probably enhanced this aridification (Houston and Hartley, 2003, and references therein). This first-order climatic pattern was overprinted by several global cold and warm phases that correlate well with plate tectonic processes (*e.g.*, Zachos et al., 2001; Ruddiman, 2008). However, the sedimentary records used to reconstruct paleo-climates during the Cenozoic are often too incomplete and resolutions are too low to draw firm conclusions about possible feedbacks. One of the best studied climatic transition occurred during the Late Cenozoic, when the global climate cooled (Zachos et al., 2001) and evolved towards high-amplitude oscillating conditions expressed by interglacial-glacial cycles throughout the Plio-Pleistocene (Shackleton et al., 1984). Many studies suggest that Pleistocene glaciation has had a global impact on the topographic evolution, relief, valley shape and erosion rates in mountainous landscapes (*e.g.*, Molnar and England, 1990; Montgomery et al., 2001; Shuster et al., 2005; Egholm et al., 2009; Shuster et al., 2011; Herman et al., 2013). Hence, past glaciations could have significantly contributed to the exhumation history of the Central Andes and we therefore summarize below evidences of past glaciations observed in the study area.

2.4.2.1 Evidence of past glaciations

The Pleistocene glaciation has had a global impact on the topographic evolution, relief, valley shape and erosion rates in mountainous landscapes (*e.g.*, Molnar and England, 1990; Montgomery et al., 2001; Shuster et al., 2005; Egholm et al., 2009; Shuster et al., 2011; Herman et al., 2013). Hence, past glaciations might have significantly contributed to the exhumation history of the Central Andes.

Glaciers can only grow if the equilibrium line altitude (ELA) is lower than the maximum elevation. North of 27° S in the semi-arid to arid Andes, the current ELA is at an altitude of around 6000 m and the presence of glaciers is restricted to few volcanic edifices exceeding 6000 m (Clapperton, 1983). The ELA also shows a steep east-west gradient due to higher precipitation on the eastern flanks of the Andes (Clapperton, 1994; Klein et al., 1999; Haselton et al., 2002). Between 27 and 40° S, the ELA drops from 6000 m to 1500 m (Schwerdtfeger, 1976; Montgomery et al., 2001; Harrison, 2004) and the east-west ELA gradient is reversed south of 30° S due to the inversion of the dominant wind direction and induced precipitation pattern (Clapperton, 1994). Today, the northernmost glaciers influenced by Westerly precipitation are found up to 27° S (Ammann et al., 2001).

Although evidence of glaciations are found throughout the Andes, most studies focused on the glacial record of Patagonia south of 40° S (*e.g.*, Clapperton, 1983, 1994; Harrison, 2004; Rabassa et al., 2005; Hein et al., 2017), where glaciation started around 7 to 4.6 Ma (Mercer and Sutter, 1982) and was followed by several glacial-interglacial cycles throughout the Plio-Pleistocene (Clapperton, 1983; Harrison, 2004). There is also considerable evidence for extensive late Pleistocene icefields and valley glaciers between 32 and 37° S on the western side of the Andes (Clapperton, 1994; Harrison, 2004; Zech et al., 2008; Charrier et al., 2019). Mapped and dated moraine deposits at 33 to 34.5° S show that valley glaciers have descended as low as 950-1300 m during the last glacial maximum (LGM) (Herrera Ossandón, 2016; Charrier et al., 2019) and thus have covered large parts of the catchments. Furthermore, radiometrically dated volcanic layers indicate that most valley incision in the higher Andes west of the drainage divide has occurred during the Pleistocene, with incision rates between 1.2 and 2.8 km/Ma during the last 1 Ma (Farías et al., 2008). Glacial growth in this region likely responded to increased precipitation associated with intensified Westerlies and may have occurred before (35-40 ka) the global LGM (Zech et al., 2008, 2011). Evidence for higher precipitation before and during the LGM, between 40 and 17 ka, also comes from grain-size and clay mineral analyses in marine sediment cores offshore Chile at 27° S (Stuut and Lamy, 2004) and 33° S (Lamy et al., 1999) and from palynological, sedimentological and isotopic data from a lake core from Laguna Tagua Tagua at 34.5° S (Heusser, 1983; Valero-Garcés et al., 2005). On the contrary, drier conditions prevailed during the early to

mid-Holocene warm phase (Lamy et al., 2001; Jenny et al., 2003; Stuut and Lamy, 2004; Valero-Garcés et al., 2005). These climatic changes might be attributed to shifts in the core zone of the Westerlies in response to sea surface temperature in the eastern South Pacific Ocean (*e.g.*, Lamy et al., 2010).

Glaciations in the semi-arid Andes up to 27° S north were less developed and restricted to higher elevations, with late Pleistocene ELA's located around 4000 m and the lowest preserved terminal moraine reaching down to 3450 m (Ammann et al., 2001; Harrison, 2004; Zech et al., 2008). Several cirque and valley glaciations are also observed in the Altiplano-Puna and in the Sierra Pampeanas which advanced during periods of intensified monsoonal precipitation (*e.g.*, Haselton et al., 2002; Zech et al., 2008; Baker and Fritz, 2015; D'Arcy et al., 2019). Colder temperatures and increased moisture on the eastern flank of the Andes led to a significant drop-down in Pleistocene snowlines of 300 m in the Puna and 900 m in the Sierra Pampeanas (Haselton et al., 2002). The extent to which these glaciations have affected the topography in the Central Andes remains debated. Montgomery et al. (2001) highlighted a strong latitudinal correlation between mean mountain height and the position of the ELA. Rehak et al. (2010) investigated the influence of climate on relief in Chile between 15.5 and 41.5° S and identified the region between 28 and 35° S as a zone of high local relief (750 m) generated by repeated glacial erosion during the Quaternary.

Precipitation modulates erosion and thus influences exhumation and sediment storage, recycling and transport out of the system. According to the sedimentary record, several climatic changes could have left a signal in the exhumation history of the Central Andes. The most important change occurred during the late Miocene, when the Andes reached elevations high enough to act as an orographic barrier and initiated the South American Monsoon system (*e.g.*, Strecker et al., 2007). This led to increased precipitation at the eastern mountain front and thus possibly to higher erosion rates in parts of the Eastern Cordillera, Santa Barbara system, Sierra Pampeanas and Subandean zone (*e.g.*, Horton and DeCelles, 2001; Starck and Anzótegui, 2001; Uba et al., 2007). In northern Chile during this time, hyperarid conditions were established (*e.g.*, Rech et al., 2010; Jordan et al., 2014) and deep canyon incision started (Farías et al., 2005; Garcia and Hérail, 2005; Hoke et al., 2007; García et al., 2011; Cooper et al., 2016). Furthermore, the mid-Pleistocene shift to a highly oscillating climate (Zachos et al., 2001) and the occurrence of Pleistocene glaciation in the Central Andes (*e.g.*, Zech et al., 2008) possibly also led to increased exhumation rates in parts of the Central Andes that experienced colder and wetter conditions (*e.g.*, Aguilar et al., 2011).

2.5 Methods

2.5.1 New and compiled data

We collected 149 bedrock samples between 21.8 and 34.9° S latitude in the Chilean Andes that we analysed for AHe (119 samples, Appendix, Table A1), ZHe (92 samples, Appendix, Table A2) and/or AFT (52 samples, Appendix, Table A3). Our sampling strategy was to increase spatial coverage where data was sparse, concentrating on the western side of the Andes. Three analysed samples out of these 149 samples were rejected for all thermochronometric systems (14NC98, CLRK3849, Clin3). The new data includes samples collected on elevation transects at six locations to define age-elevation relationships (AER): samples Clin22A-D (AER-a in Fig. 2.1), CLRK3864 and CLRK3866 to CLRK3868 (AER-b in Fig. 2.1), Clin10A-E, Clin12A-E, Clin16A-E, and Clin25A-D analysed for AHe (all profiles), AFT (Clin22A-D, Clin25A-D and CLRK3864/3865-3868) and ZHe (CLRK3864/3865-3868). Clin22A and Clin25A were additionally dated with the U-Pb method because they were collected from shallow Miocene intrusions with unknown crystallization ages (Appendix, Table A4 and Fig. S5).

The laboratory procedures are detailed in the supplementary material. We use mean ages and their standard deviation for (U-Th)/He data representation and modelling. AHe single grain ages with a U concentration over the grain mass smaller than 2 ppm and/or high He uncertainty (>15%) were rejected because of their low precision (Appendix, Table A1). We also rejected AHe single grain ages with an age difference greater than 50% relative to the average age of the sample, if the other aliquots show consistent ages similar to AHe samples in their surroundings. Additionally, two AHe single grain ages were rejected because they were older than the remaining aliquots, which gave consistent ages, and older than their crystallization (CLRK3853, age difference >17% from average age) or ZHe age (CLRK3864, age difference >35% from average age). We rejected three samples that showed large age dispersions (1σ>50% of average age, 14NC36, Clin3, CLRK3849), one sample that is significantly younger than its surroundings and whose grains have very low U concentrations (<2 ppm) and high He-uncertainties (14NC38), and one sample that was derived from a Porphyry deposit and whose age overlap with its crystallization and ZHe age (14NC98). Single ZHe grain ages were excluded if they overlap or are older than their crystallization age or if they have age differences greater than 50% relative to the average age of the sample. In total, seven ZHe samples were rejected due to magmatic cooling (14NC26, 14NC29, 14NC31, 14NC70, 14NC98, CLRK3849) and high age dispersion (Huasco87) (Appendix, Table A2).

We calculated AFT central ages, χ^2 probability and age dispersion for apatite fission-track ages (Appendix, Table A3). Although derived from igneous bedrock, nine samples failed the χ^2-test and were decomposed into age peaks using Binomfit (Brandon, 2002). We use the central age if the

major age peaks are similar to the central age and comprised a fraction of grains greater than 75% and for sample 14NC06, which yields two populations with ages similar to the central age. Track lengths could only be measured for 14 of the 54 samples (Appendix, Table A3). Of these, seven samples show bimodal track length distributions with mean track lengths between 12.2 and 14.2 μm and 1σ>2 (Gleadow et al., 1986). One additional sample (CLRK3874) has a track length of 11.72±1.4 μm but this value is based on 5 measured tracks only. Because all but one (Huasco54) of this seven samples pass the χ^2-test and because all central ages have relatively low 1σuncertainties and are consistent with other thermochronological data (AHe, AFT, ZHe) in their surroundings, the samples were included in the inversion. We cannot guarantee that samples for which no track lengths could be measured are not partially reset and these samples might lead to an underestimation of the modelled exhumation rate at their locations. Five samples show low U concentrations (<16 ppm), high uncertainties (1σ>15% of the central age), and low numbers of counted grains (<10) and were rejected. Furthermore, sample 14NC05 was rejected because it is older than its corresponding ZHe age, contains little U (5 ppm) and shows high uncertainty (1σ = 14.8% of the central age). Seven samples are close (<2 Ma, within standard deviation of the mean age) to their magmatic cooling age and were rejected to exclude data corresponding to magmatic cooling instead of exhumation-related cooling (*e.g.*, Murray et al., 2018).

Additionally, we compiled a total of 1177 AHe, AFT, ZHe and ZFT ages from previous studies in the Central Andes between 18 and 36° S (supplementary Table A5, provided in electronic form only). Of those, 255 ages were rejected because they were either of poor quality (*e.g.*, less than 10 grains analyzed for AFT/ZFT), highly dispersed for AHe/ZHe (1σ differs for more than 100% or 20 Ma from the average) or samples failing the χ^2-test, unreset detrital samples (*i.e.*, ages older than or overlapping with their formation age) or partially reset samples that were reported as such in the literature. Additionally, we excluded 80 AFT, ZHe and ZFT ages that are, within standard deviation of the sample age, less than 2 Ma younger than the sample intrusion age to exclude data corresponding to magmatic cooling instead of exhumation-related cooling. This value is a conservative estimate for magmatic cooling (Murray et al., 2018). 30 of those samples are from volcanic or porphyry rocks or dykes, the remaining ones are from intrusive rocks of which most can be related to porphyry copper deposits and associated hydrothermal circulation (*e.g.*, Maksaev and Zentilli, 1999; Deckart et al., 2005; Farías et al., 2008; Maksaev et al., 2009). We also excluded 18 samples that are derived from or located close to hydrothermally altered rocks or hot springs.

Including our 238 accepted ages, 1062 thermochronological ages from 695 samples were used in total to constrain the exhumation rate history of the central-southern Central Andes (Fig. 2.6, supplementary Table A5).
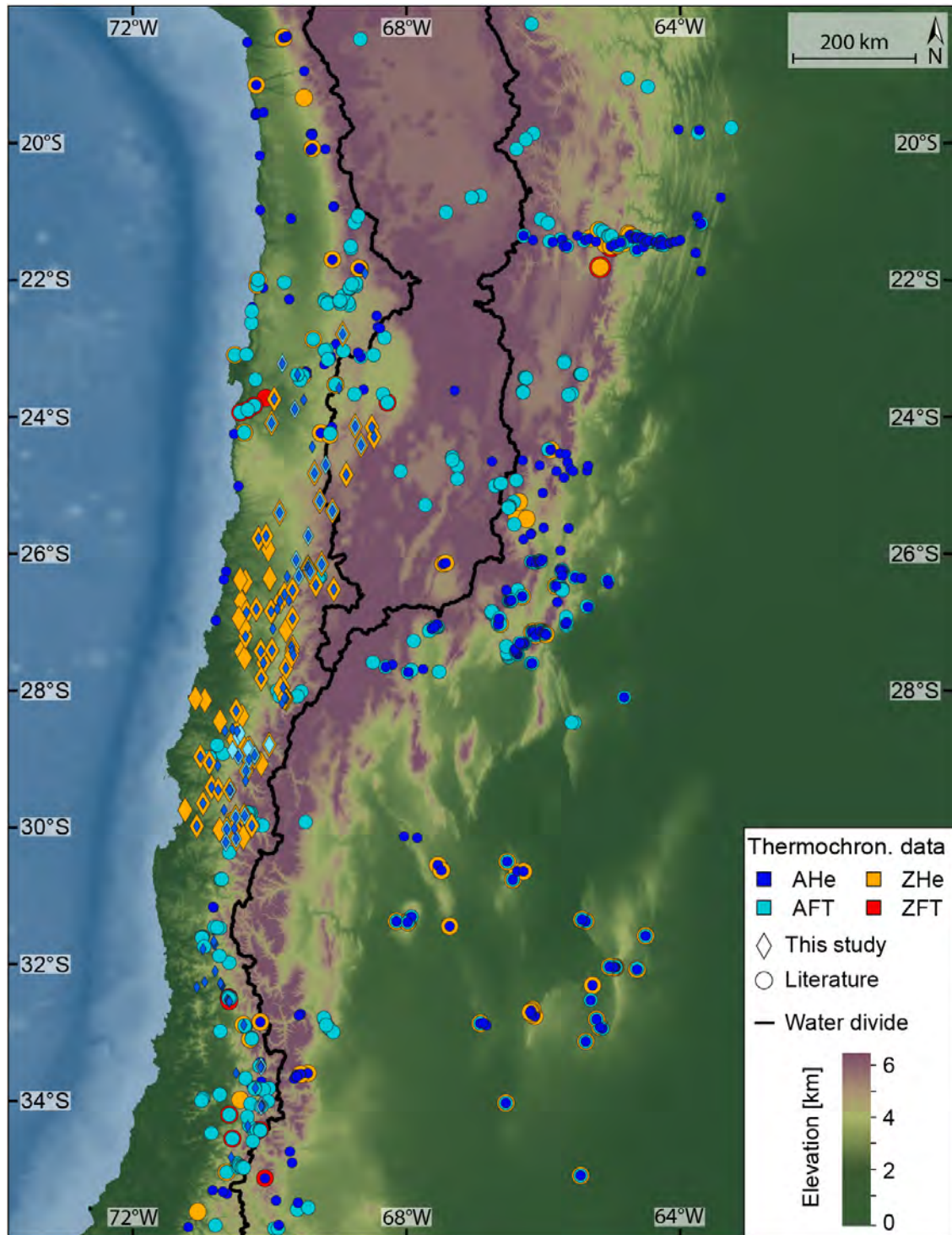
Figure 2.6: Low-temperature thermochronological ages compiled from literature and own data (see supplementary Table A5 for data and references). Topography from GMTED2010, 7.5 arc-s (Danielson and Gesch, 2011), bathymetry from GEBCO_2014 (Weatherall et al., 2015).

2.5.2 Inversion of data into exhumation rate histories

We use the inversion method described in Fox et al. (2014) and modified by Herman and Brandon (2015) to model the rate of exhumation for the last 80 Ma in the central-southern Central Andes. In this method, the depth from the surface to the closure depth, z_c, is described as the integral of the exhumation rate, $\dot{e}$, from the cooling age, tau, to the present day, which is translated to logarithmic space to avoid negative exhumation rates:

$$z_c = \int_0^\tau \dot{e} \, \mathrm{d}t \rightarrow \zeta = ln(\int_0^\tau \exp(\varepsilon) \, \mathrm{d}t) \tag{2.1}$$

where $\zeta = ln(z_c)$ and $\varepsilon = ln(\dot{e})$. The model assumes monotonic exhumation histories and therefore does not account for reburial. A thermal model that accounts for heat advection and the effects of topography is used to model the geothermal gradient and rock cooling histories. From the thermal histories, we derive the closure depth using Dodson's definition for the closure temperature, *i.e.*, the temperature at which the sample was at the time given by its apparent age (Dodson, 1973). This inverse problem is weakly non-linear and can be solved using the non-linear least-squares method (*e.g.*, Tarantola, 2005). This is achieved by discretization of the integral in Equation 2.1 into fixed time intervals Δt:

$$\zeta = ln \left(\sum_{i=0}^\tau exp(\varepsilon_i) * \Delta t \right) \tag{2.2}$$

Similar to Fox et al. (2014), we impose the condition that ε is spatially correlated by defining an a priori model covariance matrix, $\mathbf{C_M}$. This matrix is constructed for all time intervals using the horizontal distance between the ith and jth data points, d, and a Gaussian correlation function,

$$\mathbf{C_M}(i,j) = \sigma^2 exp \left(-\left(\frac{d}{L} \right)^2 \right) \tag{2.3}$$

where L is a correlation length scale, d the distance between samples, and σ^2 is the a priori variance serving primarily as a weighting factor. This covariance matrix enables, but does not impose, that data close to each other share a common exhumation history. Finally, a second non-linearity is implied because both the temperature field and closure depth calculations depend on the solution, *i.e.*, on the estimated erosion rates (Fox et al., 2014). The non-linear problem is solved using the steepest descent algorithm (Tarantola (2005), p.70),

$$\varepsilon_{m+1} = \varepsilon_m - \mu \left(\mathbf{C_M} \mathbf{G}^t \mathbf{C_D}^{-1} \left(\zeta_m - \zeta_{tm} \right) + \left(\varepsilon_m - \varepsilon_{prior} \right) \right) \tag{2.4}$$

where m is the iteration number, ε_{prior} is the logarithm of our initial guess of the erosion rate $\dot{e}_{prior}$, $\mathbf{C_D}$ is the data covariance matrix, μ is an ad hoc parameter chosen by trial and error that controls

how rapidly the model parameters change, ζ_m and ζ_{obs} are the logarithms of the modelled and observed closure depths calculated with the thermal model, and $\mathbf{G}$ is obtained by computing the derivatives of $ln\left(\sum_{i=0}^{\tau} exp(\varepsilon_i) * \Delta t\right)$ with respect to ε (Herman and Brandon, 2015).

The model and data covariance must be chosen to minimize trade-off between model and data variance, σ_d^2 (*e.g.*, Aster et al., 2011). We start the iterative process by assigning the a priori expected value of the exhumation rate, $\dot{e}_{prior}$, and a final prior geothermal gradient, G_0. As any Bayesian inversion problem (*e.g.*, Tarantola, 2005), the model solution depends on the initial $\dot{e}_{prior}$ since it remains part of the solution (Equation 2.4) (Fox et al., 2014; Herman et al., 2013; Jiao et al., 2017; Willett et al., 2020). This dependency is more pronounced when data have poor resolution capacity. Similarly, the model also depends on our choice of G_0 due to the strong coupling between the geothermal field and the exhumation rate. In particular, higher geothermal gradients lead to shallower closure depths and thus to less exhumation. Higher exhumation rates increase the geothermal gradient because heat is more efficiently advected towards the surface. We run our model for two different $\dot{e}_{prior}$ values (0.1 and 0.5 km/Ma) and geothermal gradients G_0 (25 and 50 ℃/km) to test the robustness of our results. The tested $\dot{e}_{prior}$ values are endmember values for regions that show very low Cenozoic exhumation rates like the Atacama Desert (<0.2 km/Ma, Avdievitch et al. (2018)) and regions that show higher exhumation rates like the southwestern Puna plateau (0.3 km/Ma to >1 km/Ma, Carrapa et al. (2005); Carrapa and DeCelles (2008)) or the southern Eastern Cordillera (0.1 to 0.6 km/Ma, Coutand et al. (2006); Deeken et al. (2006)). The choice of G_0 and the length of time the model is run, *i.e.*, 80 Ma, set the final geothermal gradient at the end of the prior model. We adjust the initial geothermal gradient G_{ini} (*i.e.*, at 80 Ma) to generate a final prior geothermal gradients at the end of the prior model (G_0) of 25 and 50 ℃/km, respectively, under $\dot{e}_{prior}$ values of 0.1 and 0.5 km/Ma. For example, an initial geothermal gradient G_{ini} of 22.3 ℃/km and running the model for 80 Ma with an $\dot{e}_{prior}$ of 0.1 km/Ma leads to a final prior geothermal gradient G_0 of 25 ℃/km in the most recent time step. Because the geothermal gradient is influenced by heat advection, an $\dot{e}_{prior}$ of 0.5 km/Ma requires a smaller G_{ini} (14.5 ℃/km) to get the same final prior geothermal gradient as in the inversion with an $\dot{e}_{prior}$ of 0.1 km/Ma. Similar G_0's for the different $\dot{e}_{prior}$ values are important to allow investigating the influence of the $\dot{e}_{prior}$ on the modelled exhumation rates. Finally, the modelled geothermal gradients in the most recent time step (*i.e.*, as constrained by the modelled exhumation rates) should be comparable to observed modern geothermal gradients in the Central Andes. A G_0 of 25 ℃/km and a time length of 80 Ma leads to modelled geothermal gradients in the range of 24-34 ℃/km ($\dot{e}_{prior}$ = 0.1 km/Ma) and 16-49 ℃/km ($\dot{e}_{prior}$ = 0.5 km/Ma) for the last time step. These values are consistent with most heat flow measurements of the Central Andes apart from the Coastal Cordillera, although few data are available (*e.g.*, Springer and Förster, 1998; Höfer-Öllinger and Millen, 2010; Ege et al., 2007) (supplementary Fig. S4). Nevertheless, because many data especially in the southern segment

were sampled closer to the magmatic arc and thus in areas with geothermal gradients up to 70 °C/km, we also test for a G_0 of 50 °C/km. Such a high final prior geothermal gradient results in modelled present-day values between 46-60 °C/km ($\dot{e}_{prior}$ = 0.1 km/Ma) and 31-75 °C/km ($\dot{e}_{prior}$ = 0.5 km/Ma), which are significantly higher than observed in the Central Andes.

To assess the solution, we compute the reduced variance which is the ratio between the a posteriori and a priori variance. The reduced variance ranges from 0 to 1 and is an indication of whether the solution has improved by incorporating data or not. The closer to zero, the better the solution is. We set the ratio between the a priori variance and a priori exhumation rate in logarithmic space equal to 7 for all inversions. This relatively high value permits more variation in the inverse solution and improves the fit to the data (Fox et al., 2014).

The use of the correlation structure $\mathbf{C_M}(i, j)$ was recently criticized by Schildgen et al. (2018) who argued that the increase in late Cenozoic exhumation rates observed in modelled thermochronological data (Herman et al., 2013; Fox et al., 2015) is an artifact caused by the inversion method we use here. Schildgen et al. (2018) performed synthetic tests and a reanalysis of the results reported in Herman et al. (2013). They showed test examples of uplifting blocks and argued that the correlation structure used in the inversion scheme inappropriately combines data across faults, which creates a false inference of an acceleration of erosion. Willett et al. (2020) recently reviewed their analysis. They show that Schildgen et al. (2018) used different boundary conditions in the model used to generate synthetic data and for the inversion. In the forward model, Schildgen et al. (2018) applied a fixed temperature at the base of the model, whereas they used a flux boundary condition in the inversion. The two models predict significantly different geothermal gradients, and therefore significantly different thermochronometric ages. The spurious errors that Schildgen et al. (2018) attributed to the correlation structure were a consequence of these mismatched geotherms. Willett et al. (2020) performed comparable tests, but with common geotherms between forward and inverse models, and showed that the correlation structure does not generate significant errors including the false increases of erosion. The spatial correlation may smooth exhumation rates across fault boundaries, but does not impose a common history on correlated data. Willett et al. (2020) found that with sufficient age coverage, an age inversion, such as we use here, will fully resolve spatial variability in exhumation rates. With sparse data, resolution is decreased, but does not create artifacts. Finally, Willett et al. (2020) compared inversion results for natural examples (*e.g.* the Alps) in which they include data from either side of the fault or only from one side. They found inversion results that are nearly identical to each other. To further ensure that our results are not affected by the concerns raised by Schildgen et al. (2018), we perform additional tests (1) for different correlation length scales (10, 20 and 30 km) and (2) by splitting the study area into fault blocks that are independent from each other (*i.e.*, no correlation between

data in different blocks). We find that the change of the correlation length scale or the inclusion of fault blocks does not affect our interpretation.

In total, we provide eight inversions to test different combinations of G0 and $\dot{e}_{prior}$ values (four inversions, A-D) and to explore the importance of the correlation length scales (2 inversions, E&F) and fault blocks (2 inversions, G&H). Each inversion is run for 80 Ma, which is the approximate onset of compressional deformation in the Central Andes (Fig. 2.3). Therefore, only thermochronological ages younger than or equal to 80 Ma are used in the inversions (837 ages). Finally, past and present geothermal gradients are unknown in most parts of the Central Andes. We thus compare our modelled exhumation rates with rates derived from age-elevation profiles at 3 locations, which provide independent constrains on exhumation rates (*e.g.*, Wagner et al., 1979; Gleadow and Fitzgerald, 1987; Fitzgerald et al., 1995), although Fox et al. (2014) showed that exhumation rates are robust with respect to the thermal model where data constrain exhumation rates due to age elevation relationships.

2.6 Results

2.6.1 Thermochronological ages

In the following section, we first analyse how the compiled thermochronological ages vary in time and space, including new and previously published ages (Fig. 2.6, supplementary Table A5). Whereas the Western/Principal Cordillera (348 ages), the Sierra Pampeanas (277 ages), and the Coastal (124 ages), Eastern (93 ages) and Frontal (105 ages) Cordilleras are relatively well covered with data, the other tectonomorphic units contain a maximum of 42 ages (Fig. 2.1, Fig. 2.6). Furthermore, more data are available in the western part of the orogen than in the east, where data density is high only at 21° S and in the southern Eastern Cordillera and northern Sierra Pampeanas. The absence of a certain age population in tectonomorphic structures where only few ages were dated can thus simply be a sampling bias.

We split the compiled data set along the main drainage divide to account for the climatic gradients that are opposite on the western and eastern sides of the Andes (Fig. 2.7, Fig. 2.8). Data from the internally draining Altiplano-Puna plateau are merged with data in the west. Relative frequencies of the age distributions for the western and eastern sides of the Andes are shown in the supplementary Figure S1. Furthermore, we provide latitudinal cross-sections for the northern, central and southern segments to account for their different tectonic settings (Fig. 2.9). In the data description hereafter, the numbers in brackets represent the number of samples in a given tectonomorphic or temporal unit.

2.6.1.1 Data to the west of the main drainage divide

Figure 2.7 shows the 586 thermochronological ages that are located to the west of the drainage divide. A major feature is the significant drop in ages south of ca. 32° S observed in all four thermochronological systems.

North of 32° S, the distribution of the AHe and AFT ages share many similarities and therefore we describe them here together. The AHe (226) and AFT (147) ages range from 10 to 109 Ma and from 16 to 198 Ma, respectively (Fig. 2.7, supplementary Fig. S1A and Table A5). Both systems have one exception located at 30° S in the Frontal Cordillera at 2050 m elevation with an AHe age of 6.9±0.6 Ma and an AFT age of 8.4±0.8 Ma (Rodríguez et al., 2018). Palaeocene and older ages are a minor fraction (23 AHe and 30 AFT ages). They are mainly located in the Coastal Cordillera (16 AHe and 17 AFT) and are rare and scattered from the Central Depression to the Puna Plateau. The majority of ages are Eocene to Oligocene (148 AHe and 108 AFT ages) and mostly located in the Principal Cordillera (94 AHe and 65 AFT ages), common in the Frontal Cordillera (11 AHe and 28 AFT ages) and sparse elsewhere. Miocene ages (56 AHe and 9 AFT ages) are common in the Frontal (19 AHe and 4 AFT ages) and Principal/Western Cordilleras (31 AHe and 2 AFT ages) but are sparse in the Coastal Cordillera and Puna plateau.

South of 32° S, the AHe ages (36) range from 0.5 to 35 Ma (Fig. 2.7, supplementary Fig. S1B). Only four ages are Oligocene. These are located close to 32° S in the Coastal (2) and Principal (2) Cordilleras. The remaining AHe ages are all located in the Principal Cordillera. Miocene ages (9) are located closer to the mountain front, whereas most Plio-to-Pleistocene ages (23) are located closer to the drainage divide. The AFT data (50) range from 1.9 to 51 Ma. They show a minority of Eocene ages in the Principal (5) and Coastal Cordilleras (4), one early Miocene age in the Central Depression (1), and a large majority of ages (40) younger than 13 Ma located in the Principal Cordillera. Sixteen samples are Plio-Pleistocene in age.

ZHe ages (107) north of 32° S range from 31 to 221 Ma (Fig. 2.7, supplementary Fig. S1A). Pre-Cretaceous ages (6) range between 150 and 221 Ma and are located in the Principal (5) and Frontal (1) Cordilleras. Cretaceous ages (51) are found in the Coastal Cordillera (27), the Principal (11) and Frontal Cordilleras (10), the Puna plateau (2), and the Central Depression (1). The remaining ages are Paleogene (50) and located in the Principal (34), Frontal (13), and Coastal (3) Cordilleras. South of 32° S, the Principal Cordillera yields Miocene (3) to Pliocene (3) ZHe ages between 13 and 2.8 Ma (Fig. 2.7, supplementary Fig. S1B).

Only thirteen ZFT samples located west of the Andean crest remained after excluding ages that represent magmatic cooling ages, non-reset detrital ages, or samples that were most likely hydrothermally altered (supplementary Table A5). Among the accepted samples, six are located
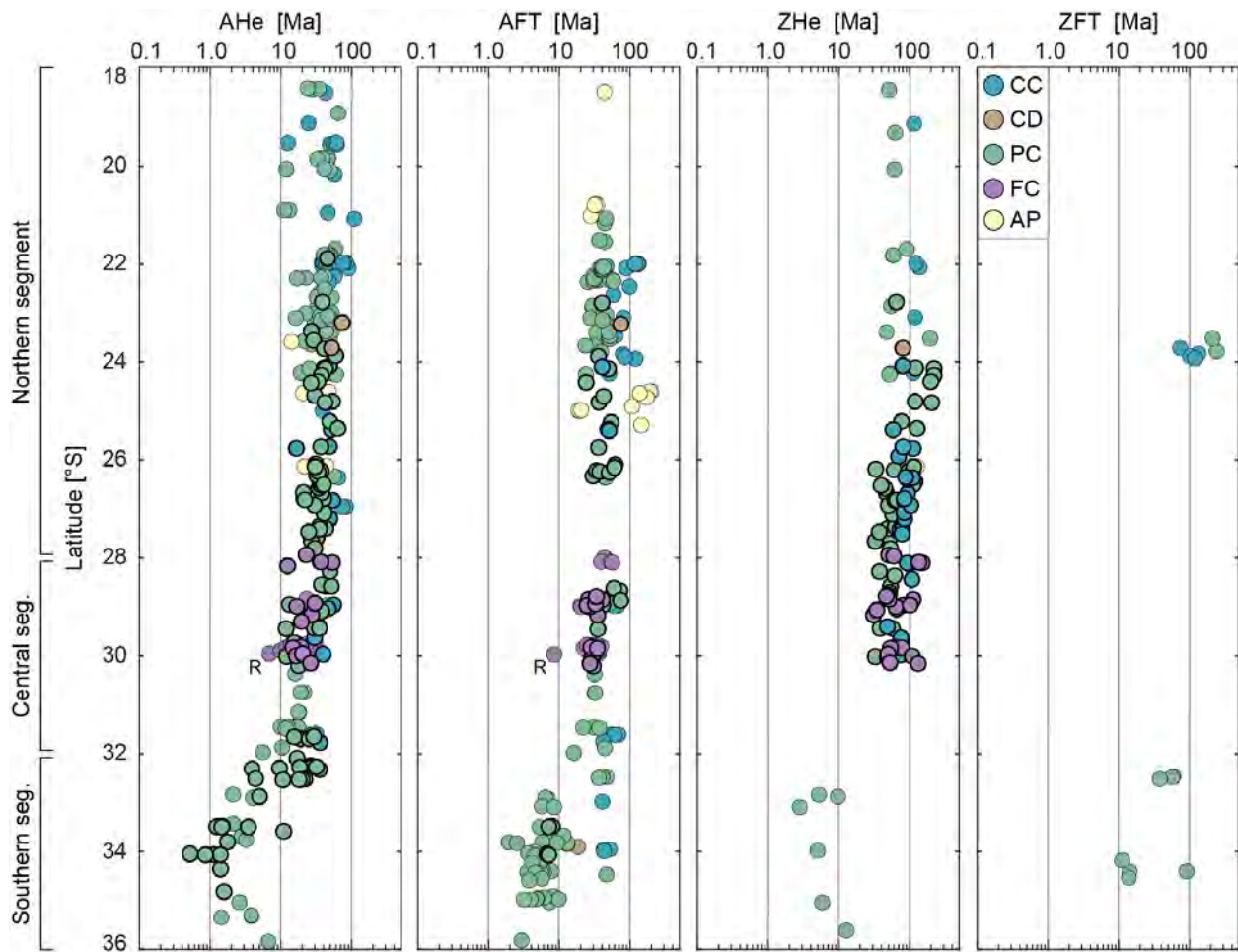
Figure 2.7: Thermochronological ages west of the drainage divide along the strike of the Andes, including the internally drained Altiplano-Puna plateau. Colors represent tectonomorphic units from Fig. 2.1: AP = Altiplano-Puna plateau; CC = Coastal Cordillera; CD = Central Depression; FC = Frontal Cordillera; PC = Western/Principal Cordillera. Data from this study are highlighted with bold black rim. Ages south of 32° S are significantly younger than in the north for all thermochronologic systems. R denotes the exceptionally young sample from Rodríguez et al. (2018).

north of 32° S (Fig. 2.7). They show Triassic ages in the Western/Principal Cordillera and Cretaceous ages in the Coastal Cordillera. South of 32° S, all ZFT samples are located in the Principal Cordillera (7). One age is Late Cretaceous, three ages are late Paleocene to Eocene and three are middle to late Miocene (Fig. 2.7).

In summary, the majority of the thermochronological ages west of the Andean water divide and north of 32° S are Paleogene (Fig. 2.7, supplementary Fig. S1A). The few ZFT ages and the ZHe additionally show a major Cretaceous population. Among the Paleogene samples, AHe and AFT ages are predominantly Eocene to Oligocene whereas ZHe ages are mostly Paleocene to Eocene (supplementary Fig. S1A). These ages are distributed from the Coastal Cordillera to the

Western/Principal and Frontal Cordilleras to the Altiplano-Puna plateau. Miocene cooling ages, mostly AHe ages and few AFT ages, are mainly located in the Western/Principal and Frontal Cordilleras. Finally, pre-Cenozoic ages of all four systems, yet frequently recorded by the ZHe system, are common in the Coastal Cordillera but are also present in other units. Ages south of 32° S are significantly younger than in the north (Fig. 2.7, supplementary Fig. S1B). Almost all ages are located in the Principal Cordillera. Plio-Pleistocene to Miocene ages prevail, whereas pre-Cenozoic ages are only observed in the ZFT system.

2.6.1.2 Data to the east of the main drainage divide

East of the Andean range crest, the quantity of data (476) is lower than to the west (Fig. 2.6). Data are dense in the northern segment along a cross-section at 21° S in the Eastern Cordillera and Inter- and Subandean zones as well as in the southern Eastern Cordillera and the northern Sierra Pampeanas, whereas they are sparse in the Frontal Cordillera, Precordillera and eastern Principal Cordillera in the middle and central segments (Fig. 2.1). Unlike to the western side of the orogen, no clear spatial pattern is observed along a north-south transect (Fig. 2.8). Young AHe ages are present all along the eastern margin of the orogen. AFT and ZHe ages are youngest between 27 and 28° S.

As observed to the west of the drainage divide, the spatial distribution of the AHe and AFT ages east of the divide share some similarities and are thus described together. AHe ages range from 1.6 to 294 Ma (168 samples) and AFT ages from 2.6 to 270 Ma (169 samples) (Fig. 2.8, supplementary Fig. S1C). All but one Pre-Cenozoic AHe ages (44) and the majority of the pre-Cenozoic AFT ages (45) are located in the Sierra Pampeanas. The pre-Cenozoic AHe age exception is located in the Frontal Cordillera. The remaining pre-Cenozoic AFT ages (9) are scattered in the foothills of the Precordillera (6), the Subandean zone (2) and the foreland close to Malargüe (1). Paleogene ages (27 AHe and 39 AFT) include a majority of mid-Eocene to Oligocene ages particularly dense in the Eastern Cordillera (7 AHe and 20 AFT) and the Sierra Pampeanas and Santa Barbara range (17 AHe and 12 AFT). The rest is scattered among the Puna (5 AFT), Interandean zone (3 AHe) and Frontal Cordillera (2 AFT). Miocene ages (77 AHe and 60 AFT) are distributed over most tectonomorphic units of the eastern side of the drainage divide and are most frequent in the Eastern Cordillera (25 AHe and 20 AFT), Sierra Pampeanas (20 AHe and 15 AFT) and Interandean zone (20 AHe and 15 AFT). The rest is found in the Subandean zone (6 AHe and 1 AFT), southern Frontal Cordillera (6 AHe), Puna (3 AFT), Precordillera (2 AFT) and in the Principal Cordillera (2 AFT) and adjacent foreland (2 AFT). Pliocene ages (16 AHe and 16 AFT) are mostly observed in the Sierra Aconquíja (4 AHe and all 16 AFT) and the Sierra de Valle Fértil (2 AHe), which are part of the Sierra Pampeanas, and in the Subandean zone (7 AHe). The remaining AHe are distributed among the Interandean zone (1 AHe) and at the southern margin of the Eastern
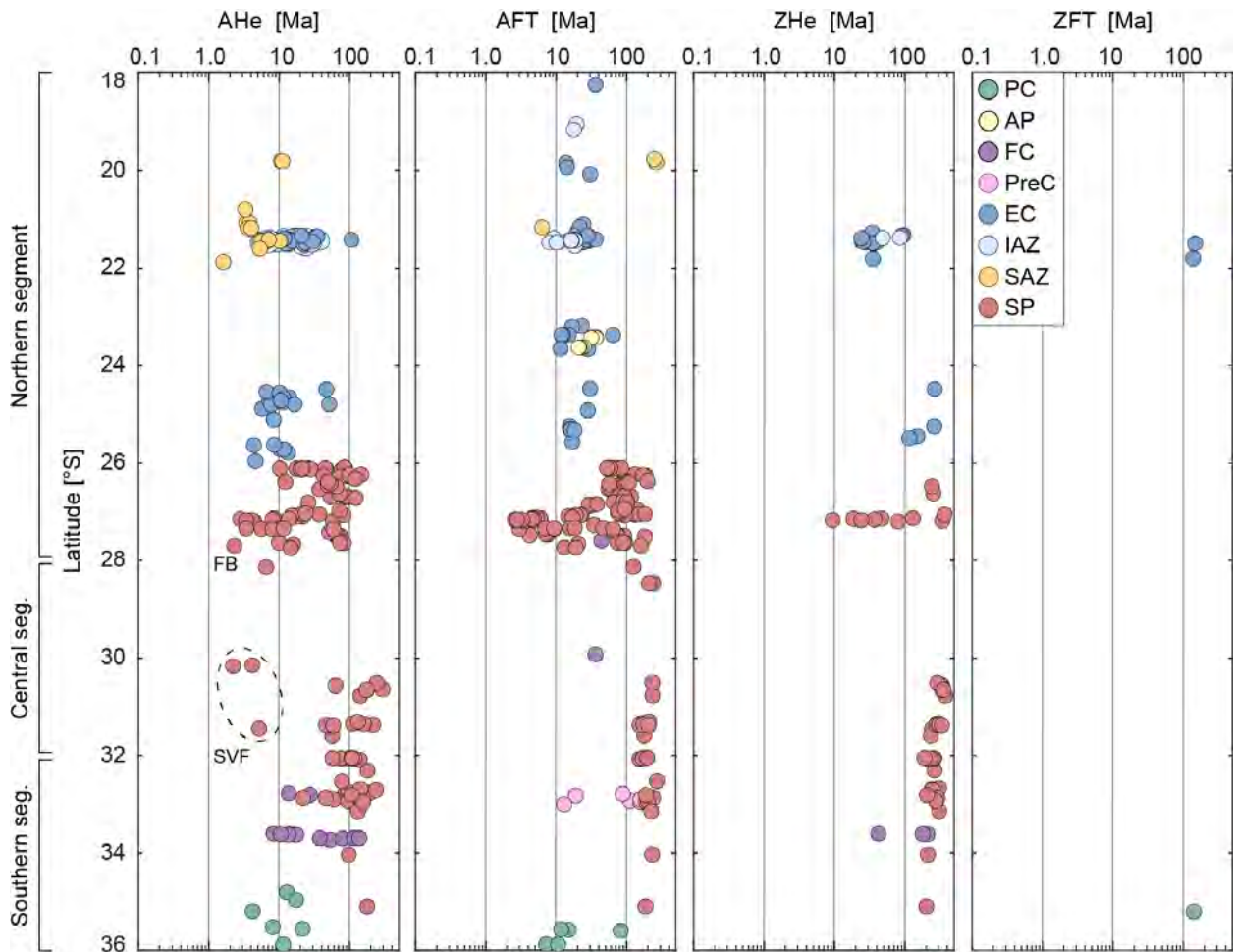
Figure 2.8: Thermochronological ages east of the drainage divide along the strike of the Andes. Colors represent tectonomorphic units from Fig. 2.1: AP = Altiplano-Puna plateau; EC = Eastern Cordillera; FC = Frontal Cordillera; IAZ = Interandean zone; PC = Western/Principal Cordillera; PreC = Precordillera; SAZ = Subandean zone; SP = Sierra Pampeanas and Santa Barbara ranges. AHe, AFT and ZHe systems all show a youngest age cluster between 26° and 28°S but no clear pattern is observed. The AHe data additionally show young ages in the Subandean zone (21-22°S) and in the Sierra de Valle Fértil (SVF; Ortiz et al., 2015). FB denotes the young sample from the Fiambalá Basin (Safipour et al., 2015).

Cordillera (2 AHe). Pleistocene data include only three AHe ages located in the Sierra de Valle Fértil (1) and Fiambalá Basin (1) of the Sierra Pampeanas and in the Subandean zone (1) (Fig. 2.8).

Among the ZHe ages, which range from 9.4 to 378 Ma (63 ages), the majority are pre-Cenozoic (45) and mainly derived from the Sierra Pampeanas (36) (Fig. 2.8, supplementary Fig. S1C). The remaining pre-Cenozoic ages are from the Eastern Cordillera (6), Interandean zone (1) and Frontal Cordillera (2). Eocene to Oligocene ages (16) occur mainly in the Eastern Cordillera (11) and few are derived from the Sierra Aconquíja in the Sierra Pampeanas (3), Interandean zone

(1) and Frontal Cordillera (1). Two ages from the Sierra Aconquíja in the Sierra Pampeanas are Miocene.

The only two ZFT ages in our compilation are from the Eastern Cordillera and yielded Upper Jurassic to Lower Cretaceous ages (Fig. 2.8).

In summary, the eastern dataset shows younger thermochronological ages compared to the western data set north of 32° S and a larger spread of ages (Figs. 2.7, 2.8, supplementary Fig. S1A,C). Pre-Cenozoic ages mainly occur in the Sierra Pampeanas and are abundant in all four thermochronometric systems. Paleogene and Miocene ages from the AHe, AFT and ZHe systems are distributed within most tectonomorphic units, although data are sparse in the Frontal and Principal Cordilleras, Precordillera and the Altiplano-Puna (Fig. 2.1). Pliocene ages are restricted to the AFT and AHe systems (Fig. 2.8). They are found commonly in the Subandean zone and the Sierra Pampeanas and only locally in the southern margin of the Eastern Cordillera. Pleistocene ages are sparse and only observed among the AHe data from the Sierra Pampeanas and the Subandean zone.

2.6.1.3 Latitudinal age distribution

Figure 9 shows the data distribution across the Andes in four latitudinal cross-sections. Thermochronological AHe and AFT ages in the cross-section between 18 and 23.5° S show an eastward decreasing age trend that is particularly important in the AHe system for the Inter- and Subandean zones (Fig. 2.9A). A similar trend can be observed in the cross-section between 23.5 and 28° S in the AHe, AFT and ZHe systems that show much younger ages and a wider age range in the northern Sierra Pampeanas (including the Fiambalá Basin) and the southern Eastern Cordillera than the data located to the west, which are all older than 10 Ma (Fig. 2.9B). The middle segment between 28 and 32° S has less data and ages on the eastern side are restricted to the Sierra Pampeanas. AFT and ZHe ages are younger on the western side, whereas AHe ages are young on both side of the orogen and especially in the Sierra de Valle Fértil located in the Sierra Pampeanas (Bense et al., 2013; Ortiz et al., 2015) (Fig. 2.9C). Finally, the southern segment between 32 and 36° S shows significantly younger ages and a much wider spread of ages in the west compared to the east (Fig. 2.9D).

In summary, most ages in our database are Eocene to Miocene. Plio-to Pleistocene ages are common in three areas: in the Subandean zone and the Sierra Pampeanas (especially in the Sierra Aconquíja) east of the drainage divide and in the southern Principal Cordillera west of the drainage divide.
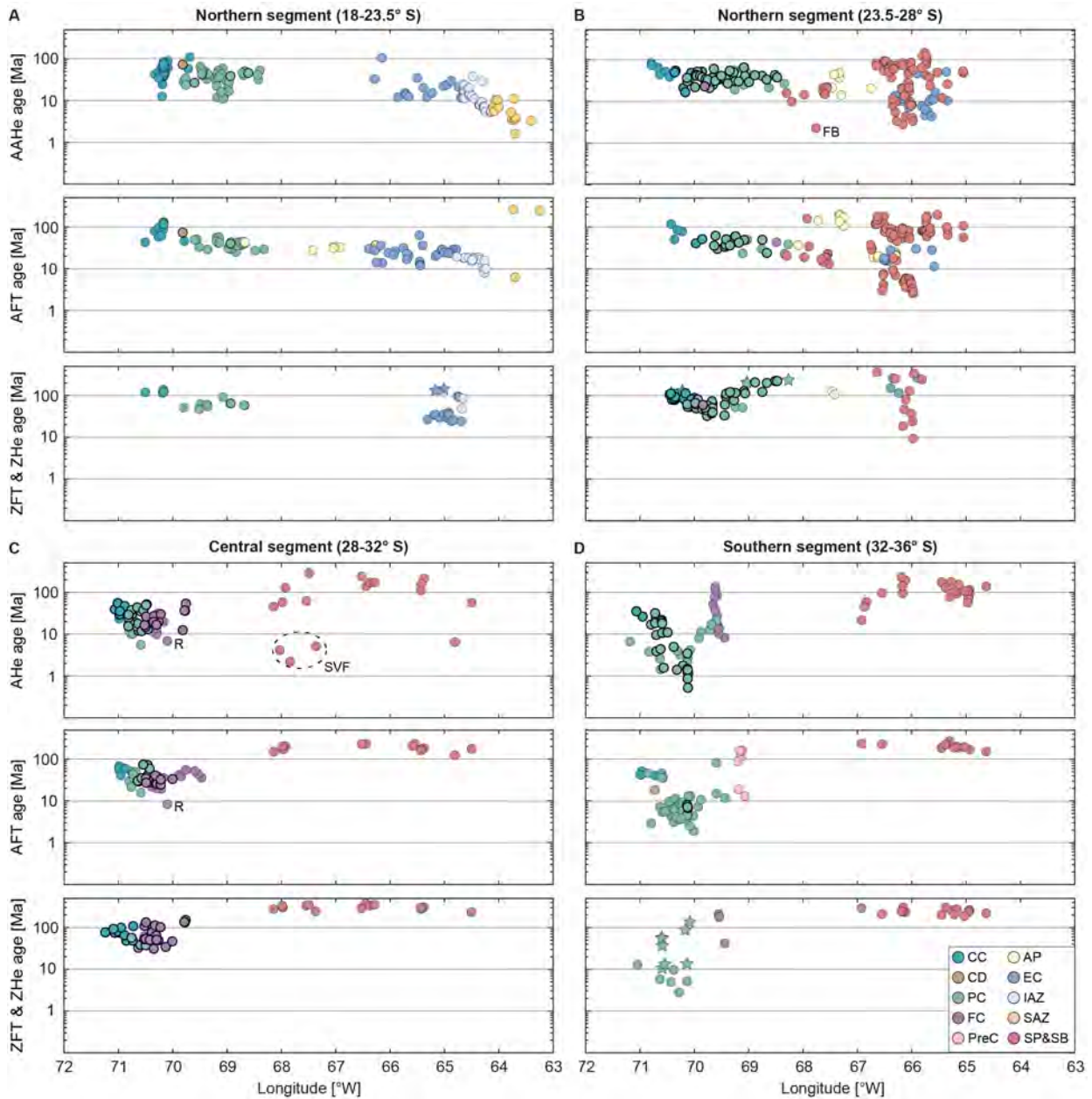
Figure 2.9: Latitudinal cross-sections of thermochronological ages. ZFT ages in B&D are shown together with ZHe ages and represented by star symbols. Colors correspond to tectonic units from Fig. 2.1: AP = Altiplano-Puna plateau; CC = Coastal Cordillera; CD = Central Depression; EC = Eastern Cordillera; FC = Frontal Cordillera; IAZ = Interandean zone; PC = Western/Principal Cordillera; PreC = Precordillera; SAZ = Subandean zone; SP = Sierra Pampeanas and Santa Barbara ranges. **A,B)** The northern segment shows cooling ages that are younger than 10 Ma east of ca. 65° W in the Inter- and Subandean zones (A) and east of ca. 65.5° W in the northern Sierra Pampeanas and southern Eastern Cordillera (B). Ages to the west are all older than 10 Ma, with the exception of the young AHe age from the Fiambalá Basin (FB; Safipour et al., 2015). **C,D)** The central (C) and southern (D) segments show the opposite age trend with ages younging to the west, apart from four AHe ages in the Sierra de Valle Fértil (SVF; Ortiz et al., 2015) and in the foreland (Zapata, 2019) in the central segment. Data from this study are highlighted with bold black rim.

2.6.2 Inversion of ages to exhumation rate histories

In this section, we first describe the inversion results for the exhumation rate history of the Central Andes for selected time intervals using a correlation length scale of 20 km, an $\dot{e}_{prior}$ of 0.1 km/Ma and a G_0 of 25 °C/km (Fig. 2.10, Fig. 2.11). The erosion rates mentioned in this section are specific for this set of parameters. This is because the prescribed G0, and to a lesser extent the $\dot{e}_{prior}$ value and the correlation length scale, directly influence the magnitude of the modelled exhumation rates (Sec. 2.6.3). Yet the general pattern (*i.e.*, acceleration, deceleration) stays the same for all inversions (supplementary material, movies InversionA-H). Furthermore, Fox et al. (2014) emphasized the importance of the reduced variance and temporal resolution when analyzing the inversion results. Because resolution degrades back in time, more recent stages of the model are better resolved than earlier stages, in which changes in exhumation rates can only be captured where multiple thermochronometers are available. Movies showing the complete exhumation rate histories since 80 Ma are provided in the supplementary material for all eight inversions.

2.6.2.1 Exhumation rate history of the Central Andes

Northern segment (18-28°S)

The exhumation rate history before 36 Ma is poorly constrained, as indicated by a reduced variance close to 1 in most parts of the Central Andes (Fig. 2.11A,B). Only the western flank of the Andes and parts of the Sierra Pampeanas, Eastern Cordillera and Interandean zone are partially resolved and show some constraints on the exhumation rates. These are mainly around 0.1 km/Ma between 60 and 36 Ma (Fig. 2.10A,B and supplementary movie, InversionA).

Such low exhumation rates prevail on the western side of the Andes during the whole modelled time period apart from localized zones in the Western Cordillera that show slightly higher (≤ 0.2 km/Ma) rates: A pulse of exhumation migrates from the south (28°S) to the north (26°S) between 50 and 38 Ma (Fig. 2.10B), and some localized spots show higher Miocene exhumation rates compared to their surroundings (Fig. 2.10G).

Fig. 2.10: Modelled exhumation rates for selected time intervals discussed in the text. Black line delineates the main water divide, black points represent thermochronological data falling into the respective time intervals. Numbers indicate specific locations referred to in the text: 1 = Santa Barbara system, 2 = Sierra Aconquíja, 3 = Fiambalá Basin, 4 = Sierra de Valle Fértil, 5 = Cuyo foreland basin, 6 = Aconcagua fold-and-thrust belt, 7 = West Andean fold-and-thrust belt, 8 = Laguna de Tagua Tagua, 9 = Malargüe fold-and-thrust belt, 10 = Malargüe foreland basin. Letters correspond to the following tectonomorphic units: AP = Altiplano, C = Coastal Cordillera, E = Eastern Cordillera, FC = Frontal Cordillera, IA = Interandean zone, P = Principal Cordillera, Pr = Precordillera, Pu = Puna, SA = Subandean zone, SE = southern Eastern Cordillera, SP = Sierra Pampeanas, W = Western Cordillera. Underlying topography from GEBCO_2014, 30 arc-s (Becker et al., 2009).

Figure 2.10
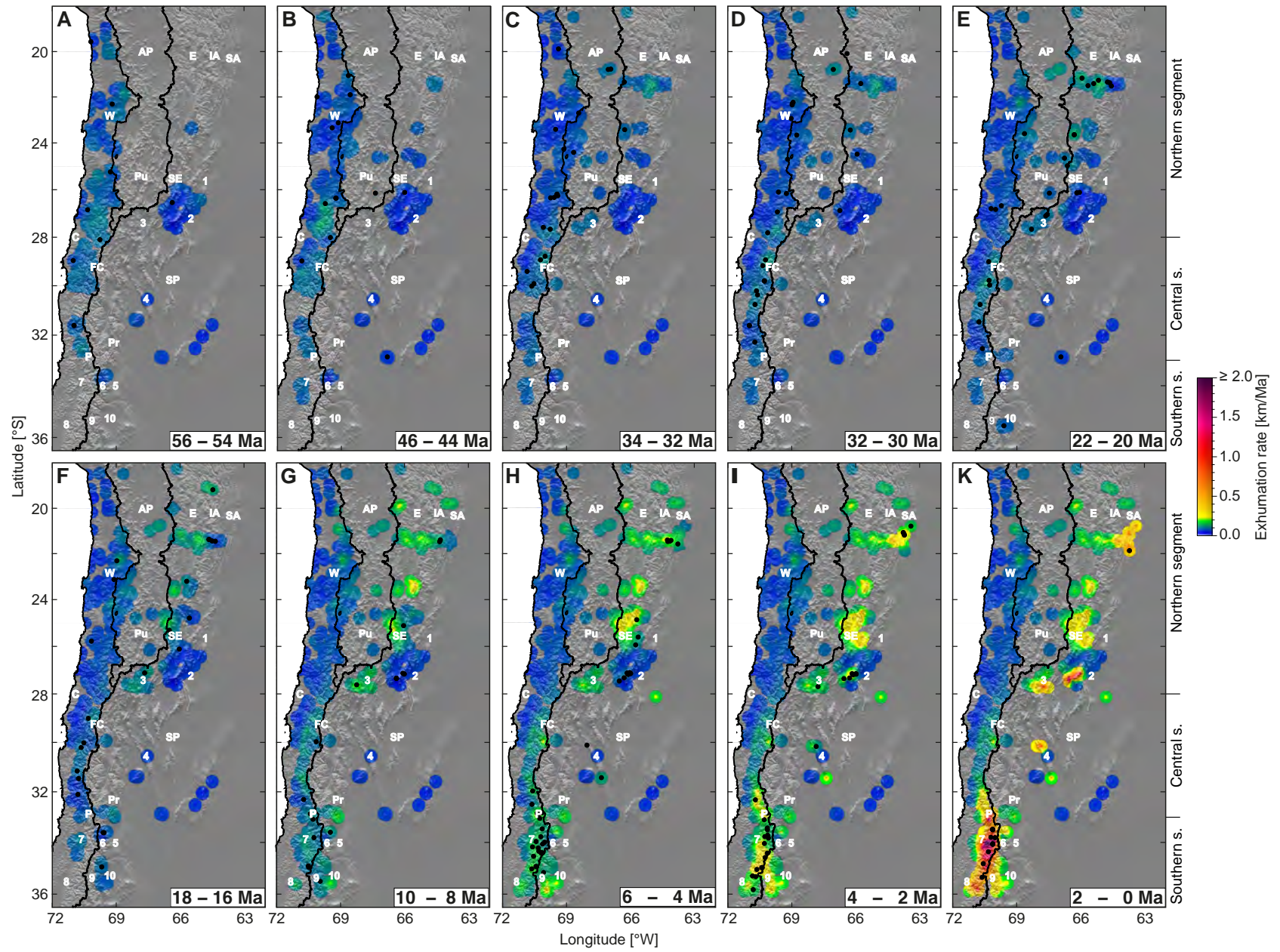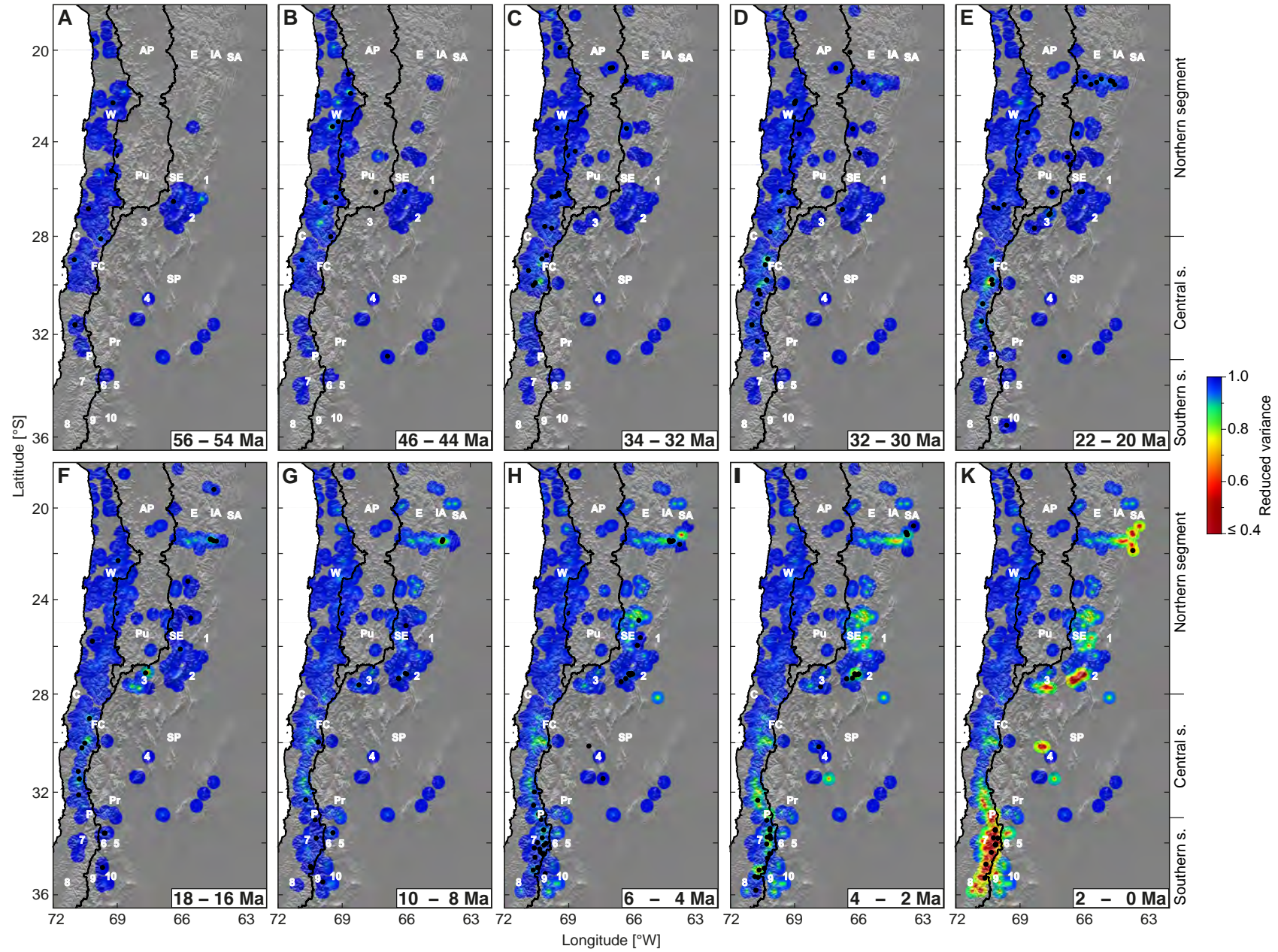
Figure 2.11: Reduced variances corresponding to the exhumation rate maps shown in Fig. 2.10. Black line delineates the main water divide, black points represent thermochronological data falling into the respective time intervals. See caption Fig. 2.10 for numbers and letters. Underlying topography from GEBCO_2014, 30 arc-s (Becker et al., 2009).

During the Late Cretaceous to the Paleocene, exhumation on the eastern side of the Andes occurs only in the northern Sierra Pampeanas with low rates (0.1 km/Ma) (Fig. 2.10A). By the middle to late Eocene, exhumation starts locally in the Eastern Cordillera and the Altiplano-Puna plateau (Fig. 2.10B) and subsequently affects larger parts of these regions and the north-western Sierra Pampeanas during the Oligocene (Fig. 2.10C,D). Exhumation rates remain smaller than 0.2 km/Ma until the middle Miocene. In the early Miocene, the Interandean zone starts exhuming with rates <0.15 km/Ma (Fig. 2.10E,F). Reduced variances <1 in the Eastern Cordillera at 22°S and the western Sierra Pampeanas indicate that the solution in these parts is now reasonable constrained by thermochronological data (Fig. 2.11E,F). During the late Miocene, exhumation accelerates up to ca. 0.25 km/Ma in parts of the Eastern Cordillera, western Puna margin and Interandean zone and propagates eastwards into the eastern part of the southern Eastern Cordillera and into Subandean zone (Fig. 2.10G-K). Exhumation rates in the eastern Interandean zone and the Subandean zone increase from <0.2 km/Ma before 6 Ma to ca. 0.6 km/Ma in the Pleistocene (Fig. 2.10H-K). Plio-Pleistocene increases in exhumation rates are also observed locally in the northern Sierra Pampeanas, namely in the Fiambalá Basin and the Sierra Aconquíja. In the latter, rates increase from <0.1 km/Ma before 6 Ma (Fig. 2.10H) to about 1.5 km/Ma in the Pleistocene (Fig. 2.10K). This region shows the highest rates observed in the northern segment of the Central Andes.

Central segment (28-32°S)

Exhumation rates west of the drainage divide in the central segment show a similar pattern as the northern segment. Until the middle Miocene, exhumation rates in the Principal and Frontal Cordilleras vary around 0.1 to 0.13 km/Ma (Fig. 2.10A-F). Between ca. 10 Ma to 6 Ma, exhumation rates in the Frontal Cordillera constantly increase and reach values up to 0.25 km/Ma at 30°S (Fig. 2.10G,H). On the eastern side, only few thermochronological data are available that restricted to the Sierra Pampeanas. There, exhumation rates are low (<0.1 km/Ma) with the exception of the Sierra de Valle Fértil that starts exhuming during the Pliocene and shows exhumation rates of ca. 0.75 km/Ma in the last 2 Ma (Fig. 2.10I,K).

Southern segment (32-36°S)

In the Central Andes south of ca. 32° S on the western side of the drainage divide, most pre-Miocene ages are located in the Coastal Cordillera or close to the mountain front in the Principal Cordillera. In this zone, a first exhumation signal is observed in the early Eocene and low exhumation rates (~0.1 km/Ma) prevail until the late Miocene (Fig. 2.10A-F). However, data are sparse

and the solution is not well resolved (Fig. 2.11A-F). After 12 Ma, exhumation is recorded in most parts of the Principal and Frontal Cordilleras with a better resolution (Fig.2.10G, 2.11G). Exhumation rates on the western side increase from <0.15 km/Ma in the latest Miocene (Fig.2.10H) to ca. 0.25 km/Ma in the Pliocene (Fig. 2.10I) and to more than 2 km/Ma in the Pleistocene (Fig. 2.10K). These are the highest exhumation rates observed in the Central Andes. On the eastern side of the Andes, exhumation rates in the Frontal and Principal Cordilleras and in the Malargüe fold-and-thrust belt accelerated relatively continuously from ca. 0.15 km/Ma in the late Miocene to ca. 0.4 km/Ma in the Pleistocene (Fig. 2.10G-K).

2.6.3 Influences of the model parameters on the inversion results

To assess the influence of fault blocks, G_0, $\dot{e}_{prior}$ values and correlation length scales on the inversion result, we compare the exhumation rate histories and reduced variances for the 2-0 Ma time interval of the eight inversions (Fig. 2.12, Fig. 2.13). The misfit between observed and predicted ages and histograms of the age differences are provided in supplementary Figure S2.

The most significant influences on the modelled exhumation rates is exerted by our choice of the $\dot{e}_{prior}$ and G_0 (Fig. 2.12). Higher G_0's lead to lower exhumation rates because heat is more efficiently advected to the surface and thus the closure depths are shallower (Fig. 2.12B,D). Higher $\dot{e}_{prior}$ values instead lead to significantly higher exhumation rates because the $\dot{e}_{prior}$ stays part of the solution (Equation 2.4) (Fig. 2.12C,D). Thus, a higher geothermal gradient partly compensates for higher exhumation rates resulting from a high $\dot{e}_{prior}$, and therefore rates are highest in the inversion with an $\dot{e}_{prior}$ of 0.5 km/Ma and a geothermal gradient of 25 °C/km (Fig. 2.12C). These differences in exhumation rates are most important in fast exhuming places (*e.g.*, in the Inter- and Subandean zones, southern Principal Cordillera or Sierra Aconquíja), whereas in places where exhumation rates are low (*e.g.*, in the Western Cordillera) recovered rates are similarly low (and mainly below 0.2 km/Ma) in all inversions (Fig. 2.12). Different values of $\dot{e}_{prior}$ and G_0 do not influence the reduced variance if the correlation length scale remains the same (Fig. 2.13A-D). Instead, a smaller correlation length scale increases the reduced variance because the number of thermochronological data to infer exhumation rates at any given location is reduced (Fig. 2.11E).

Fig. 2.12 Influence of the model parameters on the modelled exhumation rates of the most recent time step (2-0 Ma). White rectangles delineate specific locations discussed in the text: EC = southern Eastern Cordillera, IAZ/SAZ = Inter- and Subandean zones, PC = southern Principal Cordillera, SA = Sierra Aconquíja, northern Sierra Pampeanas, WC = Western Cordillera. Arrows highlight differences between inversions modelled with and without fault blocks. **A-D)** Inversions with different combinations of $\dot{e}_{prior}$ (0.1, 0.5 km/Ma) and G_0 (25, 50 °C/km). Correlation length scale is 20 km. **E,F)** Inversions with the same set of parameter as in A) but with correlation lengthscales of 10 and 30 km, respectively. **G,H)** Inversions with fault blocks and the same set of parameter as in A) and correlation lengthscales of 20 and 1000 km, respectively. Thin black lines delineate the faultblocks.
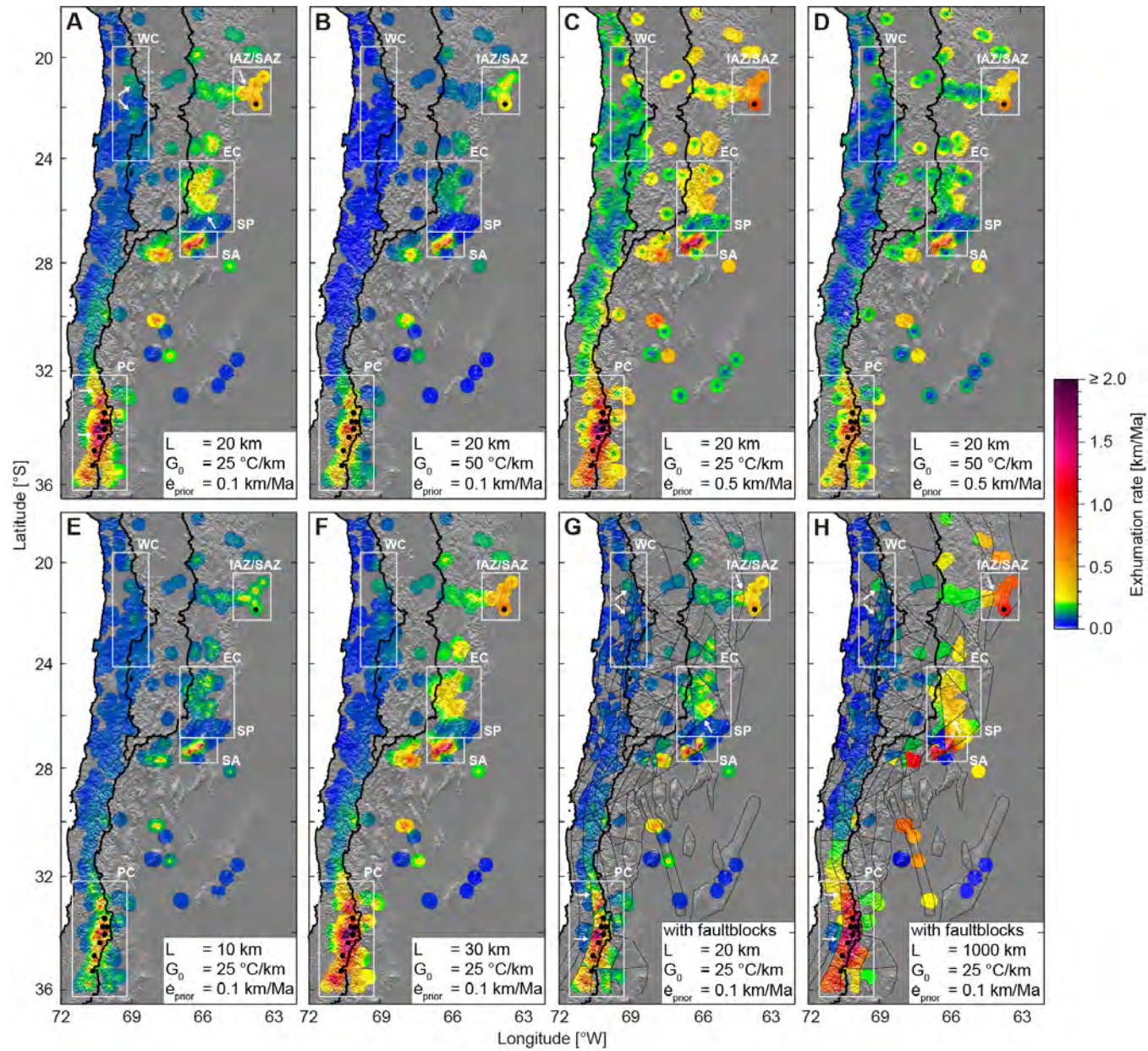
Figure 2.12
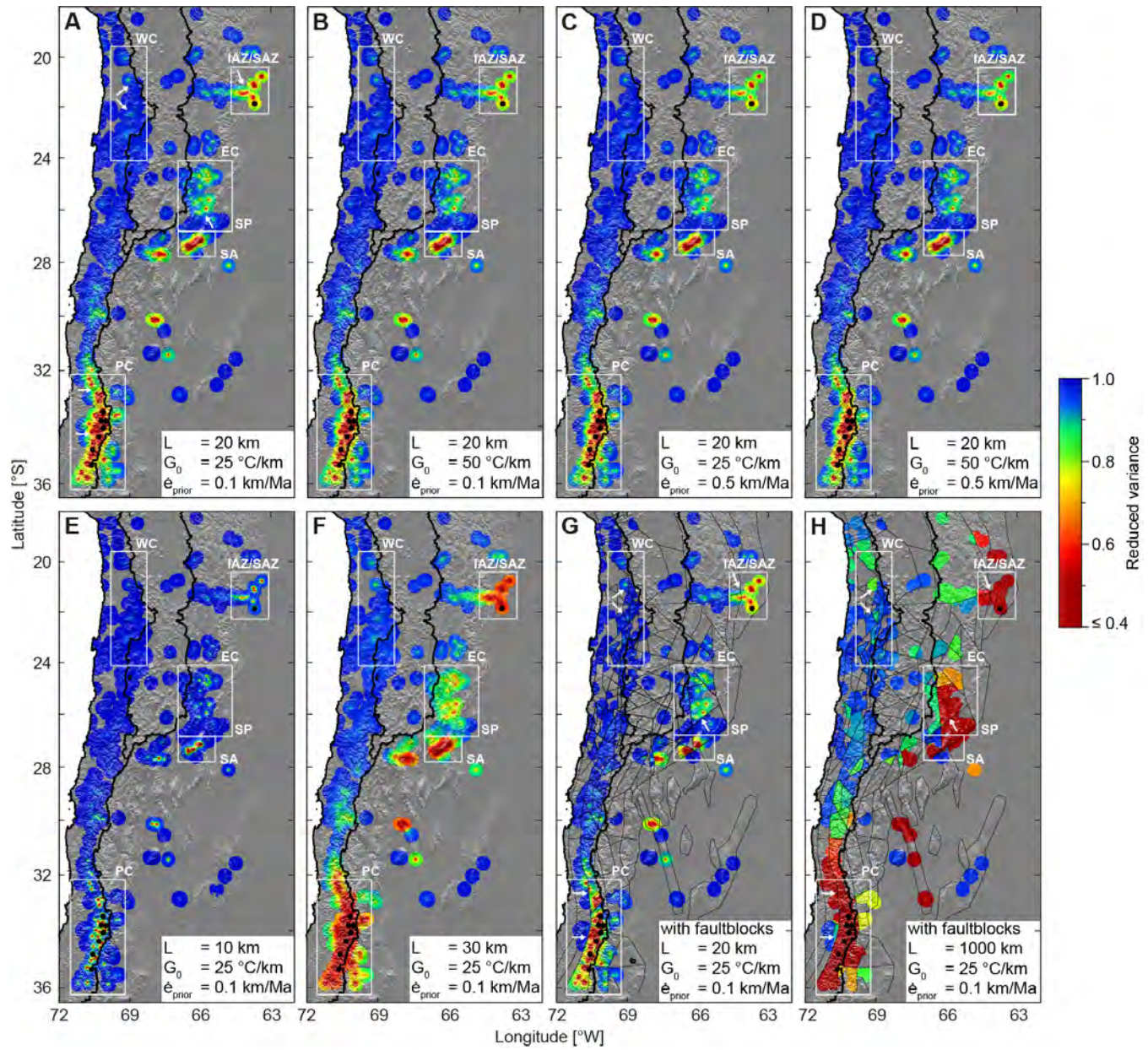
Figure 2.13: Figure caption on next page

Figure 2.13: Reduced variance of the inversion results shown in Fig. 2.12. White rectangles delineate specific locations discussed in the text: EC = southern Eastern Cordillera, IAZ/SAZ = Inter- and Subandean zones, PC = southern Principal Cordillera, SA = Sierra Aconquíja (Sierra Pampeanas), WC = Western Cordillera. Arrows highlight differences between inversions modelled with (G,H) and without (A) fault blocks.

A larger length scale results in lower reduced variances and more spatial smoothing (Fig. 2.11F). Nevertheless, the exhumation rate magnitudes and patterns remain similar despite being less pronounced when a small correlation length scale is used (Fig. 2.12A,E,F).

The influence of fault blocks on the inversion results can be investigated by comparing Figure 2.12A (without faults) with Figure 2.12G (with faults), for which the same set of parameters was used ($\dot{e}_{prior}$ = 0.1 km/Ma, G_0 = 25 °C/km, L = 20 km). In the inversion with fault blocks, the spatial extent of the modelled exhumation rates (Fig. 2.12G) and reduced variances (Fig. 2.13G) is truncated at block boundaries because information of thermochronological data does not propagate into adjacent blocks, whereas the solution is smoothed across in the inversion without fault blocks (Fig. 2.12A, Fig. 2.13A). This is for example clearly observable along the western mountain front in the southern Principal Cordillera. However, these differences are rather local and exhumation rate magnitudes and patterns are similar in most places. Besides, regional differences in exhumation rates, which are an expression of spatially different thermochronological data, are equally recovered in several locations as for example at the boundary between the southern Eastern Cordillera and northern Sierra Pampeanas, the boundary between the Inter- and Subandean zones or in the Western Cordillera (Fig. 2.12A,G). Figure 2.12H shows the inversion for which fault blocks were combined with a correlation length scale of 1000 km, *i.e.* all data can be spatially correlated if located in the same fault block. Even with such a large correlation length scale, exhumation rates vary spatially in individual blocks (*e.g.*, in the southern Principal Cordillera and northern Sierra Pampeanas). Where data resolution is high, the magnitude and pattern of the modelled exhumation rates remain comparable to the inversion without fault blocks (Fig. 2.12A), although they are heavily smoothed.

2.6.4 Age-elevation profile analysis

The slope of an age-elevation profile is an approximation of the exhumation rate that is independent of the geothermal gradient (*e.g.*, Wagner et al., 1979; Gleadow and Fitzgerald, 1987; Fitzgerald et al., 1995) and thus enables us to validate our modelling results (Fig. 2.14). However, in such age-elevation relationships it is assumed that the isotherms are flat and that the samples have undergone an identical exhumation history (*e.g.*, Mancktelow and Grasemann, 1997). This assumption is often not valid because topography disturbs the geothermal field (*e.g.*, Mancktelow and Grasemann, 1997; Braun, 2002b,a). The temperature perturbation decreases exponen-

tially with depth in proportion to the wavelength of the surface topography. The critical wavelength for this temperature disturbance can be approximated by the closure temperature divided by the geothermal gradient (Braun, 2002b,a). Assuming a geothermal gradient of 25 °C/km and a closure temperature of 70 °C (Farley, 2000) for AHe and 110 °C for AFT (Ketcham et al., 1999), the critical wavelength is 2.8 km for AHe and 4.4 km for AFT. We use three sites for the age-elevation analysis: two are located in the southern segment around 33.5° S latitude on the western (AER-a, this study) and eastern sides (AER-b, Riesner et al., 2019) of the Andes, the third one is located in the Western Cordillera at 26.2° S (AER-c, this study) (see Fig. 2.1 and supplementary Table A5 for location and data). Because AER-b and AER-c were sampled over a larger horizontal distance (5.7 and 7.5 km) than the critical wavelength λ_c, the derived exhumation rates should be considered as maximum values (Braun, 2002a).

The age-elevation profile in the southern segment on the western side of the Andes (AER-a) consists of data between 1.24±0.3 to 9.8±1.0 Ma at elevations from 1559 to 2575 m (Fig. 2.14A). The AHe data show a break in slope that indicates an increase in the exhumation rate (*e.g.*, Wagner et al., 1979; Gleadow and Fitzgerald, 1987; Fitzgerald et al., 1995) from 0.15±0.1 km/Ma before 2 Ma to 2.0±3.7 km/Ma after 2 Ma. The linear fit to the AFT data indicates an exhumation rate of 0.54±0.3 km/Ma between 7 and 10 Ma, which fits with the slower rate before 2 Ma in the AHe data. The two oldest AFT samples are close to their magmatic cooling age (10.2±0.09 Ma (this study), Appendix Table A4). However, the intrusion from which the samples were taken from is an isolated body of moderate size that was emplaced high in the crust and does not show any sign of multiple intrusive pulses and thus has cooled relatively quickly (Cornejo and Mahood, 1997). Therefore, these two ages probably represent cooling due to exhumation and can be used in the age-elevation relationship. Nevertheless, they were rejected in the inverse modelling since all thermochronological ages compiled for this study were treated uniformly (*i.e.*, at least 2 Ma younger than their intrusion age). The exhumation history as resolved by the age-elevation profile differs only partly from that derived from the inversion model (Fig. 2.14C). In the inversion, the reduced variance stays close to 1 before 15 Ma (Fig. 2.14E) indicating that the a posteriori rates are not resolved by the data. After 15 Ma, the modelled exhumation rates with $\dot{e}_{prior}$ = 0.5 km/Ma start to decrease from the prior value to $\leq$ 0.25 km/Ma at 8 Ma, whereas they start to increase slightly for the inversions with $\dot{e}_{prior}$ = 0.1 km/Ma (Fig. 2.14C). The observed decrease in exhumation rates for the inversions with an $\dot{e}_{prior}$ value of 0.5 km/Ma should thus be considered as an artefact caused by the transition from posterior rates unresolved by the data to rates resolved by the data. After 8 Ma, the reduced variance decreases significantly to values between 0.55 and 0.85 (Fig. 2.14E) due to the incorporation of the AFT data (Fig. 2.14A) and until 2 Ma all exhumation rates range between 0.08 and 0.26 km/Ma. At 2 Ma, the reduced variance drops below 0.1 and the rates increase abruptly to values between 0.65 and 0.74 km/Ma for G_0 set
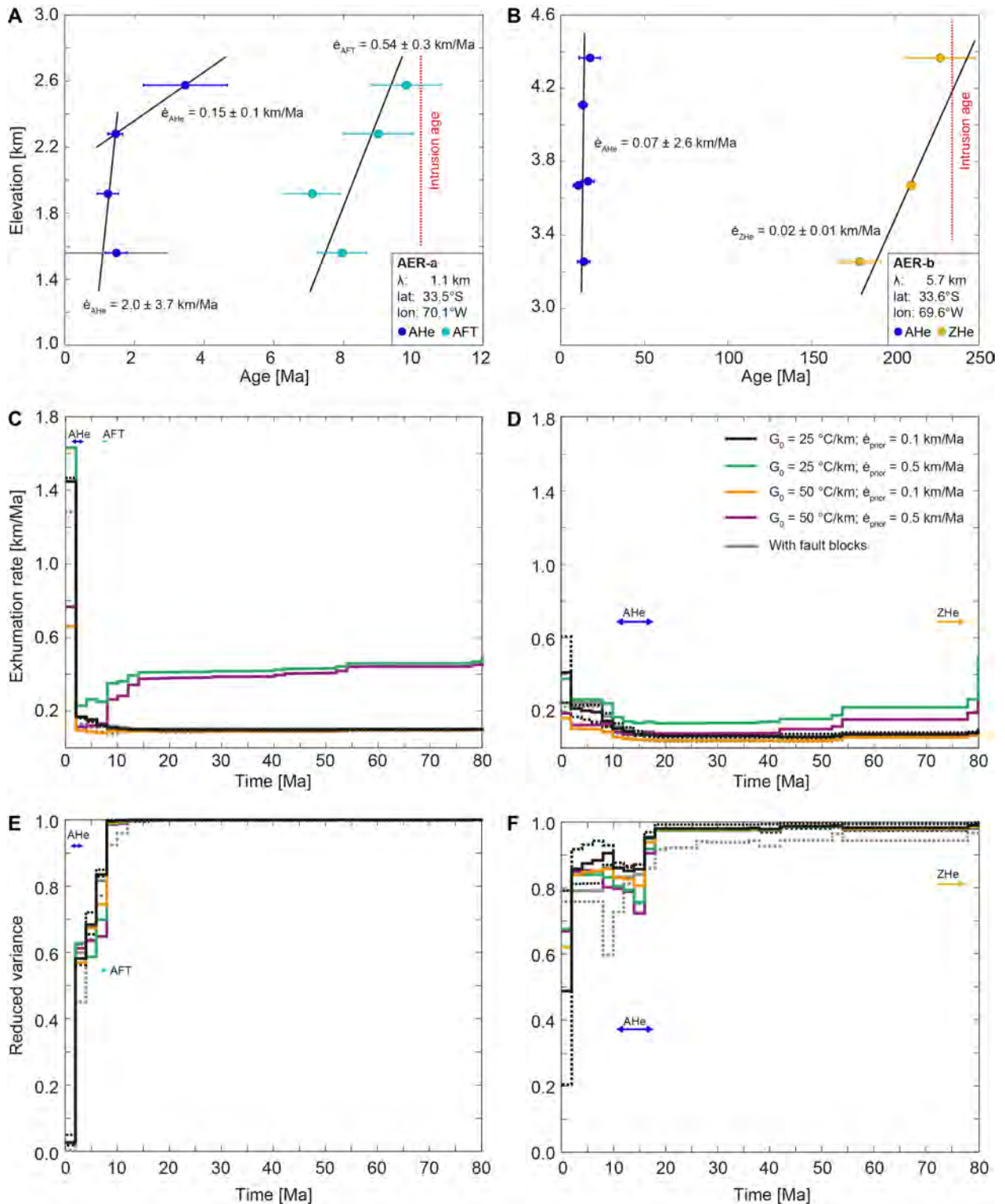
Figure 2.14: Comparison of exhumation rates derived from age-elevation profiles and from the inversions for the southern segment of our study area. See Fig. 2.1 and supplementary Table A5 for locations and data. **A,B)** Age-elevation profiles at 33.5° S to the west (AER-a) and east (AER-b) of the water divide, with linear best-fit after York et al. (2004) indicating the exhumation rate. For consistency with the inversion, average ages with standard deviation rather than individual grain ages are used. (cont. on next page)

Figure 2.14: (cont.) The AHe data of profile AER-a shows a break in slope that indicates an increase in exhumation rate from 0.15±0.1 km/Ma before 2 Ma (slope of the line connecting the two highest elevated samples) to 2.0±3.7 km/Ma after 2 Ma. To get a meaningful linear fit, a higher uncertainty (1.5 Ma instead of 0.3 Ma, grey error bar) was given to the lowermost sample. **C,D)** Exhumation rates derived from the inversions at the respective locations of the age-elevation profiles using different sets of parameters. The ZHe data from AER-b is not used in the model because ages older than 80 Ma are excluded in the inversion. Solid lines represent inversions with a correlation length scale of 20 km and varying G_0 (25 and 50 °C/km) and $\dot{e}_{prior}$'s (0.1 and 0.5 km/Ma). Black lines are inversions with our preferred parameter set ($G_0 = 25$ °C/km, $\dot{e}_{prior} = 0.1$ km/Ma) run with correlation length scales of 10 km (dotted), 20 km (solid) and 30 km (dashed). Grey lines represent the inversion with fault blocks and correlation length scales of 20 km (solid) and 1000 km (dashed), respectively. Colored arrows indicate the time span covered by the respective thermochronological systems. **E,F)** The reduced variance of the model drops when information of the thermochronological data are available.

to 50 °C/km and between 1.43 and 1.62 km/Ma for G_0 set to 25 °C/km (Fig. 2.14C), which matches the slope of the age-elevation relationship. Different correlation length scales do not significantly influence the results.

The age-elevation profile on the eastern side of the orogen (AER-b) has much older AHe and ZHe ages than the profile on the western side (Fig. 2.14B) (Riesner et al., 2019). No AFT ages were available. AHe ages span the period between 10.5±2.7 and 17.5±6.2 Ma and the linear fit to this data indicates an exhumation rate of 0.07±2.6 km/Ma. ZHe ages lie between 179±12.4 and 227±20.8 Ma and give an exhumation rate of 0.02±0.01 km/Ma. These data are from a Permo-Triassic intrusion with poor age control (one whole rock K-Ar age of 234±10 Ma, Gregori and Benedini, 2013, and references therein) and the oldest two ZHe ages may represent magmatic cooling ages. The ZHe ages were not incorporated in the inverse model because only ages younger than or equal to 80 Ma were used. The modelled exhumation rates (Fig. 2.14D) and reduced variances (Fig. 2.14F) at this location show a first signal at 80 Ma due to the influence of pre-Cenozoic AHe ages in the surrounding area in the Frontal Cordillera. This is especially important for the inversions with $\dot{e}_{prior}$ values of 0.5 km/Ma for which erosion rates drop below 0.25 km/Ma (Fig. 2.14D). The decrease is a direct consequence of the choice of the $\dot{e}_{prior}$ and occurs when the model starts to adjust to rates constrained by thermochronological data. However, the reduced variance stays close to 1, indicating poor data resolution (Fig. 2.14F). By 42 Ma, exhumation rates of all inversions are similar and smaller than 0.15 km/Ma (Fig. 2.14D). Between 18 and 16 Ma, the exhumation rate history starts to be constrained by the AHe data along the age-elevation profile, which results in a drop of the reduced variance to 0.72-0.96 (Fig. 2.14F). The reduced variance stays around these values until 10 Ma, indicating that the solution in these time intervals is better constrained. All but one inversions show exhumation rates that steadily increase from below 0.1 km/Ma before 18 Ma to values between 0.15 and 0.6 km/Ma at 2 Ma. In the last time interval, the reduced variance drops again below 0.8 due to the additional constraint that the samples need to be exhumed to the surface. In the time interval covered by the thermochronological data (10-18 Ma), the exhumation rates of most inversions (0.06 to 0.17 km/Ma) are consistent with the rates derived from the AHe age-elevation relationship (0.07±2.6 km/Ma).

A third age-elevation profile from the Western Cordillera (AER-c) also shows a good fit with the inversion results (supplementary Fig. S3). Here, ZHe, AFT and AHe data constrain the time period between 110 and 33 Ma in the age-elevation profile, giving exhumation rates of 0.01±0.001 km/Ma ($\dot{e}_{\mathrm{ZHe}}$), 0.03±0.06 km/Ma ($\dot{e}_{\mathrm{AFT}}$) and 0.2±0.09 km/Ma ($\dot{e}_{\mathrm{AHe}}$) that match well with the modelling results yielding rates between 0.04 and 0.2 km/Ma in the time interval covered by the data.

Taken together, the modelled exhumation rates are similar to the ones derived from age-elevation profiles at selected locations over the time intervals resolved by the data. Furthermore, all inversions show the same exhumation rate pattern (acceleration, deceleration) independently from the chosen parameters when data resolution is sufficient (*i.e.,* when the reduced variance $\ll$ 1), but the magnitude of the rates varies strongly with G_0 and, to a lesser extent, the $\dot{e}_{prior}$.

2.7 Discussion

2.7.1 Influence of $\dot{e}_{\mathbf{prior}}$ and G_0 on modelled exhumation rates

The inversion of low-temperature thermochronological data requires to prescribe an a priori exhumation rate ($\dot{e}_{prior}$) and a priori covariance, which are both independent of the thermochronometric data (*e.g.*, Fox et al., 2014), and a final prior geothermal gradient (G_0). Their influence can be tested by comparing inversion results with different sets of parameters or different correlation length scales (Fig. 2.12, Fig. 2.13) and by comparing the inversion solutions with age-elevation relationships at selected locations (Fig. 2.14, supplementary Fig. S3). Several conclusions can be drawn from these comparisons.

First, all tested cases converge toward similar exhumation rate histories that are consistent with the age-elevation relationships when data resolution is sufficient. At 33.5° S, all modelled exhumation rates increase significantly at 2 Ma west of the Andes (Fig. 2.14C) and moderately since 14 Ma on the eastern side of the orogen (Fig. 2.14D). The observed temporal variations of exhumation rate patterns (*i.e.*, acceleration, deceleration) are therefore independent of our prior model. This demonstrates the robustness of our approach.

On the other hand, the magnitude of the modelled exhumation rates strongly depends on G_0 and to a lesser extent on the $\dot{e}_{prior}$. Especially the model solution of the most recent time step shows a high dependency on the near surface geothermal gradient (Fox et al., 2014). This is expected for this interval as the youngest ages only provide an estimate of the exhumation from their closure depths to their present elevation, and the closure depth clearly depends on the geothermal gradient at the time of closure. In comparison, older ages in an age-elevation relationship constrain both the average exhumation since closure (which depends on the thermal field) but also the ex-

humation rate between the sample's age and the age of the sample directly below it in the profile. Therefore, parts of the model that are resolved by age-elevation relationships are less sensitive to the geothermal gradient than the youngest time step and time steps that are more recent than the youngest age. Furthermore, fast exhuming regions like the southern Principal Cordillera, the Sierra Aconquíja or the Subandean zone are more sensitive to the geothermal gradient (Fig. 2.12, Fig. 2.14C). This can be explained by the control of the exhumation rate on heat advection, which is elevated in case of faster exhumation rates.

Modelled exhumation rates in the southern Principal Cordillera (1.43 to 1.62 km/Ma, Fig. 2.14C) match better the rates derived from the age-elevation relationship (2.0±3.7 km/Ma, Fig. 2.14A) under a G_0 of 25 °C/km, although the exhumation rate is still underestimated. Such an underestimation is expected because the age-elevation relationship approach assumes that the closure isotherm is flat and therefore tends to overestimate rates as the closure isotherm is likely to be perturbed by topography. A G_0 of 25 °C/km results in modern modelled geothermal gradients in the range of 24-34 °C/km ($\dot{e}_{prior}$ = 0.1 km/Ma) and 16-49 °C/km ($\dot{e}_{prior}$ = 0.5 km/Ma) (supplementary Fig. S4), which are consistent with most heat flow measurements of the Central Andes (Springer and Förster, 1998) and with present-day geothermal gradients from the Principal Cordillera (32-35 °C/km, Höfer-Öllinger and Millen (2010)). Instead, a G_0 of 50 °C/km yields modern modelled geothermal gradients between 46 and 60 °C/km ($\dot{e}_{prior}$ = 0.1 km/Ma) that are significantly higher than the observed values. Thus, inversions using a G_0 of 25 °C/km are preferable over inversions with 50 °C/km. This means however that the magnitude of modelled exhumation rates in regions where the true geothermal gradient is lower are underestimated, *i.e.*, in the Coastal Cordillera (8 °C/km) and Subandean zone (15 °C/km), whereas rates are overestimated in regions with a higher geothermal gradient such as in parts of the Principal Cordillera close to the magmatic arc (19-69 °C/km).

Furthermore, magmatic bodies in the Andean middle-to-upper crust locally alter the geothermal field. This can lead to a misinterpretation of exhumation rates derived from thermochronological data (*e.g.*, Calk and Naeser, 1973; Murray et al., 2018). For example, a large magma reservoir with a volume of up to 500'000 km[3] (Ward et al., 2014) sits in the upper crust below the Altiplano-Puna plateau (21-24° S, 68.5-66 ° W) since the late Miocene (de Silva, 1989). However, all thermochronological ages located less than 25 km away from the intrusion boundary are older than Miocene, except for one AHe age, and the latitudinal trend does not show any anomaly in this area (Fig. 2.9A,B). The data used in this study thus seem to be unaffected by the intrusion. Volcanic and plutonic activity in the Central Andes was common during the Mesozoic in the Coastal Cordillera and during the Cenozoic in the Principal/Western Cordilleras (Fig. 2.4). Our western thermochronological dataset shows a significant decrease in cooling ages south of 32° S (Fig. 2.7). This pattern is similar to the distribution of the magmatic intrusion ages (Fig. 2.4A) that

shows mostly Miocene intrusions south of 33°S whereas pre-Miocene ages prevail to the north. Miocene and younger volcanic activity however is relatively uniformly distributed in the Principal Cordillera north of 33°S apart from the amagmatic zone delineating the modern flat slab segment between 28-32°S (Fig. 2.4B). This suggests that Miocene magmatic bodies were most probably also present in the northern segment of the Andes but are simply not exposed due to lower exhumation rates in this zone. Likewise, pre-Miocene intrusions are preserved in the north whereas higher exhumation rates in the southern Principal Cordillera may have caused their erosion and the exposure of younger magmatic bodies. No data are available in the Coastal Cordillera south of 32°S and we thus relate the absence of Cretaceous and Paleozoic igneous rocks in this area to a sampling bias. Our samples were taken at a minimum distance of 25 km from Holocene volcanoes in order to exclude possible hydrothermal disturbances of the geothermal field by volcanic activity. Few literature samples are located closer to Holocene volcanos, but their ages show no anomalies in the cross-sectional age trends depicted in Figures 2.7, 2.8 and 2.9. We thus conclude that magmatic effects on our thermochronological dataset are negligible.

Another factor that influences the magnitude of the modelled exhumation rates is the $\dot{e}_{prior}$ because it remains part of the solution (Equation 2.4) (Fox et al., 2014; Herman et al., 2013; Jiao et al., 2017; Willett et al., 2020). If the data resolution capacity is low, the model solution is especially sensitive to the prior model due to the impossibility of recovering a function not sampled by the age data. In such cases, our model parameter will not deviate from the prior value. Furthermore, this can lead to a spurious acceleration or deceleration of the exhumation rates as rates begin to deviate from the prior due to increased data resolution (*e.g.*, Fox et al., 2014; Willett et al., 2020). Figure 2.14 shows that the impact of the $\dot{e}_{prior}$ on our model solution is especially important at the beginning when the oldest thermochronological ages become available but when data resolution is still poor. For example, an overestimated $\dot{e}_{prior}$ leads to a decrease in exhumation rates when the model starts to incorporate data that indicate a lower rate than the assumed $\dot{e}_{prior}$, as observed for an $\dot{e}_{prior}$ of 0.5 km/Ma between 14 and 8 Ma at the site of AER-a (Fig. 2.14C) and at 80 Ma at the site of AER-b (Fig. 2.14D). In such cases, a diagnostic feature to recognize the validity of the inversion results is the reduced variance: if the deceleration/acceleration corresponds to an interval with reduced variance close to 1, than the model is poorly resolved over that period and the deceleration/acceleration is likely not a robust feature (*e.g.*, Fig. 2.14E,F). If the deceleration/acceleration instead corresponds to intervals with good data resolution, then the influence of the $\dot{e}_{prior}$ is negligible.

We prefer an $\dot{e}_{prior}$ value of 0.1 km/Ma over an $\dot{e}_{prior}$ of 0.5 km/Ma, despite the better model fit of the ZHe and ZFT ages with the higher prior value (supplementary Fig. S2). The reason for this is that during the late Cretaceous to the middle Eocene, a high $\dot{e}_{prior}$ predicts high exhumation rates due to the lack of resolution. However, exhumation rates were likely to be slow during this time

period as there is evidence that little topography existed. It is important to note that the exhumation rates after the middle Eocene are similar for the different $\dot{e}_{prior}$ values, with the $\dot{e}_{prior}$ = 0.5 km/Ma model showing a decrease in rates during the early Eocene to values similar to the $\dot{e}_{prior}$ = 0.1 km/Ma model as resolution increases (supplementary Fig. S3 and movie InversionC). The misfit is especially large for the pre-Oligocene ZHe and ZFT ages (supplementary Fig. S2A,A*), which are mainly located within the Western Cordillera and are locally close to or younger than their corresponding AHe or AFT age or surrounding AHe/AFT ages (supplementary Table A5). This could be related to issues with the kinetic parameters of the different systems or due to higher exhumation rates that are not recovered by the model due to damping. Yet, no evidence of higher rates during the Paleogene is observed in the inversion with a higher $\dot{e}_{prior}$ (supplementary Fig. S3 and movie, InversionC). Alternatively, the geothermal gradient could have been higher than assumed during this time interval due to the position of the Paleogene magmatic arc in the Western Cordillera (*e.g.*, Charrier et al., 2007). This could explain the better fit of the ZHe ages in the inversion with a higher geothermal gradient (supplementary Fig. S2B,B* and movie, InversionB) which predicts less age dispersion between the different systems due to smaller differences in the closure depth. Furthermore, a higher $\dot{e}_{prior}$ would be more appropriate in fast exhuming places like the southern Principal Cordillera, the eastern flank of the Andes, or the Sierra Aconquíja in the more recent time steps. Here, erosion rates might be underestimated which could explain the larger misfit of the Neogene AFT ages of the Sierra Aconquíja (supplementary Fig. S2A).

Finally, the comparison of exhumation histories derived with and without fault blocks but with the same correlation length scale (Fig. 2.12A,G and movies,InversionA,G) shows that the two versions are similar and lead to the same pattern of exhumation rates. This implies that our model is robust regarding to the fault blocks and that observed increases are not due to potential correlations across faults as suggested by Schildgen et al. (2018).

Our analysis of the influence of the model parameters and model set up on the inversion results shows that the differences in the solution are minor and that the method used in this study is robust. Whereas all inversions show a similar pattern of exhumation rates (*i.e.*, deceleration/acceleration), the magnitude of the exhumation rate depends on the chosen geothermal gradient G_0 and on the $\dot{e}_{prior}$ especially when data resolution is poor.

2.7.2 Exhumation history of the Central Andes

The large-scale spatial pattern of thermochronological cooling ages and exhumation rates strikingly mimic the present-day climatic precipitation gradients of the Central Andes (Fig. 2.5). On the western side, the northern arid to semi-arid climate is replaced by more humid conditions south of ca. 30°S due to the influence of the Westerlies. Most ages north of 32°S are Paleogene and, with

one exception (Rodríguez et al., 2018), no ages younger than 10 Ma are observed (Fig. 2.7). This results in generally low exhumation rates over the modelled time period (Fig. 2.10). South of 32° S, the ages decrease significantly and Plio-to-Pleistocene modelled exhumation rates are markedly increased relative to the north. On the eastern side, the South American Monsoon leads to high precipitation on the mountain front north of ca. 28° S, whereas the climate is semi-arid south of it (Fig. 2.5). Although no clear correlation between cooling ages and precipitation pattern is observed along the strike of the Andes on the eastern side (Fig. 2.8), latitudinal cross-sections show that ages north of 28° S are youngest along the eastern mountain front, whereas south of 32° S tehy are youngest on the western side (Fig. 2.9). Yet, the observed cooling patterns could also be explained by tectonic deformation that affected most parts of the Andes between the Eocene and the late Miocene and later focused at the eastern mountain front (Fig. 2.3). These first-order observations imply a complex interplay between tectonics, climate and erosion that is discussed below for the northern, central, and southern segments of the southern-central Central Andes.

2.7.2.1 Northern segment (18-28° S)

On the western side of the Andes, exhumation started in the Late Cretaceous to Paleocene as constrained by cooling ages mainly located in the Coastal Cordillera and Central Depression. This corroborates the idea that mountain building may have started during this time (*e.g.*, Mpodozis et al., 2005; Arriagada et al., 2006; Henriquez et al., 2019). However, the inversion results do not sufficiently resolve possible changes in exhumation rates on the western side of the drainage divide (Fig. 2.11). In fact, the data can be fitted with relatively constant exhumation rates that did not exceeded 0.2 km/Ma since 80 Ma (Fig. 2.10). This is supported by the inversion with an $\dot{e}_{prior}$ value of 0.5 km/Ma that recovers equally low rates in places with better resolution (*e.g.*, Fig. 2.12, supplementary Fig. S3 and movie, InversionC). Our results do not exclude a pulse of exhumation during the Paleogene that is expected from the deformation record (Sec. 2.2.1) and suggested by the thermo-kinematic modelling of thermochronometric data in Reiners et al. (2015), but data resolution on the western side of the orogen is too low to discriminate between constant low erosion rates and migrating pulses of exhumation during this time interval. Furthermore, our assumption of monotonic cooling might not be appropriate due to volcanic reburial (Reiners et al., 2015).

In this arid zone of the Central Andes, deformation started in the Late Cretaceous in the Central Depression and Western/Principal Cordillera (Fig. 2.3A) and was active throughout the Cenozoic, but with low shortening rates (Fig. 2.2, Victor et al., 2004; Oncken et al., 2006). A major phase of mountain building took place in the Eocene with shortening rates up to 1.2 mm/a (Fig. 2.2, Fig. 2.3, Oncken et al., 2006). Our inversion resolves a localised pulse of enhanced exhumation ($\leq$ 0.2 km/Ma) between 26 and 28° S from 58 to 38 Ma (Fig. 2.10A,B), which might be associated

with increased shortening rates during that time. Similar pulses of localized enhanced exhumation are also observed along the western Andean piedmont since the Miocene (Fig. 2.10G). These might be linked to the onset of deep canyon incision and to intensified uplift of the western Andean flank since the middle Miocene (*e.g.*, Farías et al., 2005; Garcia and Hérail, 2005; Hoke et al., 2007; Jordan et al., 2010; García et al., 2011; Cooper et al., 2016). However, exhumation rates in this part of the Central Andes were generally low and are thus consistent with low amounts of horizontal shortening and low mean annual precipitation.

On the eastern side of the Central Andes, a first signal in exhumation is observed in the northern Sierra Pampeanas in the Late Cretaceous that can be related to extensional tectonics of the Salta rift system (Grier et al., 1991; Marquillas et al., 2005). Only by the middle-to-late Eocene, exhumation starts locally in the Eastern Cordillera and the Altiplano-Puna plateau and subsequently covers larger parts of these regions during the Oligocene. This is in good agreement with the onset of syntectonic sedimentation in these regions (Fig. 2.3A, *e.g.*, Coutand et al., 2001; Elger et al., 2005; McQuarrie et al., 2005; Montero-López et al., 2016) and with the early Oligocene onset of major crustal thickening in the northern segment (*e.g.*, Mamani et al., 2010b). Shortening rates in the northern part of the Eastern Cordillera culminated in the Oligocene to the early Miocene (Müller et al., 2002; Elger et al., 2005), but exhumation rates remained relatively constant during this time period (Fig. 2.10D,E). This indicates that episodes of horizontal shortening are not necessarily followed by pulses in exhumation. During the Miocene, exhumation affected large parts of the Puna, Eastern Cordillera, north-western Sierra Pampeanas and the Interandean zone (Fig. 2.10F,G). This exhumation pattern agrees well with major tectonic deformation that affected the whole Andes except for the Subandean zone from the Oligocene until ca. 10 Ma. It also correlates with intense shortening in the Puna (Coutand et al., 2001) and with the onset of basement block uplift in the Eastern Cordillera that led to the compartmentalization of the foreland (*e.g.*, Coutand et al., 2006). In the late Miocene (~12 Ma), exhumation propagated into the Subandean zone (Fig. 2.10G) and thus reflects the eastward propagation of deformation into this area (Fig. 2.3A). Similarly, exhumation in the southern Eastern Cordillera also spreads eastwards during this time, contemporaneously with the east-directed, yet unsystematic propagation of uplifting basement blocks (*e.g.*, Coutand et al., 2006; Hain et al., 2011) (supplementary movie, InversionA). However, exhumation rates in the southern Eastern Cordillera as resolved by our inversion appear relatively constant through time (Fig. 2.10) in spite of the successive aridification of the hinterland that is associated with growing orographic barriers (Coutand et al., 2006). This can be explained by low data resolution in the western part of the southern Eastern Cordillera where only data from single thermochronometric systems (either AFT or AHe) are available, which are older than 10 Ma, or ZHe older than 80 Ma, which are not included in the modelling (Deeken et al., 2006; Carrapa et al., 2011; Pearson et al., 2013; Carrapa et al., 2014; Reiners et al., 2015).

The initiation of the South American Monsoon in the late Miocene (10-7 Ma) led to important hydrological changes at the eastern mountain front (*e.g.*, Strecker et al., 2007; Uba et al., 2007; Mulch et al., 2010). Increased exhumation rates in the eastern Interandean zone and the Subandean belt since the latest Miocene (~6 Ma) could thus be an expression of enhanced precipitation and higher climate variability associated with the onset of the monsoonal climate (Mulch et al., 2010; Rohrmann et al., 2016) and the establishment of high-amplitude climatic oscillations in the Plio-Pleistocene (Shackleton et al., 1984) (Fig. 2.10H-K, supplementary movie, InversionA). Conversely, they can also be explained by augmented shortening rates (Echavarria et al., 2003) or a combination of both. Higher moisture availability might also account for higher exhumation rates observed locally in the Eastern Cordillera during the late Miocene. Finally, the Sierra Aconquíja in the northern Sierra Pampeanas shows a strong Plio-Pleistocene acceleration in exhumation, where rates increase from <0.1 km/Ma before 6 Ma to ca. 1.5 km/Ma in the Pleistocene (Fig. 2.10H-K). The Sierra Aconquíja is a major orographic barrier for westward moisture-bearing winds from the foreland and receives more than 800 mm/a rainfall on its eastern flank (Sobel and Strecker, 2003). Major tectonically-driven surface uplift and relief development started after 6 Ma along high-angle reverse faults, intensified during the Pliocene and was most pronounced after 3 Ma (Strecker et al., 1989; Bossi et al., 2001; Zapata et al., 2019). Ensuing aridification of the adjacent intermontane basin to the west has occurred between 3 and 2.5 Ma as a result of the establishment of an efficient orographic barrier at that time (Kleinert and Strecker, 2001). Taken together, the Pleistocene increase in exhumation rate in this area can be explained by the interplay of active tectonic uplift and efficient erosion related to very high precipitation and localized Pleistocene glaciation (*e.g.*, Sobel and Strecker, 2003; Löbens et al., 2013). A similar Pleistocene increase in the exhumation rate also occurred in the Fiambalá Basin (western northern Sierra Pampeanas) but is only based on one young AHe age of 2.3±0.05 Ma (*e.g.*, Figs. 2.8, Fig. 2.9B) that has been attributed to Plio-Pleistocene tectonic activity in this area (Carrapa et al., 2008; Safipour et al., 2015).

In the northern segment of the Central Andes, the influence of both climate and tectonic processes can be observed. On the western side, exhumation rates are slow and correspond to very low shortening rates and high aridity. Although significant topography at the western flank of the Andes might have existed since the middle Miocene or earlier (Jordan et al., 2010; Evenstar et al., 2015; Scott et al., 2018), little exhumation has occurred during the Cenozoic in this part of the Andes. Reburial linked to volcanic covering and internal drainage of the Altiplano-Puna plateau, a consequence of dry climatic conditions, contributed to low exhumation rates (*e.g.*, Reiners et al., 2015). This suggests that erosion in the west is primarily inhibited due to the absence of precipitation and possibly would have been higher in a different climatic setting. The onset of exhumation on the eastern side of the Andes seems to be synchronous with the onset of tectonic activity

(Fig. 2.3A). The observed exhumation pattern also generally agrees well with phases of major tectonic deformation, but increased horizontal shortening does not necessarily result in pulses of enhanced exhumation. However, as deformation propagates into areas that were previously not subjected to shortening, so does exhumation. This is clearly observed in the eastward migration of exhumation into the Subandean zone and in the southern Eastern Cordillera during the late Miocene that reflects the eastward propagation of deformation in these areas.

Exhumation rates in the east are higher than in the west. This can be explained by higher amounts of horizontal shortening and/or higher moisture availability in a semi-arid to humid environment. Increased exhumation rates in the eastern Interandean and the Subandean zone since the latest Miocene (ca. 6 Ma) can equally be explained by either increased shortening rates (Echavarria et al., 2003) or higher precipitation associated with the onset of the South American Monsoon (*e.g.*, Strecker et al., 2007; Uba et al., 2007; Mulch et al., 2010) and the establishment of high-amplitude climatic oscillations in the Plio-Pleistocene (Shackleton et al., 1984) associated with Late Cenozoic global cooling (Zachos et al., 2001). Yet, Pleistocene exhumation rates in the northern Sierra Pampeanas are significantly higher than in the Subandean range, although both were tectonically active and received high amounts of precipitation during the last 2 Myr. They differ, however, in their tectonic style. Whereas deformation in the Subandean belt is thin-skinned (*e.g.*, Echavarria et al., 2003; Anderson et al., 2017), shortening in the northern Sierra Pampeanas is accommodated along steep (50-60° dip, Strecker et al., 1989), basement-involving reverse faults that result in important surface uplift (*e.g.*, Sobel and Strecker, 2003), steep topography and high exhumation rates. This suggest that the tectonic style that accommodates deformation is a major factor in setting the exhumation rate under similar precipitation conditions. Our results further show that the onset of exhumation agrees relatively well with the onset of tectonic activity, whereas the magnitude of exhumation rates seems to be strongly modulated by climatic conditions and the tectonic style which accommodates deformation. Therefore, in the northern segment of the Central Andes, we cannot disentangle the respective roles of deformation and climate on exhumation.

2.7.2.2 Central segment (28-32° S)

The central part of the orogen between 28 and 32° S is currently located above the Pampean flat slab segment which initiated in the latest early Miocene (*e.g.*, Kay and Mpodozis, 2002). On the western side of the range, where thermochronological data are abundant, little information about the timing and magnitude of tectonic activity exists. Contractional deformation initiated in the Late Cretaceous to the Paleocene in the Principal and Frontal Cordilleras. Similar to the northern segment, exhumation during the Paleogene is recorded with relatively low rates (<0.2 km/Ma) although data resolution is too low to infer changes in exhumation rates. This supports previous interpretations of structural and sedimentary observations (Martínez et al., 2016; Rossel et al.,

2016; Fosdick et al., 2017; Martínez et al., 2018) and thermochronological data (Lossada et al., 2017; Rodríguez et al., 2018) that indicate an early, pre-Oligocene onset of mountain building in this part of the Andes. In the Oligocene, contractional deformation was interrupted by extension and only resumed in the early Miocene by basin inversion and deformation in the Frontal Cordillera (Fig. 2.3B, Winocur et al., 2015; Martínez et al., 2016; Rossel et al., 2016). At a regional scale, exhumation rates in the Frontal Cordillera are moderately higher (0.25 km/Ma) since the late Miocene compared to the northern segment (Fig. 2.10G). This correlates with the onset of crustal thickening and the peak of slab shallowing (*e.g.*, Kay and Mpodozis, 2002; Rodríguez et al., 2018) that could have led to isostatic uplift (*e.g.*, Dávila and Lithgow-Bertelloni, 2015; Flament et al., 2015) and, in turn, enhanced exhumation rates. Higher exhumation rates could also be explained by the influence of the Westerlies, which bring higher precipitation up to 30° S in austral winter (Garreaud et al., 2009). East of the drainage divide, thermochronological data are very sparse. The main recovered signal is a relatively high Pleistocene exhumation rate (ca. 0.75 km/Ma) in the Sierra Pampeanas which can be attributed to active deformation along reactivated normal faults in the Sierra de Valle Fértil (Ortiz et al., 2015).

2.7.2.3 Southern segment (32-36° S)

Pre-Neogene thermochronological ages are sparse and limited to the Coastal Cordillera, which shows low exhumation rates since the Oligocene (Fig. 2.10), or close to the mountain front in the Principal Cordillera. Therefore, our reconstruction of the exhumation rate is restricted to the middle Miocene and onwards. Compressional deformation in the southern segment has occurred in the early Miocene after a period of regional extension (Fig. 2.3C) (*e.g.*, Jordan et al., 2001a; Horton, 2018b). A first signal in exhumation rate is recorded after 16 Ma in most parts of the Principal and Frontal Cordilleras (supplementary movie, InversionA). This is later than the suggested onset of tectonic activity in the West-Andean fault-and-thrust belt at ca. 25 Ma (Riesner et al., 2017) and crustal thickening (Kay et al., 2005), but around the same time of the initiation of the Aconcagua fold-and-thrust belt at 18-15 Ma (Giambiagi et al., 2015b). Exhumation rates on the eastern side of the drainage divide continuously accelerated since the late Miocene from 0.15 km/Ma to ca. 0.4 km/Ma in the Pleistocene (Fig. 2.10) despite decreasing (Giambiagi et al., 2015b) or constant (Riesner et al., 2017) shortening rates (Fig. 2.2). This might be explained by higher erosional efficiency related to increasing topography associated with Andean mountain building and by the onset of more humid conditions in the middle Miocene (Jordan et al., 2001b; Ruskin and Jordan, 2007; Ciccioli et al., 2014; Buelow et al., 2018) and the South American Monsoon system in the late Miocene (Strecker et al., 2007; Mulch et al., 2010; Rohrmann et al., 2016). The Principal Cordillera on the western side of the Andes shows low rates (0.1-0.25 km/Ma) during the late Miocene to the late Pliocene that drastically increase to values exceeding 2 km/Ma in the Pleis-

tocene (Fig. 2.10H-K). These high erosion rates are observed 2 Ma after the period of high surface uplift (10.5-4.6 Ma) (Farías et al., 2008), and although the Principal Cordillera was and is tectonically active, no evidence for intensified Pleistocene rates of horizontal shortening exists (Riesner et al., 2017) and we cannot explain this change in erosion nor the magnitude of Pleistocene erosion rates by tectonically-driven rock uplift only. Interestingly, this region experienced important glaciation (*e.g.*, Clapperton, 1994) and intensified precipitation (Lamy et al., 1999; Valero-Garcés et al., 2005) during the Pleistocene, processes that are commonly associated to a northward shift of the Westerlies during colder conditions (*e.g.*, Lamy et al., 1999; Zech et al., 2008). We therefore attribute the high Pleistocene erosion rates on the western side of the Andes to glacial erosion and intensified precipitation, reinforced by isostatic rock-uplift and active tectonics. Glacial overprint in this region is also evidenced by glacial relief observed from morphometric analyses (Rehak et al., 2010). Consequently, we conclude that increased erosion caused by the onset of glaciations produced a perturbation to the prevailing conditions in this part of the Central Andes that could have resulted in increased rock uplift and, in turn, further enhanced erosion in a feedback mechanism (*e.g.*, Molnar and England, 1990; Whipple and Meade, 2006).

2.7.2.4 Integrated view on the exhumation rate pattern from north to south

As shown by the critical wedge theory (*e.g.*, Dahlen and Suppe, 1988; Willett, 1999) and implied by previous case studies of the Central Andes (Masek et al., 1994; Horton, 1999; Montgomery et al., 2001), climatic conditions may control the shape of the mountain belt by influencing the erosion rate. Our study shows that the wide mountain belt in the northern segment indeed correlates with low erosion rates that prevail over most parts of the orogen, apart from focused erosion on its eastern orogenic front. Yet, reconstructed Miocene erosion rates in the southern segment, where the Andes are narrow, are comparably low as in the northern segment and only accelerated in the Plio-Pleistocene. It seems thus likely that processes such as mantle dynamics, tectonic activity and crustal thickening set the topographic expression of the Central Andes, which is then modulated by climatic conditions. In particular, the northern Central Andes experienced much more horizontal shortening and crustal thickening than the southern segment, and both processes initiated earlier in the northern segment. This may have resulted in orographic growth before (*e.g.*, Canavan et al., 2014; Scott et al., 2018) or during (*e.g.*, Fiorella et al., 2015) the Oligocene. On the contrary, the southern segment experienced a period of Oligocene extension and horizontal shortening resumed only in the early Miocene, with values significantly lower than in the north (Fig. 2.2, Fig. 2.3). Given these different tectonic settings, it remains open if the southern segment of the Central Andes would have reached similar width and height as the northern segment, although significant growth seems to be unlikely under such high Plio-Pleistocene erosion rates. Similarly, the building up of the Altiplano-Puna plateau might not have been possible under higher erosion rates.

Our analysis of the exhumation rate in the Central Andes indicates that the onset of exhumation, as constrained by the oldest cooling ages in a given region, mainly correlates with the onset of tectonic activity and major crustal thickening. However, these ages could be younger than the true onset of exhumation and therefore they represent minimum ages for initial cooling. Our results also highlights the influence of climatic conditions on the magnitude of upper crustal exhumation. Exhumation rates in the Central Andes vary most commonly between 0.05 km/Ma and 0.25 km/Ma with important regional exceptions. The highest rates are observed during the Plio-Pleistocene in the Subandean range, the Sierra Aconquíja in the northern Sierra Pampeanas and in the Principal Cordillera south of 33° S. These regions are all characterized by active tectonics and high moisture availability but show important differences that highlight several aspects of the relationships between tectonics, climate and exhumation. First, inherited structures and the presence of sediments and décollement layers in the foreland control the way how deformation is accommodated (*e.g.*, Allmendinger et al., 1983) and directly influence the exhumation rate by determining the steepness of faults and thus the amount of vertical displacement. Second, we observe similar Mio-to-Pliocene erosion rates in the western part of the southern segment (Principal Cordillera) and in the eastern part of the northern segment (Eastern Cordillera, Inter- and Subandean zones), although shortening rates are much higher in the north than in the south (Fig. 2.2). This suggests that the magnitude of erosion does not necessarily correlate with the amount of horizontal shortening and that moisture availability and the structural style of deformation have an important role in setting the exhumation rate. Finally, glacial erosion in the southern Principal Cordillera increases the exhumation rate previously set by deformation and fluvial processes by ca. one order of magnitude.

2.8 Conclusion

In this study, we provide 238 new thermochronological ages from 146 samples that we complement with 824 ages from literature to constrain the exhumation rate history of the Central Andes. To gain insights about feedback mechanisms between climate, tectonics and erosion, we compare the exhumation rate history to the past and present climatic setting and to the deformation record of the Central Andes.

In the arid region west of the Andes (18-32° S), exhumation rates are generally low (<0.2 km/Ma) and correlate well with low shortening rates and high aridity. On the eastern side of the Andes in the northern segment, the subsequent onset of exhumation in the Eastern Cordillera, Altiplano-Puna plateau and Inter- and Subandean zones reflects the onset and eastward propagation of deformation observed in this region. Accelerated exhumation since the latest Miocene in the east-

ern Interandean and the Subandean zone can be either related to increased horizontal shortening rates, the onset of the South American Monsoon, or the coupling between the two.

Highest exhumation rates are observed during the Pleistocene in the Sierra Aconquíja in the northern Sierra Pampeanas and in the Principal Cordillera south of 33° S and west of the Andes. These regions are characterized by active tectonics accommodated along steep, reactivated normal faults and affected by either particularly high rainfall (Sierra Aconquíja) or intense glacial erosion (southern Principal Cordillera). The observed exhumation rates in these regions are higher than the ones observed in the Subandean range, which is characterized by high shortening rates accommodated by thin-skinned deformation. This indicates that the inherited structures and the presence of sediments in the foreland have a significant impact on the magnitude of exhumation rates, as does glacial erosion and increased precipitation in an active tectonic setting.

2.9 Acknowledgments

2.10 Supplementary Material

2.10.1 Thermochronological analyses (AHe, ZHe and AFT)

To increase spatial coverage on the western side of the Andes, where thermochronometric data was sparse, we have collected 149 new samples from Chile during several field campaigns that were realized over the last 4 years. After crushing and sieving of the bedrock samples to gain the fraction between 25-350 μm, apatite and zircon crystals were concentrated using the traditional two-steps heavy liquid separations (3.1 and 3.3 g/cm^{-3}) and Frantz paramagnetic separation techniques. Different laboratories were involved for mineral separation and dating. Samples labelled with the prefix 14NC (Campaign 1) were separated at the Geological Institute of the Bulgarian Academy of Sciences in Sofia, Bulgaria, those with the prefix Clin (Campaign 2) by Zirchron LLC in Tucson, Arizona, and those with the prefix CLRK (Campaign 3) by the Langfang Yantuo Geological Service Company in Langfang, China. Samples from Campaign 1 and 2 (14NC-x; Clin-x) were analysed at the ARHDL lab (University of Arizona, Tucson) for (U-Th)/He dating. Fission-track analyses were conducted at the ISTerre (Grenoble, FR) (14NC-x) and at the ETH Zurich (Zurich, Switzerland) (Clin-x), respectively. CLRK-x samples were analysed at Dalhousie University (Halifax, CA) for (U-Th)/He dating and AFT.

2.10.1.1 (U-Th)/He dating of zircons and apatites

For each sample, 2 to 5 apatite and zircon crystals were manually selected under a high-magnification stereoscopic microscope for (U–Th)/He analyses. Preference was given to euhedral, transparent, inclusion- and crack-free grains with the smallest dimensions being not less than 70 μm (CLRK–x) or 60 μm (14NC-x and Clin-x). Grain dimensions of apatites were determined and photographed in at least two different orientations parallel and perpendicular to the c-axis. For zircon crystals, the bipyramidal tip heights and two different c-axis parallel widths were measured. In rare cases, where all inclusion-free grains were broken, apatite and zircon grains with one damaged tip were analysed. This was taken into account during the α-particle ejection corrections (*e.g.*, Farley et al., 1996). All selected grains were packed in Nb tubes for ^{4}He extraction.

<u>(U-Th)/He analytical procedure at University of Arizona (samples 14NC-x and Clin-x)</u>

Apatite grains were heated by a focused laser beam (either CO_2 or diode) to 900-1000 °C for 3 minutes, zircon grains were heated 3 times to ~1000-1250 °C for 20 minutes each to allow complete degassing of ^{4}He. The ^{4}He was spiked with 0.1-0.2 pmol 3He and analysed by a Balzers quadrupole mass spectrometer (QMS). Durango apatite and Fish Canyon tuff were used as external standards for apatite and zircon measurements, respectively. The ablated grains were spiked

with nitric acid solutions enriched in ^{233}U, ^{229}Th (and ^{42}Ca, ^{147}Sm for apatites, ^{90}Zr for zircon) isotopes and dissolved in acid to determine molar contents of U, Th, Sm, Ca, and Zr via isotope-dilution ICP-MS. Preparation procedure and analytical details are provided in the ARHDL Report 1 of Reiners and Nicolescu (2006). All ages were corrected for α-particle ejection by using individual grain dimensions (Reiners et al., 2018).

(U-Th)/He analytical procedure at Dalhousie University (samples CLRK-x)

^{4}He measurements were completed on a custom-built He-extraction line equipped with a 40 W diode laser and a Pfeiffer Vacuum Prisma quadrupole mass-spectrometer. Apatite crystals were heated to 1050 °C for 5 minutes, whereas zircon crystals were heated to 1250 °C for 15 minutes. After ^{4}He extraction, a precisely measured aliquot of ^{3}He was added to the sample and the ^{3}He/^{4}He ratio was measured using the quadrupole mass-spectrometer. This procedure was repeated once for apatite crystals to assure that no ^{4}He is left in the grain. Since zircon crystals retain ^{4}He to higher temperatures, the ^{4}He extraction for zircon grains was repeated minimum 3 times until the amount of ^{4}He in the last re-extraction was less than 1% of the total ^{4}He extracted from this grain. Typical analytical uncertainties are in the range of 1.5-2% (1σ) for both zircon and apatite crystals. Durango apatites and Fish Canyon tuff zircons were used as external standards for apatite and zircon measurements, respectively, that went through the same analytical procedures as unknown samples to ensure accuracy, reproducibility and reliability of the data. After ^{4}He extraction, both apatite and zircon crystals were spiked with mixed ^{235}U, ^{230}Th, and ^{149}Sm and dissolved following standard dissolution protocols for these minerals. Apatite crystals were dissolved in HNO_3 at 80 °C for 1.5 hours, whereas zircon crystals were dissolved in high-pressure dissolution vessels in mixture of concentrated HF and HNO_3 at 200 °C for 96 hours. Isotopic ratios were measured using an iCAP Q ICP-MS. Raw data were reduced using the Helios software package developed by R. Kislitsyn and D. Stockli at Dalhousie University (Halifax, CA) specifically for (U-Th)/He data reduction. The α-ejection correction was calculated based on surface to volume ratio (Farley et al., 1996).

2.10.1.2 Fission-track dating of apatites

Apatite grains were mounted into epoxy resin, polished to expose the internal grain surface and etched for 20 s at 21 °C in 5.5 M HNO_3. All mounts were prepared using the external detector method (Hurford and Green, 1983). Samples from Campaign 1 (14NC-x) were irradiated at the FRM II research reactor in Garching, Germany under a nominal neutron fluence of $8*10^{15}$ n/cm^2 and with IRMM540R dosimeter glasses (15 ppm U) and Fish Canyon tuff and Durango apatite as external standards. Samples from Campaign 2 (Clin-x) and Campaign 3 (CLRK-x) were irradiated at the Radiation Centre of the Oregon State University under a nominal neutron fluence of $1.2*10^{16}$

n/cm^2 and $1.0*10^{16}$ n/cm^2, respectively. The high flux used for samples Clin-x was chosen based on the expected young cooling ages and relatively low (~1ppm) uranium content. CN5 dosimeter glasses and Durango apatite as external standard were used for samples Clin-x and CLRK-x. After irradiation, the low-U muscovite detectors that covered apatite grain mounts and glass dosimeters were etched in 48% HF for 18 min at 23 °C (samples 14NC-x) and in 40% HF for 45 min at 21 °C (samples Clin-x and CLRK-x) to reveal induced fission tracks. Dry counting was performed under an optical microscope at a magnification of 1000 (CLRK-x) and 1250 (14NC-x and Clin-x), respectively. Fission-track ages were calculated using a weighted mean Zeta calibration factor (Hurford and Green, 1983) based on IUGS ages standards (Durango, Fish Canyon and Mount Dromedary apatites) (Hurford, 1990; Miller et al., 1985), giving Zetas of $\zeta_{ISTerre}$ = 310.4±13.8 for samples 14NC-x, ζ_{Zurich} = 354.96±12.6 for samples Clin-x and $\zeta_{Dalhousie}$ = 370.6±5 for samples CLRK-x, respectively.

2.10.2 U–Pb analyses

A total of 75 zircon crystals from two samples (Clin22A – 39 crystals, Clin25A – 36 crystals) were analysed for U-Pb ages by LA-ICP-MS (Appendix, Table A4 and Fig. S5). Zircons were hand-picked, mounted into epoxy and polished down to half thickness with a 1 µm diamond paste. Ablation spots of 50 µm were preselected on cathodoluminescence images conducted on a Cam-ScanMV2300 SEM at the University of Lausanne. Neither sample showed mineral zonations, but the zircon grains of Clin22A have inclusion-rich cores and appear in two generations that are characterized by two different crystal sizes. Zircons from both generations were analysed. ^{238}U/^{206}Pb ages were obtained by measuring ^{202}Hg, ^{204}Pb, ^{206}Pb, ^{207}Pb, ^{208}Pb, ^{232}Th, ^{235}U, and ^{238}U intensities on an UP-193FX (ESI) ablation system interfaced to an Element XR sector field, single-collector ICP-MS (Thermo Scientific) at the University of Lausanne. Operation conditions were similar to Ulianov et al. (2012) and included a repetition rate of 5 Hz, a spot size of 50 µm and an on-sample energy density of 3 Jcm^{-2}. We used GJ-1 (Jackson et al., 2004, ID-TIMS ^{206}Pb/^{238}U age of 600.4±0.4 Ma (Ulianov et al., 2012; Boekhout et al., 2012)) as a primary Reference material and Plesoviče zircon as a secondary standard (^{206}Pb/^{238}U age of 337.13±0.37 Ma, Sláma et al., 2008). The weighted mean ^{206}Pb/^{238}U age of our measurements for Plesoviče zircon is 335.6±3.5 Ma (2σ of 1.1%). The measurements of the Plesoviče zircon crystals show a day-long drift from older (344.7 Ma) to younger (328.9 Ma) ages (Appendix, Table A4 and Fig. S6), which corresponds to max. inaccuracies of ca. 2% relative to the ID-TIMS age. Such inaccuracies are considered normal for the U/Pb LA-ICP-MS dating of zircon (*e.g.*, Schaltegger et al., 2015). The drift is not observed for the samples Clin22A and Clin25A. Common Pb contamination was qualitatively assessed by controlling the measured ^{202}Hg and ^{204}Pb. Weighted mean average ages with

2σstandard errors of analytically concordant values were calculated by using Isoplot 4.1 (Ludwig, 2001) (supplementary Fig. S5, Fig. S6).

2.10.3 Inverse model using fault blocks

The fault blocks of the study area were defined by an exploration team of First Quantum Minerals FQM using a variety of sources including seismic tomography, earthquake epicentres, satellite gravity enhanced with ground station readings, regional aeromagnetics, tectonostratigraphic geological mapping at 1:100.000-500.000, mapped faults from SERNAGEOMIN (2003) and SegemAR (1997) published maps and topography (Banyard and Farrar, 2018). The boundaries between the blocks are interpreted to be long-lived, deep seated structural corridors and as such may not find their expression in a single, traceable fault at surface (Banyard and Farrar, 2018). Thermochronological data in different blocks move independently from each other even if they are located within the correlation distance. An $\dot{e}_{prior}$ of 0.1 km/Ma, a G_0 of 25 °C and correlation length scales of 20 and 1000 km, respectively, were used to test the influence of the fault blocks on the exhumation rates (Fig. 2.12G,H and supplementary movies, InversionG and InversionH).

2.10.4 Supplementary Figures
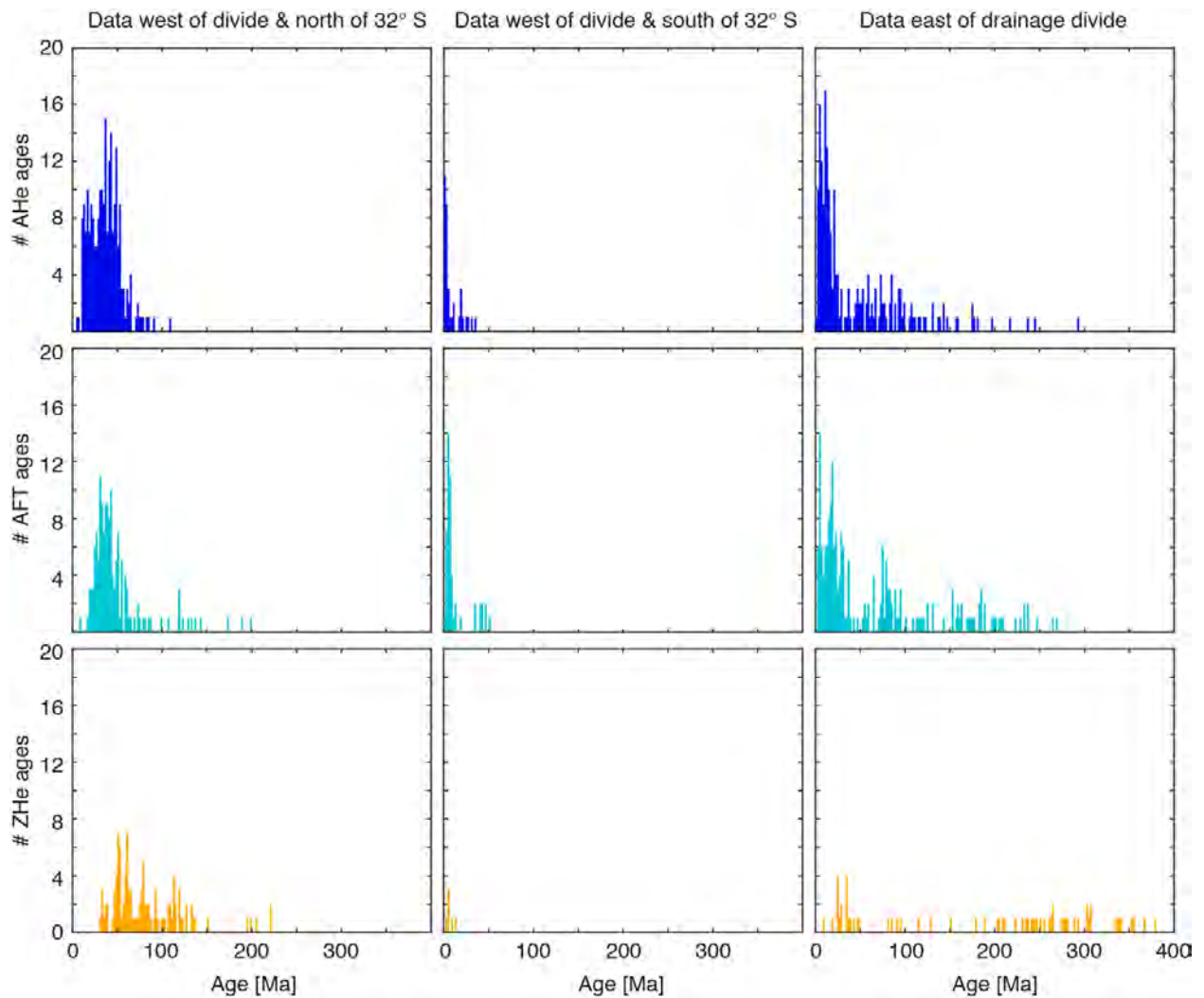
Figure S1: Histograms of AHe, AFT and ZHe ages for the different data sets described in the text. **A)** Data west of the drainage divide and north of 32° S, **B)** data west of the drainage divide and south of 32° S and **C)** data east of drainage divide.
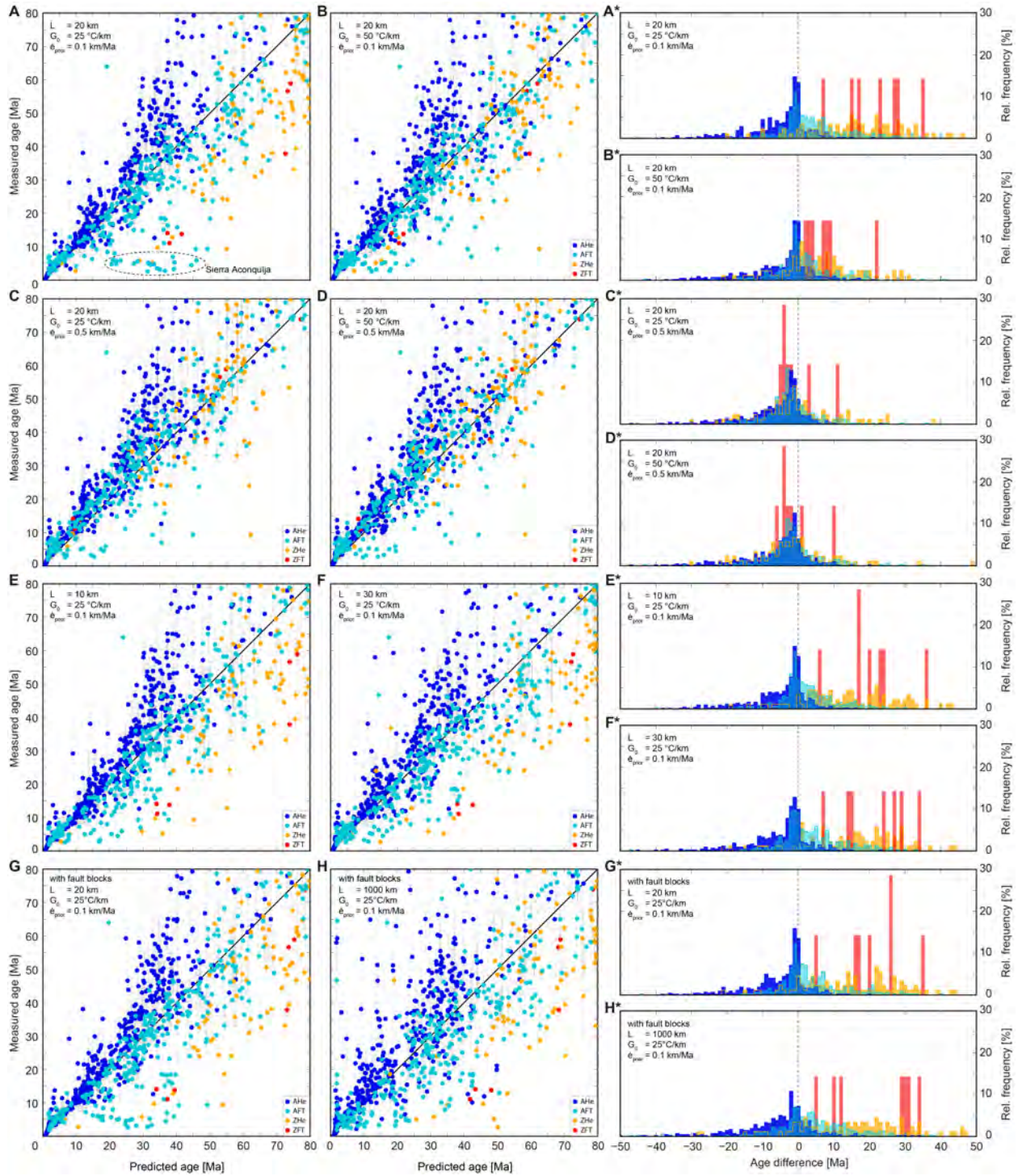
Figure S2: Misfit and histograms for the eight tested inversions. **A-D)** Inversions with different combinations of $\dot{e}_{prior}$ (0.1, 0.5 km/Ma) and G_0 (25, 50 °C/km) and a correlation length scale of 20 km. **E, F)** Inversions with the same set of parameter as in A) but with correlation lengthscales of 10 and 30 km, respectively. **G, H)** Inversions with fault blocks and the same set of parameter as in **A)** and correlation lengthscales of 20 and 1000 km, respectively. **A*-H*)** Histograms of age differences (age$_{pred}$-age$_{obs}$) corresponding to the inversions A-H.
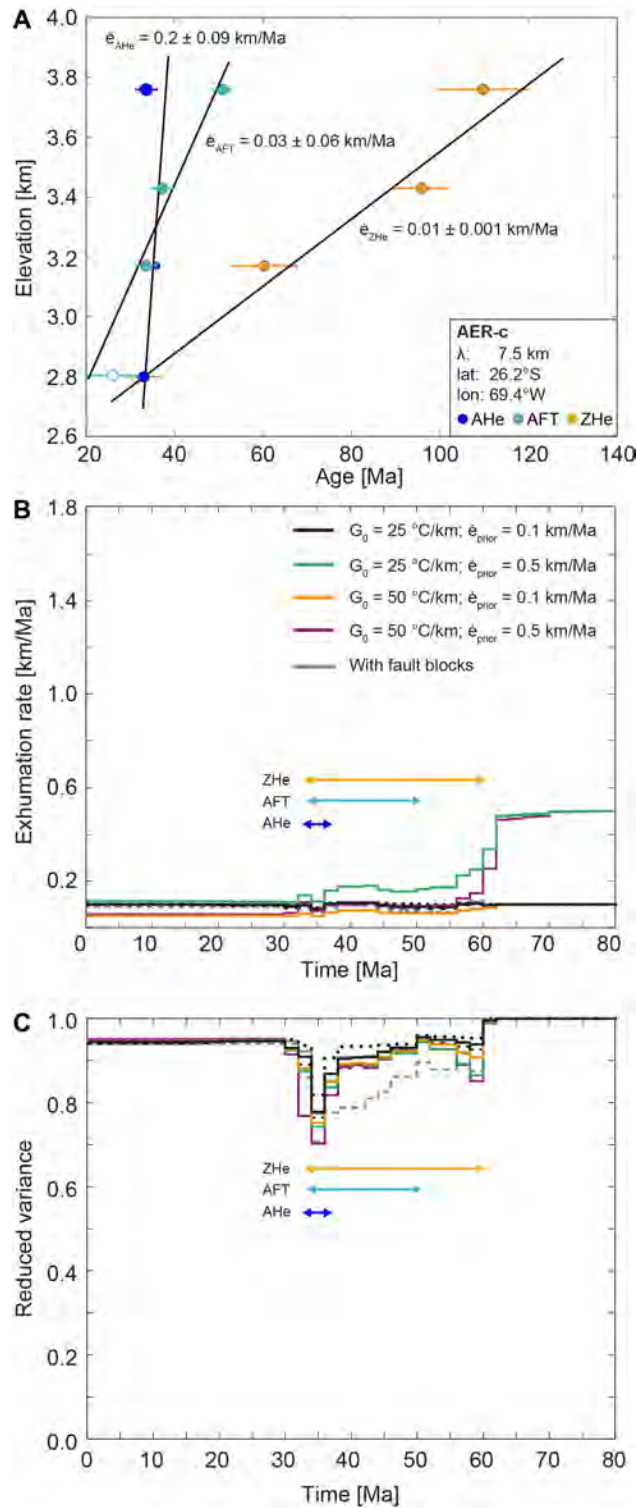
Figure S3: Comparison of exhumation rates in the northern segment of the study area (26.2° S) derived from the age-elevation profile AER-c and from our inversion (see Fig. 2.1 and supplementary Table A5 for location and data). **A)** Age-elevation profile with linear best-fit indicating the exhumation rate. For consistency with the inversion, average ages with standard deviation rather than individual grain ages are used. Open circles represent thermochronological ages excluded in the inversion. **B)** Exhumation rates derived from the inversion at the location of the age-elevation profile shown in (A) using different sets of parameters. (cont. on next page)

Figure S3: (cont.) Solid lines represent inversions with a correlation length scale of 20 km and varying G_0 (25 and 50 °C/km) and $\dot{e}_{prior}$'s (0.1 and 0.5 km/Ma). Black lines represent inversions with our preferred set of parameters ($G_0 = 25$ °C/km, $\dot{e}_{prior} = 0.1$ km/Ma) and correlation length scales of 10 km (dotted), 20 km (solid) and 30 km (dashed). Grey lines represent the inversion with fault blocks and correlation length scales of 20 km (solid) and 1000 km (dashed), respectively. Colored arrows indicate the time span covered by the respective thermochronological systems. **C)** The reduced variance of the model drops when information of the thermochronological data are available.
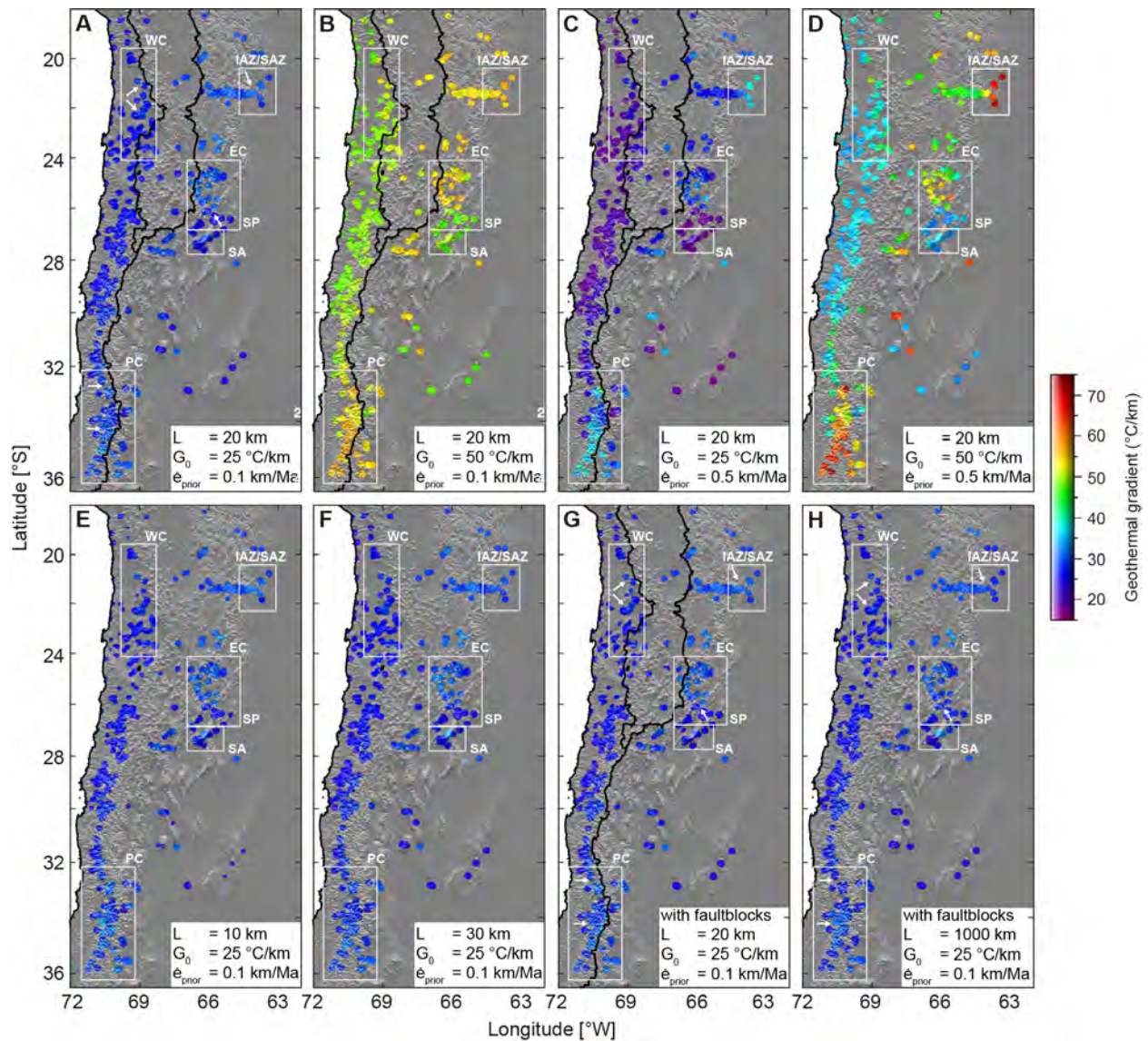
Figure S4: Modelled present-day heat flow for the tested inversions. White rectangles delineate specific locations discussed in the text: EC = southern Eastern Cordillera, IAZ/SAZ = Inter- and Subandean zones, PC = southern Principal Cordillera, SA = Sierra Aconquíja, northern Sierra Pampeanas, WC = Western Cordillera. **A-D)** Inversions with different combinations of $\dot{e}_{prior}$ (0.1 and 0.5 km/Ma) and G_0 (25 and 50 °C/km) and a correlation length scale of 20 km. **E,F)** Inversions with the same set of parameter as in (A) but with correlation lengthscales of 10 and 30 km, respectively. **G,H)** Inversions with fault blocks using the same set of parameter as in (A) and correlation lengthscales of 20 and 1000 km, respectively.
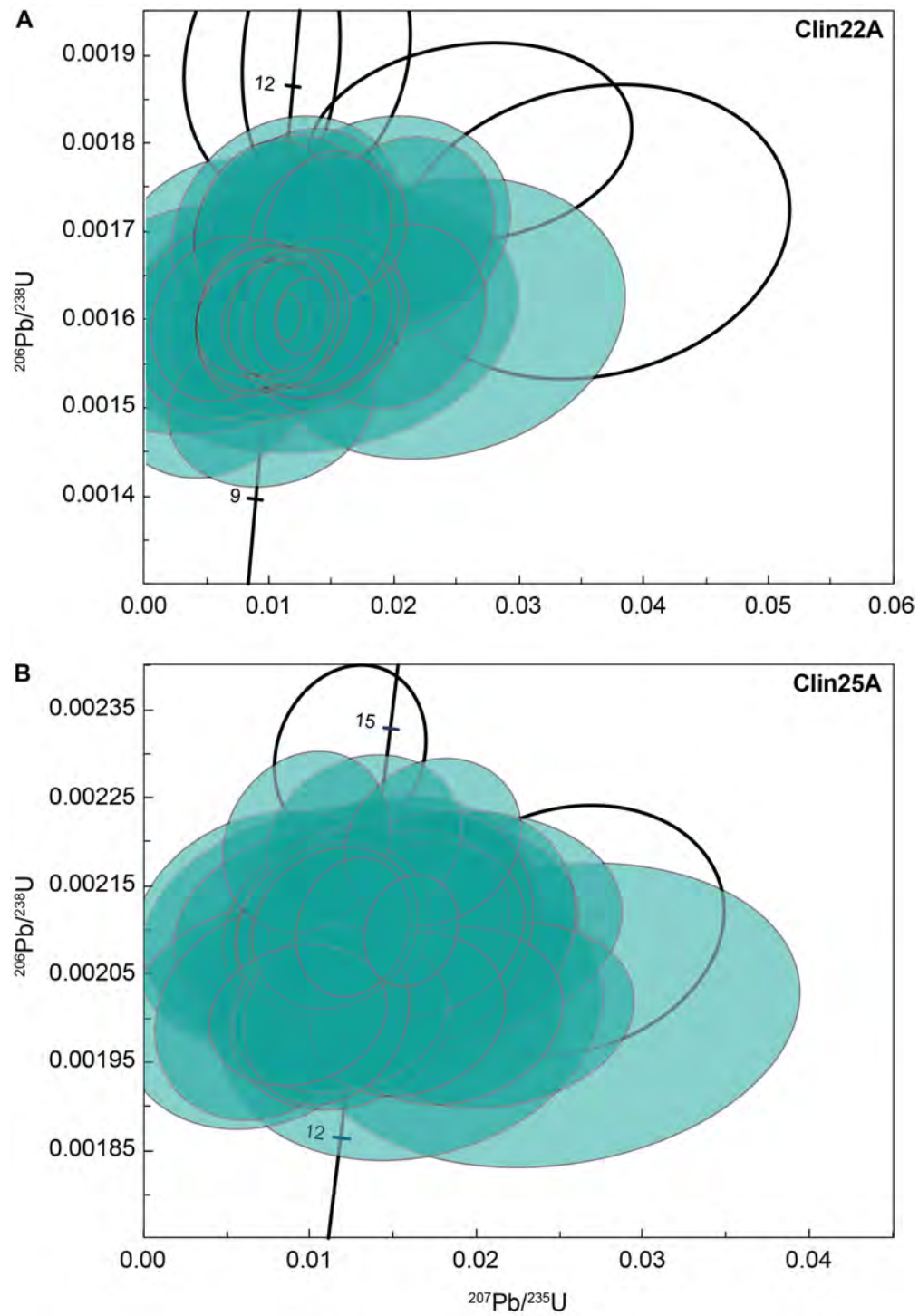
Figure S5: U-Pb Concordia diagrams for samples Clin22A and Clin25A. Discordant ages are shown as empty, black ellipses.
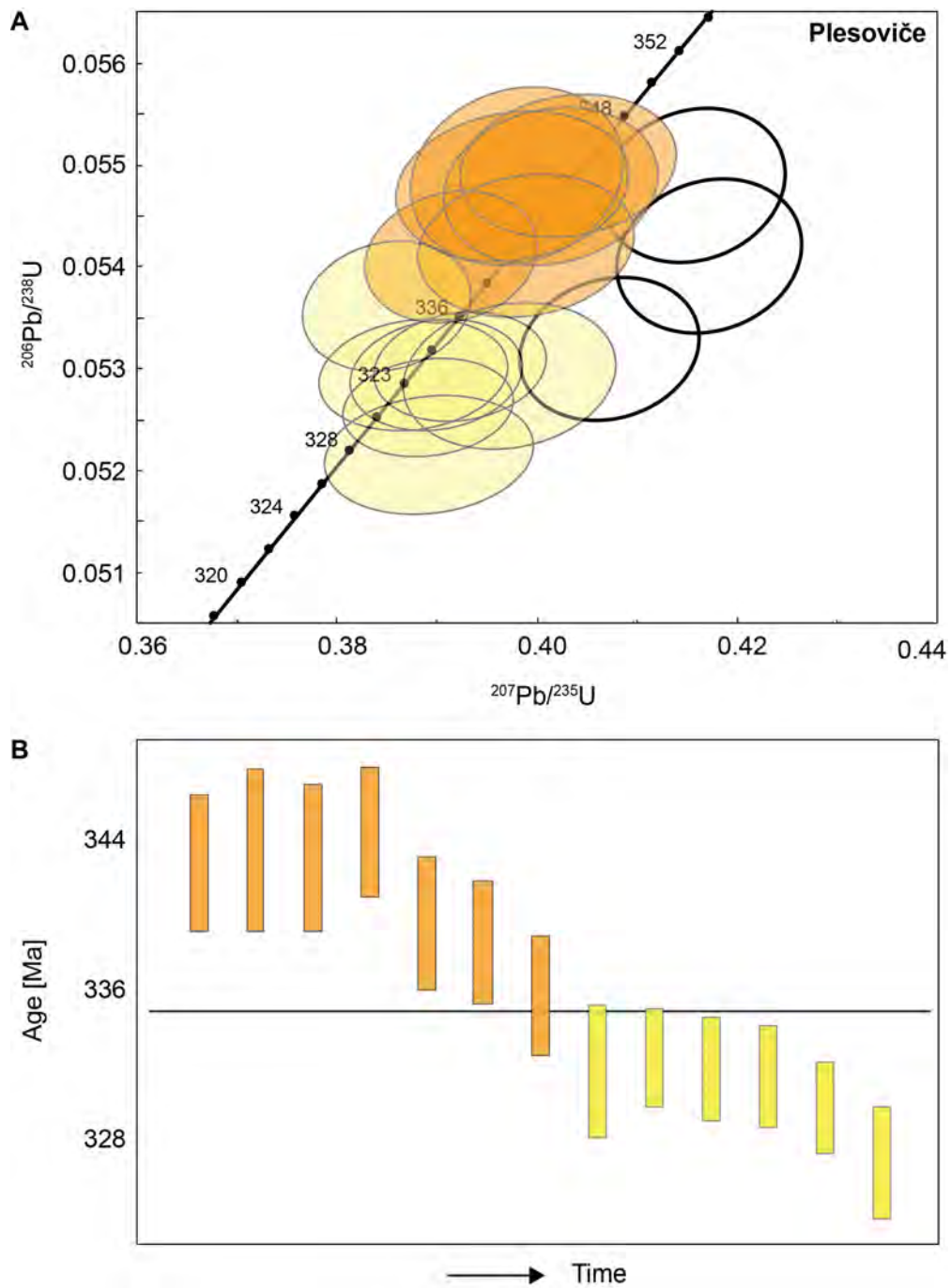
Figure S6: A) U-Pb Concordia diagram. Discordant ages are shown in empty, black ellipses. **B)** Observed day-long drift of the Plesoviče Secondary standard. Black line represents mean value of concordant ages (335.6±3.5 Ma).

Bibliography

Aguilar, G., Riquelme, R., Martinod, J., Darrozes, J., and Maire, E. (2011). Variability in erosion rates related to the state of landscape transience in the semi-arid Chilean Andes. *Earth Surf. Processes Landforms*, 36(13):1736–1748.

Allmendinger, R.W., Figueroa, D., Snyder, D., Beer, J., Mpodozis, C., and Isacks, B.L. (1990). Foreland shortening and crustal balancing in the Andes at 30°s latitude. *Tectonics*, 9(4):789–809.

Allmendinger, R.W. and Gubbels, T. (1996). Pure and simple shear plateau uplift, Altiplano-Puna, Argentina and Bolivia. *Tectonophysics*, 259(1-3):1–13.

Allmendinger, R.W., Jordan, T.E., Kay, S.M., and Isacks, B.L. (1997). The evolution of the Altiplano-Puna plateau of the Central Andes. *Annu. Rev. Earth Planet. Sci.*, 25(1):139–174.

Allmendinger, R.W. and Judge, P.A. (2014). The Argentine Precordillera: A foreland thrust belt proximal to the subducted plate. *Geosphere*, 10(6):1203–1218.

Allmendinger, R.W., Ramos, V.A., Jordan, T.E., Palma, M., and Isacks, B.L. (1983). Paleogeography and Andean structural geometry, northwest Argentina. *Tectonics*, 2(1):1–16.

Amilibia, A., Sàbat, F., McClay, K.R., Muñoz, J.A., Roca, E., and Chong, G. (2008). The role of inherited tectono-sedimentary architecture in the development of the central Andean mountain belt: Insights from the Cordillera de Domeyko. *J. Struct. Geol.*, 30(12):1520–1539.

Ammann, C., Jenny, B., Kammer, K., and Messerli, B. (2001). Late Quaternary glacier response to humidity changes in the arid Andes of Chile (18-29 °S). *Palaeogeogr. Palaeoclimatol. Palaeoecol.*, 172(3):313–326.

Anderson, R.B., Long, S.P., Horton, B.K., Calle, A.Z., and Ramirez, V. (2017). Shortening and structural architecture of the Andean fold-thrust belt of southern Bolivia (21°S): Implications for kinematic development and crustal thickening of the central Andes. *Geosphere*, 13(2):538–558.

Armijo, R., Lacassin, R., Coudurier-Curveur, A., and Carrizo, D. (2015). Coupled tectonic evolution of Andean orogeny and global climate. *Earth Sci. Rev.*, 143:1–35.

Armijo, R., Rauld, R., Thiele, R., Vargas, G., Campos, J., Lacassin, R., and Kausel, E. (2010). The West Andean thrust, the San Ramon fault, and the seismic hazard for Santiago, Chile. *Tectonics*, 29(2).

Arriagada, C., Cobbold, P.R., and Roperch, P. (2006). Salar de Atacama basin: A record of compressional tectonics in the central Andes since the mid-Cretaceous. *Tectonics*, 25(1).

Assumpção, M., Feng, M., Tassara, A., and Julià, J. (2013). Models of crustal thickness for South America from seismic refraction, receiver functions and surface wave tomography. *Tectonophysics*, 609:82–96.

Aster, R.C., Borchers, B., and Thurber, C.H. (2011). *Parameter estimation and inverse problems*, volume 90. Academic Press, Elsevier.

Avdievitch, N.N., Ehlers, T.A., and Glotzbach, C. (2018). Slow long-term exhumation of the West Central Andean plate boundary, Chile. *Tectonics*,

37(7):2243–2267.

Baby, P., Hérail, G., Salinas, R., and Sempere, T. (1992). Geometry and kinematic evolution of passive roof duplexes deduced from cross section balancing: Example from the foreland thrust system of the southern Bolivian Subandean Zone. *Tectonics*, 11(3):523–536.

Baker, P.A. and Fritz, S.C. (2015). Nature and causes of Quaternary climate variation of tropical South America. *Quat. Sci. Rev.*, 124:31–47.

Banyard, J. and Farrar, A. (2018). Mapping of structural blocks in the central andes district. *Int. Tech. Rep.* FQM First Quantum Minerals ltd. Santiago de Chile, Chile.

Barazangi, M. and Isacks, B.L. (1976). Spatial distribution of earthquakes and subduction of the Nazca plate beneath South America. *Geology*, 4(11):686–692.

Barnes, J.B. and Ehlers, T.A. (2009). End member models for Andean Plateau uplift. *Earth Sci. Rev.*, 97(1):105–132.

Barnes, J.B., Ehlers, T.A., Insel, N., McQuarrie, N., and Poulsen, C.J. (2012). Linking orography, climate, and exhumation across the central Andes. *Geology*, 40(12):1135–1138.

Barnes, J.B., Ehlers, T.A., McQuarrie, N., O'Sullivan, P.B., and Pelletier, J.D. (2006). Eocene to recent variations in erosion across the central Andean fold-thrust belt, northern Bolivia: Implications for plateau evolution. *Earth Planet. Sci. Lett.*, 248(1-2):118–133.

Barrientos, S., Vera, E., Alvarado, P., and Monfret, T. (2004). Crustal seismicity in central Chile. *J. South Am. Earth Sci.*, 16(8):759–768.

Bascuñán, S., Arriagada, C., Le Roux, J., and Deckart, K. (2016). Unraveling the Peruvian Phase of the Central Andes: stratigraphy, sed-

imentology and geochronology of the Salar de Atacama Basin (22°S 30–23°S), northern Chile. *Basin Res.*, 28(3):365–392.

Bascuñán, S., Maksymowicz, A., Martínez, F., Becerra, J., Arriagada, C., and Deckart, K. (2019). Geometry and late Mesozoic-Cenozoic evolution of the Salar de Atacama Basin (22°S 30'-24°S 30' S) in the northern Central Andes: New constraints from geophysical, geochronological and field data. *Tectonophysics*, 759:58–78.

Batt, G.E. and Braun, J. (1997). On the thermo-mechanical evolution of compressional orogens. *Geophys. J. Int.*, 128(2):364–382.

Beaumont, C., Fullsack, P., and Hamilton, J. (1992). Erosional control of active compressional orogens. In *Thrust tectonics*, pages 1–18. Springer.

Beaumont, C., Quinlan, G., and Hamilton, J. (1988). Orogeny and stratigraphy: Numerical models of the Paleozoic in the eastern interior of North America. *Tectonics*, 7(3):389–416.

Beck, S.L., Zandt, G., Myers, S.C., Wallace, T.C., Silver, P.G., and Drake, L. (1996). Crustal-thickness variations in the central Andes. *Geology*, 24(5):407–410.

Becker, J.J., Sandwell, D.T., Smith, W.H.F., Braud, J., Binder, B., Depner, J.L., Fabre, D., Factor, J., Ingalls, S., Kim, S.H., et al. (2009). Global bathymetry and elevation data at 30 arc seconds resolution: SRTM30_PLUS. *Mar. Geod.*, 32(4):355–371.

Bense, F.A., Löbens, S., Dunkl, I., Wemmer, K., and Siegesmund, S. (2013). Is the exhumation of the Sierras Pampeanas only related to Neogene flat-slab subduction? Implications from a multi-thermochronological approach. *J. South Am. Earth Sci.*, 48:123–144.

Boekhout, F., Spikings, R., Sempere, T., Chiaradia, M., Ulianov, A., and Schaltegger, U. (2012). Mesozoic arc magmatism along the southern Peruvian margin during Gondwana breakup and dispersal. *Lithos*, 146:48–64.

Bossi, G.E., Georgieff, S.M., Gavriloff, I.J.C., Ibanez, L.M., and Muruaga, C.M. (2001). Cenozoic evolution of the intramontane Santa Maria basin, Pampean Ranges, northwestern Argentina. *J. South Am. Earth Sci..*, 14(7):725–734.

Brandon, M.T. (2002). Decomposition of mixed grain age distributions using Binomfit. *On track*, 24(8):13–18.

Braun, J. (2002a). Estimating exhumation rate and relief evolution by spectral analysis of age–elevation datasets. *Terra Nova*, 14(3):210–214.

Braun, J. (2002b). Quantifying the effect of recent relief changes on age-elevation relationships. *Earth Planet. Sci. Lett.*, 200(3-4):331–343.

Braun, J. (2010). The many surface expressions of mantle dynamics. *Nat. Geosci.*, 3(12):825–833.

Buelow, E.k., Kimbrough, D.L., Mescua, J.F., Giambiagi, L.B., and Hoke, G.D. (2018). Sedimentologic and stratigraphic evolution of the Cacheuta basin: Constraints on the development of the Miocene retroarc foreland basin, south-central Andes. *Lithosphere*, 10(3):366–391.

Burns, W.M., Jordan, T.E., Copeland, P., and Kelley, S.A. (2006). The case for extensional tectonics in the Oligocene-Miocene Southern Andes as recorded in the Cura Mallin basin (36°-38°S). *Geol. Soc. Am. Spec. Paper*, 407:163.

Cahill, T. and Isacks, B.L. (1992). Seismicity and shape of the subducted Nazca plate. *J. Geophys. Res.: Solid Earth*, 97(B12):17503–17529.

Calk, L.C. and Naeser, C.W. (1973). The thermal effect of a basalt intrusion on fission tracks in quartz monzonite. *J. Geol.*, 81(2):189–198.

Calle, A.Z., Horton, B.K., Limachi, R., Stockli, D.F., Uzeda-Orellana, G.V., Anderson, R.B., and Long, S.P. (2018). Cenozoic provenance and depositional record of the Subandean foreland basin during growth and advance of the central Andean fold-thrust belt, southern Bolivia. In Zamora, G., McClay, K., and Ramos, V., editors, *Petroleum Basins and Hydrocarbon Potential of the Andes of Peru and Bolivia*, volume 117, pages 483–530. Am. Assoc. Petr. Geol. Mem.

Campetella, C.M. and Vera, C.S. (2002). The influence of the Andes mountains on the South American low-level flow. *Geophys. Res. Lett.*, 29(17):7–1.

Canavan, R.R., Carrapa, B., Clementz, M.T., Quade, J., DeCelles, P.G., and Schoenbohm, L.M. (2014). Early Cenozoic uplift of the Puna Plateau, Central Andes, based on stable isotope paleoaltimetry of hydrated volcanic glass. *Geology*, 42(5):447–450.

Carrapa, B., Adelmann, D., Hilley, G.E., Mortimer, E., Sobel, E.R., and Strecker, M.R. (2005). Oligocene range uplift and development of plateau morphology in the southern central Andes. *Tectonics*, 24(4).

Carrapa, B. and DeCelles, P.G. (2008). Eocene exhumation and basin development in the Puna of northwestern Argentina. *Tectonics*, 27(1).

Carrapa, B. and DeCelles, P.G. (2015). Regional exhumation and kinematic history of the central Andes in response to cyclical orogenic processes. *Geol. Soc. Am. Mem.*, 212:201–213.

Carrapa, B., Hauer, J., Schoenbohm, L., Strecker, M.R., Schmitt, A.K., Villanueva, A., and Sosa Gomez, J. (2008). Dynamics of deformation and sedimentation in the northern Sierras Pampeanas: An integrated study of the Neogene

Fiambalá basin, NW Argentina. *Geol. Soc. Am. Bull.*, 120(11-12):1518–1543.

Carrapa, B., Reyes-Bywater, S., Safipour, R., Sobel, Edward R .and Schoenbohm, L.M., DeCelles, P.G., Reiners, P.W., and Stockli, D. (2014). The effect of inherited paleotopography on exhumation of the Central Andes of NW Argentina. *Geol. Soc. Am. Bull.*, 126(1-2):66–77.

Carrapa, B., Trimble, J.D., and Stockli, D.F. (2011). Patterns and timing of exhumation and deformation in the Eastern Cordillera of NW Argentina revealed by (U–Th)/He thermochronology. *Tectonics*, 30(3).

Carrera, N. and Muñoz, J.A. (2008). Thrusting evolution in the southern Cordillera Oriental (northern Argentine Andes): Constraints from growth strata. *Tectonophysics*, 459(1-4):107–122.

Carretier, S., Tolorza, V., Regard, V., Aguilar, G., Bermúdez, M.A., Martinod, J., Guyot, J.L., Hérail, G., and Riquelme, R. (2018). Review of erosion dynamics along the major NS climatic gradient in Chile and perspectives. *Geomorphology*, 300:45–68.

Carvalho, L.M.V., Jones, C., and Liebmann, B. (2004). The South Atlantic convergence zone: Intensity, form, persistence, and relationships with intraseasonal to interannual activity and extreme rainfall. *J. Climate*, 17(1):88–108.

Čermák, V. and Rybach, L. (1982). Thermal Properties. Thermal conductivity and specific heat of minerals and rocks. In Angenheister, G., editor, *Landolt-Börnstein: Numerical Data and Functional Relationships in Science and Technology, New Series, Group V (Geophysics and Space Research), Volume Ia,(Physical Properties of Rocks)*, pages 305–343. Springer, Berlin-Heidelberg.

Champagnac, J.D., Molnar, P., Sue, C., and Herman, F. (2012). Tectonics, climate, and mountain topography. *J. Geophys. Res.: Solid Earth*, 117.

Charrier, R., Baeza, O., Elgueta, S., Flynn, J.J., Gans, P., Kay Mahlburg, S., Muñoz, N., Wyss, A.R., and Zurita, E. (2002). Evidence for Cenozoic extensional basin development and tectonic inversion south of the flat-slab segment, southern Central Andes, Chile (33°-36° S.L.). *J. South Am. Earth Sci.*, 15(1):117–139.

Charrier, R., Hérail, G., Pinto, L., García, M., Riquelme, R., Farías, M., and Muñoz, N. (2013). Cenozoic tectonic evolution in the Central Andes in northern Chile and west central Bolivia: implications for paleogeographic, magmatic and mountain building evolution. *Int. J. Earth Sci.*, 102(1):235–264.

Charrier, R., Iturrizaga, L., Carretier, S., and Regard, V. (2019). Geomorphologic and glacial Evolution of the Cachapoal and southern Maipo catchments in the Andean Principal Cordillera, Central Chile (34°-35° S). *Andean Geology*, 46(2):240–278.

Charrier, R., Pinto, L., and Rodríguez, M.P. (2007). Tectonostratigraphic evolution of the Andean Orogen in Chile. In *The Geology of Chile*. Geol. Soc. Spec. Pub.

Charrier, R., Ramos, V.A., Tapia, F., and Sagripanti, L. (2015). Tectono-stratigraphic evolution of the Andean Orogen between 31° and 37°S (Chile and Western Argentina). *Geol. Soc. London Spec. Pub.*, 399(1):13–61.

Chulick, G.S., Detweiler, S., and Mooney, W.D. (2013). Seismic structure of the crust and uppermost mantle of South America and surrounding oceanic basins. *J. South Am. Earth Sci.*, 42:260–276.

Ciccioli, P.L., Limarino, C.O., Friedman, R., and Marenssi, S.A. (2014). New high precision U-Pb ages for the Vinchina Formation: implications for the stratigraphy of the Bermejo Andean foreland basin (La Rioja province, western Argentina). *J. South Am. Earth Sci.*, 56:200–213.

Clapperton, C.M. (1983). The glaciation of the Andes. *Quat. Sci. Rev.*, 2(2-3):83–155.

Clapperton, C.M. (1994). The quaternary glaciation of Chile: a review. *Rev. Chil. Hist. Nat.*, 67(4):369–383.

Cooper, F.J., Adams, B.A., Blundy, J.D., Farley, K.A., McKeon, R.E., and Ruggiero, A. (2016). Aridity-induced Miocene canyon incision in the Central Andes. *Geology*, 44(8):675–678.

Cornejo, P.C. and Mahood, G.A. (1997). Seeing past the effects of re-equilibration to reconstruct magmatic gradients in plutons: La Gloria Pluton, central Chilean Andes. *Contrib. Mineral. Petrol.*, 127(1-2):159–175.

Coutand, I., Carrapa, B., Deeken, A., Schmitt, A.K., Sobel, E.R., and Strecker, M.R. (2006). Propagation of orographic barriers along an active range front: insights from sandstone petrography and detrital apatite fission-track thermochronology in the intramontane Angastaco basin, NW Argentina. *Basin Res.*, 18(1):1–26.

Coutand, I., Cobbold, P.R., de Urreiztieta, M., Gautier, P., Chauvin, A., Gapais, D., Rossello, E.A., and López-Gamundí, O. (2001). Style and history of Andean deformation, Puna plateau, northwestern Argentina. *Tectonics*, 20(2):210–234.

Dahlen, F.A. and Suppe, J. (1988). Mechanics, growth, and erosion of mountain belts. *Geol. Soc. Am. Spec. Pap.*, 218:161–178.

Danielson, J. and Gesch, D.B. (2011). Global multi-resolution terrain elevation data 2010 (GMTED2010). *US Geological Survey*, No. 2011-1073.

D'Arcy, M., Schildgen, T.F., Strecker, M.R., Wittmann, H., Duesing, W., Mey, J., Tofelde, S., Weissmann, P., and Alonso, R.N. (2019). Timing of past glaciation at the Sierra de Aconquíja, northwestern Argentina, and throughout the Central Andes. *Quat. Sci. Rev.*, 204:37–57.

Dávila, F.M. and Lithgow-Bertelloni, C. (2015). Dynamic uplift during slab flattening. *Earth Planet. Sci. Lett.*, 425:34–43.

Davis, D., Suppe, J., and Dahlen, F.A. (1983). Mechanics of fold-and-thrust belts and accretionary wedges. *J. Geophys. Res. Solid Earth*, 88(B2):1153–1172.

de Martonne, E. (1925). *Traité de Géographie Physique*, volume 2. Librarie Armand Colin, Paris.

de Silva, S.L. (1989). Altiplano-Puna volcanic complex of the central Andes. *Geology*, 17:1102–1106.

de Silva, S.L. and Kay, S.M. (2018). Turning up the Heat: High-flux Magmatism in the Central Andes. *Elements*, 14:245–250.

DeCelles, P.G., Carrapa, B., Horton, B.K., and Gehrels, G.E. (2011). Cenozoic foreland basin system in the central Andes of northwestern Argentina: Implications for Andean geodynamics and modes of deformation. *Tectonics*, 30(TC6013).

DeCelles, P.G. and Horton, B.K. (2003). Early to middle Tertiary foreland basin development and the history of Andean crustal shortening in Bolivia. *Geol. Soc. Am. Bull.*, 115:58–77.

Deckart, K., Clark, A.H., Celso, A.A., Ricardo, V.R., Bertens, A.N., Mortensen, J.K., and Fanning, M. (2005). Magmatic and hydrothermal chronology of the giant Río Blanco porphyry copper

deposit, central Chile: Implications of an integrated U-Pb and ^{40}Ar/^{39}Ar database. *Econ. Geol.*, 100(5):905–934.

Deeken, A., Sobel, E.R., Coutand, I., Haschke, M., Riller, U., and Strecker, M.R. (2006). Development of the southern Eastern Cordillera, NW Argentina, constrained by apatite fission track thermochronology: From early Cretaceous extension to middle Miocene shortening. *Tectonics*, 25(6).

del Papa, C., Hongn, F., Powell, J., Payrola, P., Do Campo, M., Strecker, M.R., Petrinovic, I., Schmitt, A.K., and Pereyra, R. (2013). Middle Eocene-Oligocene broken-foreland evolution in the Andean Calchaqui Valley, NW Argentina: insights from stratigraphic, structural and provenance studies. *Basin Res.*, 25:574–593.

Del Rey, A., Deckart, K., Arriagada, C., and Martínez, F. (2016). Resolving the paradigm of the late Paleozoic-Triassic Chilean magmatism: Isotopic approach. *Gondwana Res.*, 37:172–181.

Dewey, J.F. and Bird, J.M. (1970). Mountain belts and the new global tectonics. *J. Geophys. Res*, 75(14):2625–2647.

Di Giulio, A., Ronchi, A., Sanfilippo, A., Tiepolo, M., Pimentel, M., and Ramos, V.A. (2012). Detrital zircon provenance from the Neuquén Basin (south-central Andes): Cretaceous geodynamic evolution and sedimentary response in a retroarc-foreland basin. *Geology*, 40:559–562.

Dodson, M.H. (1973). Closure temperature in cooling geochronological and petrological systems. *Contrib. Mineral. Petrol.*, 40(3):259–274.

Dunai, T.J., López, G.A.G., and Juez-Larré, J. (2005). Oligocene-Miocene age of aridity in the Atacama Desert revealed by exposure dating of erosion-sensitive landforms. *Geology*, 33(4):321–324.

Dunn, J.F., Hartshorn, K.G., and Hartshorn, P.W. (1995). Structural styles and hydrocarbon potential of the sub-Andean thrust belt of southern Bolivia. In Tankard, A.J., Suarez, R., and Welsink, H.J., editors, *Petroleum Basins of South America*, pages 523–543. Am. Assoc. Petrol. Geol.

Echavarria, L., Hernández, R., Allmendinger, R., and Reynolds, J. (2003). Subandean thrust and fold belt of northwestern Argentina: geometry and timing of the Andean evolution. *Am. Assoc. Petrol. Geol. Bull.*, 87:965–985.

Ege, H., Sobel, E.R., Scheuber, E., and Jacobshagen, V. (2007). Exhumation history of the southern Altiplano plateau (southern Bolivia) constrained by apatite fission track thermochronology. *Tectonics*, 26(TC1004).

Egholm, D.L., Nielsen, S.B., Pedersen, V.K., and Lesemann, J.E. (2009). Glacial effects limiting mountain height. *Nature*, 460(7257):884–887.

Ehlers, T.A. and Poulsen, C.J. (2009). Influence of Andean uplift on climate and paleoaltimetry estimates. *Earth Planet. Sci. Lett.*, 281(3):238–248.

Eichelberger, N., McQuarrie, N., Ehlers, T.A., Enkelmann, E., Barnes, J.B., and Lease, R.O. (2013). New constraints on the chronology, magnitude, and distribution of deformation within the central Andean orocline. *Tectonics*, 32(5):1432–1453.

Elger, K., Oncken, O., and Glodny, J. (2005). Plateau-style accumulation of deformation: Southern Altiplano. *Tectonics*, 24(TC4020).

England, P. and Molnar, P. (1990). Surface uplift, uplift of rocks, and exhumation of rocks. *Geology*, 18:1173–1177.

Evenstar, L.A., Hartley, A.J., Stuart, F.M., Mather, A.E., Rice, C.M., and Chong, G. (2009). Multiphase development of the Atacama Planation Surface recorded by cosmogenic 3He exposure

ages: Implications for uplift and Cenozoic climate change in western South America. *Geology*, 37(1):27–30.

Evenstar, L.A., Stuart, F.M., Hartley, A.J., and Tattitch, B. (2015). Slow Cenozoic uplift of the western Andean Cordillera indicated by cosmogenic 3He in alluvial boulders from the Pacific Planation Surface. *Geophys. Res. Lett.*, 42(20):8448–8455.

Faccenna, C., Oncken, O., Holt, A.F., and Becker, T.W. (2017). Initiation of the Andean orogeny by lower mantle subduction. *Earth Planet. Sci. Lett.*, 463:189–201.

Farías, M., Charrier, R., Carretier, S., Martinod, J., Fock, A., Campbell, D., Cáceres, J., and Comte, D. (2008). Late Miocene high and rapid surface uplift and its erosional response in the Andes of central Chile (33-35 °S). *Tectonics*, 27(1).

Farías, M., Charrier, R., Comte, D., Martinod, J., and Hérail, G. (2005). Late Cenozoic deformation and uplift of the western flank of the Altiplano: Evidence from the depositional, tectonic, and geomorphologic evolution and shallow seismic activity (northern Chile at 19° 30' S). *Tectonics*, 24(4).

Farías, M., Comte, D., Charrier, R., Martinod, J., David, C., Tassara, A., Tapia, F., and Fock, A. (2010). Crustal-scale structural architecture in central Chile based on seismicity and surface geology: Implications for Andean mountain building. *Tectonics*, 29(3):1–22.

Farley, K.A. (2000). Helium diffusion from apatite: General behavior as illustrated by Durango fluorapatite. *J. Geophys. Res.*, 105(B2):2903–2914.

Farley, K.A., Wolf, R.A., and Silver, L.T. (1996). The effects of long alpha-stopping distances on (U-Th)/He ages. *Geochim. Cosmochim. Acta*, 60:4223–4229.

Fiorella, R.P., Poulsen, C.J., Zolá, R.S.P., Jeffery, M.L., and Ehlers, T.A. (2015). Modern and long-term evaporation of central Andes surface waters suggests paleo archives underestimate Neogene elevations. *Earth Planet. Sci. Lett.*, 432:59–72.

Fitzgerald, P.G., Sorkhabi, R.B., Redfield, T.F., and Stump, E. (1995). Uplift and denudation of the central Alaska Range: A case study in the use of apatite fission track thermochronology to determine absolute uplift parameters. *J. Geophys. Res.: Solid Earth*, 100(B10):20175–20191.

Flament, N., Gurnis, M., Müller, R.D., Bower, D.J., and Husson, L. (2015). Influence of subduction history on South American topography. *Earth Planet. Sci. Lett.*, 430:9–18.

Fock, A., Charrier, R., Farías, M., and Muñoz, M. (2006). Fallas de vergencia oeste en la Cordillera Principal de Chile Central: Inversión de la cuenca de Abanico (33-34°S). *Asoc. Geol. Argent. Publ. Espec*, 6:48–55.

Folguera, A., Rojas Vera, E., Bottessi, G., Zamora Valcarce, G., and Ramos, V.A. (2010). The Loncopué trough: A Cenozoic basin produced by extension in the southern central Andes. *J. Geodyn.*, 49:287–295.

Fosdick, J.C., Reat, E.J., Carrapa, B., Ortiz, G., and Alvarado, P.M. (2017). Retroarc basin reorganization and aridification during Paleogene uplift of the southern central Andes. *Tectonics*, 36(3):493–514.

Fox, M., Herman, F., Kissling, E., and Willett, S.D. (2015). Rapid exhumation in the Western Alps driven by slab detachment and glacial erosion. *Geology*, 43(5):379–382.

Fox, M., Herman, F., Willett, S.D., and May, D.A. (2014). A linear inversion method to infer exhumation rates in space and time from thermochronometric data. *Earth Surf. Dyn.*, 2(1):47.

Francis, P.W. and Hawkesworth, C.J. (1994). Late Cenozoic rats of magmatic activity in the Central Andes and the relationships to continental crust formation and thickening. *J. Geol. Soc. London*, 151:845–854.

Gans, C.R., Beck, S.L., Zandt, G., Gilbert, H., Alvarado, P., Anderson, M., and Linkimer, L. (2011). Continental and oceanic crustal structure of the Pampean flat slab region, western Argentina, using receiver function analysis: new high-resolution results. *Geophys. J. Int.*, 186(1):45–58.

Gansser, A. (1973). Facts and theories on the Andes: twenty-sixth William Smith Lecture. *J. Geol. Soc. London*, 129(2):93–131.

Garcia, M. and Hérail, G. (2005). Fault-related folding, drainage network evolution and valley incision during the Neogene in the Andean Precordillera of Northern Chile. *Geomorphology*, 65(3-4):279–300.

García, M., Riquelme, R., Farías, M., Hérail, G., and Charrier, R. (2011). Late Miocene-Holocene canyon incision in the western Altiplano, northern Chile: tectonic or climatic forcing? *J. Geol. Soc.*, 168(4):1047–1060.

García, V.H. and Casa, A.L. (2014). Quaternary tectonics and seismic potential of the Andean retrowedge at 33-34° S. In Sepúlveda, S., Giambiagi, L.B., Moreiras, S.M., Pinto, L., Tunik, M., Hoke, G.D., and Farías, M., editors, *Geodynamic Processes in the Andes of Central Chile and Argentina*, pages 311–327. Geol. Soc. London Spec. Pub., 399.

Garreaud, R. (2007). Precipitation and circulation covariability in the extratropics. *J. Climate*, 20(18):4789–4797.

Garreaud, R.D. (2009). The Andes climate and weather. *Adv. Geosci.*, 22:3–11.

Garreaud, R.D., Vuille, M., Compagnucci, R., and Marengo, J. (2009). Present-day South American climate. *Paleogeogr., Paleoclimatol., Paleoecol.*, 281(3-4):180–195. Sp. Iss. SI 514AB Times Cited:269 Cited References Count:110.

Garzione, C.N., McQuarrie, N., Perez, N.D., Ehlers, T.A., Beck, S.L., Kar, N., Eichelberger, N., Chapman, A.D., Ward, K.M., Ducea, M.N., Lease, R.O., Poulsen, C.J., Wagner, L.S., Saylor, J.E., Zandt, G., and Horton, B.K. (2017). Tectonic evolution of the Central Andean plateau and implications for the growth of plateaus. *Ann. Rev. Earth Planet. Sci.*, 45:529–559.

Gayó, E., Hinojosa, L.F., and Villagrán, C. (2005). On the persistence of Tropical Paleofloras in central Chile during the Early Eocene. *Rev. Palaeobot. Palyno.*, 137(1-2):41–50.

Gephart, J.W. (1994). Topography and subduction geometry in the central Andes: Clues to the mechanics of a noncollisional orogen. *J. Geophys. Res. Solid Earth*, 99(B6):12279–12288.

Giambiagi, L., Mescua, J., Bechis, F., Tassara, A., and Hoke, G. (2012). Thrust belts of the southern Central Andes: Along-strike variations in shortening, topography, crustal geometry, and denudation. *Geol. Soc. Am. Bull.*, 124(7-8):1339–1351.

Giambiagi, L., Spagnotto, S., Moreiras, S.M., Gómez, G., Stahlschmidt, E., and Mescua, J. (2015a). Three-dimensional approach to understanding the relationship between the Plio-Quaternary stress field and tectonic inversion in the Triassic Cuyo Basin, Argentina. *Solid Earth*, 6(2):747–763.

Giambiagi, L., Tassara, A., Mescua, J., Tunik, M., Alvarez, P.P., Godoy, E., Hoke, G., Pinto, L., Spagnotto, S., Porras, H., Tapia, F., Jara, P., Bechis, F., Garcìa, V.H., Suriano, J., Moreiras, S.M., and Pagano, S.D. (2015b). Evolution of shallow and

deep structures along the maipo–tunuyán transect (33° 40' S): from the Pacific coast to the Andean foreland. *Geol. Soc. London. Spec. Pub.*, 399(1):63–82.

Giambiagi, L.B. and Ramos, V.A. (2002). Structural evolution of the Andes in a transitional zone between flat and normal subduction (33°30'-33°45'S), Argentina and Chile. *J. S. Am. Earth Sci.*, 15(1):101–116.

Giambiagi, L.B., Ramos, V.A., Godoy, E., Alvarez, P.P., and Orts, S. (2003). Cenozoic deformation and tectonic style of the Andes, between 33° and 34° south latitude. *Tectonics*, 22(4).

Giambiagi, L.B., Tunik, M.A., and Ghiglione, M. (2001). Cenozoic tectonic evolution of the alto tunuyán foreland basin above the transition zone between the flat and normal subduction segment (33°30'-34°s), western argentina. *J. S. Am. Earth Sci.*, 14(7):707–724.

Giese, P., Scheuber, E., Schilling, F., Schmitz, M., and Wigger, P. (1999). Crustal thickening processes in the Central Andes and the different natures of the Moho-discontinuity. *J. S. Am. Earth Sci.*, 12(2):201–220.

Gillis, R.J., Horton, B.K., and Grove, M. (2006). Thermochronology, geochronology, and upper crustal structure of the Cordillera Real: Implications for Cenozoic exhumation of the central Andean plateau. *Tectonics*, 25(6).

Gleadow, A.J.W., Duddy, I.R., Green, P.F., and Lovering, J.F. (1986). Confined fission track lengths in apatite: a diagnostic tool for thermal history analysis. *Contr. Mineral. Petrol.*, 94:405–415.

Gleadow, A.J.W. and Fitzgerald, P.G. (1987). Uplift history and structure of the Transantarctic Mountains: new evidence from fission track dating of basement apatites in the Dry Valleys area, southern Victoria Land. *Earth Planet. Sci. Lett.*, 82(1-2):1–14.

Godoy, E., Yañez, G., and Vera, E. (1999). Inversion of an Oligocene volcano-tectonic basin and uplifting of its superimposed Miocene magmatic arc in the central Chilean Andes: first seismic and gravity evidences. *Tectonophysics*, 306:217–236.

Gourou, P. and Papy, L. (1966). *Compendio de Geografía General*. Ediciones RIALP, Madrid. Ediciones RIALP, Madrid.

Gregori, D. and Benedini, L. (2013). The Cordon del Portillo Permian magmatism, Mendoza, Argentina, plutonic and volcanic sequences at the western margin of Gondwana. *J. S. Am. Earth Sci.*, 42:61–73.

Grier, M.E., Salfity, J.A., and Allmendinger, R.W. (1991). Andean reactivation of the Cretaceous Salta rift, northwestern Argentina. *J. S. Am. Earth Sci.*, 4:351.

Gubbels, T.L., Isacks, B.L., and Farrar, E. (1993). High-level surfaces, plateau uplift, and foreland development, Bolivian central Andes. *Geology*, 21:695–698.

Hain, M.P., Strecker, M.R., Bookhagen, B., Alonso, R.N., and Pingel, H. Schmitt, A.K. (2011). Neogene to Quaternary broken foreland formation and sedimentation dynamics in the Andes of NW Argentina (25°S). *Tectonics*, 30(TC2006).

Harrison, S. (2004). The pleistocene glaciations of chile. In Ehlers., J. and Gibbard, P., editors, *Quaternary Glaciations - Extent and Chronology. Part III: South America, Asia, Africa, Australasia, Antarctica*, pages 89–103. Elsevier, Cambridge.

Hartley, A.J., Chong, G., Houston, J., and Mather, A.E. (2005). 150 million years of climatic stability: evidence from the Atacama Desert, northern Chile. *J. Geol. Soc.*, 162(3):421–424.

Hartley, A.J., Flint, S., Turner, P., and Jolley, E.J. (1992). Tectonic controls on the development of a semi-arid, alluvial basin as reflected in the stratigraphy of the Purilactis Group (Upper Cretaceous-Eocene), northern Chile. *J. S. Am. Earth Sci.*, 5:273–294.

Hartley, A.J., Sempéré, T., and Wörner, G. (2007). A comment on "Rapid late Miocene rise of the Bolivian Altiplano: Evidence for removal of mantle lithosphere" by CN Garzione et al.[Earth Planet. Sci. Lett. 241 (2006) 543-556]. *Earth Planet. Sci. Lett.*, 259(3):625–629.

Haselton, K., Hilley, G., and Strecker, M.R. (2002). Average Pleistocene climatic patterns in the southern Central Andes: Controls on mountain glaciation and paleoclimate implications. *J. Geol.*, 110(2):211–226.

Hein, A.S., Cogez, A., Darvill, C.M., Mendelova, M., Kaplan, M.R., Herman, F., Dunai, T.J., Norton, K., Xu, S., Christl, M., and Rodés, Á. (2017). Regional mid-Pleistocene glaciation in central Patagonia. *Quat. Sci. Rev.*, 164:77–94.

Henriquez, S., DeCelles, P.G., and Carrapa, B. (2019). Cretaceous to middle Cenozoic exhumation history of the Cordillera de Domeyko and Salar de Atacama basin, northern Chile. *Tectonics*, 38(2):395–416.

Herman, F. and Brandon, M. (2015). Mid-latitude glacial erosion hotspot related to equatorial shifts in southern Westerlies. *Geology*, 43(11):987–990.

Herman, F. and Champagnac, J. (2016). Plio-Pleistocene increase of erosion rates in mountain belts in response to climate change. *Terra Nova*, 28(1):2–10.

Herman, F., Seward, D., Valla, P.G., Carter, A., Kohn, B., Willett, S.D., and Ehlers, T.A. (2013). Worldwide acceleration of mountain erosion under a cooling climate. *Nature*, 504(7480):423–426.

Herrera, S., Pinto, L., Deckart, K., Cortés, J., and Valenzuela, J. (2017). Cenozoic tectonostratigraphic evolution and architecture of the Central Andes in northern Chile based on the Aquine region, Western Cordillera (19°-19°30' S). *Andean Geol.*, 44(2):87–122.

Herrera Ossandón, M. (2016). Estimación de las altitudes de las líneas de equilibrio en glaciares de montaña para el último ciclo glacial-interglacial en los Andes de Santiago, Chile Central. *Tesis de Posgrado*. Universidad de Chile, Departamento de Geología, Santiago, Chile.

Hervé, F., Fanning, C.M., Calderón, M., and Mpodozis, C. (2014). Early Permian to Late Triassic batholiths of the Chilean Frontal Cordillera (28°-31° S): SHRIMP U-Pb zircon ages and Lu-Hf and O isotope systematics. *Lithos*, 184:436–446.

Heusser, C.J. (1983). Quaternary pollen record from Laguna de Tagua Tagua, Chile. *Science*, 219(4591):1429–1432.

Hijmans, R.J., Cameron, S.E., Parra, J.L., Jones, P.G., and Jarvis, A. (2005). Very high resolution interpolated climate surfaces for global land areas. *Int. J. Climatol.*, 25(15):1965–1978.

Hilley, G.E., Blisniuk, P.M., and Strecker, M.R. (2005). Mechanics and erosion of basement-cored uplift provinces. *J. Geophys. Res. Solid Earth*, 110(B12).

Hilley, G.E. and Coutand, I. (2010). Links between topography, erosion, rheological heterogeneity, and deformation in contractional settings: Insights from the central Andes. *Tectonophysics*, 495(1-2):78–92.

Hilley, G.E. and Strecker, M.R. (2005). Processes of oscillatory basin filling and excavation in a tectonically active orogen: Quebrada del Toro Basin, NW Argentina. *Geol. Soc. Am. Bull.*, 117(7-8):887–901.

Hinojosa, L.F. (2005). Cambios climáticos y vegetacionales inferidos a partir de paleofloras cenozoicas del sur de Sudamérica. *Rev. Geol. Chile*, 32(1):95–115.

Höfer-Öllinger, G. and Millen, B. (2010). Geothermal prognoses for tunnels in the Andes. *Geomech. Tunnelling*, 3(5):622–633.

Hoke, G.D., Giambiagi, L.B., Garzione, C.N., Mahoney, J.B., and Strecker, M.R. (2014). Neogene paleoelevation of intermontane basins in a narrow, compressional mountain range, southern Central Andes of Argentina. *Earth Planet. Sci. Lett.*, 406:153–164.

Hoke, G.D., Isacks, B.L., Jordan, T.E., Blanco, N., Tomlinson, A.J., and Ramezani, J. (2007). Geomorphic evidence for post-10 Ma uplift of the western flank of the central Andes 18°S30'–22°S. *Tectonics*, 26(5).

Hongn, F., del Papa, C., Powell, J., Petrinovic, I., Mon, R., and Deraco, V. (2007). Middle Eocene deformation and sedimentation in the Puna-Eastern Cordillera transition (23-26°S): Control by preexisting heterogeneities on the pattern of initial Andean shortening. *Geology*, 35(3):271–274.

Horton, B. and DeCelles, P.G. (2001). Modern and ancient fluvial megafans in the foreland basin system of the central Andes, southern Bolivia: implications for drainage network evolution in fold-thrust belts. *Basin Res.*, 13:43–63.

Horton, B.K. (1999). Erosional control on the geometry and kinematics of thrust belt development in the central Andes. *Tectonics*, 18:1292–1304.

Horton, B.K. (2005). Revised deformation history of the central andes: Inferences from cenozoic foredeep and intermontane basins of the eastern cordillera, bolivia. *Tectonics*, 24.

Horton, B.K. (2018a). Sedimentary record of Andean mountain building. *Earth Sci. Rev.*, 178:279–309.

Horton, B.K. (2018b). Tectonic regimes of the central and southern Andes: Responses to variations in plate coupling during subduction. *Tectonics*, 37(2):402–429.

Horton, B.K. and DeCelles, P.G. (1997). The modern foreland basin system adjacent to the Central Andes. *Geology*, 25:895–898.

Horton, B.K., Fuentes, F., Boll, A., Starck, D., Ramirez, S.G., and Stockli, D.F. (2016). Andean stratigraphic record of the transition from backarc extension to orogenic shortening: A case study from the northern Neuquén Basin, Argentina. *J. S. Am. Earth Sci.*, 71:17–40.

Horton, B.K., Hampton, B.A., and Waanders, G.L. (2001). Paleogene synorogenic sedimentation in the Altiplano plateau and implications for initial mountain building in the central Andes. *Geol. Soc. Am. Bull.*, 113(11):1387–1400.

Houston, J. and Hartley, A.J. (2003). The central Andean west-slope rainshadow and its potential contribution to the origin of hyper-aridity in the Atacama Desert. *Int. J. Clim.*, 23(12):1453–1464.

Hurford, A.J. (1990). Standardization of fission track dating calibration: Recommendation by the Fission Track Working Group of the IUGS Subcommission on Geochronology. *Chem. Geology*, 80(2):171–178.

Hurford, A.J. and Green, P.F. (1983). The Zeta age calibration of fission-track dating. *Chem. Geology*, 41:285–317.

Insel, N., Poulsen, C.J., and Ehlers, T.A. (2010). Influence of the Andes Mountains on South American moisture transport, convection, and precipitation. *Climate Dyn.*, 35(7-8):1477–1492.

Irigoyen, M.V., Buchan, K.L., and Brown, R.L. (2000). Magnetostratigraphy of Neogene Andean foreland-basin strata, lat 33°S, Mendoza Province, Argentina. *Geol. Soc. Am. Bull.*, 112(6):803–816.

Isacks, B.L. (1988). Uplift of the central Andean plateau and bending of the Bolivian orocline. *J. Geophys. Res. Solid Earth*, 93(B4):3211–3231.

Jackson, S.E., Pearson, N.J., Griffin, W.L., and Belousova, E.A. (2004). The application of laser ablation-inductively coupled plasma-mass spectrometry to in situ U–Pb zircon geochronology. *Chem. Geol.*, 211(1):47–69.

Jenny, B., Wilhelm, D., and Valero-Garcés, B. (2003). The Southern Westerlies in Central Chile: Holocene precipitation estimates based on a water balance model for Laguna Aculeo (33°S 50' S). *Clim. Dyn.*, 20(2-3):269–280.

Jiao, R., Herman, F., and Seward, D. (2017). Late Cenozoic exhumation model of New Zealand: Impacts from tectonics and climate. *Earth-Sci. Rev*, 166:286–298.

Jones, R.E., Kirstein, L.A., Kasemann, S.A., Dhuime, B., Elliott, T., Litvak, V.D., Alonso, R., Hinton, R., and Facility, E.I.M. (2015). Geodynamic controls on the contamination of Cenozoic arc magmas in the southern Central Andes: Insights from the O and Hf isotopic composition of zircon. *Geochim. Cosmochim. Acta*, 164:386–402.

Jordan, T.E. and Allmendinger, R.W. (1986). The Sierras Pampeanas of Argentina; a modern analogue of Rocky Mountain foreland deformation. *Am. J. Sci.*, 286(10):737–764.

Jordan, T.E., Allmendinger, R.W., Damanti, J.F., and Drake, R. (1993). Chronology of Motion in a Complete Thrust Belt: The Precordillera, 30-31°S, Andes Mountains. *J. Geol.*, 101(2):135–156.

Jordan, T.E., Burns, W.M., Veiga, R., Pángaro, F., Copeland, P., Kelley, S., and Mpodozis, C. (2001a). Extension and basin formation in the southern Andes caused by increased convergence rate: A mid-Cenozoic trigger for the Andes. *Tectonics*, 20:308–324.

Jordan, T.E., Isacks, B.L., Allmendinger, R.W., Brewer, J.A., Ramos, V.A., and Ando, C.J. (1983). Andean tectonics related to geometry of subducted Nazca plate. *Geol. Soc. Am. Bull.*, 94(3):341–361.

Jordan, T.E., Kirk-Lawlor, N.E., Blanco, N.P., Rech, J.A., and Cosentino, N.J. (2014). Landscape modification in response to repeated onset of hyperarid paleoclimate states since 14 Ma, Atacama Desert, Chile. *Geol. Am. Soc. Bull.*, 126(7-8):1016–1046.

Jordan, T.E., Mpodozis, C., Muñoz, N., Blanco, N., Pananont, P., and Gardeweg, M. (2007). Cenozoic subsurface stratigraphy and structure of the salar de atacama basin, northern chile. *J. S. Am. Earth Sci.*, 23:122–146.

Jordan, T.E., Nester, P.L., Blanco, N., Hoke, G.D., Dávila, F., and Tomlinson, A.J. (2010). Uplift of the Altiplano-Puna plateau: A view from the west. *Tectonics*, 29(TC5007).

Jordan, T.E., Schlunegger, F., and Cardazo, N. (2001b). Unsteady and spatially variable evolution of the Neogene Andean Bermejo foreland basin, Argentina. *J. S. Am. Earth Sci.*, 14:775–798.

Kay, S.M., Coira, B.L., Caffe, P.J., and Chen, C.H. (2010). Regional chemical diversity, crustal and mantle sources and evolution of central Andean

Puna plateau ignimbrites. *J. Volcanol. Geotherm. Res.*, 198(1-2):81–111.

Kay, S.M., Godoy, E., and Kurtz, A. (2005). Episodic arc migration, crustal thickening, subduction erosion, and magmatism in the south-central Andes. *Geol. Am. Soc. Bull.*, 117(1):67–88.

Kay, S.M. and Mpodozis, C. (2002). Magmatism as a probe to the Neogene shallowing of the Nazca plate beneath the modern Chilean flat-slab. *Earth Planet. Sci. Lett.*, 15:39–57.

Kay, S.M., Mpodozis, C., Ramos, V.A., and Munizaga, F. (1991). Magma source variations for mid-late tertiary magmatic rocks associated with a shallowing subduction zone and a thickening crust in the central Andes (28 to 33°S). *Geol. Soc. Am. Spec. Publ.*, 265:113–137.

Kay, S.M., Mpodozis, C., Tittler, A., and Cornejo, P. (1994). Tertiary magmatic evolution of the Maricunga mineral belt in Chile. *Int. Geol. Rev.*, 36(12):1079–1112.

Ketcham, R.A., Donelick, R.A., and Carlson, W.D. (1999). Variability of apatite fission-track annealing kinetics: III. Extrapolation to geological time scales. *Am. Mineral.*, 84(9):1235–1255.

Klein, A.G., Seltzer, G.O., and Isacks, B.L. (1999). Modern and last local glacial maximum snowlines in the Central Andes of Peru, Bolivia, and Northern Chile. *Quat. Sci. Rev.*, 18(1):63–84.

Kleinert, K. and Strecker, M.R. (2001). Climate change in response to orographic barrier uplift: Paleosol and stable isotope evidence from the late Neogene Santa Maria basin, northwestern Argentina. *Geol. Soc. Am. Bull.*, 113(6):728–742.

Kley, J. (1996). Transition from basement involved to thin-skinned thrusting in the Cordillera Oriental of southern Bolivia. *Tectonics*, 15:763–775.

Kley, J. and Monaldi, C.R. (1998). Tectonic shortening and crustal thickness in the Central Andes: How good is the correlation? *Geology*, 26(8):723–726.

Kley, J. and Monaldi, C.R. (2002). Tectonic inversion in the Santa Barbara System of the central Andean foreland thrust belt, northwestern Argentina. *Tectonics*, 21(6):1061.

Kley, J., Monaldi, C.R., and Salfity, J.A. (1999). Along-strike segmentation of the Andean foreland: causes and consequences. *Tectonophysics*, 301(1-2):75–94.

Kodama, Y. (1992). Large-scale common features of subtropical precipitation zones (the Baiu frontal zone, the SPCZ, and the SACZ) Part I: Characteristics of subtropical frontal zones. *J. Meteor. Soc. Japan.*, 70(4):813–836.

Konstantinovskaia, E. and Malavieille, J. (2005). Erosion and exhumation in accretionary orogens: Experimental and geological approaches. *Geochem. Geophys. Geosyst.*, 6(2).

Koons, P.O. (1989). The topographic evolution of collisional mountain belts; a numerical look at the Southern Alps, New Zealand. *Am. J. Sci.*, 289(9):1041–1069.

Koons, P.O. (1990). Two-sided orogen: Collision and erosion from the sandbox to the Southern Alps, New Zealand. *Geology*, 18(8):679–682.

Kraemer, B., Adelmann, D., Alten, M., Schnurr, W., Erpenstein, K., Kiefer, E., Van den Bogaard, P., and G örler, K. (1999). Incorporation of the Paleogene foreland into the Neogene Puna plateau: the Salar de Antofalla area, NW Argentina. *J. S. Am. Earth Sci.*, 12(2):157–182.

Kurtz, A.C., Kay, S.M., Charrier, R., and Farrar, E. (1997). Geochronology of Miocene plutons and exhumation history of the El Teniente region,

Central Chile (34-35°S). *Andean Geol.*, 24(1):75–90.

Lamb, S. and Davis, P. (2003). Cenozoic climate change as a possible cause for the rise of the Andes. *Nature*, 425(6960):792–797.

Lamb, S., Hoke, L., Kennan, L., and Dewey, J. (1997). Cenozoic evolution of the Central Andes in Bolivia and northern Chile. *Geol. Soc. Lond. Spec. Publ.*, 121:237–264.

Lamy, F., Hebbeln, D., Röhl, U., and Wefer, G. (2001). Holocene rainfall variability in southern Chile: a marine record of latitudinal shifts of the Southern Westerlies. *Earth Planet. Sci. Lett.*, 185(3-4):369–382.

Lamy, F., Hebbeln, D., and Wefer, G. (1999). High-resolution marine record of climatic change in mid-latitude Chile during the last 28,000 years based on terrigenous sediment parameters. *Quat. Res.*, 51(1):83–93.

Lamy, F., Kilian, R., Arz, H.W., Francois, J.P., Kaiser, J., Prange, M., and Steinke, T. (2010). Holocene changes in the position and intensity of the southern westerly wind belt. *Nat. Geosci.*, 3(10):695–699.

Le Roux, J.P. (2012). A review of Tertiary climate changes in southern South America and the Antarctic Peninsula. Part 2: continental conditions. *Sediment. Geol.*, 247:21–38.

Leeman, W.P. (1983). The influence of crustal structure on compositions of subduction-related magmas. *J. Volcanol. Geoth. Res.*, 18:561–588.

Lehner, B. and Grill, G. (2013). Global river hydrography and network routing: baseline data and new approaches to study the world's large river systems. *Hydrol. Process.*, 27(15):2171–2186.

Leier, A.L., DeCelles, P.G., and Pelletier, J.D. (2005). Mountains, monsoons, and megafans. *Geology*, 33(4):289–292.

Lenters, J.D. and Cook, K.H. (1995). Simulation and diagnosis of the regional summertime precipitation climatology of South America. *J. Climate*, 8(12):2988–3005.

Lenters, J.D. and Cook, K.H. (1997). On the origin of the Bolivian high and related circulation features of the South American climate. *J. At. Sci.*, 54(5):656–678.

Lenters, J.D. and Cook, K.H. (1999). Summertime precipitation variability over South America: Role of the large-scale circulation. *Monthly Weather Rev.*, 127(3):409–431.

Litvak, V.D., Poma, S., Kay, S.M., and Valle, E. (2007). Paleogene and Neogene magmatism in the Valle del Cura region: New perspective on the evolution of the Pampean flat slab, San Juan province, Argentina. *J. S. Am. Earth Sci.*, 24:117–17.

Löbens, S., Sobel, E.R., Bense, F.A., Wemmer, K., Dunkl, I., and Siegesmund, S. (2013). Refined exhumation history of the northern Sierras Pampeanas, Argentina. *Tectonics*, 32(3):453–472.

Lossada, A.C., Giambiagi, L., Hoke, G.D., Fitzgerald, P.G., Creixell, C., Murillo, I., Mardonez, D., Velá squez, R., and Suriano, J. (2017). Thermochronologic evidence for late Eocene Andean mountain building at 30°S. *Tectonics*, 36(11):2693–2713.

Ludwig, K.R. (2001). Isoplot 4.1: A Geochronological Toolkit for Microsoft Excel. *Spec. Publ.*, 4.

Maksaev, V., Munizaga, F., Zentilli, M., and Charrier, R. (2009). Fission track thermochronology of Neogene plutons in the Principal Andean Cordillera of central Chile (33-35°S): Implications for tectonic evolution and porphyry cu-mo mineralization. *Andean Geol.*, 36(2):153–171.

Maksaev, V. and Zentilli, M. (1999). Fission Track Thermochronology of the Domeyko Cordillera, Northern Chile: Implication for Andean Tectonics and Porphyry Copper Metallogenesis. *Exploration Mining Geology*, 8(1-2):65–89.

Malavieille, J. (1984). Modelisation experimentale des chevauchements imbriques; application aux chaines de montagnes. *Bull. Soc. Geol. Fr.*, 7(1):129–138.

Mamani, M., Wörner, G., and Sempere, T. (2010a). [dataset] The Central Andes Geochemical GPS database. University of Göttingen. http://www.uni-geochem.gwdg.de/en/andes-database.

Mamani, M., Wörner, G., and Sempere, T. (2010b). Geochemical variations in igneous rocks of the Central Andean orocline (13°S to 18°S): Tracing crustal thickening and magma generation through time and space. *Geol. Soc. Am. Bull.*, 122(1-2):162–182.

Mancktelow, N.S. and Grasemann, B. (1997). Time-dependent effects of heat advection and topography on cooling histories during erosion. *Tectonophysics*, 270(3):167–195.

Marengo, J.A., Liebmann, B., Grimm, A.M., Misra, V., Silva Dias, P.L., Cavalcanti, I.F.A., et al. (2012). Recent developments on the South American monsoon system. *Int. J. Climatol.*, 32(1):1–21.

Marengo, J.A., Soares, W.R., Saulo, C., and Nicolini, M. (2004). Climatology of the low-level jet east of the andes as derived from the ncep–ncar reanalyses: Characteristics and temporal variability. *Journal of climate*, 17(12):2261–2280.

Marquillas, R.A., Del Papa, C., and Sabino, I.F. (2005). Sedimentary aspects and paleoenvironmental evolution of a rift basin: Salta Group (Cretaceous–Paleogene), northwestern Argentina. *Int. J. Earth Sci.*, 94(1):94–113.

Martínez, F., Arriagada, C., and Bascuñán, S. (2018). Mechanisms and episodes of deformation along the chilean pampean flat-slab subduction segment of the central andes in northern chile. In Folguera, A., Contreras-Reyes, E., Heredia, N., Encinas, A.B., Iannelli, S., Oliveros, V.M., Dávila, F., Collo, G., Giambiagi, L., A., M., et al., editors, *The Evolution of the Chilean-Argentinean Andes*, pages 273–290. Springer Earth System Sciences, Cham, Switzerland.

Martínez, F., Arriagada, C., Peña, M., Deckart, K., and Charrier, R. (2016). Tectonic styles and crustal shortening of the Central Andes "Pampean" flat-slab segment in northern Chile (27–29°S). *Tectonophysics*, 667:144–162.

Martinod, J., Husson, L., Roperch, P., Guillaume, B., and Espurt, N. (2010). Horizontal subduction zones, convergence velocity and the building of the Andes. *Earth Planet. Sci. Lett.*, 299(3):299–309.

Masek, J.G., Isacks, B.L., Gubbels, T.L., and Fielding, E.J. (1994). Erosion and tectonics at the margins of continental plateaus. *J. Geophys. Res. Solid Earth*, 99(B7):13941–13956.

McNutt, R.H., Crocket, J.H., Clark, A.H., Caelles, J.C., Farrar, E., Haynes, S.J., and Zentilli, M. (1975). Initial ^{87}Sr/^{86}Sr ratios of plutonic and volcanic rocks of the central Andes between latitudes 26° and 29° south. *Earth Planet. Sci. Lett.*, 27(2):305–313.

McQuarrie, N. (2002). The kinematic history of the central Andean fold-thrust belt, Bolivia: Implications for building a high plateau. *Geol. Soc. Am. Bull.*, 114(8):950–963.

McQuarrie, N. and DeCelles, P. (2001). Geometry and structural evolution of the central Andean backthrust belt, Bolivia. *Tectonics*, 20(5):669–692.

McQuarrie, N., Horton, B.K., Zandt, G., Beck, S., and DeCelles, P.G. (2005). Lithospheric evolution of the Andean fold–thrust belt, Bolivia, and the origin of the central Andean plateau. *Tectonophysics*, 399(1-4):15–37.

Mercer, J.H. and Sutter, J.F. (1982). Late Miocene - earliest Pliocene glaciation in southern Argentina: Implications for global ice sheet history. *Palaeogeogr., Palaeoclimatol., Palaeoecol.*, 38:185–206.

Miller, D.S., Duddy, I.R., Green, P.F., Hurford, A.J., and Naeser, C.W. (1985). Results of interlaboratory comparison of fission-track age standards. *Nucl. Tracks and Radiat. Meas.*, 10:381–391.

Mitrovica, J.X., Beaumont, C., and Jarvis, G.T. (1989). Tilting of continental interiors by the dynamical effects of subduction. *Tectonics*, 8(5):1079–1094.

Molnar, P. (2004). Late cenozoic increase in accumulation rates of terrestrial sediment: How might climate change have affected erosion rates? *Annu. Rev. Earth Planet. Sci.*, 32:67–89.

Molnar, P. (2009). The state of interactions among tectonics, erosion, and climate: A polemic. *GSA Today*, 19(7):44–45.

Molnar, P. and England, P. (1990). Late Cenozoic Uplift of Mountain-Ranges and Global Climate Change – Chicken or Egg. *Nature*, 346(6279):29–34.

Montero-López, C., del Papa, C., Hongn, F., Strecker, M.R., and Aramayo, A. (2016). Synsedimentary broken-foreland tectonics during the paleogene in the andes of nw argentine: new evidence from regional to centimetre-scale deformation features. *Basin Res.*, 30:142–159.

Montgomery, D.R., Balco, G., and Willett, S.D. (2001). Climate, tectonics, and the morphology of the Andes. *Geology*, 29(7):579–582.

Mpodozis, C., Arrigada, C., Basso, M., Roperch, P., Cobbold, P., and Reich, M. (2005). Late Mesozoic to Paleogene stratigraphy of the Salar de Atacama Basin, Antofagasta, Northern Chile: Implications for the tectonic evolution of the Central Andes. *Tectonophysics*, 399(1-4):125–154.

Mpodozis, C. and Ramos, V. (1989). The andes of chile and argentina. In Ericksen, G.E., Cañas Pinochet, M.T., and Reinemund, J.A., editors, *Geology of the Andes and its relation to hydrocarbon and mineral resources*, pages 59–90. Circum-Pacific Counc. Energy Miner. Resour. Earth Sci. Ser. 11, Housten, Texas.

Muir, D.D., Barfod, D.N., Blundy, J.D., Rust, A.C., Sparks, R.S.J., and Clarke, K.M. (2015). The temporal record of magmatism at Cerro Uturuncu, Bolivian Altiplano. In Caricchi, L. and Blundy, J.D., editors, *Chemical, Physical and Temporal Evolution of Magmatic Systems*, pages 1–27. Geol. Soc. London. Spec. Publ., 422, London.

Mulch, A., Uba, C.E., Strecker, M.R., Schoenberg, R., and Chamberlain, C.P. (2010). Late miocene climate variability and surface elevation in the central andes. *Earth Planet. Sci. Lett.*, 290(1-2):173–182.

Müller, J.P., Kley, J., and Jacobshagen, V. (2002). Structure and Cenozoic kinematics of the Eastern Cordillera, southern Bolivia (21°S). *Tectonics*, 21(5):1037.

Muñoz, N. and Charrier, R. (1996). Uplift of the western border of the Altiplano on a west-vergent thrust system, northern Chile. *J. South Am. Earth Sci.*, 9:171–181.

Murray, K.E., Braun, J., and Reiners, P.W. (2018). Toward robust interpretation of low-temperature thermochronometers in magmatic terranes. *Geochem., Geophys., Geosyst.*, 19(10):3739–

3763.

Mutschler, F.E., Ludington, S., and Bookstrom, A. (2001). [dataset] Giant porphyry-related metal camps of the world – a database. U.S. Geological Survey Open-file Report 99-556. `https://pubs.usgs.gov/of/1999/of99-556/`.

Nalpas, T., Dabard, M.P., Ruffet, G., Vernon, A., Mpodozis, C., Loi, A., and Hérail, G. (2008). Sedimentation and preservation of the miocene atacama gravels in the pedernales–chañaral area, northern chile: climatic or tectonic control? *Tectonophysics*, 459(1-4):161–173.

Naranjo, J.A., Villa, V., Ramírez, C., and Pérez de Arce, C. (2018). Volcanism and tectonism in the southern Central Andes: Tempo, styles, and relationships. *Geosphere*, 14(2):626–641.

Nielsen, S.N. and Glodny, J. (2009). Early Miocene subtropical water temperatures in the southeast Pacific. *Palaeogeogr., Palaeoclimatol., Palaeoecol.*, 280(3-4):480–488.

Nogués-Paegle, J., Mechoso, C.R., Fu, R., Berbery, E.H., Chao, W.C., Chen, T.C., Cook, K., Diaz, A.F., Enfield, D., Ferreira, R., et al. (2002). Progress in Pan American CLIVAR research: understanding the South American monsoon. *Meteorologica*, 27(12):1–30.

Nyström, J.O., Vergara, M., Morata, D., and Levi, B. (2003). Tertiary volcanism during extension in the Andean foothills of central Chile (33°15'-33°45'). *Geol. Am. Soc. Bull.*, 115(12):1523–1537.

Oerter, E., Amundson, R., Heimsath, A., Jungers, M., Chong, G., and Renne, P. (2016). Early to Middle Miocene climate in the Atacama Desert of Northern Chile. *Paleogeogr., Paleoclimatol. Paleoecol.*, 441:890–900.

Oliveros, V., González, J., Vargas, M.E., Vásquez, P., Rossel, P., Creixell, C., Sepúlveda, F., and Bas-

tias, F. (2018). The early stages of the magmatic arc in the southern Central Andes. In Folguera, A., Contreras-Reyes, E., Heredia, N., Ecinas, A., Iannelli, S.B., Oliveros, V., Dávila, F.M., Collo, G., Giambiagi, L., and Maksymowicz, A., editors, *The Evolution of the Chilean-Argentinean Andes*, pages 165–190. Springer Earth System Sciences, Springer, Cham, Switzerland.

Oliveros, V., Morata, D., Aguirre, L., Féraud, G., and Fornari, M. (2007). Jurassic to Early Cretaceous subduction-related magmatism in the Coastal Cordillera of northern Chile (18°30-24°S): geochemistry and petrogenesis. *Andean Geol.*, 34:209–232.

Oncken, O., Boutelier, D., Dresen, G., and Schemmann, K. (2012). Strain accumulation controls failure of a plate boundary zone: Linking deformation of the Central Andes and lithosphere mechanics. *Geochem. Geophys. Geosyst.*, 13(12).

Oncken, O., Hindle, D., Kley, J., Elger, K., Victor, P., and Schemmann, K. (2006). Deformation of the Central Andean Upper Plate System - Facts, Fiction, and Constraints for Plateau Models. In Oncken, O., G., C., Franz, G., Giese, P., Götze, H., Ramos, V., Strecker, M.R., and Wigger, P., editors, *The Andes*, pages 3–27. Frontiers in Earth Sciences. Springer, Berlin, Heidelberg.

Ortiz, G., Alvarado, P., Fosdick, J.C., Perucca, L., Sáez, M., and Venerdini, A. (2015). Active deformation in the northern Sierra de Valle Fértil, Sierras Pampeanas, Argentina. *J. S. Am. Earth Sci.*, 64:339–350.

Pananont, P., Mpodozis, C., Blanco, N., Jordan, T.E., and Brown, L.D. (2004). Cenozoic evolution of the northwestern Salar de Atacama Basin, northern Chile. *Tectonics*, 23(TC6007).

Parrish, J.T., Ziegler, A.M., and Scotese, C.R. (1982). Rainfall patterns and the distribution of

coals and evaporites in the Mesozoic and Cenozoic. *Palaeogeogr., Palaeoclim., Palaeoecol.*, 40:67–101.

Pearson, D.M., Kapp, P., DeCelles, P.G., Reiners, P.W., Gehrels, G.E., Ducea, M.N., and Pullen, A. (2013). Influence of pre-Andean crustal structure on Cenozoic thrust belt kinematics and shortening magnitude: Northwestern Argentina. *Geosphere*, 9(6):1766–1782.

Perkins, J.P., Ward, K.M., de Silva, S.L., Zandt, G., Beck, S.L., and Finnegan, N.J. (2016). Surface uplift in the Central Andes driven by growth of the Altiplano Puna Magma Body. *Nature Commun.*, 7(13185).

Plank, T. and Langmuir, C.H. (1988). An evaluation of the global variations in the major element chemistry of arc basalts. *Earth Planet. Sci. Lett.*, 90:349–370.

Porras, H., Pinto, L., Tunik, M., Giambiagi, L., and Deckart, K. (2016). Provenance of the miocene alto tunuyán basin (33° 40' S, Argentina) and its implications for the evolution of the Andean Range: Insights from petrography and U–Pb LA–ICPMS zircon ages. *Tectonophysics*, 690:298–317.

Profeta, L., Ducea, M.N., Chapman, J.B., Paterson, S.R., Gonzales, S.M.H., Kirsch, M., Petrescu, L., and DeCelles, P.G. (2015). Quantifying crustal thickness over time in magmatic arcs. *Sci. Rep.*, 5(17786).

Rabassa, J., Coronato, A.M., and Salemme, M. (2005). Chronology of the Late Cenozoic Patagonian glaciations and their correlation with biostratigraphic units of the Pampean region (Argentina). *J. S. Am. Earth Sci.*, 20(1-2):81–103.

Ramos, V. (1999). Plate tectonic setting of the Andean Cordillera. *Episodes*, 22:183–190.

Ramos, V.A., Cegarra, M., and Cristallini, E. (1996). Cenozoic tectonics of the High Andes of west-central Argentina (30-36° S latitude). *Tectonophysics*, 259(1):185–200.

Ramos, V.A. and Folguera, A. (2005). Tectonic evolution of the Andes of Neuquén: Constraints derived from the magmatic arc and foreland deformation. *Geol. Soc. London Spec. Publ.*, 252:15–35.

Ramos, V.A. and Folguera, A. (2009). Andean flat-slab subduction through time. *Geol. Soc. London. Spec. Pub.*, 327(1):31–54.

Raymo, M.E. and Ruddiman, W.F. (1992). Tectonic Forcing of Late Cenozoic Climate. *Nature*, 359(6391):117–122.

Rech, J.A., Currie, B.S., Jordan, T.E., Riquelme, R., Lehmann, S.B., Kirk-Lawlor, N.E., Li, S., and Gooley, J.T. (2019). Massive middle Miocene gypsic paleosols in the Atacama Desert and the formation of the Central Andean rain-shadow. *Earth Planet. Sci. Lett.*, 506:184–194.

Rech, J.A., Currie, B.S., Shullenberger, E.D., Dunagan, S.P., Jordan, T.E., Blanco, N., Tomlinson, A.J., Rowe, H.D., and Houston, J. (2010). Evidence for the development of the Andean rain shadow from a Neogene isotopic record in the Atacama Desert, Chile. *Earth Planet. Sci. Lett.*, 292(3-4):371–382.

Rehak, K., Bookhagen, B., Strecker, M.R., and Echtler, H.P. (2010). The topographic imprint of a transient climate episode: the western Andean flank between 15.5° and 41.5°S. *Earth Surf. Process. Landf.*, 35(13):1516–1534.

Reiners, P.W., Carlson, R.W., Renne, P.R., Cooper, K.M., Granger, D.E., McLean, N.M., and Schoene, B. (2018). *Geochronology and Thermochronology*. Wiley & Sons.

Reiners, P.W., Ehlers, T.A., Mitchell, S.G., and Montgomery, D.R. (2003). Coupled spatial variations in precipitation and long-term erosion rates across the Washington Cascades. *Nature*, 426(6967):645–647.

Reiners, P.W. and Nicolescu, S. (2006). Measurements of parent nuclides for (U–Th)/He chronometry by solution sector ICP-MS, ARHDL Report 1. Technical report, Dep. of Geosciences, University of Arizona, Tucson.

Reiners, P.W., Thomson, S.N., Vernon, A., Willett, S.D., Zattin, M., Einhorn, J., Gehrels, G., Quade, J., Pearson, D., and Murray, K.E. (2015). Low-temperature thermochronologic trends across the central andes, 21°S-28°S. *Geol. Soc. Am. Mem.*, 212:215–249.

Riesner, M., Lacassin, R., Simoes, M., Armijo, R., Rauld, R., and Vargas, G. (2017). Kinematics of the active west Andean fold-and-thrust belt (Central Chile): Structure and long-term shortening rate. *Tectonics*, 36(2):287–303.

Riesner, M., Lacassin, R., Simoes, M., Carrizo, D., and Armijo, R. (2018). Revisiting the crustal structure and kinematics of the central Andes at 33.5°S: Implications for the Mechanics of Andean Mountain Building. *Tectonics*, 37:1347–1375.

Riesner, M., Simoes, M., Carrizo, D., and Lacassin, R. (2019). Early exhumation of the Frontal Cordillera (Southern Central Andes) and implications for Andean mountain-building at ~33.5°S. *Sci. Rep.*, 9(1):1–10.

Riquelme, R., Hérail, G., Martinod, J., Charrier, R., and Darrozes, J. (2007). Late cenozoic geomorphologic signal of andean forearc deformation and tilting associated with the uplift and climate changes of the southern atacama desert (26°S-28°S). *Geomorphology*, 86(3-4):283–306.

Rodríguez, M.P., Charrier, R., Brichau, S., Carretier, S., Farías, M., de Parseval, P., and Ketcham, R.A. (2018). Latitudinal and longitudinal patterns of exhumation in the Andes of north-central Chile. *Tectonics*, 37(9):2863–2886.

Rohrmann, A., Sachse, D., Mulch, A., Pingel, H., Tofelde, S., Alonso, R.N., and Strecker, M.R. (2016). Miocene orographic uplift forces rapid hydrological change in the southern central Andes. *Sci. Rep.*, 6:35678.

Rojas Vera, E.A., Folguera, A., Valcarce, G.Z., Giménez, M., Ruiz, F., Martínez, P., Bottesi, G., and Ramos, V.A. (2010). Neogene to Quaternary extensional reactivation of a fold and thrust belt: the Agrio belt in the Southern Central Andes and its relation to the Loncopué trough (38°–39° S). *Tectonophysics*, 492:279–294.

Rossel, K., Aguilar, G., Salazar, E., Martinod, J., Carretier, S., Pinto, L., and Cabré, A. (2016). Chronology of Chilean Frontal Cordillera building from geochronological, stratigraphic and geomorphological data insights from Miocene intramontane-basin deposits. *Basin Res.*, 30:289–310.

Royden, L.H. (1993). Evolution of retreating subduction boundaries formed during continental collision. *Tectonics*, 12(2):629–638.

Ruddiman, W.F. (2008). *Earth's Climate: past and future*. Macmillan, 2 edition.

Ruskin, B.G. and Jordan, T.E. (2007). Climate change across continental sequence boundaries: paleopedology and lithofacies of Iglesia Basin, northwestern Argentina. *J. Sediment. Res.*, 77(9):661–679.

Ryan, J., Beck, S., Zandt, G., Wagner, L., Minaya, E., and Tavera, H. (2016). Central Andean crustal structure from receiver function analysis. *Tectonophysics*, 682:120–133.

Sáez, A., Cabrera, L., Garcés, M., van den Bogaard, P., Jensen, A., and Gimeno, D. (2012). The stratigraphic record of changing hyperaridity in the Atacama Desert over the last 10 Ma. *Earth Planet. Sci. Lett.*, 355:32–38.

Safipour, R., Carrapa, B., DeCelles, P.G., and Thomson, S.N. (2015). Exhumation of the Precordillera and northern Sierras Pampeanas and along-strike correlation of the Andean orogenic front, northwestern Argentina. *Geol. Soc. Am. Mem.*, 212:181–199.

Saulo, A.C., Nicolini, M., and Chou, S.C. (2000). Model characterization of the South American low-level flow during the 1997–1998 spring–summer season. *Climate Dynam.*, 16(10-11):867–881.

Schaltegger, U., Schmitt, A.K., and Horstwood, M.S.A. (2015). U-Th-Pb zircon geochronology by ID-TIMS, SIMS, and laser ablation ICP-MS: Recipes, interpretations, and opportunities. *Chem. Geol.*, 402:89–110.

Schepers, G., van Hinsbergen, D.J.J., Spakman, W., Kosters, M.E., Boschman, L.M., and McQuarrie, N. (2017). South-American plate advance and forced Andean trench retreat as drivers for transient flat subduction episodes. *Nat. Commun.*, 8(15249).

Scheuber, E. (1998). [dataset] Radiometric and Fission Track Age Determination of Central Andes. Freie Universität Berlin. www.cms.fu-berlin.de/sfb/sfb267/results/data_catalogue/central_andean_data/geochemical_data.html.

Scheuber, E., Bogdanic, T., Jensen, A., and Reutter, K.J. (1994). Tectonic development of the North Chilean Andes in relation to plate convergence and magmatism since the Jurassic. In Reutter, K.J., Scheuber, E., and Wigger, P.J., editors, *Tectonics of the Southern Central Andes*, pages 121–139. Springer, Berlin, Heidelberg.

Schildgen, T.F., van der Beek, P.A., Sinclair, H.D., and Thiede, R.C. (2018). Spatial correlation bias in late-Cenozoic erosion histories derived from thermochronology. *Nature*, 559(7712):89–93.

Schwerdtfeger, W. (1976). *World survey of climatology volume 12: Climates of Central and South America*, volume 12. Elsevier Sci. Pub., Amsterdam.

Scott, E.M., Allen, M.B., Macpherson, C.G., McCaffrey, K.J., Davidson, J.P., Saville, C., and Ducea, M.N. (2018). Andean surface uplift constrained by radiogenic isotopes of arc lavas. *Nature commun.*, 9(969).

SegemAR (1997). Mapa Geológico de la República Argentina: versión digital, escala 1:1'000'000. Instituto de Geología y Recursos Minerales, Servicio Geológico Minero Argentino, Buenos Aires.

Sempere, T., Butler, R.F., Richards, D.R., Marshall, L.G., Sharp, W., and Swisher, C.C. (1997). Stratigraphy and chronology of late Cretaceous-early Paleogene strata in Bolivia and northern Argentina. *Geol. Soc. Am. Bull.*, 109:709–727.

SERNAGEOMIN (2003). Mapa Geológico de Chile: versión digital, escala 1:1'000'000. Publicación Geológica Digital No. 4.

Shackleton, N.J., Backman, J., Zimmerman, H., Kent, D.V., Hall, M.A., Roberts, D.G., Schnitker, D., Baldauf, J.G., Desprairies, A., Homrighausen, R., and et al. (1984). Oxygen isotope calibration of the onset of ice-rafting and history of glaciation in the North Atlantic region. *Nature*, 307:620–623.

Shuster, D.L., Cuffey, K.M., Sanders, J.W., and Balco, G. (2011). Thermochronometry reveals headward propagation of erosion in an alpine

landscape. *Science*, 332(6025):84–88.

Shuster, D.L., Ehlers, T.A., Rusmoren, M.E., and Farley, K.A. (2005). Rapid glacial erosion at 1.8 Ma revealed by ^{4}He/^{3}He thermochronometry. *Science*, 310(5754):1668–1670.

Singer, D.A., Berger, V.I., and Moring, B.C. (1998). [dataset] Porphyry Copper Deposits of the World: Data base and Grade and Tonnage Models. U.S. Geological Survey Open-file Report 2008-1155. https://pubs.usgs.gov/of/2008/1155/.

Siravo, G., Faccenna, C., Gérault, M., Becker, T.W., Fellin, M.G., Herman, F., and Molin, P. (2019). Slab flattening and the rise of the Eastern Cordillera, Colombia. *Earth Planet. Sci. Lett.*, 512:100–110.

Sláma, J., Košler, J., Condon, D.J., Crowley, J.L., Gerdes, A., Hanchar, J.M., Horstwood, M.S.A., Morris, G.A., Nasdala, L., Norberg, N., et al. (2008). Plesovičce zircon – a new natural reference material for U–Pb and Hf isotopic microanalysis. *Chem. Geol.*, 249(1):1–35.

Sobel, E.R. and Strecker, M.R. (2003). Uplift, exhumation and precipitation: tectonic and climatic control of Late Cenozoic landscape evolution in the northern Sierra Pampeanas, Argentina. *Basin Res.*, 15:431–441.

Spikings, R., Dungan, M., Foeken, J., Carter, A., Page, L., and Stuart, F. (2008). Tectonic response of the central Chilean margin (35–38°S) to the collision and subduction of heterogeneous oceanic crust: a thermochronological study. *J. Geol. Soc.*, 165(5):941–953.

Springer, M. and Förster, A. (1998). Heat-flow density across the Central Andean subduction zone. *Tectonophysics*, 291:123–139.

Starck, D. and Anzótegui, L.M. (2001). The late Miocene climatic change - Persistence of a cli-

matic signal through the orogenic stratigraphic record in northwestern Argentina. *J. South Am. Earth Sci.*, 14(7):763–774.

Strecker, M.R., Alonso, R., Bookhagen, B., Carrapa, B., Coutand, I., Hain, M.P., Hilley, G.E., Mortimer, E., Schoenbohm, L., and Sobel, E.R. (2009). Does the topographic distribution of the central Andean Puna Plateau result from climatic or geodynamic processes? *Geology*, 37(7):643–646.

Strecker, M.R., Alonso, R.N., Bookhagen, B., Carrapa, B., Hilley, G.E., Sobel, E.R., and Trauth, M.H. (2007). Tectonics and Climate of the Southern Central Andes. *Annu. Rev. Earth Planet. Sci.*, 35:747–787.

Strecker, M.R., Cerveny, P., Bloom, A.L., and Malizia, D. (1989). Late Cenozoic Tectonism and Landscape Development in the Foreland of the Andes: Northern Sierras Pampeanas (26°-28°S), Argentina. *Tectonics*, 8(3):517–534.

Stuut, J.W. and Lamy, F. (2004). Climate variability at the southern boundaries of the Namib (southwestern Africa) and Atacama (northern Chile) coastal deserts during the last 120,000 yr. *Quat. Res.*, 62:301–309.

Tarantola, A. (2005). *Inverse problem theory and methods for model parameter estimation*. siam.

Thomson, S.N., Brandon, M.T., Tomkin, J.H., Reiners, P.W., Vásquez, C., and Wilson, N.J. (2010). Glaciation as a destructive and constructive control on mountain building. *Nature*, 467(7313):313–317.

Tripaldi, A. and Limarino, C.O. (2005). Vallecito Formation (Miocene): The evolution of an eolian system in an Andean foreland basin (northwestern Argentina). *J. South Am. Earth Sci.*, 19(3):343–357.

Uba, C.E., Heubeck, C., and Hulka, C. (2005). Facies analysis and basin architecture of the Neogene Subandean synorogenic wedge, southern Bolivia. *Sediment. Geol.*, 180:91–123.

Uba, C.E., Heubeck, C., and Hulka, C. (2006). Evolution of the late Cenozoic Chaco foreland basin, Southern Bolivia. *Basin Res.*, 18:145–170.

Uba, C.E., Kley, J., Strecker, M.R., and Schmitt, A.K. (2009). Unsteady evolution of the Bolivian Subandean thrust belt: The role of enhanced erosion and clastic wedge progradation. *Earth Planet. Sci. Lett.*, 281(3–4):134–146.

Uba, C.E., Strecker, M.R., and Schmitt, A.K. (2007). Increased sediment accumulation rates and climatic forcing in the central Andes during the late Miocene. *Geology*, 35(11):979–982.

Ulianov, A., Müntener, O., Schaltegger, U., and Bussy, F. (2012). The data treatment dependent variability of U–Pb zircon ages obtained using mono-collector, sector field, laser ablation ICPMS. *J. Anal. At. Spectrom.*, 27(4):663–676.

Valero-Garcés, B.L., Jenny, B., Rondanelli, M., Delgado-Huertas, A., Burns, S.J., Veit, H., and Moreno, A. (2005). Palaeohydrology of Laguna de Tagua Tagua (34° 30' S) and moisture fluctuations in Central Chile for the last 46 000 yr. *J. Quat. Sci*, 20(7-8):625–641.

van der Meijde, M., Julià, J., and Assumpção, M. (2013). Gravity derived Moho for South America. *Tectonophysics*, 609:456–467.

Vargas, G., Klinger, Y., Rockwell, T.K., Forman, S.L., Rebolledo, S., Baize, S., Lacassin, R., and Armijo, R. (2014). Probing large intraplate earthquakes at the west flank of the Andes. *Geology*, 42(12):1083–1086.

Vera, C., Higgins, W., Amdor, J., Ambrizzi, T., Garreaud, R., Gochis, D., Gutzler, D., Lettenmaier, D., Marengo, J., Mechoso, C.R., Nogues-Paegle, J., Silva Dias, P.L., and Zhang, C. (2006). Toward a unified view of the american monsoon system. *Am. Meteorolog. Soc.*, pages 4977–5000.

Victor, P., Oncken, O., and Glodny, J. (2004). Uplift of the western Altiplano plateau: Evidence form the Precordillera between 20° and 21°S (northern Chile). *Tectonics*, 23(TC4004):1–24.

Villagrán, C., Armesto, J.J., Hinojosa, F., Cuvertino, J., Pérez, C., and Medina, C. (2004). El enigmático orígen del bosque relicto de Fray Jorge. In Squeo, F., Gutiérrez, J.R., and Hernández, I.R., editors, *Historia Natural del Parque Nacional Bosque Fray Jorge*, pages 3–43. Ediciones Universidad de La Serena, La Serena, Chile.

Vuille, M. and Ammann, C. (1997). Regional snowfall patterns in the high, arid Andes. *Clim. Change*, 36:413–423.

Wagner, G.A., Miller, D.S., and Jäger, E. (1979). Fission track ages on apatite of Bergell rocks from central Alps and Bergell boulders in Oligocene sediments. *Earth Planet. Sci. Lett.*, 45(2):355–360.

Ward, K.M., Zandt, G., Beck, S.L., Christensen, D.H., and McFarlin, H. (2014). Seismic imaging of the magmatic underpinnings beneath the Altiplano-Puna volcanic complex from the joint inversion of surface wave dispersion and receiver functions. *Earth Planet. Sci. Lett.*, 404:43–53.

Weatherall, P., Marks, K.M., Jakobsson, M., Schmitt, T., Tani, S., Arndt, J.E., Rovere, M., Chayes, D., Ferrini, V., and Wigley, R. (2015). A new digital bathymetric model of the world's oceans. *Earth Space Sci.*, 2(8):331–345.

Whipple, K.X. (2009). The influence of climate on the tectonic evolution of mountain belts. *Nat. Geosci.*, 2(2):97–104.

Whipple, K.X. (2014). Can erosion drive tectonics? *Science*, 346(6212):918–919.

Whipple, K.X. and Meade, B.J. (2006). Orogen response to changes in climatic and tectonic forcing. *Earth Planet. Sci. Lett.*, 243:218–228.

Willenbring, J.K. and Jerolmack, D.J. (2016). The null hypothesis: globally steady rates of erosion, weathering fluxes and shelf sediment accumulation during Late Cenozoic mountain uplift and glaciation. *Terra Nova*, 28(1):11–18.

Willett, S.D. (1999). Orogeny and orography: The effects of erosion on the structure of mountain belts. *J. Geophys. Res.*, 104((B12)):28957–28981.

Willett, S.D., Beaumont, C., and Fullsack, P. (1993). Mechanical model for the tectonics of doubly vergent compressional orogens. *Geology*, 21(4):371–374.

Willett, S.D., Herman, F., Fox, M., Stalder, N.F., Ehlers, T.A., Jiao, R., and Yang, R. (2020). Bias and error in modelling thermochronometric data: resolving a potential increase in Plio-Pleistocene erosion rate. *Earth Surf. Dynam. Discuss., in review*.

Winocur, D.A., Litvak, V.D., and Ramos, V.A. (2015). Magmatic and tectonic evolution of the Oligocene Valle del Cura Basin, main Andes of Argentina and Chile: Evidence for generalized extension. *Geol. Soc. London Spec. Pub.*, 399:109–130.

Wotzlaw, J.F., Decou, A., von Eynatten, H., Wörner, G., and Frei, D. (2011). Jurassic to Palaeogene tectono-magmatic evolution of northern Chile and adjacent Bolivia from detrital zircon U-Pb geochronology and heavy mineral provenance. *Terra Nova*, 23(6):399–406.

York, D., Evensen, N.M., López Martínez, M., and De Basabe Delgado, J. (2004). Unified equations for the slope, intercept, and standard error of the best straight line. *Am. J. Phys*, 72:367.

Zachos, J., Pagani, M., Sloan, L., Thomas, E., and Billups, K. (2001). Trends, Rhythms, and Aberrations in Global Climate 65 Ma to present. *Science*, 292(5517):686–693.

Zapata, S. (2019). *Paleozoic to Pliocene evolution of the Andean retroarc between 26 and 28°S: interactions between tectonics, climate, and upper plate architecture*. PhD thesis, Universität Potsdam, Potsdam, Germany. PhD thesis, Universität Potsdam, Potsdam, Germany, pp. 139.

Zapata, S., Sobel, E.R., del Papa, C., Muruaga, C., and Zhou, R. (2019). Miocene fragmentation of the Central Andean foreland basins between 26 and 28 °S. *J. South Am. Earth Sci.*, 94:1–18.

Zech, R., May, J., Kull, C., Ilgner, J., Kubik, P.W., and Veit, H. (2008). Timing of the late Quaternary glaciation in the Andes from ~15 to 40°S. *J. Quat. Sci.*, 23(6):635–647.

Zech, R., Zech, J., Kull, C., Kubik, P.W., and Veit, H. (2011). Early last glacial maximum in the southern Central Andes reveals northward shift of the westerlies at similar to 39 ka. *Climate Past*, 7(1):41–46.

Zhang, P.Z., Molnar, P., and Downs, W.R. (2001). Increased sedimentation rates and grain sizes 2-4 Myr ago due to the influence of climate change on erosion rates. *Nature*, 410(6831):891–897.

Zhou, J. and Lau, K.M. (1998). Does a monsoon climate exist over South America? *J. Climate*, 11(5):1020–1040.

Maximized erosion at the last glacial maximum revealed by luminescence thermochronometry

Nadja F. Stalder[1], Frédéric Herman[1], Rabiul H. Biswas[1]

Institute of Earth Surface Dynamics, University of Lausanne, Switzerland

Abstract

Increased erosion rates during the last 2 Myr of Earth history are commonly associated with widespread glaciation and global cooling. However, whether erosion rates actually increased during that period of Earth history remains debated. This is in part because the respective role of fluvial and glacial erosion is difficult to assess, and because many existing techniques used to estimate erosion rates can be affected by a systematic averaging bias that tend to produce increased erosion rates towards the present. Here we use thermoluminescence thermochronometry, which enables us to extract unbiased time series of erosion rates, in the Chilean Andes. We focus our analysis on an area that experienced a full transition from glacial to fluvial-dominated conditions during the last 100 kyr, and find that erosion rates were systematically higher during the last glacial maximum than today. The difference in erosion rates are by more than an order of magnitude. This result indicates that glacial erosion is probably more efficient than fluvial erosion. More importantly, our findings imply that erosion has remained transient during the Quaternary, which may in part explain the observed decrease towards the present.

3.1 Introduction

The Earth's topography is shaped by erosional processes that are dictated by tectonic and climatic processes. During the Late Cenozoic, the Earth's climate cooled (e.g., Zachos et al., 2001) and entered into a state of a highly variable climate (Lisiecki and Raymo, 2005, 2007) expressed by the waxing and waning of continental ice sheets (Shackleton et al., 1984), with cycles that evolved from 41 to 100 kyr periods at the mid-Pleistocene transition around 0.9 Ma (Lisiecki and Raymo, 2007). These climatic transitions may have led to an increase in erosion rates (e.g., Valla et al., 2012; Pedersen and Egholm, 2013; Herman and Champagnac, 2016), as suggested by observations of increased terrigenous sediment flux to the ocean (Molnar and England, 1990), increased sedimentation (Zhang et al., 2001; Molnar, 2004) and erosion rates (Charreau et al., 2011) in continental basins, and thermochronological data (Shuster et al., 2005, 2011; Herman et al., 2013; Willett et al., 2020). In particular, the onset of glacial erosion has left a profound impact on topographic evolution, relief, and erosion rates in mountainous landscapes (e.g., Brozović et al., 1997; Montgomery et al., 2001; Egholm et al., 2009; Thomson et al., 2010; Herman et al., 2013; Champagnac et al., 2014). Moreover, sediment yield measurements from modern environments suggest that temperate glaciers erode faster than rivers (Hallet et al., 1996; Gurnell et al., 1996; Brocklehurst and Whipple, 2002; Montgomery, 2002). However, glacial erosion rates span up to five orders of magnitude, from 10^{-4} mm/a to >100 mm/a (Hallet et al., 1996; Delmas et al., 2009), and the idea that glaciers are more efficient than rivers is ascertained by global compilations of sediment yield and denudation rates that show that fluvial and glacial erosion rates are equal in tectonically active settings (Koppes and Montgomery, 2009).

An attractive explanation for an increase in erosion rates during the Quaternary is that both changes in amplitudes and frequency of climate during this time period have maintained a state of disequilibrium in which erosive processes continually adjusted to new conditions (Gilbert, 1900; Knox, 1972; Donnelly, 1982; Bull, 1991; Einsele, 2000; Overeem et al., 2001; Zhang et al., 2001; Molnar, 2004). Any change in erosion rate due to a shift in climate will include a transient response that usually leads to a pulse of erosion. However, maintaining erosion rates over the full Quaternary that are a higher than the flux of rocks provided by tectonics requires a response time, i.e., the time to settle back to equilibrium, that is sufficiently long. Recently, such characteristic times have been established for both fluvial and glacial erosion processes. The characteristic time for fluvial erosion is based on the stream power model and is up to a few million years, depending on uplift rate, erosional efficiency, spatial scale, and sustained transient conditions during the Late Cenozoic (Whipple, 2001; Braun et al., 2015). In contrast, work on glacial erosion suggest that the characteristic time also depends on rock uplift, erosional efficiency and precipitation rates, but that it is much shorter than for fluvial erosion, of the order of tens to hundreds of thousands of years, which corresponds to the periods of Milankovitch cycles (Herman et al., 2018). The latter findings

imply that the entry into cyclic climatic conditions during the Quaternary may have enabled the persistence of transient conditions.

Assessing the relative efficacy of fluvial and glacial erosion is debated because of our limited means to measure erosion rates at the timescales of Quaternary glacial cycles. Measurements of erosion rates, particularly for glacial settings, may depend on the applied method and the time span over which they are averaged (Spotila et al., 2004; Delmas et al., 2009; Koppes and Montgomery, 2009), which may lead to a timescale bias (Ganti et al., 2016). This timescale bias can be explained by either the stochastic nature of erosional processes (Finnegan et al., 2014; Ganti et al., 2016) or by the incompleteness of the sedimentary record (Barrell, 1917; Sadler, 1981). The net effect is that erosion rates scale with the time interval they are averaged with, producing higher erosion rates towards the present (Ganti et al., 2016). Therefore, studies measuring erosion rates that could give insights into the respective efficiency of fluvial and glacial erosion can be biased when compared at different timescales (Gardner et al., 1987), and in turn require time series of erosion rates that are reliable. Yet, studies reporting such time series of erosion rates are sparse and mostly rely on ^{10}Be data (Schaller et al., 2004; Haeuselmann et al., 2007; Charreau et al., 2011; Knudsen et al., 2015; Marshall et al., 2017). Here, we apply thermoluminescence thermochronology on rock samples from the Chilean Andes (Fig. 3.1) to constrain erosion rate histories during the last 100 kyr. This new technique does not suffer from a timescale bias, as we show here. Our data indicate a decrease of erosion rates at the transition from fully glaciated to cold conditions, showing that erosion rates remained transient at the timescale of Quaternary cycles.

3.2 The Chilean Andes and their glacial overprint

To estimate the erosional response at the transition between glacial and fluvial conditions, we collected samples in the central Chilean Andes (33 to 35° S). This region shows a strong, highly seasonal precipitation gradient from north to south, with average yearly precipitation of ca. 400 mm/a in the north to ca. 750 mm/a in the south (Fick and Hijmans, 2017) (Fig. 3.1). Most precipitation falls during austral winter when the mid-latitude storm-tracks expand as far as 32° S north. Modern perennial snowline measurements reflect this precipitation gradient by showing decreasing elevations from north (3800 m) to south (3500 m) (Fig. 3.2). Several lines of evidence suggest that the Westerlies in this region intensified during cold, glacial periods (Lamy et al., 1999; Moreno et al., 1999; Valero-Garcés et al., 2005; Lamy et al., 2010), leading to the lowering of the snow lines by about 1 km (Broecker and Denton, 1989) and hence to the growth of glaciers (Zech et al., 2008) that shaped the modern relief (Clapperton, 1994). Moreover, this region is (Vargas et al., 2014) and has been tectonically active since the Miocene (Riesner et al., 2018). This area is thus
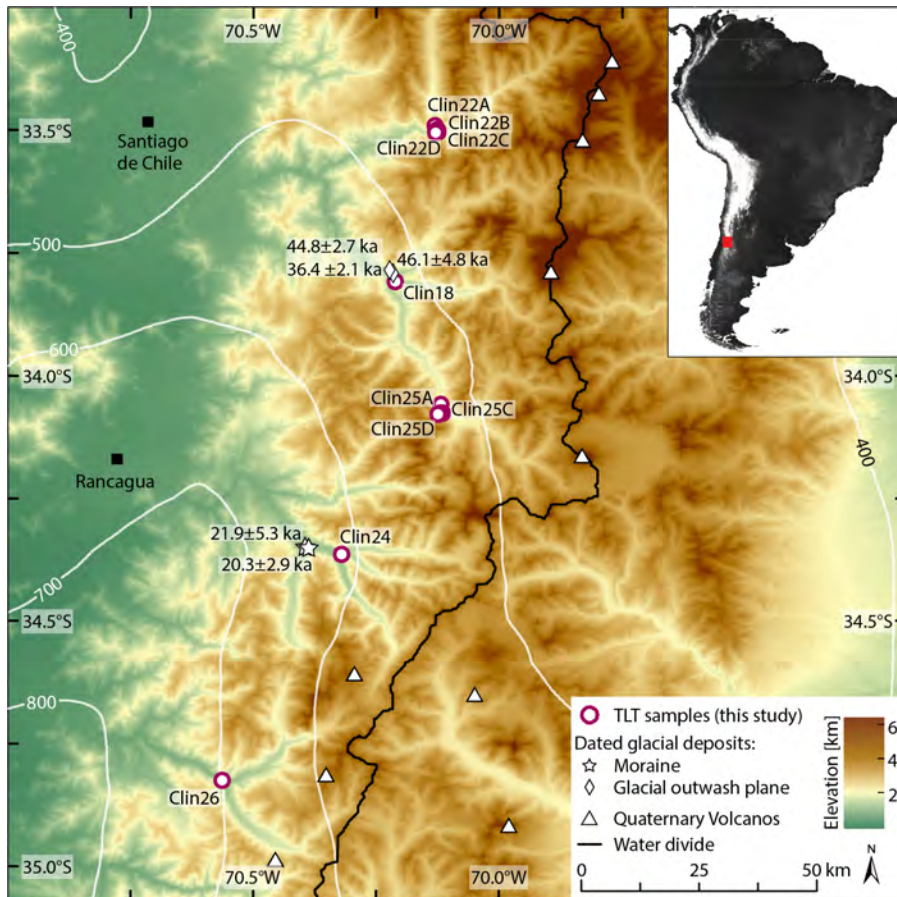
Figure 3.1: Study area with TL sample locations and dated moraine (Charrier et al., 2019) and glacier outwash (Herrera Ossandón, 2016) deposits delimiting the extent of the last glacial maximum. Digital elevation model from Danielson and Gesch (2011). White lines delineate the average yearly precipitation [mm/yr] (data from Fick and Hijmans (2017)).

subjected to changes in climatic conditions, and in particular to pronounced interglacial and glacial cycles. Therefore, if higher climate variability is one of the main drivers of the Late Cenozoic increase in erosion rates (Zhang et al., 2001; Molnar, 2004; Herman et al., 2013), this area should show high erosion rates during the last glacial-interglacial cycle and offers a unique opportunity to investigate the role of glaciations on erosion rates.

Two main studies quantified erosion rates in the central Chilean Andes and found erosion rates that vary by an order of magnitude between decadal to millennial timescales (<0.3 mm/a, Carretier et al., 2013) and Ma-timescales (>2 mm/a, Stalder et al., 2020). However, the difference in erosion rates at different timescales remains unexplained beyond the stochastic nature of erosional processes. To bridge the mismatch between long- and short-term erosion rates and to therefore rule out any timescale bias, we collected samples around the formerly glaciated area at different elevations to extract erosion histories of the last 100 kyr using thermoluminescence thermochronometry (Fig. 3.1).
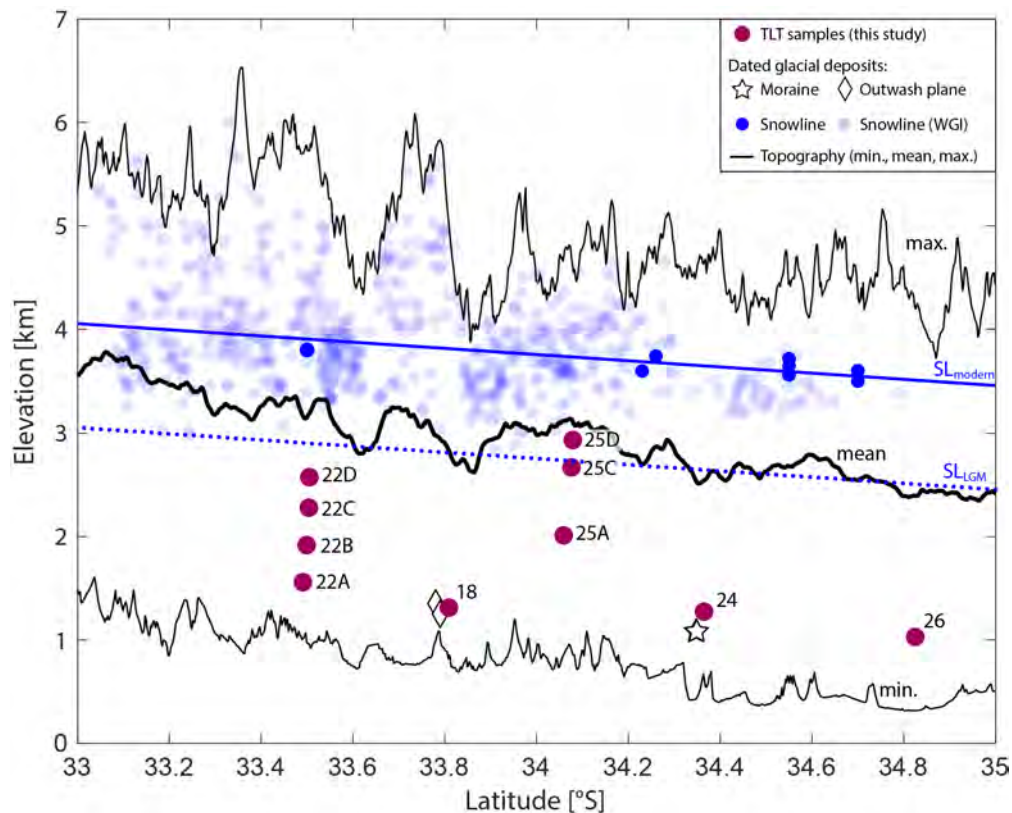
Figure 3.2: TL sample elevations relative to topography and snowlines. Maximum, mean and minimum topography were calculated from a Swath profile of the Chilean Andes (mountain front to water divide) using digital elevation data from Danielson and Gesch (2011). The estimate of the modern snowline (blue line) is the best fit for modern snowline observations (dark blue dots, Appendix Table B4). Additional snowline data (light blue dots) from WGMS (1989). The snowline during the last glacial maximum (stippled blue line) is estimated to be 1 km lower than the modern snowline (Broecker and Denton, 1989). Dated glacial deposits from Charrier et al. (2019) and Herrera Ossandón (2016).

3.3 Deciphering time series of erosion rates using thermoluminescence thermochronometry

Thermoluminescence thermochronology exploits the thermal dependency of luminescence signals generated by the release of electrons from traps under the stimulation of heat in the laboratory. In nature, ambient radiation from decaying radioactive elements (U, Th, K) excites electrons in the crystal lattice of feldspars so that they move freely through the crystal lattice until being trapped in trapping centers located at different energy levels. During rock exhumation, and thus rock cooling, electrons are released or not, depending on their energy level, which corresponds to temperatures ranging from 30 to 80 °C (Biswas et al., 2018). This process can be exploited as a multiple thermochronometer (Brown et al., 2017; Biswas et al., 2018) that records the cooling history of rock samples at Quaternary timescales (Herman and King, 2018). Combining such

measurements with a thermal model and a Bayesian inverse approach enables the extraction of time series of erosion rates (Biswas et al., 2018).

Most samples that we analyzed show a decrease in erosion rates by an order of magnitude, from ~40-60 mm/a down to ~3-5 mm/a during the last 50 kyr (Fig. 3.3); except for one sample that lies above the Equilibrium Line Altitude (ELA) of the Last Glacial Maximum (LGM), about 20 kyr ago, and two samples that are located very close to the limit of the LGM extent (Fig. 3.2). The decrease in erosion rates occurs before the expected climatic transition at 20-40 ka (Zech et al., 2008; Charrier et al., 2019). The erosion rates between 100 and 40 kyr are higher than erosion rates measured for this region during the Pleistocene (Stalder et al., 2020). However, erosion rates estimated over several hundreds of thousands of years are expected to be lower as they are integrated over longer timescales (Ganti et al., 2016). Similarly, the erosion rates estimated using thermoluminescence thermochronology remain higher than the erosion rates estimated by suspended sediment-load and ^{10}Be data in the same area (Carretier et al., 2013).

To test the robustness of our inverse results and the ability of our method to detect the timing of the change, we conducted a series of synthetic tests. The results show that our method cannot detect abrupt changes in erosion rates (Fig. 3.3), leading to a smooth but unbiased solution. One can recover the pattern of changes, but the magnitude of erosion rates and the timing of the change must be interpreted with caution. The smoothing is caused by the diffusion of heat within the crust. Also, the synthetic tests show that the time series inferred using thermoluminescence cannot recover very low erosion rates towards the present (supplementary Fig. S16). This can be explained by the very low cooling rates associated with low erosion, which are below the detection limit of thermoluminescence thermochronology with its closure temperatures between 30 and 80 °C (Biswas et al., 2018). In all synthetic tests, the inversions never cause a change in erosion rates that does not exist.
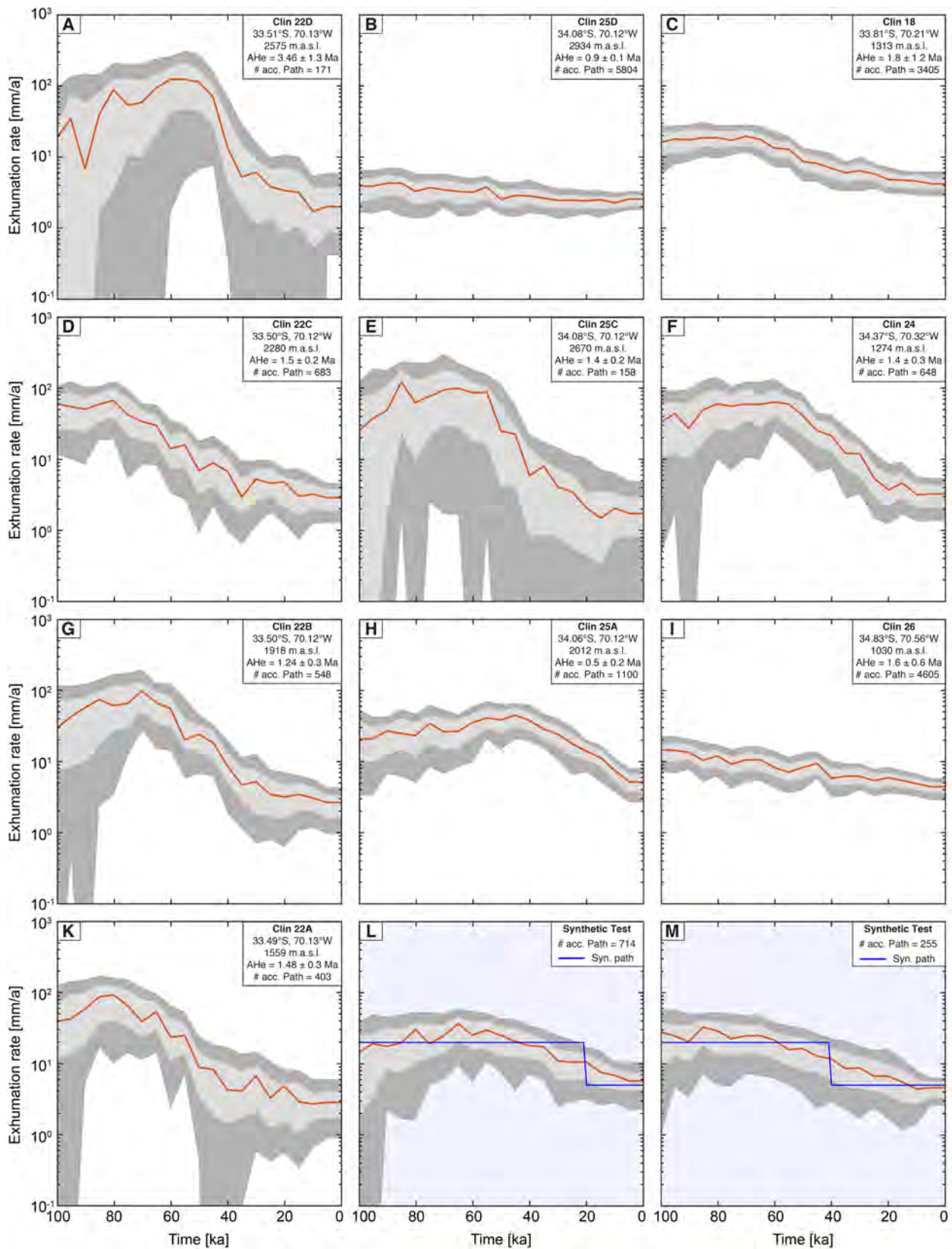
Figure 3.3: Time series of erosion rates. **A-K)** Most samples show a decrease in erosion rates of an order of magnitude. Exceptions are samples (B) Clin25D, which is located above the estimated LGM snowline, (C) Clin18 (cont. on next page)

Figure 3.3: (cont.) which is located very close to the LGM extent, and (I) Clin26 which is the lowest sample and also probably located close to the limit of the LGM extent (Figs. 3.1&3.2). AHe is the corresponding apatite (U-Th)/He age of the same sample (from Stalder et al. (2020)). **L, M)** Synthetic tests for decreasing erosion rates at 20 ka (L) and 40 ka (M) indicate that the method cannot resolve the exact timing of the change in erosion rates.

3.4 Impact of Quaternary glaciations on erosion rates

Debates about the impact of late Cenozoic cooling on erosion has been focused on the difficulty of finding direct observations for (Zhang et al., 2001; Molnar, 2004; Herman et al., 2013; Caves Rugenstein et al., 2019), or against an increase of erosion (Willenbring and von Blanckenburg, 2010; Ganti et al., 2016; Schildgen et al., 2018). Everyone agrees that geomorphic processes must have been transient (e.g., Koppes and Montgomery, 2009; Ganti et al., 2016; Willenbring and Jerolmack, 2016; Herman et al., 2018), but evidence of erosion variability during glacial cycles has been lacking. Here we show that erosion rates can vary by an order of magnitude within a single glacial cycle, and be highest during glacial periods.

Such large variations may have several explanations. First, the characteristic timescale for glacial erosion is comparable to Milankovitch periods, i.e., 23, 41 and 100 kyr, and one may expect to see the largest response to Quaternary glaciations in regions where the uplift rate is moderate (0.3-1 mm/yr) and precipitation is high (Herman et al., 2018). This matches our observations of large changes in erosion rates in the central Chilean Andes, where the uplift rates are likely moderate and precipitation rates were high during glacial periods. Furthermore, our results agree with several studies that have argued that the impact of glaciations on mountain erosion rates is maximized at mid-latitude (Shuster et al., 2005; Haeuselmann et al., 2007; Thomson et al., 2010; Valla et al., 2012; Champagnac et al., 2014), where ice accumulation rates during glacial periods were highest.

Existing studies have argued about the transiency of processes by comparing erosion rates estimated with independent methods and independent timescales (Koppes and Montgomery, 2009; Ganti et al., 2016). In contrast, we report here a time serie of erosion rate that is smoother than the true erosion rate history, but which is unbiased. Time series of erosion or weathering rates also exist in other context and have shown contrasting results. For example, Cogez et al. (2015) used Neodymium isotopes from marine sediment cores to estimate weathering fluxes from the east and west coasts of New Zealand. In the east, where rock uplift and precipitation are moderate, erosion and/or weathering fluxes were 2 to 10 times higher during glacial periods than during interglacial times. On the western side instead, little variation was observed during the last 300 kyr, thus supporting the idea that glacial and fluvial erosion are similar and landscapes quickly reestablish equilibrium after climatic disturbances in regions where both rock-uplift and precipitation rates are sustained. Using ^{10}Be data from a sedimentary section in the North Tianshan Piedmont,

spanning 9 Ma to the present, Charreau et al. (2011) observed that erosion rates peaked with up to 2.5 mm/a between 3 and 1.7 Myr, contemporaneously with the onset of Quaternary ice ages. More recent rates show again values similar to the rates observed before 3 Ma (0.1 to 1 mm/a), indicating that the transient glacial erosion rates could be sustained at timescales longer than the characteristic time of glacial erosion. In areas that did not experience glaciations, [10]Be data from sedimentary archives point towards either higher (Marshall et al., 2017) or lower (Hidy et al., 2014) denudation rates during glacial periods, depending on the environmental conditions. While cold periods may increase periglacial processes such as frost cracking (Marshall et al., 2017), temperature-dependent processes such as chemical weathering, changes in vegetation cover or changes in soil thickness may enhance denudation rates during warm periods (Hidy et al., 2014). Finally, a sediment record from the Bay of Bengal documents an increase in chemical weathering products since the LGM, when weathering fluxes from the Himalaya might have been reduced by 90 % (Lupker et al., 2013), although von Blanckenburg et al. (2015) finds that global silicate weathering fluxes did not change over the Quaternary. Except for the latter study, these studies all imply that erosion rates have remained transient during Quaternary.

To conclude, thermoluminescence thermochronology enables us to directly measure bedrock erosion in a region that experienced a full transition from glacial-humid to fluvial-dry conditions and reconciles measurements made on the short term (10 kyr, [10]Be) with measurements made on the long term (Myr, AHe and AFT dating). The inferred time series of erosion show that erosion was maximized during the LGM and then slowed down, implying that erosion rates remain transient during the Quaternary and that glacial valleys are progressively carved during each glacial cycle. More broadly, our results imply that changes in amplitudes and frequency of climate oscillations during the Quaternary remain a viable mechanism through which erosion rates may have increased during the Quaternary, at least in glaciated areas (Molnar, 2004; Herman et al., 2013).

3.5 Methods

3.5.1 Sampling campaign and sample preparation

We collected 12 granitic bedrocks samples (ca. 10x10x10 cm^3 dimension) in the Chilean Andes (33-35° S). The samples are distributed in the main river valleys (Clin18,24,26) and along two elevation profiles (Clin22A-D and Clin25A-D) that were sampled from valley bottom to mountain peak (Appendix Table B1). The rock samples were prepared under subdued red light conditions (wavelength ~650 nm) to avoid exposure of higher light flux and energy that may reduce the TL signal. For each sample, the outer rim (>1 cm) was removed with a diamond saw to extract the light protected portion, which was then gently crushed with pestle and mortar and sieved to retrieve grain fractions between 150 and 250 µm. The sieved samples were treated with 10% hydrochloric acid and 35% hydrogen peroxide to remove potential carbonates. Magnetic minerals were removed with a strong hand magnet. K-feldspars were separated from quartz and other minerals through density separation using Sodiumpolytungsten (ρ= 2.58 gcm^{-3}), applied to ca. 6 g of the sample material. The K-feldspar grains were finally mounted on stainless steel discs in a diameter of 2 mm, each containing ~100 grains.

3.5.2 Measurements of TL data

Thermoluminescence (TL) thermochronology exploits the thermal dependency of luminescence signals generated by the release of electrons from traps under the stimulation of heat in the laboratory. In nature, ambient radiation from decaying radioactive elements (e.g., U, Th, K) excites electrons in the crystal lattice of feldspars so that they move freely through the crystal lattice until being trapped in trapping centers. These centers are located at different energy levels, which correspond to closure temperatures between 30 and 80 °C (Biswas et al., 2018), and can be exploited as multiple thermochronometer (Brown et al., 2017; Biswas et al., 2018) that record the Quaternary cooling history of rock samples (Herman and King, 2018). This cooling history can be converted into an erosion rate history if the temperature field near the Earth's surface is known (e.g., Reiners and Brandon, 2006).

For each trap depth, the natural TL signal is controlled by the rate of irradiation-induced growth and the rates of thermal and athermal loss, and can be described by a general order kinetic model (Guralnik et al., 2015; Biswas et al., 2018):

$$\frac{\mathrm{d}}{\mathrm{d}t}\left(\bar{n}(r',t)\right) = \underbrace{\frac{\dot{D}}{D_0} * \left(1 - \bar{n}(r',t)\right)^a}_{\text{Growth}} - \underbrace{se^{-\frac{E}{kT}} * \left(\bar{n}(r',t)\right)^b}_{\text{Thermal loss}} - \underbrace{\tilde{s}e^{-\rho'(-\frac{1}{3}r')}\bar{n}(r',t)}_{\text{Athermal fading}} \tag{3.1}$$

where $\bar{n}$ is the ratio of number of trapped electrons (n) at time t and temperature T and the total number of available traps (N), $\dot{D}$ is the dose rate due to ambient radioactivity, D_0 is the onset of dose saturation, a and b are the kinetic orders of trapping and thermal detrapping, respectively, E is the activation energy, s and $\tilde{s}$ are the thermal and athermal frequency factors, and ρ' is the dimensionless recombination center density, which is a measure for athermal fading and depends on the distance r' between a trapped electron and its nearest hole (Huntley, 2006). For each sample, these kinetic parameters are individually estimated for each trapping depth, or TL signals, during three experiments. Details of the model and procedures to constrain the kinetic parameters are described in Biswas et al. (2018) and shortly outlined below. The validity of the model was tested on KTB borehole samples for optical luminescence of feldspar (Guralnik et al., 2015) and TL of feldspar (Biswas et al., 2018).

All TL measurements were carried out at the University of Lausanne on a Risø TL/OSL reader (TL/OSL-DA-20; Bøtter-Jensen et al., 2010) equipped with a $^{90}Sr/^{90}Y$ irradiation source (~0.2 Gy/s). Linear heating was conducted with a rate of 1 °C/s under inert atmospheric conditions (N$_2$ gas). Luminescence was measured in the violet-blue emission bands with an EMI9235QA photomultiplier and using a combination of BG3 and BG39 filters.

3.5.2.1 Growth parameters

We use the single aliquot regeneration protocol (SAR; Murray and Wintle, 2000) on three aliquots per sample to measure the natural TL signal, $\bar{n}$, and to extract growth parameters, i.e., the onset of dose saturation, D_0, and the kinetic orders of trapping, a. The aliquots underwent several cycles of regeneration doses and measurements of TL to constrain individual regenerative dose response curves for each of the seven TL signals (250-320 °C, with 10 °C interval) or thermochronometers used in this study. For each cycle, we applied a preheat of 200 °C to remove unstable, shallowly trapped electrons (residence times at room temperature of <ka) and used a post glow TL for a fixed test dose (50 Gy) to correct changes in TL sensitivity. Regeneration doses of 0, 24, 48, 120, 240, 480, 960, 1910, and 3820 Gy were given for all samples except for Clin25A that was measured on a different Risø-reader with regeneration doses of 0, 24, 60, 120, 240, 470, 950, 1890, and 3780 Gy. Note that for Clin25A, one of the three disk was discarded because grains on it were lost during measurement. To test recuperation and luminescence signal recycling, we additionally applied a dose of 0 Gy and repeated one regeneration point of 24 Gy, respectively. A recycling of ±20% was tolerated. D_0, a and $\bar{n}$ were estimated from these regenerative dose response curves after correction for athermal fading during laboratory irradiation (Biswas et al., 2018). The kinetic order of trapping, a, determines the shape of the growth curve and is constrained between 1 and 2 (Biswas et al., 2018). The natural TL level, $\bar{n}_{obs}$, is finally derived from the dose response curve,

which is normalized by the maximum (saturated) intensity equal to 1. The results are listed in Appendix, Table B2 and illustrated in supplementary Figures S1 and S2.

Another growth parameter, the environmental dose rate $\dot{D}$, must be estimated for each sample to assess the amount of ambient radiation in the feldspar crystals. Bulk samples were crushed to powder and sent to the ACT-lab in Ontario, Canada to estimate the concentrations of the radioactive elements U, Th, K and Rb using inductively coupled mass spectrometer (Appendix, Table B3). The environmental dose rates were calculated with DRAC, v. 1.2 (Durcan et al., 2015), taking into account α-, β- and γ-radiation from radioelements and contribution from cosmic rays. The grain size distributions of K-feldspars were estimated in thin sections under the microscope, using a lower limit of 150 μm (min. sieving size) and an upper limit of 1000 μm (crystals bigger than 1000 μm were carefully removed during the sieving procedure) (Appendix, Table B1). We assumed a water content of 2±2%, internal K of 12.5±0.5% and a burial depth of 0.1±0.05 m. The α-efficiency factor was considered to be 0.15±0.05, assuming that alpha efficiencies of TL and IRSL are similar (Biswas et al., 2013; Kreutzer et al., 2014; Biswas et al., 2018).

3.5.2.2 Thermal decay parameters

Thermal decay parameters, i.e. the activation energy E, frequency factor s, and kinetic order of detrapping b, were estimated for each TL signal using the T_m-T_{stop} experiment (McKeever, 1980). In this experiment, fractional growth curves (0-450 °C) are generated by measuring the TL signal after applying a dose rate of 75 Gy and heating to T_{stop}, which was varied from 50 to 430 °C in 5 °C intervals. Every fractional growth curve was normalized by an arbitrarily chosen test dose (15 Gy) to account for changes in the luminescence signal sensitivity. The subtraction between two consecutive fractional glow curves provides a number of subpeaks. Each subpeak can be considered as TL glow with a single activation energy (Pagonis et al., 2014; Biswas et al., 2018). All subpeaks were fitted with the general order TL glow curve equation from which the distribution of the kinematic parameters E, b and s were evaluated (Biswas et al., 2018). These distributions finally allowed to extract mean values for each TL thermochronometers (Biswas et al., 2018) (supplementary Figs. S3,S4&S5).
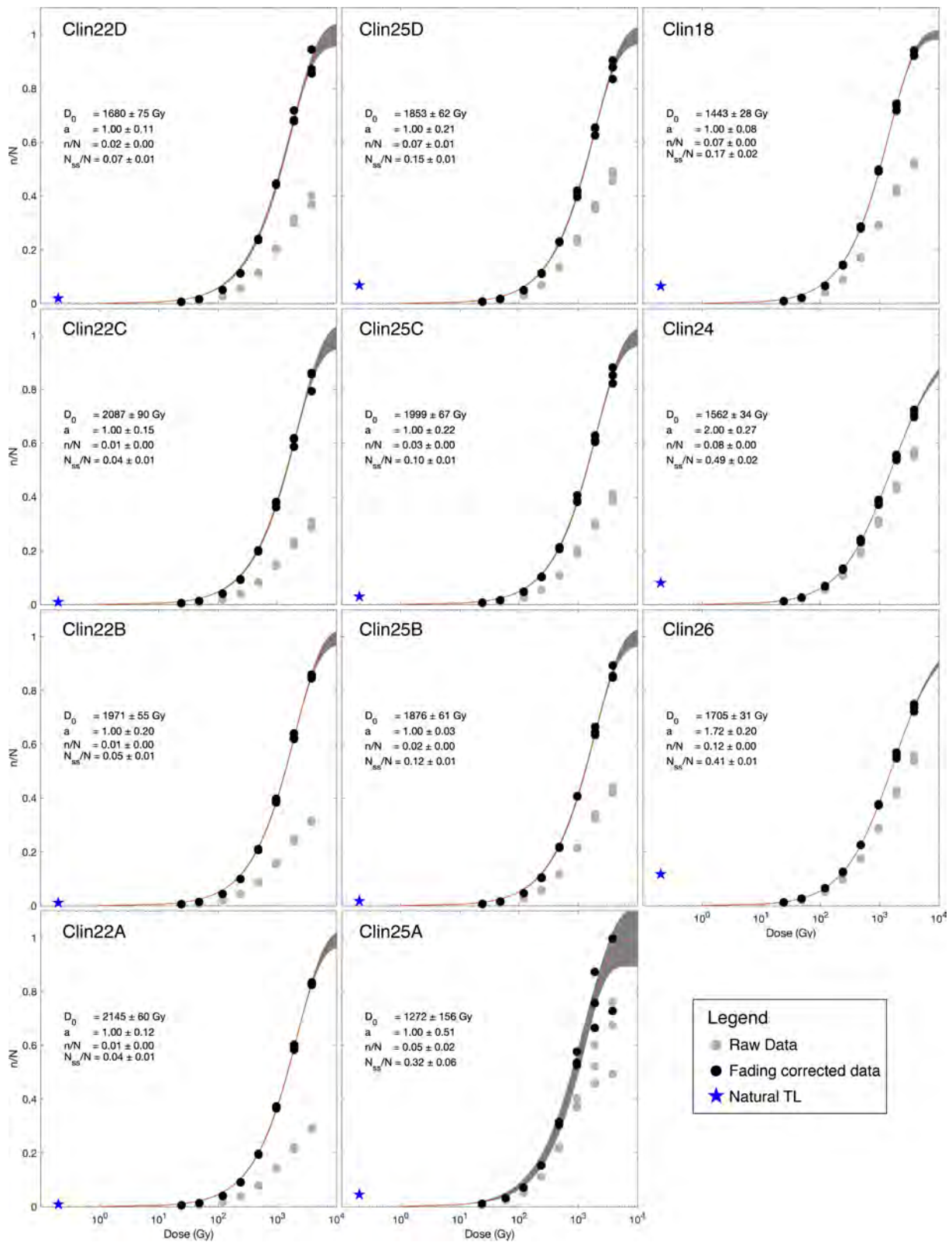
Figure S1: Regenerative dose response curve for the first signal (temperature range = 250-260 °C). Black dots represent athermal fading-corrected data of the measurements (grey dots) and were used for fitting of the data (red line). Blue star is the normalized natural luminescence signal.
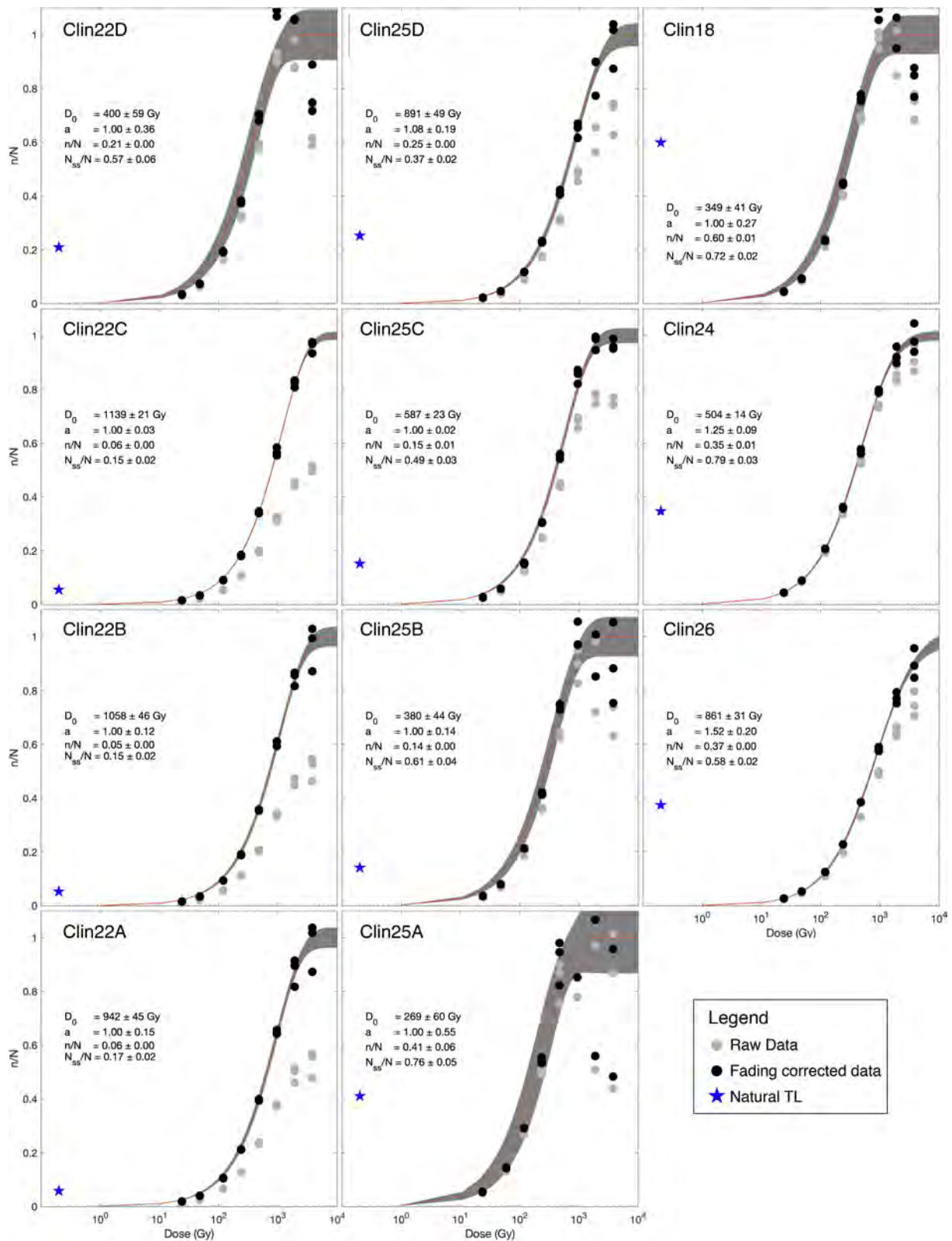
Figure S2: Regenerative dose response curve for the last signal (temperature range = 310-320 °C). Black dots represent athermal fading-corrected data of the measurements (grey dots) and were used for fitting of the data (red line). Blue star is the normalized natural luminescence signal.
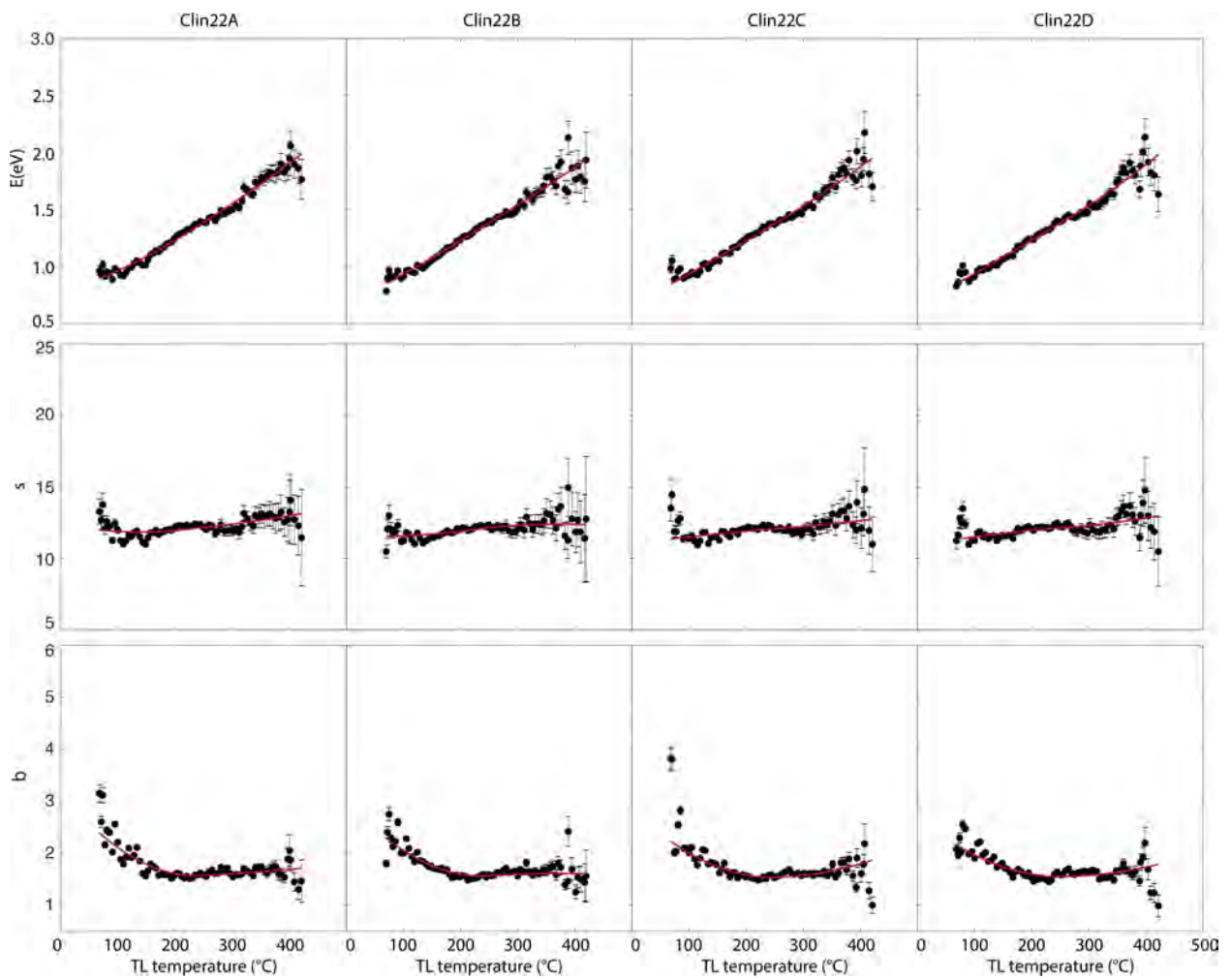
Figure S3: Distribution of kinetic parameters for thermal loss, samples Clin22A-D. Red line shows fitting of the data.
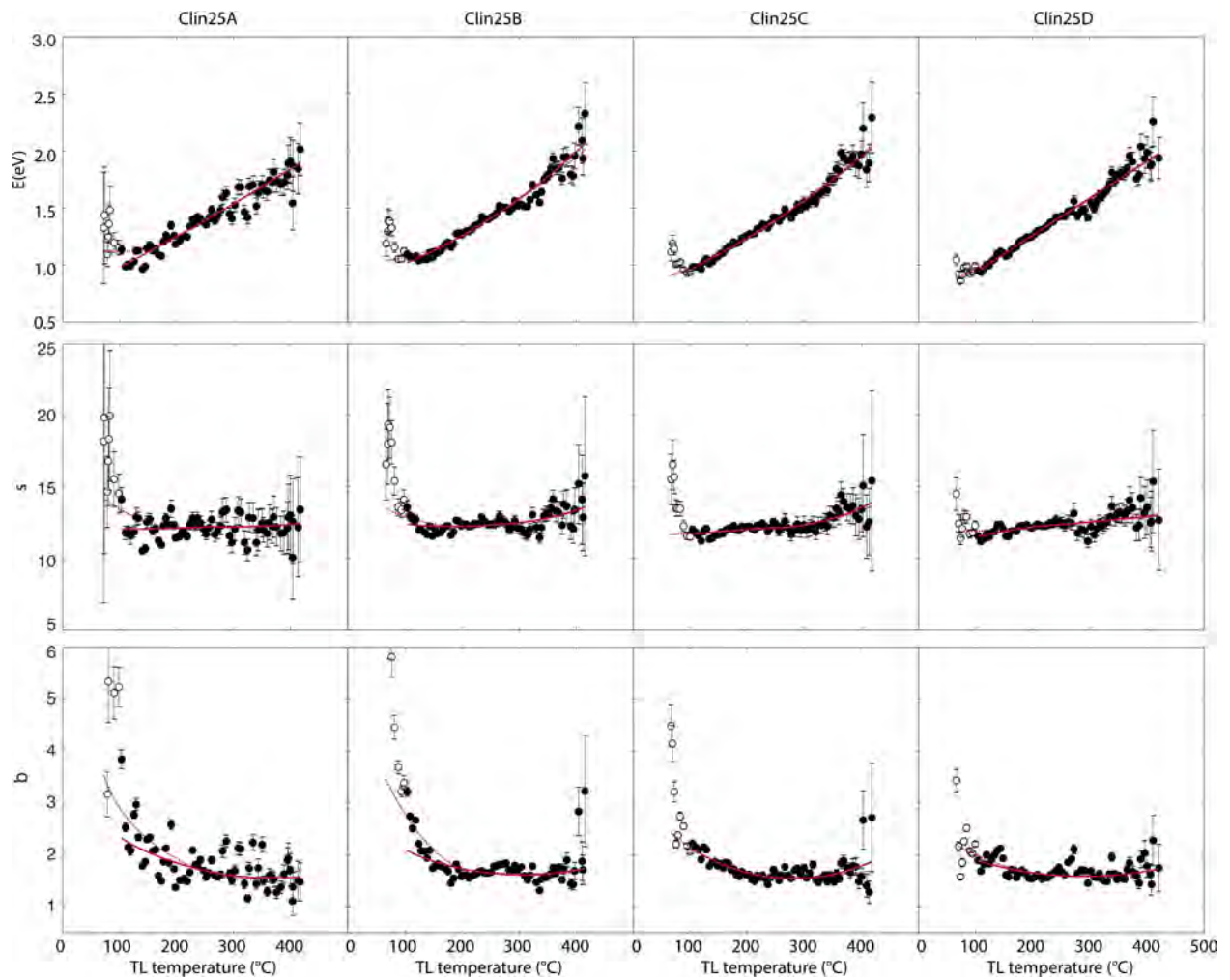
Figure S4: Distribution of kinetic parameters for thermal loss, samples Clin25A-D. Red line shows fitting of the data, under exclusion of measurements at temperatures <100 °C (open circles) that deviate from the general trend (black circles), and was used for estimation of kinetic parameters. Stippled red line represents fitting of all data points.
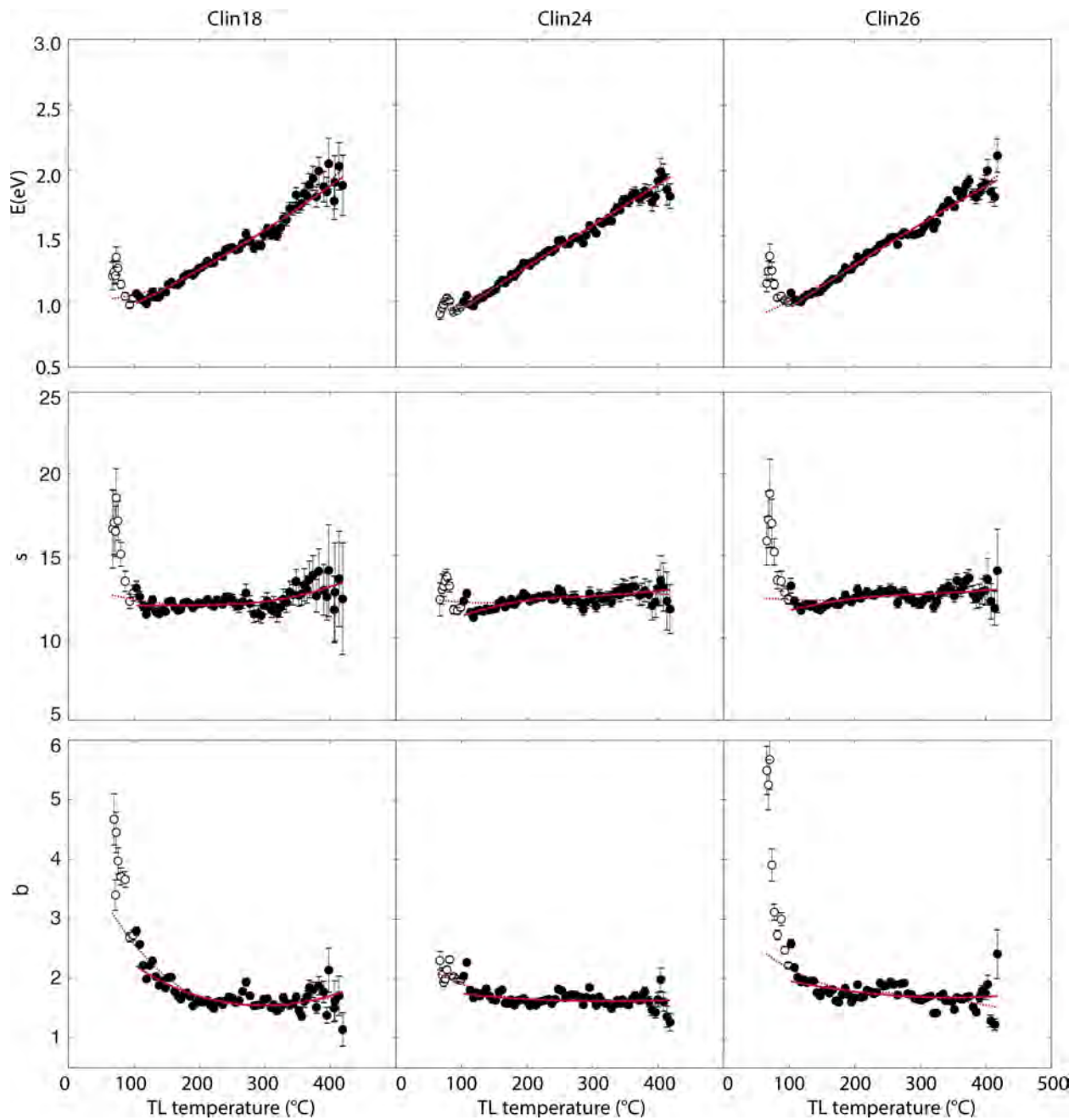
Figure S5: Distribution of kinetic parameters for thermal loss, samples Clin18,24&26. Red line shows fitting of the data, under exclusion of measurements at temperatures <100 °C (open circles) that deviate from the general trend (black circles), and was used for estimation of kinetic parameters. Stippled red line represents fitting of all data points.

3.5.2.3 Athermal decay parameters

Athermal fading (Wintle, 1973) was measured for different delay times ranging from minutes to months after applying an irradiation dose of 75 Gy. Three discs were repeatedly used for the measurement. Similar to the experiments described above, a cut-off heat of 200 °C was used in between irradiation and delay time measurements to remove shallowly trapped electrons. Each signal was normalized by a test dose of 25 Gy. The athermal fading parameter ρ' (Huntley, 2006) were finally determined by fitting the measured data as described in Biswas et al. (2018). ρ' parameters of the different thermochronometers are listed in Appendix, Table B2 and illustrated in supplementary Figures S6&S7.

3.5.2.4 Evidence of thermal loss

Because the number of electron traps in feldspar is finite, samples from slowly eroding areas can reach an equilibrium state where signal growth equals athermal decay. In this case, no thermal history can be extracted. In the absence of thermal loss, the maximum possible luminescence level, taking athermal fading into account, is called the field saturation $\bar{N}_{ss}$ (Kars et al., 2008) and can be theoretically obtained by equating the rate of growth and the rate of athermal decay (Eq. 3.1). Thermal loss is the difference between $\bar{N}_{ss}$ and $\bar{n}_{obs}$. Since none of our samples reach the saturation limit (supplementary Fig. S8), they can be used to extract erosion histories.
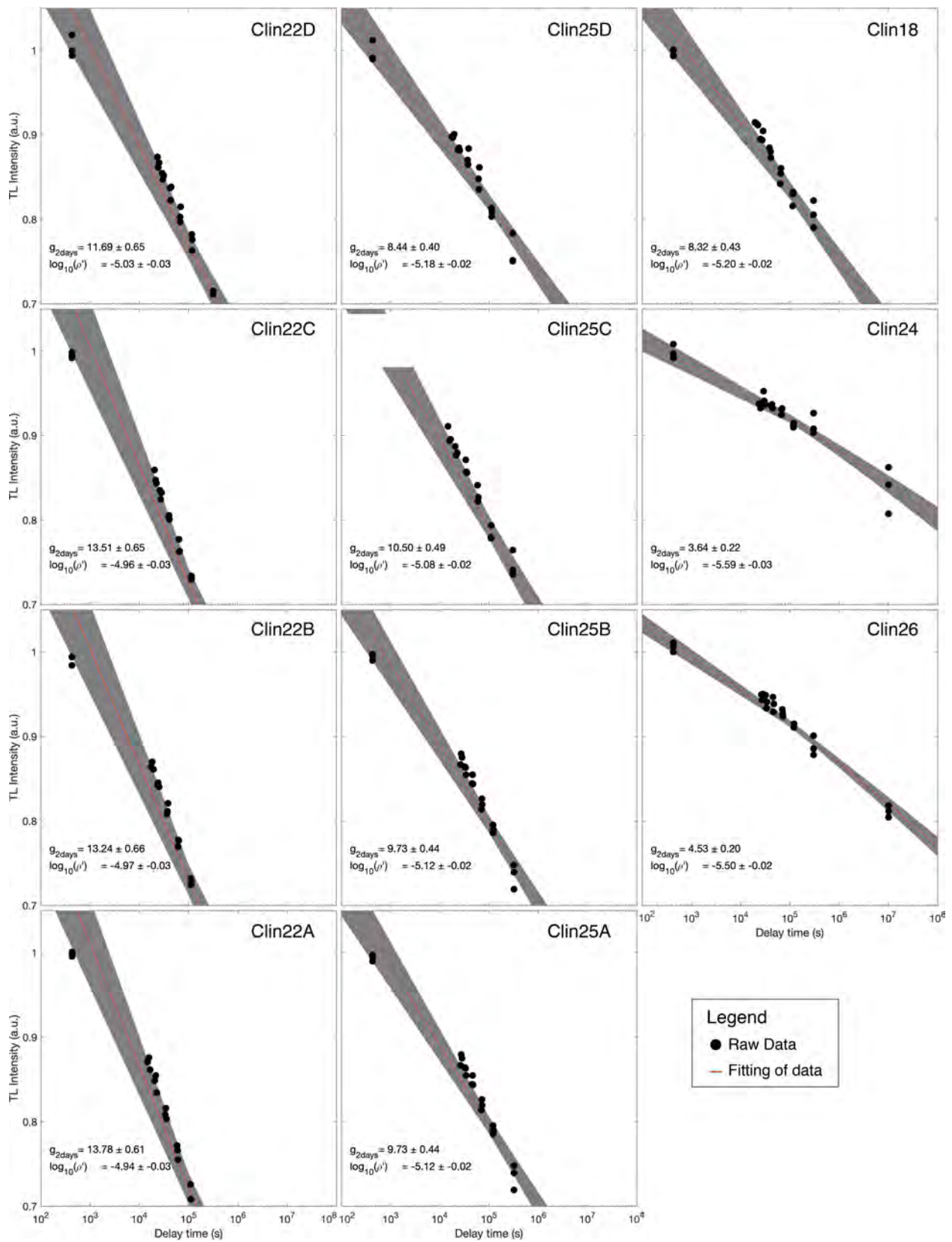
Figure S6: Athermal fading measurements and fit of the data for the first signal (temperature range = 250-260 °C).
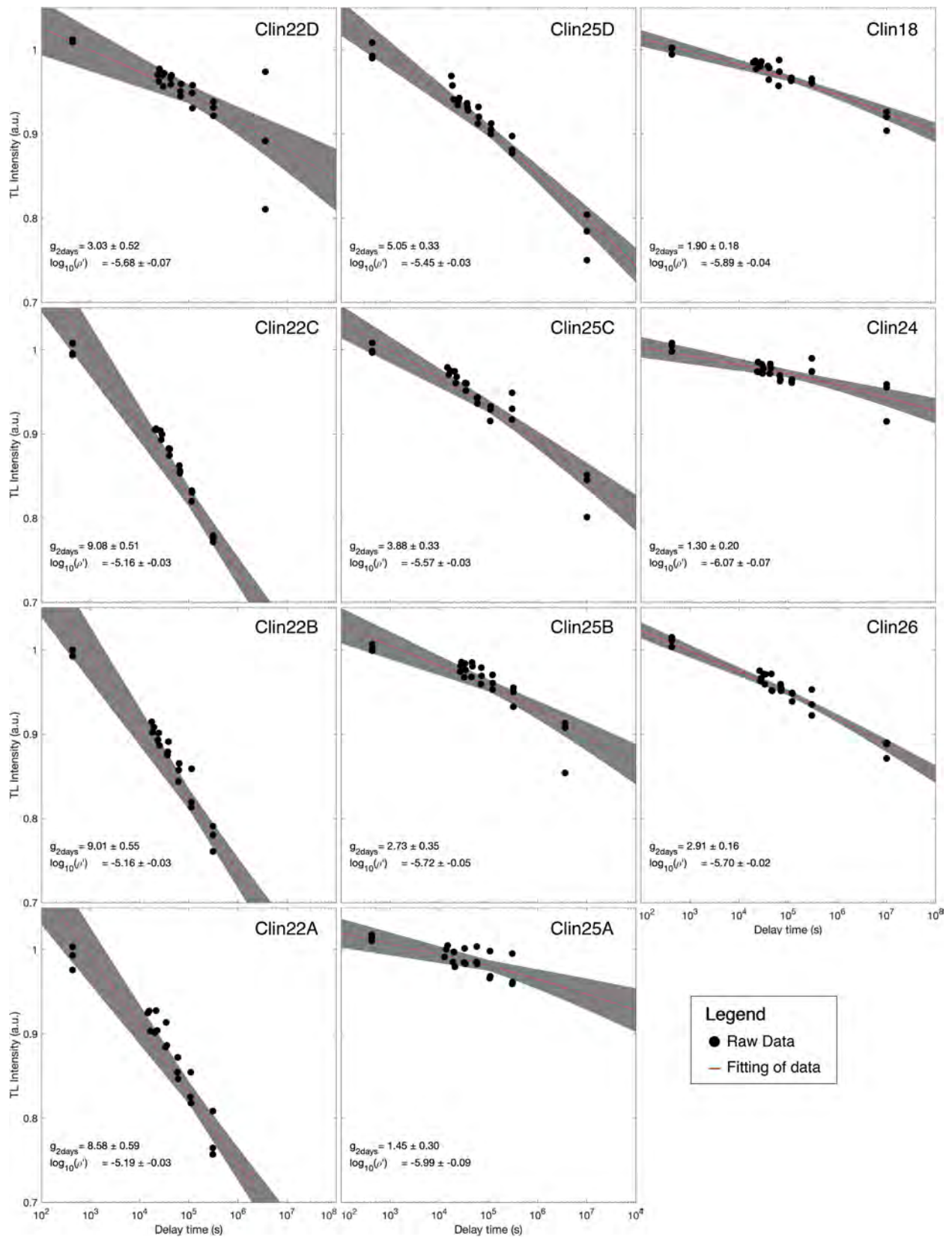
Figure S7: Athermal fading measurements and fit of the data for the last signal (temperature range = 310-320 °C).
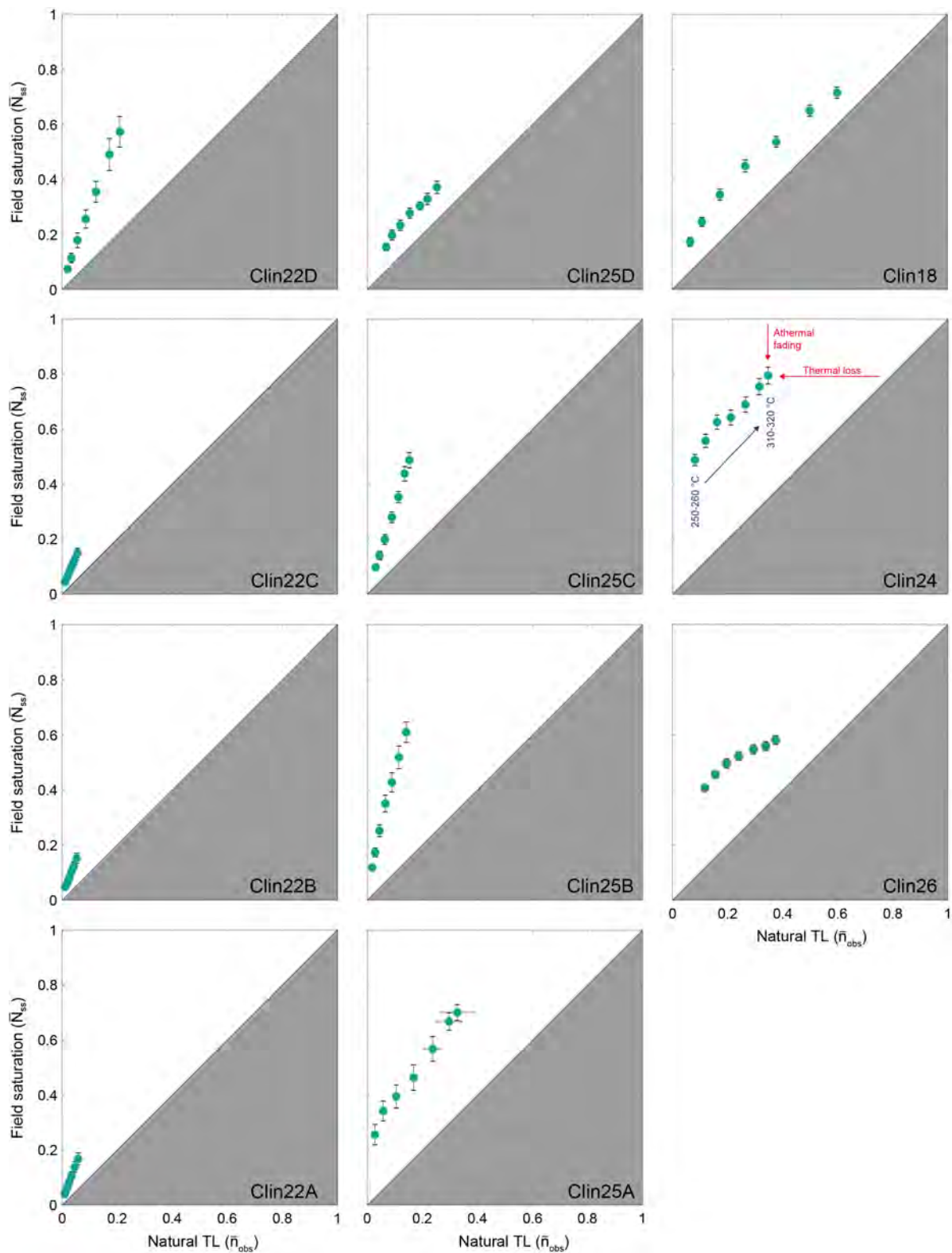
Figure S8: Field saturation ($\bar{N}_{ss}$) versus natural TL signals ($\bar{n}$) for the 250 to 320 °C temperature intervals. The grey triangle represents the zone of saturation. All samples plot in the white areas, indicating thermal loss, and can be used to model erosion rates. Samples Clin22A-C show very high athermal fading and are therefore highly dependent on the assumption of the fading-correction model.

3.5.3 Inversion of TL-signals

We use the inversion algorithm developed in Biswas et al. (2018) with some refinements to extract erosion histories of the collected samples. We also investigate the sensitivity and limitation of the method by providing 12 synthetic tests in which we prescribe decreasing, increasing and oscillating exhumation rates. The inverse model solves the 1D heat transfer equation for diffusion and advection:

$$\frac{\partial T}{\partial t} = \underbrace{\kappa \frac{\mathrm{d}^2 T}{\mathrm{d}z^2}}_{\text{Diffusion}} + \underbrace{\dot{e}(t) \frac{\mathrm{d}T}{\mathrm{d}z}}_{\text{advection}} \tag{3.2}$$

where κ is the thermal diffusivity (30 km^2/Ma), T is the temperature, z is the depth, and $\dot{e}$ is the time-dependent exhumation rate. For each inversion, we randomly generate a large number of monotonically decreasing time-depth paths (tZ-paths; 75'000 for synthetic tests; 100'000 for samples) for which we individually solve the heat transfer equation (Eq. 3.2), recording temperature at any depth in time. For each path, the present-day TL signal is predicted ($\bar{n}_{pred}$) using Equation 3.1 and compared to the observed natural signals ($\bar{n}_{obs}$) using a logarithmic misfit function (Wheelock et al., 2015, Eq. 7):

$$misfit = \frac{1}{l} * \sum_{i=1}^{l} \left(\frac{1}{2} \frac{(\bar{n}_{obs})_i}{\sigma_i} * \log \left(\frac{(\bar{n}_{obs})_i}{(\bar{n}_{pred})_i} \right) \right)^2 \tag{3.3}$$

where l is the number of signals (here l = 7), and σ_i is the error on the observed TL signals ($\bar{n}_{obs}$).

The best fitting paths (i.e., lowest misfit) are selected if their normalized likelihood, expressed as $exp(-misfit)$, are higher than a random number R:

$$\frac{likelihood}{max(likelihood)} > R, \quad R \, \epsilon \, [0, 1] \tag{3.4}$$

To calculate the probability distribution, median and 95%- and 68%- confidence intervals, the time-depth space (6-0 Ma; 10-0 km) is divided into a 1200 x 1200 grid and the number of accepted tZ-paths passing through each cell is summed. The erosion rate is finally calculated by taking the time derivative of the median in the tZ-space. The 95%- and 68% confidence intervals of erosion rates are estimated by Monte-Carlo resampling of the tZ-median (resampling 10% of accepted paths for 200 times).

Erosion rates and the geothermal field are strongly coupled. Because the advection of heat associated with exhumation increases the geothermal gradient with time, geothermal gradients at

the end of the model (G_{final} at t = 0) will be higher than at the beginning (G_{ini} at t = 6 Ma). A higher geothermal gradient leads to lower erosion rates because closure depths are shallower, and vice versa. Higher erosion rates, in turn, increase the geothermal gradient because heat is more efficiently transported towards the surface. The inversion results are thus highly sensitive to our choice of the initial geothermal gradient, G_{ini}. Heat flow measurements allowing the estimation of modern geothermal gradients are very sparse in central Chile and can show significant temporal and spatial variations (Springer and Förster, 1998; Hamza and Muñoz, 1996; Hamza et al., 2005). Three heat flow measurements are located close to our study area and document values of 61 mW/m² (33.47° S, 70.17° W), 63 mW/m² (33.25° S, 68.75° W) and 79 mW/m² (33.34° S, 70.75° W), with inferred geothermal gradients of 16, 29 and 29 °C/km, respectively (Uyeda and Watanabe (1982), data downloaded from IHFC (2011)). Because the final geothermal gradient, G_{final}, of each accepted path from the inverse model should be comparable to observed geothermal gradients, we resample the accepted solutions to exclude solutions with unrealistically high G_{final}'s as detailed below.

We explore the effect of the geothermal gradient on the erosion history for sample Clin24 by comparing inverse model results achieved with G_{ini}'s of 5, 10, 20 and 30 °C/km (supplementary Fig. S9). Since most accepted solutions of the inversion with a G_{ini} of 30 °C/km yield G_{final}'s exceeding 60 °C/km (supplementary Fig. S9D), we use a threshold of 80 °C/km for G_{final} to allow comparison with the other inversions. All four cases show a similar pattern of the erosion rate history but differ in magnitude. Modelled rates drop from rates exceeding 10 mm/a to rates below 10 mm/a between 60 and 40 ka. The inversion with a G_{ini} of 5 °C/km shows highest erosion rates, exceeding 50 mm/a (supplementary Fig. S9A). This inversion also shows highest misfits, especially for the three deepest TL-signals, and thus has the smallest number of accepted paths. The inversion with a G_{ini} of 30 °C/km, and lowest erosion rates, fits better the data but most solutions show unrealistically high G_{final}'s that exceed 60 °C/km (supplementary Fig. S9D). We prefer the inversion with a G_{ini} of 10 °C/km because the fit of the data is good and the G_{final}'s are closest to the modern observations of 30 °C/km (supplementary Fig. S9B). Therefore, to obtain solutions with G_{final}'s clustering around 30 to 40 °C/km, we use an initial geothermal gradient (G_{ini}) of 10 °C/km for all our samples (supplementary Figs. S10,S11&S12). Because the final geothermal gradient is not known with confidence, accepted paths are resampled for G_{final} smaller or equal to 60 °C/km to avoid including solutions with unrealistically high gradients.
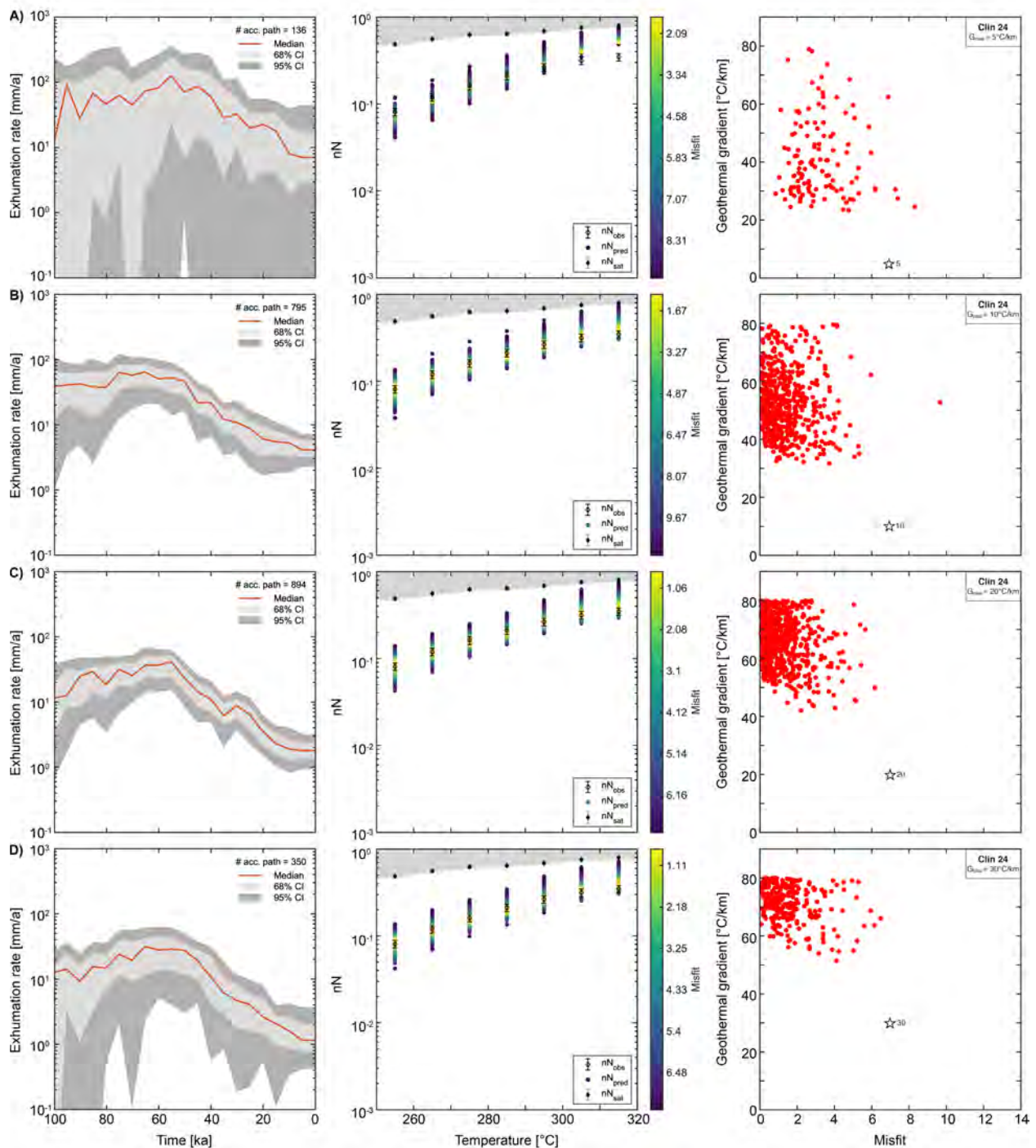
Figure S9: Modelling results of Clin24 showing the influence of the initial geothermal gradient on the erosion rate. Left column shows the erosion rate, i.e., the time derivative of the median in the tZ-space (red line), and Monte-Carlo resampled confidence intervals of the accepted paths (# acc. path). Middle column shows the observed and modelled TL signals of the accepted paths. The grey zone shows the zone of saturation (see supplementary Fig. S8). Right column shows the final geothermal gradients (red dots) of accepted solutions. Initial geothermal gradients are shown as open black stars.
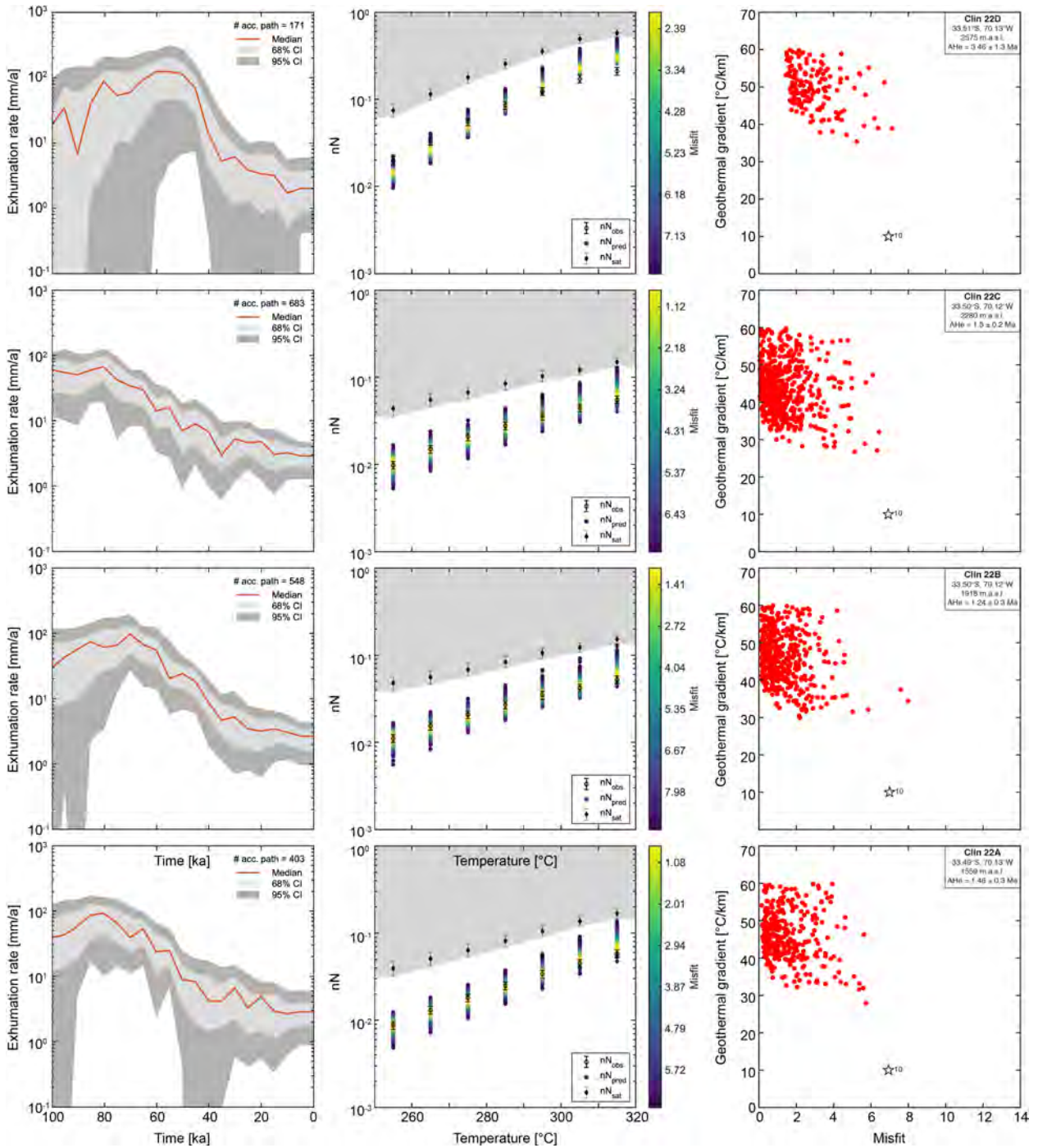
Figure S10: Modelling results for Clin22A-D. Left column shows the erosion rate, i.e., the time derivative of the median in the tZ-space (red line), and Monte-Carlo resampled confidence intervals of the accepted paths (# acc. path). Middle column shows the observed and modelled TL signals of the accepted paths. Right column shows the initial (10 °C/km, open star) and final geothermal gradients (red dots) of the accepted solutions. Only paths with final geothermal gradients <60 °C/km are accepted. Please note that samples Clin22A-C show very high fading (see supplementary Fig. S8), which makes them highly dependent on the assumptions behind the fading correction model. These samples are thus less reliable when extracting thermal histories.
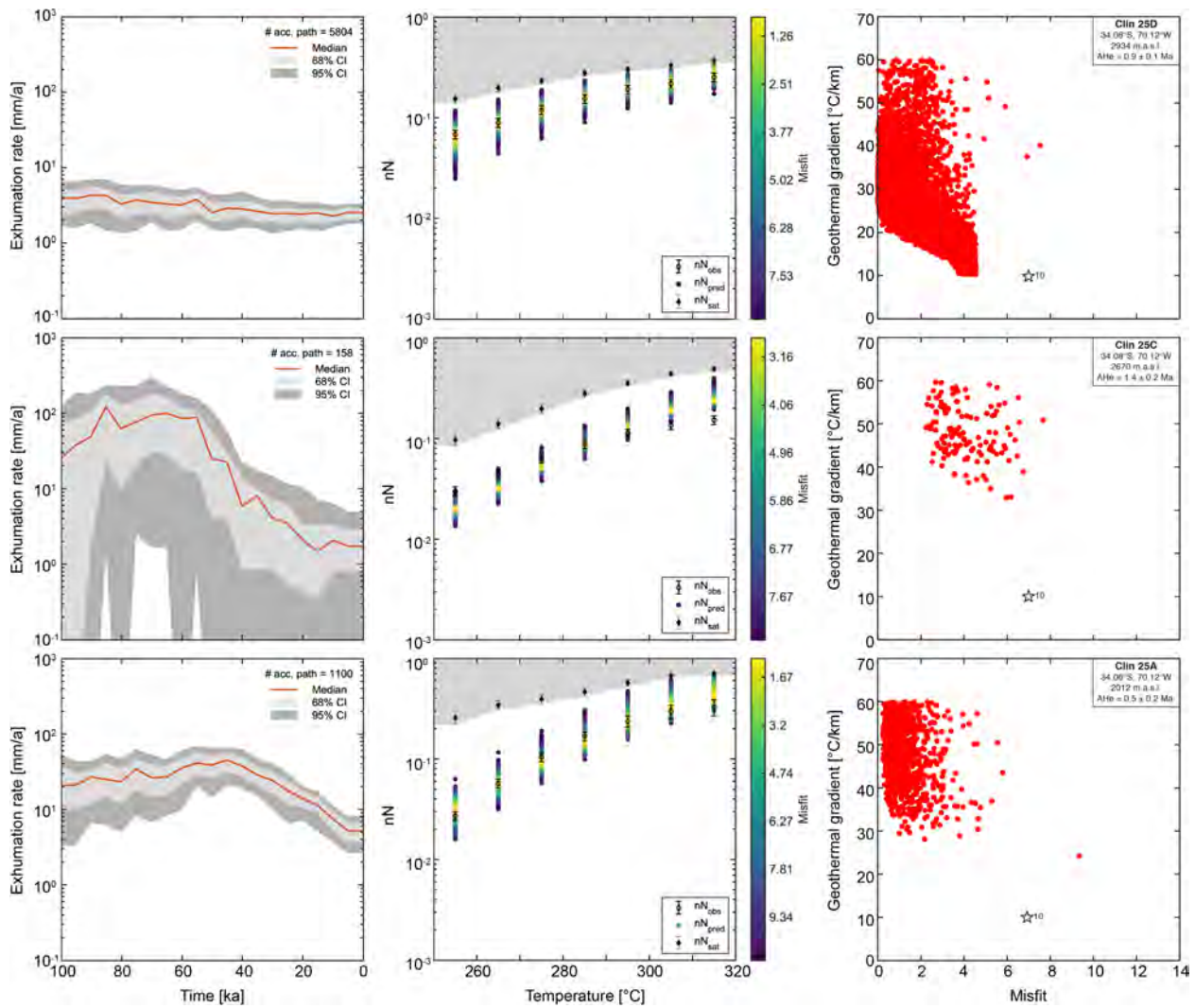
Figure S11: Modelling results for Clin25A,C&D. Left column shows the erosion rate, i.e., the time derivative of the median in the tZ-space (red line), and Monte-Carlo resampled confidence intervals of the accepted paths (# acc. path). Middle column shows the observed and modelled TL signals of the accepted paths. Right column shows the initial (10 °C/km, open star) and final geothermal gradients (red dots) of the accepted solutions. Only paths with final geothermal gradients <60 °C/km are accepted. Data of Clin25B could not be fitted with confidence and is therefore not shown.
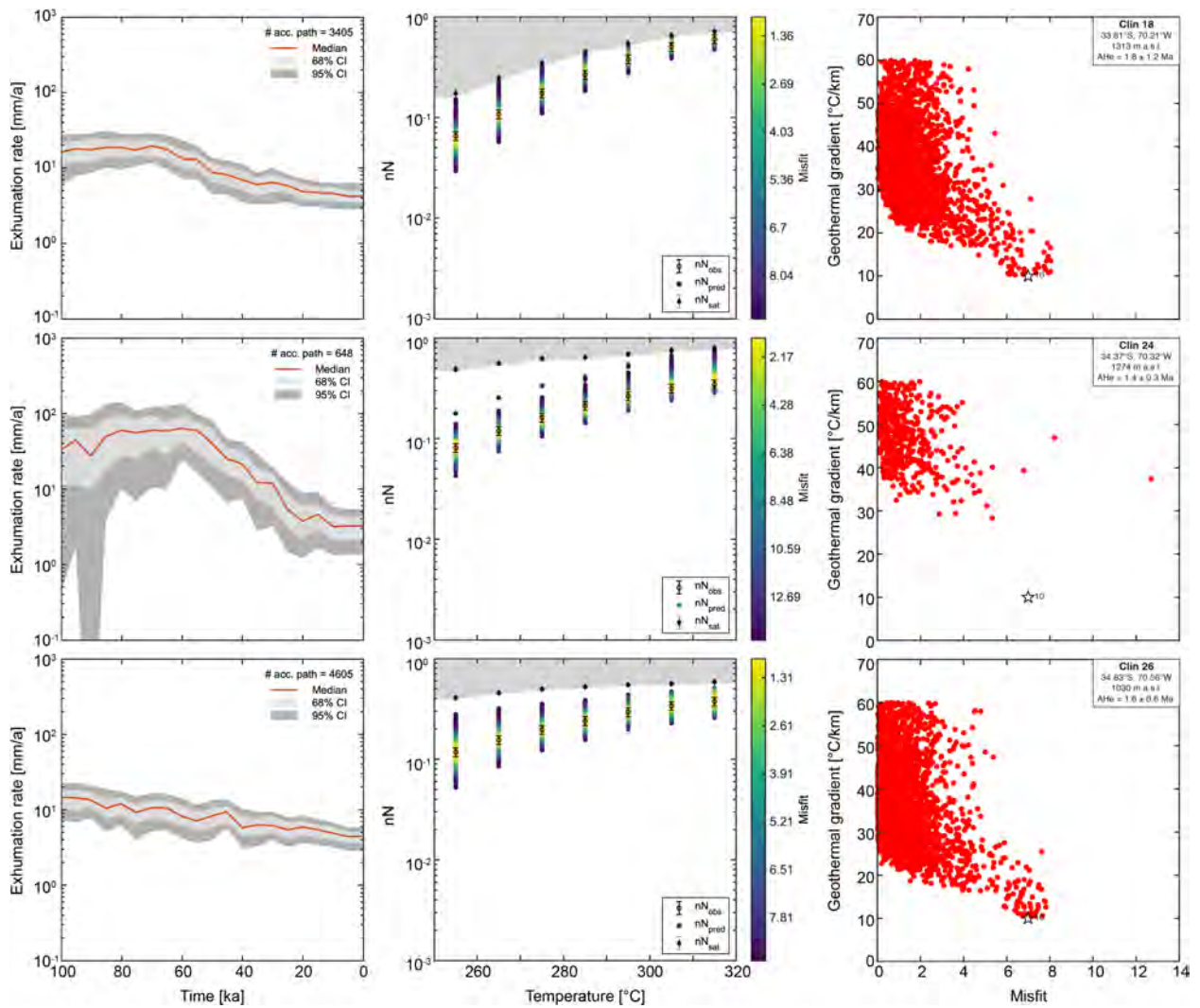
Figure S12: Modelling results for samples Clin18, 24 & 26. Left column shows the erosion rate, i.e., the time derivative of the median in the tZ-space (red line), and Monte-Carlo resampled confidence intervals of the accepted paths (# acc. path). Middle column shows the observed and modelled TL signals of the accepted paths. Right column shows the initial (10 °C/km, open star) and final geothermal gradients (red dots) of the accepted solutions. Only solutions with final geothermal gradients <60 °C/km are accepted.

To better understand the sensitivity and limitations of TL thermoluminescence to predict erosion rate histories, we use a forward model to generate synthetic TL data for given erosion rate histories that we try to recover using our inverse model. For these synthetic tests, we employ the kinetic parameters of Clin24 (Appendix, Table B2) and we tune G_{ini} to get a G_{final} of 30 °C/km or 45 °C/km (for scenarios with very high erosion rates) at the end of the forward model. Accepted paths are resampled for solutions yielding G_{final}'s smaller than 45 °C/km or 60 °C/km, respectively. We test for step-function decreases and increases in erosion rates, with the change occurring at 20 ka (supplementary Figs. S13&S15), and for oscillating rates that peak at 120 ka and 20 ka (supplementary Fig. S14). The magnitudes of the erosion rates vary by a factor of min. 2 and max. 20. Erosion rates before 240 ka are constant and adjusted so that the rock starts at a depth of 10 km at 6 Ma. Because TL is sensitive only to low temperatures between 30 and 80 °C, the erosion rate history before ~200 ka does not affect the TL signals. The inversion results with modelled erosion rates, predicted and observed present-day TL data and G_{final}'s of the accepted paths are depicted in supplementary Figures S13,S14&S15.

The erosion rate histories of the decreasing and cyclic scenarios are generally well recovered if the maximum erosion rate is high (Fig. S13C-E and Fig. S14C-E), but the decrease is smoother and occurs earlier, around 30 to 40 ka. On the contrary, models with low erosion rates are not well reproduced and erosion rates remain constant (supplementary Fig. S13A&B, Fig. S14A&B). Furthermore, our method does not resolve increases in erosion rates (supplementary Fig. S15) with the given synthetic scenarios. Better results can be obtained by choosing a higher initial geothermal gradient (Biswas et al., 2018) or by using higher erosion rates (e.g., supplementary Fig. S15E). TL thermochronometry can thus be used to predict changes in erosion rates in rapidly eroding areas or regions with high geothermal gradients (King et al., 2016). The lack of prediction in slowly eroding areas is due to the fact that temperature differences are too small to be detected by TL thermoluminescence, which has closure temperatures between 80 and 30 °C. For instance, assuming a geothermal gradient of 30 °C/km, an erosion rate of 10 mm/a during the last 20 ka corresponds to only 6 °C of cooling over a temperature range that is lower than the lowest closure temperature of 30 °C.
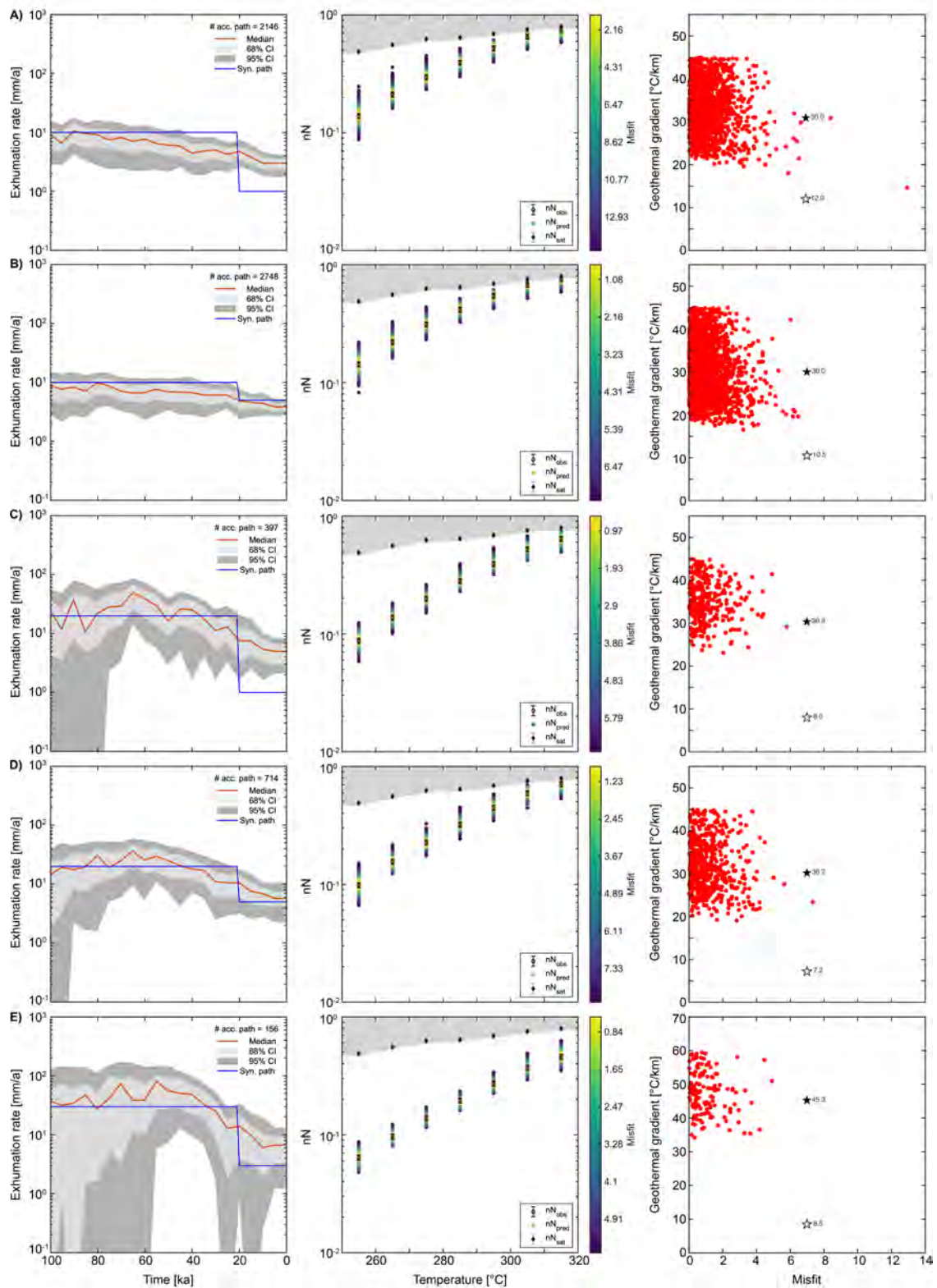
Figure S13: Modelling results for synthetic tests with step-function decreases in erosion rates in the last 20 ka. Synthetic data are generated using forward models with prescribed tT-paths representing the step-function decreases in erosion rates (blue lines). Only solutions with final geothermal gradients <45 °C **(A-D)** or <60 °C/km **(E)** are accepted. See Figure S9 caption for additional description.
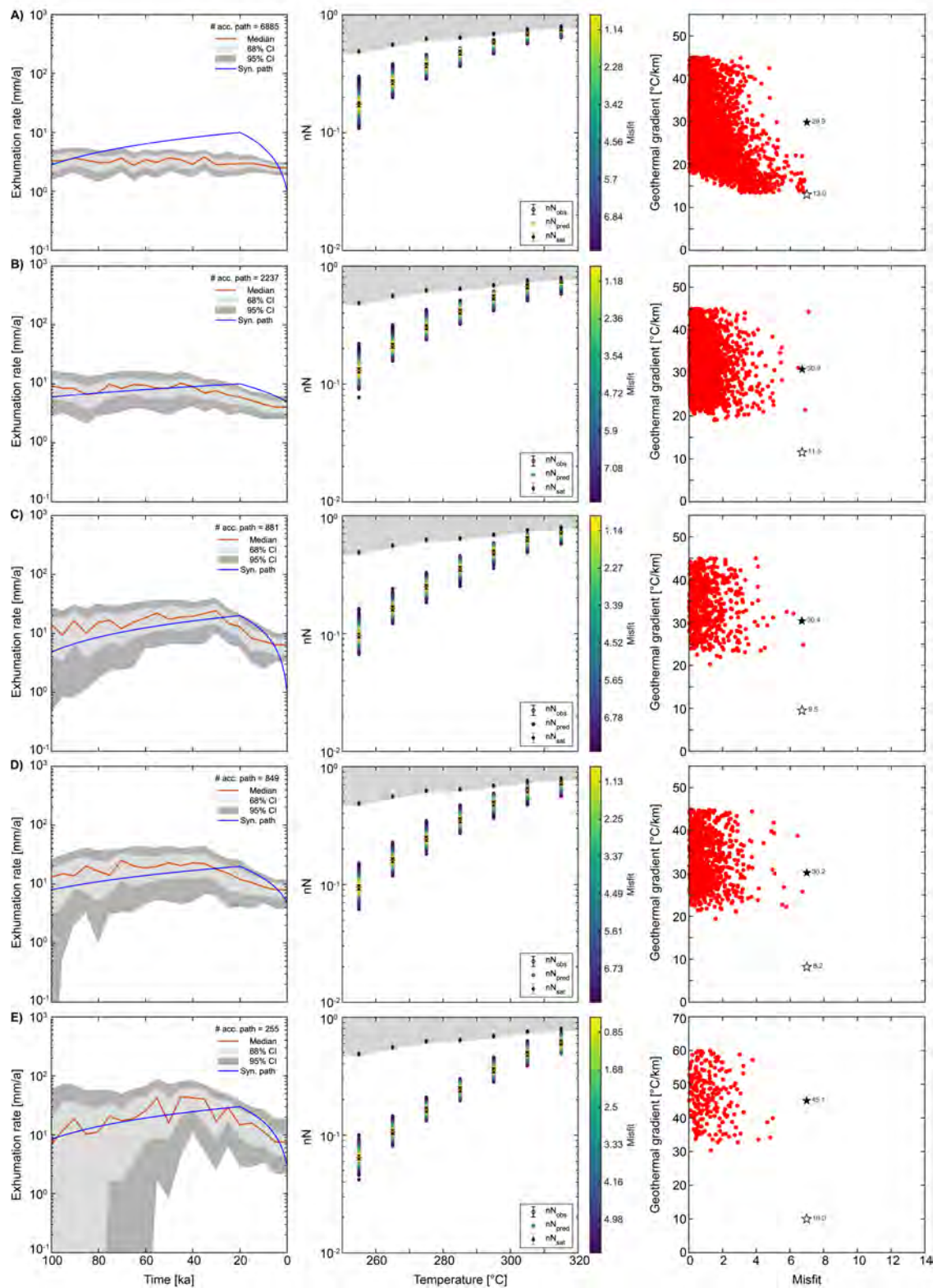
Figure S14: Modelling results for synthetic tests with erosion rates showing cyclic variations. Synthetic data are generated using forward models with prescribed tT-paths representing oscillating erosion rates (blue lines). Only solutions with final geothermal gradients <45 °C **(A-D)** or <60 °C/km **(E)** are accepted. See Figure S9 caption for additional description.
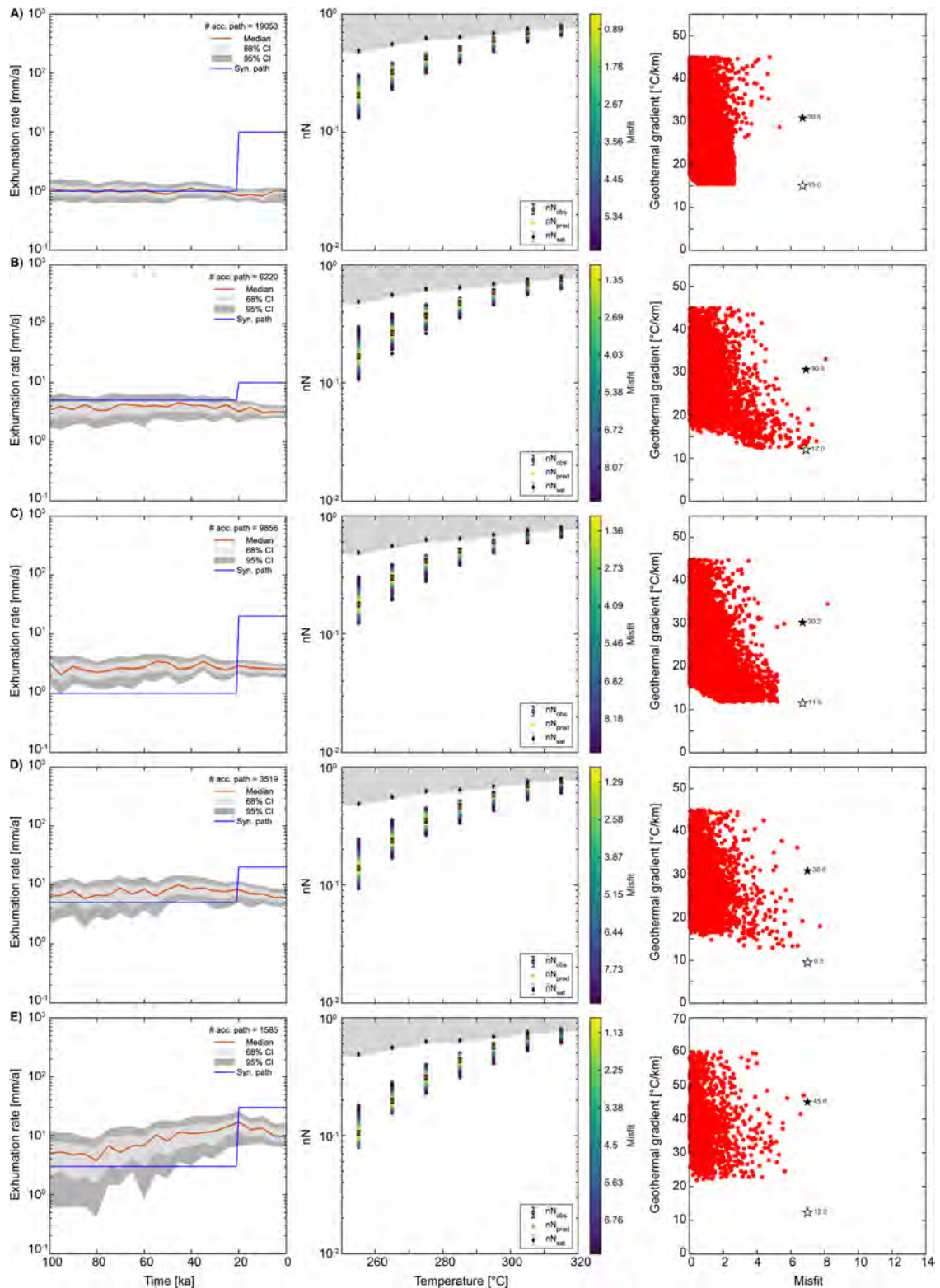
Figure S15: Modelling results for synthetic tests with step-function increases in erosion rates in the last 20 ka. Synthetic data are generated using forward models with prescribed tT-paths representing step-function increases in erosion rates (blue lines). Only solutions with final geothermal gradients <45 °C **(A-D)** or <60 °C/km **(E)** are accepted. See Figure S9 caption for additional description.
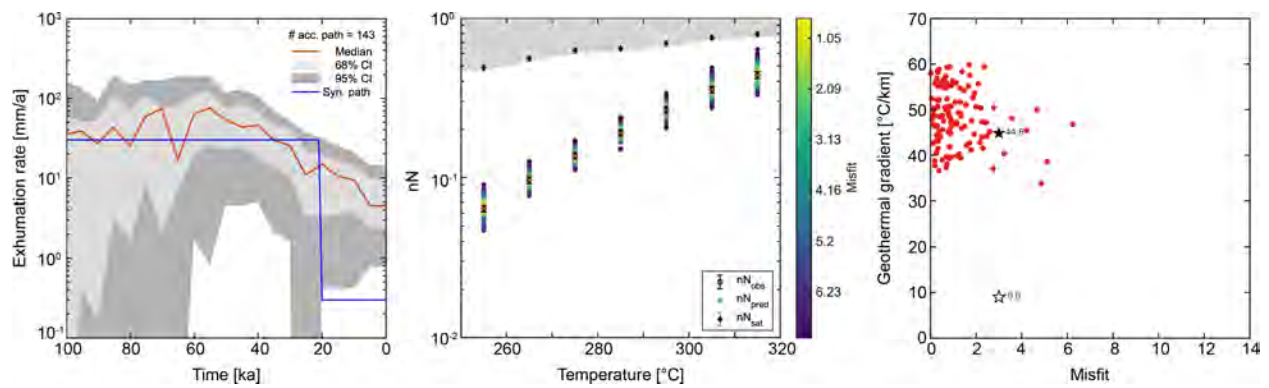
Figure S16: Modelling result for synthetic test with a step-function decrease in erosion rates from 30 to 0.3 km/Ma in the last 20 ka (blue lines). The method recovers the general decrease in erosion rates but fails to reproduce the low rates observed with [10]Be and sediment yield (Carretier et al., 2013). The initial geothermal gradient (open black star) is chosen so that the final geothermal gradient of the forward model of the synthetic paths is 45 °C/km (filled black star). Only solutions with final geothermal gradients <60 °C/km are accepted.

Bibliography

Barrell, J. (1917). Rhythms and the measurements of geologic time. *Geol. Soc. Am. Bull.*, 28(1):745–904.

Biswas, R.H., Herman, F., King, G.E., and Braun, J. (2018). Thermoluminescence of feldspar as a multi-thermochronometer to constrain the temporal variation of rock exhumation in the recent past. *Earth Planet. Sci. Lett.*, 495:56–68.

Biswas, R.H., Williams, M.A.J., Raj, R., Juyal, N., and Singhvi, A.K. (2013). Methodological studies on luminescence dating of volcanic ashes. *Quat. Geochronol.*, 17:14–25.

Bøtter-Jensen, L., Thomsen, K.J., and Jain, M. (2010). Review of optically stimulated luminescence (OSL) instrumental developments for retrospective dosimetry. *Radiat. Meas.*, 45(3-6):253–257.

Braun, J., Voisin, C., Gourlan, A.T., and Chauvel, C. (2015). Erosional response of an actively uplifting mountain belt to cyclic rainfall variations. *Earth Surf. Dyn.*, 3(1):1.

Brocklehurst, S.H. and Whipple, K.X. (2002). Glacial erosion and relief production in the Eastern Sierra Nevada, California. *Geomorphology*, 42(1-2):1–24.

Broecker, W.S. and Denton, G.H. (1989). The role of ocean-atmosphere reorganizations in glacial cycles. *Geochim. Cosmochim. Acta*, 53(10):2465–2501.

Brown, N.D., Rhodes, E.J., and Harrison, T.M. (2017). Using thermoluminescence signals from feldspars for low-temperature thermochronology. *Quat. Geochronol.*, 42:31–41.

Brozović, N., Burbank, D.W., and Meigs, A.J. (1997). Climatic limits on landscape development in the northwestern Himalaya. *Science*, 276(5312):571–574.

Bull, W.B. (1991). *Geomorphic responses to climatic change*. Oxford University Press.

Carretier, S., Regard, V., Vassallo, R., Aguilar, G., Martinod, J., Riquelme, R., Pepin, E., Charrier, R., Hérail, G., Farías, M., et al. (2013). Slope and climate variability control of erosion in the Andes of central Chile. *Geology*, 41(2):195–198.

Caves Rugenstein, J.K., Ibarra, D.E., and von Blanckenburg, F. (2019). Neogene cooling driven by land surface reactivity rather than increased weathering fluxes. *Nature*, 571(7763):99–102.

Champagnac, J.D., Valla, P.G., and Herman, F. (2014). Late-Cenozoic relief evolution under evolving climate: A review. *Tectonophysics*, 614:44–65.

Charreau, J., Blard, P.H., Puchol, N., Avouac, J.P., Lallier-Vergès, E., Bourlès, D., Braucher, R., Gallaud, A., Finkel, R., Jolivet, M., et al. (2011). Paleo-erosion rates in Central Asia since 9 Ma: A transient increase at the onset of Quaternary glaciations? *Earth Planet. Sci. Lett.*, 304(1-2):85–92.

Charrier, R., Iturrizaga, L., Carretier, S., and Regard, V. (2019). Geomorphologic and glacial Evolution of the Cachapoal and southern Maipo catchments in the Andean Principal Cordillera, Central Chile (34°-35° S). *Andean Geology*, 46(2):240–278.

Clapperton, C.M. (1994). The quaternary glaciation of Chile: a review. *Rev. Chil. Hist. Nat.*, 67(4):369–383.

Cogez, A., Meynadier, L., Allègre, C., Limmois, D., Herman, F., and Gaillardet, J. (2015). Constraints on the role of tectonic and climate on erosion revealed by two time series analysis of marine cores around new zealand. *Earth Planet. Sci. Lett.*, 410:174–185.

Danielson, J. and Gesch, D.B. (2011). Global multi-resolution terrain elevation data 2010 (GMTED2010). *US Geological Survey*, No. 2011-1073.

Delmas, M., Calvet, M., and Gunnell, Y. (2009). Variability of Quaternary glacial erosion rates–A global perspective with special reference to the Eastern Pyrenees. *Quat. Sci. Rev.*, 28(5-6):484–498.

Donnelly, T.W. (1982). Worldwide continental denudation and climatic deterioration during the late Tertiary: Evidence from deep-sea sediments. *Geology*, 10(9):451–454.

Durcan, J.A., King, G.E., and Duller, G.A.T. (2015). DRAC: Dose rate and age calculator for trapped charge dating. *Quat. Geochronol.*, 28:54–61.

Egholm, D.L., Nielsen, S.B., Pedersen, V.K., and Lesemann, J.E. (2009). Glacial effects limiting mountain height. *Nature*, 460(7257):884–887.

Einsele, G. (2000). *Sedimentary Basins: Evolution, Facies, and Sediment Budget*. Springer-Verlag.

Fick, S.E. and Hijmans, R.J. (2017). Worldclim 2: New 1-km spatial resolution climate surfaces for global land areas. *Int. J. Climatol.*

Finnegan, N.J., Schumer, R., and Finnegan, S. (2014). A signature of transience in bedrock river incision rates over timescales of 10^4–10^7 years. *Nature*, 505(7483):391–394.

Ganti, V., von Hagke, C., Scherler, D., Lamb, M.P., Fischer, W.W., and Avouac, J.P. (2016). Time scale bias in erosion rates of glaciated landscapes. *Sci. Adv.*, 2(e1600204).

Gardner, T.W., Jorgensen, D.W., Shuman, C., and Lemieux, C.R. (1987). Geomorphic and tectonic process rates: Effects of measured time interval. *Geology*, 15(3):259–261.

Gilbert, G.K. (1900). Rhythms and geologic time. *Science*, pages 1001–1012.

Guralnik, B., Jain, M., Herman, F., Ankjærgaard, C., Murray, A.S., Valla, P.G., Preusser, F., King, G.E., Chen, R., Lowick, S.E., Kook, M., and Rhodes, E.J. (2015). OSL-thermochronometry of feldspar from the KTB borehole, Germany. *Earth Planet. Sci. Lett.*, 423:232–243.

Gurnell, A., Hannah, D., and Lawler, D. (1996). Suspended sediment yield from glacier basins. *Intl. Assoc. Hydro. Sci. Publ.*, 236:97–104.

Haeuselmann, P., Granger, D.E., Jeannin, P.Y., and Lauritzen, S.E. (2007). Abrupt glacial valley incision at 0.8 Ma dated from cave deposits in Switzerland. *Geology*, 35(2):143–146.

Hallet, B., Hunter, L., and Bogen, J. (1996). Rates of erosion and sediment evacuation byglaciers: A review of field data and their implications. *Glob. Planet. Change*, 12:213–235.

Hamza, V.M., Dias, F.J.S., Gomes, A.J.L., and Terceros, Z.G.D. (2005). Numerical and functional representations of regional heat flow in South America. *Physics Earth Planet. Inter.*, 152(4):223–256.

Hamza, V.M. and Muñoz, M. (1996). Heat flow map of South America. *Geothermics*, 25(6):599–646.

Herman, F., Braun, J., Deal, E., and Prasiček, G. (2018). The response time of glacial erosion. *J. Geophys. Res.: Earth Surface*, 123(4):801–817.

Herman, F. and Champagnac, J. (2016). Plio-Pleistocene increase of erosion rates in mountain belts in response to climate change. *Terra Nova*, 28(1):2–10.

Herman, F. and King, G.E. (2018). Luminescence thermochronometry: Investigating the link between mountain erosion, tectonics and climate. *Elements*, 14(1):33–38.

Herman, F., Seward, D., Valla, P.G., Carter, A., Kohn, B., Willett, S.D., and Ehlers, T.A. (2013). Worldwide acceleration of mountain erosion under a cooling climate. *Nature*, 504(7480):423–426.

Herrera Ossandón, M. (2016). Estimación de las altitudes de las líneas de equilibrio en glaciares de montaña para el último ciclo glacial-interglacial en los Andes de Santiago, Chile Central. *Tesis de Posgrado*. Universidad de Chile, Departamento de Geología, Santiago, Chile.

Hidy, A.J., Gosse, J.C., Blum, M.D., and Gibling, M.R. (2014). Glacial-interglacial variation in denudation rates from interior Texas, USA, established with cosmogenic nuclides. *Earth Planet. Sci. Lett.*, 390:209–221.

Huntley, D.J. (2006). An explanation of the power-law decay of luminescence. *J. Phys. Condens. Matter*, 18:1359–1365.

IHFC (2011). Global Heat Flow Database of the International Heat Flow Commission 2011. University of North Dakota, USA. Data downloaded Jan 2020 from https://engineering.und.edu/research/global-heat-flow-database/data.html.

Kars, R.H., Wallinga, J., and Cohen, K.M. (2008). A new approach towards anomalous fading correction for feldspar IRSL dating–tests on samples in field saturation. *Radiat. Meas.*, 43:786–790.

King, G.E., Guralnik, B., Valla, P.G., and Herman, F. (2016). Trapped-charge thermochronometry and thermometry: A status review. *Chem. Geol.*, 446:3–17.

Knox, J.C. (1972). Valley alluviation in southwestern Wisconsin. *Annu. Assoc. of Am. Geogr.*, 62(3):401–410.

Knudsen, M.F., Egholm, D.L., Jacobsen, B.H., Larsen, N.K., Jansen, J.D., Andersen, J.L., and Linge, H.C. (2015). A multi-nuclide approach to constrain landscape evolution and past erosion rates in previously glaciated terrains. *Quat. Geochron.*, 30:100–113.

Koppes, M.N. and Montgomery, D.R. (2009). The relative efficacy of fluvial and glacial erosion over modern to orogenic timescales. *Nat. Geosci.*, 2(9):644–647.

Kreutzer, S., Schmidt, C., DeWitt, R., and Fuchs, M. (2014). The a-value of polymineral fine grain samples measured with the post-IR IRSL protocol. *Radiat. Meas.*, 69:18–29.

Lamy, F., Hebbeln, D., and Wefer, G. (1999). High-resolution marine record of climatic change in mid-latitude Chile during the last 28,000 years based on terrigenous sediment parameters. *Quat. Res.*, 51(1):83–93.

Lamy, F., Kilian, R., Arz, H.W., Francois, J.P., Kaiser, J., Prange, M., and Steinke, T. (2010). Holocene changes in the position and intensity of the southern westerly wind belt. *Nat. Geosci.*, 3(10):695–699.

Lisiecki, L.E. and Raymo, M.E. (2005). A Pliocene-Pleistocene stack of 57 globally distributed benthic δ^{18}O records. *Paleoceanography*, 20(1).

Lisiecki, L.E. and Raymo, M.E. (2007). Plio-Pleistocene climate evolution: trends and transitions in glacial cycle dynamics. *Quat. Sci. Rev.*,

26(1-2):56–69.

Lupker, M., France-Lanord, C., Galy, V., Lavé, J., and Kudrass, H. (2013). Increasing chemical weathering in the Himalayan system since the Last Glacial Maximum. *Earth Planet. Sci. Lett.*, 365:243–252.

Marshall, J.A., Roering, J.J., Gavin, D.G., and Granger, D.E. (2017). Late Quaternary climatic controls on erosion rates and geomorphic processes in western Oregon, USA. *Geol. Soc. Am. Bull.*, 129(5-6):715–731.

McKeever, S.W.S. (1980). On the analysis of complex thermoluminescence. Glow-curves: Resolution into individual peaks. *physica status solidi (a)*, 62(1):331–340.

Molnar, P. (2004). Late cenozoic increase in accumulation rates of terrestrial sediment: How might climate change have affected erosion rates? *Annu. Rev. Earth Planet. Sci.*, 32:67–89.

Molnar, P. and England, P. (1990). Late Cenozoic Uplift of Mountain-Ranges and Global Climate Change – Chicken or Egg. *Nature*, 346(6279):29–34.

Montgomery, D.R. (2002). Valley formation by fluvial and glacial erosion. *Geology*, 30(11):1047–1050.

Montgomery, D.R., Balco, G., and Willett, S.D. (2001). Climate, tectonics, and the morphology of the Andes. *Geology*, 29(7):579–582.

Moreno, P.I., Lowell, T.V., Jacobson Jr., G.L., and Denton, G.H. (1999). Abrupt vegetation and climate changes during the last glacial maximum and last termination in the Chilean Lake district: a case study from Canal de la Puntilla (41 °S). *Geografiska Annaler: Series A, Physical Geography*, 81(2):285–311.

Murray, A.S. and Wintle, A.G. (2000). Luminescence dating of quartz using an improved single-aliquot regenerative-dose protocol. *Radiat. Meas.*, 32:57–73.

Overeem, I., Weltje, G.J., Bishop-Kay, C., and Kroonenberg, S.B. (2001). The Late Cenozoic Eridanos delta system in the Southern North Sea Basin: a climate signal in sediment supply? *Basin Res.*, 13(3):293–312.

Pagonis, V., Morthekai, P., and Kitis, G. (2014). Kinetic analysis of thermoluminescence glow curves in feldspar: evidence for a continuous distribution of energies. *Geochronometria*, 41(2):168–177.

Pedersen, V.K. and Egholm, D.L. (2013). Glaciations in response to climate variations preconditioned by evolving topography. *Nature*, 493(7431):206–210.

Reiners, P.W. and Brandon, M.T. (2006). Using thermochronology to understand orogenic erosion. *Annu. Rev. Earth Planet. Sci.*, 34:419–466.

Riesner, M., Lacassin, R., Simoes, M., Carrizo, D., and Armijo, R. (2018). Revisiting the crustal structure and kinematics of the central Andes at 33.5°S: Implications for the Mechanics of Andean Mountain Building. *Tectonics*, 37:1347–1375.

Sadler, P.M. (1981). Sediment accumulation rates and the completeness of stratigraphic sections. *J. Geol.*, pages 569–584.

Schaller, M., von Blanckenburg, F., Hovius, N., Veldkamp, A., van den Berg, M.W., and Kubik, P.W. (2004). Paleoerosion rates from cosmogenic [10]Be in a 1.3 Ma terrace sequence: Response of the River Meuse to changes in climate and rock uplift. *J. Geol.*, 112(2):127–144.

Schildgen, T.F., van der Beek, P.A., Sinclair, H.D., and Thiede, R.C. (2018). Spatial correlation bias in late-Cenozoic erosion histories derived from thermochronology. *Nature*, 559(7712):89–93.

Shackleton, N.J., Backman, J., Zimmerman, H., Kent, D.V., Hall, M.A., Roberts, D.G., Schnitker, D., Baldauf, J.G., Desprairies, A., Homrighausen, R., and et al. (1984). Oxygen isotope calibration of the onset of ice-rafting and history of glaciation in the North Atlantic region. *Nature*, 307:620–623.

Shuster, D.L., Cuffey, K.M., Sanders, J.W., and Balco, G. (2011). Thermochronometry reveals headward propagation of erosion in an alpine landscape. *Science*, 332(6025):84–88.

Shuster, D.L., Ehlers, T.A., Rusmoren, M.E., and Farley, K.A. (2005). Rapid glacial erosion at 1.8 Ma revealed by ^{4}He/^{3}He thermochronometry. *Science*, 310(5754):1668–1670.

Spotila, J.A., Buscher, J.T., Meigs, A.J., and Reiners, P.W. (2004). Long-term glacial erosion of active mountain belts: Example of the Chugach–St. Elias Range, Alaska. *Geology*, 32(6):501–504.

Springer, M. and Förster, A. (1998). Heat-flow density across the Central Andean subduction zone. *Tectonophysics*, 291:123–139.

Stalder, N.F., Herman, F., Fellin, M.G., Coutand, I., Aguilar, G., Reiners, P.W., and Fox, M. (2020). The relationships between tectonics, climate and exhumation in the Central Andes (18-36°S): evidence from low-temperature thermochronology. *Earth-Science Reviews*, 210:1–37.

Thomson, S.N., Brandon, M.T., Tomkin, J.H., Reiners, P.W., Vásquez, C., and Wilson, N.J. (2010). Glaciation as a destructive and constructive control on mountain building. *Nature*, 467(7313):313–317.

Uyeda, S. and Watanabe, T. (1982). Terrestrial heat flow in western South America. *Tectonophysics*, 83(1-2):63–70.

Valero-Garcés, B.L., Jenny, B., Rondanelli, M., Delgado-Huertas, A., Burns, S.J., Veit, H., and Moreno, A. (2005). Palaeohydrology of Laguna de Tagua Tagua (34° 30' S) and moisture fluctuations in Central Chile for the last 46 000 yr. *J. Quat. Sci*, 20(7-8):625–641.

Valla, P.G., van der Beek, P.A., Shuster, D.L., Braun, J., Herman, F., Tassan-Got, L., and Gautheron, C. (2012). Late Neogene exhumation and relief development of the Aar and Aiguilles Rouges massifs (Swiss Alps) from low-temperature thermochronology modeling and ^{4}He/^{3}He thermochronometry. *J. Geophys. Res.: Earth Surf.*, 117(F01004).

Vargas, G., Klinger, Y., Rockwell, T.K., Forman, S.L., Rebolledo, S., Baize, S., Lacassin, R., and Armijo, R. (2014). Probing large intraplate earthquakes at the west flank of the Andes. *Geology*, 42(12):1083–1086.

von Blanckenburg, F., Bouchez, J., Ibarra, D.E., and Maher, K. (2015). Stable runoff and weathering fluxes into the oceans over Quaternary climate cycles. *Nat. Geosci.*, 8(7):538–542.

WGMS (1989). World glacier inventory – status 1988. IAHS (ICSI)/UNEP/UNESCO, World Glacier Monitoring Service, Zurich, Switzerland. Data downloaded Jan 2020 from http://nsidc.org/data/glacier_inventory/browse.html.

Wheelock, B., Constable, S., and Key, K. (2015). The advantages of logarithmically scaled data for electromagnetic inversion. *Geophys. J. Int.*, 201(3):1765–1780.

Whipple, K.X. (2001). Fluvial landscape response time: how plausible is steady-state denudation? *Am. J. Sci.*, 301(4-5):313–325.

Willenbring, J.K. and Jerolmack, D.J. (2016). The null hypothesis: globally steady rates of erosion, weathering fluxes and shelf sediment accumu-

lation during Late Cenozoic mountain uplift and glaciation. *Terra Nova*, 28(1):11–18.

Willenbring, J.K. and von Blanckenburg, F. (2010). Long–term stability of global erosion rates and weathering during late–Cenozoic cooling. *Nature*, 465(7295):211–214.

Willett, C.D., Ma, K.F., Brandon, M.T., Hourigan, J.K., Christeleit, E.C., and Shuster, D.L. (2020). Transient glacial incision in the Patagonian Andes from ̃6 Ma to present. *Science Advances*, 6(7):1–9.

Wintle, A.G. (1973). Anomalous fading of thermo-luminescence in mineral samples. *Nature*, 245:143–144.

Zachos, J., Pagani, M., Sloan, L., Thomas, E., and Billups, K. (2001). Trends, Rhythms, and Aberrations in Global Climate 65 Ma to present. *Science*, 292(5517):686–693.

Zech, R., May, J., Kull, C., Ilgner, J., Kubik, P.W., and Veit, H. (2008). Timing of the late Quaternary glaciation in the Andes from ̃15 to 40°S. *J. Quat. Sci.*, 23(6):635–647.

Zhang, P.Z., Molnar, P., and Downs, W.R. (2001). Increased sedimentation rates and grain sizes 2-4 Myr ago due to the influence of climate change on erosion rates. *Nature*, 410(6831):891–897.

CHAPTER **4**

Drivers of Pleistocene erosion in the Chilean Andes (33-35° S) – active tectonics or climate change?

Nadja F. Stalder[1], Frédéric Herman[1], Magali Riesner[2], Martine Simoes[3], Robin Lacassin[3]

[1]Institute of Earth Surface Dynamics, University of Lausanne, Switzerland
[2]Earth Observatory Singapore, Nanyang Technological University, Singapore
[3]Institut de Physique du Globe de Paris, University of Paris, France

Abstract

The respective roles of tectonics and climate on erosion remains debated. This is in part due to the complexity of the relationships between climate, tectonics and erosion and to the difficulty of quantifying tectonics and climate independently. The Chilean Andes at 33-35° S combine a well-constrained active tectonic setting and a climate characterized by a strongly increasing N-S precipitation gradient. For the tectonics, thrusting initiated around 23 Ma ago in the Principal Cordillera and was relatively constant since then, with average orogenic shortening rates around 2.2 mm/yr. For the climate, precipitation increases from ~400 mm/yr to ~800 mm/yr from north to south. This region therefore offers the possibility to investigate how erosion varies under relatively uniform tectonics and changing precipitation. To quantify erosion, we collected 11 new apatite (U-Th)/He ages and 8 new apatite fission-track ages from the Principal Cordillera that we interpret using thermal models. AFT ages show cooling ages between 6.7 and 9.8 Ma, whereas (U-Th)/He ages are extremely young and range from 0.5 to 3.5 Ma. Our results imply a significant increase in erosion rates in the mid-Pleistocene, with rates being an order of magnitude higher than their pre-Pleistocene values and higher than erosion rates observed from thermochronological data in the north. Using a thermo-kinematic model constrained by the existing knowledge on fault kinematics and shortening rates, we find that the cooling ages cannot be explained by tectonically-driven rock uplift only or by changes in the activity of mapped faults. Several studies have suggested that the peak precipitation rate associated with the Westerlies migrated northward during cold periods, which may have enhanced precipitation and thus erosion rates. Furthermore, the geomorphology shows an increasingly glacial imprint from north to south, with wider, glacial U-shaped valleys compared to the north. Our results indicate that the impact of Pleistocene glaciations can be significant in tectonically active areas.

4.1 Introduction

The Earth's topography reflects the balance between tectonic and climatic processes, which are linked by erosion and coupled through a system of complex feedback mechanisms (e.g., Molnar and England, 1990; Raymo and Ruddiman, 1992; Reiners et al., 2003; Molnar, 2009; Whipple, 2009; Champagnac et al., 2012). Plate tectonic processes create new mountain belts, oceans and islands and control the distribution and topography of landmass, thus controlling atmospheric CO_2 and weathering rates (e.g., Berner et al., 1983; Hay, 1996). Climate, in turn, can change the lithospheric stress regime of mountain belts through erosion and re-deposition of sediment and may ultimately control the topographic height and width of orogens (Dahlen and Suppe, 1988; Koons, 1990; Molnar and England, 1990; Beaumont et al., 1992; Willett, 1999; Montgomery et al., 2001).

However, our understanding of the feedbacks between climate, erosion and tectonics are hindered by the lack of knowledge of erosional processes, which act on different spatial and temporal scales (Chap. 3), and by the scarcity of data reporting tectonic and climatic changes in geological time (Chap. 2). Furthermore, the idea that increased climate variability during the Plio-Pleistocene transition (Lisiecki and Raymo, 2005, 2007) and the change from 41 ka to 100 ka climatic cycles in the mid-Pleistocene (~0.9 Ma; Lisiecki and Raymo, 2007), with its associated widespread glaciations, have led to increased erosion rates in mountainous landscapes (Molnar and England, 1990; Zhang et al., 2001; Molnar, 2004; Herman et al., 2013; Herman and Champagnac, 2016) has been challenged by studies demonstrating that erosion rates have remained constant through the Late Cenozoic (Willenbring and von Blanckenburg, 2010; von Blanckenburg et al., 2015; Willenbring and Jerolmack, 2016) and that any observed increase may be associated to a time-scale bias caused by comparing measurements averaged over different time-scales (e.g., Ganti et al., 2016).

In Chapter 2, new thermochronological data and inverse modeling have revealed that the youngest apatite (U-Th)/He ages and highest Pleistocene erosion rates of the Central Andes are observed between 33 and 36°S in Chile (Fig. 4.1). This region is also characterized by a climatic transition, evolving from semi-arid conditions in the north to humid conditions in the south, along with a change in morphology from fluvial- to glacial-dominated landscapes. Accordingly, the high erosion rates have been explained by increased precipitation related to the northward shift of the Westerlies and the onset of glaciations.

However, this region is and has been tectonically active and uncertainties about the respective role of climate and tectonics setting the Pleistocene erosion rates remain. Using syn-tectonic sediments, Riesner et al. (2017, 2018) recently investigated the Miocene-to-Pleistocene deformation
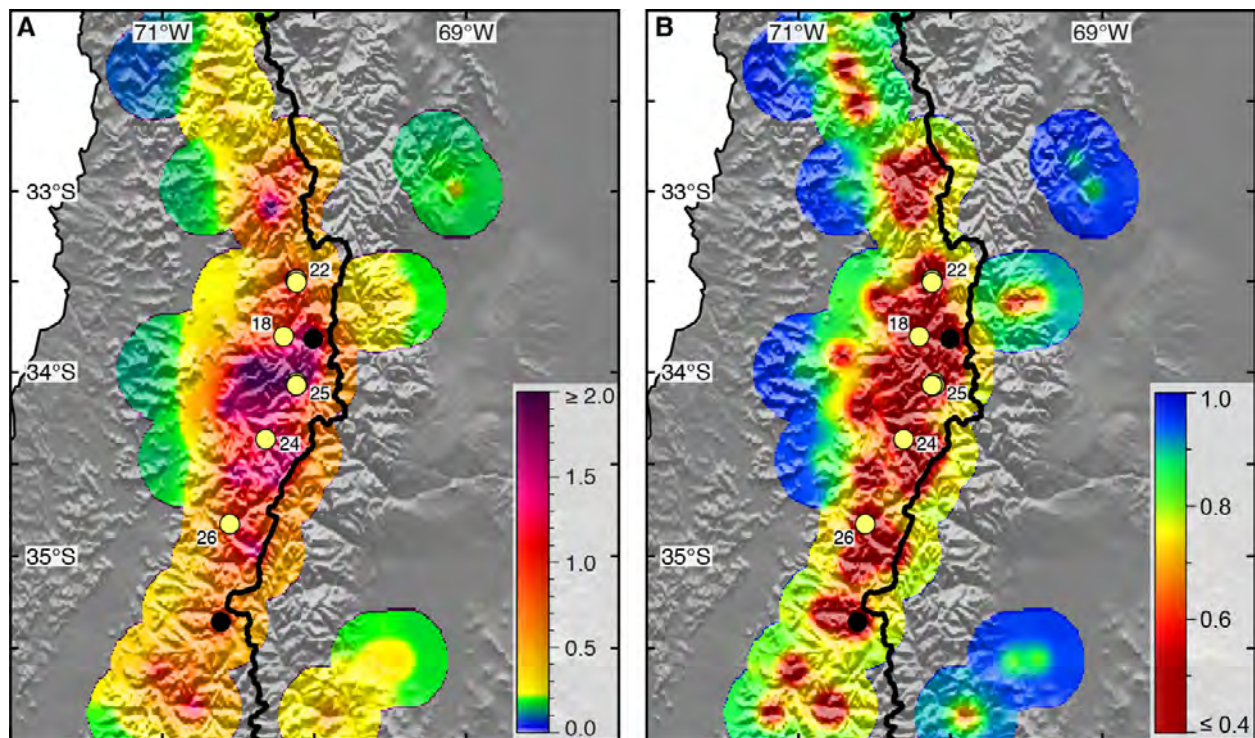
Figure 4.1: Inversely modelled **A)** exhumation rates and **B)** reduced variance from Chapter 2 for the most recent time interval (2-0 Ma). A correlation length scale of 20 km, an $\dot{e}_{prior}$ of 0.1 km/Ma and a G_0 of 25 °C/km has been used. The reduced variance is an indication of whether the solution has improved by incorporating data or not; the closer to zero, the better the solution is. Black line delineates the main water divide, black and yellow dots represent the thermochronological literature and new data, respectively, falling into the time interval (2-0 Ma). Underlying topography from GEBCO_2014, 30 arc-s (Becker et al., 2009). See Chapter 2 for details.

history in this area and constrained the average orogenic shortening rate as well as the fault-kinematics of individual thrusts. Furthermore, a thermo-kinematic model has been developed to predict thermochronological ages associated with the observed tectonic activity (Riesner, 2017). Application of this thermo-kinematic model on low-temperature thermochronological data compiled in Chapter 2 and own data (apatite and zircon (U-Th)/He (AHe, ZHe) and fission-track (AFT, ZFT) dating) enables us to further investigate the interactions between climate, tectonics and erosion between 33 and 35°S.

Below we show how we have developed a thermo-kinematic model that is constrained by existing geological knowledge. We find that tectonic-driven rock uplift alone cannot explain the observed ages. We also demonstrate that a significant increase in erosion rates during the Plio-Pleistocene is necessary to explain the observed ages, and that this increase cannot be explained by tectonics. These findings support the conclusions drawn in Chapters 2&3 and highlight once more the importance of Pleistocene glaciations on erosion rates.

4.2 Geological setting

At the latitude of Santiago, the Andes comprise from west to east the Coastal Cordillera, the Central Depression, the Principal Cordillera, and the Frontal Cordillera, which disappears around 34.5° S (Fig. 4.2). The Central Depression is separated from the Principal Cordillera by the active
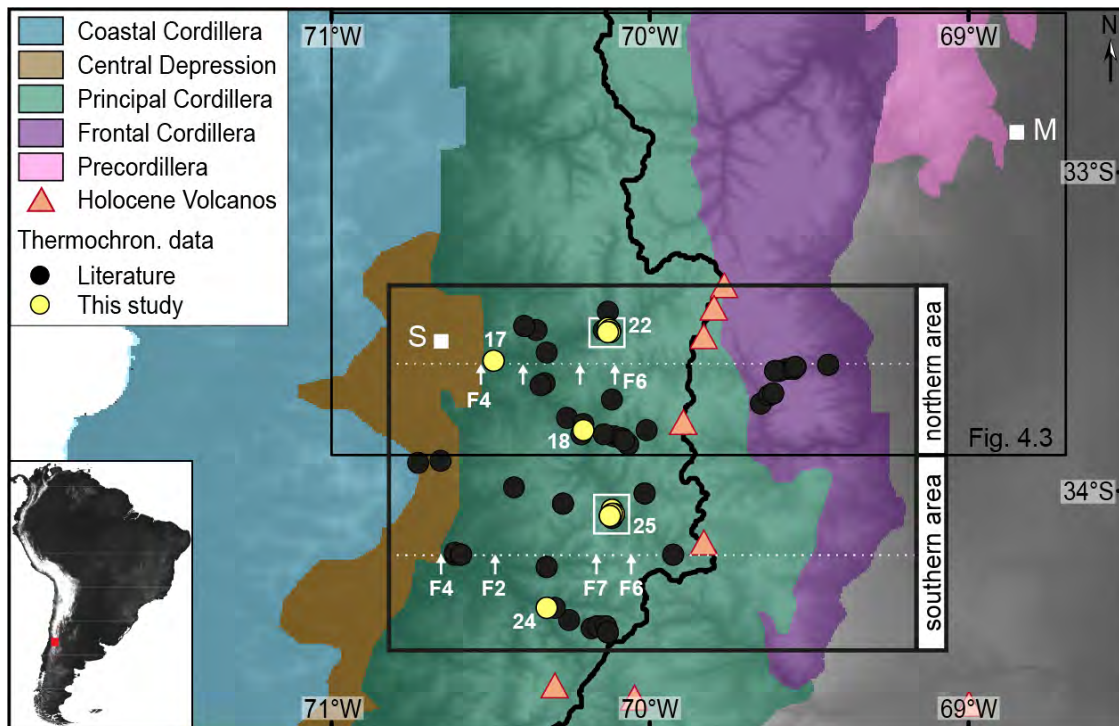
Figure 4.2: Tectonomorphic structure of the Central Andes at 33-36° S with thermochronological sample locations. The study area is divided into a northern and a southern area for the thermo-kinematic modeling. White arrows and stippled lines indicate the fault positions used in the thermo-kinematic model. White rectangles show locations of the age-elevation profiles Clin22 and Clin25 shown in Fig. 4.10.

San Ramón thrust fault, which is located directly east of Santiago de Chile (Fig. 4.3). The Principal Cordillera can be divided into the west-vergent West Andean fold-and-thrust belt (WAFTB, Armijo et al., 2010) in the west and the east-vergent Aconcagua fold-and-thrust belt (AFTB) in the east (Ramos et al., 2004; Giambiagi et al., 2003). These two belts are separated from each other by tight west-vergent folds deforming Mesozoic sediments (WVF, Armijo et al., 2010). The WAFTB consists of late Eocene to Oligocene volcaniclastics of the Abanico Fm. and the unconformably overlying Miocene Farellones Fm. (Nyström et al., 2003; Charrier et al., 2002). The sedimentary sequences are intruded by porphyric dykes and small intrusions of Miocene age like the Gloria and San Gabriel plutonites. The AFTB contains a thick sequence of Mesozoic sedimentary rocks and the Pliocene to recent volcanic arc (Ramos et al., 1996, 2004; Giambiagi et al., 2003). East
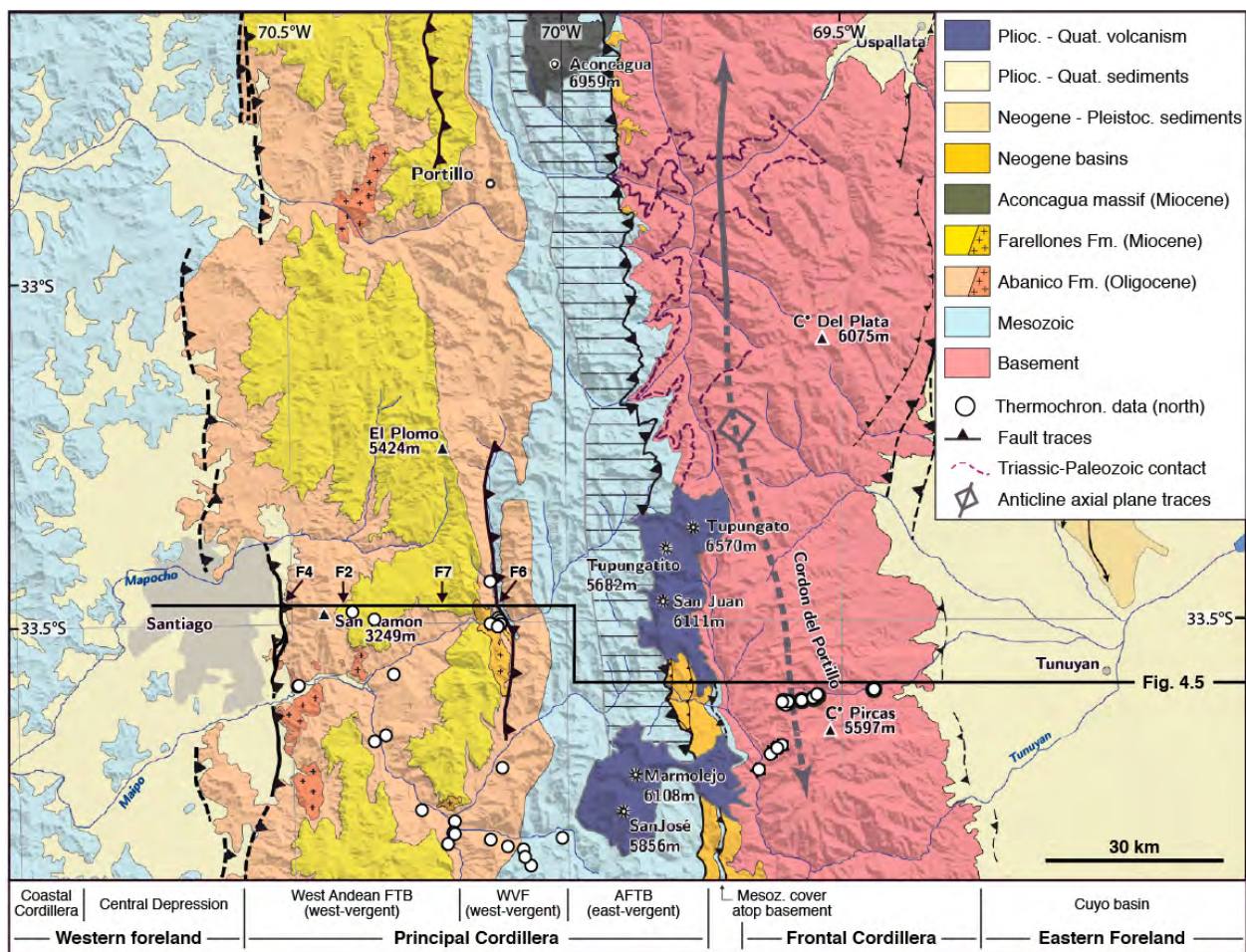
Figure 4.3: Structural map of the Andes at 33.5° S, modified from Riesner et al. (2018). Black line represents the location of the geological cross-section depicted in Fig. 4.5.

of the Principal Cordillera lies the Frontal Cordillera, composed of pre-Andean units of Early-mid Paleozoic to Permo-Triassic age. The Precordillera finally marks the eastern termination of the Andean orogen.

Deformation in this part of the Andes started in the late Oligocene by tectonic inversion of the former extensional basins after a period of large-scale extension and crustal thinning, (e.g., Godoy et al., 1999; Charrier et al., 2002). As discussed in Chapter 2, Section 2.2.3 and repeated here, the widely accepted east-vergent tectonic model (e.g., Giambiagi and Ramos, 2002; Giambiagi et al., 2012, 2015) has recently been contested by studies suggesting a doubly-vergent tectonic model (Armijo et al., 2010; Riesner et al., 2018, 2019) (Fig. 4.4).

In the traditional, east-vergent model, deformation is mainly accommodated by the hybrid thick- and thin-skinned AFTB in the eastern Principal Cordillera, which separates the modern volcanic
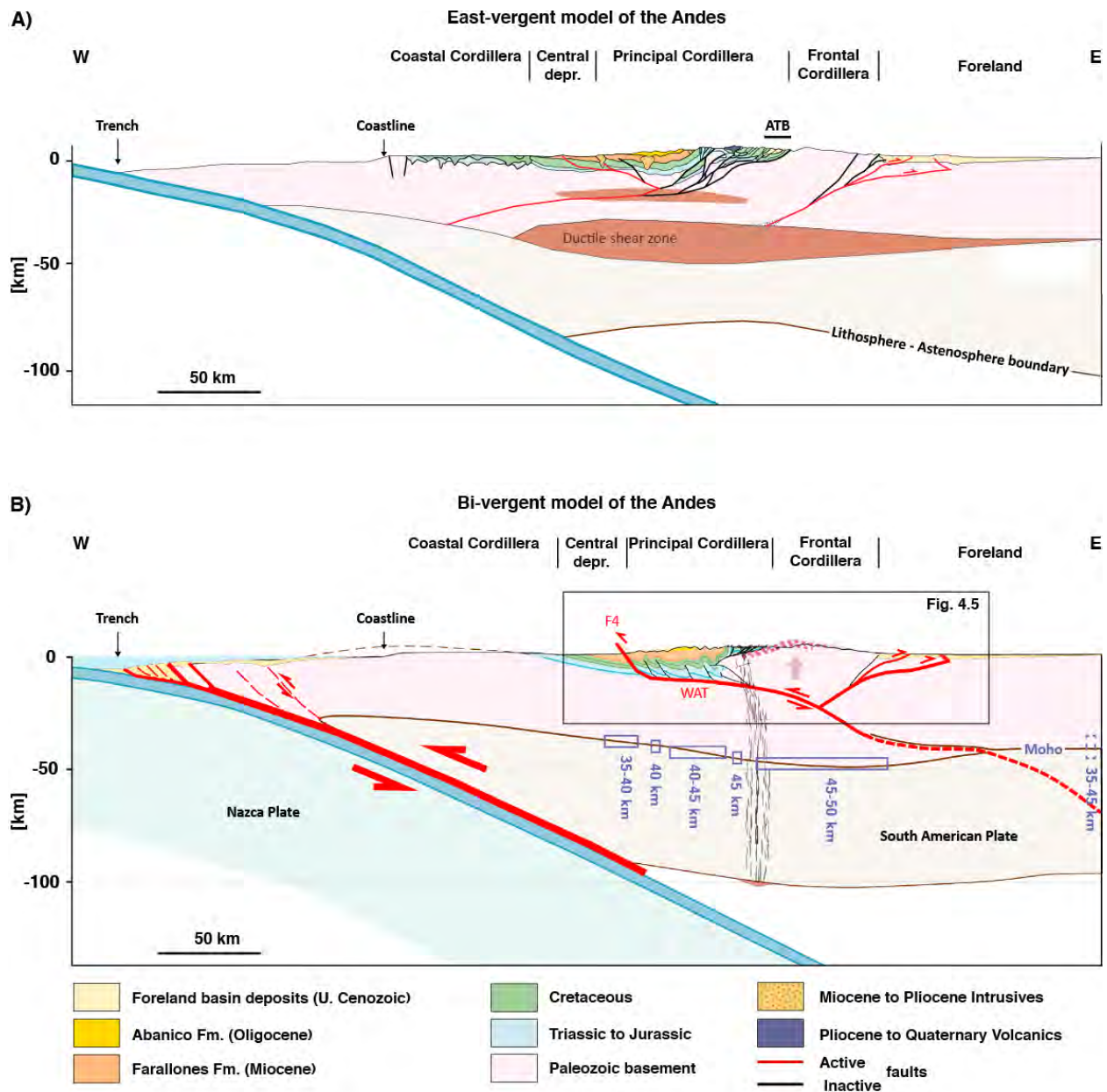
Figure 4.4: Lithospheric-scale cross-sections showing the conflicting interpretations of the structural setting of the Central Andes at 33.5° S. **A)** East-vergent model of Giambiagi et al. (2015), where the Principal Cordillera is uplifted passively. Redrawn from Giambiagi et al. (2015) to match colors in (B). ATB = Alto Tunuyán basin. **B)** Bivergent model of Riesner et al. (2018), where most shortening is accommodated by west-vergent structures in the Principal Cordillera. WAT = West Andean Thrust.

arc and the basement culmination of the Frontal Cordillera (Giambiagi et al., 2015, and references therein) (Fig. 4.4A). Shortening in the AFTB initiated around 18-15 Ma and was active until the early Pliocene (~5 Ma), as revealed by syntectonic sediments deposited in the Alto Tunuyán wedge-top basin adjacent to the east (Irigoyen et al., 2000; Giambiagi et al., 2001; Giambiagi and Ramos, 2002; Giambiagi et al., 2003, 2015). The Frontal Cordillera started uplifting in the middle to late Miocene (~12 to 9 Ma) (Giambiagi et al., 2015; Porras et al., 2016). Compressional deformation in the eastern Principal Cordillera finally stopped in the Pliocene (~4 Ma) and propagated to the eastern Frontal Cordillera and the Cuyo foreland (Irigoyen et al., 2000; Giambiagi et al., 2003; García and Casa, 2014; Giambiagi et al., 2015). In this model, the Coastal Cordillera and the western Principal Cordillera were uplifted passively due to the tectonic activity of the AFTB (Giambiagi et al., 2015). Shortening peaks between 17 and 11 Ma, with rates of 4.7-6.5 mm/a, and is low before 17 Ma (2 mm/a) and during the Pliocene (1.6 mm/a) (Giambiagi et al., 2015) (Chap. 2, Fig. 2.2).

The second, doubly-vergent model (Fig. 4.4B) is based on detailed analysis of high-resolution satellite and aerial images and digital elevation models of the western part of the orogen, a region which had gained little attention in previous studies. There, Oligocene to Miocene syntectonic deposits from the WAFTB indicate continuous activity of west-vergent thrusts since ca. 23 Ma (Riesner et al., 2017, 2018) (Figs. 4.3&4.5). These faults inverted and folded the former Oligocene to Miocene Abanico basin. Its western-most fault, the San Ramón fault (F4), delineates the modern orogenic front and is still active (Barrientos et al., 2004; Vargas et al., 2014). The WAFTB and AFTB are connected by the WFV, a series of out-of-sequence thrusts that deformed Jurassic to Miocene sediments in west-vergent folds between 15 Ma to 5 Ma (Riesner et al., 2018) (Fig. 4.5). These studies indicate that the western part of the Andean mountain belt might have accommodated more shortening than previously thought and primarily along westward structures (Armijo et al., 2010; Riesner et al., 2017, 2018). According to this view, shortening was relatively continuous with long-term average shortening rates of 1.2 - 2.2 mm/a and total shortening of ca. 31-55 km, of which 27-42 km were accommodated by the west-vergent thrusts located in the Principal Cordillera (Riesner et al., 2018).

Although both models suggest tectonic deformation in the Principal Cordillera during the last 25 Myr, the way this deformation is expressed (passive vs. active), the amount of shortening accommodated, and the spatial and temporal resolution of the fault kinematics are significantly different. Compared to the east-vergent model favoring uplift and deformation in the eastern part of the orogen in the Frontal Cordillera, the doubly-vergent model can be understood as an end-member for tectonic activity in the Principal Cordillera. Because most of our thermochronological data is located in the Principal Cordillera, where the detailed fault activity has been constrained by Riesner
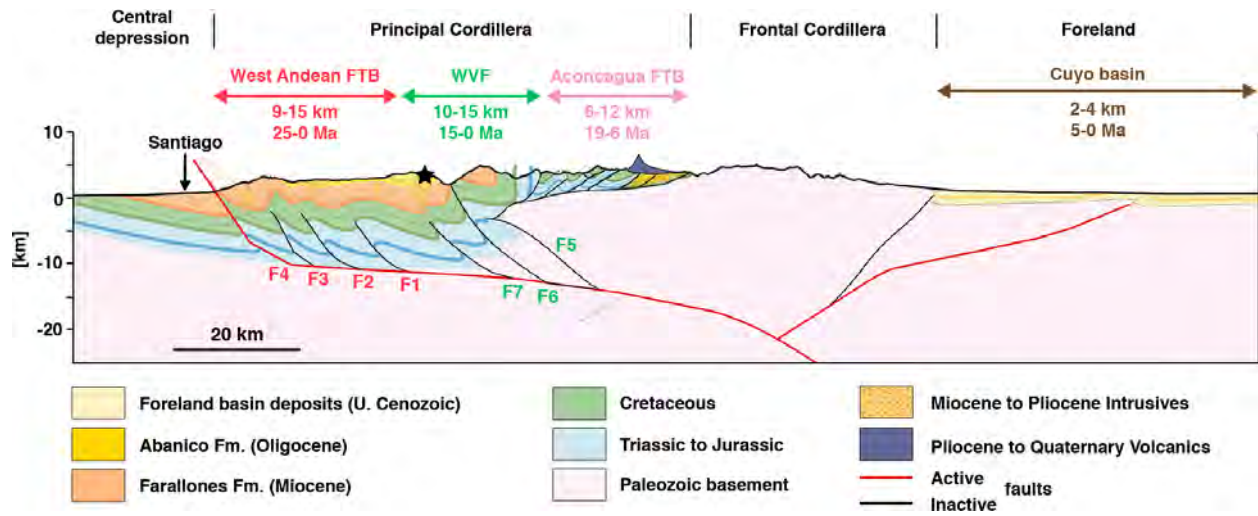
Figure 4.5: Geological cross-section at 33.5° S from Riesner (2017) with the timing and cumulative shortening of each structural unit. Black star indicates location of age-elevation profile Clin22. See Fig. 4.3 for location.

et al. (2017, 2018), we use the doubly-vergent model for our thermo-kinematic modelling, keeping in mind that the main structural setting, doubly- or east-vergent, is still a matter of debate.

4.3 Methods

4.3.1 Thermo-kinematic fault model

Thermochronological ages between 33.4 and 34.5° S were extracted from the data compiled in Chapter 2. In total, 66 ages from literature (AHe, AFT, ZHe, ZFT) and 19 new ages (AHe, AFT) were used (Fig. 4.2 and Appendix, Table C1). To account for differences in the fault position and because AHe ages in the south are significantly younger than in the north, the study area is split into a northern (33.4 to 33.9° S; 47 ages) and a southern (33.9 to 34.5° S; 38 ages) segment, which are modeled separately. For both areas, the minimum elevation is derived from Swath profiles that have been extracted from a digital elevation model (GTOPO30, 1997) and smoothed with a 1-km resolution. All sample elevations were projected on the minimum topography for the modeling. This is appropriate because most samples were collected at the valley floor and the elevations of the samples are thus similar to the elevations of the minimum topography. Differences between modeled ages using minimum and maximum topographies are addressed in Appendix, supplementary Fig. C.2, where ages interpolated on the true sample elevations using:

$$Age_{interp} = Age_{min} + (Age_{max} - Age_{min}) * \left(\frac{h - h_{min}}{h_{max} - h_{min}} \right) \tag{4.1}$$

are also shown. Differences between the modeled and interpolated ages are minor, and interpolated ages are closest to the ones where the minimum topography has been used.

Longitudinal coordinates and fault positions are expressed as distances relative to the surface trace of the San Ramón fault (F4), which delineates the current mountain front (Fig. 4.3). To do so, the coordinates of the San Ramón fault have been extracted from Google Earth and the minimum distances between the San Ramón fault and the thermochronological samples have been calculated to assure that the samples are located at the right position relative to the fault.

We solve the heat transfer equation in two dimensions to account for the role of fault kinematics on the geothermal field and exhumation rates. The fault kinematics and geometry has been constrained in the northern sector of our study area (Fig. 4.3) by Riesner et al. (2017, 2018) and is based on a series of west-vergent faults (F1 to F7) rooting at 10 to 15 km depth in a crustal ramp dipping with 15-20° (Riesner, 2017) (Figs.4.5&4.6A). The faults are located close to each other and most of them are blind thrusts - only F4 and F6 have mapped surface traces (Riesner, 2017) (Fig. 4.3). Therefore, the locations of the thermochronological ages relative to the faults is difficult to constrain and we simplified the fault geometry by merging F1, F2 and F3 into one fault (F2) in our thermo-kinematic model set-up (Figs. 4.6C&4.7). Moreover, shortening in the Aconcagua fold-and-thrust belt is accommodated by the west-vergent fault F6.
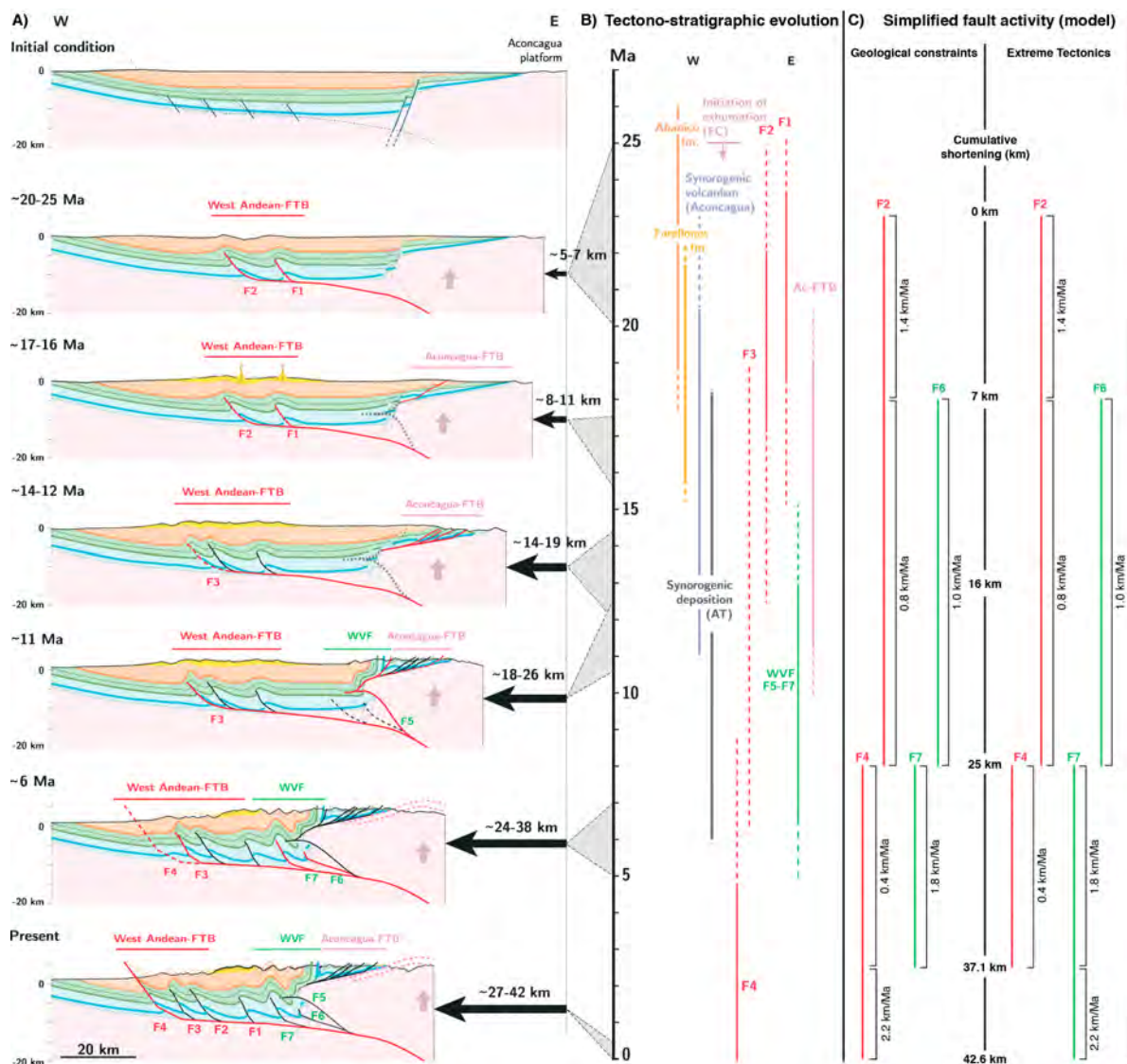
Figure 4.6: A,B) Kinematic evolution of the Principal Cordillera and chronological constraints for the fault kinematics derived from syn-tectonic sediments (Abanico and Farellones Fm. and Alto Tunuyán (AT) basin) (from Riesner et al., 2018). Active thrusts are indicated in red, inactive thrusts in black. FTB = fold-and-thrust belt; WVF = west vergent folds; Ac-FTB = Aconcagua fold-and-thrust belt. Initiation of exhumation of the Frontal Cordillera (FC) has been defined from thermochronological data in Riesner et al. (2018). Total cumulative shortening for each time interval is indicated with black arrows. **C)** Simplified fault kinematics of the two model scenarios used in this study.

Although the fault kinematic is relatively well constrained in the study area, uncertainties about the onset and duration of individual fault activities remain. We therefore test for two scenarios (Fig. 4.6C): scenario 1 – "geological observations" is closest to the geological observation, with the San Ramón fault (F4) being the only active fault since the Pleistocene, and scenario 2 – "extreme tectonics" where all shortening during the last 2.5 Ma is accommodated by F7. This latter scenario is the tectonic end-member model that results in highest rock-uplift and exhumation rates in the hanging wall of F7 where the youngest AHe data are observed (age-elevation profiles Clin22 and
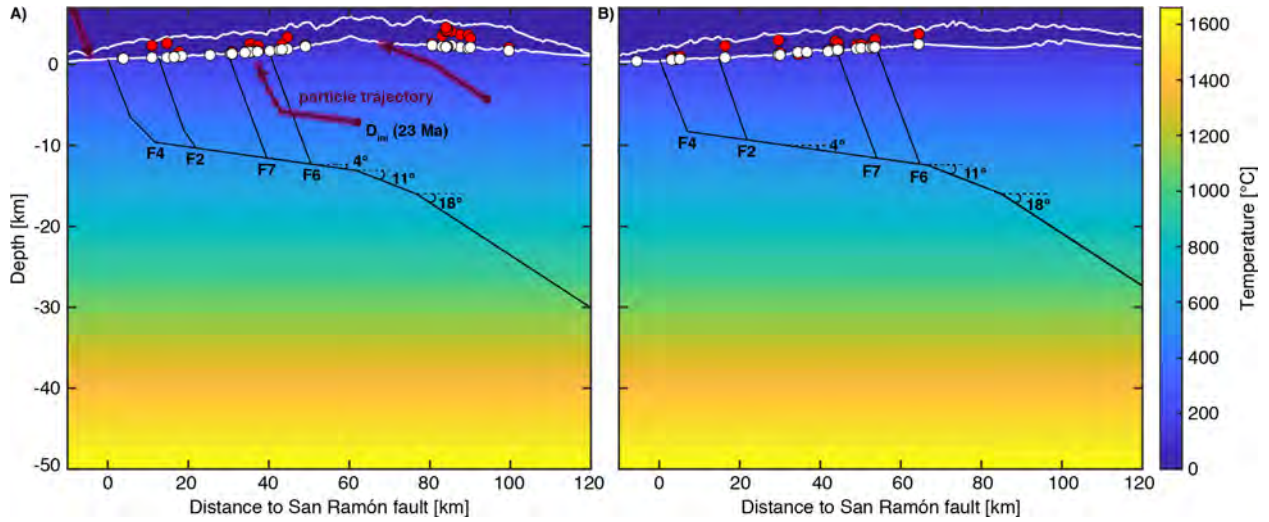
Figure 4.7: Thermo-kinematic model set up for the northern (**A**) and southern (**B**) area. Sample elevations are represented as red circles, projected elevations on the minimum topography in white. Purple arrows shows particle trajectories during advection to the surface, with D_{ini} being the starting point at 23 Ma.

Clin25; Fig. 4.2). Simultaneous fault activities between 18 and 2.5 Ma are modelled by moving the faults individually each other time step with doubled shortening rates. Shortening is accommodated by four faults – F4, F2, F7 and F6 – with slip rates approximated by the average orogenic shortening rates as follows: 1.4 km/Ma between 23 and 18 Ma, 1.8 km/Ma between 18 and 8 Ma and 2.2 since 8 Ma (Figs. 4.6C&4.7). We test for a constant topography approximated by the minimum elevation of the Swath profiles, thus maximizing exhumation, and one which continuously evolves from sea level at 23 Ma to the present-day minimum topography, thus minimizing exhumation. A box size of 140 km length and 60 km depth is used so that a complete west-east cross section from the Central Depression to the eastern foreland basin is included.

The thermo-kinematic model defines the thermal structure of the upper crust by solving the 2D heat conservation equation for diffusion and advection, including heat production from radioactive decay:

$$\frac{\partial T}{\partial t} = \kappa \nabla^2 T - \vec{v} * \nabla T + H(z) \tag{4.2}$$

where κ is the thermal diffusivity (km²/Ma), $\vec{v}$ the velocity field in x and z direction (m/s), and $H(z) = H_0 exp(-z/\lambda_H)$ is the depth-dependent radiogenic heat production (µW/m). The temperature at the base of the lithosphere, T_{bottom}, is chosen so that the average final geothermal gradient at the surface is between 30 and 33 °C. The initial geothermal gradient is set to 30 °C/km for scenario 1 and to 34 °C/km for scenario 2. The orientation of the velocity vectors is directly derived from the fault geometry and kinematics using the fault-bend approach (Suppe, 1983), which only allows for

Table 4.1: Thermo-kinematic model parameters

Heat diffusivity	κ	30	km^2/Ma
Heat production	H	3	µW/m^3
Decay depth	λ_H	10	km
Surface temperature	T_{surf}	0	°C
Temperature at depth	T_{bottom}	1500 / 1700	°C
Overthrusting		73.40	%
Dip of crustal ramp		18°	
Modelled time span	t_{max}	23	Ma
Length of model box	L_x	160	km
Depth of model box	L_z	60	km

simple shear parallel to the fault (Herman et al., 2010). The magnitude of the velocity is set by the individual fault slip rates and their partitioning between overthrusting of the hanging wall and underthrusting of the footwall, here kept constant at 73.4 % overthrusting following M. Riesner (*pers. comm*). This relatively high value has been found to explain best the thermochronological data in the eastern part of the Andes (Riesner, 2017). The thermal structure is then used to predict thermochronological ages using the Pecube routine. Finally, differences between predicted and observed ages are calculated to derive a misfit. All parameters are listed in Table 4.1.

The thermo-kinematic model routine can be summarized as follows (Fig. 4.7):

1. Samples are retro-displaced from the surface to their initial position in the crust using the velocity vector defined by the fault kinematics.

2. The heat conservation equation (Eq. 4.2) is solved to derive the temperature-time (Tt) path of each sample while being advected to the surface.

3. Misfits are calculated for each thermochronological age.

4.3.2 QTQt and 1D heat transport model for age-elevation profiles

Two age-elevation profiles (Clin22A-D and Clin25A-D) are additionally investigated with the QTQt software (Gallagher, 2012) and an 1D inverse thermal model. The age-elevation profiles were sampled along two mountain ridges exposing small granitic bodies of Miocene age and spanning elevation differences of 1010 and 920 m, respectively. The profiles are located in the hanging wall of F7 in the northern (33.5° S) and southern (34.1° S) area (Fig. 4.2).

The thermal history of the QTQt model is constrained to start at 200 °C at the time of the emplacement of the intrusion (10.4 Ma and 13.4 Ma U-Pb age for Clin22 and Clin25, Appendix Table A4), following a recommendation of K. Gallagher. The initial prior range is chosen relatively widely (time = 7±7 Ma; T = 70±70 °C) (Appendix, supplementary Fig. C.3). A lapse rate of ~5 °C/km is assumed by providing individual surface temperatures for each sample using the "constrained present day" option of QTQt (Gallagher, 2012). We used the AFT annealing model from Ketcham et al. (2007) and the radiation damage model from Gautheron et al. (2009) for AHe data. Four to five apatite crystals were used for AHe (Appendix, Table A1). Unfortunately, no apatite fission track lengths could be measured due to bad quality of the apatites. MCMC model parameters are provided in Appendix, supplementary Fig. C.4.

In the 1D thermal model, a tabular intrusion containing the samples, with 7.0 x 2.5 km dimension in x-z direction, is emplaced in the upper crust at 6.75 km depth (center of the intrusion) at the time of the U-Pb closure age, t_{max}, with an initial temperature of 700 °C (Appendix, supplementary Fig. C.5). The samples are then advected towards the surface with an initial velocity, $\dot{e}_{before}$, randomly chosen between 0.1 and 4.5 km/Ma, until a randomly chosen time, t_{Acc}, between 3 and 0 Ma. After this time, the samples are advected with a new velocity, $\dot{e}_{after}$, calculated by the remaining distance to the surface and the remaining time, t_{max} - t_{Acc}. By recording the temperature-time path of each sample, the thermochronological age can be predicted using the Pecube age routine. The misfit for each inversion is calculated as follows:

$$ misfit = \sqrt{\sum_{i=1}^{N} \left(\frac{age_{obs(i)} - age_{pred(i)}}{\sigma_{obs(i)}} \right)^2 } \qquad (4.3) $$

The two inversions are run for 10'000 iterations. Model parameters are provided in Table 4.2.

Table 4.2: Parameters for 1D inversion model

Heat diffusivity	κ	34	km²/Ma
Surface temperature	T_{surf}	15	°C
Temperature at depth	T_{bottom}	1250	°C
Modelled time span	t_{max}	10.4 / 13.4	Ma
Intrusion dimension (x,y)		7, 2.5	km
Temperature of intrusion	$T_{intrusion}$	700	°C
Lapse rate		5	°C
Length of model box	L_x	20	km
Depth of model box	L_z	50	km
Iterations		10'000	

4.4 Results

Figure 4.8 shows the thermo-kinematic modelling results for both tested scenarios, "geological observation" and "extreme tectonics" (Fig. 4.6C), for the northern and southern areas. For clarity, predicted ages are shown as colored lines representing predicted ages of the minimum topography calculated at 2 km resolution. The omitted predicted ages of the samples fall on these lines since the minimum topography has been used for the modelling.

The scenario following most closely the geological observations, i.e., the San Ramón fault being the only active fault during the Pleistocene, fits most of the AFT and ZFT data but not the AHe ages (Fig. 4.8A). In the northern area, predicted AHe (~2 Ma) and AFT (~2-4 Ma) data in the hanging wall of the San Ramón fault (x = 0-20 km) are younger than the observed ages, which are greater than 10 Ma for both systems, whereas AFT data in the hanging wall of F2 (x = 15-20 km) is fitted relatively well. Further to the east in the Principal Cordillera, predicted AHe ages located in the hanging wall of F7 (x = 20-40 km) are around 5 Ma and therefore significantly older than the observed Pleistocene AHe ages, whereas AFT and ZFT ages fit relatively well. Predicted ages in the Frontal Cordillera (x = 80-100 km) are also younger than observed. A similar result can be observed in the southern area, although less data is available here. Data located in the hanging wall of the San Ramón fault (x = 10-18 km) are mostly underestimated and the model does not represent the zone of young thermochronological ages defined by all four systems in the hanging wall of F2 (x = 18-40 km). Here, observed AHe, AFT and ZHe ages are younger than 5 Ma and ZFT are between 5-10 Ma, whereas modelled ages are ~23 Ma and were thus not affected by the tectonic activity prescribed by the thermo-kinematic model. Finally, the fit of the data is relatively good in the hanging wall of F7 (x = 40-60 km) for AFT and ZFT ages, whereas the Pleistocene AHe ages are again significantly overestimated (~5 Ma).

The scenario where all Pleistocene shortening has been accommodated by F7 was chosen as a tectonic end-member model to test if the young AHe ages observed in the hanging wall of F7 can be explained mainly by tectonic-induced rock-uplift (Fig. 4.8B). AHe ages in the northern area show indeed a good fit to the data, and also the AHe ages located in the Frontal Cordillera (x = 80-100 km) fit better. However, most observed AFT ages are older than 5 Ma and are now significantly underestimated, since predicted AHe and AFT ages are both ~2 Ma. This discrepancy is even more pronounced in the southern area. Even with this end-member model, AHe ages located in the hanging wall of F7 are still overestimated while AFT ages are highly underestimated. Only the ZFT ages fit reasonably well. Moreover, we observe a high mismatch between observed and predicted ages for all four systems for all the data to the west of the hanging wall of F7 (x = -20 - 45 km) .
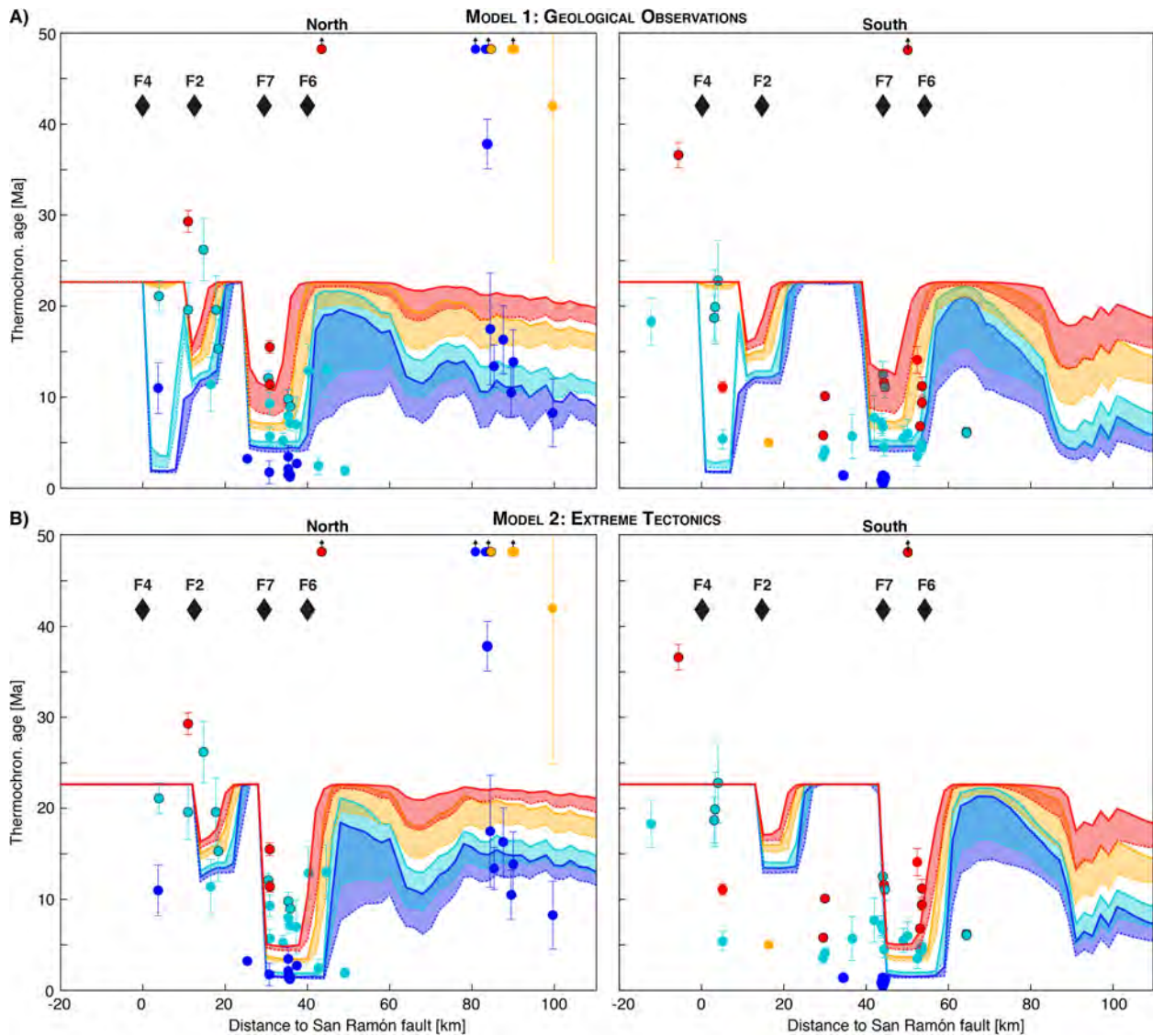
Figure 4.8: Thermo-kinematic modelling results for both scenarios and areas. AHe data is represented in blue, AFT in light blue, ZHe in orange and ZFT in red. Observed thermochronological ages are represented as colored circles. Ages that may represent magmatic cooling ages (see Chap. 2) are indicated with a black rim; ages older than 50 Ma are indicated with black arrows on top of the figures. Predicted ages of the minimum topography, calculated at 2 km resolution, are shown as stippled (constant topography) and solid (evolving topography) lines. Black diamonds indicate fault positions in the West-Andean FTB (F4, F2) and WVF (F7, F6). **A)** Modelling results for the northern and southern areas using fault kinematics closest to the geological observations, i.e., with the San Ramón fault (F4) being the only active fault during the Pleistocene. **B)** Modelling results for the northern and southern areas using the tectonic end-member model, where all shortening during the Pleistocene is accommodated by F7.

The poor fit between predicted and observed ages is also apparent in Figure 4.9, where observed vs. predicted ages are shown for the two model scenarios using constant topography. Misfits for the models with evolving topography are shown in Appendix, supplementary Figure C.1. In the northern area, most thermochronological ages are underestimated whereas many ages are
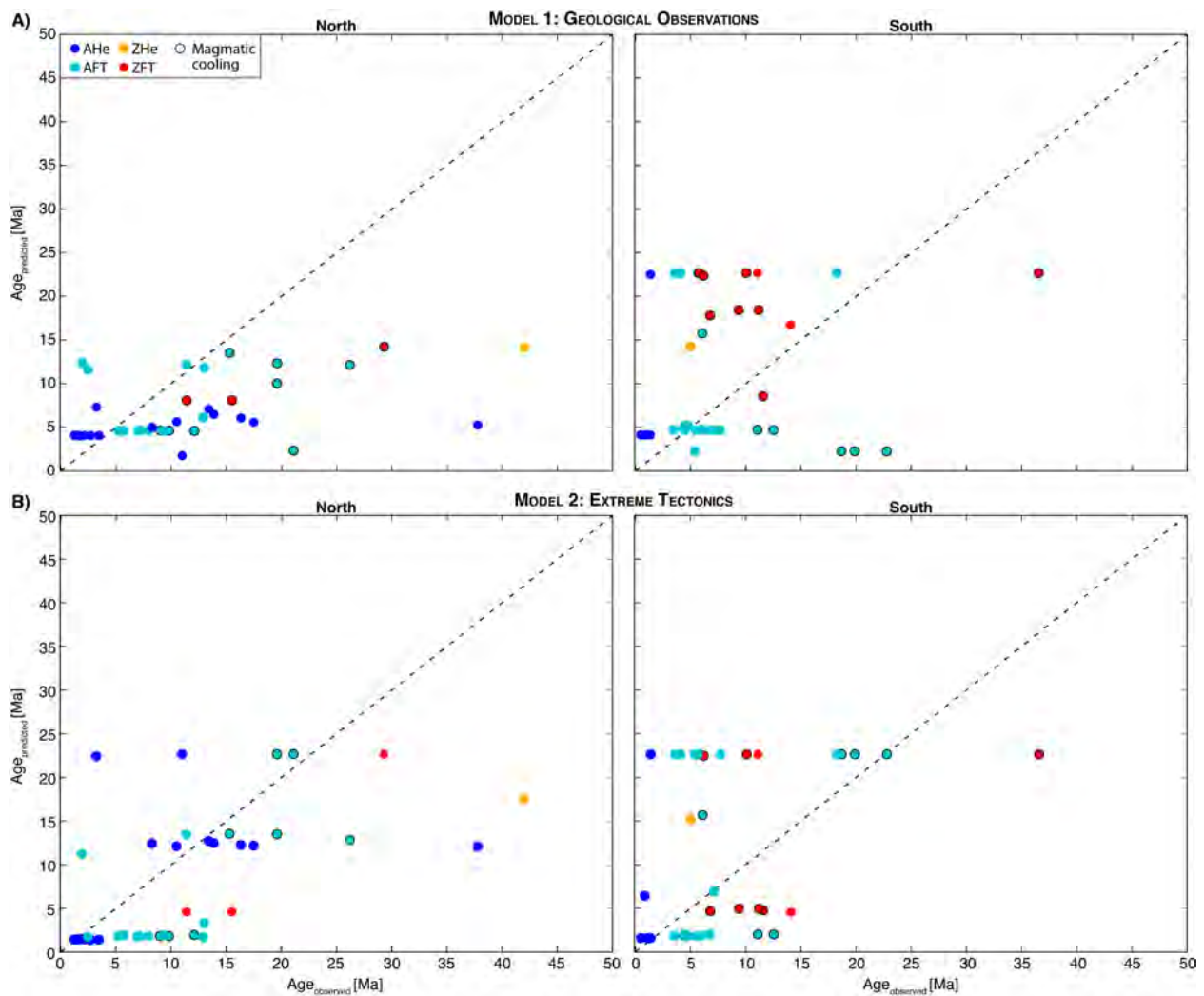
Figure 4.9: Observed versus predicted ages of the thermo-kinematic model using constant topography. See Appendix, supplementary Fig. C.1 for the case with evolving topography.

overestimated in the southern region. Hence, neither of the two tested models can explain the observed thermochronological ages in a satisfactory manner. The "geological observation" model generates to little tectonic uplift to reproduce the Pleistocene AHe data located in the hanging wall of F7, whereas fitting of the Pleistocene AHe data in the tectonic end-member model leads to an underestimation of the AFT and ZFT data. Furthermore, the mismatch between observed and predicted data is especially high in the southern area between 0 and 40 km distance to the San Ramón fault.

In a second step, we investigated more closely the Pleistocene AHe ages located in the hanging wall of F7 in the Principal Cordillera. Here, two age elevation profiles have been sampled for AHe
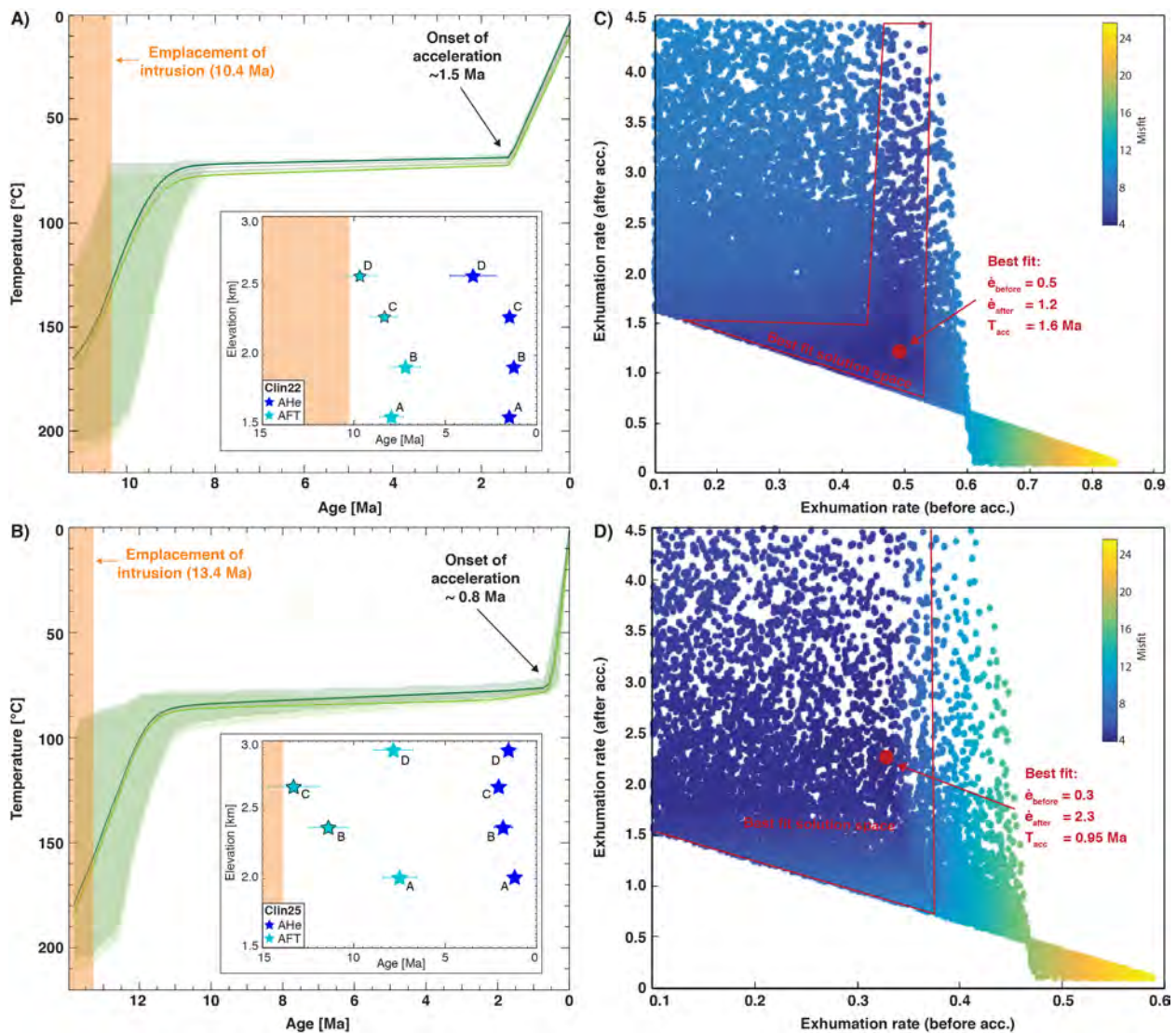
Figure 4.10: QTQt modelling results for (**A**) Clin22 (33.5° S; northern area) and (**B**) Clin25 (34.1° S; southern area) showing accelerated cooling in the middle Pleistocene. Insets show age-elevation profiles of the modelled AHe (blue stars) and AFT (light blue stars) ages. Stars with a black rim are close to the magmatic cooling age and have been excluded in the inversion of Chapter 2. **C,D)** 1D modelling results for the northern and southern areas.

and AFT over ~1 km elevation in the northern (33.5° S; Clin22A-D) and the southern (34.1° S; Clin25A-D) area (Appendix, Table C1). In the northern area, AFT ages lie between 7.1±0.8 and 9.8±1.0 and AHe between 1.2±0.3 and 3.5±1.2 Ma (Fig. 4.10). AFT ages for the southern region range between 6.7±1.0 and 12.5±1.4 Ma; AHe ages are between 0.5±0.2 and 1.4±0.2 Ma. Note that Clin22C,D and Clin25B,C are less than 2 Ma younger than the intrusion age and have been excluded in the thermochronological data compiled in Chapter 2. Since the timing of the intrusion

emplacement is accounted for in the QTQt and 1D model set-ups, all the data have been included here.

After an initial rapid cooling, most probably associated to the cooling of the intrusion, temperature-time paths derived from QTQt show very low cooling rates of ~1-1.5 °C/Ma until the late Pleistocene (Fig. 4.10 A,B). Most cooling takes place in the last 1.5 Ma (north) to 0.8 Ma (south), when cooling rates increase to around 40-50 and 90-100 °C/Ma, respectively. Assuming a geothermal gradient of 25 °C/km, as used in the 1D model (Table 4.2), estimated exhumation rates are in the order of 0.4-0.6 km/Ma before the Pleistocene and 1.9-3.8 km/Ma in the last 1.5 to 0.8 Ma. The 1D heat transport model shows a very similar result (Fig. 4.10 C,D). The best fitting inversion for the northern area predicts exhumation rates of 0.5 km/Ma before 1.6 Ma and 1.2 km/Ma since then (Fig. 4.10 C). In the southern area, exhumation rates accelerate from 0.3 km/Ma to 2.3 km/Ma at 0.95 Ma (Fig. 4.10 D).

Such a Pleistocene acceleration is not observed in the thermo-kinematic fault model, where predicted AFT and AHe data in the hanging wall of F7 show little differences and do not fit the observed ages. QTQt and the 1D model thus show cooling/exhumation histories that are not re-produced in the thermo-kinematic fault model scenarios.

4.5 Discussion and Conclusion

In Chapter 2, it has been shown that exhumation rates in the Chilean Andes between 33 and 36° S have increased from ~0.25 km/Ma in the Pliocene to more than 2 km/Ma in the Pleistocene (Fig. 4.1). These results are based on an inversion algorithm that searches for patterns in exhumation rates given the thermochronological ages (see Chap. 2 for details). Here, we have explicitly used the reconstructed fault activities observed in this region to predict thermochronological ages. This is done with a thermo-kinematic model in which two scenarios are tested, the "geological observation" and the "extreme tectonics" case.

Neither of the two tested scenarios in the thermo-kinematic fault model can satisfactorily fit the observed thermochronological data. Discrepancies between predicted and observed data may be explained by several factors. First, high uncertainties exist about the timing and magnitude of shortening accommodated by the individual faults and their position relative to the San Ramón fault. Dipping angles and fault geometries are largely unknown. These uncertainties are especially high in the southern region which was not investigated by Riesner (2017) and for which the fault locations had to be estimated. Second, the prescribed model scenarios are highly oversimplified. Only four out of seven faults are modelled, and their fault slip rates have been approximated by the average orogenic shortening rates derived from geological observations. Moreover, the timing of

the different fault activities has been simplified. Thirdly, the positions of some thermochronological samples relative to the modelled faults might be inaccurate. All these factors might lead to under- and overestimations of predicted ages and might explain parts of the mismatch between modelled and observed data. Finally, the modelling results also depend on the assumption of the crustal thermal structure, here mainly controlled by the temperature at 50 km depth, T_{bottom}, defining the geothermal gradient. Yet, although our thermo-kinematic model has severe limitations, these factors alone cannot explain the large discrepancies between modelled and observed data. In fact, the scenario "geological observations" fits relatively well the ZFT and AFT data in both areas, if ages located in the hanging wall of F2 (x = 18-40) in the southern area are ignored (Fig. 4.8A,B). These latter data might be fitted by moving the position of F7 further to the west, to a distance of ~30 km from the San Ramón fault. Such a more western position cannot be excluded because the structural setting of the southern area has not be investigated in detail and the exact position of F7 is unknown. Furthermore, underestimation of data located in the hanging wall of F4 could indicate that shortening accommodated by the San Ramón fault might have been less than prescribed in the model. Hence, data might be fitted better with a lower shortening rate than used in the model. This is not incompatible with geological observations that do not allow to estimate shortening rates with such high temporal resolution. One could therefore argue that the thermo-kinematic model of scenario 1 agrees with the thermochronological AFT and ZFT data during the Neogene until ca. 5 Ma; especially in the northern region. However, the model fails to correctly predict the Pleistocene AHe ages in both areas. Even if all shortening has been accommodated by F7 during the last 2.5 Ma, AHe ages in the southern area are still overestimated (Fig. 4.8C).

Thermochronological modelling of the two age-elevation profiles, located in the hanging wall of F7 in the eastern part of the Principal Cordillera, clearly show an increase in Pleistocene exhumation rates that exceeds one order of magnitude. This change in exhumation rates occurs at ~1.5 and 0.8-1.0 Ma and is surprisingly similar for the QTQt and the 1D model (Fig. 4.10). The result also corroborates the findings from Chapter 2, in which a Pleistocene increase from ~0.25 km/Ma to more than 2 km/Ma is documented (Fig. 4.1). Reconstructed fault kinematics from Riesner et al. (2018) do not show any geological evidence that shortening and tectonic activity was enhanced during the Pleistocene or that F7 was still active during this time. Hence, such a Pleistocene acceleration in exhumation cannot be explained by tectonic-induced rock uplift alone, even when uncertainties linked to the thermo-kinematic model described above are taken into account. It is therefore likely that the onset of glaciations and the change from 41 ka to 100 ka climatic oscillation in the mid-Pleistocene (~0.9 Ma; Lisiecki and Raymo, 2007) has played an important role on setting the Pleistocene exhumation rate.

The Andes between 33 and 36° S are located in an unique climatic and tectonic setting not observed elsewhere in South America. Influenced by the Westerlies, this region shows an important

climatic gradient from the north to the south, with almost twice as much precipitation in the south relative to the north. Since most precipitation falls during winter, it also experiences significant seasonal differences. Intensified winter precipitation and colder summers during glacial periods might have led to important glacial growth, while the more northern part of the Andes stayed too dry to establish significant glaciers. This is also expressed in the relief, which changes from a fluvial at ~32°S to a glacial landscape further south (see Chapter 1, Fig. 1.4). Climatic forcing might lead to changes in the rock uplift rates by a factor of 1.5 to 2 relative to steady state conditions in active tectonic settings (Whipple and Meade, 2006). The coupling between tectonic activity and climate change could thus explain the high exhumation rates observed in our study area. Our results show that tectonic-induced rock uplift alone cannot explain the observed thermochronological ages derived from own and literature data. While pre-Pleistocene exhumation rates might have been mainly set by erosion controlled by tectonic uplift, Pleistocene exhumation rates have been primarily set by glacial growth associated with increased precipitation and global cooling. The unique climatic and tectonic setting of the Chilean Andes between 33 and 36°S have led to the highest exhumation rates observed in the Central Andes.

Bibliography

Armijo, R., Rauld, R., Thiele, R., Vargas, G., Campos, J., Lacassin, R., and Kausel, E. (2010). The West Andean thrust, the San Ramon fault, and the seismic hazard for Santiago, Chile. *Tectonics*, 29(2).

Barrientos, S., Vera, E., Alvarado, P., and Monfret, T. (2004). Crustal seismicity in central Chile. *J. South Am. Earth Sci.*, 16(8):759–768.

Beaumont, C., Fullsack, P., and Hamilton, J. (1992). Erosional control of active compressional orogens. In *Thrust tectonics*, pages 1–18. Springer.

Becker, J.J., Sandwell, D.T., Smith, W.H.F., Braud, J., Binder, B., Depner, J.L., Fabre, D., Factor, J., Ingalls, S., Kim, S.H., et al. (2009). Global bathymetry and elevation data at 30 arc seconds resolution: SRTM30_PLUS. *Mar. Geod.*, 32(4):355–371.

Berner, R.A., Lasaga, A.C., and Garrels, R.M. (1983). The carbonate-silicate geochemical cycle and its effect on atmospheric carbon dioxide over the past 100 million years. *Am. J. Sci.*, 283:641–683.

Champagnac, J.D., Molnar, P., Sue, C., and Herman, F. (2012). Tectonics, climate, and mountain topography. *J. Geophys. Res.: Solid Earth*, 117.

Charrier, R., Baeza, O., Elgueta, S., Flynn, J.J., Gans, P., Kay Mahlburg, S., Muñoz, N., Wyss, A.R., and Zurita, E. (2002). Evidence for Cenozoic extensional basin development and tectonic inversion south of the flat-slab segment, southern Central Andes, Chile (33°-36° S.L.). *J. South Am. Earth Sci.*, 15(1):117–139.

Dahlen, F.A. and Suppe, J. (1988). Mechanics, growth, and erosion of mountain belts. *Geol. Soc. Am. Spec. Pap.*, 218:161–178.

Gallagher, K. (2012). Transdimensional inverse thermal history modeling for quantitative thermochronology. *J. Geophys. Res.: Solid Earth*, 117(B2).

Ganti, V., von Hagke, C., Scherler, D., Lamb, M.P., Fischer, W.W., and Avouac, J.P. (2016). Time scale bias in erosion rates of glaciated landscapes. *Sci. Adv.*, 2(e1600204).

García, V.H. and Casa, A.L. (2014). Quaternary tectonics and seismic potential of the Andean retrowedge at 33-34° S. In Sepúlveda, S., Giambiagi, L.B., Moreiras, S.M., Pinto, L., Tunik, M., Hoke, G.D., and Farías, M., editors, *Geodynamic Processes in the Andes of Central Chile and Argentina*, pages 311–327. Geol. Soc. London Spec. Pub., 399.

Gautheron, C., Tassan-Got, L., Barbarand, J., and Pagel, M. (2009). Effect of alpha-damage annealing on apatite (U–Th)/He thermochronology. *Chem. Geol.*, 266(3):157–170.

Giambiagi, L., Mescua, J., Bechis, F., Tassara, A., and Hoke, G. (2012). Thrust belts of the southern Central Andes: Along-strike variations in shortening, topography, crustal geometry, and denudation. *Geol. Soc. Am. Bull.*, 124(7-8):1339–1351.

Giambiagi, L., Tassara, A., Mescua, J., Tunik, M., Alvarez, P.P., Godoy, E., Hoke, G., Pinto, L., Spagnotto, S., Porras, H., Tapia, F., Jara, P., Bechis, F., Garcìa, V.H., Suriano, J., Moreiras, S.M., and Pagano, S.D. (2015). Evolution of shallow and deep structures along the maipo–tunuyán transect (33° 40' S): from the Pacific coast to the An-

dean foreland. *Geol. Soc. London. Spec. Pub.*, 399(1):63–82.

Giambiagi, L.B. and Ramos, V.A. (2002). Structural evolution of the Andes in a transitional zone between flat and normal subduction (33°30'-33°45'S), Argentina and Chile. *J. S. Am. Earth Sci.*, 15(1):101–116.

Giambiagi, L.B., Ramos, V.A., Godoy, E., Alvarez, P.P., and Orts, S. (2003). Cenozoic deformation and tectonic style of the Andes, between 33° and 34° south latitude. *Tectonics*, 22(4).

Giambiagi, L.B., Tunik, M.A., and Ghiglione, M. (2001). Cenozoic tectonic evolution of the alto tunuyán foreland basin above the transition zone between the flat and normal subduction segment (33°30'-34°s), western argentina. *J. S. Am. Earth Sci.*, 14(7):707–724.

Godoy, E., Yañez, G., and Vera, E. (1999). Inversion of an Oligocene volcano-tectonic basin and uplifting of its superimposed Miocene magmatic arc in the central Chilean Andes: first seismic and gravity evidences. *Tectonophysics*, 306:217–236.

GTOPO30 (1997). *USGS 30 ARC-second Global Elevation Data, GTOPO30.* Earth Resources Observation and Science Center, U.S. Geological Survey. Data downloaded Nov. 2015 from https://earthexplorer.usgs.gov.

Hay, W.W. (1996). Tectonics and climate. *Geol. Rundsch.*, 85(3):409–437.

Herman, F. and Champagnac, J. (2016). Plio-Pleistocene increase of erosion rates in mountain belts in response to climate change. *Terra Nova*, 28(1):2–10.

Herman, F., Copeland, P., Avouac, J.P., Bollinger, L., Mahéo, G., Le Fort, P., Rai, S., Foster, D., Pêcher, A., Stüwe, K., et al. (2010). Exhumation, crustal deformation, and thermal structure of the Nepal Himalaya derived from the inversion of thermochronological and thermobarometric data and modeling of the topography. *J. Geophys. Res.: Solid Earth*, 115(B6).

Herman, F., Seward, D., Valla, P.G., Carter, A., Kohn, B., Willett, S.D., and Ehlers, T.A. (2013). Worldwide acceleration of mountain erosion under a cooling climate. *Nature*, 504(7480):423–426.

Irigoyen, M.V., Buchan, K.L., and Brown, R.L. (2000). Magnetostratigraphy of Neogene Andean foreland-basin strata, lat 33°S, Mendoza Province, Argentina. *Geol. Soc. Am. Bull.*, 112(6):803–816.

Ketcham, R.A., Carter, A., Donelick, R.A., Barbarand, J., and Hurford, A.J. (2007). Improved modeling of fission-track annealing in apatite. *American Mineralogist*, 92(5-6):799–810.

Koons, P.O. (1990). Two-sided orogen: Collision and erosion from the sandbox to the Southern Alps, New Zealand. *Geology*, 18(8):679–682.

Lisiecki, L.E. and Raymo, M.E. (2005). A Pliocene-Pleistocene stack of 57 globally distributed benthic $\delta\,^{18}O$ records. *Paleoceanography*, 20(1).

Lisiecki, L.E. and Raymo, M.E. (2007). Plio-Pleistocene climate evolution: trends and transitions in glacial cycle dynamics. *Quat. Sci. Rev.*, 26(1-2):56–69.

Molnar, P. (2004). Late cenozoic increase in accumulation rates of terrestrial sediment: How might climate change have affected erosion rates? *Annu. Rev. Earth Planet. Sci.*, 32:67–89.

Molnar, P. (2009). The state of interactions among tectonics, erosion, and climate: A polemic. *GSA Today*, 19(7):44–45.

Molnar, P. and England, P. (1990). Late Cenozoic Uplift of Mountain-Ranges and Global Climate

Change – Chicken or Egg. *Nature*, 346(6279):29–34.

Montgomery, D.R., Balco, G., and Willett, S.D. (2001). Climate, tectonics, and the morphology of the Andes. *Geology*, 29(7):579–582.

Nyström, J.O., Vergara, M., Morata, D., and Levi, B. (2003). Tertiary volcanism during extension in the Andean foothills of central Chile (33°15'-33°45'). *Geol. Am. Soc. Bull.*, 115(12):1523–1537.

Porras, H., Pinto, L., Tunik, M., Giambiagi, L., and Deckart, K. (2016). Provenance of the miocene alto tunuyán basin (33° 40' S, Argentina) and its implications for the evolution of the Andean Range: Insights from petrography and U–Pb LA–ICPMS zircon ages. *Tectonophysics*, 690:298–317.

Ramos, V.A., Cegarra, M., and Cristallini, E. (1996). Cenozoic tectonics of the High Andes of west-central Argentina (30-36° S latitude). *Tectonophysics*, 259(1):185–200.

Ramos, V.A., Zapata, T., Cristallini, E., and Introcaso, A. (2004). The Andean thrust system: latitudinal variations in structural styles and orogenic shortening. In Mcclay, K.R., editor, *Thrust Tectonics and Hydrocarbon Systems*, pages 30–50. American Association of Petroleum Geology.

Raymo, M.E. and Ruddiman, W.F. (1992). Tectonic Forcing of Late Cenozoic Climate. *Nature*, 359(6391):117–122.

Reiners, P.W., Ehlers, T.A., Mitchell, S.G., and Montgomery, D.R. (2003). Coupled spatial variations in precipitation and long-term erosion rates across the Washington Cascades. *Nature*, 426(6967):645–647.

Riesner, M. (2017). *Évolution tectonique des Andes centrales (33°S): implications sur la mécanique des chaînes de subduction*. PhD thesis, Institut de Physique du Globe de Paris (IPGP).

Riesner, M., Lacassin, R., Simoes, M., Armijo, R., Rauld, R., and Vargas, G. (2017). Kinematics of the active west Andean fold-and-thrust belt (Central Chile): Structure and long-term shortening rate. *Tectonics*, 36(2):287–303.

Riesner, M., Lacassin, R., Simoes, M., Carrizo, D., and Armijo, R. (2018). Revisiting the crustal structure and kinematics of the central Andes at 33.5°S: Implications for the Mechanics of Andean Mountain Building. *Tectonics*, 37:1347–1375.

Riesner, M., Simoes, M., Carrizo, D., and Lacassin, R. (2019). Early exhumation of the Frontal Cordillera (Southern Central Andes) and implications for Andean mountain-building at ~33.5°S. *Sci. Rep.*, 9(1):1–10.

Suppe, J. (1983). Geometry and kinematics of fault-bend folding. *Am. J. Sci.*, 283(7):684–721.

Vargas, G., Klinger, Y., Rockwell, T.K., Forman, S.L., Rebolledo, S., Baize, S., Lacassin, R., and Armijo, R. (2014). Probing large intraplate earthquakes at the west flank of the Andes. *Geology*, 42(12):1083–1086.

von Blanckenburg, F., Bouchez, J., Ibarra, D.E., and Maher, K. (2015). Stable runoff and weathering fluxes into the oceans over Quaternary climate cycles. *Nat. Geosci.*, 8(7):538–542.

Whipple, K.X. (2009). The influence of climate on the tectonic evolution of mountain belts. *Nat. Geosci.*, 2(2):97–104.

Whipple, K.X. and Meade, B.J. (2006). Orogen response to changes in climatic and tectonic forcing. *Earth Planet. Sci. Lett.*, 243:218–228.

Willenbring, J.K. and Jerolmack, D.J. (2016). The null hypothesis: globally steady rates of erosion, weathering fluxes and shelf sediment accumulation during Late Cenozoic mountain uplift and

glaciation. *Terra Nova*, 28(1):11–18.

Willenbring, J.K. and von Blanckenburg, F. (2010). Long–term stability of global erosion rates and weathering during late–Cenozoic cooling. *Nature*, 465(7295):211–214.

Willett, S.D. (1999). Orogeny and orography: The effects of erosion on the structure of mountain belts. *J. Geophys. Res.*, 104((B12)):28957–28981.

Zhang, P.Z., Molnar, P., and Downs, W.R. (2001). Increased sedimentation rates and grain sizes 2-4 Myr ago due to the influence of climate change on erosion rates. *Nature*, 410(6831):891–897.

CHAPTER 5 ■

Conclusion

In this thesis, I use thermochronology as a tool to better understand the exhumation history of the Central Andes and to draw conclusions about the relationships between exhumation, climate and tectonics on different temporal and spatial scales.

Although many numerical models and analogue experiments have investigated the relationships between the tectonic evolution of mountain belts and climate-modulated erosion (e.g., Dahlen and Suppe, 1988; Willett, 1999), validation of these concepts through field studies remains challenging (Whipple, 2009, 2014). The objective of Chapter 2 is to provide field evidence about the role of climate and tectonics on the exhumation rate on the spatial scale of a mountain belt and on a Ma-time scale, using the Central Andes (18-36° S) as a natural laboratory. To do so, I have modelled the exhumation rate history of the Central Andes during the last 80 Ma using the inversion method described in Fox et al. (2014) and modified by Herman and Brandon (2015). The inversion is based on a literature compilation of 744 thermochronological ages (AHe, AFT, ZHe, ZFT; 543 samples) and 238 new ages (AHe, AFT, ZHe; 146 samples) that were collected in Chile during three field campaigns. Furthermore, I have reviewed current knowledge about the past and present South American climate and compiled the onset and duration of tectonic activity from syn-tectonic sediments observed in the different structural units of the Central Andes. This framework has allowed me to compare changes in the modelled exhumation rates with observed changes in climatic and tectonic conditions. I find that the onset of exhumation correlates well with the on-set of tectonic activity and major crustal thickening, and that the climate strongly influences the magnitude of the exhumation rate. Exhumation rates in the Central Andes vary most commonly between 0.05 km/Ma and 0.25 km/Ma with important regional exceptions. In the Western Cordillera in the north-western part of the Andes, (hyper-)aridity and primarily low shortening rates result in very low exhumation rates that do not exceed 0.2 km/Ma during the Cretaceous and Cenozoic. In the Eastern Cordillera and in the Inter- and Subandean belts east of the Andean range crest,

the subsequent onset and eastward propagation of deformation is reflected in the observed ex-humation rate patterns, whereas accelerated erosion since the Miocene is probably connected to the establishment of the South American Monsoon system bringing high precipitation to the eastern flank of the Andes. A strong influence of climate on erosion rates is also observed in the Principal Cordillera in the south-western part of the Andes. Here, increased Plio-Pleistocene ero-sion rates are most probably associated with intense glacial erosion and enhanced precipitation related to a northward expansion of the mid-latitude storm-tracks during glacial periods. Higher Plio-Pleistocene erosion rates are also observed in the Sierra Aconquíja, where high precipitation is combined with active tectonics accommodated along steep, reactivated normal faults.

The results from Chapter 2 seem to indicate that tectonic activity and crustal thickening sustain a background erosion rate by setting the topography and rock-uplift rate, which is then modulated by regional climatic conditions. For instance, diminished precipitation in the Atacama Desert leads to low erosion rates, whereas enhanced precipitation and glaciations in the Principal Cordillera sustain high erosion rates. Yet, any conclusions about the role of erosion on tectonic activity and climate change predicted by the critical wedge theory are hindered by the high uncertainties in the tectonic and climatic records and the low temporal resolutions. For instance, I could not ob-serve any tectonic response to increased exhumation rates suggested in numerical and analogue experiments (e.g., out-of-sequence thrusting or retreat of the deformation front to the interior of the orogen). The different tectonic settings in the northern and southern parts also impede the establishment of correlations between the morphology of the Andes and the climatic setting.

Furthermore, the influence of Late Cenozoic cooling on erosion rates remains debated due to several studies that have questioned the techniques used to quantify erosion rates and how erosion rate measurements can be compared across timescales (e.g., Schumer and Jerolmack, 2009; Willenbring and von Blanckenburg, 2010; Ganti et al., 2016). In Chapters 3 and 4, I con-tribute to this debate by further exploring the role of climate and tectonics on erosion on a smaller spatial scale (km). In particular, I provide new evidence for the idea that global cooling and the onset of glaciations have had a significant impact on the magnitude of late Cenozoic erosion rates in mountainous regions. To do so, I focus on the southern part of the Chilean Andes (33-35° S), where the new AHe data from Chapter 2 imply a significant acceleration in Plio-Pleistocene ero-sion. This region is characterized by an important N-S precipitation gradient that connects the arid Atacama Desert in the north with humid conditions of Patagonia in the south, and by an active tectonic setting that has recently been investigated by Riesner et al. (2017, 2018).

In Chapter 3, I apply thermoluminescence thermochronology (TLT) to eleven samples from Chapter 2 and inversely model them to extract time series of erosion rates over the Quaternary. To better understand the sensitivity of the new technique and the inverse model, I conduct a series of

synthetic tests which show that the method can recover the pattern of erosion rate changes, but that the timing and magnitude of the change might not be accurate. The ability to constrain continuous erosion rates rather than averaged rates over time intervals dictated by thermochronological age differences allows me to compare Quaternary erosion rates over the last glacial-interglacial cycle with rates derived from ^{10}Be and sediment yield measurements, without introducing a time scale bias (e.g., Ganti et al., 2016). TLT-derived erosion rates in the Principal Cordillera are highest during the last glacial maximum (40-60 mm/yr) and then slow down to ~4 mm/yr. This result suggests that glaciations and increased precipitation have a significant impact on erosion rates and documents the transient nature of Quaternary erosion.

Finally, the high Plio-Pleistocene erosion rates observed in the Chilean Andes between 33 and 36° S might also be explained by tectonic-induced rock uplift rather than climate change. Therefore in Chapter 4, I further explore the respective contributions of climate-modulated erosion and tectonic-induced rock uplift on exhumation in this region. Thermochronological ages (AHe, AFT, ZHe, ZFT) from the region between 33 and 34.5° S are predicted with a modified version of the 2D thermo-kinematic model developed by Riesner (2017) and compared to the observed ages. The thermo-kinematic model accounts for the role of fault kinematics on the geothermal field and exhumation rate. Using the fault activities constrained by Riesner et al. (2017, 2018), I show that tectonic rock-uplift alone cannot correctly predict the observed thermochronological ages. Furthermore, QTQt modelling (Gallagher, 2012) and a simple 1D model applied on two new age-elevations profiles from Chapter 2 (AHe and AFT data) document an increase in erosion rates by an order of magnitude during the Pleistocene. Since there is no geological evidence that tectonic activity increased during this time, the results from Chapter 4 reinforce the interpretations from Chapters 2&3 about the importance of climate on setting Late Cenozoic erosion rates in mountainous regions.

Bibliography

Dahlen, F.A. and Suppe, J. (1988). Mechanics, growth, and erosion of mountain belts. *Geol. Soc. Am. Spec. Pap.*, 218:161–178.

Fox, M., Herman, F., Willett, S.D., and May, D.A. (2014). A linear inversion method to infer exhumation rates in space and time from thermochronometric data. *Earth Surf. Dyn.*, 2(1):47.

Gallagher, K. (2012). Transdimensional inverse thermal history modeling for quantitative thermochronology. *J. Geophys. Res.: Solid Earth*, 117(B2).

Ganti, V., von Hagke, C., Scherler, D., Lamb, M.P., Fischer, W.W., and Avouac, J.P. (2016). Time scale bias in erosion rates of glaciated landscapes. *Sci. Adv.*, 2(e1600204).

Herman, F. and Brandon, M. (2015). Mid-latitude glacial erosion hotspot related to equatorial shifts in southern Westerlies. *Geology*, 43(11):987–990.

Riesner, M. (2017). *Évolution tectonique des Andes centrales (33°S): implications sur la mécanique des chaînes de subduction*. PhD thesis, Institut de Physique du Globe de Paris (IPGP).

Riesner, M., Lacassin, R., Simoes, M., Armijo, R., Rauld, R., and Vargas, G. (2017). Kinematics of the active west Andean fold-and-thrust belt (Central Chile): Structure and long-term shortening rate. *Tectonics*, 36(2):287–303.

Riesner, M., Lacassin, R., Simoes, M., Carrizo, D., and Armijo, R. (2018). Revisiting the crustal structure and kinematics of the central Andes at 33.5°S: Implications for the Mechanics of Andean Mountain Building. *Tectonics*, 37:1347–1375.

Schumer, R. and Jerolmack, D.J. (2009). Real and apparent changes in sediment deposition rates through time. *J. Geophys. Res.: Earth Surf.*, 114(F3).

Whipple, K.X. (2009). The influence of climate on the tectonic evolution of mountain belts. *Nat. Geosci.*, 2(2):97–104.

Whipple, K.X. (2014). Can erosion drive tectonics? *Science*, 346(6212):918–919.

Willenbring, J.K. and von Blanckenburg, F. (2010). Long–term stability of global erosion rates and weathering during late–Cenozoic cooling. *Nature*, 465(7295):211–214.

Willett, S.D. (1999). Orogeny and orography: The effects of erosion on the structure of mountain belts. *J. Geophys. Res.*, 104((B12)):28957–28981.

CHAPTER 6 ■

Perspectives

This thesis provides a framework for the tectonic, climatic and erosional evolution of the Central Andes and discusses several aspects about the influence of climate and tectonic activity on erosion rates. This work also offers new perspectives and open questions for future research in the Central Andes and for studies investigating the relationships between climate, tectonic and erosion, which are outlined below.

6.1 Relations between climate, tectonics and erosion

The interactions between climate, tectonics and erosion act on a global-scale and thus also require long-term, orogen-to-global scale investigations. Yet, dealing with such a large region as the Central Andes has made it necessary to reduce the complexity of the feedback mechanisms to three principal factors: tectonic activity, represented by the onset, magnitude and duration of compression or extension, paleoclimate, represented by the amount of precipitation and glaciations, and exhumation representing erosion. This has led to the negligence of other key parameters influencing the Earth's topography such as vegetation cover (e.g., Acosta Torres et al., 2015; Starke et al., 2020), dynamic mantle processes (e.g., Braun, 2010), relief construction and destruction (e.g., Champagnac et al., 2014) or erosional thresholds (e.g., Carretier et al., 2013). For instance, it would be interesting to investigate more closely possible correlations between erosion rates and geomorphological features observed in the Central Andes, or to look deeper into the paleogeography and paleotopographic evolution of the Andean orogen.

Many uncertainties also remain considering the correlation between tectonic activities, paleoclimate, and exhumation rates established in this work. This is partially due to the low temporal resolution when reconstructing these parameters in geological time. Paleoclimate reconstructions on Myr-time scales mainly rely on sedimentary features, pollen analyses and $\delta^{18}O$ records de-

rived from the sedimentary archives. Studies quantifying tectonic activities also rely on the sedimentary record and, more recently, on thermochronological data. Tectonic studies that use thermochronometry often equal a thermochronometric signal with tectonic activity, neglecting the climate as exhumation component. If exhumation is quantified by thermochronology, as in this work, the use of these studies introduces circularity when investigating the links between exhumation and tectonics. Hence, the resolution of the climatic and tectonic histories largely depend on the availability and preservation of the sedimentary records, which are especially sparse on the western side of the Andes. Furthermore, although many new thermochronological ages have been produced in this study, some tectonic units only contain little data, as for instance the Precordillera or the Frontal Cordillera, and the resolution of the exhumation rate depends heavily on how many thermochronometric systems have been analyzed per sample and on their thermochronological age differences. More data will improve the exhumation rate histories in certain areas, but not necessarily its resolution.

In field studies, any conclusion about the interactions between climate, tectonics and erosion predicted by the critical wedge theory are strongly limited by the data coverage. Obviously, these limitations will also be encountered in other study areas of similar size and it might be wiser, although eventually not more appropriate when studying large-scale interactions, to focus on smaller regions that have well constrained settings. More studies that test specific model predictions with high data resolution are needed to better understand the interactions between climate, tectonics and erosion (e.g., Whipple, 2009, 2014).

6.2 Thermoluminescence thermochronology

In Chapter 3, I have successfully applied a recently developed thermochronometer (TLT) (Biswas et al., 2018) to samples in the Chilean Andes. To better understand the sensitivity of the technique and the inverse model, I have conducted a series of synthetic tests that show that step-function decreases and oscillating erosion rates can be relatively well recovered. However, the results from the synthetic tests with step-function increases in erosion rates were less promising. These could be tested more thoroughly with different parameters. For example, higher geothermal gradients or higher erosion rates will significantly increase the fit of the synthetic data, and applications of TLT in regions with high geothermal gradients will lead to better results.

Regarding the study area, it would be interesting to apply TLT to samples that are located outside of the formerly glaciated area. This would allow a direct comparison of fluvial and glacial erosion rates under similar amounts of precipitation and similar tectonic activity. It would also be interesting to apply TLT in a region where the limit of the glacial extent and the timing of the last

glacial maximum is better constrained, as for example in the Chilean Lake district (~40° S) or the Sierra Aconquíja in Argentina.

6.3 Thermo-kinematic modelling

Finally, in Chapter 4, I have investigated the respective contributions of tectonic-induced rock-uplift and climate-modulated erosion. I have shown that the thermochronological data cannot be fitted with the model set-up used in this study. Yet it remains unclear if the data could be better fitted with a different set of parameters and a different fault geometry. For example, the effects of the dipping angles of the crustal ramp and the individual faults could be tested, and the timing and shortening rates could be varied more rigorously. Moreover, the fault positions relative to the thermochronological samples could be adjusted, especially in the southern part where the locations of the individual faults are not constrained. Once a "best-fit" model is found that explains most of the pre-(Plio-)Pleistocene thermochronological data while respecting the geological observations, a second advection component representing erosional unloading (i.e., decreasing topography) during the Plio-Pleistocene could be added to the model. The total erosion rate, $\dot{e}$, would then be composed of a tectonic component, $\dot{e}_{tectonic}$, and a climate component, $\dot{e}_{climate}$, which would directly quantify the respective roles of tectonic-induced rock uplift and climate on the exhumation rate.

Bibliography

Acosta Torres, V., Schildgen, T.F., Clarke, B.A., Scherler, D., Bookhagen, B., Wittmann, H., von Blanckenburg, F., and Strecker, M.R. (2015). Effect of vegetation cover on millennial-scale landscape denudation rates in East Africa. *Lithosphere*, 7(4):408–420.

Biswas, R.H., Herman, F., King, G.E., and Braun, J. (2018). Thermoluminescence of feldspar as a multi-thermochronometer to constrain the temporal variation of rock exhumation in the recent past. *Earth Planet. Sci. Lett.*, 495:56–68.

Braun, J. (2010). The many surface expressions of mantle dynamics. *Nat. Geosci.*, 3(12):825–833.

Carretier, S., Regard, V., Vassallo, R., Aguilar, G., Martinod, J., Riquelme, R., Pepin, E., Charrier, R., Hérail, G., Farías, M., et al. (2013). Slope and climate variability control of erosion in the Andes of central Chile. *Geology*, 41(2):195–198.

Champagnac, J.D., Valla, P.G., and Herman, F. (2014). Late-Cenozoic relief evolution under evolving climate: A review. *Tectonophysics*, 614:44–65.

Starke, J., Ehlers, T.A., and Schaller, M. (2020). Latitudinal effect of vegetation on erosion rates identified along western South America. *Science*, 367(6484):1358–1361.

Whipple, K.X. (2009). The influence of climate on the tectonic evolution of mountain belts. *Nat. Geosci.*, 2(2):97–104.

Whipple, K.X. (2014). Can erosion drive tectonics? *Science*, 346(6212):918–919.

APPENDIX A ■

Supplementary Tables, Chapter 2

A1. AHe Data

A2. ZHe Data

A3. AFT Data

A4. U-Pb Data

A6. Deformation history

Tables **A5. Thermochronological data compilation** and **A7. Igneous data compilation** are provided in electronic form only

A1. AHe Data

Table A1: Apatite (U-Th)/He data with average and standard deviation for each sample. Rejected ages are in Italic. Intrusion ages refer to the closest U-Pb, K-Ar or Ar-Ar age from the same lithology (see numbers for references, provided at the end of the thermochronological data tables). Rock compositions result from field observations and are thus approximative. Tectonic units: CC = Coastal Cordillera, CD = Central Depression, FC = Frontal Cordillera, PC = Principal Cordillera.

Sample	Lon	Lat	Elev.	Lithology	Tect. unit	^{4}He	± 1σ	± 1σ	U	Th	Sm	U	Th	Sm	eU	F_T	F_T	R_s	Raw Age	± 2σ	Corr. Age	± 1σ	6% err
	(°)	(°)	(m)			(pmol)	(pmol)	(%)	(ng)	(ng)	(ng)	(ppm)	(ppm)	(ppm)	(ppm)	^{238}U	^{232}Th	(μm)	(Ma)	(Ma)	(Ma)	(Ma)	(Ma)
14NC01_Ap1						0.0237	0.0003	1.4	0.1841	0.3615	0.5433	72.74	142.81	214.64	107.16	0.730	0.693	52.66	16.25	0.58	**22.6**	**0.4**	1.4
14NC01_Ap2						0.0227	0.0003	1.4	0.2318	0.3915	0.5353	110.60	186.77	255.34	155.51	0.687	0.646	44.86	12.96	0.46	**19.2**	**0.3**	1.2
14NC01_Ap3						0.0063	0.0001	1.8	0.1019	0.0190	0.0837	65.74	12.27	54.03	68.87	0.679	0.636	43.57	10.90	0.50	**16.1**	**0.4**	1.0
14NC01	**-70.369**	**-29.834**	**1460**	**Felsic Intrusive (288.2 Ma U-Pb[1])**	**FC**																**19.3**	**3.3**	
14NC03_Ap1						0.0026	0.0001	2.9	0.0256	0.0276	2.1330	4.72	5.09	393.60	7.76	0.773	0.741	63.47	14.11	0.88	**18.2**	**0.6**	1.1
14NC03_Ap2						0.0027	0.0001	2.1	0.0396	0.0128	1.1359	14.77	4.80	423.98	17.89	0.700	0.660	46.97	11.46	0.57	**16.3**	**0.4**	1.0
14NC03_Ap3						0.0007	0.0001	7.2	0.0142	0.0131	0.7612	7.36	6.77	393.41	10.79	0.709	0.670	48.65	7.15	1.05	**10.0**	**0.7**	0.6
14NC03	**-70.499**	**-29.854**	**1057**	**Felsic Intrusive (291.2 Ma U-Pb[1])**	**FC**																**14.8**	**4.3**	
14NC05_Ap1						0.0028	0.0001	1.9	0.0254	0.0648	0.6782	7.67	19.60	205.07	13.22	0.736	0.700	54.00	12.62	0.54	**17.4**	**0.4**	1.0
14NC05_Ap2						0.0067	0.0001	1.9	0.0518	0.1200	1.7242	7.80	18.06	259.47	13.24	0.790	0.760	68.94	15.14	0.65	**19.4**	**0.4**	1.2
14NC05_Ap3						0.0024	0.0001	3.5	0.0298	0.0663	0.8350	8.11	18.02	227.07	13.39	0.750	0.715	57.22	9.61	0.71	**13.0**	**0.5**	0.8
14NC05	**-70.519**	**-30.018**	**976**	**Felsic Intrusive (291.2 Ma U-Pb[1])**	**FC**																**16.6**	**3.3**	
14NC06_Ap1						0.0281	0.0004	1.3	0.5443	0.4062	1.1425	104.20	77.77	218.71	123.42	0.784	0.754	67.10	8.13	0.28	**10.4**	**0.2**	0.6
14NC06_Ap2						0.0758	0.0009	1.2	1.1126	1.1466	3.0418	70.51	72.66	192.77	88.42	0.846	0.824	95.60	10.13	0.34	**12.0**	**0.2**	0.7
14NC06_Ap3						0.0988	0.0012	1.2	1.2641	1.2636	2.8659	83.40	83.36	189.07	103.80	0.849	0.827	97.66	11.70	0.39	**13.9**	**0.2**	0.8
14NC06	**-70.631**	**-30.026**	**732**	**Felsic Intrusive (62.4 Ma[2])**	**PC**																**12.1**	**1.7**	
14NC08_Ap1						0.0942	0.0031	3.3	0.4091	0.5642	6.0789	20.77	28.65	308.69	28.93	0.847	0.825	96.34	31.69	2.23	**37.6**	**1.3**	2.3
14NC08_Ap2						0.1056	0.0035	3.3	0.4094	0.6298	8.3528	18.22	28.03	371.82	26.53	0.848	0.827	97.35	34.39	2.42	**40.7**	**1.4**	2.4
14NC08_Ap3						0.0900	0.0030	3.3	0.3730	0.4129	5.7135	25.68	28.43	393.38	34.19	0.874	0.856	117.93	34.85	2.46	**40.0**	**1.4**	2.4
14NC08	**-71.066**	**-29.983**	**212**	**Felsic Intrusive (95 Ma K-Ar[3])**	**CC**																**39.4**	**1.6**	
14NC10_Ap1						0.0057	0.0000	0.9	0.0291	0.0627	1.1992	13.17	28.34	542.31	22.35	0.722	0.684	51.00	23.28	0.64	**32.6**	**0.4**	2.0
14NC10_Ap2						0.0070	0.0001	0.9	0.0560	0.0790	1.3494	23.05	32.50	555.41	33.26	0.710	0.671	48.68	17.10	0.50	**24.3**	**0.4**	1.5
14NC10_Ap3						0.0035	0.0000	1.1	0.0164	0.0506	0.4962	9.33	28.82	282.64	17.41	0.702	0.662	47.36	22.67	0.74	**32.9**	**0.5**	2.0
14NC10	**-70.976**	**-29.649**	**950**	**Felsic Intrusive (89-109.5 Ma K-Ar[3])**	**CC**																**29.9**	**4.9**	
14NC12_Ap1						0.0036	0.0001	2.3	0.0275	0.0861	1.1721	7.09	22.16	301.72	13.69	0.783	0.752	66.56	13.54	0.68	**17.5**	**0.4**	1.0
14NC12_Ap2						0.0057	0.0001	1.9	0.0457	0.1590	2.6289	7.04	24.48	404.81	14.67	0.802	0.775	73.67	12.20	0.52	**15.4**	**0.3**	0.9
14NC12_Ap3						0.0042	0.0001	2.2	0.0382	0.1381	1.9710	9.71	35.11	500.90	20.28	0.785	0.756	67.50	10.63	0.50	**13.7**	**0.3**	0.8
14NC12	**-70.666**	**-29.749**	**1875**	**Felsic Intrusive (48 - 55.6 Ma K-Ar[4])**	**PC**																**15.5**	**1.9**	
14NC14_Ap2						0.0026	0.0001	2.8	0.0294	0.0425	0.6898	10.66	15.41	250.00	15.44	0.757	0.724	59.14	12.11	0.73	**16.1**	**0.5**	1.0
14NC14_Ap3						0.0048	0.0001	1.7	0.0369	0.0589	0.2225	22.21	35.47	134.03	31.14	0.723	0.686	51.27	17.44	0.71	**24.5**	**0.5**	1.5
14NC14	**-70.263**	**-29.977**	**1599**	**Felsic Intrusive (288.2 Ma U-Pb[1])**	**FC**																**20.3**	**5.9**	
14NC15_Ap1						0.0489	0.0006	1.2	0.2695	0.9418	1.4382	82.08	286.86	438.03	151.26	0.721	0.684	50.92	18.34	0.59	**26.0**	**0.4**	1.6
14NC15_Ap2						0.0338	0.0004	1.3	0.2087	0.5575	1.2838	54.58	145.79	335.70	90.27	0.770	0.738	62.58	18.28	0.59	**24.1**	**0.4**	1.4
14NC15_Ap3						0.0756	0.0009	1.2	0.3638	1.1889	2.2945	92.90	303.58	585.88	166.69	0.766	0.733	61.47	21.59	0.68	**28.7**	**0.4**	1.7
14NC15	**-70.491**	**-30.164**	**1389**	**Felsic Intrusive (289.7 Ma U-Pb[1])**	**FC**																**26.3**	**2.3**	
14NC18_Ap1						0.0039	0.0001	1.9	0.0649	0.0981	0.4666	33.59	50.77	241.36	46.60	0.715	0.677	49.75	8.15	0.37	**11.5**	**0.3**	0.7
14NC18_Ap2						0.0738	0.0009	1.2	0.6350	0.8241	1.5300	70.35	91.29	169.48	92.51	0.816	0.790	79.60	16.44	0.55	**20.3**	**0.3**	1.2
14NC18_Ap3						0.0375	0.0005	1.3	0.3153	0.4064	0.9615	71.64	92.33	218.45	94.27	0.780	0.750	65.88	16.84	0.57	**21.8**	**0.4**	1.3
14NC18	**-70.645**	**-30.217**	**2015**	**Felsic Intrusive (42.4 Ma K-Ar[2])**	**PC**																**17.9**	**5.5**	
14NC20_Ap1						0.0098	0.0001	0.8	0.0470	0.1360	1.5168	25.53	73.81	823.24	46.67	0.694	0.653	45.90	22.40	0.58	**32.9**	**0.4**	2.0
14NC20_Ap2						0.0030	0.0000	1.3	0.0105	0.0561	0.8158	7.55	40.53	589.00	19.80	0.652	0.607	39.84	22.77	0.79	**35.8**	**0.6**	2.1
14NC20_Ap3						0.0103	0.0001	0.9	0.0444	0.1557	1.7967	19.01	66.68	769.62	38.23	0.712	0.673	49.14	22.95	0.61	**32.8**	**0.4**	2.0
14NC20	**-70.854**	**-29.413**	**590**	**Felsic intrusive (83.6 Ma U-Pb[5])**	**CC**																**33.8**	**1.7**	
14NC21_Ap1						0.0035	0.0001	1.8	0.0174	0.0537	0.7190	8.11	25.06	335.50	15.55	0.673	0.630	42.67	21.01	0.86	**31.8**	**0.7**	1.9
14NC21_Ap2						0.0023	0.0001	3.2	0.0146	0.0227	0.3539	15.68	24.38	380.77	23.18	0.637	0.589	37.92	20.63	1.41	**32.8**	**1.1**	2.0
14NC21_Ap3						0.0014	0.0001	7.0	0.0119	0.0235	0.3219	14.65	28.99	397.25	23.31	0.596	0.545	33.57	14.17	2.00	**24.2**	**1.7**	1.5
14NC21	**-70.755**	**-29.451**	**1056**	**Felsic Intrusive (63.2 Ma U-Pb[5])**	**PC**																**29.6**	**4.7**	
14NC22_Ap1						0.0007	0.0000	3.0	0.0117	0.0369	0.4743	7.48	23.63	303.64	14.44	0.703	0.663	47.49	5.81	0.37	**8.4**	**0.3**	0.5
14NC22_Ap2						0.0015	0.0001	7.6	0.0203	0.0744	1.0691	7.42	27.22	391.07	15.63	0.747	0.713	56.62	6.89	1.06	**9.3**	**0.7**	0.6

Sample	Lon (°)	Lat (°)	Elev. (m)	Lithology	Tect. unit	^{4}He (pmol)	± 1σ (pmol)	± 1σ (%)	U (ng)	Th (ng)	Sm (ng)	U (ppm)	Th (ppm)	Sm (ppm)	eU (ppm)	F_T ^{238}U	F_T ^{232}Th	R_s (µm)	Raw Age (Ma)	± 2σ (Ma)	Corr. Age (Ma)	± 1σ (Ma)	6% err (Ma)	Comments
14NC22_Ap3						0.0041	0.0001	2.2	0.0286	0.1029	1.2094	7.77	28.01	329.13	15.87	0.784	0.754	67.14	13.83	0.66	**17.9**	**0.4**	1.1	
14NC22	**-70.575**	**-29.462**	**2630**	**Felsic Intrusive (78 - 68 Ma[5])**	**PC**																**11.9**	**5.2**		
14NC23_Ap1						0.0052	0.0001	2.0	0.0246	0.0406	0.4325	20.24	33.35	355.47	29.72	0.647	0.601	39.15	27.46	1.25	**43.1**	**1.0**	2.6	Older than ZHe (37.4), but ZHe is single age
14NC23_Ap2						0.0036	0.0001	1.9	0.0171	0.0405	0.5861	11.67	27.67	399.92	20.03	0.683	0.641	44.20	24.38	1.07	**36.2**	**0.8**	2.2	Close to ZHe age
14NC23_Ap3						0.0021	0.0001	4.4	0.0123	0.0415	0.4639	9.67	32.61	364.69	19.01	0.669	0.625	42.07	17.13	1.55	**26.2**	**1.2**	1.6	
14NC23	**-70.592**	**-29.451**	**2390**	**Felsic Intrusive (78 - 68 Ma[5])**	**PC**																**35.2**	**8.5**		
14NC24_Ap1						0.0083	0.0001	0.8	0.0283	0.0499	0.5628	22.73	40.02	451.24	34.22	0.624	0.576	36.50	37.72	1.46	**61.4**	**1.2**	3.7	
14NC24_Ap2						0.0036	0.0000	1.1	0.0186	0.0183	0.1286	33.10	32.60	229.49	41.81	0.597	0.546	33.71	29.19	0.99	**49.6**	**0.8**	3.0	
14NC24_Ap3						*0.0007*	*0.0000*	*2.6*	*0.0019*	*0.0212*	*0.1501*	*1.36*	*15.36*	*108.80*	*5.47*	*0.694*	*0.653*	*45.90*	*19.01*	*1.32*	*28.4*	*1.0*	*1.7*	*low U => rejected*
14NC24	**-71.014**	**-28.972**	**610**	**Felsic Intrusive (127 - 124 Ma[5])**	**CC**																**55.5**	**8.4**		
14NC25_Ap1						0.0173	0.0001	0.7	0.0666	0.1020	0.9519	31.77	48.64	454.03	45.28	0.687	0.646	44.87	34.91	0.90	**51.4**	**0.7**	3.1	
14NC25_Ap2						0.0136	0.0001	0.7	0.0505	0.0795	0.8423	27.14	42.73	452.71	39.27	0.680	0.638	43.81	35.65	0.92	**53.1**	**0.7**	3.2	
14NC25_Ap3						0.0072	0.0001	0.8	0.0446	0.0394	0.4700	33.21	29.35	350.33	41.72	0.670	0.626	42.26	24.35	0.69	**36.7**	**0.5**	2.2	
14NC25	**-70.886**	**-29.052**	**861**	**Felsic Intrusive (99 Ma K-Ar[5])**	**CC**																**47.1**	**9.0**		
14NC26_Ap1						0.0264	0.0003	1.3	0.1275	0.2064	0.6371	50.37	81.51	251.61	70.62	0.739	0.704	54.78	27.57	0.94	**37.8**	**0.6**	2.3	
14NC26_Ap2						0.0186	0.0002	1.2	0.1104	0.1487	0.4394	80.39	108.30	320.00	107.23	0.660	0.616	40.94	23.55	0.76	**36.2**	**0.6**	2.2	
14NC26_Ap3						0.0191	0.0004	2.3	0.0894	0.1812	0.5298	48.43	98.18	287.09	72.75	0.696	0.655	46.23	26.66	1.33	**39.0**	**1.0**	2.3	
14NC26	**-70.761**	**-29.103**	**1386**	**Felsic Intrusive (68.6 Ma U-Pb[5])**	**PC**																**37.7**	**1.4**		
14NC27_Ap1						0.0797	0.0004	0.5	0.3056	0.3679	2.3854	29.13	35.07	227.36	38.40	0.790	0.760	68.97	37.28	0.92	**47.6**	**0.6**	2.9	
14NC27_Ap2						0.0199	0.0001	0.6	0.1036	0.0856	0.4716	44.32	36.61	201.79	53.83	0.713	0.674	49.26	29.56	0.79	**41.8**	**0.6**	2.5	
14NC27_Ap3						0.0103	0.0001	1.0	0.0577	0.0561	0.3376	43.22	41.99	252.82	54.23	0.649	0.603	39.42	26.80	0.80	**41.8**	**0.6**	2.5	
14NC27	**-70.654**	**-28.592**	**733**	**Felsic Intrusive (93 Ma[6])**	**PC**																**43.7**	**3.3**		
14NC29_Ap1						0.0034	0.0001	2.8	0.0569	0.0711	0.4644	44.77	55.90	365.12	59.57	0.653	0.608	40.01	8.43	0.51	**13.1**	**0.4**	0.8	
14NC29_Ap2						0.0023	0.0001	3.2	0.0351	0.0692	0.5140	32.33	63.71	473.38	49.46	0.615	0.565	35.46	8.05	0.54	**13.4**	**0.4**	0.8	
14NC29_Ap3						0.0027	0.0001	2.8	0.0492	0.0520	0.3450	44.14	46.67	309.77	56.51	0.625	0.577	36.64	8.16	0.49	**13.2**	**0.4**	0.8	
14NC29	**-70.461**	**-28.962**	**1285**	**Felsic Intrusive (44 Ma[7])**	**PC**																**13.2**	**1.0**		
14NC30_Ap1						0.0056	0.0002	2.7	0.0296	0.1245	0.9315	17.51	73.54	550.42	37.30	0.664	0.620	41.44	17.28	1.01	**26.7**	**0.8**	1.6	
14NC30_Ap2						0.0072	0.0002	2.4	0.0403	0.1456	0.9004	18.23	65.89	407.40	35.56	0.675	0.632	43.01	17.65	0.93	**26.8**	**0.7**	1.6	
14NC30_Ap3						0.0237	0.0005	2.3	0.1038	0.5851	1.2276	80.18	451.89	948.17	190.38	0.663	0.619	41.33	18.03	0.90	**28.2**	**0.7**	1.7	
14NC30	**-70.347**	**-29.178**	**1885**	**Granite (Devon. - Perm.[8])**	**FC**																**27.3**	**0.8**		Similar to ZHe age (30.95 Ma)
14NC31_Ap1						0.0020	0.0001	3.0	0.0172	0.0495	0.6974	17.11	49.40	695.61	31.94	0.590	0.539	33.08	12.46	0.79	**21.6**	**0.4**	1.3	
14NC31_Ap2						0.0056	0.0001	2.6	0.0362	0.1401	1.8978	11.12	42.97	582.04	23.91	0.721	0.684	50.96	14.45	0.81	**20.4**	**0.6**	1.2	
14NC31_Ap3						0.0020	0.0001	2.9	0.0267	0.0373	0.6889	22.91	32.01	591.69	33.18	0.629	0.582	37.09	10.34	0.64	**16.6**	**0.5**	1.0	
14NC31	**-70.354**	**-29.322**	**2170**	**Granite (Upper Cretaceous[5,8])**	**FC**																**19.5**	**2.6**		
14NC32_Ap1						0.0039	0.0001	2.6	0.0636	0.0124	0.0826	40.96	7.99	53.25	43.08	0.689	0.647	45.12	10.87	0.64	**15.8**	**0.5**	1.0	
14NC32_Ap2						0.0077	0.0002	2.4	0.1031	0.0106	0.1298	41.43	4.27	52.17	42.67	0.721	0.683	50.81	13.45	0.75	**18.7**	**0.5**	1.1	
14NC32_Ap3						0.0025	0.0001	3.4	0.0422	0.0112	0.0928	38.75	10.32	85.26	41.57	0.648	0.602	39.33	10.24	0.74	**15.9**	**0.6**	1.0	
14NC32	**-70.302**	**-29.007**	**1690**	**Felsic Intrusive (Permian[7,8])**	**FC**																**16.8**	**1.6**		
14NC34_Ap1						0.0061	0.0001	1.6	0.0254	0.0789	0.8775	8.96	27.82	309.52	16.93	0.737	0.701	54.25	25.13	0.97	**34.6**	**0.7**	2.1	
14NC34_Ap2						0.0069	0.0001	1.4	0.0240	0.0786	0.8725	7.05	23.09	256.31	13.66	0.726	0.689	51.81	29.42	1.01	**41.2**	**0.7**	2.5	
14NC34_Ap3						0.0027	0.0001	2.0	0.0136	0.0371	0.2771	10.38	28.19	210.72	17.96	0.622	0.574	36.29	22.29	1.01	**36.7**	**0.8**	2.2	
14NC34	**-70.543**	**-28.565**	**1121**	**Felsic Intrusive (68 Ma U-Pb[6])**	**PC**																**37.5**	**3.4**		
14NC35_Ap2						0.0118	0.0001	1.1	0.0353	0.1166	0.9389	22.57	74.43	599.48	42.80	0.673	0.630	42.74	34.09	1.02	**51.8**	**0.8**	3.1	Single grain age
14NC35	**-70.480**	**-28.595**	**2078**	**Felsic Intrusive (68.85 Ma U-Pb[7])**	**PC**																**51.8**	**0.8**		
14NC36_Ap1						*0.0009*	*0.0001*	*9.0*	*0.0224*	*0.0477*	*0.4892*	*17.46*	*37.24*	*381.67*	*27.97*	*0.676*	*0.634*	*43.19*	*4.80*	*0.87*	*7.2*	*0.7*	*0.4*	
14NC36_Ap2						*0.0041*	*0.0001*	*2.5*	*0.0152*	*0.0582*	*0.2842*	*14.86*	*56.99*	*278.23*	*29.50*	*0.617*	*0.568*	*35.75*	*25.82*	*1.41*	*43.3*	*1.2*	*2.6*	
14NC36_Ap3						*0.0062*	*0.0001*	*1.0*	*0.0442*	*0.0643*	*0.6244*	*23.98*	*34.88*	*338.66*	*33.73*	*0.734*	*0.698*	*53.66*	*19.13*	*0.57*	*26.3*	*0.4*	*1.6*	
14NC36	*-70.409*	*-28.376*	*1053*	*Felsic Intrusive (64-66 Ma K-Ar[7])*	*PC*																*25.6*	*18.0*		*High age dispersion => reject*
14NC37_Ap1						0.0120	0.0001	0.9	0.0643	0.0392	0.5797	53.78	32.78	484.58	63.73	0.646	0.600	39.07	29.77	0.93	**46.4**	**0.7**	2.8	
14NC37_Ap2						0.0251	0.0002	0.7	0.1113	0.0667	1.1049	57.11	34.24	567.02	67.79	0.684	0.642	44.41	36.15	1.01	**53.1**	**0.7**	3.2	
14NC37_Ap3						0.0108	0.0001	1.1	0.0593	0.0481	0.4689	86.42	70.11	683.74	106.04	0.574	0.521	31.64	28.07	0.92	**49.5**	**0.8**	3.0	

Sample	Lon	Lat	Elev.	Lithology	Tect. unit	^{4}He	± 1σ	± 1σ	U	Th	Sm	U	Th	Sm	eU	F_T	F_T	R_s	Raw Age	± 2σ	Corr. Age	± 1σ	6% err	Comments
	(°)	(°)	(m)			(pmol)	(pmol)	(%)	(ng)	(ng)	(ng)	(ppm)	(ppm)	(ppm)	(ppm)	[238]U	[232]Th	(µm)	(Ma)	(Ma)	(Ma)	(Ma)	(Ma)	
14NC37	**-70.493**	**-28.295**	**850**	*Felsic Intrusive (66 ± 2 K-Ar[7])*	**PC**																**49.6**	**3.4**		Older than ZHe age (37.4)
14NC38_Ap1						0.0002	0.0000	5.8	0.0036	0.0339	0.0817	2.00	18.73	45.19	6.60	0.713	0.674	49.31	3.33	0.39	*4.8*	*0.3*	0.3	*High He error, low U*
14NC38_Ap2						0.0001	0.0000	18.3	0.0014	0.0078	0.0176	1.82	10.49	23.64	4.38	0.580	0.527	32.08	2.96	1.09	*5.4*	*1.0*	0.3	*High He error, low U*
14NC38_Ap3						0.0000	0.0000	27.9	0.0024	0.0054	0.0312	1.66	3.74	21.62	2.64	0.669	0.626	42.16	1.54	0.86	*2.4*	*0.7*	0.1	*High He error, low U*
14NC38	**-70.724**	**-28.455**	**678**	*Micro-diorite (127.3 Ma[3,6])*	**CC**																**4.2**	**1.6**		*High He error, low U => reject*
14NC42_Ap1						0.0201	0.0002	1.1	0.0797	0.0963	0.6769	37.28	45.04	316.49	49.31	0.715	0.676	49.61	36.00	1.13	**50.9**	**0.8**	3.1	
14NC42_Ap2						0.0081	0.0001	1.1	0.0370	0.0442	0.3129	37.48	44.78	317.33	49.45	0.636	0.588	37.80	31.20	0.98	**49.8**	**0.8**	3.0	
14NC42_Ap3						0.0139	0.0001	1.0	0.0495	0.0657	0.3782	46.84	62.09	357.69	63.05	0.646	0.600	39.11	39.11	1.21	**61.4**	**1.0**	3.7	
14NC42	**-70.340**	**-26.855**	**1075**	**Felsic Intrusive (119.9 Ma[9,10])**	**CC**																**54.0**	**6.4**		
14NC45_Ap1						0.0157	0.0004	2.7	0.0897	0.1498	0.4346	50.83	84.82	246.16	71.84	0.675	0.632	42.93	23.07	1.36	**34.8**	**1.0**	2.1	
14NC45_Ap2						0.0097	0.0003	2.7	0.0499	0.1388	0.2980	27.46	76.31	163.84	46.08	0.683	0.640	44.13	21.59	1.27	**32.4**	**1.0**	1.9	
14NC45_Ap3						0.0076	0.0002	2.7	0.0476	0.1080	0.4136	31.82	72.27	276.75	50.04	0.653	0.608	39.98	19.13	1.12	**30.0**	**0.9**	1.8	
14NC45	**-70.090**	**-27.594**	**984**	**Felsic Intrusive (60.6 Ar-Ar[11])**	**PC**																**32.4**	**2.4**		
14NC47_Ap1						0.0337	0.0002	0.7	0.2177	0.2577	1.9715	35.03	41.48	317.29	46.23	0.785	0.755	67.45	22.20	0.57	**28.5**	**0.4**	1.7	
14NC47_Ap2						0.0336	0.0004	1.2	0.2503	0.2346	1.6334	38.92	36.48	253.99	48.65	0.791	0.762	69.55	20.25	0.67	**25.8**	**0.4**	1.5	
14NC47_Ap3						0.0462	0.0005	1.1	0.3028	0.4085	2.5532	39.86	53.77	336.03	54.02	0.798	0.770	72.10	21.23	0.64	**26.8**	**0.4**	1.6	
14NC47	**-69.768**	**-27.672**	**2436**	**Porphyry (42.1 Ma K-Ar[12])**	**PC**																**27.0**	**1.4**		
14NC48_Ap1						0.0126	0.0001	0.8	0.0969	0.1276	0.9433	12.28	16.17	119.55	16.63	0.801	0.773	73.07	18.15	0.49	**22.8**	**0.3**	1.4	
14NC48_Ap2						0.0063	0.0001	1.0	0.0450	0.0295	0.5077	10.49	6.87	118.36	12.65	0.790	0.761	69.07	22.17	0.70	**28.2**	**0.4**	1.7	
14NC48_Ap3						0.0021	0.0000	1.6	0.0221	0.0414	0.3959	11.55	21.60	206.74	17.57	0.709	0.670	48.61	12.25	0.48	**17.5**	**0.3**	1.1	
14NC48	**-69.806**	**-27.956**	**1704**	**Granite, deformed (Carb. - Perm.[7])**	**FC**																**22.8**	**5.3**		
14NC52_Ap1						0.0101	0.0001	1.1	0.0779	0.1132	0.4896	72.94	106.02	458.63	99.90	0.646	0.600	39.11	17.84	0.55	**28.1**	**0.4**	1.7	
14NC52_Ap2						0.0070	0.0001	1.1	0.0530	0.0821	0.4630	42.82	66.31	373.80	60.09	0.662	0.617	41.09	17.88	0.56	**27.5**	**0.4**	1.6	
14NC52_Ap3						0.0114	0.0001	0.8	0.0669	0.0975	0.4600	44.57	64.96	306.35	61.21	0.673	0.630	42.74	23.32	0.63	**35.2**	**0.5**	2.1	
14NC52	**-70.126**	**-27.822**	**918**	**Felsic Intrusive (61.8 Ma K-Ar[11,12])**	**PC**																**30.2**	**4.3**		
14NC54_Ap1						0.0005	0.0000	2.8	0.0146	0.0166	0.0423	11.10	12.62	32.21	14.20	0.628	0.580	36.95	5.49	0.34	**8.9**	**0.3**	0.5	
14NC54_Ap2						0.0019	0.0000	1.4	0.0327	0.0267	0.1707	14.77	12.09	77.16	17.96	0.713	0.675	49.38	8.77	0.32	**12.4**	**0.2**	0.7	
14NC54_Ap3						0.0022	0.0000	1.5	0.0301	0.0310	0.1057	13.49	13.85	47.29	16.95	0.693	0.652	45.82	11.08	0.42	**16.2**	**0.3**	1.0	
14NC54	**-69.818**	**-28.186**	**1732**	**Felsic Intrusive (234 Ma K-Ar[7])**	**FC**																**12.5**	**3.6**		
14NC56_Ap1						0.0594	0.0014	2.4	0.2608	0.0727	0.5729	176.11	49.07	386.80	189.41	0.682	0.640	44.05	39.42	2.15	**58.0**	**1.6**	3.5	
14NC56_Ap2						0.0161	0.0004	2.4	0.0855	0.0120	0.2646	65.24	9.12	201.80	68.32	0.664	0.620	41.39	33.57	1.87	**50.7**	**1.4**	3.0	
14NC56_Ap3						0.0371	0.0009	2.4	0.1628	0.0173	0.7594	43.40	4.62	202.46	45.43	0.779	0.748	65.37	40.87	2.25	**52.5**	**1.4**	3.1	
14NC56	**-69.760**	**-28.116**	**2386**	**Felsic Intrusive (234 Ma K-Ar[7])**	**FC**																**53.7**	**3.8**		
14NC57_Ap1						0.0224	0.0002	1.0	0.1035	0.2781	0.3472	44.80	120.31	150.24	73.66	0.700	0.660	47.01	24.39	0.69	**35.6**	**0.5**	2.1	
14NC57_Ap2						0.0187	0.0002	1.1	0.0823	0.2076	0.2606	36.51	92.13	115.66	58.61	0.730	0.693	52.70	26.33	0.81	**36.8**	**0.6**	2.2	
14NC57_Ap3						0.0124	0.0001	1.0	0.0533	0.1730	0.7868	36.07	117.11	532.64	65.98	0.691	0.649	45.41	24.19	0.68	**35.9**	**0.5**	2.2	
14NC57	**-69.775**	**-28.104**	**3416**	**Felsic Intrusive (234 Ma K-Ar[7])**	**FC**																**36.1**	**0.6**		
14NC58_Ap1						0.0038	0.0001	2.2	0.0212	0.0243	0.2252	11.66	13.38	123.72	15.38	0.657	0.612	40.50	25.74	1.30	**39.6**	**1.0**	2.4	
14NC58_Ap2						0.0034	0.0001	1.8	0.0207	0.0302	0.2956	11.30	16.43	161.03	15.90	0.635	0.587	37.69	22.39	1.00	**35.8**	**0.8**	2.1	
14NC58_Ap3						0.0025	0.0000	2.0	0.0155	0.0201	0.2612	6.96	9.06	117.70	9.64	0.647	0.601	39.13	22.58	1.03	**35.4**	**0.8**	2.1	
14NC58	**-69.785**	**-28.104**	**3641**	**Felsic Intrusive (234 Ma K-Ar[7])**	**FC**																**36.9**	**2.4**		
14NC59_Ap1						0.0015	0.0001	6.4	0.0098	0.0169	0.2587	3.51	6.04	92.53	5.36	0.722	0.684	51.06	19.48	2.55	**27.3**	**1.8**	1.6	High He error
14NC59_Ap2						0.0050	0.0001	1.4	0.0179	0.0402	0.6103	2.47	5.54	84.10	4.16	0.787	0.758	68.15	32.97	1.15	**42.2**	**0.7**	2.5	
14NC59_Ap3						0.0026	0.0001	2.1	0.0113	0.0216	0.4150	2.59	4.94	95.13	4.19	0.735	0.698	53.69	28.95	1.38	**39.7**	**1.0**	2.4	
14NC59	**-70.131**	**-27.427**	**929**	**Porphyric diorite (83 ± 6 Ma K-Ar[13])**	**PC**																**36.4**	**8.0**		
14NC61_Ap1						0.0172	0.0001	0.7	0.0726	0.0781	0.2383	14.03	15.09	46.08	17.78	0.789	0.759	68.63	34.83	0.94	**44.5**	**0.6**	2.7	
14NC61_Ap2						0.0155	0.0001	0.8	0.0727	0.1122	0.6119	27.18	41.93	228.74	38.06	0.684	0.642	44.35	28.63	0.79	**42.5**	**0.6**	2.5	
14NC61_Ap3						0.0077	0.0001	1.0	0.0363	0.0532	0.4390	24.18	35.47	292.82	33.86	0.675	0.632	42.93	28.78	0.84	**43.2**	**0.6**	2.6	
14NC61	**-69.967**	**-27.414**	**1363**	**Felsic Intrusive (60.4 Ma K-Ar[12])**	**PC**																**43.4**	**1.0**		
14NC63_Ap1						0.0046	0.0000	1.1	0.0244	0.0657	0.4710	17.52	47.23	338.47	30.17	0.613	0.563	35.25	20.99	0.63	**35.2**	**0.5**	2.1	
14NC63_Ap2						0.0031	0.0000	1.4	0.0180	0.0444	0.2423	24.73	61.05	333.04	40.58	0.588	0.536	32.87	20.18	0.73	**35.3**	**0.6**	2.1	

Sample	Lon (°)	Lat (°)	Elev. (m)	Lithology	Tect. unit	⁴He (pmol)	±1σ (pmol)	±1σ (%)	U (ng)	Th (ng)	Sm (ng)	U (ppm)	Th (ppm)	Sm (ppm)	eU (ppm)	F_T ²³⁸U	F_T ²³²Th	R_s (µm)	Raw Age (Ma)	±2σ (Ma)	Corr. Age (Ma)	±1σ (Ma)	6% err (Ma)	Comments
14NC63_Ap3						0.0171	0.0001	0.8	0.0802	0.2141	1.2885	29.49	78.76	474.05	50.15	0.679	0.636	43.53	23.92	0.62	**36.0**	**0.5**	2.2	
14NC63	**-69.679**	**-27.360**	**2728**	**Felsic Intrusive (Carb.-Perm[14])**	**PC**																**35.5**	**0.4**		
14NC65_Ap1						0.0059	0.0001	2.4	0.0363	0.0584	0.3269	23.03	37.09	207.45	32.69	0.680	0.637	43.68	21.71	1.16	**32.5**	**0.9**	1.9	
14NC65_Ap2						0.0036	0.0001	2.4	0.0216	0.0192	0.0407	11.51	10.23	21.71	14.00	0.709	0.670	48.52	25.41	1.36	**36.2**	**1.0**	2.2	
14NC65_Ap3						0.0147	0.0003	2.4	0.0692	0.1428	0.7058	27.77	57.32	283.26	42.51	0.721	0.683	50.79	26.18	1.36	**36.9**	**1.0**	2.2	
14NC65	**-69.677**	**-27.427**	**3128**	**Felsic Intrusive (Carb.-Perm[14])**	**PC**																**35.2**	**2.4**		
14NC66_Ap1						0.0093	0.0001	1.5	0.0739	0.1263	0.6642	54.45	93.14	489.64	78.54	0.661	0.617	41.04	16.50	0.61	**25.4**	**0.5**	1.5	
14NC66_Ap2						0.0225	0.0002	1.1	0.1922	0.2240	0.7235	89.60	104.42	337.18	115.61	0.700	0.660	46.96	16.91	0.53	**24.5**	**0.4**	1.5	
14NC66_Ap3						0.0230	0.0003	1.2	0.1977	0.2724	0.8366	117.21	161.47	495.99	157.32	0.677	0.635	43.33	16.23	0.53	**24.3**	**0.4**	1.5	
14NC66	**-69.655**	**-27.484**	**2739**	**Felsic Intrusive (Carb.-Perm[14])**	**PC**																**24.7**	**0..6**		
14NC70_Ap1						0.0110	0.0001	1.0	0.0392	0.1526	2.1246	9.97	38.82	540.42	21.60	0.771	0.740	63.03	26.22	0.74	**34.4**	**0.5**	2.1	
14NC70_Ap2						0.0162	0.0002	1.0	0.0480	0.1735	2.5197	10.67	38.61	560.69	22.34	0.782	0.752	66.47	32.58	0.90	**42.1**	**0.6**	2.5	
14NC70_Ap3						0.0420	0.0004	0.9	0.1022	0.3980	5.5535	11.27	43.91	612.68	24.43	0.834	0.811	88.82	38.21	1.01	**46.2**	**0.6**	2.8	
14NC70	**-69.952**	**-27.100**	**1724**	**Porphyry (60.6 Ma K-Ar[12])**	**PC**																**40.9**	**6.0**		
14NC71_Ap1						0.0190	0.0004	2.4	0.0869	0.1480	1.5486	31.37	53.40	558.76	46.49	0.727	0.691	52.18	28.45	1.47	**39.6**	**1.0**	2.4	
14NC71_Ap2						0.0072	0.0002	2.4	0.0218	0.1064	1.3626	7.78	38.03	487.21	18.97	0.738	0.702	54.38	27.42	1.41	**37.8**	**1.0**	2.3	
14NC71_Ap3						0.0195	0.0005	2.3	0.0614	0.1656	2.7367	10.22	27.55	455.42	18.81	0.786	0.756	67.68	34.64	1.78	**44.5**	**1.1**	2.7	
14NC71	**-69.890**	**-26.813**	**1740**	**Felsic Intrusive (63 Ma K-Ar[15])**	**PC**																**40.6**	**3.4**		
14NC72_Ap1						0.0004	0.0000	3.4	0.0019	0.0036	0.0728	2.52	4.67	95.23	4.06	0.613	0.564	35.33	23.39	1.75	**38.6**	**1.4**	2.3	
14NC72_Ap2						0.0003	0.0000	3.9	0.0021	0.0045	0.0678	2.49	5.37	81.18	4.13	0.606	0.555	34.54	18.29	1.50	**30.7**	**1.3**	1.8	
14NC72_Ap3						0.0024	0.0001	2.6	0.0100	0.0273	0.4455	10.82	29.67	484.12	20.04	0.627	0.579	36.81	26.72	1.47	**43.4**	**1.2**	2.6	
14NC72	**-69.852**	**-26.694**	**1764**	**Felsic Intrusive (63 Ma[16])**	**PC**																**37.6**	**6.4**		
14NC74_Ap1						0.0136	0.0001	1.0	0.1186	0.2089	1.9501	28.10	49.51	462.20	41.85	0.772	0.741	63.33	14.81	0.43	**19.4**	**0.3**	1.2	
14NC74_Ap2						0.0173	0.0002	1.0	0.1086	0.2400	1.6976	17.79	39.30	277.95	28.29	0.796	0.768	71.27	19.17	0.54	**24.3**	**0.3**	1.5	
14NC74_Ap3						0.0168	0.0002	1.0	0.1320	0.2852	2.6727	17.24	37.26	349.20	27.60	0.828	0.804	85.35	15.38	0.44	**18.7**	**0.3**	1.1	
14NC74	**-69.718**	**-26.685**	**1966**	**Porphyry (55 - 53 Ma[15])**	**PC**																**20.8**	**3.1**		
14NC78_Ap1						0.0098	0.0001	1.2	0.0395	0.1462	1.1374	9.50	35.14	273.38	19.01	0.773	0.741	63.53	24.14	0.77	**31.7**	**0.5**	1.9	
14NC78_Ap2						0.0049	0.0001	1.5	0.0225	0.0853	0.3758	8.83	33.49	147.60	17.36	0.723	0.686	51.35	21.15	0.78	**29.9**	**0.6**	1.8	
14NC78_Ap3						0.0121	0.0002	1.3	0.0509	0.1993	1.6025	6.89	27.00	217.08	14.23	0.799	0.771	72.53	22.41	0.73	**28.4**	**0.5**	1.7	
14NC78	**-69.667**	**-26.947**	**2708**	**Felsic Intrusion (62.5 Ma Ar-Ar[15])**	**PC**																**30.0**	**1.7**		
14NC81_Ap1						0.0082	0.0001	1.1	0.0365	0.0466	0.1260	32.16	41.03	110.89	42.28	0.647	0.601	39.23	31.93	1.01	**50.1**	**0.8**	3.0	
14NC81_Ap2						0.0105	0.0001	1.1	0.0500	0.0541	0.2018	34.97	37.89	141.26	44.50	0.663	0.619	41.33	30.95	0.97	**47.3**	**0.7**	2.8	
14NC81_Ap3						0.0099	0.0001	1.1	0.0388	0.0572	0.3123	20.69	30.51	166.47	28.62	0.696	0.656	46.31	34.89	1.08	**50.8**	**0.8**	3.0	
14NC81	**-70.356**	**-27.212**	**831**	**Felsic Intrusion (103 Ma K-Ar[13])**	**CC**																**49.4**	**1.9**		
14NC84_Ap1						0.0028	0.0001	2.5	0.0151	0.0569	0.5265	5.17	19.50	180.27	10.58	0.749	0.714	57.01	17.81	0.96	**24.2**	**0.7**	1.5	
14NC84_Ap2						0.0013	0.0000	2.5	0.0068	0.0293	0.3160	4.18	17.99	194.16	9.30	0.685	0.643	44.43	17.49	0.95	**26.1**	**0.7**	1.6	
14NC84_Ap3						0.0004	0.0000	3.8	0.0052	0.0149	0.2523	2.46	7.08	119.46	4.68	0.714	0.675	49.48	8.89	0.69	**12.6**	**0.5**	0.8	
14NC84	**-70.197**	**-26.809**	**1305**	**Felsic Intrusive (119.9 Ma[9,10])**	**CC**																**21.0**	**7.3**		
14NC88_Ap1						0.0098	0.0003	2.7	0.0689	0.1539	1.5099	10.94	24.44	239.85	17.79	0.783	0.753	66.71	17.02	0.98	**22.0**	**0.6**	1.3	
14NC88_Ap2						0.0065	0.0002	2.4	0.0599	0.0622	0.6933	23.85	24.75	275.85	30.94	0.740	0.705	54.92	15.91	0.86	**21.7**	**0.6**	1.3	
14NC88_Ap3						*0.0277*	*0.0007*	*2.4*	*0.0634*	*0.1063*	*0.7113*	*30.21*	*50.63*	*338.69*	*43.65*	*0.709*	*0.670*	*48.61*	*57.12*	*3.02*	*81.6*	*2.2*	*4.9*	*He injection => rejected*
14NC88	**-69.984**	**-26.840**	**1952**	**Porphyry (Triassic[15])**	**PC**																**21.8**	**0.2**		
14NC89_Ap1						0.0036	0.0001	2.5	0.0313	0.0384	0.2021	63.59	77.93	410.28	83.75	0.526	0.469	27.85	16.41	0.91	**31.9**	**0.9**	1.9	
14NC89_Ap2						0.0800	0.0019	2.3	0.4172	0.4430	2.6938	59.54	63.23	384.49	76.15	0.785	0.755	67.40	28.21	1.47	**36.2**	**0.9**	2.2	
14NC89_Ap3						0.0395	0.0009	2.3	0.2113	0.2869	1.4454	54.13	73.48	370.22	73.07	0.754	0.720	58.25	26.03	1.35	**34.9**	**0.9**	2.1	
14NC89	**-69.786**	**-26.592**	**1784**	**Felsic Intrusive (64 ± 2 Ma K-Ar[15])**	**PC**																**34.3**	**2.2**		
14NC90_Ap1						0.0349	0.0002	0.6	0.1802	0.1578	0.9286	85.01	74.45	438.10	104.49	0.699	0.659	46.77	29.52	0.78	**42.6**	**0.6**	2.6	Older than ZHe age
14NC90_Ap2						0.0078	0.0001	0.9	0.0634	0.0581	0.3347	41.46	37.96	218.74	51.37	0.678	0.636	43.47	18.60	0.54	**27.7**	**0.4**	1.7	
14NC90_Ap3						0.0295	0.0002	0.6	0.1550	0.1677	0.4636	75.37	81.51	225.36	95.50	0.708	0.669	48.42	27.93	0.73	**39.9**	**0.5**	2.4	Older than ZHe age
14NC90	**-69.665**	**-26.538**	**2338**	**Felsic Intrusive (47.8 - 48.1 Ma K-Ar[15])**	**PC**																**36.7**	**7.9**		
14NC95_Ap1						0.0036	0.0001	2.4	0.0158	0.0647	0.5235	9.72	39.70	321.22	20.52	0.687	0.645	44.74	21.23	1.12	**31.7**	**0.8**	1.9	

Sample	Lon (°)	Lat (°)	Elev. (m)	Lithology	Tect. unit	^{4}He (pmol)	±1σ (pmol)	±1σ (%)	U (ng)	Th (ng)	Sm (ng)	U (ppm)	Th (ppm)	Sm (ppm)	eU (ppm)	F_T ^{238}U	F_T ^{232}Th	R_s (µm)	Raw Age (Ma)	±2σ (Ma)	Corr. Age (Ma)	±1σ (Ma)	6% err (Ma)	Comments
14NC95_Ap2						0.0045	0.0001	2.3	0.0184	0.0809	0.6578	12.65	55.74	453.45	27.83	0.664	0.620	41.48	21.90	1.31	**33.9**	**1.0**	2.0	
14NC95_Ap3						0.0021	0.0001	2.5	0.0096	0.0394	0.4147	8.38	34.51	363.06	18.16	0.640	0.593	38.30	20.28	1.10	**32.5**	**0.9**	2.0	
14NC95	**-69.749**	**-26.339**	**1336**	**Porphyry (69 - 66 Ma[17])**	**PC**																**32.7**	**1.1**		
14NC97_Ap1						0.0125	0.0003	2.7	0.0497	0.1620	0.9440	31.23	101.72	592.71	57.82	0.651	0.606	39.71	25.92	1.51	**40.9**	**1.2**	2.5	
14NC97_Ap2						0.0065	0.0002	2.8	0.0316	0.0876	0.5498	27.71	76.92	482.59	47.98	0.629	0.581	37.00	22.79	1.34	**37.2**	**1.1**	2.2	
14NC97_Ap3						0.0018	0.0001	2.9	0.0102	0.0297	0.2825	10.75	31.41	298.57	19.51	0.618	0.569	35.84	19.44	1.20	**32.2**	**1.0**	1.9	
14NC97	**-69.328**	**-26.458**	**2758**	**Felsic Intrusive (Carb. - Perm.[18])**	**PC**																**36.8**	**4.3**		
14NC98_Ap1						*0.0032*	*0.0001*	*1.8*	*0.0130*	*0.0465*	*0.6630*	*3.28*	*11.77*	*167.98*	*6.83*	*0.730*	*0.693*	*52.68*	*24.24*	*1.00*	***33.7***	***0.7***	*2.0*	
14NC98_Ap2						*0.0043*	*0.0001*	*1.6*	*0.0190*	*0.0747*	*0.6100*	*4.89*	*19.22*	*157.03*	*10.12*	*0.733*	*0.697*	*53.38*	*21.36*	*0.82*	***29.7***	***0.6***	*1.8*	
14NC98_Ap3						*0.0023*	*0.0001*	*2.8*	*0.0085*	*0.0293*	*0.4004*	*3.46*	*11.96*	*163.35*	*7.03*	*0.714*	*0.676*	*49.53*	*26.28*	*1.55*	***37.4***	***1.1***	*2.2*	
14NC98	***-69.554***	***-27.119***	***2738***	***Porphyry (Eocene[14])***	***PC***																***33.6***	***3.8***		***Magmatic cooling***
Huasco87_Ap1						0.0072	0.0001	1.6	0.0552	0.0525	0.1377	33.27	31.66	83.03	41.07	0.693	0.652	45.83	19.56	0.78	**28.5**	**0.6**	1.7	
Huasco87_Ap3						0.0125	0.0002	1.4	0.0889	0.1069	0.3423	41.25	49.60	158.84	53.60	0.643	0.597	38.75	20.17	0.73	**31.9**	**0.6**	1.9	
Huasco87	**-70.223**	**-28.941**	**2864**	**Gneiss (310 Ma K-Ar[7])**	**FC**																**30.2**	**2.3**		
Clin2_Ap1						0.0012	0.0000	1.9	0.0115	0.0240	0.3699	8.46	17.72	272.88	13.89	0.663	0.618	41.24	12.53	0.54	**19.2**	**0.4**	1.15	
Clin2_Ap2						0.0004	0.0000	3.9	0.0046	0.0108	0.1433	8.15	19.19	254.89	13.83	0.569	0.515	31.14	10.45	0.85	**18.8**	**0.8**	1.13	
Clin2_Ap3						0.0004	0.0000	4.0	0.0061	0.0128	0.1897	8.54	17.93	265.17	13.99	0.584	0.531	32.44	7.47	0.63	**13.1**	**0.5**	0.78	
Clin2_Ap4						0.0018	0.0001	3.2	0.0146	0.0288	0.4250	8.92	17.65	260.04	14.27	0.665	0.621	41.51	15.16	1.02	**23.1**	**0.8**	1.39	
Clin2_Ap5						0.0004	0.0000	3.1	0.0091	0.0160	0.2069	10.00	17.61	228.34	15.19	0.588	0.536	32.86	6.06	0.41	**10.5**	**0.4**	0.63	
Clin2 Av	**-32.104**	**-70.797**	**960**	**Granite (79 - 80 Ma K-Ar[19])**	**PC**																**16.9**	**5.1**		
Clin3_Ap1						*0.0008*	*0.0000*	*2.0*	*0.0048*	*0.0205*	*0.3752*	*6.83*	*29.38*	*537.93*	*16.23*	*0.586*	*0.534*	*32.65*	*15.27*	*0.68*	***26.7***	***0.6***	*1.60*	
Clin3_Ap2						*0.0004*	*0.0000*	*6.9*	*0.0107*	*0.0366*	*0.7981*	*6.33*	*21.63*	*471.33*	*13.60*	*0.687*	*0.645*	*44.82*	*3.77*	*0.52*	***5.6***	***0.4***	*0.33*	
Clin3_Ap3						*0.0012*	*0.0000*	*1.8*	*0.0060*	*0.0252*	*0.7619*	*3.56*	*14.89*	*449.94*	*9.16*	*0.665*	*0.621*	*41.61*	*16.54*	*0.67*	***25.0***	***0.5***	*1.50*	
Clin3_Ap4						*0.0009*	*0.0000*	*2.3*	*0.0112*	*0.0372*	*0.5286*	*11.19*	*37.26*	*529.51*	*22.39*	*0.634*	*0.586*	*37.56*	*8.16*	*0.40*	***13.2***	***0.3***	*0.79*	
Clin3_Ap5						*0.0014*	*0.0000*	*1.5*	*0.0040*	*0.0210*	*0.4278*	*4.35*	*23.08*	*470.35*	*11.96*	*0.617*	*0.568*	*35.76*	*27.38*	*0.98*	***45.2***	***0.8***	*2.71*	
Clin3 Av	*-32.232*	*-70.706*	*1229*	*Granite (45.5 -47.2 Ma K-Ar[19])*	*PC*																*23.1*	*15.1*		*High age dispersion => rejected*
Clin4_Ap1						0.0034	0.0000	1.3	0.0235	0.0873	0.9381	10.78	40.13	431.01	22.19	0.718	0.680	50.23	14.10	0.47	**20.0**	**0.3**	1.20	
Clin4_Ap2						0.0088	0.0001	0.7	0.0513	0.1734	2.1745	11.28	38.15	478.31	22.45	0.768	0.735	61.96	17.07	0.41	**22.5**	**0.3**	1.35	
Clin4_Ap3						0.0082	0.0001	0.8	0.0364	0.1210	1.1694	13.15	43.74	422.76	25.38	0.727	0.690	52.15	22.76	0.57	**31.8**	**0.4**	1.91	
Clin4_Ap4						0.0026	0.0000	1.2	0.0140	0.0489	0.4518	14.14	49.50	456.87	27.87	0.644	0.597	38.77	18.32	0.61	**29.2**	**0.5**	1.75	
Clin4_Ap5						0.0020	0.0000	1.5	0.0102	0.0393	0.3790	11.25	43.50	419.43	23.40	0.665	0.621	41.52	18.18	0.69	**28.0**	**0.5**	1.68	
Clin4 Av	**-32.257**	**-70.951**	**524**	**Granite (86 ± 3 Ma K-Ar[19])**	**CC**																**26.3**	**4.9**		
Clin5_Ap1						0.0068	0.0002	2.2	0.0409	0.0810	0.1655	31.94	63.15	129.07	47.32	0.640	0.593	38.30	21.03	1.03	**33.7**	**0.8**	2.02	
Clin5_Ap3						0.0070	0.0002	2.2	0.0335	0.0688	0.2307	29.11	59.84	200.49	44.06	0.623	0.574	36.36	25.87	1.25	**42.6**	**1.0**	2.55	
Clin5_Ap4						0.0062	0.0001	2.0	0.0249	0.0940	0.4725	11.96	45.11	226.66	23.58	0.702	0.662	47.33	23.85	1.07	**34.8**	**0.8**	2.09	
Clin5_Ap5						0.0078	0.0002	2.0	0.0584	0.0787	0.3472	31.87	42.98	189.65	42.82	0.676	0.633	43.13	18.73	0.85	**28.1**	**0.6**	1.69	
Clin5_Ap6						0.0089	0.0002	2.0	0.0446	0.0919	0.3041	25.86	53.24	176.22	39.15	0.678	0.636	43.46	24.61	1.10	**37.0**	**0.8**	2.22	
Clin5 Av	**-32.336**	**-71.067**	**306**	**Granite (123 Ma U-Pb[19])**	**CC**																**35.2**	**5.2**		
Clin6_Ap1						0.0193	0.0002	0.8	0.0660	0.2273	2.5390	14.07	48.45	541.13	27.95	0.788	0.759	68.53	29.04	0.75	**37.3**	**0.5**	2.24	
Clin6_Ap2						0.0145	0.0001	0.9	0.0535	0.1572	0.8005	21.48	63.14	321.57	37.76	0.684	0.642	44.35	29.27	0.79	**43.8**	**0.6**	2.63	
Clin6_Ap4						0.0042	0.0001	2.0	0.0310	0.1035	1.0612	13.59	45.43	465.72	26.41	0.690	0.648	45.25	13.76	0.60	**20.4**	**0.4**	1.22	
Clin6_Ap5						0.0124	0.0001	0.8	0.0524	0.1611	1.7168	16.36	50.25	535.50	30.63	0.725	0.688	51.68	24.74	0.63	**34.7**	**0.4**	2.08	
Clin6_Ap6						0.0130	0.0001	1.1	0.0506	0.1489	0.6182	27.26	80.16	332.91	47.58	0.686	0.645	44.70	27.77	0.82	**41.4**	**0.6**	2.48	
Clin6 Av	**-31.784**	**-70.975**	**508**	**Granite (109 ± 10 Ma U-Pb[20])**	**PC**																**35.5**	**9.2**		
Clin10A_Ap1						0.0004	0.0000	3.9	0.0056	0.0241	0.3543	7.08	30.42	447.30	16.30	0.605	0.555	34.50	6.43	0.52	**10.9**	**0.4**	0.65	
Clin10A_Ap2						0.0435	0.0002	0.5	0.2768	0.3510	4.1795	38.19	48.43	576.75	52.24	0.791	0.762	69.39	22.06	0.54	**28.1**	**0.3**	1.68	
Clin10A_Ap3						0.0079	0.0001	1.8	0.0724	0.1395	1.0792	43.77	84.37	652.53	66.58	0.672	0.629	42.61	13.78	0.57	**20.9**	**0.4**	1.25	
Clin10A_Ap4						0.0086	0.0001	1.0	0.0758	0.1930	1.9198	22.95	58.44	581.32	39.36	0.693	0.652	45.82	12.90	0.36	**18.9**	**0.3**	1.14	
Clin10A_Ap5						0.0020	0.0000	2.3	0.0203	0.0576	0.9864	8.98	25.50	436.78	17.00	0.692	0.651	45.57	10.67	0.53	**15.6**	**0.4**	0.94	
Clin10A Av	**-31.708**	**-70.796**	**1114**	**Granite (64 ± 10 Ma U-Pb[20])**	**PC**																**18.9**	**6.4**		
Clin10B_Ap1						0.0294	0.0003	1.0	0.1985	0.2564	5.2100	17.21	22.23	451.75	24.54	0.830	0.806	86.34	20.51	0.59	**24.8**	**0.4**	1.49	

Sample	Lon	Lat	Elev.	Lithology	Tect. unit	^{4}He	±1σ	±1σ	U	Th	Sm	U	Th	Sm	eU	F_T	F_T	R_s	Raw Age	±2σ	Corr. Age	±1σ	6% err	Comments
	(°)	(°)	(m)			(pmol)	(pmol)	(%)	(ng)	(ng)	(ng)	(ppm)	(ppm)	(ppm)	(ppm)	^{238}U	^{232}Th	(µm)	(Ma)	(Ma)	(Ma)	(Ma)	(Ma)	
Clin10B_Ap2						0.0300	0.0003	1.0	0.1607	0.2509	6.2036	10.71	16.72	413.46	16.57	0.845	0.823	95.04	24.44	0.70	29.0	0.4	1.74	
Clin10B_Ap3						0.0676	0.0006	0.9	0.4225	0.6267	9.0821	25.86	38.36	555.87	37.45	0.836	0.813	89.75	21.53	0.60	25.9	0.4	1.55	
Clin10B_Ap4						0.0101	0.0002	1.8	0.0749	0.0813	1.6838	17.20	18.69	386.83	23.40	0.758	0.724	59.25	19.47	0.83	25.8	0.6	1.55	
Clin10B_Ap5						0.0064	0.0001	1.8	0.0592	0.0881	1.4033	15.30	22.78	362.65	22.34	0.743	0.707	55.52	14.48	0.62	19.7	0.4	1.18	
Clin10B Av	**-31.707**	**-70.817**	**1392**	**Granite (64 ± 10 Ma U-Pb[20])**	**PC**																**25.0**	**3.4**		
Clin10D_Ap1						0.0052	0.0001	1.8	0.0813	0.1080	0.3203	80.21	106.55	316.13	106.62	0.618	0.569	35.78	9.05	0.39	14.9	0.3	0.90	
Clin10D_Ap2						0.0016	0.0001	4.1	0.0143	0.0496	0.4728	13.40	46.40	442.27	26.34	0.654	0.609	40.10	11.44	0.96	17.9	0.8	1.07	
Clin10D_Ap4						0.0041	0.0001	2.5	0.0491	0.0690	0.4233	40.21	56.51	346.71	55.07	0.658	0.613	40.62	11.54	0.63	17.8	0.5	1.07	
Clin10D_Ap5						0.0164	0.0003	1.6	0.2471	0.4168	2.1335	32.56	54.92	281.13	46.73	0.793	0.764	70.05	8.75	0.34	11.1	0.2	0.67	
Clin10D Av	**-31.669**	**-70.818**	**2065**	**Granite (64 ± 10 Ma U-Pb[20])**	**PC**																**15.5**	**3.2**		
Clin10E_Ap1						0.0024	0.0001	2.3	0.0104	0.0414	0.6624	5.07	20.22	323.38	11.32	0.675	0.632	42.97	20.82	1.06	31.4	0.8	1.89	
Clin10E_Ap2						*0.0002*	*0.0000*	*5.4*	*0.0012*	*0.0090*	*0.0185*	*0.44*	*3.15*	*6.47*	*1.20*	*0.700*	*0.660*	*46.92*	*10.43*	*1.21*	*15.4*	*0.9*	*0.93*	*Low U => rejected*
Clin10E_Ap3						0.0051	0.0001	1.4	0.0234	0.0782	0.5636	15.94	53.20	383.64	30.20	0.676	0.634	43.21	21.97	0.74	33.2	0.6	1.99	
Clin10E_Ap4						0.0019	0.0001	2.8	0.0123	0.0449	0.5918	8.55	31.21	411.33	17.79	0.676	0.633	43.12	15.14	0.89	22.8	0.7	1.37	
Clin10E_Ap5						*0.0007*	*0.0001*	*9.5*	*0.0156*	*0.0394*	*0.7409*	*9.87*	*24.94*	*469.50*	*17.92*	*0.688*	*0.646*	*44.96*	*4.90*	*0.93*	*7.2*	*0.7*	*0.43*	*High He error, younger than surrounding*
Clin10E Av	**-31.663**	**-70.816**	**2259**	**Granite (64 ± 10 Ma U-Pb[20])**	**PC**																**29.2**	**5.6**		
Clin12A_Ap2						0.0011	0.0001	8.7	0.0257	0.1008	0.5406	6.93	27.15	145.59	13.96	0.737	0.701	54.26	4.17	0.73	5.8	0.5	0.35	
Clin12A_Ap3						0.0003	0.0000	5.3	0.0178	0.0623	0.4281	3.41	11.90	81.82	6.58	0.776	0.744	64.34	1.68	0.18	2.2	0.1	0.13	
Clin12A_Ap4						0.0002	0.0000	11.3	0.0065	0.0316	0.1733	3.17	15.48	85.00	7.19	0.694	0.653	45.96	2.01	0.46	3.0	0.3	0.18	
Clin12A_Ap5						0.0001	0.0000	9.4	0.0042	0.0161	0.1062	4.04	15.63	103.17	8.18	0.628	0.580	36.96	2.85	0.54	4.7	0.4	0.28	
Clin12A Av	**-32.320**	**-70.697**	**1062**	**Granite (55.4 - 60 Ma K-Ar[19])**	**PC**																**3.9**	**1.6**		
Clin12B_Ap1						0.0003	0.0000	3.7	0.0041	0.0211	0.0827	7.26	37.62	147.21	16.75	0.577	0.524	31.84	5.16	0.44	9.4	0.4	0.56	
Clin12B_Ap2						0.0002	0.0000	5.7	0.0034	0.0140	0.0738	3.49	14.45	76.40	7.23	0.597	0.546	33.73	5.50	0.64	9.6	0.6	0.57	
Clin12B_Ap3						0.0004	0.0000	6.9	0.0069	0.0223	0.1878	8.20	26.42	222.97	15.43	0.604	0.554	34.43	5.78	0.81	9.8	0.7	0.59	
Clin12B Av	**-32.308**	**-70.701**	**1470**	**Granite (55.4 - 60 Ma K-Ar[19])**	**PC**																**9.6**	**0.2**		
Clin12C_Ap1						0.0037	0.0001	2.0	0.0473	0.0376	0.5207	19.17	15.23	211.05	23.72	0.708	0.669	48.42	11.96	0.57	17.0	0.4	1.02	
Clin12C_Ap2						0.0049	0.0001	2.2	0.0360	0.0514	0.2603	17.46	24.93	126.34	23.89	0.671	0.628	42.45	18.76	0.91	28.4	0.7	1.70	
Clin12C_Ap3						0.0207	0.0003	1.6	0.1350	0.1366	0.6113	63.11	63.85	285.74	79.39	0.695	0.654	46.05	22.84	0.88	33.2	0.6	1.99	
Clin12C_Ap4						0.0042	0.0001	2.1	0.0432	0.0455	0.3351	34.56	36.47	268.35	44.35	0.630	0.582	37.17	14.34	0.69	23.1	0.6	1.38	
Clin12C_Ap5						*0.0176*	*0.0003*	*1.8*	*0.0365*	*0.0913*	*0.3240*	*20.07*	*50.17*	*177.98*	*32.65*	*0.664*	*0.620*	*41.42*	*55.51*	*2.31*	*85.5*	*1.8*	*5.13*	*He injection => rejected*
Clin12C Av	**-32.297**	**-70.709**	**1858**	**Granite (55.4 - 60 Ma K-Ar[19])**	**PC**																**25.4**	**7.0**		
Clin12D_Ap1						0.0013	0.0000	2.1	0.0095	0.0391	0.6051	4.70	19.35	299.51	10.64	0.696	0.655	46.29	12.68	0.60	18.5	0.4	1.11	
Clin12D_Ap2						*0.0016*	*0.0000*	*1.9*	*0.0073*	*0.0217*	*0.4151*	*4.89*	*14.62*	*279.86*	*9.63*	*0.661*	*0.616*	*41.01*	*22.36*	*0.96*	*34.3*	*0.7*	*2.06*	*He injection => rejected*
Clin12D_Ap3						0.0005	0.0000	3.2	0.0056	0.0191	0.3590	5.07	17.30	324.51	10.64	0.646	0.600	39.12	9.09	0.61	14.3	0.5	0.86	
Clin12D_Ap4						0.0009	0.0000	2.0	0.0058	0.0276	0.4542	4.62	21.89	359.98	11.44	0.657	0.612	40.51	12.45	0.55	19.3	0.4	1.16	
Clin12D_Ap5						0.0021	0.0000	1.6	0.0114	0.0504	0.9597	4.30	19.09	363.24	10.47	0.732	0.696	53.22	15.59	0.57	21.6	0.4	1.29	
Clin12D Av	**-32.288**	**-70.719**	**2267**	**Granite (55.4 - 60 Ma K-Ar[19])**	**PC**																**18.4**	**3.0**		
Clin12E_Ap1						0.0005	0.0000	3.1	0.0030	0.0136	0.2752	2.46	11.13	224.89	6.12	0.637	0.590	37.99	13.99	1.26	22.4	1.0	1.34	
Clin12E_Ap2						0.0004	0.0000	3.6	0.0034	0.0164	0.4250	2.81	13.35	346.99	7.56	0.673	0.630	42.68	9.22	0.70	13.9	0.5	0.83	
Clin12E_Ap3						0.0010	0.0000	1.9	0.0030	0.0134	0.1350	3.29	14.79	148.66	7.45	0.621	0.572	36.13	30.35	1.35	50.4	1.1	3.02	
Clin12E_Ap4						0.0017	0.0000	1.8	0.0058	0.0302	0.5423	3.68	19.05	342.33	9.75	0.681	0.639	43.94	23.75	1.01	35.5	0.8	2.13	
Clin12E_Ap5						0.0010	0.0000	1.9	0.0035	0.0193	0.3460	3.46	19.28	344.81	9.59	0.612	0.563	35.24	22.11	0.95	37.0	0.8	2.22	
Clin12E Av	**-32.281**	**-70.721**	**2645**	**Granite (55.4 - 60 Ma K-Ar[19])**	**PC**																**31.8**	**14.1**		
Clin15_Ap1						0.0006	0.0000	2.4	0.0151	0.0503	0.6705	12.44	41.47	553.19	24.74	0.640	0.593	38.33	4.13	0.22	6.6	0.2	0.40	
Clin15_Ap2						0.0001	0.0000	7.9	0.0075	0.0137	0.2134	10.61	19.42	301.74	16.57	0.557	0.502	30.18	2.47	0.40	4.5	0.4	0.27	
Clin15_Ap3						0.0001	0.0000	14.0	0.0017	0.0082	0.1247	4.80	23.51	358.72	11.98	0.621	0.573	36.18	2.85	0.83	4.7	0.7	0.28	
Clin15_Ap4						0.0005	0.0000	2.6	0.0257	0.0466	0.6310	20.51	37.14	502.77	31.56	0.643	0.597	38.73	2.61	0.15	4.1	0.1	0.25	
Clin15 Av	**-32.886**	**-70.380**	**1160**	**Granite (19.8 ± 0.5 Ma K-Ar[21])**	**PC**																**5.0**	**1.1**		
Clin16A_Ap1						0.0003	0.0000	5.0	0.0094	0.0359	0.5704	3.99	15.20	241.39	8.68	0.698	0.657	46.55	3.24	0.33	4.7	0.2	0.28	
Clin16A_Ap3						0.0003	0.0000	4.7	0.0093	0.0305	0.4609	4.69	15.33	231.54	9.37	0.690	0.648	45.25	3.05	0.29	4.5	0.2	0.27	
Clin16A_Ap4						0.0004	0.0000	2.7	0.0143	0.0540	0.4408	8.18	30.84	251.91	16.58	0.685	0.643	44.43	2.65	0.15	4.0	0.1	0.24	

Sample	Lon (°)	Lat (°)	Elev. (m)	Lithology	Tect. unit	^{4}He (pmol)	± 1σ (pmol)	± 1σ (%)	U (ng)	Th (ng)	Sm (ng)	U (ppm)	Th (ppm)	Sm (ppm)	eU (ppm)	F_T ^{238}U	F_T ^{232}Th	R_s (µm)	Raw Age (Ma)	± 2σ (Ma)	Corr. Age (Ma)	± 1σ (Ma)	6% err (Ma)	Comments
Clin16A Av	**-32.523**	**-70.621**	**1116**	**Granite (63.7 ± 7 Ma U-Pb[19])**	**PC**																**4.4**	**0.4**		
Clin16B_Ap1						0.0049	0.0001	1.5	0.0283	0.1212	1.9612	5.50	23.59	381.71	12.82	0.784	0.754	67.04	15.44	0.54	**19.9**	**0.3**	1.20	
Clin16B_Ap2						0.0052	0.0001	1.0	0.0211	0.0974	1.3838	4.46	20.64	293.15	10.67	0.764	0.731	60.92	21.00	0.59	**27.9**	**0.4**	1.67	
Clin16B_Ap3						0.0039	0.0001	1.5	0.0204	0.0831	1.3926	4.97	20.21	338.65	11.29	0.735	0.698	53.71	17.30	0.61	**23.9**	**0.4**	1.43	
Clin16B_Ap4						0.0013	0.0001	5.6	0.0103	0.0336	0.6826	6.34	20.60	418.71	13.13	0.669	0.625	42.05	12.80	1.46	**19.4**	**1.1**	1.16	
Clin16B_Ap5						0.0030	0.0001	2.6	0.0193	0.0850	1.4273	4.83	21.29	357.37	11.49	0.757	0.723	59.05	13.53	0.75	**18.1**	**0.5**	1.09	
Clin16B Av	**-32.532**	**-70.602**	**1515**	**Granite (63.7 ± 7 Ma U-Pb[19])**	**PC**																**21.8**	**4.0**		
Clin16C_Ap1						0.0011	0.0000	2.1	0.0119	0.0276	1.1079	5.82	13.49	540.98	11.52	0.701	0.661	47.15	10.04	0.53	**14.3**	**0.4**	0.86	
Clin16C_Ap2						0.0033	0.0000	1.3	0.0315	0.0365	1.2564	13.44	15.57	535.39	19.60	0.714	0.675	49.46	14.70	0.51	**20.6**	**0.4**	1.24	
Clin16C_Ap3						0.0023	0.0000	1.3	0.0177	0.0581	1.6916	5.48	18.00	524.18	12.16	0.723	0.686	51.29	12.57	0.41	**17.5**	**0.3**	1.05	
Clin16C_Ap4						0.0070	0.0001	1.1	0.0392	0.1265	3.7950	4.64	14.98	449.65	10.26	0.804	0.776	74.20	17.70	0.52	**22.1**	**0.3**	1.33	
Clin16C_Ap5						0.0012	0.0000	1.8	0.0084	0.0239	0.3855	6.16	17.50	282.35	11.59	0.641	0.594	38.42	15.87	0.67	**25.2**	**0.5**	1.51	
Clin16C Av	**-32.540**	**-70.597**	**1908**	**Granite (63.7 ± 7 Ma U-Pb[19])**	**PC**																**20.0**	**4.2**		
Clin16D_Ap3						0.0003	0.0000	5.0	0.0040	0.0123	0.1760	4.10	12.48	178.85	7.86	0.618	0.569	35.80	6.80	0.70	**11.3**	**0.6**	0.68	
Clin16D_Ap4						0.0003	0.0000	4.1	0.0025	0.0103	0.2434	4.18	17.22	405.92	10.12	0.595	0.544	33.51	10.32	0.90	**17.6**	**0.8**	1.06	
Clin16D_Ap6						0.0006	0.0000	2.9	0.0038	0.0115	0.2134	5.13	15.63	291.25	10.16	0.621	0.572	36.14	15.46	0.96	**25.3**	**0.8**	1.52	
Clin16D Av	**-32.545**	**-70.593**	**2260**	**Granite (63.7 ± 7 Ma U-Pb[19])**	**PC**																**18.1**	**7.1**		
Clin16E_Ap1						0.0002	0.0000	7.3	0.0034	0.0099	0.1556	3.97	11.65	183.42	7.56	0.614	0.565	35.44	5.66	0.83	**9.4**	**0.7**	0.56	
Clin16E_Ap3						0.0001	0.0000	7.5	0.0027	0.0084	0.1322	4.87	15.03	235.91	9.50	0.580	0.528	32.14	5.07	0.77	**9.0**	**0.7**	0.54	
Clin16E_Ap4						0.0003	0.0000	4.0	0.0045	0.0144	0.3409	4.21	13.48	318.55	8.86	0.667	0.623	41.84	7.32	0.61	**11.1**	**0.5**	0.67	
Clin16E_Ap5						0.0008	0.0001	10.3	0.0094	0.0309	0.4291	5.92	19.41	269.15	11.73	0.647	0.602	39.24	8.53	1.77	**13.4**	**1.4**	0.81	
Clin16E Av	**-32.548**	**-70.592**	**2474**	**Granite (63.7 ± 7 Ma U-Pb[19])**	**PC**																**10.7**	**2.0**		
Clin17_Ap1						*0.0245*	*0.0001*	*0.4*	*0.0444*	*0.0912*	*1.5488*	*18.44*	*37.89*	*643.23*	*30.33*	*0.707*	*0.668*	*48.24*	*66.56*	*1.47*	*95.0*	*1.1*	*5.70*	*He injection => rejected*
Clin17_Ap2						*0.0113*	*0.0001*	*0.7*	*0.0198*	*0.0353*	*0.5605*	*27.16*	*48.47*	*770.35*	*42.12*	*0.571*	*0.518*	*31.34*	*72.23*	*1.86*	*128.3*	*1.7*	*7.70*	*He injection => rejected*
Clin17_Ap3						0.0019	0.0000	1.6	0.0386	0.0644	1.4595	17.32	28.87	654.69	27.15	0.718	0.680	50.35	6.41	0.25	**9.0**	**0.2**	0.54	
Clin17_Ap4						0.0004	0.0000	10.4	0.0069	0.0160	0.2737	10.72	24.87	425.99	18.54	0.620	0.572	36.08	6.18	1.29	**10.1**	**1.1**	0.61	
Clin17_Ap5						0.0010	0.0000	3.5	0.0293	0.0475	0.6106	23.80	38.49	495.16	35.13	0.642	0.596	38.58	4.40	0.32	**6.9**	**0.3**	0.42	
Clin17_Ap6						0.0003	0.0000	13.8	0.0057	0.0074	0.1184	18.39	23.55	379.45	25.68	0.450	0.388	23.21	7.19	2.00	**16.3**	**2.3**	0.98	
Clin17_Ap7						0.0005	0.0000	8.6	0.0109	0.0151	0.3368	12.75	17.70	395.42	18.76	0.563	0.509	30.70	6.06	1.05	**10.9**	**0.9**	0.65	
Clin17_Ap8						0.0005	0.0000	8.2	0.0123	0.0113	0.1770	28.36	26.07	408.39	36.38	0.609	0.559	34.88	6.02	1.01	**10.0**	**0.8**	0.60	
Clin17_Ap9						0.0022	0.0001	2.5	0.0377	0.0483	1.1621	21.23	27.20	653.77	30.67	0.675	0.632	43.01	8.07	0.44	**12.0**	**0.3**	0.72	
Clin17_Ap11						0.0007	0.0000	6.5	0.0133	0.0191	0.3675	16.19	23.26	446.79	23.74	0.564	0.510	30.78	7.06	0.93	**12.7**	**0.8**	0.76	
Clin17 Av	**-33.596**	**-70.492**	**790**	**Granite (19-22 Ma[22])**	**PC**																**11.0**	**2.8**		
Clin18_Ap1						0.0003	0.0000	4.9	0.0310	0.1042	0.3357	21.38	71.89	231.56	39.29	0.659	0.615	40.78	0.92	0.09	**1.4**	**0.1**	0.09	
Clin18_Ap2						0.0001	0.0000	7.7	0.0309	0.0711	0.2360	20.86	48.00	159.31	32.84	0.673	0.630	42.71	0.46	0.07	**0.7**	**0.1**	0.04	
Clin18_Ap4						0.0017	0.0000	1.8	0.0774	0.2659	0.7468	26.10	89.66	251.78	48.26	0.744	0.709	55.84	2.28	0.09	**3.1**	**0.1**	0.19	
Clin18 Av	**-33.809**	**-70.211**	**1313**	**Granite (9.3 - 11.4 Ma U-Pb[23])**	**PC**																**1.8**	**1.2**		**High age dispersion**
Clin22A_Ap1						0.0024	0.0000	1.4	0.2509	0.4176	1.0587	46.91	78.06	197.91	66.10	0.765	0.732	61.17	1.26	0.04	**1.7**	**0.0**	0.10	
Clin22A_Ap2						0.0007	0.0000	2.9	0.0947	0.1367	0.4328	42.93	61.97	196.25	58.36	0.689	0.647	45.10	1.03	0.06	**1.5**	**0.0**	0.09	
Clin22A_Ap3						0.0006	0.0000	2.9	0.0582	0.2581	1.2117	12.12	53.69	252.06	25.86	0.747	0.713	56.61	0.87	0.05	**1.2**	**0.0**	0.07	
Clin22A_Ap4						0.0015	0.0000	1.6	0.2041	0.3590	1.2633	33.64	59.17	208.19	48.47	0.774	0.743	63.96	0.96	0.04	**1.2**	**0.0**	0.07	
Clin22A_Ap5						0.0011	0.0000	2.0	0.1206	0.1720	0.7270	40.60	57.90	244.75	55.30	0.711	0.673	49.01	1.24	0.06	**1.8**	**0.0**	0.11	
Clin22A Av	**-33.491**	**-70.130**	**1559**	**Granite (10.37 ± 0.1 Ma U-Pb[24])**	**PC**																**1.5**	**0.3**		
Clin22B_Ap1						0.0019	0.0000	2.4	0.1337	0.6442	2.7523	14.85	71.53	305.57	33.02	0.807	0.780	75.60	1.24	0.07	**1.6**	**0.0**	0.09	
Clin22B_Ap2						0.0012	0.0001	10.6	0.1628	0.2328	0.7063	30.32	43.35	131.57	41.08	0.768	0.736	62.17	1.05	0.22	**1.4**	**0.1**	0.08	
Clin22B_Ap3						0.0003	0.0000	5.1	0.0547	0.0777	0.1988	35.82	50.91	130.25	48.35	0.627	0.578	36.76	0.65	0.07	**1.1**	**0.1**	0.06	
Clin22B_Ap5						0.0003	0.0000	4.0	0.0407	0.1538	0.5043	17.74	67.09	220.02	34.48	0.689	0.648	45.13	0.64	0.05	**1.0**	**0.0**	0.06	
Clin22B Av	**-33.499**	**-70.125**	**1918**	**Granite (10.37 ± 0.1 Ma U-Pb[24])**	**PC**																**1.2**	**0.3**	0.07	
Clin22C_Ap1						0.0003	0.0000	2.9	0.0272	0.0924	0.3938	13.17	44.73	190.54	24.53	0.700	0.660	46.92	1.17	0.07	**1.7**	**0.1**	0.10	
Clin22C_Ap2						0.0004	0.0000	3.1	0.0422	0.1046	0.4636	21.51	53.32	236.27	35.10	0.675	0.632	42.92	1.06	0.07	**1.6**	**0.1**	0.10	
Clin22C_Ap3						0.0003	0.0000	3.2	0.0454	0.0916	0.3642	27.17	54.85	218.02	41.03	0.680	0.637	43.67	0.95	0.06	**1.4**	**0.0**	0.09	

Sample	Lon (°)	Lat (°)	Elev. (m)	Lithology	Tect. unit	^{4}He (pmol)	±1σ (pmol)	±1σ (%)	U (ng)	Th (ng)	Sm (ng)	U (ppm)	Th (ppm)	Sm (ppm)	eU (ppm)	F_T ^{238}U	F_T ^{232}Th	R_s (µm)	Raw Age (Ma)	±2σ (Ma)	Corr. Age (Ma)	±1σ (Ma)	6% err (Ma)	Comments
Clin22C_Ap4						0.0003	0.0000	4.2	0.0424	0.0997	0.4425	22.10	51.98	230.66	35.35	0.679	0.637	43.66	0.84	0.07	**1.3**	**0.1**	0.08	
Clin22C_Ap5						0.0005	0.0000	4.0	0.0732	0.1339	0.6238	26.58	48.66	226.60	39.03	0.686	0.644	44.65	0.86	0.07	**1.3**	**0.1**	0.08	
Clin22C Av	**-33.504**	**-70.124**	**2280**	**Granite (10.37 ± 0.1 Ma U-Pb[24])**	**PC**																**1.5**	**0.2**		
Clin22D_Ap1						0.0020	0.0001	2.8	0.1332	0.3443	1.3953	47.62	123.10	498.92	78.77	0.725	0.687	51.58	1.68	0.10	**2.4**	**0.1**	0.14	
Clin22D_Ap2						0.0085	0.0001	1.7	0.3335	0.9039	2.7320	45.44	123.15	372.23	76.01	0.775	0.744	64.27	2.86	0.11	**3.7**	**0.1**	0.22	
Clin22D_Ap3						0.0067	0.0001	2.2	0.1659	0.5755	2.9356	27.42	95.14	485.34	51.96	0.783	0.753	66.83	4.04	0.19	**5.2**	**0.1**	0.31	
Clin22D_Ap4						0.0011	0.0001	7.8	0.0706	0.2760	0.9977	33.41	130.66	472.21	66.20	0.709	0.670	48.52	1.50	0.24	**2.2**	**0.2**	0.13	
Clin22D_Ap5						0.0054	0.0001	1.3	0.2170	0.5432	1.7022	42.25	105.79	331.49	68.56	0.768	0.735	61.97	2.86	0.10	**3.8**	**0.1**	0.23	
Clin22D Av	**-33.505**	**-70.129**	**2575**	**Granite (10.37 ± 0.1 Ma U-Pb[24])**	**PC**																**3.5**	**1.2**		
Clin24_Ap1						0.0001	0.0000	9.4	0.0137	0.0353	0.4014	13.52	34.78	395.29	23.52	0.624	0.576	36.50	0.96	0.18	**1.6**	**0.2**	0.09	
Clin24_Ap2						0.0002	0.0000	4.3	0.0269	0.1017	1.1307	9.49	35.84	398.37	19.75	0.731	0.695	52.98	0.88	0.08	**1.2**	**0.1**	0.07	
Clin24_Ap3						*0.0000*	*0.0000*	*30.0*	*0.0057*	*0.0271*	*0.2052*	*9.28*	*43.94*	*332.82*	*21.13*	*0.634*	*0.586*	*37.58*	*0.37*	*0.22*	***0.6***	***0.2***	*0.04*	*High He error => rejected*
Clin24_Ap4						*0.0001*	*0.0000*	*14.0*	*0.0117*	*0.0233*	*0.3191*	*14.72*	*29.35*	*401.38*	*23.47*	*0.681*	*0.639*	*43.89*	*0.58*	*0.16*	***0.9***	***0.1***	*0.05*	*Partly broken grain, high He error => rej.*
Clin24_Ap5						*0.0000*	*0.0000*	*17.0*	*0.0106*	*0.0226*	*0.3173*	*12.48*	*26.64*	*373.70*	*20.47*	*0.727*	*0.690*	*52.07*	*0.48*	*0.16*	***0.7***	***0.1***	*0.04*	*High He error => rejected*
Clin24 Av	**-34.365**	**-70.321**	**1274**	**Granite (11.7 ± 0.5 Ma k-Ar[25])**	**PC**																**1.4**	**0.3**		
Clin25A_Ap1						0.0001	0.0000	11.3	0.0482	0.1212	0.5017	17.27	43.41	179.64	28.27	0.722	0.684	51.01	0.28	0.06	**0.4**	**0.0**	0.02	
Clin25A_Ap2						0.0001	0.0000	7.5	0.0609	0.1000	0.5772	18.95	31.08	179.45	27.06	0.744	0.709	55.89	0.32	0.05	**0.4**	**0.0**	0.03	
Clin25A_Ap4						0.0002	0.0000	6.6	0.0700	0.1295	0.6978	20.63	38.18	205.75	30.53	0.726	0.689	51.88	0.34	0.05	**0.5**	**0.0**	0.03	
Clin25A_Ap5						0.0002	0.0000	4.9	0.0393	0.0918	0.4736	16.73	39.11	201.65	26.83	0.695	0.654	46.10	0.56	0.06	**0.8**	**0.0**	0.05	
Clin25A_Ap6						0.0001	0.0000	11.3	0.0339	0.0501	0.2186	28.90	42.73	186.35	39.78	0.623	0.574	36.35	0.29	0.07	**0.5**	**0.1**	0.03	
Clin25A Av	**-34.059**	**-70.118**	**2012**	**Granite (13.39 ± 0.13 Ma U-Pb[24])**	**PC**																**0.5**	**0.2**		
Clin25B_Ap1						0.0006	0.0000	6.2	0.0623	0.1313	2.6033	10.60	22.33	442.65	17.90	0.790	0.760	68.98	1.23	0.16	**1.6**	**0.1**	0.09	
Clin25B_Ap2						0.0008	0.0001	6.3	0.0719	0.1459	1.9696	14.12	28.67	387.02	22.65	0.779	0.748	65.33	1.36	0.17	**1.8**	**0.1**	0.11	
Clin25B_Ap3						0.0001	0.0000	12.5	0.0114	0.0498	0.7662	6.02	26.19	403.29	14.04	0.675	0.632	42.94	0.42	0.11	**0.6**	**0.1**	0.04	
Clin25B_Ap4						0.0001	0.0000	10.6	0.0148	0.0504	0.9936	6.53	22.22	438.19	13.79	0.695	0.655	46.20	0.53	0.11	**0.8**	**0.1**	0.05	
Clin25B_Ap5						0.0001	0.0000	13.3	0.0095	0.0367	0.3048	10.00	38.85	322.64	20.61	0.631	0.583	37.24	0.59	0.16	**1.0**	**0.1**	0.06	
Clin25B Av	**-34.076**	**-70.115**	**2374**	**Granite (13.39 ± 0.13 Ma U-Pb[24])**	**PC**																**1.1**	**0.5**		
Clin25C_Ap1						0.0003	0.0000	4.1	0.0449	0.0587	0.9837	22.30	29.18	488.78	31.43	0.704	0.664	47.61	0.93	0.08	**1.3**	**0.1**	0.08	
Clin25C_Ap2						0.0003	0.0000	3.9	0.0410	0.0529	1.0091	21.30	27.47	523.75	30.18	0.694	0.654	46.01	1.14	0.09	**1.7**	**0.1**	0.10	
Clin25C_Ap3						0.0002	0.0000	3.7	0.0397	0.0526	0.9605	20.79	27.55	502.67	29.60	0.692	0.651	45.63	0.86	0.07	**1.3**	**0.0**	0.08	
Clin25C_Ap4						0.0001	0.0000	7.4	0.0180	0.0383	0.8424	11.85	25.18	554.19	20.35	0.671	0.628	42.41	0.95	0.14	**1.4**	**0.1**	0.09	
Clin25C_Ap5						0.0006	0.0000	7.5	0.0855	0.1213	1.8012	23.93	33.94	503.97	34.24	0.728	0.691	52.22	0.90	0.14	**1.3**	**0.1**	0.08	
Clin25C Av	**-34.076**	**-70.120**	**2670**	**Granite (13.39 ± 0.13 Ma U-Pb[24])**	**PC**																**1.4**	**0.2**		
Clin25D_Ap1						0.0004	0.0000	3.3	0.0526	0.2139	2.8880	6.29	25.56	345.03	13.89	0.802	0.774	73.57	0.62	0.04	**0.8**	**0.0**	0.05	
Clin25D_Ap2						0.0001	0.0000	7.5	0.0294	0.0565	0.7837	18.70	35.88	497.67	29.43	0.664	0.619	41.37	0.61	0.09	**0.9**	**0.1**	0.06	
Clin25D_Ap3						0.0004	0.0000	5.4	0.0745	0.1717	1.5609	24.09	55.53	504.68	39.45	0.735	0.699	53.74	0.66	0.07	**0.9**	**0.0**	0.05	
Clin25D_Ap4						*0.0000*	*0.0000*	*23.8*	*0.0079*	*0.0425*	*0.4128*	*3.40*	*18.28*	*177.62*	*8.51*	*0.716*	*0.678*	*49.86*	*0.33*	*0.15*	***0.5***	***0.1***	*0.03*	*High He error => rejected*
Clin25D_Ap5						0.0002	0.0000	6.1	0.0429	0.0655	0.5080	33.16	50.65	392.99	46.86	0.644	0.597	38.76	0.50	0.06	**0.8**	**0.0**	0.05	
Clin25D Av	**-34.079**	**-70.124**	**2934**	**Granite (13.39 ± 0.13 Ma U-Pb[24])**	**PC**																**0.9**	**0.1**		
Clin26_Ap1						0.0003	0.0000	3.7	0.0248	0.0468	0.6424	14.89	28.05	385.33	23.27	0.699	0.658	46.75	1.65	0.13	**2.4**	**0.1**	0.14	
Clin26_Ap2						0.0001	0.0000	10.6	0.0096	0.0251	0.7228	5.49	14.41	414.41	10.81	0.656	0.611	40.38	0.91	0.19	**1.4**	**0.1**	0.08	
Clin26_Ap3						*0.0001*	*0.0000*	*10.6*	*0.0007*	*0.0002*	*0.0007*	*1.09*	*0.35*	*1.22*	*1.18*	*0.660*	*0.615*	*40.88*	*32.36*	*11.44*	***49.3***	***8.7***	*2.96*	*Low U => rejected*
Clin26_Ap4						0.0001	0.0000	10.0	0.0158	0.0721	1.0018	11.66	53.37	741.28	27.63	0.622	0.573	36.24	0.79	0.16	**1.3**	**0.1**	0.08	
Clin26_Ap5						0.0001	0.0000	10.1	0.0178	0.0535	0.9903	6.86	20.64	381.82	13.48	0.740	0.705	55.00	0.87	0.18	**1.2**	**0.1**	0.07	
Clin26 Av	**-34.825**	**-70.564**	**1030**	**Granite (Miocene[26])**	**PC**																**1.6**	**0.6**		
CLRK3848_Ap1						0.0111	0.0002	2.0	0.0358	0.0417	0.2690	8.39	9.78	63.07	10.95	0.752	0.718	57.72	42.87	0.47	**58.5**	n.a.	3.51	
CLRK3848_Ap2						*0.0005*	*0.0000*	*3.6*	*0.0023*	*0.0072*	*0.0995*	*0.70*	*2.24*	*30.82*	*1.37*	*0.726*	*0.688*	*51.80*	*21.25*	*0.27*	***30.5***	*n.a.*	***1.83***	*High He error, low U => rejected*
CLRK3848_Ap3						0.0068	0.0001	2.1	0.0175	0.0666	1.0374	5.12	19.44	302.84	11.11	0.714	0.676	49.53	30.25	0.32	**44.2**	n.a.	2.65	
CLRK3848_Ap4						0.0074	0.0002	2.2	0.0247	0.0721	0.5331	11.83	34.55	255.50	21.06	0.685	0.643	44.50	29.53	0.33	**45.2**	n.a.	2.71	
CLRK3848_Ap5						0.0062	0.0001	2.3	0.0208	0.0527	0.4942	10.52	26.59	249.38	17.89	0.669	0.626	42.18	30.49	0.35	**47.8**	n.a.	2.87	
CLRK3848	**-69.972**	**-24.098**	**1088**	**Granite (168 Ma[27,37])**	**CC**																**48.9**	**6.5**		

Sample	Lon	Lat	Elev.	Lithology	Tect. unit	^{4}He	± 1σ	± 1σ	U	Th	Sm	U	Th	Sm	eU	F_T ^{238}U	F_T ^{232}Th	R_s	Raw Age	± 2σ	Corr. Age	± 1σ	6% err	Comments
	(°)	(°)	(m)			(pmol)	(pmol)	(%)	(ng)	(ng)	(ng)	(ppm)	(ppm)	(ppm)	(ppm)			(µm)	(Ma)	(Ma)	(Ma)	(Ma)	(Ma)	
CLRK3849_Ap2						*0.0005*	*0.0000*	*4.1*	*0.0022*	*0.0017*	*0.0575*	*1.24*	*0.95*	*32.11*	*1.62*	*0.674*	*0.631*	*42.86*	*32.20*	*0.56*	**49.1**	*n.a.*	**2.95**	*High He error, low U => rejected*
CLRK3849_Ap3						*0.0003*	*0.0000*	*5.4*	*0.0004*	*0.0010*	*0.0053*	*0.19*	*0.44*	*2.27*	*0.30*	*0.701*	*0.661*	*47.12*	*77.73*	*3.46*	**115.5**	*n.a.*	**6.93**	*High He error, low U => rejected*
CLRK3849_Ap4						*0.0008*	*0.0000*	*2.9*	*0.0027*	*0.0288*	*0.0307*	*1.28*	*13.65*	*14.60*	*4.50*	*0.694*	*0.653*	*45.97*	*14.59*	*0.18*	**22.2**	*n.a.*	**1.33**	*High He error, low U => rejected*
CLRK3849	**-70.146**	**-24.691**	**2243**	**Granodiorite (108 Ma K-Ar [28,37])**	**CC**																**62.3**	**48.0**		***High He error, low U => rejected***
CLRK3851_Ap1						0.0254	0.0005	2.0	0.0882	0.0762	1.8282	48.42	41.83	######	63.07	0.669	0.626	42.18	38.71	0.50	**59.6**	n.a.	**3.58**	
CLRK3851_Ap2						0.0035	0.0001	2.1	0.0157	0.0518	0.4912	7.22	23.76	225.20	13.81	0.694	0.653	45.98	20.47	0.22	**30.9**	n.a.	**1.85**	
CLRK3851_Ap3						0.0082	0.0002	2.0	0.0136	0.0719	0.7475	6.01	31.86	331.34	15.00	0.687	0.645	44.77	41.38	0.46	**63.5**	n.a.	**3.81**	
CLRK3851_Ap4						0.0059	0.0001	2.3	0.0108	0.0674	0.5649	4.03	25.12	210.53	10.86	0.705	0.665	47.77	34.52	0.38	**51.5**	n.a.	**3.09**	
CLRK3851_Ap5						0.0085	0.0002	2.3	0.0394	0.0666	0.8045	22.89	38.64	467.06	34.12	0.652	0.607	39.85	25.51	0.31	**40.9**	n.a.	**2.45**	
CLRK3851	**-69.271**	**-25.235**	**3817**	**Granite (289 Ma K-Ar [29])**	**PC**																**49.3**	**13.4**		
CLRK3852_Ap1						0.0238	0.0005	2.0	0.0910	0.0297	0.9620	47.13	15.39	498.21	53.17	0.675	0.633	43.06	41.47	0.58	**62.4**	n.a.	**3.74**	
CLRK3852_Ap2						*0.1888*	*0.0037*	*2.0*	*0.2267*	*0.1713*	*2.5225*	*45.47*	*34.36*	*505.96*	*55.91*	*0.751*	*0.717*	*57.53*	*120.51*	*1.41*	**163.7**	*n.a.*	**9.82**	*He injection => rejected*
CLRK3852_Ap3						0.0220	0.0004	2.0	0.0818	0.0342	0.9346	48.44	20.22	553.13	55.86	0.641	0.595	38.49	41.71	0.61	**66.5**	n.a.	**3.99**	
CLRK3852	**-69.084**	**-25.380**	**4020**	**Monzonite (Permian, 323.9 Ma U-Pb [29])**	**PC**																**64.4**	**2.9**		
CLRK3853_Ap1						0.0021	0.0000	2.3	0.0068	0.0258	0.5298	4.28	16.27	334.42	9.70	0.659	0.614	40.68	22.81	0.27	**36.6**	n.a.	**2.20**	
CLRK3853_Ap2						*0.0052*	*0.0001*	*2.1*	*0.0149*	*0.0511*	*0.9621*	*7.80*	*26.68*	*502.79*	*16.46*	*0.668*	*0.624*	*41.98*	*27.50*	*0.31*	**43.4**	*n.a.*	**2.60**	*Magmatic cooling age => rejected*
CLRK3853_Ap3						0.0031	0.0001	2.1	0.0102	0.0388	0.5873	5.49	20.86	315.49	11.87	0.679	0.637	43.65	23.86	0.27	**36.9**	n.a.	**2.22**	
CLRK3853	**-69.436**	**-25.746**	**2700**	**Monzonite (43.3 Ma K-Ar [30])**	**PC**																**36.8**	**0.2**		
CLRK3859_Ap1						0.0004	0.0000	3.8	0.0017	0.0164	0.1583	0.59	5.88	56.81	2.23	0.708	0.669	48.44	10.24	0.13	**15.2**	n.a.	**0.91**	
CLRK3859_Ap2						0.0006	0.0000	2.9	0.0046	0.0150	0.3189	2.83	9.27	197.25	5.96	0.664	0.620	41.39	10.42	0.13	**16.5**	n.a.	**0.99**	
CLRK3859_Ap3						0.0003	0.0000	4.3	0.0022	0.0079	0.1546	1.06	3.79	74.34	2.30	0.683	0.641	44.18	11.31	0.15	**17.4**	n.a.	**1.04**	
CLRK3859	**-70.163**	**-25.781**	**1091**	**Tonalite (149.4 Ma [31])**	**CC**																**16.5**	**1.0**		
CLRK3862_Ap1						0.0044	0.0001	2.1	0.0167	0.0568	0.6914	7.95	27.10	329.82	15.84	0.676	0.633	43.15	22.60	0.25	**35.2**	n.a.	**2.11**	
CLRK3862_Ap2						*0.0166*	*0.0003*	*2.1*	*0.0310*	*0.1290*	*1.6019*	*11.88*	*49.46*	*614.11*	*26.33*	*0.706*	*0.667*	*48.08*	*41.09*	*0.43*	**60.9**	*n.a.*	**3.66**	*Magmatic cooling age => rejected*
CLRK3862_Ap3						0.0044	0.0001	2.2	0.0342	0.0470	0.3180	23.86	32.81	222.11	32.52	0.640	0.593	38.32	17.15	0.22	**28.0**	n.a.	**1.68**	
CLRK3862_Ap4						0.0064	0.0001	2.3	0.0262	0.0901	1.3714	10.83	37.17	566.03	22.21	0.682	0.640	44.02	20.03	0.22	**30.8**	n.a.	**1.85**	
CLRK3862_Ap5						0.0049	0.0001	2.3	0.0260	0.0563	0.6599	23.59	51.05	598.83	38.34	0.621	0.573	36.20	20.24	0.26	**34.4**	n.a.	**2.06**	
CLRK3862	**-69.577**	**-26.332**	**2604**	**Porphyritic Monzonite (59 ±2 Ma [17])**	**PC**																**32.1**	**3.3**		
CLRK3863_Ap1						0.0083	0.0002	2.0	0.0507	0.0497	0.4772	21.01	20.63	197.95	26.75	0.699	0.658	46.73	23.20	0.28	**34.2**	n.a.	**2.05**	
CLRK3863_Ap2						0.0137	0.0003	2.0	0.0788	0.0978	0.9670	15.89	19.72	195.01	21.40	0.752	0.718	57.70	23.10	0.25	**31.5**	n.a.	**1.89**	
CLRK3863_Ap3						0.0088	0.0002	2.0	0.0611	0.0744	0.6402	18.39	22.37	192.62	24.50	0.721	0.683	50.87	19.32	0.22	**27.6**	n.a.	**1.66**	
CLRK3863	**-69.612**	**-26.099**	**2007**	**Tonalite (68.5 Ma K-Ar [17])**	**PC**																**31.1**	**3.3**		
CLRK3864_Ap1						*0.0025*	*0.0001*	*2.2*	*0.0084*	*0.0223*	*0.4372*	*7.76*	*20.56*	*402.66*	*14.50*	*0.624*	*0.576*	*36.53*	*26.25*	*0.33*	**44.5**	*n.a.*	**2.67**	*He injection? Older than ZHe age => rej.*
CLRK3864_Ap2						*0.0018*	*0.0000*	*2.2*	*0.0062*	*0.0138*	*0.2130*	*6.11*	*13.69*	*210.72*	*10.32*	*0.619*	*0.570*	*35.91*	*29.57*	*0.39*	**50.6**	*n.a.*	**3.03**	*He injection? Older than ZHe age => rej.*
CLRK3864_Ap3						0.0010	0.0000	2.4	0.0060	0.0131	0.1714	7.09	15.47	202.29	11.66	0.591	0.539	33.08	18.45	0.26	**33.2**	n.a.	**1.99**	
CLRK3864_Ap4						0.0018	0.0000	2.5	0.0101	0.0174	0.4262	11.21	19.20	471.62	17.99	0.603	0.553	34.29	19.09	0.26	**33.4**	n.a.	**2.01**	
CLRK3864_Ap5						0.0015	0.0000	2.6	0.0076	0.0178	0.4340	7.69	18.12	441.31	14.07	0.598	0.547	33.83	18.00	0.25	**32.0**	n.a.	**1.92**	
CLRK3864	**-69.445**	**-26.201**	**2804**	**Granite (Permian [18])**	**PC**																**32.9**	**0.8**		
CLRK3866_Ap1						0.0446	0.0009	2.0	0.2519	0.3674	0.6463	114.55	167.06	293.89	154.48	0.681	0.639	43.91	24.02	0.29	**36.6**	n.a.	**2.20**	
CLRK3866_Ap2						0.0600	0.0012	2.0	0.3207	0.4624	0.8387	89.48	129.01	234.03	120.35	0.737	0.701	54.19	25.41	0.27	**35.5**	n.a.	**2.13**	
CLRK3866_Ap3						0.1222	0.0024	2.0	0.6288	0.9321	1.5390	111.32	165.01	272.44	150.66	0.763	0.730	60.71	26.25	0.28	**35.3**	n.a.	**2.12**	
CLRK3866	**-69.438**	**-26.220**	**3166**	**Granite (Permian [18])**	**PC**																**35.8**	**0.7**		
CLRK3867_Ap1						0.0236	0.0005	2.0	0.0901	0.2779	0.6697	29.15	89.91	216.71	50.93	0.711	0.673	49.01	27.12	0.28	**39.8**	n.a.	**2.39**	
CLRK3867_Ap2						0.0255	0.0005	2.0	0.1040	0.2686	1.1137	23.07	59.59	247.10	38.02	0.748	0.714	56.89	26.74	0.27	**37.0**	n.a.	**2.22**	
CLRK3867_Ap3						0.0136	0.0003	2.0	0.0564	0.2030	0.3393	21.52	77.44	129.42	39.99	0.703	0.663	47.46	23.44	0.25	**34.9**	n.a.	**2.09**	
CLRK3867	**-69.421**	**-26.242**	**3433**	**Granite (Permian [18])**	**PC**																**37.2**	**2.4**		
CLRK3868_Ap1						0.0440	0.0009	2.0	0.2393	0.3656	0.8900	50.15	76.62	186.51	68.72	0.753	0.719	57.99	24.45	0.26	**33.4**	n.a.	**2.00**	
CLRK3868_Ap2						0.0322	0.0006	2.0	0.2055	0.2568	0.8546	60.51	75.62	251.69	79.18	0.726	0.689	51.83	21.85	0.25	**31.0**	n.a.	**1.86**	
CLRK3868_Ap3						0.0548	0.0011	2.0	0.2707	0.4315	0.8352	57.98	92.42	178.91	80.15	0.750	0.716	57.36	26.71	0.28	**36.6**	n.a.	**2.20**	
CLRK3868	**-69.415**	**-26.258**	**3762**	**Granite (Permian [18])**	**PC**																**33.7**	**2.8**		
CLRK3871_Ap1						0.0098	0.0002	2.0	0.0352	0.1919	0.8937	11.95	65.21	303.71	28.48	0.706	0.667	48.07	20.69	0.22	**30.7**	n.a.	**1.84**	

Sample	Lon	Lat	Elev.	Lithology	Tect. unit	^{4}He	±1σ	±1σ	U	Th	Sm	U	Th	Sm	eU	F_T	F_T	R_s	Raw Age	±2σ	Corr. Age	±1σ	6% err	Comments
	(°)	(°)	(m)			(pmol)	(pmol)	(%)	(ng)	(ng)	(ng)	(ppm)	(ppm)	(ppm)	(ppm)	^{238}U	^{232}Th	(µm)	(Ma)	(Ma)	(Ma)	(Ma)	(Ma)	
CLRK3871_Ap2						*0.0073*	*0.0001*	*2.0*	*0.0179*	*0.0572*	*0.7482*	*2.93*	*9.38*	*122.62*	*5.70*	*0.778*	*0.747*	*64.99*	*36.03*	*0.35*	***47.8***	*n.a.*	***2.87***	*He injection? => rejected*
CLRK3871_Ap3						0.0020	0.0000	2.2	0.0067	0.0203	0.7462	2.33	7.09	260.69	5.26	0.711	0.673	49.00	20.73	0.23	**30.4**	n.a.	**1.82**	
CLRK3871_Ap4						0.0110	0.0002	2.1	0.0553	0.1179	0.9599	10.78	22.99	187.12	17.00	0.752	0.718	57.76	22.38	0.23	**30.7**	n.a.	**1.84**	
CLRK3871_Ap5						0.0039	0.0001	2.3	0.0155	0.0643	0.5572	5.10	21.22	183.82	10.91	0.711	0.673	49.01	20.47	0.21	**30.1**	n.a.	**1.81**	
CLRK3871	**-69.243**	**-26.156**	**3304**	**Sandstone (Middle Jurassic[17])**	**PC**																**30.5**	**0.3**		
CLRK3872_Ap1						0.0017	0.0000	2.3	0.0057	0.0189	0.4621	4.99	16.64	407.07	10.86	0.620	0.572	36.08	22.07	0.30	**37.9**	n.a.	**2.27**	
CLRK3872_Ap2						0.0008	0.0000	2.8	0.0023	0.0088	0.2078	2.96	11.51	272.69	6.97	0.585	0.533	32.57	23.69	0.44	**43.6**	n.a.	**2.61**	
CLRK3872_Ap3						0.0011	0.0000	2.5	0.0038	0.0127	0.3102	5.24	17.75	433.01	11.49	0.576	0.523	31.78	21.10	0.34	**39.4**	n.a.	**2.36**	
CLRK3872	**-69.066**	**-26.524**	**3614**	**Granite (Permian[32])**	**PC**																**40.3**	**3.0**		
CLRK3873_Ap1						0.0037	0.0001	2.1	0.0110	0.0233	0.4166	4.57	9.70	173.38	7.67	0.696	0.655	46.24	34.60	0.40	**51.8**	n.a.	**3.11**	
CLRK3873_Ap2						0.0039	0.0001	2.1	0.0113	0.0230	0.4635	4.52	9.23	186.05	7.57	0.707	0.668	48.25	35.11	0.40	**51.6**	n.a.	**3.09**	
CLRK3873_Ap3						0.0072	0.0001	2.0	0.0230	0.0339	0.6615	6.20	9.12	178.09	9.18	0.735	0.699	53.85	36.42	0.40	**51.0**	n.a.	**3.06**	
CLRK3873	**-69.856**	**-25.404**	**1716**	**Tonalite (188.8 - 180 Ma[33])**	**CC**																**51.5**	**0.4**		
CLRK3874_Ap1						0.0667	0.0012	1.9	0.2774	0.0976	1.6751	50.24	17.67	303.42	55.83	0.748	0.713	56.70	39.26	0.49	**53.2**	n.a.	**3.19**	
CLRK3874_Ap2						0.0163	0.0003	2.0	0.0505	0.0660	1.1420	28.12	36.73	635.85	39.75	0.670	0.626	42.23	39.85	0.49	**61.8**	n.a.	**3.71**	
CLRK3874_Ap3						0.0421	0.0008	2.0	0.1662	0.2177	1.9332	45.51	59.64	529.56	61.89	0.736	0.700	53.96	33.40	0.37	**46.7**	n.a.	**2.80**	
CLRK3874	**-69.345**	**-24.825**	**2814**	**Granite (Carb.-Perm.[34])**	**PC**																**53.9**	**7.6**		
CLRK3875_Ap1						0.0062	0.0001	2.0	0.0401	0.0343	0.9414	14.45	12.35	339.38	18.99	0.711	0.672	48.86	20.61	0.25	**29.8**	n.a.	**1.79**	
CLRK3875_Ap2						0.0034	0.0001	2.0	0.0221	0.0313	0.4810	15.48	21.96	336.96	22.22	0.643	0.597	38.69	18.86	0.24	**30.6**	n.a.	**1.84**	
CLRK3875_Ap3						*0.0014*	*0.0000*	*1.9*	*0.0027*	*0.0126*	*0.2799*	*1.23*	*5.85*	*129.64*	*3.23*	*0.691*	*0.650*	*45.46*	*32.08*	*0.45*	***48.8***	*n.a.*	***2.93***	*Low U => rejected*
CLRK3875_Ap4						0.0133	0.0003	2.3	0.0745	0.0972	2.1888	10.23	13.34	300.50	14.80	0.787	0.757	67.91	21.26	0.22	**27.6**	n.a.	**1.66**	
CLRK3875_Ap5						0.0032	0.0001	2.4	0.0195	0.0190	0.5585	12.32	12.04	353.02	16.86	0.661	0.616	40.98	20.67	0.27	**32.4**	n.a.	**1.94**	
CLRK3875	**-69.181**	**-24.701**	**3625**	**Porphyric Tonalite (Permian[34])**	**PC**																**30.1**	**2.0**		
CLRK3876_Ap1						0.0221	0.0004	1.9	0.1230	0.1000	0.3855	52.13	42.39	163.38	62.71	0.692	0.651	45.66	27.26	0.34	**40.5**	n.a.	**2.43**	
CLRK3876_Ap2						0.0324	0.0006	2.0	0.1715	0.1748	0.4143	81.43	83.00	196.78	101.52	0.682	0.639	43.98	27.78	0.35	**42.1**	n.a.	**2.52**	
CLRK3876_Ap3						*0.0463*	*0.0009*	*2.0*	*0.1548*	*0.1150*	*0.4064*	*67.64*	*50.25*	*177.57*	*80.09*	*0.690*	*0.649*	*45.34*	*46.21*	*0.59*	***68.7***	*n.a.*	***4.12***	*Older than AFT age. He-injection? => rej.*
CLRK3876_Ap4						0.0173	0.0004	2.3	0.0962	0.0749	0.2884	47.81	37.20	143.31	57.09	0.679	0.636	43.53	27.58	0.36	**41.8**	n.a.	**2.51**	
CLRK3876_Ap5						0.0225	0.0005	2.3	0.1322	0.0992	0.3549	64.85	48.64	174.11	76.91	0.683	0.641	44.18	26.28	0.34	**39.5**	n.a.	**2.37**	
CLRK3876	**-68.750**	**-24.140**	**3054**	**Granite (Permian[35])**	**PC**																**41.0**	**1.2**		
CLRK3877_Ap1						0.0094	0.0002	2.0	0.0353	0.0851	0.2883	19.56	47.20	159.82	31.22	0.658	0.613	40.60	29.96	0.35	**47.8**	n.a.	**2.87**	
CLRK3877_Ap2						*0.0004*	*0.0000*	*3.7*	*0.0012*	*0.0026*	*0.0205*	*0.48*	*1.05*	*8.33*	*0.76*	*0.683*	*0.641*	*44.14*	*34.28*	*0.99*	***52.4***	*n.a.*	***3.15***	*Low U => rejected*
CLRK3877_Ap3						0.0068	0.0001	2.1	0.0367	0.0677	0.2743	22.54	41.53	168.32	32.94	0.643	0.597	38.71	22.90	0.28	**37.3**	n.a.	**2.24**	
CLRK3877	**-68.512**	**-24.155**	**3441**	**Porphyric granite (Carb.-Perm.[35])**	**PC**																**42.6**	**7.4**		
CLRK3879_Ap1						*0.0164*	*0.0003*	*1.9*	*0.0251*	*0.0472*	*0.4501*	*10.75*	*20.21*	*192.65*	*16.36*	*0.691*	*0.650*	*45.50*	*75.58*	*0.86*	***113.8***	*n.a.*	***6.83***	*He injection => rejected*
CLRK3879_Ap2						*0.0055*	*0.0001*	*2.0*	*0.0166*	*0.0354*	*0.2942*	*14.44*	*30.80*	*256.00*	*22.82*	*0.619*	*0.570*	*35.95*	*37.18*	*0.48*	***63.5***	*n.a.*	***3.81***	*He injection? small grain => rejected*
CLRK3879_Ap3						0.0120	0.0002	2.0	0.0452	0.0919	0.9076	9.71	19.75	195.04	15.23	0.754	0.720	58.19	29.93	0.31	**41.0**	n.a.	**2.46**	
CLRK3879_Ap4						*0.0148*	*0.0003*	*2.1*	*0.0268*	*0.0512*	*0.4095*	*11.09*	*21.21*	*169.54*	*16.82*	*0.701*	*0.661*	*47.14*	*64.70*	*0.72*	***95.9***	*n.a.*	***5.75***	*He injection => rejected*
CLRK3879_Ap5						0.0079	0.0002	2.3	0.0419	0.0688	0.6322	16.92	27.73	255.01	24.58	0.706	0.667	48.02	23.11	0.26	**33.9**	n.a.	**2.03**	
CLRK3879	**-68.475**	**-24.289**	**3506**	**(Syeno-)Granite (Ordovician[36])**	**PC**																**37.4**	**5.0**		
CLRK3880_Ap1						0.0070	0.0001	2.0	0.0360	0.0585	0.8258	12.71	20.68	291.75	18.93	0.715	0.676	49.62	22.96	0.26	**33.2**	n.a.	**1.99**	
CLRK3880_Ap2						0.0042	0.0001	2.0	0.0194	0.0509	0.6316	7.36	19.35	239.96	13.02	0.712	0.673	49.07	21.44	0.23	**31.4**	n.a.	**1.88**	
CLRK3880_Ap3						0.0195	0.0004	2.0	0.0841	0.1598	1.8274	16.85	31.99	365.90	26.04	0.760	0.727	59.87	26.30	0.27	**35.6**	n.a.	**2.14**	
CLRK3880	**-68.666**	**-24.415**	**3619**	**Granite (Carb.-Perm.[35])**	**PC**																**33.4**	**2.1**		
CLRK3881_Ap1						0.0138	0.0003	2.0	0.0338	0.1369	1.1209	9.54	38.61	316.10	20.01	0.730	0.693	52.73	33.78	0.34	**48.2**	n.a.	**2.89**	
CLRK3881_Ap2						0.0057	0.0001	2.1	0.0138	0.0583	0.3116	6.65	27.96	149.52	13.83	0.687	0.645	44.77	35.02	0.38	**53.6**	n.a.	**3.22**	
CLRK3881_Ap3						0.0071	0.0001	2.0	0.0162	0.0670	0.5238	5.82	24.06	188.16	12.30	0.716	0.678	49.95	35.93	0.37	**52.4**	n.a.	**3.14**	
CLRK3881	**-69.938**	**-23.740**	**653**	**Granite (90 - 110 Ma[37])**	**CD**																**51.4**	**2.8**		
CLRK3882_Ap1						*0.0004*	*0.0000*	*3.1*	*0.0170*	*0.0507*	*0.2424*	*8.67*	*25.88*	*123.73*	*15.25*	*0.668*	*0.624*	*41.99*	*2.57*	*0.03*	***4.0***	*n.a.*	***0.24***	*He problem => rejected*
CLRK3882_Ap2						0.0056	0.0001	2.0	0.0146	0.0330	1.0900	8.68	19.55	645.70	16.41	0.658	0.613	40.60	32.84	0.39	**52.4**	n.a.	**3.14**	
CLRK3882_Ap3						0.0069	0.0001	2.0	0.0178	0.0257	0.8101	13.46	19.47	613.11	21.01	0.642	0.596	38.62	41.58	0.54	**67.6**	n.a.	**4.06**	
CLRK3882	**-69.636**	**-23.890**	**1265**	**Granite (Carbon - Perm.[37])**	**PC**																**60.0**	**10.8**		

Sample	Lon (°)	Lat (°)	Elev. (m)	Lithology	Tect. unit	^{4}He (pmol)	± 1σ (pmol)	± 1σ (%)	U (ng)	Th (ng)	Sm (ng)	U (ppm)	Th (ppm)	Sm (ppm)	eU (ppm)	F$_T$ ^{238}U	F$_T$ ^{232}Th	R$_s$ (µm)	Raw Age (Ma)	± 2σ (Ma)	Corr. Age (Ma)	± 1σ (Ma)	6% err (Ma)	Comments
CLRK3883_Ap1						0.0217	0.0004	2.0	0.0434	0.0610	1.8783	9.36	13.17	405.51	14.42	0.749	0.714	56.95	54.71	0.59	75.1	n.a.	4.51	
CLRK3883_Ap2						0.0064	0.0001	2.0	0.0155	0.0222	0.6773	8.17	11.70	357.57	12.65	0.673	0.630	42.72	44.84	0.55	69.2	n.a.	4.15	
CLRK3883_Ap3						0.0140	0.0003	2.0	0.0313	0.0435	1.0946	10.93	15.22	382.44	16.34	0.714	0.675	49.44	51.15	0.59	74.0	n.a.	4.44	
CLRK3883	**-69.815**	**-23.224**	**1254**	**Granite (191 Ma U-Pb[38])**	**CD**																**72.8**	**3.1**		
CLRK3884_Ap1						*0.0066*	*0.0001*	*2.0*	*0.0178*	*0.0621*	*0.9891*	*7.30*	*25.46*	*405.82*	*15.19*	*0.697*	*0.656*	*46.40*	*30.10*	*0.32*	*45.3*	*n.a.*	*2.72*	*Older than AFT age. He-injection? => rej.*
CLRK3884_Ap2						*0.0207*	*0.0004*	*2.0*	*0.0408*	*0.0543*	*1.8011*	*9.01*	*11.99*	*397.70*	*13.76*	*0.755*	*0.721*	*58.48*	*55.78*	*0.60*	*75.8*	*n.a.*	*4.55*	*Magmatic cooling age => rejected*
CLRK3884_Ap3						0.0016	0.0000	2.1	0.0069	0.0282	0.3546	5.25	21.34	268.53	11.51	0.641	0.595	38.48	17.95	0.22	29.7	n.a.	1.78	
CLRK3884_Ap4						0.0012	0.0000	2.5	0.0082	0.0227	0.2648	3.34	9.22	107.61	6.00	0.698	0.658	46.63	14.39	0.16	21.5	n.a.	1.29	
CLRK3884_Ap5						0.0016	0.0000	2.5	0.0069	0.0273	0.3869	5.01	19.98	282.66	11.02	0.645	0.599	38.92	18.03	0.22	29.7	n.a.	1.78	
CLRK3884	**-69.598**	**-23.388**	**1510**	**Granite (78.6 Ma K-Ar[39])**	**PC**																**27.0**	**4.7**		
CLRK3886_Ap1						0.0367	0.0007	2.0	0.1672	0.2858	0.9212	28.51	48.73	157.07	40.51	0.773	0.742	63.55	28.00	0.28	37.2	n.a.	2.23	
CLRK3886_Ap2						0.0189	0.0004	2.0	0.1160	0.1281	0.2303	39.13	43.22	77.69	49.46	0.721	0.683	50.77	23.64	0.28	33.7	n.a.	2.02	
CLRK3886_Ap3						0.0291	0.0006	2.0	0.1206	0.1619	0.4481	26.44	35.50	98.26	35.11	0.756	0.723	58.87	33.12	0.36	44.9	n.a.	2.70	
CLRK3886	**-68.937**	**-22.791**	**2755**	**Granite (Carboniferous[40])**	**PC**																**38.6**	**5.7**		
CLRK3887_Ap1						0.0880	0.0018	2.0	0.2887	0.7405	0.8553	48.53	124.49	143.80	77.91	0.775	0.743	64.03	34.56	0.33	46.0	n.a.	2.76	
CLRK3887_Ap2						0.0433	0.0009	2.0	0.1045	0.5628	0.6010	32.19	173.33	185.07	73.01	0.727	0.690	52.05	33.02	0.34	47.5	n.a.	2.85	
CLRK3887_Ap3						0.0113	0.0002	2.0	0.0306	0.1570	0.4686	12.57	64.49	192.51	28.38	0.705	0.666	47.92	29.32	0.31	43.6	n.a.	2.62	
CLRK3887	**-68.608**	**-21.906**	**3132**	**Tonalite (66.6 Ma K-Ar[39,41])**	**PC**																**45.7**	**1.9**		
CLRK3888_Ap1						0.0122	0.0002	2.0	0.0793	0.0987	0.6085	34.69	43.15	266.08	45.96	0.700	0.660	46.99	21.02	0.25	31.0	n.a.	1.86	
CLRK3888_Ap2						*0.0049*	*0.0001*	*2.0*	*0.0102*	*0.0379*	*0.6242*	*5.28*	*19.67*	*324.44*	*11.43*	*0.671*	*0.628*	*42.40*	*37.65*	*0.43*	*59.1*	*n.a.*	*3.55*	*Older than AFT age. He-injection? => rej.*
CLRK3888_Ap3						0.0109	0.0002	2.0	0.0856	0.0884	0.6072	37.28	38.52	264.56	47.47	0.696	0.656	46.37	18.18	0.22	26.9	n.a.	1.61	
CLRK3888	**-68.990**	**-23.582**	**2436**	**Granodiorite (Permian, 260-273 Ma[42])**	**PC**																**29.0**	**2.9**		
CLRK3889_Ap1						0.0173	0.0003	2.0	0.0773	0.1084	0.7239	22.66	31.78	212.20	31.04	0.728	0.692	52.37	29.36	0.33	41.5	n.a.	2.49	
CLRK3889_Ap2						0.0150	0.0003	2.0	0.0680	0.0846	0.6084	22.36	27.83	200.22	29.77	0.715	0.677	49.78	29.81	0.34	42.9	n.a.	2.58	
CLRK3889_Ap3						0.0080	0.0002	2.1	0.0432	0.0460	0.3724	18.14	19.31	156.35	23.36	0.695	0.654	46.06	26.01	0.32	38.6	n.a.	2.32	
CLRK3889	**-69.501**	**-23.755**	**1907**	**Tonalite (66 - 69 Ma K-Ar[37,43])**	**PC**																**41.0**	**2.2**		
CLRK3890_Ap1						0.0223	0.0004	2.0	0.0820	0.3066	1.1656	18.16	67.92	258.20	35.09	0.751	0.717	57.55	25.18	0.25	34.8	n.a.	2.09	
CLRK3890_Ap2						0.0025	0.0001	2.2	0.0102	0.0492	0.5761	4.99	23.96	280.81	11.91	0.681	0.639	43.95	17.71	0.20	27.4	n.a.	1.64	
CLRK3890_Ap3						0.0027	0.0001	2.2	0.0162	0.0686	0.9601	5.14	21.84	305.43	11.70	0.719	0.681	50.44	12.40	0.13	18.0	n.a.	1.08	
CLRK3890	**-69.381**	**-24.444**	**2098**	**Monzonite (42.2 Ma K-Ar[44])**	**PC**																**26.7**	**8.4**		
CLRK3891_Ap1						0.0140	0.0003	2.0	0.0719	0.0973	0.4521	42.33	57.33	266.23	56.86	0.665	0.621	41.54	26.24	0.32	41.0	n.a.	2.46	
CLRK3891_Ap2						0.0188	0.0004	2.0	0.0951	0.0961	0.5526	38.10	38.50	221.33	48.07	0.702	0.662	47.33	28.38	0.34	41.6	n.a.	2.50	
CLRK3891_Ap3						0.0188	0.0004	2.0	0.0887	0.1268	0.7270	49.99	71.49	409.93	68.50	0.667	0.623	41.86	27.98	0.34	43.6	n.a.	2.62	
CLRK3891	**-68.883**	**-24.845**	**3410**	**Granite (Permian 282 Ma[45])**	**PC**																**42.1**	**1.4**		
CLRK3892_Ap1						0.0228	0.0005	2.0	0.0962	0.0823	0.4892	57.08	48.85	290.41	69.77	0.649	0.603	39.41	35.23	0.47	56.1	n.a.	3.37	
CLRK3892_Ap2						0.0960	0.0019	2.0	0.3725	0.4786	1.1726	177.25	227.72	557.95	232.46	0.690	0.649	45.34	35.87	0.43	53.8	n.a.	3.23	
CLRK3892_Ap3						0.0145	0.0003	2.0	0.0601	0.1124	0.6154	19.68	36.83	201.59	29.16	0.722	0.684	50.97	29.34	0.32	42.1	n.a.	2.53	
CLRK3892_Ap4						0.0306	0.0007	2.2	0.1368	0.1023	0.5920	48.64	36.37	210.41	58.06	0.708	0.669	48.41	34.18	0.43	49.4	n.a.	2.97	
CLRK3892_Ap5						0.0104	0.0002	2.3	0.0577	0.0606	0.4615	36.53	38.34	292.01	46.82	0.663	0.618	41.23	25.41	0.33	39.7	n.a.	2.38	
CLRK3892	**-70.054**	**-25.743**	**1319**	**Granite (149.4 Ma U-Pb[31])**	**CC**																**48.2**	**7.2**		

A2. ZHe Data

Table A2: Zircon (U-Th)/He data with average and standard deviation for each sample. Rejected ages are in Italic. Intrusion ages refer to the closest U-Pb, K-Ar or Ar-Ar age from the same lithology (see numbers for references, provided at the end of the thermochronological data tables). Rock compositions result from field observations and are thus approximative. Tectonic units: CC = Coastal Cordillera, CD = Central Depression, FC = Frontal Cordillera, PC = Principal Cordillera.

Sample	Lon	Lat	Elev.	Lithology	Tect. unit	^{4}He	± 1σ	U	Th	Sm	U	Th	Sm	eU	F_T	F_T	R_s	Raw Age	± 2σ	Corr. Age	± 1σ	6% err	Comment
	(°)	(°)	(m)			(pmol)	(pmol)	(ng)	(ng)	(ng)	(ppm)	(ppm)	(ppm)	(ppm)	^{238}U	^{232}Th	(µm)	(Ma)	(Ma)	(Ma)	(Ma)	(Ma)	
14NC01_Zr1						0.81968	0.02369	2.8001	1.3987		349.61	174.64	n.a.	390.65	0.792	0.762	58.54	48.40	3.06	**61.4**	**1.9**	3.68	
14NC01	**-70.369**	**-29.834**	**1460**	**Felsic Intrusive (288.2 Ma U-Pb[1])**	**FC**															**61.4**	**1.9**		**Single age**
14NC02_Zr1						0.62554	0.00335	1.6201	1.1062		288.91	197.25	n.a.	335.26	0.775	0.743	53.88	61.38	1.63	**79.6**	**1.1**	4.78	
14NC02_Zr2						0.35943	0.00202	1.0819	0.6666		415.48	255.98	n.a.	475.64	0.728	0.689	43.75	53.58	1.45	**74.1**	**1.0**	4.45	
14NC02	**-70.379**	**-29.842**	**1386**	**Felsic Intrusive (288.2 Ma U-Pb[1])**	**FC**															**76.9**	**3.9**		
14NC03_Zr1						0.13520	0.00393	0.6873	0.1540		291.45	65.29	n.a.	306.80	0.711	0.670	40.96	34.58	2.22	**48.8**	**1.6**	2.93	
14NC03_Zr2						0.07995	0.00165	0.3322	0.1846		95.60	53.14	n.a.	108.09	0.685	0.641	37.22	39.36	1.90	**58.0**	**1.4**	3.48	
14NC03	**-70.499**	**-29.854**	**1057**	**Felsic Intrusive (291.2 Ma U-Pb[1])**	**FC**															**53.4**	**6.4**		
14NC05_Zr1						1.47114	0.02944	2.6000	1.3583		216.57	113.14	n.a.	243.16	0.819	0.792	67.78	92.74	4.40	**113.6**	**2.7**	6.82	
14NC05_Zr2						0.76885	0.01550	1.4597	0.9928		143.59	97.66	n.a.	166.54	0.807	0.778	63.32	83.62	3.96	**104.1**	**2.5**	6.25	
14NC05	**-70.519**	**-30.018**	**976**	**Felsic Intrusive (291.2 Ma U-Pb[1])**	**FC**															**108.8**	**6.7**		
14NC06_Zr1						2.85162	0.05703	19.9859	5.3940		2204.36	594.93	n.a.	2344.16	0.803	0.774	61.98	24.85	1.19	**31.0**	**0.7**	1.86	
14NC06_Zr2						0.67087	0.00295	4.1895	2.2529		407.23	218.98	n.a.	458.69	0.769	0.736	52.35	26.31	0.69	**34.4**	**0.5**	2.06	
14NC06	**-70.631**	**-30.026**	**732**	**Felsic Intrusive (62.4 Ma[2])**	**PC**															**32.7**	**2.4**		
14NC07_Zr1						0.12447	0.00126	0.6358	0.4181		492.13	323.61	n.a.	568.17	0.655	0.609	33.71	31.36	0.99	**48.4**	**0.8**	2.90	
14NC07_Zr2						*0.13415*	*0.00140*	*0.3402*	*0.2339*		*427.73*	*294.12*	*n.a.*	*496.84*	*0.620*	*0.570*	*30.15*	*62.62*	*2.03*	*102.1*	*1.7*	*6.13*	*Older than intrusion age => rejected*
14NC07	**-70.734**	**-30.038**	**600**	**Felsic Intrusive (62.4 Ma[2])**	**PC**															**48.4**	**1.5**		
14NC08_Zr1						1.71196	0.01701	4.4606	2.1899		141.63	69.53	n.a.	157.97	0.848	0.825	81.49	63.48	2.04	**75.1**	**1.2**	4.50	
14NC08_Zr2						2.06692	0.02027	5.0107	2.3045		211.18	97.13	n.a.	234.01	0.866	0.846	93.11	68.65	2.19	**79.4**	**1.3**	4.77	
14NC08_Zr3						0.97967	0.01296	2.8148	0.9679		193.85	66.65	n.a.	209.51	0.857	0.835	86.57	59.44	2.20	**69.5**	**1.3**	4.17	
14NC08	**-71.066**	**-29.983**	**212**	**Felsic Intrusive (95 Ma K-Ar[3])**	**CC**															**74.7**	**5.0**		
14NC09_Zr1						*1.86407*	*0.02460*	*3.7511*	*2.8764*		*313.98*	*240.77*	*n.a.*	*370.56*	*0.841*	*0.817*	*77.59*	*77.57*	*2.77*	*92.6*	*1.7*	*5.56*	*Magmatic cooling => rejected*
14NC09_Zr2						0.65227	0.00866	1.5969	1.2996		429.20	349.29	n.a.	511.28	0.789	0.759	57.77	63.24	2.27	**80.6**	**1.5**	4.84	
14NC09_Zr3						2.28574	0.02205	6.0661	4.2393		538.77	376.52	n.a.	627.25	0.831	0.806	73.04	59.72	1.85	**72.1**	**1.1**	4.33	
14NC09	**-71.239**	**-29.748**	**265**	**Felsic Intrusive (89-109.5 Ma K-Ar[3])**	**CC**															**76.4**	**6.0**		
14NC10_Zr1						3.20278	0.03086	7.7587	7.5363		1128.16	1095.81	n.a.	1385.67	0.806	0.778	63.10	61.98	1.88	**77.4**	**1.2**	4.64	
14NC10_Zr2						4.68439	0.04566	11.8940	11.0017		1454.64	1345.51	n.a.	1770.83	0.823	0.796	69.34	59.68	1.81	**72.9**	**1.1**	4.38	
14NC10_Zr3						2.61465	0.02558	6.5974	6.1131		1470.93	1362.96	n.a.	1791.22	0.803	0.774	61.94	60.03	1.83	**75.3**	**1.2**	4.52	
14NC10	**-70.976**	**-29.649**	**950**	**Felsic Intrusive (89-109.5 Ma K-Ar[3])**	**CC**															**75.2**	**2.2**		
14NC14_Zr1						0.32622	0.00325	1.4644	0.6551		583.11	260.83	n.a.	644.40	0.737	0.700	45.47	37.28	1.20	**50.9**	**0.8**	3.05	
14NC14_Zr2						0.69213	0.01290	3.2054	1.3634		926.14	393.92	n.a.	1018.71	0.761	0.727	50.48	36.31	1.65	**47.9**	**1.1**	2.88	
14NC14	**-70.263**	**-29.977**	**1599**	**Felsic Intrusive (288.2 Ma U-Pb[1])**	**FC**															**49.4**	**2.1**		
14NC15_Zr1						0.78306	0.01449	1.1742	0.6491		158.86	87.82	n.a.	179.50	0.737	0.700	45.54	108.46	4.89	**147.7**	**3.3**	8.86	
14NC15_Zr2						0.46001	0.00848	0.8070	0.4467		128.39	71.06	n.a.	145.09	0.795	0.765	59.49	92.81	4.15	**117.1**	**2.6**	7.03	
14NC15	**-70.491**	**-30.164**	**1389**	**Felsic Intrusive (289.7 Ma U-Pb[1])**	**FC**															**132.4**	**21.6**		
14NC16_Zr1						0.09650	0.00180	0.3040	0.2413		77.78	61.74	n.a.	92.29	0.752	0.717	48.49	49.40	2.20	**66.2**	**1.5**	3.97	
14NC16_Zr2						0.21425	0.00362	1.3270	0.2669		493.81	99.31	n.a.	517.14	0.737	0.700	45.44	28.54	1.23	**38.9**	**0.8**	2.33	
14NC16	**-70.388**	**-30.146**	**1552**	**Felsic Intrusive (289.7 Ma U-Pb[1])**	**FC**															**52.5**	**19.3**		
14NC20_Zr1						*1.35287*	*0.01325*	*2.9457*	*2.9338*		*422.84*	*421.13*	*n.a.*	*521.81*	*0.788*	*0.757*	*57.36*	*68.59*	*2.10*	*87.7*	*1.3*	*5.26*	*Magmatic cooling => rejected*
14NC20_Zr2						0.27802	0.00076	1.0674	1.3918		216.25	281.98	n.a.	282.51	0.811	0.783	64.93	36.83	0.85	**45.8**	**0.5**	2.75	
14NC20_Zr3						0.44157	0.00112	1.6795	2.2922		654.11	892.74	n.a.	863.90	0.731	0.693	44.41	36.77	0.85	**50.9**	**0.6**	3.06	
14NC20	**-70.854**	**-29.413**	**590**	**Felsic intrusive (83.6 Ma U-Pb[5])**	**CC**															**48.4**	**3.7**		
14NC21_Zr1						0.23559	0.00394	0.7662	0.6562		106.26	91.01	n.a.	127.65	0.794	0.764	59.22	47.26	1.94	**59.9**	**1.2**	3.59	
14NC21_Zr2						0.19267	0.00319	0.7283	0.6884		126.67	119.73	n.a.	154.80	0.753	0.718	48.67	39.99	1.62	**53.6**	**1.1**	3.22	

Sample	Lon	Lat	Elev.	Lithology	Tect. unit	^{4}He	± 1σ	U	Th	Sm	U	Th	Sm	eU	F_T	F_T	R_s	Raw Age	± 2σ	Corr. Age	± 1σ	6% err	Comment
	(°)	(°)	(m)			(pmol)	(pmol)	(ng)	(ng)	(ng)	(ppm)	(ppm)	(ppm)	(ppm)	^{238}U	^{232}Th	(µm)	(Ma)	(Ma)	(Ma)	(Ma)	(Ma)	
14NC21	**-70.755**	**-29.451**	**1056**	**Felsic Intrusive (63.2 Ma U-Pb[5])**	**PC**															**56.7**	**4.5**		
14NC23_Zr2						0.33135	0.00546	1.8736	0.8516		324.86	147.66	n.a.	359.56	0.781	0.749	55.28	29.57	1.23	**38.1**	**0.8**	2.28	
14NC23_Zr2	**-70.592**	**-29.451**	**2390**	**Felsic Intrusive (78 - 68 Ma[5])**	**PC**															**38.1**	**0.8**		**Single age**
14NC24_Zr1						0.36878	0.00301	0.8806	0.4540		88.32	45.53	n.a.	99.02	0.833	0.808	73.89	68.88	2.05	**82.9**	**1.2**	4.98	
14NC24_Zr2						0.68889	0.00564	1.5370	1.1310		144.10	106.03	n.a.	169.02	0.839	0.815	76.58	70.44	2.06	**84.3**	**1.2**	5.06	
14NC24_Zr3						0.73296	0.00291	1.8117	1.4795		159.11	129.93	n.a.	189.65	0.846	0.823	80.26	62.60	1.57	**74.3**	**0.9**	4.46	
14NC24	**-71.014**	**-28.972**	**610**	**Felsic Intrusive (127 - 124 Ma[5])**	**CC**															**80.5**	**5.4**		
14NC25_Zr1						1.18421	0.00485	3.7927	1.2846		396.03	134.14	n.a.	427.55	0.846	0.823	80.57	53.42	1.45	**63.2**	**0.9**	3.79	
14NC25_Zr2						0.31212	0.00414	1.2531	0.4355		721.51	250.73	n.a.	780.43	0.717	0.677	41.94	42.57	1.58	**59.7**	**1.1**	3.58	
14NC25_Zr3						0.42294	0.00558	1.2518	0.5496		263.84	115.83	n.a.	291.06	0.786	0.755	56.79	56.54	2.07	**72.2**	**1.3**	4.33	
14NC25	**-70.886**	**-29.052**	**861**	**Felsic Intrusive (99 Ma[5])**	**CC**															**65.0**	**6.5**		
14NC26_Zr1						*0.45098*	*0.00745*	*1.0754*	*1.0551*		*436.08*	*427.85*	*n.a.*	*536.63*	*0.734*	*0.697*	*44.98*	*62.84*	*2.55*	***86.4***	***1.8***	*5.18*	*Magmatic cooling => rejected*
14NC26_Zr2						*0.95389*	*0.02079*	*2.9212*	*2.8569*		*1142.55*	*1117.40*	*n.a.*	*1405.14*	*0.725*	*0.686*	*43.26*	*49.02*	*2.43*	***68.3***	***1.7***	*4.10*	*Magmatic cooling => rejected*
14NC26	***-70.761***	***-29.103***	***1386***	***Felsic Intrusive (68.6 Ma U-Pb[5])***	***PC***															***77.4***	***12.8***		***Magmatic cooling => rejected***
14NC29_Zr1						*0.55370*	*0.01212*	*2.4926*	*1.9701*		*309.34*	*244.49*	*n.a.*	*366.79*	*0.804*	*0.775*	*62.32*	*34.63*	*1.73*	***43.3***	***1.1***	*2.60*	*Magmatic cooling => rejected*
14NC29_Zr2						*0.52385*	*0.01145*	*2.1275*	*1.5291*		*465.01*	*334.22*	*n.a.*	*543.55*	*0.835*	*0.810*	*74.63*	*38.93*	*1.95*	***46.9***	***1.2***	*2.81*	*Magmatic cooling => rejected*
14NC29	***-70.461***	***-28.962***	***1285***	***Felsic Intrusive (44 Ma[7])***	***PC***															***45.1***	***2.5***		***Magmatic cooling => rejected***
14NC30_Zr1						0.94219	0.02054	5.1865	4.5917		532.11	471.10	n.a.	642.82	0.820	0.793	68.10	27.81	1.38	**34.1**	**0.8**	2.05	
14NC30_Zr2						0.50054	0.01089	3.7260	3.2693		491.69	431.42	n.a.	593.07	0.750	0.714	47.93	20.61	1.02	**27.8**	**0.7**	1.67	Younger than AHe age
14NC30	**-70.347**	**-29.178**	**1885**	**Granite (Devon. - Perm.[8])**	**FC**															**30.9**	**4.5**		
14NC31_Zr1						*0.24404*	*0.00535*	*0.5386*	*0.5324*		*175.17*	*173.17*	*n.a.*	*215.87*	*0.736*	*0.699*	*45.27*	*67.77*	*3.37*	***92.9***	***2.3***	*5.58*	
14NC31_Zr2						*0.79923*	*0.00512*	*1.2462*	*1.2744*		*206.64*	*211.31*	*n.a.*	*256.29*	*0.773*	*0.740*	*53.31*	*95.09*	*2.53*	***123.9***	***1.7***	*7.44*	
14NC31	***-70.354***	***-29.322***	***2170***	***Granite (Upper Cretaceous[5,8])***	***PC***															***108.4***	***21.9***		***Magmatic cooling***
14NC32_Zr1						1.10090	0.00716	3.9007	0.8533		589.27	128.91	n.a.	619.57	0.782	0.750	55.67	49.60	1.46	**63.6**	**0.9**	3.81	
14NC32	**-70.302**	**-29.007**	**1690**	**Felsic Intrusive (Permian[7,8])**	**FC**															**63.6**	**0.9**		**Single age**
14NC33_Zr2						0.19620	0.00192	1.2618	0.7172		348.36	198.01	n.a.	394.89	0.746	0.710	47.20	25.39	0.80	**34.3**	**0.5**	2.06	
14NC33	**-70.127**	**-29.074**	**1855**	**Felsic Intrusive (Triassic[7,8])**	**FC**															**34.3**	**0.5**		**Single age**
14NC35_Zr1						0.38527	0.00208	1.9407	1.0953		370.99	209.37	n.a.	420.19	0.728	0.690	43.86	32.42	0.87	**44.8**	**0.6**	2.69	younger than AHe age
14NC35_Zr2						0.36739	0.00210	1.2174	1.0895		216.11	193.41	n.a.	261.56	0.749	0.713	47.82	46.05	1.21	**62.0**	**0.8**	3.72	
14NC35	**-70.480**	**-28.595**	**2078**	**Felsic Intrusive (68.85 Ma U-Pb[7])**	**PC**															**53.4**	**12.1**		
14NC36_Zr1						1.47086	0.01434	4.2745	4.4690		260.66	272.52	n.a.	324.70	0.838	0.814	76.33	50.98	1.54	**61.2**	**0.9**	3.67	
14NC36	**-70.409**	**-28.376**	**1053**	*Felsic Intrusive (64-66 Ma K-Ar[7])*	**PC**															**61.2**	**0.9**		
14NC37_Zr2						0.37134	0.00358	2.3427	0.4121		682.18	120.00	n.a.	710.38	0.755	0.720	49.09	28.19	0.93	**37.4**	**0.6**	2.25	Younger than AHe age
14NC37	**-70.493**	**-28.295**	**850**	*Felsic Intrusive (66 ± 2 K-Ar[7])*	**PC**															**37.4**	**0.6**		**Single age - Younger than AHe**
14NC38_Zr1						0.93198	0.01306	1.7945	1.7023		276.72	262.50	n.a.	338.41	0.841	0.818	77.96	78.22	2.87	**93.4**	**1.7**	5.60	
14NC38_Zr3						1.39355	0.01949	2.6271	1.7235		525.63	344.83	n.a.	606.66	0.784	0.753	56.31	84.62	3.15	**108.4**	**2.0**	6.50	
14NC38_Zr4						1.16247	0.01064	1.9019	2.1768		318.86	364.95	n.a.	404.62	0.781	0.749	55.40	88.62	2.61	**114.4**	**1.7**	6.86	
14NC38_Zr4						1.16247	0.01064	1.9019	2.1768		318.86	364.95	n.a.	404.62	0.781	0.749	55.40	88.62	2.61	**114.4**	**1.7**	6.86	
14NC38	**-70.724**	**-28.455**	**678**	*Micro-diorite (127.3 Ma[3,6])*	**CC**															**107.6**	**9.9**		
14NC39_Zr1						1.47409	0.02108	2.5610	3.2189		419.08	526.75	n.a.	542.87	0.795	0.765	59.54	81.79	2.99	**103.7**	**1.9**	6.22	
14NC39_Zr2						1.32189	0.00757	2.4731	2.4748		326.92	327.15	n.a.	403.80	0.800	0.771	61.14	79.69	2.06	**100.2**	**1.3**	6.01	
14NC39_Zr3						2.81367	0.01575	5.3792	6.0603		546.79	616.02	n.a.	691.56	0.821	0.795	68.71	76.17	1.93	**93.4**	**1.2**	5.60	
14NC39	**-70.949**	**-28.146**	**206**	**Felsic Intrusive (148 - 151 Ma K-Ar[3])**	**CC**															**99.1**	**5.3**		
14NC40_Zr2						3.04610	0.01773	5.4117	4.3137		253.99	202.45	n.a.	301.57	0.858	0.837	87.61	87.26	2.32	**102.0**	**1.4**	6.12	
14NC40_Zr3						2.06776	0.05360	4.1370	2.8289		195.10	133.41	n.a.	226.45	0.864	0.844	91.59	79.32	4.57	**92.1**	**2.7**	5.52	
14NC40_Zr7						0.28975	0.00269	0.7939	0.4377		708.67	390.68	n.a.	800.48	0.688	0.645	37.65	59.63	1.86	**87.3**	**1.4**	5.24	

Sample	Lon	Lat	Elev.	Lithology	Tect. unit	^{4}He	± 1σ	U	Th	Sm	U	Th	Sm	eU	F_T	F_T	R_s	Raw Age	± 2σ	Corr. Age	± 1σ	6% err	Comment
	(°)	(°)	(m)			(pmol)	(pmol)	(ng)	(ng)	(ng)	(ppm)	(ppm)	(ppm)	(ppm)	^{238}U	^{232}Th	(µm)	(Ma)	(Ma)	(Ma)	(Ma)	(Ma)	
14NC40_Zr7						0.28975	0.00269	0.7939	0.4377		708.67	390.68		800.48	0.688	0.645	37.65	59.63	1.86	**87.3**	**1.4**	5.24	
14NC40	**-71.089**	**-28.118**	**90**	**Felsic Intrusive (143 - 139 Ma[3,46])**	**CC**															**92.2**	**6.9**		
14NC41_Zr1						1.01901	0.01356	2.1401	1.4415		355.05	239.15	n.a.	411.25	0.822	0.795	68.89	75.74	2.73	**92.6**	**1.7**	5.55	
14NC41_Zr2						1.06015	0.00571	2.2207	1.5814		459.61	327.30	n.a.	536.52	0.799	0.769	60.55	75.35	1.99	**94.8**	**1.3**	5.69	
14NC41_Zr3						1.02991	0.00546	2.2132	1.5029		468.14	317.91	n.a.	542.85	0.802	0.772	61.55	73.96	1.95	**92.7**	**1.2**	5.56	
14NC41	**-70.422**	**-26.696**		**Gabbro (Upper Jurassic[47])**	**CC**															**93.4**	**1.3**		
14NC42_Zr1						0.48225	0.00165	1.1163	0.6684		109.77	65.72	n.a.	125.21	0.846	0.823	80.34	69.82	1.78	**82.8**	**1.1**	4.97	
14NC42_Zr2						0.27962	0.00089	0.6565	0.4033		121.39	74.56	n.a.	138.91	0.788	0.757	57.33	68.62	1.76	**87.5**	**1.1**	5.25	
14NC42_Zr3						0.46827	0.00138	1.1176	0.7440		137.12	91.29	n.a.	158.58	0.820	0.793	68.08	66.81	1.68	**81.9**	**1.0**	4.91	
14NC42	**-70.340**	**-26.855**	**1075**	**Felsic Intrusive (119.9 Ma[9,10])**	**CC**															**84.1**	**3.0**		
14NC45_Zr2						0.44436	0.00232	1.6399	1.3075		348.26	277.68	n.a.	413.52	0.786	0.755	56.75	42.16	1.09	**54.0**	**0.7**	3.24	
14NC45_Zr3						0.30122	0.00210	1.2600	0.7254		806.44	464.29	n.a.	915.55	0.709	0.669	40.73	38.93	1.10	**55.3**	**0.8**	3.32	
14NC45_Zr4						0.79318	0.00533	3.6996	1.1498		1423.99	442.58	n.a.	1528.00	0.748	0.712	47.70	36.96	1.42	**49.6**	**1.0**	2.97	
14NC45	**-70.090**	**-27.594**	**984**	**Felsic Intrusive (60.6 Ar-Ar[11])**	**PC**															**53.0**	**3.0**		
14NC47_Zr1						1.78354	0.02187	11.2029	3.7157		655.50	217.41	n.a.	706.59	0.852	0.830	83.84	27.34	0.97	**32.2**	**0.6**	1.93	
14NC47_Zr2						0.88562	0.01079	5.9229	2.1585		603.75	220.03	n.a.	655.45	0.844	0.821	79.53	25.50	0.90	**30.3**	**0.5**	1.82	
14NC47_Zr3						1.63549	0.01922	8.6571	6.8588		608.00	481.71	n.a.	721.20	0.843	0.820	78.84	29.46	0.98	**35.1**	**0.6**	2.11	
14NC47	**-69.768**	**-27.672**	**2436**	**Porphyry (42.1 Ma K-Ar[12])**	**PC**															**32.5**	**2.4**		
14NC48_Zr1						0.40569	0.00503	1.5081	0.7498		198.13	98.50	n.a.	221.28	0.788	0.757	57.41	44.51	1.57	**56.7**	**1.0**	3.40	
14NC48_Zr2						0.26805	0.00335	1.2131	0.6643		194.61	106.57	n.a.	219.65	0.803	0.774	62.04	36.20	1.27	**45.3**	**0.8**	2.72	
14NC48_Zr3						0.34888	0.00430	1.4274	0.6797		158.53	75.49	n.a.	176.27	0.826	0.800	70.65	40.64	1.43	**49.4**	**0.9**	2.96	
14NC48	**-69.806**	**-27.956**	**1704**	**Granite, deformed (Carb. - Perm.[7])**	**FC**															**50.5**	**5.8**		
14NC51_Zr1						0.19289	0.00137	0.8758	0.5658		500.37	323.28	n.a.	576.34	0.712	0.671	41.12	35.36	0.99	**50.1**	**0.7**	3.01	
14NC51_Zr2						0.43046	0.00696	1.4894	0.5616		504.85	190.35	n.a.	549.58	0.758	0.723	49.80	49.05	2.02	**65.0**	**1.3**	3.90	
14NC51_Zr3						0.39133	0.00633	1.4621	0.5183		793.90	281.42	n.a.	860.03	0.729	0.690	43.92	45.66	1.89	**63.0**	**1.3**	3.78	
14NC51	**-69.844**	**-27.980**	**1578**	**Granite, deformed (Carb. - Perm.[7])**	**FC**															**59.3**	**8.1**		
14NC52_Zr1						0.30494	0.00286	1.1718	0.9332		320.67	255.38	n.a.	380.68	0.747	0.711	47.36	40.50	1.23	**54.7**	**0.8**	3.28	
14NC52_Zr2						0.10228	0.00138	0.4384	0.3310		215.08	162.39	n.a.	253.24	0.724	0.685	43.14	36.63	1.32	**51.0**	**0.9**	3.06	
14NC52_Zr3						1.02172	0.01344	3.8731	2.1667		628.67	351.69	n.a.	711.32	0.795	0.765	59.44	43.09	1.55	**54.5**	**1.0**	3.27	
14NC52	**-70.126**	**-27.822**	**918**	**Felsic Intrusive (61.8 Ma K-Ar[11,12])**	**PC**															**53.4**	**2.0**		
14NC56_Zr1						0.76957	0.01020	1.3970	0.3248		996.94	231.78	n.a.	1051.41	0.682	0.638	36.87	96.11	3.61	**141.2**	**2.7**	8.47	
14NC56_Zr2						2.66588	0.03526	4.7141	1.4224		1185.74	357.78	n.a.	1269.82	0.759	0.724	49.86	97.15	3.61	**128.3**	**2.4**	7.70	
14NC56_Zr3						1.71535	0.02247	2.2082	0.3620		706.93	115.88	n.a.	734.16	0.749	0.713	47.86	137.12	5.16	**182.9**	**3.5**	10.98	
14NC56	**-69.760**	**-28.116**	**2386**	**Felsic Intrusive (234 Ma K-Ar[7])**	**FC**															**150.8**	**28.5**		
14NC57_Zr1						1.40423	0.01770	1.9049	1.5083		315.00	249.41	n.a.	373.61	0.793	0.763	58.93	114.14	4.03	**144.6**	**2.6**	8.67	
14NC57_Zr2						0.84685	0.01069	1.3265	1.0940		340.67	280.99	n.a.	406.71	0.761	0.727	50.54	98.34	3.46	**130.0**	**2.3**	7.80	
14NC57_Zr3						0.92057	0.01163	1.5843	0.9436		391.28	233.04	n.a.	446.04	0.760	0.726	50.24	93.78	3.37	**123.9**	**2.2**	7.44	
14NC57	**-69.775**	**-28.104**	**3416**	**Felsic Intrusive (234 Ma K-Ar[7])**	**FC**															**132.8**	**10.6**		
14NC58_Zr1						0.90410	0.00702	1.7234	0.8524		228.13	112.83	n.a.	254.64	0.819	0.792	67.68	86.53	2.57	**106.0**	**1.6**	6.36	
14NC58_Zr2						1.35505	0.01043	1.7736	0.9342		294.65	155.20	n.a.	331.12	0.785	0.753	56.39	124.76	3.69	**159.5**	**2.4**	9.57	
14NC58_Zr3						1.80212	0.00598	2.7124	1.1804		448.53	195.19	n.a.	494.40	0.785	0.753	56.37	110.75	2.99	**141.5**	**1.9**	8.49	
14NC58	**-69.785**	**-28.104**	**3641**	**Felsic Intrusive (234 Ma K-Ar[7])**	**FC**															**135.7**	**27.2**		
14NC59_Zr1						0.22040	0.00064	0.7346	0.3854		110.49	57.97	n.a.	124.11	0.794	0.764	59.08	49.34	1.29	**62.4**	**0.8**	3.75	
14NC59_Zr2						0.28027	0.00157	0.8286	1.1208		128.45	173.75	n.a.	169.28	0.806	0.778	63.15	47.37	1.17	**59.3**	**0.7**	3.56	
14NC59_Zr3						0.09653	0.00058	0.3298	0.1792		81.68	44.38	n.a.	92.10	0.778	0.746	54.65	47.95	1.33	**61.9**	**0.9**	3.72	
14NC59	**-70.131**	**-27.427**	**929**	**Porphyric diorite (83 ± 6 Ma K-Ar[13])**	**PC**															**61.2**	**1.7**		

Sample	Lon	Lat	Elev.	Lithology	Tect. unit	4He	± 1σ	U	Th	Sm	U	Th	Sm	eU	F_T 238U	F_T 232Th	R_s	Raw Age	± 2σ	Corr. Age	± 1σ	6% err	Comment
	(°)	(°)	(m)			(pmol)	(pmol)	(ng)	(ng)	(ng)	(ppm)	(ppm)	(ppm)	(ppm)			(µm)	(Ma)	(Ma)	(Ma)	(Ma)	(Ma)	
14NC61_Zr1						0.54610	0.00181	2.5348	1.1664		854.27	393.10	n.a.	946.64	0.752	0.716	48.44	35.96	0.93	**48.1**	**0.6**	2.88	
14NC61_Zr2						0.34760	0.00506	1.6430	0.6930		899.26	379.28	n.a.	988.39	0.714	0.674	41.48	35.60	1.38	**50.2**	**1.0**	3.01	
14NC61_Zr3						*0.57982*	*0.00857*	*2.3503*	*0.6315*		*1093.00*	*293.66*	*n.a.*	*1162.01*	*0.728*	*0.689*	*43.75*	*42.90*	*1.69*	***59.2***	***1.2***	*3.55*	*Magmatic cooling => rejected*
14NC61	**-69.967**	**-27.414**	**1363**	**Felsic Intrusive (60.4 Ma K-Ar[12])**	**PC**															**49.1**	**1.5**		
14NC64_Zr1						0.44383	0.00715	1.2392	0.5841		512.21	241.45	n.a.	568.95	0.744	0.707	46.80	59.51	2.43	**80.4**	**1.6**	4.82	
14NC64_Zr2						0.58106	0.00937	2.3457	1.0964		1018.08	475.83	n.a.	1129.91	0.747	0.711	47.49	41.26	1.68	**55.5**	**1.1**	3.33	
14NC64_Zr3						0.07037	0.00126	0.3316	0.1652		368.20	183.40	n.a.	411.30	0.684	0.641	37.16	35.14	1.53	**51.8**	**1.1**	3.11	
14NC64	**-69.666**	**-27.375**	**2954**	**Felsic Intrusive (Carb.-Perm.[14])**	**PC**															**62.5**	**15.6**		
14NC65_Zr1						0.68944	0.00361	2.1839	1.0466		581.64	278.75	n.a.	647.14	0.768	0.735	52.07	52.40	1.43	**68.5**	**0.9**	4.11	
14NC65_Zr2						0.27539	0.00158	0.8817	0.5265		248.03	148.12	n.a.	282.84	0.759	0.724	49.93	50.58	1.37	**67.1**	**0.9**	4.02	
14NC65_Zr3						0.44388	0.00236	1.2115	0.6650		506.64	278.07	n.a.	571.99	0.730	0.692	44.16	59.89	1.62	**82.5**	**1.1**	4.95	
14NC65	**-69.677**	**-27.427**	**3128**	**Felsic Intrusive (Carb.-Perm.[14])**	**PC**															**72.7**	**8.5**		
14NC67_Zr1						0.81212	0.01435	4.0886	2.1922		444.84	238.51	n.a.	500.89	0.837	0.813	75.79	32.63	1.41	**39.1**	**0.8**	2.35	
14NC67_Zr2						0.28124	0.00498	1.8738	0.6699		456.55	163.23	n.a.	494.91	0.791	0.760	58.23	25.63	1.12	**32.5**	**0.7**	1.95	
14NC67_Zr3						0.53546	0.00948	2.8007	1.2574		465.53	209.00	n.a.	514.64	0.808	0.780	63.90	32.00	1.39	**39.7**	**0.9**	2.38	
14NC67	**-69.681**	**-27.481**	**2632**	**Felsic Intrusive (Carb.-Perm.[14])**	**PC**															**37.1**	**4.0**		
14NC68_Zr1						1.31664	0.01544	3.6746	1.5661		862.32	367.52	n.a.	948.68	0.790	0.759	57.85	60.11	2.07	**76.4**	**1.3**	4.58	
14NC68_Zr2						3.79526	0.04372	9.1078	8.7715		3694.04	3557.62	n.a.	4530.08	0.743	0.706	46.59	62.66	2.05	**85.1**	**1.4**	5.11	
14NC68_Zr3						2.28124	0.02614	6.9631	1.7771		2369.10	604.63	n.a.	2511.18	0.778	0.746	54.65	57.07	1.98	**73.5**	**1.3**	4.41	
14NC68	**-70.411**	**-27.431**	**982**	**Diorite (106.9 Ma K-Ar[12])**	**CC**															**78.3**	**6.0**		
14NC69_Zr1						0.72828	0.00384	2.4091	0.6640		306.44	84.46	n.a.	326.29	0.817	0.789	66.86	52.45	1.47	**64.4**	**0.9**	3.86	
14NC69_Zr2						0.31498	0.00149	0.7214	0.3854		73.01	39.01	n.a.	82.18	0.823	0.796	69.36	71.51	1.90	**87.2**	**1.2**	5.23	
14NC69_Zr3						0.33935	0.00155	0.8596	0.3481		106.27	43.04	n.a.	116.38	0.807	0.779	63.40	66.50	1.80	**82.6**	**1.1**	4.96	
14NC69	**-70.365**	**-27.522**	**950**	**Felsic Intrusive (106.9 Ma K-Ar[11,12])**	**CC**															**78.1**	**12.1**		
14NC70_Zr1						*0.83185*	*0.01482*	*1.8226*	*1.7271*		*166.70*	*157.97*	*n.a.*	*203.83*	*0.842*	*0.819*	*78.49*	*68.80*	*2.95*	***82.1***	***1.8***	*4.92*	*Magmatic cooling => rejected*
14NC70_Zr2						*0.60867*	*0.01085*	*1.6276*	*1.3696*		*163.07*	*137.22*	*n.a.*	*195.31*	*0.812*	*0.784*	*65.24*	*57.61*	*2.47*	***71.3***	***1.5***	*4.28*	*Magmatic cooling => rejected*
14NC70_Zr3						*0.60966*	*0.01083*	*1.1863*	*1.0867*		*345.17*	*316.17*	*n.a.*	*419.47*	*0.770*	*0.737*	*52.55*	*77.89*	*3.32*	***101.9***	***2.2***	*6.11*	*Magmatic cooling => rejected*
14NC70	***-69.952***	***-27.100***	***1724***	***Porphyry (60.6 Ma K-Ar[12])***	***PC***															***85.1***	***15.5***		***Magmatic cooling => rejected***
14NC72_Zr1						0.18541	0.00157	0.8290	0.9746		376.34	442.40	n.a.	480.31	0.728	0.690	43.82	32.39	0.93	**45.0**	**0.7**	2.70	
14NC72_Zr2						0.26590	0.00223	1.0831	1.0383		288.79	276.84	n.a.	353.85	0.796	0.767	59.87	37.03	1.08	**46.8**	**0.7**	2.81	
14NC72_Zr3						0.17063	0.00142	0.7137	0.6195		254.37	220.77	n.a.	306.25	0.767	0.734	51.86	36.70	1.09	**48.2**	**0.7**	2.89	
14NC72	**-69.852**	**-26.694**	**1764**	**Felsic Intrusive (63 Ma[16])**	**PC**															**46.7**	**1.6**		
14NC77_Zr1						0.45880	0.00383	1.7744	1.0109		202.17	115.18	n.a.	229.24	0.822	0.796	69.17	42.14	1.28	**51.5**	**0.8**	3.09	
14NC77_Zr2						0.39303	0.00111	1.2893	0.5647		545.43	238.89	n.a.	601.56	0.734	0.696	44.85	51.05	1.35	**69.9**	**0.9**	4.20	
14NC77_Zr3						0.30488	0.00096	1.3695	0.6450		585.83	275.92	n.a.	650.67	0.738	0.701	45.68	37.06	0.98	**50.5**	**0.7**	3.03	
14NC77	**-69.765**	**-27.119**	**1510**	**Sandstone (Lower Triassic[14])**	**PC**															**57.3**	**11.0**		
14NC78_Zr1						0.26100	0.00700	1.0157	1.5360		229.91	347.66	n.a.	311.61	0.782	0.751	55.72	35.02	2.04	**45.3**	**1.3**	2.72	
14NC78_Zr2						0.17074	0.00458	0.7305	0.5119		277.58	194.51	n.a.	323.29	0.769	0.736	52.35	37.10	2.20	**48.6**	**1.4**	2.91	
14NC78_Zr3						0.70048	0.00309	2.4254	1.5022		177.35	109.84	n.a.	203.17	0.830	0.805	72.62	46.57	1.24	**56.3**	**0.8**	3.38	
14NC78	**-69.667**	**-26.947**	**2708**	**Felsic Intrusion (62.5 Ma Ar-Ar[15])**	**PC**															**50.0**	**5.7**		
14NC81_Zr1						*0.14491*	*0.00074*	*0.3766*	*0.1405*		*219.32*	*81.82*	*n.a.*	*238.55*	*0.718*	*0.679*	*42.19*	*65.27*	*1.80*	***91.2***	***1.3***	*5.47*	
14NC81_Zr2						*0.22754*	*0.00107*	*0.7353*	*0.2613*		*192.90*	*68.55*	*n.a.*	*209.01*	*0.764*	*0.730*	*51.06*	*52.75*	*1.44*	***69.3***	***1.0***	*4.16*	
14NC81_Zr3						*0.45553*	*0.00314*	*1.0655*	*0.5900*		*384.35*	*212.82*	*n.a.*	*434.36*	*0.755*	*0.720*	*49.16*	*69.75*	*1.97*	***92.8***	***1.3***	*5.57*	
14NC81	**-70.356**	**-27.212**	**831**	**Felsic Intrusion (103 Ma K-Ar[13])**	**CC**															**84.5**	**13.1**		
14NC82_Zr1						0.74987	0.00359	1.7792	1.2387		304.27	211.84	n.a.	354.06	0.804	0.775	62.37	66.79	1.74	**83.5**	**1.1**	5.01	
14NC82_Zr2						*1.70013*	*0.00595*	*3.3560*	*2.5709*		*1311.62*	*1004.80*	*n.a.*	*1547.75*	*0.759*	*0.724*	*49.92*	*79.08*	*1.97*	***104.9***	***1.3***	*6.29*	*Magmatic cooling => rejected*

Sample	Lon	Lat	Elev.	Lithology	Tect. unit	^{4}He	± 1σ	U	Th	Sm	U	Th	Sm	eU	F_T ^{238}U	F_T ^{232}Th	R_s	Raw Age	± 2σ	Corr. Age	± 1σ	6% err	Comment
	(°)	(°)	(m)			(pmol)	(pmol)	(ng)	(ng)	(ng)	(ppm)	(ppm)	(ppm)	(ppm)			(µm)	(Ma)	(Ma)	(Ma)	(Ma)	(Ma)	
14NC82_Zr3						*0.49844*	*0.00170*	*1.0887*	*0.7576*		*248.53*	*172.96*	*n.a.*	*289.18*	*0.761*	*0.727*	*50.42*	*72.52*	*1.82*	**95.9**	**1.2**	*5.75*	*Magmatic cooling => rejected*
14NC82	**-70.374**	**-27.084**	**1423**	**Felsic Intrusion (95+-3 Ma K-Ar[13])**	**CC**															**83.5**	**2.2**		
14NC83_Zr1						0.84708	0.00974	1.8568	1.6392		1423.44	1256.59	n.a.	1718.74	0.698	0.656	39.00	69.64	2.30	**100.8**	**1.7**	6.05	
14NC83_Zr2						0.10084	0.00045	0.3802	0.1364		306.86	110.12	n.a.	332.74	0.702	0.661	39.71	45.20	1.24	**64.7**	**0.9**	3.88	
14NC83_Zr3						1.89292	0.01184	3.6039	2.7761		1300.00	1001.38	n.a.	1535.32	0.773	0.740	53.31	81.90	2.20	**106.6**	**1.4**	6.39	
14NC83	**-70.454**	**-26.946**	**800**	**Felsic Intrusion (135 - 130 Ma[10])**	**CC**															**103.7**	**4.1**		
14NC84_Zr1						0.67236	0.00323	1.6497	0.4298		242.49	63.17	n.a.	257.33	0.814	0.786	65.78	70.83	2.03	**87.2**	**1.3**	5.23	
14NC84_Zr2						0.46844	0.00211	1.1191	0.7238		159.23	102.99	n.a.	183.43	0.846	0.823	80.26	67.01	1.78	**79.5**	**1.1**	4.77	
14NC84_Zr3						0.12066	0.00154	0.3089	0.1638		72.78	38.59	n.a.	81.85	0.761	0.727	50.44	64.07	2.33	**84.6**	**1.5**	5.08	
14NC84	**-70.197**	**-26.809**	**1305**	**Felsic Intrusive (119.9 Ma[9,10])**	**CC**															**83.8**	**3.9**		
14NC87_Zr1						0.16812	0.00064	0.5499	0.2533		131.28	60.47	n.a.	145.49	0.748	0.712	47.65	50.96	1.35	**68.4**	**0.9**	4.11	
14NC87_Zr2						0.56865	0.00172	1.7356	1.3476		141.09	109.55	n.a.	166.83	0.834	0.810	74.50	51.15	1.29	**61.6**	**0.8**	3.70	
14NC87_Zr3						0.13860	0.00051	0.5108	0.5525		203.72	220.34	n.a.	255.50	0.728	0.689	43.77	39.96	0.95	**55.5**	**0.7**	3.33	
14NC87	**-69.969**	**-26.850**	**2135**	**Porphyry (95 - 88 Ma[15])**	**PC**															**61.9**	**6.5**		
14NC88_Zr1						0.77439	0.02006	2.2885	1.1166		137.63	67.15	n.a.	153.41	0.863	0.842	90.54	56.04	3.24	**65.1**	**1.9**	3.91	
14NC88_Zr2						1.00203	0.00732	2.9006	1.4232		125.79	61.72	n.a.	140.29	0.861	0.839	89.13	57.18	1.66	**66.6**	**1.0**	4.00	
14NC88_Zr3						0.74483	0.00546	2.2153	1.2537		187.86	106.31	n.a.	212.84	0.838	0.813	76.04	54.78	1.57	**65.6**	**0.9**	3.94	
14NC88	**-69.984**	**-26.840**	**1952**	**Porphyry (Triassic[15])**	**FC**															**65.8**	**0.8**		
14NC89_Zr1						0.48519	0.00172	2.1117	1.3886		265.07	174.30	n.a.	306.03	0.827	0.802	71.28	36.79	0.93	**44.7**	**0.6**	2.68	
14NC89_Zr2						0.83717	0.00275	3.5380	2.5240		255.89	182.55	n.a.	298.79	0.831	0.806	72.84	37.46	0.93	**45.3**	**0.6**	2.72	
14NC89_Zr3						0.12105	0.00048	0.5721	0.4197		143.48	105.27	n.a.	168.22	0.776	0.743	53.95	33.37	0.84	**43.3**	**0.6**	2.60	
14NC89	**-69.786**	**-26.592**	**1784**	**Felsic Intrusive (64 +- 2 Ma K-Ar[15])**	**PC**															**44.4**	**1.0**		
14NC90_Zr1						0.37037	0.00277	1.8336	1.0890		176.24	104.67	n.a.	200.84	0.831	0.806	72.96	32.78	0.94	**39.6**	**0.6**	2.38	
14NC90_Zr2						0.93868	0.00222	4.9658	3.4925		382.52	269.04	n.a.	445.75	0.829	0.803	71.82	30.00	0.74	**36.4**	**0.4**	2.18	
14NC90_Zr3						0.23517	0.00047	1.0516	0.7521		103.65	74.13	n.a.	121.07	0.840	0.817	77.44	35.39	0.86	**42.3**	**0.5**	2.54	
14NC90	**-69.665**	**-26.538**	**2338**	**Felsic Intrusive (47.8 - 48.1 Ma K-Ar[15])**	**PC**															**39.4**	**3.0**		
14NC91_Zr1						1.88641	0.07219	3.8914	2.3003		182.32	107.77	n.a.	207.64	0.862	0.841	89.98	78.42	6.36	**91.2**	**3.7**	5.47	
14NC91_Zr2						0.66392	0.02540	1.2949	0.6954		244.34	131.22	n.a.	275.18	0.861	0.840	89.58	83.84	6.81	**97.6**	**4.0**	5.86	
14NC91_Zr3						0.97166	0.02602	2.1042	1.3501		162.39	104.20	n.a.	186.88	0.841	0.817	77.62	73.95	4.40	**88.3**	**2.6**	5.30	
14NC91	**-70.356**	**-26.411**	**352**	**Felsic Intrusive (123 Ma K-Ar[48])**	**CC**															**92.4**	**4.8**		
14NC92_Zr1						2.45042	0.01560	4.1583	2.7429		459.41	303.03	n.a.	530.62	0.848	0.825	81.36	93.87	2.59	**111.1**	**1.5**	6.66	
14NC92_Zr2						4.09079	0.02585	6.5351	4.7971		390.42	286.58	n.a.	457.77	0.845	0.822	79.86	98.18	2.65	**116.6**	**1.6**	7.00	
14NC92_Zr3						1.81636	0.01145	3.5181	1.7517		508.00	252.94	n.a.	567.44	0.815	0.787	66.10	85.11	2.38	**104.8**	**1.5**	6.29	
14NC92	**-70.434**	**-26.384**	**251**	**Felsic Intrusive (148 Ma K-Ar[48])**	**CC**															**110.8**	**5.9**		
14NC94_Zr1						0.51994	0.00352	1.1649	0.6485		75.60	42.08	n.a.	85.49	0.852	0.830	84.00	72.75	2.06	**85.6**	**1.2**	5.14	
14NC94_Zr2						0.58103	0.00396	1.2704	0.8405		103.11	68.22	n.a.	119.14	0.853	0.831	84.35	72.95	2.03	**85.8**	**1.2**	5.15	
14NC94_Zr4						0.20706	0.00416	0.4550	0.3434		99.09	74.78	n.a.	116.67	0.782	0.750	55.61	71.24	3.35	**91.7**	**2.2**	5.50	
14NC94	**-70.001**	**-26.367**	**873**	**Porphyry (Middle Jurassic[17])**	**CC**															**87.7**	**3.4**		
14NC97_Zr1						0.83054	0.00529	1.4237	1.0126		408.06	290.23	n.a.	476.26	0.778	0.745	54.50	91.97	2.50	**118.9**	**1.6**	7.13	
14NC97_Zr2						0.92549	0.00579	1.3102	0.8646		338.33	223.25	n.a.	390.79	0.803	0.774	62.02	112.33	3.07	**140.4**	**1.9**	8.42	
14NC97_Zr3						0.74885	0.00477	1.7013	1.2694		1044.14	779.06	n.a.	1227.22	0.710	0.669	40.79	69.04	1.87	**98.1**	**1.3**	5.89	
14NC97	**-69.328**	**-26.458**	**2758**	**Felsic Intrusive (Carb. - Perm.[18])**	**FC**															**119.1**	**21.2**		
14NC98_Zr1						*0.02518*	*0.00023*	*0.2038*	*0.1228*		*90.66*	*54.65*	*n.a.*	*103.50*	*0.728*	*0.690*	*43.83*	*20.04*	*0.63*	**27.7**	**0.4**	*1.66*	
14NC98_Zr2						*0.01678*	*0.00018*	*0.1170*	*0.0871*		*41.19*	*30.67*	*n.a.*	*48.39*	*0.770*	*0.737*	*52.57*	*22.59*	*0.73*	**29.6**	**0.5**	*1.77*	
14NC98_Zr3						*0.01832*	*0.00019*	*0.1104*	*0.1109*		*40.92*	*41.09*	*n.a.*	*50.57*	*0.731*	*0.693*	*44.38*	*24.84*	*0.78*	**34.3**	**0.5**	*2.06*	
14NC98	***-69.554***	***-27.119***	***2738***	***Porphyry (Eocene[14])***	***PC***															***30.5***	***3.4***		*Magmatic cooling => rejected*

Sample	Lon	Lat	Elev.	Lithology	Tect. unit	^{4}He	± 1σ	U	Th	Sm	U	Th	Sm	eU	F_T	F_T	R_s	Raw Age	± 2σ	Corr. Age	± 1σ	6% err	Comment
	(°)	(°)	(m)			(pmol)	(pmol)	(ng)	(ng)	(ng)	(ppm)	(ppm)	(ppm)	(ppm)	^{238}U	^{232}Th	(µm)	(Ma)	(Ma)	(Ma)	(Ma)	(Ma)	
Huasco52_Zr1						0.44675	0.01006	1.4795	0.9292		244.37	153.48	n.a.	280.44	0.784	0.753	56.29	48.60	2.50	**62.3**	**1.6**	3.74	
Huasco52_Zr2						0.59850	0.01345	3.0294	2.6208		553.25	478.62	n.a.	665.72	0.801	0.772	61.48	30.36	1.54	**38.1**	**1.0**	2.29	
Huasco52	-70.420	-28.775	876	Felsic Intrusive (Carb. - Perm.[7])	FC															50.2	17.1		
Huasco54_Zr1						0.37030	0.00259	1.9845	1.0779		239.11	129.88	n.a.	269.64	0.804	0.775	62.36	30.61	0.87	**38.3**	**0.5**	2.30	
Huasco54_Zr2						0.91274	0.00669	2.8591	1.8426		275.79	177.73	n.a.	317.55	0.810	0.782	64.47	51.20	1.46	**63.5**	**0.9**	3.81	
Huasco54	-70.295	-28.850	1089	Tonalite (310 Ma K-Ar[7])	FC															50.9	17.8		
Huasco55_Zr1						0.07904	0.00109	0.3297	0.2921		196.31	173.90	n.a.	237.17	0.713	0.673	41.39	36.67	1.35	**51.9**	**1.0**	3.12	
Huasco55	-70.523	-28.722	710	Felsic Intrusive (69 Ma Ar-Ar[6])	PC															51.9	1.0		Single age
Huasco73_Zr1						0.50305	0.00379	0.9007	0.6308		382.80	268.09	n.a.	445.80	0.705	0.664	40.15	88.27	2.56	**126.0**	**1.8**	7.56	
Huasco73_Zr2						0.32149	0.00228	0.7613	0.4079		329.47	176.51	n.a.	370.95	0.707	0.667	40.44	69.16	2.01	**98.4**	**1.4**	5.90	
Huasco73	-70.324	-28.859	2032	Tonalite (310 Ma K-Ar[7])	FC															112.2	19.6		
Huasco75_Zr1						0.73695	0.00433	1.6000	0.6118		487.19	186.30	n.a.	530.97	0.769	0.735	52.23	77.88	2.21	**101.6**	**1.5**	6.10	
Huasco75	-70.223	-28.970	1298	Gneiss (310 Ma K-Ar[7])	FC															101.6	1.5		Single age, but similar to Huasco73
Huasco87_Zr1						*0.74420*	*0.01677*	*1.0214*	*0.4125*		*584.21*	*235.96*	*n.a.*	*639.66*	*0.686*	*0.643*	*37.40*	*122.15*	*6.40*	***178.6***	***4.7***	*10.71*	
Huasco87_Zr2						*1.06746*	*0.01437*	*0.8489*	*0.4791*		*294.05*	*165.97*	*n.a.*	*333.05*	*0.724*	*0.685*	*43.10*	*202.34*	*7.53*	***280.0***	***5.3***	*16.80*	
Huasco87	*-70.223*	*-28.941*	*2864*	*Felsic Intrusive (310 Ma K-Ar[7])*	*FC*															*229.3*	*71.7*		*High age dispersion => rejected*
Laguna57_Zr2						0.06424	0.00145	0.2989	0.2770		140.18	129.93	n.a.	170.71	0.709	0.669	40.72	32.63	1.68	**46.5**	**1.2**	2.79	
Laguna57	-70.007	-28.792	2570	Granodiorite (260 Ma[7])	FC															46.5	1.2		Single age
CLRK3848_Zr1						0.60297	0.01102	1.7532	1.0744	0.0208	204.03	125.03	2.42	232.82	0.801	0.779	57.46	55.49	0.62	**70.0**	n.a.	4.20	
CLRK3848_Zr2						0.57732	0.00819	1.2651	0.9843	0.0337	148.41	115.47	3.95	175.01	0.803	0.781	58.02	71.09	0.77	**89.6**	n.a.	5.38	
CLRK3848_Zr3						0.41283	0.00825	1.0187	0.8560	0.0219	137.23	115.31	2.95	163.79	0.793	0.770	55.23	62.41	0.67	**79.7**	n.a.	4.78	
CLRK3848	-69.972	-24.098	1088	Granite (168 Ma[27,37])	CC															79.8	9.8		
CLRK3849_Zr1						*0.26372*	*0.00520*	*0.4810*	*0.2291*	*0.0113*	*174.89*	*83.30*	*4.12*	*194.09*	*0.724*	*0.693*	*40.19*	*90.74*	*1.15*	***127.1***	*n.a.*	*7.63*	*Magmatic cooling => rejected*
CLRK3849_Zr2						*0.61975*	*0.01234*	*0.7159*	*0.5156*	*0.0073*	*273.18*	*196.72*	*2.78*	*318.48*	*0.721*	*0.691*	*39.83*	*135.69*	*1.65*	***191.5***	*n.a.*	*11.49*	*Magmatic cooling => rejected*
CLRK3849_Zr3						*0.09332*	*0.00185*	*0.2062*	*0.1219*	*0.0045*	*84.29*	*49.81*	*1.83*	*95.76*	*0.713*	*0.681*	*38.51*	*73.22*	*0.92*	***104.5***	*n.a.*	*6.27*	*Magmatic cooling => rejected*
CLRK3849	*-70.146*	*-24.691*	*2243*	*Granodiorite (108 Ma K-Ar[28,37])*	*CC*															*141.0*	*45.2*		*Magmatic cooling => rejected*
CLRK3851_Zr1						0.68425	0.01354	2.0028	0.9513	0.0450	352.58	167.47	7.93	391.17	0.779	0.754	51.28	56.73	0.66	**73.6**	n.a.	4.42	
CLRK3851_Zr2						0.91066	0.01817	2.6634	1.1737	0.0606	400.88	176.65	9.12	441.60	0.788	0.764	53.73	57.19	0.66	**73.2**	n.a.	4.39	
CLRK3851_Zr3						*1.20103*	*0.02257*	*1.9124*	*0.9966*	*0.0733*	*275.58*	*143.60*	*10.57*	*308.69*	*0.784*	*0.760*	*52.72*	*102.83*	*1.18*	***132.5***	*n.a.*	*7.95*	*He injection => rejected*
CLRK3851_Zr4						0.71284	0.01579	1.7083	1.1891	0.2658	194.64	135.49	30.28	225.98	0.804	0.782	58.42	66.06	0.72	**83.1**	n.a.	4.99	
CLRK3851_Zr5						0.67209	0.01490	1.9290	0.9981	0.0437	380.41	196.83	8.61	425.77	0.765	0.739	48.00	57.33	0.68	**75.8**	n.a.	4.55	
CLRK3851	-69.271	-25.235	3817	Granite (289 Ma K-Ar[29])	FC															76.4	4.6		
CLRK3852_Zr1						0.48187	0.00947	1.0901	0.4507	0.0263	192.68	79.65	4.65	211.04	0.777	0.752	50.84	74.25	0.88	**96.5**	n.a.	5.79	
CLRK3852_Zr2						1.82637	0.03231	2.6711	0.7683	0.0573	246.10	70.79	5.28	262.42	0.811	0.790	60.64	117.58	1.37	**145.9**	n.a.	8.75	
CLRK3852_Zr3						1.41052	0.02797	2.1245	1.2830	0.0501	353.57	213.54	8.34	402.77	0.770	0.745	49.19	106.83	1.24	**140.5**	n.a.	8.43	
CLRK3852	-69.084	-25.380	4020	Monzonite (Permian, 323.9 Ma U-Pb[29])	FC															127.6	27.1		
CLRK3859_Zr1						3.04344	0.06045	4.6704	8.5153	0.0653	1034.97	1886.98	14.48	1469.42	0.759	0.733	46.80	83.92	0.86	**113.1**	n.a.	6.79	
CLRK3859_Zr2						0.23366	0.00464	0.4465	0.3910	0.0216	80.88	70.83	3.91	97.20	0.782	0.757	51.98	79.90	0.87	**103.8**	n.a.	6.23	
CLRK3859_Zr3						3.07738	0.05901	4.5777	5.4109	0.1360	383.41	453.20	11.39	487.79	0.821	0.801	64.24	96.72	0.96	**119.4**	n.a.	7.17	
CLRK3859	-70.163	-25.781	1091	Tonalite (149.4 Ma[31])	CC															112.1	7.9		
CLRK3860_Zr1						*0.00090*	*0.00003*	*0.0004*	*0.0004*	*0.0015*	*0.04*	*0.05*	*0.17*	*0.06*	*0.811*	*0.790*	*60.78*	*340.38*	*####*	***425.3***	*n.a.*	*25.52*	*He injection => rejected*
CLRK3860_Zr2						0.09083	0.00175	0.2071	0.0990	0.0180	9.46	4.52	0.82	10.51	0.855	0.839	80.34	72.63	0.77	**85.5**	n.a.	5.13	
CLRK3860_Zr3						1.09901	0.02196	4.0092	1.8198	0.0721	165.08	74.93	2.97	182.35	0.859	0.843	82.51	45.77	0.49	**53.6**	n.a.	3.22	
CLRK3860	-70.018	-25.942	1162	Porphyritic Dacite (123.7 Ma U-Pb[31])	CC															69.6	22.5		
CLRK3864_Zr1						0.50804	0.01006	3.5901	0.9279	0.0167	480.10	124.09	2.24	508.67	0.799	0.777	56.95	24.71	0.29	**31.1**	n.a.	1.87	
CLRK3864_Zr2						0.71724	0.01422	4.2039	1.3653	0.0171	751.27	243.99	3.06	807.45	0.769	0.743	48.84	29.34	0.36	**38.5**	n.a.	2.31	

Sample	Lon	Lat	Elev.	Lithology	Tect. unit	^{4}He	±1σ	U	Th	Sm	U	Th	Sm	eU	F_T	F_T	R_s	Raw Age	±2σ	Corr. Age	±1σ	6% err	Comment
	(°)	(°)	(m)			(pmol)	(pmol)	(ng)	(ng)	(ng)	(ppm)	(ppm)	(ppm)	(ppm)	^{238}U	^{232}Th	(µm)	(Ma)	(Ma)	(Ma)	(Ma)	(Ma)	
CLRK3864_Zr3						0.39426	0.00782	1.1665	0.4892	0.0092	136.35	57.19	1.07	149.52	0.802	0.780	57.92	56.80	0.65	71.4	n.a.	4.28	He injection => rejected
CLRK3864_Zr4						0.77302	0.01716	4.8196	1.9516	0.0594	462.12	187.13	5.69	505.22	0.818	0.798	63.20	27.11	0.31	33.4	n.a.	2.00	
CLRK3864_Zr5						0.52477	0.01143	4.0869	1.1098	0.0233	869.50	236.11	4.96	923.88	0.763	0.737	47.62	22.36	0.28	29.5	n.a.	1.77	
CLRK3864	**-69.445**	**-26.201**	**2804**	**Granite (Permian[18])**	**FC**															**33.1**	**3.9**		
CLRK3866_Zr1						0.85260	0.01702	2.6260	1.0824	0.0514	198.33	81.75	3.88	217.17	0.822	0.802	64.84	54.65	0.61	66.9	n.a.	4.02	
CLRK3866_Zr2						0.80060	0.01601	3.2715	1.1576	0.0268	342.92	121.34	2.81	370.86	0.805	0.783	58.73	41.77	0.48	52.3	n.a.	3.14	
CLRK3866_Zr3						0.49704	0.00992	1.6043	0.9309	0.0157	132.15	76.68	1.29	149.80	0.828	0.809	67.15	50.35	0.54	61.3	n.a.	3.68	
CLRK3866	**-69.438**	**-26.220**	**3166**	**Granite (Permian[18])**	**FC**															**60.2**	**7.4**		
CLRK3867_Zr1						0.57379	0.01137	1.2292	0.6206	0.0103	142.83	72.12	1.20	159.44	0.807	0.785	59.33	76.89	0.86	96.2	n.a.	5.77	
CLRK3867_Zr2						0.31697	0.00624	0.7302	0.4567	0.0118	112.37	70.28	1.81	128.55	0.786	0.763	53.27	69.77	0.79	89.8	n.a.	5.39	
CLRK3867_Zr3						0.55477	0.01100	1.1048	0.7889	0.0119	164.19	117.24	1.77	191.19	0.789	0.766	54.10	79.20	0.88	101.6	n.a.	6.09	
CLRK3867	**-69.421**	**-26.242**	**3433**	**Granite (Permian[18])**	**FC**															**95.8**	**5.9**		
CLRK3868_Zr1						1.03409	0.02046	2.1892	0.7806	0.0147	235.29	83.89	1.58	254.61	0.806	0.784	58.96	80.30	0.93	100.4	n.a.	6.02	
CLRK3868_Zr2						1.68355	0.03347	3.2401	1.2486	0.0209	267.77	103.19	1.73	291.54	0.818	0.797	63.17	87.72	0.99	108.0	n.a.	6.48	
CLRK3868_Zr3						0.63435	0.01212	1.0628	0.8123	0.0204	145.41	111.13	2.79	171.01	0.782	0.758	52.13	93.07	1.03	120.6	n.a.	7.24	
CLRK3868	**-69.415**	**-26.258**	**3762**	**Granite (Permian[18])**	**FC**															**109.7**	**10.2**		
CLRK3871_Zr1						1.26725	0.02502	2.3243	1.2208	0.0226	367.31	192.93	3.57	411.74	0.776	0.751	50.67	89.32	1.04	116.4	n.a.	6.98	
CLRK3871_Zr2						1.01334	0.01986	1.3984	0.9859	0.0278	166.35	117.28	3.31	193.37	0.802	0.779	57.66	114.14	1.25	144.0	n.a.	8.64	
CLRK3871_Zr3						0.31965	0.00635	0.7874	0.6175	0.0161	135.41	106.20	2.76	159.87	0.769	0.743	48.90	63.21	0.71	83.4	n.a.	5.01	
CLRK3871	**-69.243**	**-26.156**	**3304**	**Granite (Middle Jurassic[18])**	**PC**															**114.6**	**30.3**		
CLRK3872_Zr1						0.37063	0.00742	1.1170	0.6435	0.0263	258.60	148.98	6.10	292.92	0.756	0.729	46.06	53.95	0.64	72.3	n.a.	4.34	
CLRK3872_Zr2						0.54650	0.01040	0.7843	0.4670	0.0217	111.04	66.11	3.07	126.28	0.785	0.761	52.77	112.25	1.28	144.7	n.a.	8.68	
CLRK3872_Zr3						0.21245	0.00426	0.5365	0.2166	0.0154	118.80	47.95	3.41	129.86	0.758	0.731	46.54	66.70	0.81	88.9	n.a.	5.33	
CLRK3872_Zr4						0.29272	0.00629	0.6170	0.3794	0.0204	113.14	69.57	3.74	129.17	0.774	0.749	50.23	76.36	0.88	99.8	n.a.	5.99	
CLRK3872_Zr5						0.60259	0.01291	0.7962	0.5557	0.0305	145.49	101.55	5.57	168.90	0.775	0.750	50.32	119.32	1.35	156.1	n.a.	9.36	
CLRK3872	**-69.066**	**-26.524**	**3614**	**Granite (Permian[32])**	**FC**															**112.4**	**36.3**		
CLRK3873_Zr1						0.34814	0.00700	1.1279	0.8025	0.0200	147.40	104.87	2.62	171.55	0.796	0.773	55.97	48.83	0.54	62.1	n.a.	3.73	
CLRK3873_Zr2						0.71221	0.01414	2.7417	1.4276	0.0404	264.01	137.47	3.89	295.68	0.815	0.794	62.08	42.77	0.47	53.0	n.a.	3.18	
CLRK3873_Zr3						0.70814	0.01413	2.4390	1.2931	0.0366	226.92	120.31	3.41	254.63	0.818	0.798	63.21	47.69	0.53	58.8	n.a.	3.53	
CLRK3873	**-69.856**	**-25.404**	**1716**	**Tonalite (188.8 - 180 Ma[33])**	**CC**															**58.0**	**4.6**		
CLRK3874_Zr1						0.65592	0.01314	1.1853	0.3367	0.0177	298.91	84.91	4.47	318.48	0.745	0.716	43.85	95.44	1.21	129.3	n.a.	7.76	
CLRK3874_Zr2						0.55451	0.01101	1.4919	0.6040	0.0216	296.74	120.15	4.30	324.42	0.766	0.740	48.28	62.62	0.75	82.5	n.a.	4.95	
CLRK3874_Zr3						0.38165	0.00759	0.7103	0.3328	0.0233	189.60	88.82	6.21	210.08	0.739	0.710	42.83	89.07	1.10	122.0	n.a.	7.32	
CLRK3874_Zr4						0.84011	0.01857	1.3735	0.5219	0.0230	315.34	119.81	5.28	342.94	0.762	0.735	47.31	103.22	1.26	136.8	n.a.	8.21	
CLRK3874_Zr5						0.41142	0.00913	0.7261	0.3487	0.0210	191.75	92.08	5.56	212.98	0.741	0.712	43.11	93.66	1.15	128.1	n.a.	7.68	
CLRK3874	**-69.345**	**-24.825**	**2814**	**Granite (Carb.-Perm.[34])**	**FC**															**119.8**	**21.5**		
CLRK3876_Zr1						1.75164	0.03471	3.4276	1.1997	0.0417	512.45	179.36	6.24	553.77	0.794	0.771	55.28	86.94	1.02	110.4	n.a.	6.62	
CLRK3876_Zr2						0.79862	0.01528	1.4563	0.6320	0.0162	350.78	152.24	3.91	385.85	0.753	0.726	45.51	91.58	1.12	123.0	n.a.	7.38	
CLRK3876_Zr3						0.66085	0.01319	1.0224	0.7984	0.0127	181.85	142.00	2.26	214.55	0.777	0.752	50.84	100.40	1.12	131.1	n.a.	7.86	
CLRK3876	**-68.750**	**-24.140**	**3054**	**Granite (Permian[35])**	**FC**															**121.5**	**10.4**		
CLRK3877_Zr1						1.14838	0.02296	1.1178	0.6029	0.0342	268.34	144.73	8.22	301.70	0.755	0.728	46.00	166.62	1.99	223.4	n.a.	13.40	
CLRK3877_Zr2						1.42920	0.02863	1.5191	0.8857	0.0948	267.15	155.77	16.66	303.10	0.780	0.755	51.50	151.38	1.74	196.4	n.a.	11.79	
CLRK3877_Zr3						0.71699	0.01418	0.6340	0.3617	0.0089	153.86	87.77	2.17	174.07	0.755	0.728	45.99	181.98	2.16	244.1	n.a.	14.64	
CLRK3877	**-68.512**	**-24.155**	**3441**	**Poprhyric granite (Carb.-Perm.[35])**	**FC**															**221.3**	**23.9**		
CLRK3879_Zr1						1.56224	0.02966	1.6018	0.6854	0.0160	290.47	124.28	2.90	319.10	0.762	0.736	47.39	162.02	1.95	214.8	n.a.	12.89	
CLRK3879_Zr2						1.62064	0.03198	1.5856	0.7253	0.0202	251.16	114.89	3.20	277.63	0.761	0.734	47.10	168.63	2.03	224.1	n.a.	13.45	

Sample	Lon	Lat	Elev.	Lithology	Tect. unit	^{4}He	± 1σ	U	Th	Sm	U	Th	Sm	eU	F_T	F_T	R_s	Raw Age	± 2σ	Corr. Age	± 1σ	6% err	Comment
	(°)	(°)	(m)			(pmol)	(pmol)	(ng)	(ng)	(ng)	(ppm)	(ppm)	(ppm)	(ppm)	^{238}U	^{232}Th	(µm)	(Ma)	(Ma)	(Ma)	(Ma)	(Ma)	
CLRK3879_Zr3						1.36676	0.02482	1.3633	0.5689	0.0156	315.09	131.49	3.59	345.38	0.750	0.722	44.93	166.84	2.05	224.9	n.a.	13.49	
CLRK3879	**-68.475**	**-24.289**	**3506**	**(Syeno-)Granite (Ordovician[36])**	**FC**															**221.3**	**5.6**		
CLRK3880_Zr1						1.23222	0.02392	1.1275	0.9475	0.0153	312.31	262.45	4.23	372.75	0.737	0.708	42.45	166.80	1.95	230.5	n.a.	13.83	
CLRK3880_Zr2						1.42432	0.02781	1.4183	1.5962	0.0212	349.08	392.87	5.21	439.54	0.756	0.729	46.13	145.43	1.59	196.0	n.a.	11.76	
CLRK3880_Zr3						0.60120	0.01193	0.6960	0.4956	0.0172	103.07	73.39	2.55	119.98	0.797	0.774	56.17	135.60	1.49	172.2	n.a.	10.33	
CLRK3880	**-68.666**	**-24.415**	**3619**	**Granite (Carb.-Perm.[35])**	**FC**															**199.6**	**29.3**		
CLRK3881_Zr1						0.38674	0.00515	0.9061	0.6012	0.0112	140.56	93.26	1.74	162.03	0.787	0.763	53.31	68.08	0.76	87.6	n.a.	5.26	
CLRK3881_Zr2						0.44498	0.00819	1.1753	0.9474	0.0169	162.66	131.12	2.33	192.85	0.789	0.765	53.93	58.72	0.64	75.4	n.a.	4.53	
CLRK3881_Zr3						0.32644	0.00613	0.8654	0.6476	0.0119	129.13	96.64	1.78	151.39	0.785	0.761	52.86	59.19	0.66	76.4	n.a.	4.58	
CLRK3881	**-69.938**	**-23.740**	**653**	**Granite (90 - 110 Ma[37])**	**CC**															**79.8**	**6.8**		
CLRK3886_Zr1						0.18423	0.00366	0.6882	0.3221	0.0091	215.44	100.82	2.86	238.67	0.739	0.710	42.88	44.57	0.55	61.0	n.a.	3.66	
CLRK3886_Zr2						0.19239	0.00384	0.6169	0.3878	0.0080	213.19	134.02	2.75	244.05	0.725	0.695	40.41	50.18	0.62	70.4	n.a.	4.22	
CLRK3886_Zr3						0.21799	0.00436	0.7960	0.4822	0.0081	310.12	187.86	3.14	353.38	0.720	0.689	39.58	44.30	0.55	62.6	n.a.	3.75	
CLRK3886	**-68.937**	**-22.791**	**2755**	**Granite (Carboniferous[40])**	**FC**															**64.7**	**5.0**		
CLRK3891_Zr1						1.32116	0.02635	1.3633	0.6209	0.0279	210.12	95.69	4.31	232.17	0.790	0.767	54.38	160.07	1.85	204.4	n.a.	12.26	
CLRK3891_Zr2						2.32159	0.04397	2.9731	0.9016	0.0705	287.01	87.04	6.80	307.08	0.817	0.796	62.83	133.62	1.54	164.5	n.a.	9.87	
CLRK3891_Zr3						1.13739	0.02196	0.9433	0.5732	0.0141	148.94	90.51	2.22	169.78	0.787	0.763	53.42	192.37	2.18	247.3	n.a.	14.84	
CLRK3891	**-68.883**	**-24.845**	**3410**	**Granite (Permian 282 Ma[45])**	**FC**															**205.4**	**41.4**		
CLRK3892_Zr1						0.82449	0.01606	1.9844	1.1009	0.0329	198.69	110.23	3.29	224.08	0.807	0.785	59.24	67.78	0.75	84.8	n.a.	5.09	
CLRK3892_Zr2						0.14185	0.00281	0.3889	0.2220	0.0136	56.47	32.24	1.97	63.91	0.797	0.774	56.18	59.34	0.67	75.3	n.a.	4.52	
CLRK3892_Zr3						0.46388	0.00916	1.0859	0.6761	0.0791	44.97	28.00	3.28	51.43	0.860	0.844	83.49	68.68	0.71	80.4	n.a.	4.82	
CLRK3892	**-70.054**	**-25.743**	**1319**	**Granite (149.4 Ma U-Pb[31])**	**CC**															**80.2**	**4.8**		

A3. AFT Data

Table A3: AFT data. Zeta-values are $\zeta_{ISTerre}$= 310.4 ± 13.8 for samples 14NC-x , ζ_{ETHZ} = 354.96 ± 12.6 for samples Clin-x and $\zeta_{Dalhousie}$ = 370.6 ± 5 for samples CLRK-x. P(χ^2)-values were calculated with RadialPlotter (Vermeesch, 2009), age populations (P1, P2, P3) with Binomfit (Brandon, 2002). Rejected samples are highlighted in Italic. Intrusion ages refer to the closest U-Pb, K-Ar or Ar-Ar age from the same lithology (see numbers for references, provided at the end of the thermochronological data tables). Rock compositions result from field observations and are thus approximate. Tectonic units: CC = Coastal Cordillera, CD = Central Depression, FC = Frontal Cordillera, PC = Principal Cordillera. * = samples overlapping with AHe age, within error, § = samples younger than AHe age. # gr = number of grains; conf. TL = confined track length; TD = track density.

Sample	Lon (°)	Lat (°)	Elev. (m)	Lithology	Tect. unit	# gr	Spont. TD (ρ_s) (cm^{-2})	Ns	Ind. TD (ρ_i) (cm^{-2})	Ni	Dosim. TD (ρ_d) (cm^{-2})	Nd	P (χ^2) (%)	Cent. Age (Ma)	1σ (Ma)	U (ppm)	Dpar (μm)	1σ Dpar (μm)	Conf. TL (#)	MTL (μm ± σ)	P1 (Frac.) (Ma) (%)	95% - CI (P1) (Ma)	P2 (Frac.) (Ma) (%)	95% - CI (P2) (Ma)	P3 (Frac.) (Ma) (%)	95% - CI (P3) (Ma)	Comment
14NC01	-70.369	-29.834	1460	Felsic Intrusive (288.2 Ma U-Pb[1])	FC	20	968160	524	5245430	2839	979000	4986	32	28.0	1.3	80.4	1.43	0.13									
14NC03	-70.499	-29.854	1057	Felsic Intrusive (291.2 Ma U-Pb[1])	FC	20	198437	176	899731	798	980000	4986	3	34.6	3.6	13.8	1.20	0.15			30.1 (83.9)	7.5	67.4 (16.1)	63.75			
14NC05	*-70.519*	*-30.018*	*976*	*Felsic Intrusive (291.2 Ma U-Pb[1])*	*FC*	*20*	*238665*	*219*	*328028*	*301*	*980000*	*4986*	*0*	*128*	*19.0*	*5.0*	*1.25*	*0.22*			*72.3(55.4)*	*20.95*	*192.5 (44.6)*	*87.7*			*low U, high error*
14NC06	-70.631	-30.026	732	Felsic Intrusive (62.4 Ma[2])	PC	20	1344764	568	7036335	2972	981000	4986	0	29.3	2.1	107.6	1.53	0.41			22.8 (52.6)	4.85	36.7 (47.2)	7.95			
14NC15	-70.491	-30.164	1389	Felsic Intrusive (289.7 Ma U-Pb[1])	FC	19	373248	332	2149551	1912	982000	4986	4	27.2	2.1	32.8	1.35	0.34			24.5 (88.1)	4.1	45.9 (11.9)	26.15			
14NC18	-70.645	-30.217	2015	Felsic Intrusive (42.4 Ma K-Ar[2])	PC	20	697138	482	3503047	2422	982000	4986	68	30.3	1.5	53.5	1.70	0.19									
14NC21	*-70.755*	*-29.451*	*1056*	*Felsic Intrusive (63.2 Ma U-Pb Ma[5])*	*PC*	*20*	*373831*	*247*	*871768*	*576*	*983000*	*4986*	*4*	*65.5*	*6.4*	*13.3*	*1.39*	*0.19*			*56.2 (79.5)*	*13.1*	*112.2 (20.5)*	*56.15*			*Magmatic cooling*
14NC22	-70.575	-29.462	2630	Felsic Intrusive (78 - 68 Ma[5])	PC	20	571999	515	2473480	2227	983000	4986	18	35.1	2.0	37.7	1.64	0.21									
14NC29	-70.461	-28.962	1285	Felsic Intrusive (44 Ma[7])	PC	20	830800	765	3344921	3080	984000	4986	0	41.4	3.4	51.0	1.91	0.16			35.0 (86.3)	4.55	81.1 (13.7)	33.1			
14NC30	-70.347	-29.178	1885	Granite (Devon. - Perm.[8])	FC	30	450766	407	1801957	1627	984000	4986	0	35.0	5.0	27.5	1.27	0.56			23.4 (80.1)	4.25	101.8 (19.9)	42.1			
14NC32	-70.302	-29.007	1690	Felsic Intrusive (Permian[7,8])	FC	20	454141	370	2670840	2176	985000	4986	0	26.7	2.7	40.7	1.32	0.12			21.6 (76.1)	3.6	48.2 (23.9)	12.2			
14NC34	*-70.543*	*-28.565*	*1121*	*Felsic Intrusive (68 Ma U-Pb[6])*	*PC*	*20*	*274142*	*223*	*529844*	*431*	*986000*	*4986*	*0*	*80.0*	*11.0*	*8.1*	*1.14*	*0.16*			*57.4 (62.5)*	*32.15*	*134.0 (37.5)*	*90.65*			*Magmatic cooling*
14NC36	*-70.409*	*-28.376*	*1053*	*Granite, Oligocene (64-66 Ma K-Ar[7])*	*PC*	*20*	*927696*	*428*	*1959433*	*904*	*986000*	*4986*	*0*	*77.0*	*8.5*	*29.8*	*1.57*	*0.20*			*58.3 (64.6)*	*10.65*	*125.6 (35.4)*	*36.3*			*Magmatic cooling*
Huasco54	-70.295	-28.850	1089	Tonalite (310 Ma K-Ar[7])	FC	20	1370471	599	8080974	3532	975000	4986	0	25.9	1.8	124.3	1.96	0.16	100	12.6 ± 2.2	14.6 (16.0)	5.15	27.1 (77.8)	3.9	46.4 (6.2)	26.15	
Huasco73	-70.324	-28.859	2032	Tonalite (310 Ma K-Ar[7])	FC	20	299403	238	1115841	887	976000	4986	39	40.5	3.0	17.1	1.64	0.14									
Huasco75	-70.223	-28.970	1298	Gneiss (310 Ma K-Ar[7])	FC	20	693818	630	4278545	3885	976000	4986	6	24.6	1.3	65.8	1.47	0.14									
Huasco87	-70.223	-28.941	2864	Gneiss (310 Ma K-Ar[7])	FC	20	564337	401	2633105	1871	977000	4986	53	32.6	1.9	40.4	1.86	0.10									
Laguna57	-70.007	-28.792	2570	Granodiorite (260 Ma[7])	FC	20	209236	121	954530	552	977000	4986	24	33.4	3.5	14.7	1.73	0.22									
Relincho19	-70.464	-28.674	2220	Granodiorite (64.02 Ma U-Pb K-Ar[7])	PC	20	359610	253	751913	529	978000	4986	28	72.2	5.7	11.5	1.93	0.18									
Relincho20	-70.430	-28.627	2225	Granodiorite (64.02 Ma U-Pb K-Ar[7])	PC	20	549619	524	1404465	1339	978000	4986	42	59.1	3.0	21.5	1.59	0.21									
Sauce31	-70.546	-28.871	2398	Granodiorite (65-64 Ma[6])	PC	20	776923	350	1589363	716	979000	4986	9	73.9	5.8	24.4	1.43	0.19									
Clin22A	-33.491	-70.130	1559	Granite (10.37 ± 0.1 Ma U-Pb[24])	PC	30	161272	157	5520231	5374	1525500	8845	5	7.96	0.7	44.04	2.56	0.44									
Clin22B	-33.499	-70.125	1918	Granite (10.37 ± 0.1 Ma U-Pb[24])	PC	40	72917	80	2911205	3194	1604500	12238	47	7.13	0.8	22.08	2.58	0.48									
Clin22C	*-33.504*	*-70.124*	*2280*	*Granite (10.37 ± 0.1 Ma U-Pb[24])*	*PC*	*50*	*100870*	*154*	*3624788*	*5534*	*1683500*	*12769*	*0*	*8.99*	*1.0*	*26.20*	*3.13*	*0.76*			*7.3 (91.8)*	*1.55*	*29.0 (8.2)*	*21.45*			*Magmatic cooling*
Clin22D	*-33.505*	*-70.129*	*2575*	*Granite (10.37 ± 0.1 Ma U-Pb[24])*	*PC*	*20*	*187918*	*129*	*6118257*	*4200*	*1763000*	*10203*	*18*	*9.81*	*1.0*	*42.23*	*2.71*	*0.32*									*Magmatic cooling*
Clin25A	-34.059	-70.118	2012	Granite (13.39 ± 0.13 Ma U-Pb[24])	PC	43	45840	53	2294586	2653	1900500	11009	37	6.73	1.0	14.69	3.74	1.60									
Clin25B	*-34.076*	*-70.115*	*2374*	*Granite (13.39 ± 0.13 Ma U-Pb[24])*	*PC*	*50*	*70333*	*105*	*2282805*	*3408*	*1949000*	*13212*	*3*	*11.1*	*1.2*	*14.25*	*1.62*	*0.23*			*9.1 (85.4)*	*3.25*	*23.7 (14.6)*	*26.95*			*Magmatic cooling*
Clin25C	*-34.076*	*-70.120*	*2670*	*Granite (13.39 ± 0.13 Ma U-Pb[24])*	*PC*	*40*	*98755*	*84*	*2473577*	*2104*	*1772000*	*9070*	*61*	*12.5*	*1.4*	*16.99*	*2.18*	*0.26*									*Magmatic cooling*
Clin25D	-34.079	-70.124	2934	Granite (13.39 ± 0.13 Ma U-Pb[24])	PC	40	32026	45	1397775	1964	1752000	12625	92	7.1	1.1	9.71	2.77	0.52									
CLRK3848*	-69.972	-24.098	1088	Granite (168 Ma[27,37])	CC	20	128500	117	717100	653	1223500	6139	69	40.8	4.3	9.0	2.29	0.18	11	13.32 ± 0.57							
CLRK3851	-69.271	-25.235	3817	Granite (289 Ma K-Ar[29])	PC	18	354700	129	1490300	542	1232800	6139	97	54.1	5.4	18.0	1.99	0.16	3	14.65 ± 0.86							
CLRK3852§	-69.084	-25.380	4020	Monzonite (Permian 323.9 Ma U-Pb[29])	PC	21	1003300	682	4732400	3217	1242100	6139	14	48.9	2.8	47.0	2.07	0.11	98	13.47 ± 2.48							
CLRK3853*	-69.436	-25.746	2700	Monzonite (43.3 Ma K-Ar[30])	PC	20	81500	61	525400	393	1251300	6139	100	35.9	5.0	5.0	2.19	0.28									
CLRK3860	*-70.018*	*-25.942*	*1162*	*Porphyritic Dacite (123.7 Ma U-Pb[31])*	*CC*	*11*	*125600*	*30*	*464700*	*111*	*1269900*	*6139*	*68*	*63.3*	*13.1*	*5.0*	*3.84*	*0.53*									*Low U, high dispersion*
CLRK3862*	-69.577	-26.332	2604	Porphyritic Monzonite (59 +-2 Ma[17])	PC	16	95700	55	753400	433	1279200	6139	71	30.0	4.3	8.0	2.23	0.2									
CLRK3863	-69.612	-26.099	2007	Tonalite (68.5 Ma K-Ar[17])	PC	20	471900	203	1815700	781	1288400	6139	64	61.8	5.0	19.0	4.09	0.48	24	14.11 ± 2.24							
*CLRK3864**	*-69.445*	*-26.201*	*2804*	*Granite (Permian[18])*	*PC*	*10*	*109300*	*21*	*1004300*	*193*	*1297700*	*6139*	*100*	*26.1*	*6.0*	*13.0*	*2.28*	*0.21*									*Low U, high dispersion*
CLRK3866*	-69.438	-26.220	3166	Granite (Permian[18])	PC	10	1120800	312	8125600	2262	1307000	6139	26	33.5	2.4	82.0	2.35	0.53	54	12.14 ± 2.46							
CLRK3867*	-69.421	-26.242	3433	Granite (Permian[18])	PC	20	576500	381	3767400	2490	1316300	6139	78	37.2	2.2	37.0	1.99	0.11	26	13.78 ± 1.22							
CLRK3868	-69.415	-26.258	3762	Granite (Permian[18])	PC	20	1032300	965	4942100	4620	1325500	6139	19	50.8	2.3	48.0	2.63	0.18	100	12.19 ± 2.83							
CLRK3871	-69.243	-26.156	3304	Sandstone (Middle Jurassic[18])	PC	14	170300	137	694700	559	1334800	6139	91	60.3	5.9	7.0	3.47	0.31									
CLRK3872	*-69.066*	*-26.524*	*3614*	*Granite (Permian[32])*	*PC*	*11*	*101200*	*12*	*607400*	*72*	*1344100*	*6139*	*81*	*41.4*	*12.9*	*7.0*	*n.a.*									*Low U, high dispersion*
CLRK3873*	-69.856	-25.404	1716	Tonalite (188.8 - 180 Ma[33])	CC	21	139000	72	677400	351	1353400	6139	100	51.2	6.7	7.0	2.1	0.36									
CLRK3874§	-69.345	-24.825	2814	Granite (Carb.-Perm.[34])	PC	18	517600	165	3585400	1143	1362600	6139	39	36.4	3.3	35.0	2.41	0.2	5	11.72 ± 1.41							
CLRK3875	-69.181	-24.701	3625	Porphyric Tonalite (Permian[34])	PC	14	367900	151	2132100	875	1371900	6139	15	42.3	4.8	29.0	2.79	0.29	58	13.75 ± 2.31							
CLRK3876	-68.750	-24.140	3054	Granite (Permian[35])	PC	16	891700	442	4589500	2275	1382100	6139	61	49.6	2.7	43.0	2.56	0.14	62	13.84 ± 1.36							
CLRK3880§	-68.666	-24.415	3619	Granite (Carb.-Perm.[35])	PC	15	147400	65	1608000	709	1399700	6139	23	24.0	3.3	15.0	2.57	0.25	3	15.00 ± 1.13							
CLRK3881	*-69.938*	*-23.740*	*653*	*Granite (90 - 110 Ma[37])*	*CD*	*9*	*373800*	*48*	*1682100*	*216*	*1409000*	*6139*	*74*	*57.8*	*9.3*	*16.0*	*3.38*	*0.65*									*Low U, high dispersion*
CLRK3882§	-69.636	-23.890	1265	Granite (Carbon - Perm.[37])	FC	9	407900	74	2976900	540	1418300	6139	81	35.9	4.5	29.0	1.92	0.1									
CLRK3883	-69.815	-23.224	1254	Granite (191 Ma U-Pb[38])	CD	18	355900	412	1262200	1461	1427500	6139	96	74.2	4.4	12.0	2.26	0.17	10	12.92 ± 1.96							
CLRK3884	*-69.598*	*-23.388*	*1510*	*Granite (78.6 Ma K-Ar[39])*	*PC*	*7*	*192000*	*40*	*1142400*	*238*	*1436800*	*6139*	*39*	*44.6*	*7.8*	*10.0*	*2.68*	*0.26*									*Low U, high dispersion*
CLRK3886	-68.937	-22.791	2755	Granite (Carboniferous[40])	PC	20	424000	455	2832900	3040	1446100	6139	40	40.2	2.3	27.0	2.04	0.18	78	12.53 ± 2.25							

References for intrusion ages documented in thermochronological data Tables

1 Hervé, F., Fanning, C. M., Calderón, M., Mpodozis, C. (2014). Early Permian to Late Triassic batholiths of the Chilean Frontal Cordillera (28°–31°S): SHRIMP U–Pb zircon ages and Lu–Hf and O isotope systematics. Lithos, 184, 436-446.

2 Mpodozis, C., Cornejo, P. (1986). Hoja Pisco Elqui, 1:250.000. Servicio Nacional de Geología y Minería, Carta Geológico de Chile, No.66, Santiago

3 Moscoso, R. (1982). Hoja Vallenar y parte norte de La Serena, 1:250.000. Servicio Nacional de Geología y Minería, Carta Geológico de Chile, No.55, Santiago

4 Emparan, C., Pineda, G. (1999). Geología del área Condoriaco - Rivadavia, Región de Coquimbo, 1:100.000. Serv. Nac. Geol. Min., Mapas Geol. de Chile, No.12, Santiago

5 Creixell, C., Labbé, M., Arévalo, C., Salazar, E. (2013). Área Estación Chañar-Junta de Chingoles, Regiones de Atacama y Coquimbo, 1:100.000. Servicio Nacional de Geología y Minería, Serie Geología Básica, No. 150, Santiago

6 Arévalo, C., Mourgues, F.A., Chávez, R. (2009). Geología del área Vallenar-Domeyko, Región de Atacama, 1:100.000. Servicio Nacional de Geología y Minería, Carta Geológica de Chile, Serie Geología Básica, No. 120, Santiago

7 Mpodozis, C., Moscoso, R., Nasi, C., Ribba, L., Arévalo, C., Soffia, J., Abad, E. (2007). Hoja El Transito - Mapa de Compilación, Región de Atacama, 1:250.000. Servicio Nacional de Geología y Minería, Carta Geológica de Chile, Santiago

8 Nasi, C., Moscoso, R., Maksaev, V. (1990). Hoja Guanta, Regiones de Atacama y Coquimbo, 1:250.000. Serv. Nac. Geol. Min., Carta Geológica de Chile, No. 67, Santiago

9 McNutt, R.H., Crocket, J.H., Clark, A.H., Caelles, J.C., Farrar, E., Haynes, S.J., Zentilli, M. (1975). Initial 87Sr/86Sr ratios of plutonic and volcanic rocks of the central Andes between latitudes 26° and 29° south. *Earth and Planetary Science Letters* , *27* (2), 305-313.

10 Lara, L., Godoy, E. (1998). Hoja Quebrada Salitrosa, Región de Atacama, 1:100.000. Servicio Nacional de Geología y Minería, Serie Geología Básica, No. 4, Santiago

11 Arévalo, C. (2005). Carta Los Loros, Región de Atacama, 1:100.000. Servicio Nacional de Geología y Minería, Serie Geología Básica, No. 92, Santiago

12 Farrar, E., Clark, A. H., Haynes, S. J., Quirt, G. S., Conn, H., Zentilli, M. (1970). K-Ar evidence for the post-Paleozoic migration of granitic intrusion foci in the Andes of northern Chile. *Earth and Planetary Science Letters* , *10* (1), 60-66.

13 Arévalo, C. (2005). Carta Copiapó, Región de Atacama, 1:100.000. Servicio Nacional de Geología y Minería, Serie Geología Básica, No. 91, Santiago

14 Sepúlveda, P., Naranjo, J.A. (1982). Hoja Carrera Pinto, 1:100.000. Servicio Nacional de Geología y Minería, Carta Geologica de Chile, No. 53, Santiago

15 Matthews, S.J., Cornejo, P., Riquelme, R. (2006). Carta Inca Oro, Región de Atacama, 1:100.000. Serv. Nac. Geol. Min., Carta Geol. Chile, Serie Geol. Básica, 102, Santiago

16 Singer, D.A., Berger, V.I., Moring, B.C. (2008): Porphyry Copper Deposits of the World: Database and Grade and Tonnage Models, USGS, Open-File Report 2008-1155, v. 1.0, https://pubs.usgs.gov/of/2008/1155/

17 Cornjeo, P., Matthews, S., Mpodozis, C., Riquelme, R. (2013). Carta El Salvador, Región de Atacama, 1:100'000. Servicio Nacional de Geología y Minería, Carta Geológica de Chile, Serie Geología Básica, No. 158, Santiago

18 Tomlinson, A.J., Cornejo, P., Mpodozis, C. (1999). Hoja Potrerillos, Región de Atacama, 1:100'000. Serv. Nac. Geol. Min., Mapas Geológicos de Chile, No. 14, Santiago.

19 Rivano, S., Sepúlveda, P., Boric, R., Espiñeira, D. (1993). Hojas Quillota y Portillo, 1:250.000. Serv. Nac. Geol. Min., Carta Geológica de Chile, No. 73, Santiago

20 Rivano, S., Sepúlveda, P. (1986). Hoja Illapel, 1:250.000. Servicio Nacional de Geología y Minería, Carta Geológica de Chile, No. 69, Santiago

21 Moscoso, R., Padilla H., Rivano, S. (1982). Hoja Los Andes, 1:250.000. Servicio Nacional de Geología y Minería, Carta Geológica de Chile, No. 52, Santiago

22 Sellés, D., Gana, P. (2001). Geología del área Talagante-San Francisco de Mostazal, Regiones Metropolitana de Santiago y del Libertador General Bernardo O'Higgins, 1:100.000. Servicio Nacional de Geología y Minería, Carta Geológica de Chile, Serie Geología Básica, No. 74, Santiago.

23 Piquer, J., Hollings, P., Rivera, O., Cooke, D. R., Baker, M., Testa, F. (2017). Along-strike segmentation of the Abanico Basin, central Chile: New chronological, geochemical and structural constraints. *Lithos* , *268* , 174-197.

24 This study

25 Godoy, E., Koeppen, R. (1993). Geología del Área entre los Rios Claro del Maipo y Cachapoal, 1:100.000. Servicio Nacional de Geología y Minería

26 SERNAGEOMIN (2003). Mapa Geológico de Chile: versión digital, 1:1.000.000. Serv. Nac. Geol. Min., Publicación Geológica Digital, No. 4, versión 1.0, Santiago

27 Ferrando, R., Espinoza, F., Matthews, S., Cornejo, P., Arévalo, C. (2013). Carta Aguas Blancas, Región de Antofagasta, 1:100.000. Serv. Nac. Geol. Min., Carta Geológica de Chile, Serie Geología Básica, No. 160, Santiago

28 Marinovic, N., Smoje, I.,Maksaev, V., Hervé, M., Mpodozis, C. (1995). Hoja Aguas Blancas, Región de Antofagasta, 1:250.000. Servicio Nacional de Geología y Minería, Carta Geológica de Chile, No. 70, Santiago

29 Venegas, C., Cervetto, M., Astudillo, N., Espinoza, F., Cornejo, P., Mpodozis, C., Rivera, O. (2013). Carta Sierra Vaquillas Altas, Regiones de Antofagasta y Atacama, 1:100.000. Servicio Nacional de Geología y Minería, Carta Geológica de Chile, Serie Geología Básica, No. 159, Santiago

30 Cornejo, P., Mpodozis, C., Rivera, O., Matthews, S. (2009). Carta Exploradora, Regiones de Antofagasta y Atacama, 1:100.000. Serv. Nac. Geol. Min., Carta Geológica de Chile, Serie Geología Básica, No. 119, 1 mapa, Santiago.

31 Espinoza, M., Contreras, J. P., Jorquera, R., De la Cruz, R., Kraus, S., Ramírez, C., Naranjo, J. A. (2014). Carta Cerro del Pingo, Regiones de Antofagasta y de Atacama, 1:100.000. Serv. Nac. Geol. Min., Carta Geológica de Chile, Serie Geología Básica, No. 169, Santiago.

32 Cornejo, P., Mpodozis, C., Tomlinson, A.J. (1998). Hoja Salar de Maricunga, Región de Atacama, 1:100.000. Servicio Nacional de Geología y Minería, Carta Geológica de Chile, Serie Geología Básica, No. 7, Santiago.

33 Espinoza, F.; Matthews, S.; Cornejo, P.; Venegas, C. 2011. Carta Catalina, Región de Antofagasta, 1:100.000. Servicio Nacional de Geología y Minería, Carta Geológica de Chile, Serie Geología Básica, No.129, Santiago.

34 González, R., Wilke, G.H., Menzies, A.H., Riquelme, R., Herrera, C., Matthews, S., Espinoza, F., Cornejo, P. (2015). Carta Sierra de Varas, Región de Antofagasta, 1:100.000. Servicio Servicio Nacional de Geología y Minería, Carta Geológica de Chile, Serie Geología Básica, No. 178, Santiago.

35 Gardeweg, M., Pino, H., Ramírez, C.F., Davidson, J. (1994). Mapa geológica del área de Imilac y Sierra Almeida, Región de Antofagasta, 1:100.000. Servicio Nacional de Geología y Minería, Documentos de Trabajo, No. 7, Santiago.

36 Ramirez, C., Gardeweg, M., Davidson, J., Pino, H. (1991). Mapa geológica del área de los volcanes Socompa y Pular, Región de Antofagasta, 1:100.000. Serv. Nac. Geol. Min., Documentos de Trabajo, No. 4, Santiago.

37 Cortés, J. (2000). Hoja Palestina, Región de Antofagasta, 1:100.000. Servicio Nacional de Geología y Minería, Mapas Geológicos, No. 19, Santiago.

38 Basso, M. (20014). Carta Baquedano, Región de Antofagasta, 1:100.000. Serv. Nac. Geol. Min., Carta Geológica de Chile, Serie Geología Básica, No. 82, Santiago

39 Scheuber, E., Gonzalez, G. (1999). Tectonics of the Jurassic-Early Cretaceous magmatic arc of the north Chilean Coastal Cordillera (22°–26°S): A story of crustal deformation along a convergent plate boundary. *Tectonics* , *18* (5), 895-910.

40 Marinović, N., Lahsen, A. (1984). Hoja Calama, 1:100.000. Servicio Nacional de Geología y Minería, Carta Geológica de Chile, No. 58, Santiago

41 Ramírez, C.F., Huete, C. (1981). Geología de la Hoja Ollagüe, Región de Antofagasta, 1:250.000. Serv. Nac. Geol. Min., Carta Geológica de Chile, Santiago

42 Mpodozis, C. (1993). Hoja Sierra del Jardín - Sierra Mariposas, Región de Antofagasta, 1:100.000. Serv. Nac. Geol. Min., Carta Geológica de Chile, Santiago

43 Marinović, N. (2007). Carta Oficina Domeyko, Región de Antofagasta, 1:100.000. Servicio Nacional de Geología y Minería, Carta Geológica de Chile, Santiago

44 Maksaev, V., Marinovic, N., Smoje, I., Mpodozis, C. (1991). Mapa Geológico de la hoja Augusta Victoria, Región de Antofagasta, 1:100.000. Servicio Nacional de Geología y Minería, Documentos de Trabajo, No. 1, Santiago.

45 Gardeweg, P., Ramírez, R., Davidson, M. (1993). Mapa geológico del área del Salar de Punta Negra y del volcán Llullaillaco, Región de Antofagasta, 1:100.000. Serv. Nac. Geol. Min., Documentos de Trabajo, No. 5, Santiago.

46 Blanco, N.P., Godoy, E., Marquardt, C.R. (2003). Carta Castilla y Totoral Bajo, Región de Atacama, 1:100.000. Servicio Nacional de Geología y Minería, Carta Geológica de Chile, Serie Geología Básica, No. 77/78, Santiago.

47 Mercado, M. (1977). Avance geológico de las Hojas Chañaral y Potrerillos, Región de Antofagasta, 1:250.000. Serv. Nac. Geol. Min., Carta Geol. de Chile, No. 2, Santiago

48 Godoy, E., Lara, L. (1998). Hojas Chañaral y Diego de Almagro, Región de Atacama, 1:100.000. SServ. Nac. Geol. Min., Mapas Geológica de Chile, No. 5/6, Santiago.

A4. U-Pb Data

Table A4: Results from LA-ICP-MS U-Pb age determination. Average ages are provided as weighted mean ± 2σ [Ma] standard error. Rejected measurements are highlighted in Italic (see comments). CD = Concordia diagram

	Sample	$^{206}Pb/^{238}U$ Ratio	1σ (%)	$^{207}Pb/^{235}U$ Ratio	1σ (%)	$^{207}Pb/^{206}Pb$ Ratio	1σ (%)	$^{206}Pb/^{238}U$ Age (Ma)	2σ (Ma)	$^{207}Pb/^{235}U$ Age (Ma)	2σ (Ma)	$^{207}Pb/^{206}Pb$ Age (Ma)	2σ (Ma)	Comments
	Clin22A_Zr01	0.0017	3.2	0.0114	33.59	0.04957	42.37	10.8	0.7	11.5	7.7	174	944	
	Clin22A_Zr02	0.0016	3.98	0.0137	48.29	0.06143	162.31	10.4	0.8	13.9	13.3	654	2466	
	Clin22A_Zr03	0.0016	2.98	0.0068	48.98	0.03166	53.65	10.2	0.6	6.9	6.7	0	130	
	Clin22A_Zr04	0.0016	2.04	0.0129	16.86	0.0589	17.86	10.3	0.4	13.1	4.4	562	794	
	Clin22A_Zr05	0.0016	2.16	0.0132	24.29	0.05885	24.04	10.4	0.4	13.3	6.4	560	1012	
	Clin22A_Zr06	*0.0018*	*2.59*	*0.0261*	*20.35*	*0.10646*	*17.77*	*11.4*	*0.6*	*26.2*	*10.5*	*1738*	*662*	*discordant*
	Clin22A_Zr07	0.0016	2.15	0.0089	23.01	0.04126	22.82	10.2	0.4	9	4.1	0	224	
	Clin22A_Zr08	0.0016	3.07	0.0101	33.47	0.04489	37.07	10.3	0.6	10.2	6.8	0	658	
	Clin22A_Zr09	0.0016	4.13	0.0236	25.81	0.10911	35.32	10	0.8	23.7	12.1	1784	1374	
	Clin22A_Zr10	0.0016	2.33	0.0088	22.50	0.04036	25.10	10.1	0.5	8.9	4	0	216	
	Clin22A_Zr11	0.0016	2.46	0.0062	38.49	0.02844	41.08	10.2	0.5	6.3	4.8	0	0	
	Clin22A_Zr12	0.0016	2.7	0.0199	15.04	0.09213	15.01	10.2	0.5	20	5.9	1470	576	
	Clin22A_Zr13	0.0017	3.19	0.0187	22.92	0.07814	24.59	11	0.7	18.8	8.5	1150	1008	
	Clin22A_Zr14	0.0017	2.47	0.0096	24.96	0.04116	28.67	10.8	0.5	9.7	4.8	0	326	
	Clin22A_Zr15	0.0016	3.44	0.0052	105.06	0.02365	139.53	10.4	0.7	5.3	11.1	0	476	
	Clin22A_Zr16	*0.0027*	*4.67*	*0.1366*	*10.29*	*0.36648*	*8.07*	*17.5*	*1.6*	*130*	*25.1*	*3776*	*246*	*comm. Pb. Discord., not shown in CD*
	Clin22A_Zr17	0.0017	2.2	0.0145	14.44	0.06412	15.58	10.7	0.5	14.6	4.2	744	668	
	Clin22A_Zr18	0.0017	2.62	0.0205	14.91	0.08783	22.19	10.9	0.6	20.6	6.1	1378	876	
Clin 22A	Clin22A_Zr19	0.0016	1.61	0.0116	10.42	0.05368	10.61	10.1	0.3	11.7	2.4	356	482	
	Clin22A_Zr20	0.0016	2.1	0.0112	17.06	0.04992	18.09	10.5	0.4	11.4	3.9	190	564	
	Clin22A_Zr21	0.0016	1.72	0.0093	23.73	0.04156	24.77	10.5	0.4	9.4	4.5	0	278	
	Clin22A_Zr22	0.0016	2.85	0.012	26.30	0.05525	29.90	10.1	0.6	12.1	6.3	422	978	
	Clin22A_Zr23	0.0016	1.67	0.0098	13.52	0.04549	14.39	10.2	0.3	9.9	2.7	0	286	
	Clin22A_Zr25	0.0016	1.78	0.0112	18.76	0.04922	19.78	10.5	0.4	11.3	4.2	158	564	
	Clin22A_Zr26	0.0016	2.13	0.0094	23.40	0.04336	20.41	10.1	0.4	9.5	4.4	0	294	
	Clin22A_Zr27	*0.0019*	*3.06*	*0.0118*	*13.54*	*0.04686*	*15.53*	*11.9*	*0.7*	*12*	*3.2*	*42*	*376*	*discordant*
	Clin22A_Zr28	0.0016	4.73	0.0055	76.05	0.02457	137.91	10.5	1	5.6	8.5	0	546	
	Clin22A_Zr29	0.0016	1.11	0.0126	7.68	0.05815	8.05	10.3	0.2	12.7	1.9	534	354	
	Clin22A_Zr30	0.0016	1.99	0.0115	14.22	0.05303	14.47	10.2	0.4	11.6	3.3	330	628	
	Clin22A_Zr31	*0.0035*	*7.32*	*0.2244*	*13.58*	*0.46132*	*4.31*	*22.4*	*3.3*	*205.6*	*50.6*	*4000*	*0*	*comm. Pb. Discord., not shown in CD*
	Clin22A_Zr32	0.0016	2.77	0.0142	18.64	0.06667	22.22	10	0.6	14.3	5.3	826	954	
	Clin22A_Zr33	0.0017	2.07	0.0147	17.31	0.06455	20.55	10.7	0.4	14.8	5.1	758	890	
	Clin22A_Zr34	*0.0017*	*4.01*	*0.0359*	*18.03*	*0.15233*	*28.98*	*10.7*	*0.9*	*35.9*	*12.7*	*2372*	*1028*	*discordant*
	Clin22A_Zr35	0.0017	2.65	0.0111	26.68	0.04823	30.74	10.9	0.6	11.2	5.9	110	708	
	Clin22A_Zr36	0.0015	2.6	0.01	33.60	0.04767	46.13	9.8	0.5	10.1	6.7	82	918	
	Clin22A_Zr37	*0.0019*	*3.5*	*0.0122*	*30.36*	*0.04742*	*32.79*	*12*	*0.8*	*12.3*	*7.4*	*70*	*706*	*discordant*
	Clin22A_Zr38	0.0016	2.37	0.0131	20.48	0.05888	31.73	10.4	0.5	13.2	5.4	562	1134	
	Clin22A_Zr39	0.0016	2.38	0.0135	20.20	0.06281	22.99	10.1	0.5	13.6	5.4	700	1010	
	Clin22A - weighted mean							**10.209**	**0.09**	**(0.88 %)**				
	Clin25A_Zr10	0.002	2.06	0.0183	14.86	0.0652	16.00	13.1	0.5	18.4	5.4	780	682	
	Clin25A_Zr11	0.0021	2.66	0.0188	15.21	0.06479	16.93	13.3	0.7	19	5.7	766	726	
	Clin25A_Zr12	0.0021	2.27	0.0117	22.52	0.03999	22.47	13.6	0.6	11.8	5.3	0	146	
	Clin25A_Zr13	0.0021	1.96	0.0166	14.91	0.05859	15.97	13.3	0.5	16.8	5	550	708	
	Clin25A_Zr14	0.0021	2.32	0.0126	17.34	0.04351	18.19	13.3	0.6	12.7	4.4	0	258	
	Clin25A_Zr15	0.0021	2.97	0.0142	27.25	0.04885	31.01	13.7	0.8	14.3	7.7	140	740	
	Clin25A_Zr29	*0.0028*	*3.58*	*0.0383*	*15.47*	*0.09488*	*17.58*	*18.3*	*1.3*	*38.2*	*11.6*	*1524*	*674*	*very discordant, not shown in CD*
	Clin25A_Zr32	0.0021	2.27	0.0124	20.94	0.04334	21.41	13.4	0.6	12.5	5.2	0	312	
	Clin25A_Zr33	0.0021	1.57	0.0124	11.17	0.04365	11.04	13.4	0.4	12.5	2.8	0	122	
	Clin25A_Zr8	0.002	1.67	0.009	24.38	0.03208	25.56	13.1	0.4	9.1	4.4	0	0	
	Clin25A_Zr9	0.0022	1.8	0.0172	12.42	0.05655	13.14	14	0.5	17.3	4.3	472	588	
	Clin25A_Zr1	0.0021	2.64	0.0168	15.47	0.05746	15.90	13.7	0.7	16.9	5.2	508	710	
	Clin25A_Zr16	0.0021	1.95	0.0112	21.27	0.03884	21.41	13.4	0.5	11.3	4.8	0	56	
	Clin25A_Zr17	0.0021	2.78	0.0117	42.05	0.04058	46.45	13.5	0.7	11.8	9.8	0	582	
	Clin25A_Zr18	0.0021	2.68	0.0172	27.28	0.05885	28.55	13.7	0.7	17.4	9.4	560	1084	
	Clin25A_Zr19	0.0021	1.81	0.0113	18.19	0.03864	19.45	13.6	0.5	11.4	4.1	0	6	
Clin 25A	Clin25A_Zr2	0.002	3.41	0.0159	29.94	0.05665	46.20	13.1	0.9	16	9.5	476	1264	
	Clin25A_Zr20	0.0021	2.23	0.0155	16.34	0.05448	16.59	13.2	0.6	15.6	5.1	390	724	
	Clin25A_Zr21	0.0021	2.18	0.0143	20.35	0.04813	19.88	13.8	0.6	14.4	5.8	104	518	
	Clin25A_Zr22	0.0021	1.26	0.0159	7.51	0.05547	7.24	13.6	0.3	16	2.4	430	324	
	Clin25A_Zr23	0.0021	2.69	0.0075	45.95	0.02614	56.24	13.4	0.7	7.6	6.9	0	0	
	Clin25A_Zr24	0.002	2.64	0.0066	50.17	0.02384	54.10	12.8	0.7	6.7	6.7	0	0	
	Clin25A_Zr25	0.002	3.57	0.0245	24.68	0.08775	32.23	13	0.9	24.6	12	1376	1312	
	Clin25A_Zr26	0.002	1.91	0.0157	15.26	0.05626	14.71	13.1	0.5	15.8	4.8	462	660	
	Clin25A_Zr27	*0.0021*	*2.74*	*0.0255*	*15.04*	*0.08703*	*17.60*	*13.5*	*0.7*	*25.6*	*7.6*	*1360*	*690*	*discordant*
	Clin25A_Zr28	0.002	2.17	0.021	16.17	0.07351	17.56	13.2	0.6	21.1	6.8	1028	722	
	Clin25A_Zr3	0.002	2.08	0.0108	19.00	0.03978	19.09	12.8	0.5	10.9	4.1	0	66	
	Clin25A_Zr30	0.0022	1.94	0.0096	21.39	0.03248	22.22	14	0.5	9.7	4.1	0	0	
	Clin25A_Zr31	0.0021	2.37	0.0126	26.22	0.04274	27.08	13.6	0.6	12.7	6.6	0	384	
	Clin25A_Zr34	*0.0023*	*1.79*	*0.0124*	*14.99*	*0.03939*	*15.20*	*14.6*	*0.5*	*12.5*	*3.7*	*0*	*0*	*discordant*
	Clin25A_Zr35	0.0021	2.28	0.0104	34.63	0.03669	35.45	13.3	0.6	10.5	7.2	0	180	
	Clin25A_Zr36	0.002	1.83	0.0116	22.81	0.04251	22.70	13	0.5	11.7	5.3	0	292	
	Clin25A_ZrT1	0.0016	0.71	0.0114	3.54	0.05341	3.56	10	0.1	11.5	0.8	346	162	
	Clin25A_ZrT2	0.0017	2.85	0.0126	23.98	0.05456	23.61	10.7	0.6	12.7	6	394	850	
	Clin25A_Zr4	0.002	2.25	0.0118	23.57	0.04173	23.41	13.1	0.6	11.9	5.6	0	262	
	Clin25A_Zr5	0.0021	2.46	0.0156	27.40	0.05407	28.45	13.4	0.7	15.7	8.6	372	912	
	Clin25A_Zr6	0.002	2.47	0.0069	38.35	0.02456	44.44	13	0.6	6.9	5.3	0	0	
	Clin25A_Zr7	0.0022	1.86	0.013	18.51	0.04465	19.57	13.9	0.5	13.1	4.8	0	344	
	Clin25A - weighted mean							**13.39**	**0.11**	**(0.86 %)**				

	Sample	206Pb/238U Ratio	1σ (%)	207Pb/235U Ratio	1σ (%)	207Pb/206Pb Ratio	1σ (%)	206Pb/238U Age (Ma)	2σ (Ma)	207Pb/235U Age (Ma)	2σ (Ma)	207Pb/206Pb Age (Ma)	2σ (Ma)	Comments
	GJ-1 01	0.0973	0.53	0.8178	0.98	0.0608	0.75	598.7	6	606.8	9	632	32	
	GJ-1 02	0.0979	0.66	0.8109	0.97	0.0596	0.83	601.9	7.6	603	8.8	588	36	
	GJ-1 03	0.0971	0.74	0.8057	1.09	0.06029	0.83	597.3	8.4	600	9.8	612	36	
	GJ-1 04	0.0982	0.64	0.8033	1.00	0.05991	0.75	603.6	7.4	598.7	9	600	34	
	GJ-1 05	0.098	0.49	0.8114	0.98	0.05994	0.73	602.6	5.6	603.2	8.9	600	32	
	GJ-1 06	0.0973	0.54	0.8159	1.16	0.06057	0.96	598.5	6.1	605.8	10.6	624	42	
	GJ-1 07	0.0976	0.69	0.8053	1.08	0.06019	0.82	600.6	7.9	599.8	9.8	610	36	
	GJ-1 08	0.0975	0.5	0.8051	1.14	0.0599	0.87	599.8	5.7	599.7	10.4	598	38	
	GJ-1 09	0.0977	0.58	0.8092	1.03	0.05998	0.81	601	6.6	602	9.3	602	36	
	GJ-1 10	0.0975	0.58	0.8125	0.91	0.06063	0.80	599.8	6.7	603.8	8.3	626	34	
	GJ-1 11	0.098	0.61	0.8167	0.90	0.06021	0.78	602.7	7	606.2	8.2	610	34	
	GJ-1 12	0.0972	0.64	0.7993	1.06	0.05978	0.95	598	7.3	596.4	9.6	594	42	
	GJ-1 14	0.0983	0.59	0.8065	1.00	0.05978	0.85	604.7	6.8	600.5	9.1	594	36	
	GJ-1 15	0.098	0.5	0.811	0.96	0.05972	0.81	602.8	5.8	603	8.7	592	36	
	GJ-1 16	0.0971	0.58	0.8074	0.98	0.06037	0.85	597.1	6.6	601	8.9	616	36	
	GJ-1 17	*0.0894*	*0*	*0.7445*	*0.00*	*0.05777*	*0.00*	*551.8*	*0*	*565*	*0*	*520*	*0*	*wrong measurement*
	GJ-1 18	0.0983	0.69	0.806	1.16	0.06003	0.86	604.6	7.9	600.2	10.6	604	38	
	GJ-1 19	0.0968	0.74	0.8164	1.05	0.06067	0.76	595.7	8.4	606	9.6	626	34	
	GJ-1 20	0.0976	0.73	0.805	1.06	0.05971	0.80	600.4	8.4	599.7	9.6	592	36	
	GJ-1 21	0.0971	0.83	0.8165	1.15	0.06106	0.85	597.1	9.5	606.1	10.5	640	36	
	GJ-1 22	0.0979	0.56	0.7988	1.20	0.05944	0.91	602.2	6.4	596.2	10.8	582	40	
GJ-1	GJ-1 23	0.0978	0.62	0.8225	1.13	0.06023	0.97	601.7	7.1	609.4	10.3	610	42	
	GJ-1 24	0.0976	0.56	0.7999	1.17	0.05986	1.07	600.6	6.4	596.8	10.5	598	46	
	GJ-1 25	0.099	0.5	0.8287	1.03	0.06058	0.84	608.8	5.9	612.9	9.5	624	38	
	GJ-1 26	0.0982	0.64	0.8077	1.11	0.06025	0.90	603.8	7.4	601.2	10.1	612	40	
	GJ-1 27	0.0966	0.66	0.8034	1.20	0.05954	0.86	594.6	7.5	598.8	10.8	586	36	
	GJ-1 28	0.0966	0.68	0.7979	1.17	0.06023	0.90	594.3	7.7	595.6	10.5	610	38	
	GJ-1 29	0.098	0.5	0.8193	1.03	0.06048	0.84	602.8	5.7	607.7	9.4	620	36	
	GJ-1 30	0.0971	0.59	0.8142	1.14	0.06048	0.81	597.2	6.7	604.8	10.4	620	36	
	GJ-1 31	0.0976	0.57	0.7964	1.10	0.05998	0.89	600.6	6.5	594.8	9.9	602	40	
	GJ-1 32	0.0977	0.73	0.8079	1.19	0.05965	0.84	601	8.3	601.3	10.8	590	36	
	GJ-1 33	0.0978	0.68	0.8228	1.15	0.06076	0.96	601.5	7.9	609.6	10.6	630	42	
	GJ-1 34	0.0974	0.78	0.8115	1.14	0.0605	0.88	598.9	8.9	603.3	10.4	620	38	
	GJ-1 35	0.0979	0.7	0.8137	1.05	0.06012	0.89	601.9	8	604.6	9.5	606	38	
	GJ-1 36	0.0974	0.75	0.7897	1.12	0.05922	0.92	599.2	8.6	591	10	574	40	
	GJ-1 37	0.0971	0.79	0.8078	1.23	0.05983	0.93	597.6	9.1	601.2	11.1	596	40	
	GJ-1 38	0.0975	0.55	0.8078	1.05	0.06043	0.73	600	6.3	601.2	9.5	618	32	
	GJ-1 39	0.0973	0.53	0.8101	0.97	0.06048	0.79	598.6	6	602.5	8.8	620	34	
	GJ-1 40	0.0985	0.8	0.8121	1.12	0.05986	0.93	605.3	9.3	603.6	10.2	598	40	
	GJ-1 41	0.0978	0.63	0.8227	1.07	0.06048	0.81	601.5	7.2	609.6	9.8	620	36	
	GJ-1 42	0.0981	0.62	0.8071	1.17	0.05994	0.94	603.1	7.1	600.8	10.7	600	40	
	GJ-1 43	0.0978	0.59	0.804	1.07	0.05994	0.91	601.3	6.8	599.1	9.7	600	40	
	GJ-1 44	0.0968	0.66	0.8039	1.15	0.06024	0.94	595.6	7.5	599	10.4	612	42	
	GJ-1 - weighted mean							**600.7**	**2.1**	**(0.35%)**				
	Plesoviče 01	0.0548	0.56	0.3973	1.18	0.05276	0.97	343.7	3.7	339.7	6.8	318	44	
	Plesoviče 02	0.0549	0.66	0.3978	1.05	0.05282	0.92	344.4	4.4	340	6.1	320	42	
	Plesoviče 03	0.0548	0.59	0.4013	1.08	0.05302	0.89	344	4	342.6	6.3	328	40	
	Plesoviče 04	0.055	0.53	0.403	1.15	0.05272	1.00	345.4	3.5	343.8	6.7	316	46	
	Plesoviče 05	*0.0541*	*0.57*	*0.4172*	*0.86*	*0.05573*	*0.74*	*339.7*	*3.8*	*354.1*	*5.2*	*440*	*34*	*discordant*
	Plesoviče 06	0.0542	0.54	0.3987	1.05	0.05379	0.84	340.4	3.6	340.7	6.1	362	38	
Plesoviče	*Plesoviče 07*	*0.0548*	*0.56*	*0.4156*	*0.91*	*0.05529*	*0.82*	*344.1*	*3.7*	*352.9*	*5.4*	*422*	*36*	*common Pb*
	Plesoviče 08	0.0541	0.5	0.3912	0.85	0.05277	0.77	339.4	3.3	335.2	4.9	318	36	
	Plesoviče 09	*0.0532*	*0.54*	*0.4073*	*0.92*	*0.05587*	*0.83*	*333.9*	*3.5*	*347*	*5.4*	*446*	*36*	*discordant*
	Plesoviče 10	0.0536	0.49	0.3847	0.86	0.05284	0.83	336.5	3.2	330.5	4.8	320	38	
	Plesoviče 11	0.0529	0.56	0.3971	1.09	0.0542	1.03	332.4	3.6	339.5	6.3	378	46	
	Plesoviče 12	0.053	0.42	0.392	0.90	0.05364	0.81	333.1	2.7	335.9	5.1	356	38	
	Plesoviče 13	0.0529	0.43	0.3897	0.88	0.05376	0.80	332.5	2.8	334.1	5	360	36	
	Plesoviče 14	0.0529	0.43	0.3874	1.04	0.05293	0.82	332.1	2.8	332.4	5.9	324	38	
	Plesoviče 15	0.0526	0.38	0.3888	0.88	0.05395	0.88	330.4	2.5	333.5	5	368	40	
	Plesoviče 16	0.0521	0.46	0.389	1.07	0.05396	0.96	327.4	3	333.6	6.1	368	44	
	Plesoviče - weighted mean							**335.6**	**3.5**	**(1.1%)**				

A6. Deformation history

Table A5: Geological observations of tectonic activities (e.g., growth structures, angular unconformities) for the northern, central, and southern segments of the Central Andes. References are provided in main text.

	Region	Formation	Lat$_{min}$ (°S)	Lat$_{max}$ (°S)	Lon$_{min}$ (°W)	Lon$_{max}$ (°W)	t$_{start}$ (Ma)	t$_{end}$ (Ma)	Comments	Reference
Northern segment (18-24°S)	West Andean flank	Altos de Pica Fm.	-20	-21	-69.5	-69	30	7 to 5.3	Compression - west-vergent high-angle faults	Victor et al. (2004)
	West Andean flank	Coposa Fm.	-20	-21	-69.5	-69	5.3	0	Transtensional - Normal Faults	Victor et al. (2004)
	Pre-Cordillera	Altos de Pica Fm., El Diabolo Fm.	-19	-19.5	-69.5	-69.25	26	8	Compression - mainly west-vergent thrusts	Farías et al. (2005)
	Pre-Cordillera	Altos de Pica Fm., El Diabolo Fm.	-19	-19.5	-69.5	-69.25	8	0	Westward tilting	Farías et al. (2005)
	Salar de Atacama	Tonel Fm., Purilactis group	-22	-24	-69	68	U. Cretaceous	84	Compression / transpressional	Mpodozis et al. (2005)
	Salar de Atacama	Barros Arana Fm., Purilactis group	-22	-24	-69	68	Maastrichtian	Danian	Compression / transpressional	Mpodozis et al. (2005)
	Salar de Atacama	Naranjo Fm.	-22	-24	-69	68	early Paleocene	early Paleocene	Compression	Arrigada et al. (2006)
	Salar de Atacama	Loma Amarilla Fm.	-22	-24	-69	68	late Eocene (44)	Oligocene (28)	Compression / Transpressional.	Mpodozis et al. (2005), Arrigada et al. (2006)
	Salar de Atacama	Paciencia Group	-22	-24	-69	68	Oligocene (30)	middle Miocene (10)	Compressional / Transtensional; debated	Jordan et al. (2007), Arrigada et al. (2006)
	Salar de Atacama	Vilama Fm.	-22	-24	-69	68	late Miocene	Quaterny	Compression - reverse faults	Jordan et al. (2007), Arrigada et al. (2006)
	Western Cordillera	Aquine fault	-19	-19.5	-69.3	-69	pre-Oligoc. (inferred: 49-27 Ma)	6	Compression - High-angle east-verg. Thrusts	Herrera et al. (2017)
	Western Cordillera	Puchuldiza Fm.	-19	-19.5	-69	68.75	19	2	Compression - east-vergent thrusts	Herrera et al. (2017)
	Altiplano/Eastern Cordillera									Compilation of Elger et al. (2005)
	easternmost IAZ	u. Tariquia and l. Guandacay Fms	-19.8	-22	-64.3	-64.16	22	9	Compression	Calle et al. (2018)
	Subandean zone	Cinco Picachos Range	-22	-23	-64.8	-63.5	9	7.5	Compression - east-vergent thrusts	Echavarria et al. (2003)
	Subandean zone	Pescado Range	-22	-23	-64.8	-63.5	7.6	0	Compression - east-vergent	Echavarria et al. (2003)
	Subandean zone	Pintascayo	-22	-23	-64.8	-63.5	7.6	0	Compression - east-vergent	Echavarria et al. (2003)
	Subandean zone	Baja Oran	-22	-23	-64.8	-63.5	6.9	0	Compression - east-vergent thrusts	Echavarria et al. (2003)
	Subandean zone	San Antoni Range	-22	-23	-64.8	-63.5	4.5	2.2	Compression - east-vergent thrusts	Echavarria et al. (2003)
	Subandean zone	Aguarague Range	-22	-23	-64.8	-63.5	3	1.2	Compression - east-vergent thrusts	Echavarria et al. (2003)
Central segment (28-32°S)	Principal Cordillera	Viñitas Fm. (Chañarcillo Basin)	-28	-29	-70.4	-70	81.6	65	Compression - inversion of normal faults	Martinez et al. (2016; 2018)
	Frontal Cordillera (western margin)	Lautaro basin (Calquis fault)	-28	-29	-70	-69.9	78	n.a.	Compression - inversion of normal faults	Martinez et al. (2016; 2018)
	Frontal Cordillera (CL)	Quebrada Seca Fm. (Lagunillas Basin)	-28	-29	-69.8	-69.3	83.3	60.4	Compression - inversion of normal faults	Martinez et al. (2016; 2018)
	Frontal Cordillera (CL)	Potrerillos/Doña Ana Fm. (Lagunillas B.)	-28	-29	-69.8	-69.1	23.2	20	Compression - inversion of normal faults	Martinez et al. (2016; 2018)
	Frontal Cordillera (CL)	Valeriana Fault	-28.5	-29	-70	-69.5	63	45	Compression	Rossel et al. (2016)
	Frontal Cordillera (CL)	La Coipa-El Potro Fault System	-28.5	-29	-70	-69.5	19	13	Compression	Rossel et al. (2016)
	Frontal Cordillera (AR)	Río La Sal (24-22 Ma)	-29	-30	-70	-69.5	24	22	synextensional growth strata	Winocur et al.(2015)
	Frontal Cordillera (AR)	Tilito Fm.	-29	-30	-70	-69.5	27	23	synextensional growth strata	Winocur et al.(2015)
	Frontal Cordillera (AR)	Valle del Cura Fm. (24.7-18.5 Ma)	-29	-30	-70	-69.5	26 end of Oligoc., Min. 18.5		synextensional growth strata	Winocur et al.(2015)
	Frontal Cordillera (AR)	Escarbroso	-29	-30	-70	-69.5	21	17	transitional arc	Winocur et al.(2015)
	Precordillera	Tranca thrust	-29	-31	-69.1	-69.05	21.5	19		Jordan et al. (2001a)
	Precordillera	Tranca thrust	-29	-31	-69.1	-69.05	14	1		Jordan et al. (2001a)
	Precordillera	Caracol thrust	-29	-31	-69	-69.05	21.5	19		Jordan et al. (2001a)
	Precordillera	Caracol thrust	-29	-31	-69	-69.05	15	12		Jordan et al. (2001a)
	Precordillera	Blanco thrust	-29	-31	-69	-69.01	13.5	9		Jordan et al. (2001a)
	Precordillera	Blanquitos thrust	-29	-31	-68.9	-68.96	11.5	9.5		Jordan et al. (2001a)
	Precordillera	San Roque thrust	-29	-31	-68.8	-68.88	10.5	1.5		Jordan et al. (2001a)
	Precordillera	Niquivil thrust	-29	-31	-68.5	-68.83	5	1		Jordan et al. (2001a)
	Precordillera	Niquivil Anticline	-29	-31	-68.5	-68.5	2.6	0		Jordan et al. (2001a)
	Precordillera	Las Salinas Anticline	-29	-31	-68.6	-68.45	2.5	0		Jordan et al. (2001a)
	Precordillera	Bermejo Anticline	-29	-31	-68	-68.57	2	0		Jordan et al. (2001a)
	Precordillera	Pie de Palo	-29	-31	-67.9	-68	7	3		Jordan et al. (2001a)
	Precordillera	Sierra dell Valle Fertil	-29	-31	-67.9	-67.9	6	0		Jordan et al. (2001a)
	Precordillera	Sierra Maz	-29	-31	-67.9	-67.85	7.7	0		Jordan et al. (2001a)
	Precordillera	Sierra Famatina	-29	-31	-67.5	-67.5	6	0		Jordan et al. (2001a)
Southern segment (32-34°S)	Coastal Cordillera	Las Chilcas	-32.5	-33.5	-71.3	-70.5	100	83		Charrier et al. (2014)
	Principal Cordillera F4	San Ramos Fault (F4)	-32.5	-34	-70.5	-70.45	9	0		Riesner et al. (2017; 2018)
	Principal Cordillera F3	F3	-32.5	-34	-70.5	-70.4	19	6.5		Riesner et al. (2017; 2018)
	Principal Cordillera F2	F2	-32.5	-34	-70.4	-70.3	25	13		Riesner et al. (2017; 2018)
	Principal Cordillera F1	F1	-32.5	-34	-70.3	-70.2	25	15		Giambiagi et al. (2001; 2003), García & Casa (2014)
	Principal Cordillera	West-vergent folds	-32.5	-34	-70.2	-70.1	15	5		Giambiagi et al. (2001; 2003)
	Principal/Frontal Cordillera	U. Tunuyán Conglomerate/Marinño Fm.	-33.5	-34.1	-69.8	-69.7	16	9	Uplift of Aconcagua fold-and-thrust belt	Giambiagi et al. (2001; 2003)
	Principal/Frontal Cordillera	Palomares Fm.	-33.5	-34.1	-69.8	-69.7	8.5	7	Provenance from Cordillera del Tigre (FC)	Giambiagi et al. (2001; 2003)
	Principal/Frontal Cordillera	Butaló Fm.	-33.5	-34.1	-69.8	-69.7	7	5.9	Proven. from FC&PC, thrusts cutting through	Giambiagi et al. (2001; 2003)
	Principal Cordillera, east	Neuquén Group	-35.5	-37	-70.3	-69.25	100	83		Fennell et al.(2015)
	Cuyo Basin	La Pilona Fm./Tobas Angosura	-33.5	-34.1	-69.8	-69.7	11.7	9		Giambiagi et al. (2001; 2003)
	Cuyo Basin	Rio de los Pozos Fm.	-33.5	-34.1	-69.8	-69.7	8.7	5.8		Giambiagi et al. (2001; 2003)
	Cuyo Basin	Mogotes Fm.	-33.5	-34.1	-69.8	-69.7	3	0		Giambiagi et al. (2001; 2003)

APPENDIX B ■

Supplementary Tables, Chapter 3

B1. Sample locations

B2. TL kinetic parameters

B3. Element concentrations

B4. Glacial features

B1. Sample locations

Table B1: Sample locations and grainsize distribution

Sample	Lat (°S)	Lon (°W)	Elevation (m)	Grainsize (µm)
Clin18	33.809	70.211	1313	150 - 1000
Clin22A	33.491	70.130	1559	150 - 820
Clin22B	33.499	70.125	1918	150 - 1000
Clin22C	33.504	70.124	2280	150 - 1000
Clin22D	33.505	70.129	2575	150 - 1000
Clin24	34.365	70.321	1274	150 - 840
Clin25A	34.059	70.118	2012	150 - 690
Clin25B	34.076	70.115	2374	150 - 860
Clin25C	34.076	70.120	2670	150 - 650
Clin25D	34.079	70.124	2934	150 - 880
Clin26	34.825	70.564	1030	150 - 1000

B2. TL kinematic parameters

Table B2: Kinematic parameters for growth, thermal loss and athermal decay, natural TL signal and predicted field saturation.

	TL temperature [°C]	Growth parameters						Thermal decay			Athermal decay		Natural TL		TL Field saturation	
		$\dot{D}$	$\dot{D}$ err	D_0	D_0 err	a	a err	E	$\log_{10}(s)$	b	$\log_{10}(\rho')$	$\log_{10}(\rho')$ err	n/N_{obs}	n/N_{obs} err	N_{ss}/N	N_{ss}/N err
			[Gy/ka]		[Gy]			[eV]								
Clin18	220-230	6.813	1.444	2205	66	1.00	0.14	1.32	12.06	1.63	-5.02	-0.02	0.01	0.00	0.07	0.01
	230-240			1986	49	1.00	0.12	1.35	12.07	1.61	-5.07	-0.02	0.02	0.00	0.09	0.01
	240-250			1733	40	1.00	0.14	1.37	12.09	1.59	-5.13	-0.02	0.04	0.00	0.12	0.01
	250-260			1443	28	1.00	0.08	1.41	12.10	1.58	-5.20	-0.02	0.07	0.00	0.17	0.02
	260-270			1152	26	1.00	0.08	1.44	12.10	1.56	-5.29	-0.02	0.11	0.00	0.25	0.02
	270-280			858	24	1.00	0.08	1.47	12.14	1.55	-5.41	-0.02	0.17	0.00	0.34	0.02
	280-290			633	25	1.00	0.08	1.49	12.16	1.55	-5.53	-0.03	0.27	0.00	0.45	0.02
	290-300			489	31	1.00	0.07	1.53	12.22	1.55	-5.63	-0.03	0.38	0.00	0.54	0.02
	300-310			399	36	1.00	0.23	1.56	12.27	1.55	-5.79	-0.03	0.50	0.01	0.65	0.02
	310-320			349	41	1.00	0.27	1.61	12.36	1.55	-5.89	-0.04	0.60	0.01	0.72	0.02
Clin22A	220-230	5.661	1.15	2757	124	1.00	0.05	1.31	12.06	1.57	-4.86	-0.03	0.00	0.00	0.02	0.00
	230-240			2550	98	1.00	0.06	1.34	12.11	1.57	-4.89	-0.03	0.00	0.00	0.03	0.01
	240-250			2353	76	1.00	0.17	1.37	12.14	1.57	-4.92	-0.03	0.01	0.00	0.03	0.01
	250-260			2145	60	1.00	0.12	1.41	12.18	1.58	-4.94	-0.03	0.01	0.00	0.04	0.01
	260-270			1915	45	1.00	0.14	1.44	12.22	1.58	-4.98	-0.03	0.01	0.00	0.05	0.01
	270-280			1720	42	1.00	0.13	1.47	12.27	1.59	-5.01	-0.03	0.02	0.00	0.06	0.01
	280-290			1481	36	1.00	0.08	1.51	12.33	1.60	-5.05	-0.03	0.02	0.00	0.08	0.01
	290-300			1279	46	1.00	0.16	1.54	12.38	1.60	-5.09	-0.03	0.03	0.00	0.11	0.02
	300-310			1092	45	1.00	0.14	1.58	12.43	1.61	-5.15	-0.03	0.05	0.00	0.14	0.02
	310-320			942	45	1.00	0.15	1.61	12.48	1.62	-5.19	-0.03	0.06	0.00	0.17	0.02
Clin22B	220-230	6.485	1.436	14572	358	1.00	Inf	1.31	12.02	1.56	-4.89	-0.03	0.00	0.00	0.02	0.01
	230-240			2340	86	1.00	0.01	1.34	12.08	1.56	-4.92	-0.03	0.00	0.00	0.03	0.01
	240-250			2164	69	1.00	0.24	1.37	12.12	1.56	-4.94	-0.03	0.01	0.00	0.04	0.01
	250-260			1971	55	1.00	0.20	1.40	12.16	1.57	-4.97	-0.03	0.01	0.00	0.05	0.01
	260-270			1808	45	1.00	0.11	1.43	12.20	1.58	-4.99	-0.03	0.02	0.00	0.06	0.01
	270-280			1625	39	1.00	0.11	1.46	12.24	1.59	-5.02	-0.03	0.02	0.00	0.07	0.01
	280-290			1455	44	1.00	0.13	1.50	12.27	1.59	-5.05	-0.02	0.03	0.00	0.08	0.01
	290-300			1296	46	1.00	0.10	1.53	12.30	1.60	-5.09	-0.03	0.03	0.00	0.11	0.02
	300-310			1185	49	1.00	0.05	1.56	12.32	1.60	-5.12	-0.03	0.04	0.00	0.12	0.02
	310-320			1058	46	1.00	0.12	1.59	12.34	1.60	-5.16	-0.03	0.05	0.00	0.15	0.02
Clin22C	220-230	6.023	1.432	2572	132	1.00	0.06	1.31	11.99	1.55	-4.88	-0.03	0.00	0.00	0.02	0.01
	230-240			2427	104	1.00	0.00	1.34	12.03	1.54	-4.90	-0.03	0.00	0.00	0.03	0.01
	240-250			2266	98	1.00	0.21	1.36	12.05	1.54	-4.93	-0.03	0.01	0.00	0.03	0.01
	250-260			2087	90	1.00	0.15	1.39	12.08	1.54	-4.96	-0.03	0.01	0.00	0.04	0.01
	260-270			1893	76	1.00	0.19	1.42	12.11	1.55	-4.99	-0.03	0.01	0.00	0.06	0.01
	270-280			1731	68	1.00	0.20	1.46	12.14	1.55	-5.02	-0.03	0.02	0.00	0.07	0.01
	280-290			1558	57	1.00	0.18	1.49	12.18	1.56	-5.05	-0.03	0.03	0.00	0.08	0.01
	290-300			1383	42	1.00	0.10	1.53	12.22	1.57	-5.09	-0.03	0.04	0.00	0.10	0.02
	300-310			1250	29	1.00	0.09	1.56	12.25	1.58	-5.12	-0.03	0.04	0.00	0.12	0.02
	310-320			1139	21	1.00	0.03	1.59	12.29	1.60	-5.16	-0.03	0.06	0.00	0.15	0.02
Clin22D	220-230	5.836	1.426	2527	121	1.00	0.03	1.31	12.06	1.56	-4.88	-0.03	0.00	0.00	0.02	0.01
	230-240			2270	99	1.00	0.03	1.34	12.09	1.56	-4.92	-0.03	0.01	0.00	0.03	0.01
	240-250			2021	86	1.00	0.26	1.37	12.12	1.55	-4.97	-0.03	0.01	0.00	0.05	0.01
	250-260			1680	75	1.00	0.11	1.40	12.13	1.55	-5.03	-0.03	0.02	0.00	0.07	0.01
	260-270			1333	69	1.00	0.15	1.43	12.16	1.56	-5.11	-0.03	0.03	0.00	0.11	0.02
	270-280			1008	62	1.00	0.14	1.46	12.20	1.56	-5.20	-0.04	0.06	0.00	0.18	0.03
	280-290			751	58	1.00	0.21	1.50	12.24	1.56	-5.30	-0.04	0.09	0.00	0.26	0.03
	290-300			578	57	1.00	0.21	1.53	12.29	1.57	-5.41	-0.04	0.12	0.00	0.35	0.04
	300-310			467	59	1.00	0.24	1.57	12.33	1.58	-5.57	-0.07	0.17	0.00	0.49	0.06
	310-320			400	59	1.00	0.36	1.60	12.38	1.59	-5.68	-0.07	0.21	0.00	0.57	0.06
Clin24	220-230	5.602	1.182	2030	48	1.41	0.24	1.34	12.42	1.64	-5.34	-0.03	0.02	0.00	0.27	0.03
	230-240			1946	52	1.63	0.31	1.37	12.46	1.64	-5.44	-0.02	0.03	0.00	0.35	0.02
	240-250			1818	42	1.91	0.31	1.40	12.49	1.64	-5.52	-0.02	0.05	0.00	0.42	0.02
	250-260			1562	34	2.00	0.27	1.43	12.50	1.63	-5.59	-0.03	0.08	0.00	0.49	0.02
	260-270			1258	22	2.00	0.19	1.47	12.51	1.63	-5.68	-0.03	0.12	0.00	0.56	0.02
	270-280			1013	15	2.00	0.13	1.50	12.52	1.63	-5.77	-0.04	0.16	0.00	0.62	0.03

TL temperature [°C]	Growth parameters						Thermal decay			Athermal decay		Natural TL		TL Field saturation	
	$\dot{D}$	$\dot{D}$ err [Gy/ka]	D_0	D_0 err [Gy]	a	a err	E [eV]	$\log_{10}(s)$	b	$\log_{10}(\rho')$	$\log_{10}(\rho')$ err	n/N_{obs}	n/N_{obs} err	N_{ss}/N	N_{ss}/N err
280-290			789	10	1.82	0.08	1.54	12.55	1.62	-5.79	-0.04	0.21	0.00	0.64	0.03
290-300			638	10	1.55	0.08	1.57	12.57	1.62	-5.86	-0.04	0.26	0.00	0.69	0.03
300-310			546	12	1.39	0.08	1.60	12.60	1.62	-5.98	-0.06	0.31	0.01	0.75	0.03
310-320			504	14	1.25	0.09	1.63	12.62	1.62	-6.07	-0.07	0.35	0.01	0.79	0.03
Clin25A 220-230	3.912	0.922	2689	131	1.00	0.10	1.32	12.18	1.76	-5.12	-0.04	0.00	0.00	0.11	0.02
230-240			2331	112	1.00	0.20	1.35	12.20	1.73	-5.18	-0.04	0.00	0.00	0.15	0.03
240-250			1946	122	1.00	0.09	1.38	12.22	1.70	-5.24	-0.04	0.01	0.00	0.19	0.03
250-260			1530	117	1.00	0.37	1.41	12.24	1.68	-5.32	-0.05	0.03	0.00	0.26	0.04
260-270			1159	107	1.03	0.35	1.44	12.24	1.65	-5.42	-0.04	0.06	0.00	0.34	0.04
270-280			850	89	1.00	0.29	1.47	12.23	1.63	-5.48	-0.05	0.10	0.00	0.39	0.04
280-290			615	69	1.00	0.26	1.50	12.23	1.62	-5.55	-0.06	0.17	0.01	0.46	0.05
290-300			474	55	1.00	0.29	1.53	12.23	1.60	-5.68	-0.06	0.24	0.03	0.57	0.05
300-310			380	47	1.00	0.32	1.54	12.23	1.59	-5.82	-0.05	0.30	0.05	0.67	0.03
310-320			327	43	1.00	0.33	1.59	12.24	1.57	-5.88	-0.05	0.33	0.06	0.70	0.03
Clin25B 220-230	7.589	1.257	2908	136	1.00	0.05	1.33	12.29	1.68	-4.94	-0.02	0.00	0.00	0.04	0.01
230-240			2585	109	1.00	0.04	1.36	12.32	1.66	-4.98	-0.02	0.01	0.00	0.05	0.01
240-250			2251	81	1.00	0.04	1.39	12.36	1.65	-5.04	-0.02	0.01	0.00	0.08	0.01
250-260			1876	61	1.00	0.03	1.43	12.39	1.64	-5.12	-0.02	0.02	0.00	0.12	0.01
260-270			1492	58	1.00	0.17	1.46	12.40	1.63	-5.20	-0.02	0.03	0.00	0.17	0.02
270-280			1134	52	1.00	0.17	1.50	12.43	1.62	-5.30	-0.03	0.04	0.00	0.25	0.02
280-290			832	50	1.00	0.08	1.54	12.46	1.61	-5.41	-0.04	0.07	0.00	0.35	0.03
290-300			617	46	1.00	0.18	1.57	12.50	1.61	-5.50	-0.04	0.09	0.00	0.43	0.03
300-310			470	43	1.00	0.22	1.60	12.54	1.61	-5.60	-0.05	0.11	0.00	0.52	0.04
310-320			380	44	1.00	0.14	1.64	12.60	1.61	-5.72	-0.05	0.14	0.00	0.61	0.04
Clin25C 220-230	6.481	0.895	2804	118	1.00	0.35	1.32	12.13	1.59	-4.94	-0.02	0.01	0.00	0.04	0.01
230-240			2566	101	1.00	0.06	1.35	12.16	1.57	-4.97	-0.02	0.01	0.00	0.05	0.01
240-250			2290	81	1.00	0.27	1.38	12.17	1.56	-5.02	-0.02	0.02	0.00	0.07	0.01
250-260			1999	67	1.00	0.22	1.41	12.18	1.55	-5.08	-0.02	0.03	0.00	0.10	0.01
260-270			1693	46	1.03	0.16	1.45	12.19	1.54	-5.15	-0.02	0.04	0.00	0.14	0.02
270-280			1365	30	1.04	0.10	1.48	12.23	1.54	-5.23	-0.02	0.06	0.01	0.20	0.02
280-290			1072	24	1.05	0.08	1.50	12.26	1.54	-5.33	-0.02	0.09	0.01	0.28	0.02
290-300			857	16	1.00	0.06	1.54	12.32	1.54	-5.42	-0.02	0.11	0.01	0.35	0.02
300-310			691	17	1.00	0.06	1.58	12.39	1.55	-5.51	-0.03	0.14	0.01	0.44	0.03
310-320			587	23	1.00	0.02	1.62	12.48	1.56	-5.57	-0.03	0.15	0.01	0.49	0.03
Clin25D 220-230	5.035	1.235	2605	96	1.00	0.06	1.35	12.33	1.62	-5.01	-0.03	0.02	0.00	0.06	0.01
230-240			2351	81	1.00	0.21	1.38	12.36	1.61	-5.07	-0.02	0.03	0.00	0.09	0.01
240-250			2092	66	1.00	0.14	1.41	12.39	1.60	-5.13	-0.02	0.05	0.00	0.12	0.01
250-260			1853	62	1.00	0.21	1.44	12.40	1.59	-5.18	-0.02	0.07	0.01	0.15	0.01
260-270			1708	83	1.16	0.32	1.48	12.43	1.58	-5.24	-0.02	0.09	0.00	0.20	0.02
270-280			1418	80	1.19	0.33	1.50	12.45	1.58	-5.29	-0.02	0.12	0.00	0.23	0.02
280-290			1218	69	1.21	0.29	1.54	12.51	1.58	-5.34	-0.02	0.15	0.00	0.28	0.02
290-300			1040	59	1.11	0.23	1.58	12.56	1.58	-5.37	-0.02	0.19	0.00	0.30	0.01
300-310			963	59	1.18	0.25	1.61	12.60	1.58	-5.40	-0.02	0.22	0.01	0.33	0.02
310-320			891	49	1.08	0.19	1.64	12.64	1.59	-5.45	-0.03	0.25	0.00	0.37	0.02
Clin26 220-230	6.441	1.445	1934	32	1.00	0.10	1.35	12.52	1.75	-5.33	-0.02	0.04	0.00	0.27	0.02
230-240			1797	32	1.04	0.11	1.38	12.56	1.74	-5.39	-0.02	0.06	0.00	0.31	0.02
240-250			1746	33	1.34	0.16	1.42	12.59	1.73	-5.44	-0.02	0.09	0.00	0.36	0.01
250-260			1705	31	1.72	0.20	1.45	12.62	1.72	-5.50	-0.02	0.12	0.00	0.41	0.01
260-270			1525	34	1.90	0.25	1.48	12.63	1.71	-5.55	-0.02	0.16	0.00	0.46	0.01
270-280			1331	36	2.00	0.30	1.51	12.64	1.70	-5.60	-0.02	0.20	0.00	0.50	0.02
280-290			1153	36	2.00	0.31	1.55	12.67	1.70	-5.63	-0.02	0.24	0.00	0.52	0.02
290-300			995	36	1.83	0.29	1.58	12.69	1.69	-5.66	-0.02	0.29	0.00	0.55	0.02
300-310			910	36	1.67	0.26	1.61	12.71	1.69	-5.67	-0.02	0.34	0.01	0.56	0.02
310-320			861	31	1.52	0.20	1.63	12.72	1.69	-5.70	-0.02	0.37	0.00	0.58	0.02

B3. Element concentrations

Table B3: Element concentrations for environmental dose rate calculation

Sample	U (ppm)	U err (ppm)	Th (ppm)	Th err (ppm)	Rb (ppm)	Rb err (ppm)	K (wt-\%)	K err (wt-\%)
Clin18	3.2	0.18	16.20	0.60	107	8.23	2.92	0.003
Clin22A	3.3	0.20	11.60	0.43	68	2.79	2.41	0.023
Clin22B	4.1	0.25	15.00	0.56	68	2.79	2.64	0.025
Clin22C	3.5	0.21	8.40	0.31	81	3.32	2.76	0.026
Clin22D	2.3	0.14	13.00	0.48	57	2.34	2.47	0.024
Clin24	2.8	0.17	10.80	0.40	76	3.11	2.53	0.024
Clin25A	1.6	0.04	5.90	0.33	82	2.69	1.44	0.037
Clin25B	3.9	0.24	17.20	0.64	147	6.02	3.98	0.038
Clin25C	5.3	0.32	9.90	0.37	115	4.71	3.09	0.030
Clin25D	2.1	0.13	6.20	0.23	83	3.40	2.25	0.022
Clin26	2.9	0.18	11.50	0.43	119	4.88	3.27	0.031

B4. Glacial features

Table B4: Dated glacier deposits and modern snowline observations depicted in Fig. 3.2

Feature	Glacier	Lat	Lon	Elev. (m)	Age (ka)	1σ(ka)	Method	Reference
Outwash plane	San Gabriel	33.78	70.21	1340	46.1	4.8	OSL	Herrera (2016)
Outwash plane	San Gabriel	33.79	70.22	1270	44.8	2.7	OSL	Herrera (2016)
Outwash plane	San Gabriel	33.79	70.22	1270	36.4	2.1	OSL	Herrera (2016)
Moraine ridge	Los Cerrillos	34.35	70.39	1080	20.3	2.9	[10]Be	Charrier et al. (2019)
Moraine ridge	Los Cerrillos	34.35	70.40	1080	21.9	5.3	[10]Be	Charrier et al. (2019)
Modern snowline	Echaurren Norte	33.50	69.91	3800			In-situ observation, 1975-1993	Escobar et al. (1995)
Modern snowline	Palomo	34.23	70.13	3596			Satelites images, 2000	Lequesne pers. comm in Carrasco et al. (2005)
Modern snowline	Cortaderal	34.26	70.13	3740			Satelites images, 2000	Lequesne pers. comm in Carrasco et al. (2005)
Modern snowline	Cipreses	34.55	70.37	3559			Satelites images, 2000	Lequesne pers. comm in Carrasco et al. (2005)
Modern snowline	Cipreses	34.55	70.37	3715			Satelites images, 2015	Sagredo et al. (2016)
Modern snowline	Cipreses	34.55	70.37	3645			Satelites images, 2015	Sagredo et al. (2016)
Modern snowline	Universidad	34.70	70.33	3497			Satelites images, 2000	Lequesne pers. comm in Carrasco et al. (2005)
Modern snowline	Universidad	34.70	70.33	3600			In-situ observation, 2009/2010	Bravo et al. (2017)

References:

Bravo, C., Loriaux, T., Rivera, A., and Brock, B. W., 2017. Assessing glacier melt contribution to streamflow at Universidad Glacier, central Andes of Chile, Hydrol. Earth Syst. Sci. 21, 3249–3266.

Carrasco, J.F., G. Casassa and J. Quintana, 2005. Changes of the 08C isotherm and the equilibrium line altitude in central Chile during the last quarter of the 20th century. Hydrol. Sci. J., 50(6), 933–948.

Charrier, R., Iturrizaga, L., Carretier, S., and Regard, V., 2019. Geomorphologic and glacial evolution of the Cachapoal and southern Maipo catchments in the Andean Principal Cordillera, Central Chile (34°-35° S). Andean Geology, 46 (2), 240-278.

Escobar, F., Casassa, G., Pozo, V., 1995. Variaciones de un Glaciar de Montaña en los Andes de Chile central en las últimas dos décadas. *Bull. Inst. Fr. études andines*, 24 (3), 683-695.

Herrera, M., 2016. Estimación de las altitudas de las líneas de equilibrio en glaciares de montaña para el último ciclo glacial-interglacial en los Andes de Santiago, Chile Central. PhD Thesis, Universidad de Chile, Chile.

Sagredo, E. A., Lowel, T. V., Kelly, M. A., Rupper, S., Aravena, J. C., Ward, D. J., and Malone, A. GO., 2016. Equilibrium line altitude along the Andes during the Last millennium: paleoclimatic implications. The Holocene. 1-15.

Supplementary Material, Chapter 4

C1. **Thermochron. data used in the thermo-kinematic model**

C2. **Supplementary Figures**

Table C1: Thermochronological data compilation used in the thermokinematic model. CD: Central Depression; FC: Frontal Cordillera; PC: Principal Cordillera. Dist. F4: distance to F4. See Chapter 2 for references.

Northern Area (33.4-33.9° S)										
Dist. F4 (km)	Lon	Lat	Elev. (m)	Age (Ma)	1σ (Ma)	Sys.	Tect. unit	Reference	Sample name	Comments
3.7	-70.492	-33.596	790	11.0	2.8	AHe	PC	This study	Clin17	
30.7	-70.211	-33.809	1313	1.8	1.2	AHe	PC	This study	Clin18	High age dispersion
35.3	-70.130	-33.491	1559	1.5	0.3	AHe	PC	This study	Clin22A	AER-a
35.3	-70.130	-33.491	1559	8.0	0.7	AFT	PC	This study	Clin22A	AER-a
35.8	-70.125	-33.499	1918	1.2	0.3	AHe	PC	This study	Clin22B	AER-a
35.8	-70.125	-33.499	1918	7.1	0.8	AFT	PC	This study	Clin22B	AER-a
35.8	-70.124	-33.504	2280	1.5	0.2	AHe	PC	This study	Clin22C	AER-a
35.8	*-70.124*	*-33.504*	*2280*	*9.0*	*1.0*	*AFT*	*PC*	*This study*	*Clin22C*	*AER-a; Magmatic cooling*
35.3	-70.129	-33.505	2575	3.5	1.2	AHe	PC	This study	Clin22D	AER-a
35.3	*-70.129*	*-33.505*	*2575*	*9.8*	*1.0*	*AFT*	*PC*	*This study*	*Clin22D*	*AER-a; Magmatic cooling*
99.6	-69.439	-33.604	2095	8.3	3.7	AHe	FC	Riesner et al. (2019)	CL-10	
87.6	-69.572	-33.621	3693	16.3	3.7	AHe	FC	Riesner et al. (2019)	CL-7	
90.0	-69.544	-33.612	3256	13.9	3.5	AHe	FC	Riesner et al. (2019)	CL-8	
84.4	-69.607	-33.623	4366	17.5	6.2	AHe	FC	Riesner et al. (2019)	CHL15-02B_a	
85.3	-69.597	-33.624	4110	13.4	2.3	AHe	FC	Riesner et al. (2019)	CHL15-03_a	
89.5	-69.551	-33.617	3671	10.5	2.7	AHe	FC	Riesner et al. (2019)	CHL15-07_a	
84.4	*-69.607*	*-33.623*	*4366*	*226.9*	*20.8*	*ZHe*	*FC*	*Riesner et al. (2019)*	*CHL15-02B_z*	*Magmatic cooling*
89.5	-69.551	-33.617	3671	209.5	2.7	ZHe	FC	Riesner et al. (2019)	CHL15-07_z	
90.0	-69.544	-33.612	3256	178.9	12.4	ZHe	FC	Riesner et al. (2019)	CL-8	
99.6	-69.439	-33.604	2095	42.0	17.1	ZHe	FC	Riesner et al. (2019)	CL-10	
37.4	-70.121	-33.716	2330	2.7	0.1	AHe	PC	Piquer et al. (2017)	AN12JP001	
25.4	-70.261	-33.775	1220	3.2	0.2	AHe	PC	Piquer et al. (2017)	AN12JP003	
35.3	-70.135	-33.441	1878	2.1	0.1	AHe	PC	Piquer et al. (2017)	AN12JP005	
14.7	*-70.353*	*-33.497*	*2652*	*26.2*	*3.4*	*AFT*	*PC*	*Farias et al. (2008)*	*a7*	*Magmatic cooling*
17.7	*-70.332*	*-33.667*	*1550*	*19.6*	*3.7*	*AFT*	*PC*	*Farias et al. (2008)*	*a10*	*Magmatic cooling*
11.0	*-70.396*	*-33.486*	*2360*	*19.6*	*3.0*	*AFT*	*PC*	*Farias et al. (2008)*	*a11*	*Magmatic cooling*
44.6	-70.071	-33.858	3387	13.0	3.0	AFT	PC	Farias et al. (2008)	a13	
18.3	*-70.322*	*-33.571*	*1000*	*15.3*	*3.3*	*AFT*	*PC*	*Farias et al. (2008)*	*a22*	*Magmatic cooling*
40.3	-70.111	-33.832	1720	12.9	2.9	AFT	PC	Farias et al. (2008)	a23	
16.5	-70.345	-33.674	1010	11.4	3.0	AFT	PC	Farias et al. (2008)	a24	
37.2	-70.142	-33.822	1700	7.0	3.0	AFT	PC	Farias et al. (2008)	a26	
34.1	-70.143	-33.499	1540	5.2	0.8	AFT	PC	Farias et al. (2008)	a30	
49.1	-70.009	-33.814	2386	1.9	0.5	AFT	PC	Farias et al. (2008)	a32	
42.7	-70.085	-33.834	1835	2.5	0.9	AFT	PC	Farias et al. (2008)	a33	
11.0	*-70.396*	*-33.486*	*2360*	*29.3*	*1.2*	*ZFT*	*PC*	*Farias et al. (2008)*	*z5*	*Magmatic cooling*
43.2	*-70.082*	*-33.845*	*2480*	*112.0*	*6.0*	*ZFT*	*PC*	*Farias et al. (2008)*	*z6*	*Magmatic cooling*
3.9	*-70.490*	*-33.595*	*760*	*21.1*	*1.7*	*AFT*	*PC*	*Maksaev et al. (2009)*	*TT-115*	*Magmatic cooling*
30.5	*-70.209*	*-33.793*	*1370*	*12.1*	*0.8*	*AFT*	*PC*	*Maksaev et al. (2009)*	*TT-118*	*Magmatic cooling*
30.9	-70.210	-33.810	1315	5.7	1.0	AFT	PC	Maksaev et al. (2009)	ETP-4	failed χ2-test but granitic sample
30.8	-70.215	-33.825	1560	9.3	1.2	AFT	PC	Maksaev et al. (2009)	ETP-3	
30.8	*-70.215*	*-33.825*	*1560*	*15.5*	*0.7*	*ZFT*	*PC*	*Maksaev et al. (2009)*	*ETP-3*	*Magmatic cooling. Failed χ2-test*
30.9	*-70.210*	*-33.810*	*1315*	*11.4*	*0.6*	*ZFT*	*PC*	*Maksaev et al. (2009)*	*ETP-4*	*Magmatic cooling*
80.6	-69.654	-33.729	2600	53.1	7.3	AHe	FC	Hoke et al. (2015)	Tunu2600A	
83.0	-69.626	-33.700	3565	79.3	5.7	AHe	FC	Hoke et al. (2015)	Tunu3565A	Single grain age
83.9	-69.616	-33.696	4100	37.8	2.7	AHe	FC	Hoke et al. (2015)	Tunu4010B	Single grain age
84.2	-69.613	-33.695	4200	114.7	15.0	AHe	FC	Hoke et al. (2015)	Tunu4200F	
84.0	-69.615	-33.696	4580	137.8	19.0	AHe	FC	Hoke et al. (2015)	Tunu4580E	Single grain age

Table C1: continued

Dist. F4 (km)	Lon	Lat	Elev. (m)	Age (Ma)	1σ (Ma)	Sys.	Tect. unit	Reference	Sample name	Comments
								Southern Area (33.9-34.5° S)		
34.5	-70.321	-34.365	1274	1.4	0.3	AHe	PC	This study	Clin24	
44.1	-70.118	-34.059	2012	0.5	0.2	AHe	PC	This study	Clin25A	AER-b
44.1	-70.118	-34.059	2012	6.7	1.0	AFT	PC	This study	Clin25A	AER-b
44.6	-70.115	-34.076	2374	1.1	0.5	AHe	PC	This study	Clin25B	AER-b
44.6	*-70.115*	*-34.076*	*2374*	*11.1*	*1.2*	*AFT*	*PC*	*This study*	*Clin25B*	*AER-b; Magmatic cooling*
44.0	-70.120	-34.076	2670	1.4	0.2	AHe	PC	This study	Clin25C	AER-b
44.0	*-70.120*	*-34.076*	*2670*	*12.5*	*1.4*	*AFT*	*PC*	*This study*	*Clin25C*	*AER-b; Magmatic cooling*
43.8	*-70.124*	*-34.079*	*2934*	*0.9*	*0.1*	*AHe*	*PC*	*This study*	*Clin25D*	*AER-b*
43.8	-70.124	-34.079	2934	7.1	1.1	AFT	PC	This study	Clin25D	AER-b
16.3	*-70.426*	*-33.990*	*2345*	*5.0*	*0.3*	*ZHe*	*PC*	*Piquer et al. (2017)*	*AN12JP018*	
-12.2	-70.727	-33.911	429	18.3	2.6	AFT	CD	Farias et al. (2008)	a2	
4.0	*-70.602*	*-34.202*	*936*	*22.8*	*4.4*	*AFT*	*PC*	*Farias et al. (2008)*	*a8*	*Magmatic cooling*
3.3	*-70.610*	*-34.202*	*848*	*19.9*	*4.1*	*AFT*	*PC*	*Farias et al. (2008)*	*a9*	*Magmatic cooling*
3.1	*-70.612*	*-34.197*	*820*	*18.7*	*2.5*	*AFT*	*PC*	*Farias et al. (2008)*	*a12*	*Magmatic cooling*
42.0	-70.253	-34.404	1788	7.7	2.4	AFT	PC	Farias et al. (2008)	a25	
50.1	-70.166	-34.423	2472	6.0	1.5	AFT	PC	Farias et al. (2008)	a27	
36.6	-70.298	-34.370	1486	5.7	2.4	AFT	PC	Farias et al. (2008)	a28	
49.0	-70.185	-34.435	2471	5.5	1.3	AFT	PC	Farias et al. (2008)	a29	
52.4	-70.140	-34.426	2482	3.5	1.1	AFT	PC	Farias et al. (2008)	a31	
5.1	*-70.590*	*-34.203*	*1036*	*5.4*	*1.1*	*AFT*	*PC*	*Farias et al. (2008)*	*a34*	*Next to porphyry copper deposit*
-5.6	*-70.655*	*-33.906*	*438*	*36.6*	*1.4*	*ZFT*	*CD*	*Farias et al. (2008)*	*z1*	*Magmatic cooling*
50.1	*-70.166*	*-34.423*	*2472*	*90.9*	*8.4*	*ZFT*	*PC*	*Farias et al. (2008)*	*z12*	
52.4	*-70.140*	*-34.426*	*2482*	*14.1*	*1.5*	*ZFT*	*PC*	*Farias et al. (2008)*	*z13*	
5.1	*-70.590*	*-34.203*	*1036*	*11.1*	*0.6*	*ZFT*	*PC*	*Farias et al. (2008)*	*z14*	
53.1	-70.020	-34.010	2700	4.4	0.7	AFT	PC	Maksaev et al. (2009)	ETP-11	
29.6	-70.275	-34.043	3030	3.6	0.6	AFT	PC	Maksaev et al. (2009)	ETP-12	
44.3	-70.119	-34.087	2650	4.5	0.9	AFT	PC	Maksaev et al. (2009)	ETP-10A	
64.4	*-69.927*	*-34.203*	*3790*	*6.1*	*0.6*	*AFT*	*PC*	*Maksaev et al. (2009)*	*ETP-14*	*Magmatic cooling*
30.0	-70.323	-34.238	1490	4.1	0.6	AFT	PC	Maksaev et al. (2009)	ETP-13	
53.6	-70.135	-34.442	3150	4.8	0.7	AFT	PC	Maksaev et al. (2009)	ETP-8A	
53.6	-70.135	-34.442	3150	4.5	0.6	AFT	PC	Maksaev et al. (2009)	ETP-8B	
53.1	*-70.020*	*-34.010*	*2700*	*6.8*	*0.5*	*ZFT*	*PC*	*Maksaev et al. (2009)*	*ETP-11*	*Magmatic cooling. Failed χ2-test*
29.6	*-70.275*	*-34.043*	*3030*	*5.8*	*0.3*	*ZFT*	*PC*	*Maksaev et al. (2009)*	*ETP-12*	*Magmatic cooling*
44.3	*-70.119*	*-34.087*	*2650*	*11.6*	*1.0*	*ZFT*	*PC*	*Maksaev et al. (2009)*	*ETP-10A*	*Magmatic cooling. Failed χ2-test*
64.4	*-69.927*	*-34.203*	*3790*	*6.2*	*0.4*	*ZFT*	*PC*	*Maksaev et al. (2009)*	*ETP-14*	*Magmatic cooling*
30.0	*-70.323*	*-34.238*	*1490*	*10.1*	*0.4*	*ZFT*	*PC*	*Maksaev et al. (2009)*	*ETP-13*	*Magmatic cooling*
53.6	*-70.135*	*-34.442*	*3150*	*11.2*	*1.0*	*ZFT*	*PC*	*Maksaev et al. (2009)*	*ETP-8A*	*Magmatic cooling. Failed χ2-test*
53.6	*-70.135*	*-34.442*	*3150*	*9.4*	*0.6*	*ZFT*	*PC*	*Maksaev et al. (2009)*	*ETP-8B*	*Magmatic cooling. Failed χ2-test*

C2 Supplementary Figures
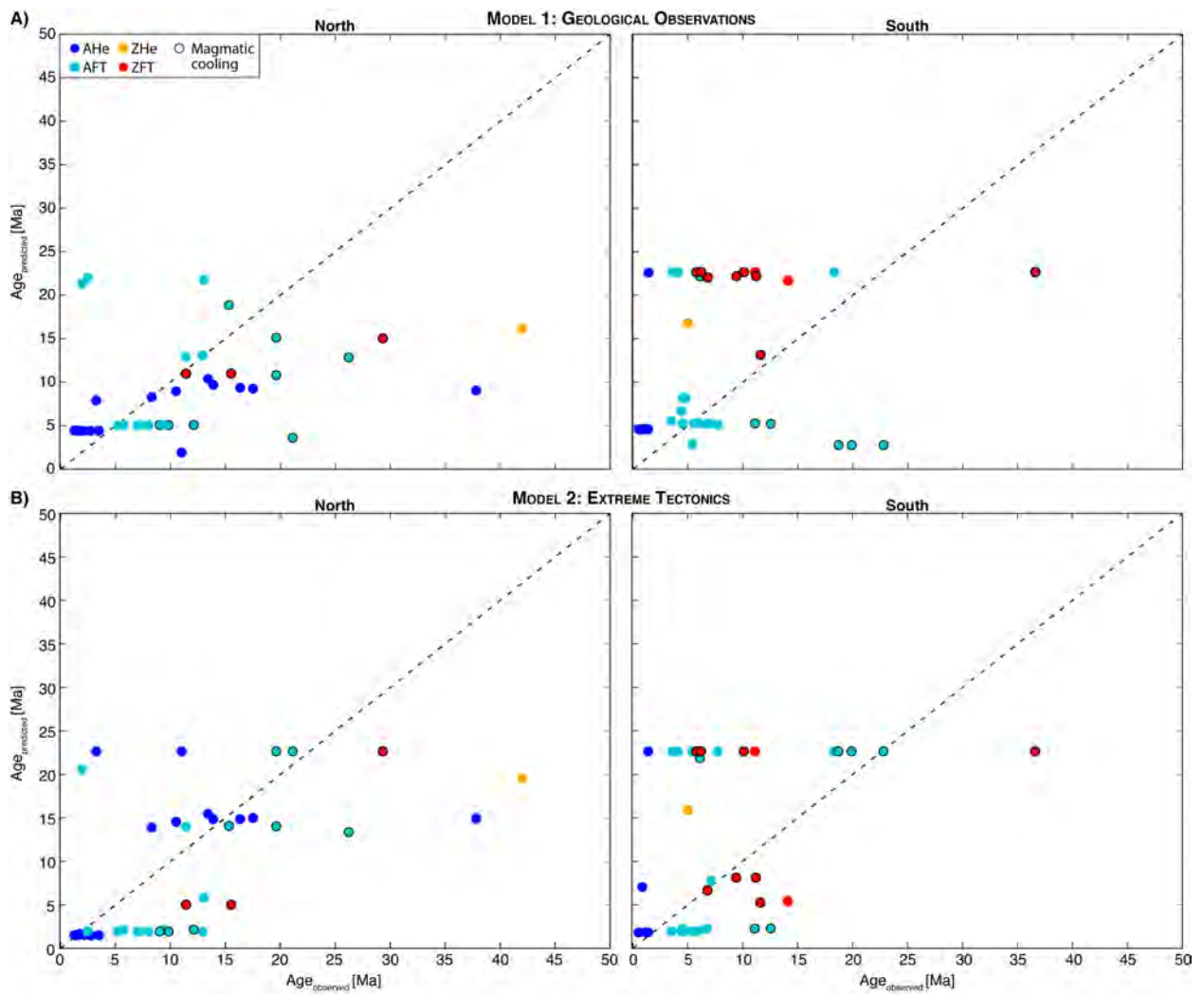
Figure C.1: Observed versus predicted ages of the thermo-kinematic model using evolving topography.
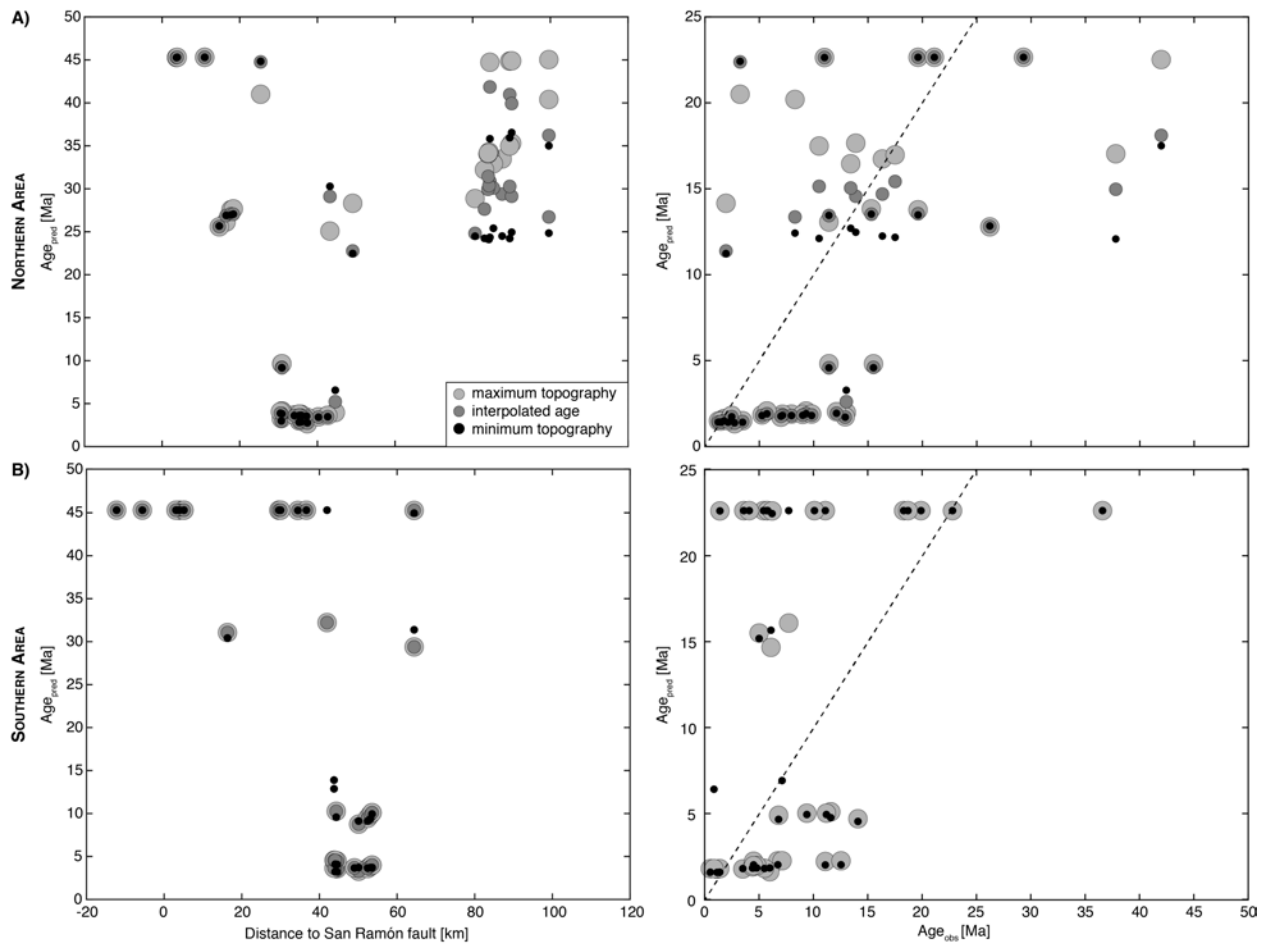
Figure C.2: Influence of topography on ages predicted with the thermo-kinematic model for the northern (**A**) and southern area (**B**), using the tectonic end-member model with steady-state topography.

Prior Parameters

Clin22

Oldest Age in profile = 13.2 Ma

Ranges for General Prior	Time (m.y.) Mean	± Range	Temperature (°C) Mean	± Range	Maximum ∂T/∂t (°C/m.y.)
	7	7	70	70	1000

Temp. Offset (°C)	5.00	5.00	☑ Allow offset to vary over time	🔘 No reheating
Gradient (°C/km)	*4.921*	*4.921*		

Present day temperature (°C)	10	10	Present day temp. Offset (°C)	5.00	0

Elevation difference = 1010.0 m 1010.0 m   Gradient (°C/km)   *4.921*   *0.000*

	Time (m.y.) Mean	± Range	Temperature (°C) Mean	± Range
☑ Constrain	10.4	3	200	10

Clin25

Oldest Age in profile = 13.6 Ma

Ranges for General Prior	Time (m.y.) Mean	± Range	Temperature (°C) Mean	± Range	Maximum ∂T/∂t (°C/m.y.)
	7	7	70	70	1000

Temp. Offset (°C)	5.00	5.00	☑ Allow offset to vary over time	🔘 No reheating
Gradient (°C/km)	*5.423*	*5.423*		

Present day temperature (°C)	10	10	Present day temp. Offset (°C)	5.00	0

Elevation difference = 920.0 m 920.0 m   Gradient (°C/km)   *5.423*   *0.000*

	Time (m.y.) Mean	± Range	Temperature (°C) Mean	± Range
☑ Constrain	13.4	1	200	10

Figure C.3: QTQt prior model parameters for Clin22 and Clin25.

Figure C.4: QTQt MCMC model parameters for Clin22 and Clin25.
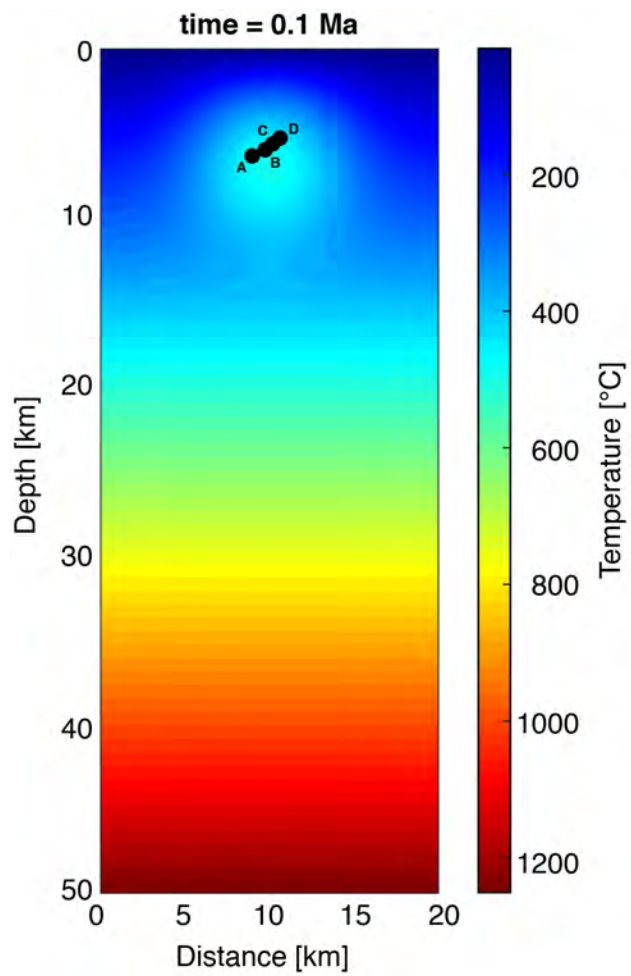
Figure C.5: Exhumation of an intrusion - 1D model set-up

Curriculum Vitae & List of Publications

Nadja Stalder

linkedin.com/nadjastalder

EDUCATION	**PhD in Earth Sciences** Université de Lausanne, Lausanne, Switzerland	Oct. 2015 – Sep. 2020
	Master in Earth Sciences ETH Zurich, Zurich, Switzerland NTNU Trondheim, Norway (Exchange semester)	Sep. 2012 – Sep. 2014
	Bachelor in Earth Sciences ETH Zurich, Switzerland	Sep. 2008 – July 2011

EXPERIENCE

Junior Researcher, University of Lausanne　　　　Oct. 2015 – Sep. 2020

Techniques: Thermochronology, Numerical Modelling

- Teaching assistant:
  - Interactions between tectonics, climate and erosion (Bsc.)　2015 – 2019
  - Numerical modelling (Bsc.)　　　　　　　　　　　　　　　　2018
- Collaborations with national and international Universities and private sector
- Scientific communication and discussions in French and English
- Publication of peer-reviewed articles and presentation of work at conferences
- Planning and management of research projects
- Data collection, analysis, modelling and interpretation
- Organisation and leading of two field expeditions in Chile, including successful applications for funding
- Organisation of weekly seminars and reading group for the Institute
- Co-responsable of the Institute and group webpages

Technical Assistant, ETH Zurich　　　　　　　　Oct. 2014 – June 2015

Techniques: FT, EMP, CL/SEM images, LA-ICPMS

- Publication of Master thesis in a peer-reviewed journal
- Development of new laboratory approaches
- Field assistant for sample collection in remote areas in Taiwan

Teaching Assistant, ETH Zurich　　　　　　　　Feb. 2010 – June 2014

- Supervision of students in Bachelor courses
- Corrections and evaluation of exercises
- Designing repetition courses for exam preparation

Internship at Nagra (CH) and Seismik s.r.o (CZ)　　　　2011/2012

- Processing of geological data with Matlab and Excel

TECHNICAL SKILLS

Matlab	LaTeX	MS Office
Adobe Illustrator	Webdesign	ArcGIS

LANGUAGES

(Swiss-)German: Native	**French**: Professional (C2; DELF A1-A6)
English: Professional (C2)	**Spanish**: Elementary proficiency

AWARDS　　Willy Studer Prize 2014 (best Master in Geosciences)

MEMBERSHIPS　　ETH Alumni, Swiss Geological Society, Geological Society Zurich

Publications in peer-reviewed scientific journals

1. **Stalder, N.F.**, Herman, F., and Biswas, R. (in prep for *Nature Geoscience*). Maximized erosion at the last glacial maximum revealed by luminescence thermochronometry.

2. Willett, S.D., Herman, F., Fox, M., **Stalder, N.F.**, Ehlers, T.A., Jiao, R., Yang, R., 2020. Bias and error in modelling thermochronometric data: resolving a potential increase in Plio-Pleistocene erosion rate. *Earth Surf. Dynam. Discuss., in review*

3. **Stalder, N.F.**, Herman, F., Fellin, M.G., Coutand, I., Aguilar, G., Reiners, P.W., and Fox, M., 2020. The relationships between tectonics, climate and exhumation in the Central Andes (18-36°S): evidence from low-temperature thermochronology. *Earth-Science Reviews*.

4. **Stalder, N.F.**, Fellin, M.G., Caracciolo, L., Guillong, M., Winkler, W., Milli, S., Moscatelli, M., Critelli, S., 2018. Dispersal pathways in the early Messinian Adriatic foreland and provenance of the Laga Formation (Central Apennines, Italy). *Sedimentary Geology*, 375, 289-308.

5. Glur, L., **Stalder, N.F.**, Wirth, S.B., Gilli, A., Anselmetti, F.S., 2015. Alpine lacustrine varved record reveals summer temperature as main control of glacier fluctuations over the past 2250 years. *The Holocene*, 25, 2, 280-287.

Invited talks

1. Erosion Hotspot in the south-western Central Andes: A Thermochronology Study to assess Feedbacks between Climate, Tectonics and Erosion. University of Arizona, Tucson (U.S.), May 2018.

2. Low-Temperature Thermochronology: (U-Th)/He and fission-track dating. Monique lecture, University of Potsdam, June 2017.

Conference participations

1. **Stalder, N.F**, Herman, F., Fellin, M.G., Coutand, I., Reiners, P.W., Aguilar, G., 2019. Exhumation rate and tectonic histories of the Central Andes (18-36°S). European Geosciences Union 2019, Vienna, Austria. Pico

2. **Stalder, N.F**, Herman, F., Fellin, M.G., Riesner, M., Simoes, M.,, Lacassin, R., Reiners, P.W., 2018. Low-temperature thermochronology reveals increased Pliocene erosion in the Western Cordillera (Central Andes, Chile), Thermo 2018, Quedlingburg, Germany. Talk

3. **Stalder, N.F.**, Herman, F., Biswas, R.H., Fellin, M.G., 2018. Bridging erosion rate measurements across timescales. European Geosciences Union 2018, Vienna, Austria. Poster

4. **Stalder, N.F.**, Herman, F., Fellin, M.G., Riesner, M., Simoes, M.,, Lacassin, R., Reiners, P.W., 2018: Erosion hotspot in the south-western Central Andes revealed by low-temperature thermochronology. European Geosciences Union 2018, Vienna, Austria. Pico

5. **Stalder, N.F.**, Herman, F., Reiners, P.W., Aguilar, G., 2017. Late Cenozoic acceleration of erosion in the Southern Central Andes revealed by low-temperature thermochronology. European Geosciences Union 2017, Vienna, Austria. Poster

6. **Stalder, N.F.**, Herman, F., Reiners, P.W., Aguilar, G., 2016. Effects of climate and tectonics on mountain erosion: Low-temperature thermochronology in the Chilean Andes. Swiss Geoscience Meeting 2016, Geneva, Switzerland. Poster

7. **Stalder, N.F.**, Fellin, M.G., Caracciolo, L., Critelli, S., Winkler, W., Guillong, M., 2015. Provenance of the Laga basin reveals early Messinian linkage between the Alps and the Apenninic realm. GeoBerlin Conference Annual Meeting 2015, Berlin, Germany. Poster

Co-authored conference presentations

1. Herman, F., Willett, S., Matt, F., Yang, R., **Stalder, N.F.**, Ehlers, T., 2019. Does spatial averaging of thermochronometric data contain a bias towards acceleration?, European Geosciences Union 2019, Vienna, Austria.

2. Fellin, M.G., **Stalder, N.F.**, Guillong, M., Winkler, W., Milli, S., Moscatelli, M., Critelli, S., 2018. Dispersal pathways in the early Messinian Adriatic foreland and provenance of the Laga Formation (Central Apennines, Italy), European Geosciences Union 2018, Vienna, Austria.

3. Sue, C., **Stalder, N.F.**, Ghiglione, M., Martinod, J., Herman, F., Salze, M., 2018. Exhumation of the Fitz Roy Granite: How Efficient are the Mantellic and Glaciations Processes?, American Geosciences Union 2018, Washington DC, USA.

4. Herman, F., Deal, E., Braun, J., Chanard, K., de Anna, P., **Stalder, N.F.**, 2017. Extracting an unbiased erosion history of glacial landscapes, European Geosciences Union 2018, Vienna, Austria.

5. Riesner, M., Lacassin, R., Simoes, M., **Stalder, N.F.**, Herman, F., Aguilar, G., Carrizo, D., Reiners, P.W., 2017. Orogen-parallel growth of the central Andes of Chile and Argentina: constraints from thermochronology. American Geosciences Union 2017, New Orleans, Louisana, USA.

APPENDIX **E**

Publications
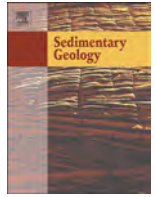
Special Issue Contribution: ANALYSIS OF SEDIMENT PROPERTIES AND PROVENANCE

Dispersal pathways in the early Messinian Adriatic foreland and provenance of the Laga Formation (Central Apennines, Italy)

Nadja Franziska Stalder [a,*], Maria Giuditta Fellin [a], Luca Caracciolo [b], Marcel Guillong [a], Wilfried Winkler [a], Salvatore Milli [c], Massimiliano Moscatelli [d], Salvatore Critelli [e]

[a] Department of Earth Sciences, ETH Zurich, Sonneggstrasse 5, 8092 Zurich, Switzerland
[b] FAU Erlangen-Nürnberg, Geozentrum Nordbayern, Lehrstuhl für Geologie, Schlossgarten 5, 91054 Erlangen, Germany
[c] Dipartimento di Scienze della Terra, SAPIENZA Università di Roma, Piazzale Aldo Moro 5, 00185 Rome, Italy
[d] Istituto di Geologia Ambientale e Geoingegneria, Consiglio Nazionale delle Ricerche (CNR), Via Salaria km 29,300, 00015 Monterotondo RM, Italy
[e] Dipartimento di Biologia, Ecologia e Scienze della Terra, Università della Calabria, 87036 Arcavacata di Rende, CS, Italy

ABSTRACT

The early Messinian Laga Formation represents a turbidite complex deposited in the Late Neogene foreland basin system of the growing Apenninic chain. While the stratigraphy and physiography of the Laga Basin are well known, the source of its sediments is contentiously claimed to be either recycled Apenninic or primary Alpine. Furthermore, a shift in paleocurrent was proposed as a marker of provenance change around 6 Ma. By combining double-dating of detrital zircons (fission-track and U-Pb dating) with compositional analyses, the sedimentary provenance of the lower Laga arenites and differences between the proximal channelized and distal lobe facies are addressed. Due to sediment sorting processes, the lobe facies shows a reduced heavy mineral spectrum relative to the channelized facies. Hence, proximal deposits reflect their hinterland lithologies better than their distal counterpart and should be preferred in provenance analyses. The petrographic composition of the Laga units implies a major metamorphic source combined with an additional dolomite and carbonate source. No compositional difference spanning the shift in paleocurrents is observed, which therefore likely reflects the evolving topography of the foreland due to syn-sedimentary tectonics. Detrital zircon fission-track data reveal youngest age populations at ~16–17 Ma and lag times in the range of 9 to 11 Ma that can be related to modern fission-track ages observed in the Central Alps. The two major $^{238}U/^{206}Pb$ age populations, centered at 277.5 and 37.5 Ma, represent (post-)Variscan events and the Paleogene magmatic activity in the Central Alps, specifically the Adamello complex. The Central and Southern Alps are thus inferred as the major source for the early Messinian Laga arenites. The pathways of the sediments from the Alps to the Laga Basin crossed the Alps-Apennines foreland and passed on the outer Apenninic wedge-top along elongated and tectonically controlled basins and channels that entered the basin from the north and northwest. The transfer could have been direct along the Apenninic depozones. Additionally, late Tortonian sediments from the Alps could have been temporarily stored on top of the Apenninic wedge, e.g. in the Marnoso-arenacea Basin, and then seamlessly cannibalized into the Laga Basin.

© 2017 Elsevier B.V. All rights reserved.

1. Introduction

The modal composition of sandstones is largely controlled by its hinterland lithology, plate tectonic setting, and surface processes (e.g., Garzanti et al., 2004). Provenance studies are thus a powerful tool to gain insights into the geology and geographic position of ancient (sub-)emergent lands, drainage patterns, exhumation histories, and climate changes (e.g., Ingersoll, 1990; Haughton et al., 1991; Garver et al., 1999; Garzanti et al., 2007). In the Adriatic region, a complete tectonostratigraphic history from the early Mesozoic rifting to the Cenozoic collision between the European and the African-Adrian plates is recorded by the infill of the ancient and present foreland basin systems. From the Oligocene through the Miocene, the Adriatic foreland was mainly fed by the Alps and subordinately by the partly emerged Apennines and the Mesomediterranean microplate (Ricci Lucchi, 1975; Argnani and Ricci Lucchi, 2001; Gandolfi et al., 2007; Amendola et al., 2016). At the end of the Miocene and during the Pliocene, the Apennines became emergent and turned into a major sediment source (Bartolini, 1999). Contemporaneously, the Adriatic foreland topography underwent severe changes related to the dynamics of the subduction zone below the Apennines (Royden et al., 1987; Patacca et al., 1990) and anticipated the opening of the Plio-Pleistocene

foredeep (Ricci Lucchi, 1975; Chiocchini et al., 1987; Boccaletti et al., 1990; Centamore et al., 1993).

The *syn*-sedimentary deformation related to the propagation of the Apenninic front as well as local significant erosion during the Messinian salinity crisis complicate the reconstruction of the source-to-sink routes of the Messinian foreland (Ricci Lucchi, 1975; Centamore et al., 1993; Milli and Moscatelli, 2000; Scisciani et al., 2001; Bigi et al., 2003; Manzi et al., 2005; Critelli et al., 2007). In this study, we address this problem by investigating the siliciclastic deposits of the Lower Messinian Laga tur-bidites, which were deposited in the central Adriatic foreland and which record the evolution from a foredeep to a wedge-top depozone (Centamore et al., 1991b; Milli et al., 2007; Bigi et al., 2009; Marini et al., 2015). While the provenance of the Upper Messinian Laga Fm clearly has an Apenninic signature, indicated by gypsum reworked from Apenninic marginal basins into its marker bed (Roveri et al., 2001; Milli et al., 2007), the provenance of the Lower Messinian Laga detritus could be Apenninic, Alpine, or mixed Alpine/Apenninic. Previous studies ad-dressing the source of the Laga Fm involved physical sedimentology and basin analysis (Ricci Lucchi, 1975; Centamore et al., 1993; Milli et al., 2007, 2013) as well as sedimentary petrography (Chiocchini et al., 1987; Chiocchini and Cipriani, 1989, 1992; Corda and Morelli, 1996; Valloni et al., 2002; Le Pera and Critelli, 2009a, 2009b). The petrographic analyses indicate metamorphic and carbonate sources of Alpine provenance. The composition shows moderate variations with time despite a major change in paleocurrents, which was interpreted as a shift from a large catchment to the NNW to a local Apenninic catchment to the NW (Milli et al., 2007; Bigi et al., 2009). The Alpine footprint can be explained by four different scenarios: 1) a direct northern supply from the Alps either with transport along the foredeep main axis or along the Apenninic wedge-top, 2) a prod-uct of recycling of older foredeep deposits exposed by the active thrusts of the Apenninic chain, 3) a seamless cannibalization of the Tortonian Marnoso-arenacea foredeep and/or other wedge-top deposits, 4) a frag-ment of continental crust showing Alpine-age metamorphism and which was exposed in the northern Apennines until the Early Pliocene (Chiocchini and Cipriani, 1992). A tool to test these alternative hypotheses is low-temperature detrital thermochronology (i.e., zircon fission-track dating) combined with U-Pb geochronological dating. In the case of recycling, the detrital thermochronologic age spectra should be similar to the one of the recycled sandstones. In the case of a direct linkage to the Alps, the age spectra should show rejuvenation of the detrital ages with time related to the actively exhuming basement rocks (e.g., Garver et al., 1999). The case of cannibalization is difficult to assess, because this process reworks the detritus within the basin with lag-times likely too short to be detected via detrital thermochronology and with minimal changes in the sandstone composition. Zircon U-Pb geochronology allows the identification of sedimentary contributions from rapidly cooled zir-cons from volcanic and crustal magmatic sources and slowly cooled zir-cons from exhumed igneous basement. The distinction between zircons in a metamorphic basement and xenochrystals in volcanic and magmatic rocks inherited from the protolith or scavenged from host rocks requires additional compositional and isotopic analysis. In this study, heavy miner-al analysis and sandstone petrography are combined with double-dating of detrital zircons on samples from the Lower Messinian Laga units to ad-dress compositional differences between the channelized and the lobe fa-cies and to unravel the sedimentary provenance of the Laga turbidite complex. Based on this information, we provide insights into the Messinian sediment-dispersal pathway in the Adriatic foreland which may ultimately give important constraints on the dynamic of the Apenninic wedge and foredeep system and its topographic gradient.

2. Geological setting

2.1. The Adriatic foreland

The Adriatic Basin is the pro-foreland of the Apennines and the retro-wedge of the Alps. In the Oligocene, the Apennines started

to evolve above the northwestward subducting Adriatic plate (Malinverno and Ryan, 1986). Since the middle to late Burdigalian, slab retreat led to a northeastward thrust migration at the front and to extension at the rear of the Apenninic wedge. This caused a continu-ous migration of the related foredeep and the incorporation of its sediments into the growing wedge, leading to the opening of new depozones towards the northeast (Ricci Lucchi, 1975, 1986; Boccaletti et al., 1990; Argnani and Ricci Lucchi, 2001). The advancing foredeeps are the Macigno-Modino (Chattian-Aquitanian; Cita Sironi et al., 2006), Cervarola (Aquitanian-Langhian; Delfrati et al., 2002), Marnoso-arenacea (late Burdigalian-Tortonian; Pialli et al., 2000; Barchi et al., 2007; Benini et al., 2009; Plesi et al., 2010) and the Plio-Pleistocene basins (Fig. 1). Until the Tortonian, the foredeeps were mainly fed from the north by Alpine detritus which was transported along the foredeep main axis (Ricci Lucchi, 1975; Gandolfi et al., 1983; Gandolfi et al., 2007; Di Giulio, 1999; Dunkl et al., 2001; Zattin and Zuffa, 2004; Garzanti and Malusà, 2008). An additional Alpine source was the Corsica-Sardinia massif and the Mesomediterranean microplate, which were located to the west at the rear of the Apennines with transport crossing the Apenninic wedge (e.g., Wildi, 1985; Gandolfi et al., 2007; Critelli et al., 2008; Amendola et al., 2016). By the Messinian, this route from the Corsica-Sardinia block and the Mesomediterranean microplate to the Northern Apennines was cut by the opening of the Northern Tyrrhenian Sea and specifically of the Corsica Basin (Mauffret and Contrucci, 1999; Carmignani et al., 2004; Thinon et al., 2016). At the end of the Tortonian, the elongated and continuous Marnoso-arenacea foredeep was incorporated into the Apenninic wedge. Sedimentation in the early Messinian occurred further to the south in the Laga Basin and in a system of fragmented and confined basins, the satellite basins (Ricci Lucchi, 1975, 1986; Cosentino et al., 2010; Ghielmi et al., 2013). To understand possible source-to-sink routes, the Messinian Adriatic foreland is described below by considering its northern and central sectors and their connection.

2.2. The Early Messinian Adriatic foreland

During the early Messinian, the northern Adriatic foreland was subdivided into independent depozones separated by ridges currently buried below the Po Plain (Fig. 2). The westernmost depozone was segmented into a northern foredeep and into a southern uplifting basin (Tertiary Piedmont Basin) fed by the Western Alps (e.g., Maino et al., 2013 and references therein). The eastern depozone was subdivided into a western confined sector connected to an eastern open one (Ghielmi et al., 2013). The western sector was restricted between structural highs (Mantova and Pavia highs) and opposite Alpine and Apenninic frontal thrusts (Pieri and Groppi, 1981). The eastern sector was a typical foredeep with incipient thrusts along the internal margin, a ramp, and a forebulge along the outer margin to the north. The forebulge separated it from the eastern foreland basin of the Southern Alps, the Venetian-Friuli Basin (e.g., Barbieri et al., 2004 and references therein). Along the Apenninic margin, thrusts defined local structural highs which confined intraslope deposits and wedge-top basins filled by turbidites. Locally, the tops of these highs were starved of terrigenous detritus and covered only by condensed sedi-ments, anoxic mudstones and/or contourite deposits. The turbidite deposits in this sector of the foreland covered the outer Marnoso-arenacea foredeep and the Serravallian-Tortonian foreland ramp (Ghielmi et al., 2013). The major entry points to the northern foreland were located to the north-west, where canyons fed by fan-delta systems from the Central and Southern Alps delivered over 1000 m of early Messinian turbiditic sand- and mudstones (Ghielmi et al., 2013). Whether these turbidite currents reached the central foreland along the major foredeep axis or along the wedge-top basins is unclear.

At present, the largest early Messinian depozone of the Central Apennines, the Laga Basin, is separated from the coeval northern fore-land by a structural and topographic culmination (Pesaro-Ancona high)
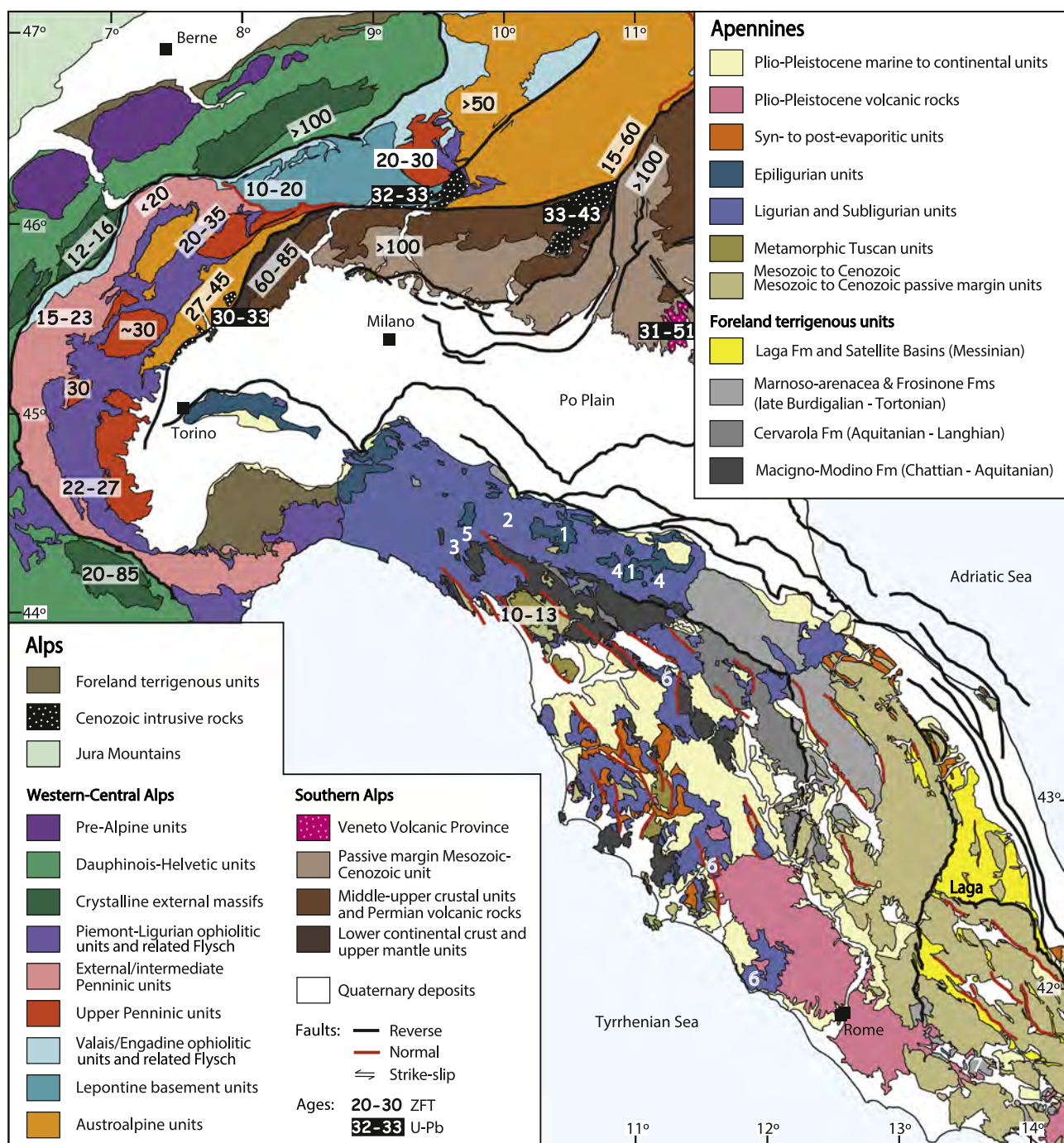
Fig. 1. Schematic structural map of the Apennines and the Alps modified after the Structural model of Italy (Bigi et al., 1990, 1992a, 1992b), with reference ranges for bedrock zircon fission-track (ZFT) and U-Pb ages of igneous rocks (see text for references). Numbers refer to approximate locations of siliciclastic deposits shown in Fig. 8: 1 = Bismantova Fm (after Cibin et al., 2001); 2 = Petrignacola Fm (Aveto Valley, after Valloni and Zuffa, 1984; Cibin et al., 2001); 3 = Monte Gottero (after Argnani et al., 2006); 4 = Monghidoro (after Argnani et al., 2006); 5 = Ostia-sandstones (Val di Taro and Val Baganza, after Mezzadri, 1964); 6 = Pietraforte Fm (after Fontana, 1991); 7 = Frosinone unit (after Cipollari and Cosentino, 1995).

that marks the southeastern termination of the Po Plain and that was a less subsiding area throughout the Neogene (Ori et al., 1986; Roveri et al., 2004). In this zone, the lower Messinian succession displays strong lateral variability both in thickness and facies indicating a complex basin physiography (Savelli and Wezel, 1978; Capuano and D'Antonio, 1992; Coward et al., 1999; Roveri et al., 2004, 2005). Proximal and distal sand lobe reached at least as far as the northern end of the Pesaro-Ancona high (Ghielmi et al., 2013), but no clastic sediments reached the external sector of the Pesaro-Ancona high and the basin to the east (Ori et al., 1986; Roveri et al., 2004). Only limited terrigenous supplies were deposited in the middle sector of the Pesaro-Ancona high (Roveri et al., 2004).

In the internal sector of this structural high, the Ligurian nappe had already advanced over the early Tortonian outer Marnoso-arenacea to the north and west of an active anticline (Zattin et al., 2002). The lower Messinian formations are overlain by sediments related to the Messinian salinity crisis. A lasting foredeep on this structural culmination first established in the Pliocene with the deposition of massive turbiditic sandstones.

In the Messinian, large portions of the Apenninic wedge emerged and provided increasing supplies from the west to the Apenninic foreland, which now consisted of several inner wedge-top basins and of the Laga Basin that evolved at the front of the growing wedge
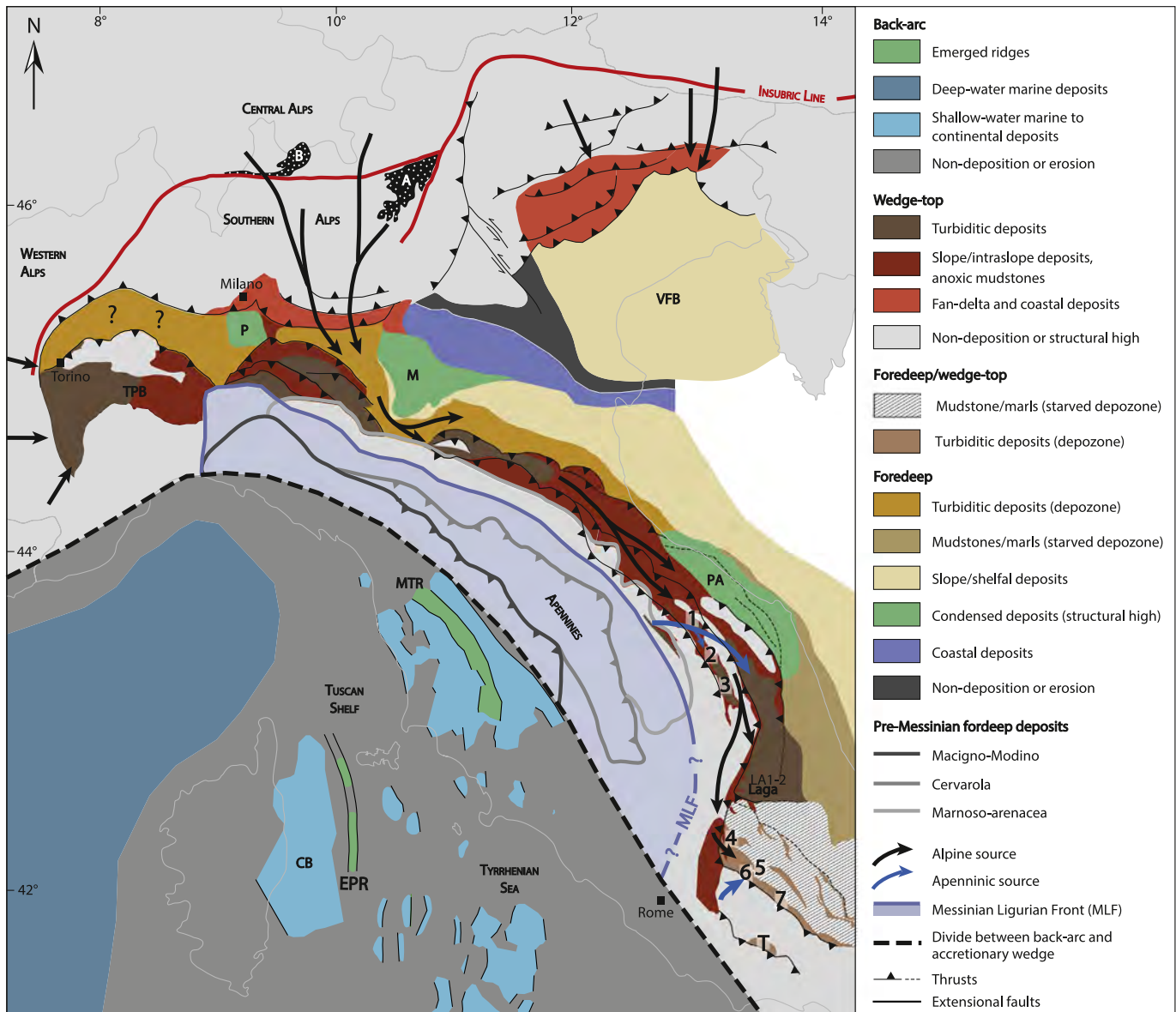
Fig. 2. Schematic map of the early to middle Messinian sediment-dispersal pattern in the northern-central Adriatic foreland and paleotopographic reconstruction modified after Bigi et al. (1990, 1992a, 1992b), Martini and Sagri (1993), Mauffret and Contrucci (1999), Roveri et al. (2004, 2005), Ghielmi et al. (2013). The Laga Basin rapidly evolved from a foredeep to a distal wedge-top depozone at the beginning of Laga 2. The shallow-water marine to continental deposits in the southern Tyrrhenian Sea are indicatively reconstructed based on the distribution of Messinian evaporites as in Fabbri and Curzi (1979). The position of the Messinian Ligurian front is reconstructed after Rossi et al. (2002), Brogi and Liotta (2008), Funiciello et al. (2008), and Caricchi et al. (2014). Its southern extent is still debated and could have reached as far as the Lepini Mountains (Cosentino et al., 2002, 2010; Centamore et al., 2007). A = Adamello; B: Bergell; CB = Corsica Basin; EPR = Elba-Pianosa Ridge; M = Mantova high; MTR = Mid-Tuscany ridge; P = Pavia high; PA = Pesaro-Ancona high; T = Torrice wedge-top basin (Latina Valley); TPB = Tertiary Piedmont Basin; VFB = Venetian-Friulian Basin. Northern satellite basins: 1 = Serraspinosa; 2 = San Donato-Cantia; 3 = Camerino. Southern satellite basins: 4 = Salto; 5 = Tagliacozzo; 6 = Brecce della Renga; 7 = Liri.

(Boccaletti et al., 1990; Centamore et al., 1993; Argnani and Ricci Lucchi, 2001; Scisciani et al., 2001; Bigi et al., 2003, 2009). The inner wedge-top depozones were elongated, tectonically controlled basins fed by coarse, locally sourced mass-flows from the west and by turbidite currents from the north (Centamore et al., 1978; Calamita et al., 1979; Chiocchini et al., 1981; Chiocchini and Cipriani, 1984, 1986, 1989; Critelli et al., 2007). The Laga Basin was triangular-shaped, elongated to the north and confined by active thrusts and growing anticlines.

2.3. Stratigraphy and structural setting of the Laga Basin

The Laga Basin is subdivided into two sectors (Cantalamessa et al., 1986; Calamita et al., 1995 with references therein): an elongated, less-subsiding sector to the north and a triangular-shaped, strongly

subsiding sector to the south with an extent of approximately 60 × 40 km^2, which is the focus of this study (Fig. 3). The Gran Sasso Range to the South, the Sibillini Mountains to the west, and the Montagna dei Fiori-Montagnone anticline to the east border the basin. Since the early Messinian, the Southern Laga Basin collected up to 3 km thick marine siliciclastic turbidites which entered the basin from NNW and NW and covered pelagic and hemipelagic marls. Different stratigraphic subdivisions have been proposed based on lithostratigraphy and facies analysis. This study adopts the stratigraphic scheme of Milli et al. (2007, 2013) which distinguishes the three major units Laga 1, Laga 2, and Laga 3 bounded by unconformity surfaces (Fig. 3). These units are correlatable to the regional Messinian-Pliocene chronostratigraphic scheme as well as to the main Messinian events recognized in the northern Apennines (Hilgen et al., 1995; Krijgsman et al., 1999; Roveri et al., 2014, and references therein). Additional age
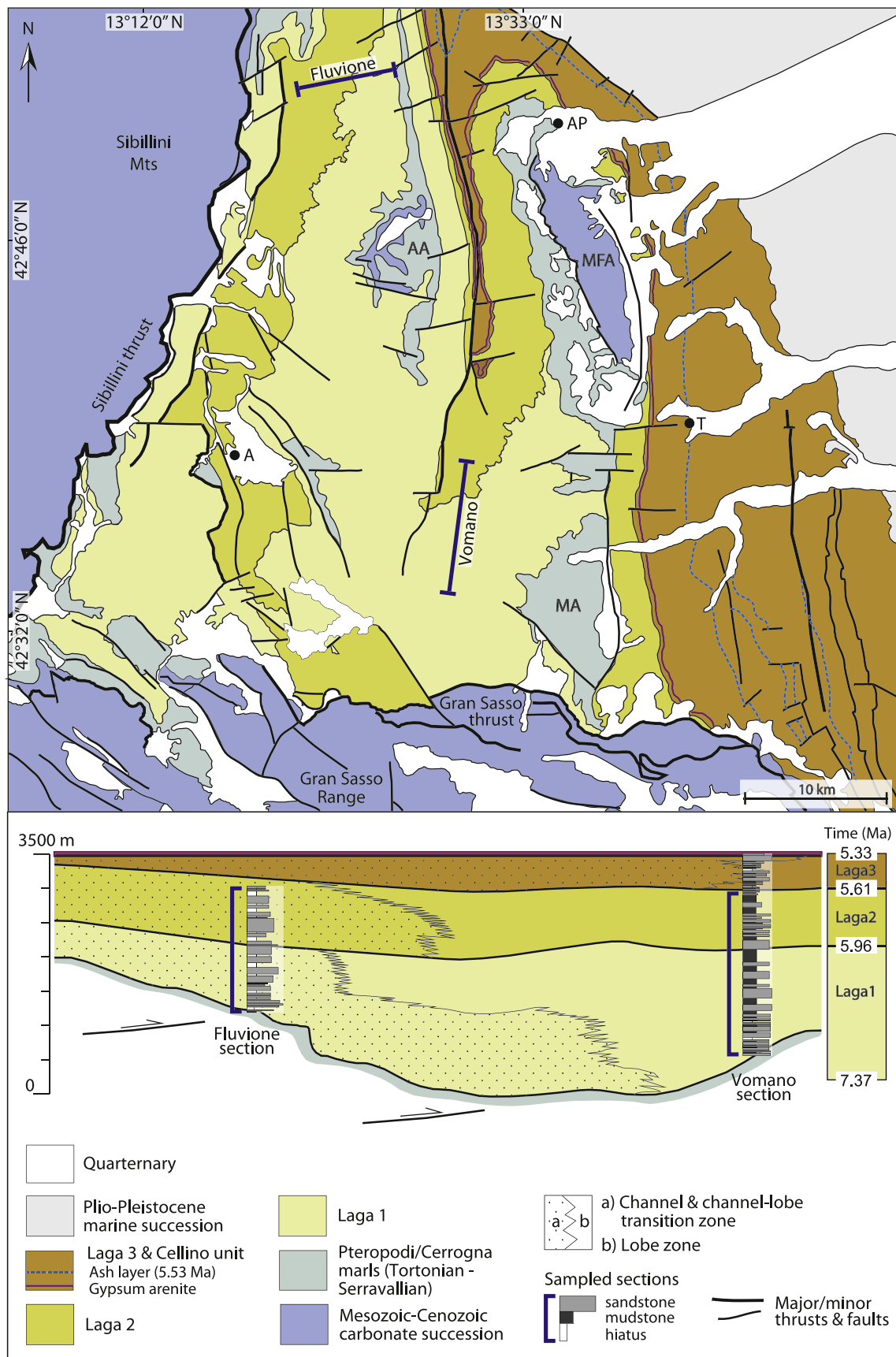
Fig. 3. Geological map of the southern Laga Basin and its surroundings, based on Centamore et al. (1991b) and modified after Marini et al. (2015), as well as a correlation scheme of the Laga Fm modified after Milli et al. (2013). The scheme is vertically exaggerated. AA = Acquasanta Anticline, MA = Montagnone Anticline, MFA = Montagna dei Fiori Anticline.

constraints are provided by biostratigraphy in the marls under- and overlying the Laga deposits as well as by radiometric dating of a volcanic ash bed within the Laga 3 (Centamore et al., 1991a; Cosentino et al., 2013). The Laga 1 unit (7.37–5.97 Ma) was deposited during the pre-evaporitic stage, a time-interval characterized by a reduced deep-water circulation in the Mediterranean Sea. The Laga 2 unit (5.97–5.60 Ma) was deposited during the evaporitic stage, while the Laga 3 unit (5.60–5.33 Ma) was deposited during the post-evaporitic Lago-Mare stage and partially during the lowermost part of the Pliocene (Milli et al., 2007, 2013). Laga 2 and Laga 3 are separated by the Messinian Erosional Surface (Krijgsman et al., 1999) which is followed by the deposition of a gypsum-arenite key bed. During the deposition of Laga 3, the depocenter migrated eastward and large areas of the Apennines were exposed to erosion, providing an increasing clastic flux to the foreland (Morelli, 1994; Corda and Morelli, 1996; Roveri et al., 2001, 2003; Valloni et al., 2002; Milli et al., 2007). This change in provenance is only modestly observed in the main sandstone composition, which indicates a quartzofeldspatholithic composition for both the pre- and *syn*-evaporitic (Laga 1+2: $Q_{m49}F_{23}L_{t28}$) and the post-evaporitic units (Laga 3: $Q_{m43}F_{22}L_{t35}$) (Chiocchini et al., 1987; Morelli, 1994). Nevertheless, the pre- and syn-evaporitic units have larger proportions of metamorphic lithic fragments (+13% relative to Laga 3), while the post-evaporitic unit shows slightly higher percentages of extrabasinal carbonates (+15% relative to Laga 1+2) and contains evaporitic clasts, which are absent in the pre-evaporitic units (Chiocchini et al., 1987; Morelli, 1994).

The turbidites of the Laga 1 and 2 units (hereafter collectively named lower Laga) constitute a submarine turbidite complex (sensu Mutti and Normark, 1987) with channelized facies in the proximal north-western part and lobe facies in the distal south-eastern part of the basin (Milli et al., 2007; Marini et al., 2011, 2015, and references therein). The channelized facies show 5 to 10 m thick, fining-upwards facies sequences and record several episodes of incision and refilling. These sequences are characterized by medium- to coarse-grained sands with rip-up clasts and scours in the basal part and thick sandstone bodies with 3D–bedforms in the upper part. The lobe facies shows amalgamated to non-amalgamated bed packages of 5 to 10 m thickness with water escape structures and climbing ripples interbedded with thin layers of very-fine grained sandstones and siltstones (Milli et al., 2007, 2013; Marini et al., 2015). The sandstones are rich in well-preserved organic material like tree trunks or leaves.

The basin morphology and turbidite sedimentation was mainly controlled by the diachronous activation of three main thrust systems and two thrust-related anticlines (Scisciani and Montefalcone, 2006; Milli et al., 2007; Bigi et al., 2009, 2011). The propagation of the Gran Sasso and Sibillini thrusts occurred contemporaneously with the deposition of the lower Laga. At the beginning of Laga 2, the Acquasanta anticline started to rise underneath the Laga Basin and probably caused the observed change in paleocurrent direction from mainly N-S in Laga 1 to NW-SE in Laga 2 (Milli et al., 2007). The thrust activity during deposition of Laga 2 is responsible for the depocenter migration to the east. The onset and major growth activity of the Montagna dei Fiori-Montagnone anticline occurred in the late stage of Laga 2 and in the lower Pliocene, respectively. Thus, the Laga Basin started as a foredeep that rapidly evolved into a distal wedge-top depozone sensu De Celles and Giles (1996) since the deposition of Laga 2, when the turbidites were deposited on top of active frontal wedge thrusts.

2.4. From the Tortonian to the early Messinian: The outer Marnoso-arenacea and satellite basins

The deposition of the Marnoso-arenacea started in the late Burdigalian (Pialli et al., 2000; Barchi et al., 2007; Plesi et al., 2010). During the inner stage, from the late Burdigalian to Serravallian, laterally continuous turbiditic sandstone lobes were deposited in a large, flat basin plain (Ricci Lucchi, 1986). During the outer stage, in the Tortonian,

thick, locally channelized sandstone turbidite bodies bearing coarse to pebbly sandstone were deposited in a segmented basin shifted towards the foreland (Roveri et al., 2002). Both north-derived and south-derived petrofacies characterize the two stages of the Marnoso-arenacea Fm (Gandolfi et al., 2007, and references therein). All facies contain high amounts of extrabasinal carbonate. The north-derived quartzofeldspatholithic petrofacies ($Q_{m50}F_{19}L_{t31}$) have been attributed predominantly to the Alpine chain based on the high fraction of metamorphic lithic clasts and the occurrence of blue amphibole. The south-derived petrofacies ($Q_{m34}F_{22}L_{t45}$), dominated by sedimentary rock fragments and containing intrabasinal carbonate clasts, were shed from the submerged Apennines. During the Tortonian, north-derived, turbidity currents carrying quartzofeldspatholithic detritus reached also a foredeep further south in the Lazio-Abruzzi domain of the Central Apennines (Frosinone Fm; $Q_{m46}F_{27}L_{t27}$) (Cipollari and Cosentino, 1995; Critelli et al., 2007). At the end of the Tortonian, the basins of the outer Marnoso-arenacea and of the Frosinone Fm were closed by active thrusts to the east. A satellite basin filled with coarse-grained clastic deposits (Torrice Fm) developed in a wedge-top position above the Frosinone Fm (Cipollari and Cosentino, 1995).

In the early Messinian, several confined depozones developed in Apenninic wedge-top and/or foredeep positions. To the north and south of the Laga Basin, active early Messinian depocenters of both siliciclastic and carbonate detritus were located in two different structural, inherited domains (Castellarin et al., 1978, 1982).

In the northern domain, early Messinian clastic sediments were deposited in three small basins (Serraspinosa, San Donato-Cantia, and Camerino Basins) that were roughly aligned from N to S along a structural depression in an internal position relative to the Laga Basin (Fig. 2). The northernmost basin (Serraspinosa Basin) consists of massive siliciclastic turbidite deposits interfingered with lenses of chaotic, locally sourced mass-flow deposits (Centamore et al., 1978, 1991a). The composition of the siliciclastic sandstones is quartzofeldspatholithic with abundant lithic fragments consisting of over 40% plutonic-metamorphic detritus ($Q_{m27}F_{37}L_{t35}$) (Chiocchini and Cipriani, 1992) (Fig. 4). A transverse structural channel fed a fan delta in the central basin (San Donato-Cantia Basin), providing mainly carbonate detritus from the west (Centamore et al., 1978; Chiocchini et al., 1981). The conglomeratic deposits contain pebbles of Apenninic marls and limestones but also phyllites and turbiditic sandstones (Canavari, 1910). The composition of the sandstones is quartzofeldspatholitic ($Q_{m24}F_9L_{t67}$) with 59% metamorphic lithics (Chiocchini and Cipriani, 1992) (Fig. 4). The deposits of the southernmost basin of the northern domain (Camerino Basin) are up to 1500–1700 m thick with strong lateral and up-section variations of both thickness and facies (Centamore et al., 1978, 1991a). They consist mostly of turbidite deposits that display channelized facies in the more confined part of the basin and lobe- to fringe-facies in the distal zones. The sediments entered the basin from several entry points to the west and were mainly dispersed from the SW along the axis to the NNW. Along the eastern margin, coarse mass-flow deposits were derived from unstable slopes consisting of Cretaceous to Miocene limestones. The sandstone composition is quartzofelspatholitic ($Q_{m40}F_{15}L_{t45}$) with abundant metamorphic (21%) and sedimentary lithics (73%) (Chiocchini and Cipriani, 1992).

In the southern domain during the early Messinian, a Mesozoic-to-Miocene carbonate platform was subsiding due to flexural loading to the east while fragments of the same platform and Apenninic internal nappes were exposed to the west (Cosentino et al., 2003; Critelli et al., 2007, and references therein). The physiography of the drowning area was characterized by alternating intrabasinal highs and elongated depressions (Tagliacozzo and Liri Basins) which merged to the north to form the Salto Basin (Fig. 2). Several extrabasinal and intrabasinal sources produced mass-flows (Brecce della Renga Fm) and turbiditic flows (Argilloso-Arenacea Fm) that were deposited in areas very proximal to the feeder systems (Milli and Moscatelli, 2000; Moscatelli, 2003). The arenites detrital
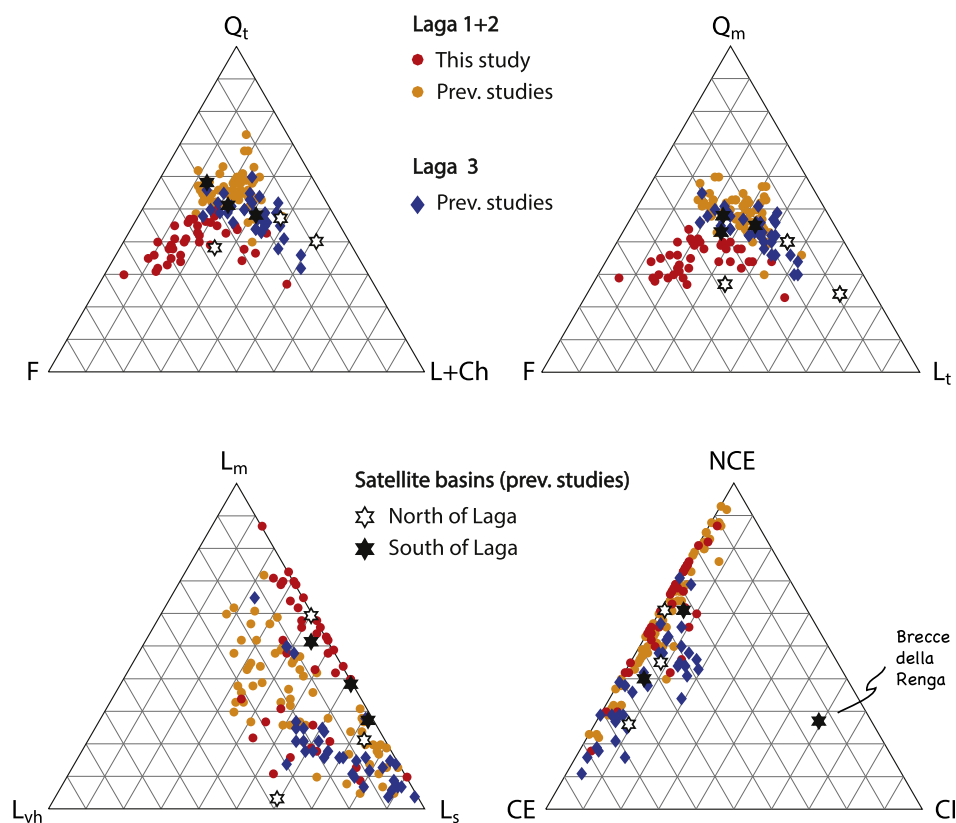
Fig. 4. Ternary diagrams for the Laga arenites and the lower Messinian Satellite basins. Previous studies: Chiocchini et al. (1987) and Morelli (1994) for the Laga Fm, Chiocchini and Cipriani (1992) for the Serraspinosa, Urbania, and San Donato-Cantia Fms and Critelli et al. (2007) for the Brecce della Renga and Argilloso-Arenacea Fms.

modes have two main petrofacies, a quartzofeldspatholithic one and a calclithite one (Critelli et al., 2007). The calclithite petrofacies (Brecce della Renga Fm, $Q_{m45}F_{21}L_{t34}$) was derived from a carbonate platform exposed along a ridge which provided mostly non-coeval intrabasinal detritus (Fig. 4). The quartzofeldspatholithic sandstones (Argilloso-Arenacea Fm, $Q_{m45}F_{29}L_{t25}$) contain abundant quartz and equal proportions of feldspar and lithic fragments (Fig. 4). Aphanitic lithics include abundant sedimentary and metasedimentary fragments and minor volcanic, metavolcanic, and ophiolitic clasts. The depozones of the southern domain have been described as part of a large foredeep characterized by a complex topography (Centamore et al., 1978; Cosentino et al., 2003; Critelli et al., 2007). The ridges have been interpreted as related to either anticlines growing over blind thrusts (Centamore et al., 2002; Centamore and Rossi, 2009) or to extensional reactivation of inherited faults (Carminati et al., 2014). In the first case, the ridges would confine the depozones to the east in a wedge-top position, while in the latter case they would represent confinement structures within the foredeep sensu *strictu*. Anyhow, during the late Messinian, this whole sector became rapidly part of the deforming wedge as the frontal thrust of the Central Apennines progressively migrated to the east.

The Apenninic signature of the calclithite facies of the satellite basins is well-defined and here not further discussed. However, based on the interfingering with detritus from Apenninic sources, the provenance of their arkosic detritus has also been debated as either recycled material from the Apennines, primary Alpine, or related to an Alpine fragment located in the Apennines (Chiocchini and Cipriani, 1992). The composition of the arkosic sediments of the satellite basins is practically undistinguishable from the composition of the Laga arenites. We thus consider their arkosic sediments within the common frame of the evolution of the Adriatic foreland and of the Apenninic wedge.

2.5. Thermo-tectonic units of the potential source areas

The provenance of clastic sediments can be traced by identifying possible source areas and comparing their compositional and geo- and thermochronometric signatures with those preserved in the detrital record. Here, we present the main thermo-tectonic features of the Alps and the Apennines that are the potential source areas of the Apennine turbidite deposits (Fig. 1). Contributions from the Corsica-Sardinia block and/or the Mesomediterranean microplate to the Laga Basin are excluded due to their paleogeographic position to the west of the opening Tyrrhenian Sea and are thus not further discussed.

The main tectonic domains of the Alps comprise the Penninic and Helvetics nappes, which are derived from the European margin, and the Austroalpine nappe and Southern Alps, which belonged to the Adriatic micro-continent (see Schmid et al., 2004; Handy et al., 2010 for plate-tectonic reconstructions and descriptions of tectonic units). Throughout the Cenozoic, the Helvetic nappes were located north of the Alpine drainage divide and did not contribute detritus to the Adriatic foreland (Spiegel et al., 2001). The Penninic nappes comprise oceanic rocks and basement slivers (Schmid et al., 2004), which show Cenozoic metamorphic overprints and Neogene zircon fission-track ages (Hunziker et al., 1989, 1992; Hurford et al., 1989; Seward and Mancktelow, 1994; Bernet et al., 2001; Fügenschuh and Schmid, 2003; Malusà et al., 2005; Bigot-Cormier et al., 2006; Schwartz et al., 2007). The Lower Penninic units are the high-grade metamorphic core of the Alps exposed in the Lepontine dome (Central Alps), which was the focus of fast exhumation during the Neogene and exposes the youngest zircon fission-track ages observed in the Alpine realm (Hurford, 1986; Hunziker et al., 1992; Campani et al., 2010). The Lepontine dome was the main contributor of sediments to the Swiss Molasse basins and to the Chattian-Tortonian Adriatic foreland (von Eynatten, 2003; Spiegel et al., 2001, 2004; Gandolfi et al., 2007; Garzanti and Malusà, 2008).

At the top of the Alpine edifice, the Austroalpine units register extensively the Cretaceous metamorphic event at ca. 100–110 Ma but only locally the Cenozoic thermal overprint. They consist of Variscan polymetamorphic basement and its Mesozoic sedimentary cover with zircon fission-track ages between ca. 50 and 100 Ma (Frank et al., 1987; Hunziker et al., 1992; Thöni, 1999; Bernet et al., 2001, and references therein; Dunkl et al., 2003). Ages younger than 50 Ma are locally observed along major faults (e.g., Fügenschuh et al., 1997; Viola et al., 2001). The basement and sedimentary cover of the Southern Alps were unaffected by the Alpine metamorphism and show zircon fission-track ages older than 50 Ma outside the area close to the Periadriatic lineament (Bürgi and Klötzli, 1990; Viola et al., 2001; Stipp et al., 2004; Wolff et al., 2012).

The Cenozoic collisional phase resulted in several magmatic intrusions along the Periadriatic Lineament, i.e. the Adamello batholiths (~31–43 Ma U-Pb zircon ages, Mayer et al., 2003; Schaltegger et al., 2009, and references therein; Schoene et al., 2012), the Bergell plutonite (~29–32 Ma U-Pb zircon ages, Oberli et al., 2004; Gianola et al., 2014 and references therein), the Biella volcanic suite and intrusions (~30–33 Ma U-Pb zircon ages, Berger et al., 2012; Kapferer et al., 2012), and the Rieserferner intrusion (31 ± 3 Ma Rb/Sr whole rock analysis, Borsi et al., 1979; Müller et al., 2000).

The northern-central Apenninic orogen consists mostly of oceanic and sedimentary rocks that show a very low-grade Apenninic thermal overprint. Its metamorphic core is only exposed in small domes as for instance the Alpi Apuane, which shows 10–13 Ma old zircon fission-track ages (Fellin et al., 2007). The structurally highest unit is the Ligurian nappe, which comprises the Ligurian-Piedmont oceanic crust with its Jurassic to Oligocene sedimentary cover and Epiligurian basins. This unit overrode the Tuscan nappe, the metamorphic complexes, and the Oligocene to Miocene Apenninic foredeep deposits. It shows lower greenschist-facies metamorphism and contains zircon fission-track ages older than 100 Ma (Balestrieri et al., 1996; Bortolotti et al., 2001). The Mesozoic rift sediments together with the Cenozoic foredeep deposits are now part of three domains: 1) the Tuscan domain, (e.g., Macigno and Modino sandstones), 2) the Umbro-Romagna-Marche (e.g., Cervarola, Marnoso-arenacea, and Laga sandstones) and 3) the Lazio domains (e.g., Frosinone, Salto, and Argilloso-Arenacea sandstones). These sediments contain zircon fission-track ages of Alpine provenance with age populations from 15 to 140 Ma (Bernet et al., 2001, 2009; Dunkl et al., 2001).

3. Methodology

We merge two datasets of the lower Laga Fm that are derived from successive independent sampling and analysis performed at the University of Calabria, Italy (data set 1) and at ETH Zürich, Switzerland (data set 2). Both datasets span the base of Laga 1 to the top of Laga 2 (Fig. 3). The post-evaporitic Laga 3 unit has a dominant Apenninic provenance and is thus not considered in our study.

First, a detailed study of the modal analysis of the channelized facies was performed (Fluvione section, 27 samples). Then, a complementary study integrated modal, heavy mineral, and detrital geo- and thermochronologic analyses on a selected number of samples. The second study included samples from both the channelized facies (Fluvione section, 7 samples) and the lobe facies (Vomano section, 5 samples) to test for compositional variations along the turbiditic pathway. The two studies sampled common sites in the channelized facies (Fluvione section) to assure homogeneity of samples and results. Zircon fission-track and U-Pb dating was performed on the lowermost (Laga 1, L1FNS1) and topmost (Laga 2, L2FNS24) samples of the Fluvione section. Details about sample locations and applied methodologies are provided in the Appendix, Table A1.

3.1. Sandstone petrography

The modal sandstone composition was determined by mid-point ribbon counting (Chayes, 1956) on stained thin sections. Methodological procedures differ slightly between the two datasets due to different practices at the two laboratories where the analysis were performed independently before merging of the data was undertaken. Staining was performed by following the procedure of Lindholm and Finkelmann (1972) for the first dataset. The second dataset followed the procedure of Houghton (1980) for feldspars and Dickson (1966) for Fe-content of carbonate minerals. All samples were counted using the Gazzi-Dickinson method as described in Ingersoll et al. (1984) and modified by Zuffa (1987). 500 points were counted on the first samples, 200 on the second one. Counted grains were assigned to the monomineralic and polymineralic compositional categories and to the spatial categories (extrabasinal versus intrabasinal) using the criteria by Zuffa (1980, 1985, 1987). Grain types and recalculated parameters are those of Dickinson (1970, 1985), Zuffa (1985, 1987), Critelli and Le Pera (1994), and Critelli and Ingersoll (1995).

3.2. Heavy mineral analyses

The samples were crushed and sieved to retrieve the 63–400 μm sand fractions for heavy mineral analysis. The residual carbonate cement and organic material was dissolved with a mixture of acetic acid and hydrogen-peroxide at 50°C. The heavy fraction was separated from low density grains by using Bromoform and mounted in Piperin to allow petrographic analysis under the microscope (Martens, 1932). Following the mid-point ribbon counting method suggested by Van der Plas (1962), the heavy mineral assemblages were counted in a 0.1 mm thick ribbon using a 20× magnification. 300 grains per sample were counted for the Fluvione section, but only 200 grains could be counted in the Vomano section due to the low heavy mineral concentrations and large amount of micas.

3.3. Zircon fission-track analysis

Zircon fission-track dating was performed on two samples of the Fluvione section at the base of Laga 1 (96 grains) and top of Laga 2 (94 grains). This ensures on a 95% percent confidence level that no fraction ≥6% of the age spectra is missing (Vermeesch, 2004). Zircons were separated with standard magnetic and heavy liquid separation techniques from the crushed 63–400 μm fractions and mounted into Teflon pads, which were polished to expose internal surfaces. Adopting the multiple-etch technique of Naeser et al. (1987), five mounts per sample were etched in an eutectic melt of NaOH and KOH at 228°C for either 14, 21, or 28 H. Mica laminas were attached to the samples as external detectors. The mounts were irradiated at the Radiation Center of Oregon State University, using a nominal neutron fluence of $1 \cdot 10^{15}$ ncm^{-2}. Induced tracks were revealed by etching in 40% HF at 23°C for 45 min. Fission tracks were analyzed on grains from all 3 etch times, using the Fish Canyon tuff as a standard for the zeta calibration (Hurford and Green, 1983). The age distribution was decomposed into dominant age peaks using the BinomFit program of Brandon (2002), version 1.2.63 (2007), where each fitted peak represents an age population representative for its source area.

3.4. $^{238}U/^{206}Pb$ dating

U-Pb isotope intensities were measured by laser ablation inductively-coupled plasma mass-spectrometry (LA-ICPMS) at the ETH Zurich on the same etched and polished detrital zircons as used for the fission-track analysis (97 grains for base Laga 1, including one underetched grain which was not counted for FT, and 93 for top Laga 2, excluding one unmeasurable grain). The ablation areas with a spot diameter of 20 μm were pre-selected with the aid of cathodoluminescence images and of

the fission-track distributions to identify zonations and crystal defects which were avoided. Zircons were analyzed using a Resonetic Resolution 155 laser ablation system with a repetition rate of 5 Hz and an energy density of 2 Jcm^{-2} coupled to a Thermo Element XR Sector-field ICP-MS measuring ^{202}Hg, ^{204}Pb, ^{206}Pb, ^{207}Pb, ^{208}Pb, ^{232}Th, ^{235}U, and ^{238}U intensities (see Guillong et al., 2014 for further information and meta data of the measurements in Appendix, Table A5). GJ-1 (Jackson et al., 2004) was used as primary Reference material, and accuracy of the method was confirmed by four secondary standards (Z5, OD-3, Temora2, and 91500). Ages and ratios corrected for instrumental drift and down hole fractionation were obtained using the Iolite 2.5 (Paton et al., 2010; Paton et al., 2011) and VizualAge software (Petrus and Kamber, 2012). No common Pb correction was applied, since contaminated signals are recognized as discordant ages in the Concordia plots, which were produced with Isoplot 4.1 (Ludwig, 2001). Error ellipses represent 2σ analytical errors of the ^{207}Pb/^{235}U and ^{206}Pb/^{238}U ratios, respectively. Histograms and probability density functions were calculated using a bin size of 15 Ma and a bandwidth of 8.

4. Results

4.1. Sandstone petrography

Recalculated values for ternary diagrams are shown in Table 1, raw point-count results and categories are tabulated in the Appendix, Tables A2 and A3. All framework categories show approximate normal distributions (Appendix, Fig. A1), except L$_{vh}$ which is skewed towards low values due to low counts in dataset 1 (see below). We thus represent data as average values in ternary diagrams, but log-transformed plots (Vermeesch, 2006) are provided in the Appendix, Fig. A2.

All samples have similar mean modal values indicating quartzofeldspatholithic composition (Q$_{t40}$F$_{41}$L$_{19}$, Q$_{m35}$F$_{41}$L$_{t24}$; Fig. 4). The majority of the lithic components are sedimentary and metamorphic grains. The total metamorphic rock fragments (Rm), including phaneritic rock fragments counted as quartz, feldspars, and micas in metamorphic rock fragments, are 84% and mostly gneiss and schists. The sedimentary fragments are almost exclusively carbonate extraclasts (CE) with dolomite dominating over limestone. A few siltites and cherts are also present. Plutonic grains are found primarily in Laga 1 along the Fluvione section. Ophiolitic detritus comprise 4% of the noncarbonate lithic clasts and consist of serpentinoschist, serpentinite and metavolcanic lithic fragments. The framework is grain-supported with moderate sorting, low maturity, and subangular clasts. This indicates, together with the lithic composition and the high feldspar content, 1st-cycle sandstones rather than 2nd-cycle sandstones derived from recycled material (Pettijohn et al., 1987). No significant modal difference occurs between the lobe and channelized facies.

Discrepancies occur between the two datasets in the proportions of lithic grains (L$_t$) versus feldspars (F) and of metamorphic (L$_m$) versus volcanic (L$_{vh}$) lithic grains. Relative to the first data set, the second one yielded more lithic (35% instead of 19%) and volcanic grains (23% instead of 3%). The higher lithic content of the second sample set likely reflects the sampling strategy aimed at maximizing the zircon yield. In fact, the samples were collected exclusively from the base of the turbiditic layers where sediments are coarser and the potential content of heavy minerals and lithic fragments are highest. The higher content of volcanic and metavolcanic grains is not easily explained but might also be related to the difference in the sampled grain size.

4.2. Heavy mineral analysis

The average percentage of the heavy fraction constitutes 2.1% and 1.2% of the insoluble material for the Fluvione (7 samples) and Vomano (4 samples) sections, respectively. Although dissolution effects can

be observed in all samples, the mineral diversity does not change significantly over the stratigraphic record. The samples should thus largely represent the main composition of their source rock, but a probable loss of amphibole and pyroxene during transport cannot be excluded (e.g., Morton and Hallsworth, 2007). Recalculated data is provided in Table 2, raw point-count results are tabulated in the Appendix Table A4.

4.2.1. Fluvione section

The average heavy mineral assemblage of the Fluvione section consists of garnet (58.4%, mean average in % of total transparent heavy minerals), epidote and zoisite (17.4%), apatite (6.5%), staurolite (3.1%), tourmaline (2.2%), kyanite (1.5%), blue amphibole (1.4%), chloritoid (0.9%), allanite (0.7%) as well as the ultradense minerals rutile (2.8%), sphene (3.1%), and zircon (1.1%). Monazite, xenotime, brookite, barite, and Cr-spinel are present in very low percentages. The bulk composition does not change over the stratigraphic section, but the relative percentages of garnet and Cr-spinel increase while epidote, kyanite, and blue amphibole decrease upsection (Fig. 5). While no influence of bed thickness can be observed, these trends slightly correlate with the average grain-size of the samples.

4.2.2. Vomano section

The heavy mineral assemblage comprises the same minerals as observed in the Fluvione section but in very different proportions (Fig. 5). The percentages of epidote and zoisite (4.9%), staurolite (0.5%), sphene (0.2%), and kyanite (0.0%) are strongly reduced, whereas the percentages of apatite (18.5%) and tourmaline (4.1%) are enhanced. Xenotime, monazite, and brookite were not observed. In addition, the amount of micas is strikingly higher in the Vomano section (≤98%) compared to the Fluvione section (≤48%). Sample L1VNS32 could not be counted because it contains almost no transparent grains. Only sample L1VNS42 shows similar percentages as the Fluvione section. This sample was retrieved from an 8 m thick deposit, while the others were derived from thinner beds with thicknesses between 0.5 m to 4.5 m. It is thus possible that this deposit is the product of a bypassing process in the channelized sector that allowed the preservation of its heavy mineral diversity. Like in the Fluvione section, no compositional difference was observed between Laga 1 and Laga 2.

4.3. ^{238}U/^{206}Pb ages

Most ^{238}U/^{206}Pb ages are concordant and plot within error on the Concordia line (Fig. 6A). 18 and 19 detrital zircons of the Laga 1 and Laga 2 units, respectively, show discordant ages. These grains represent either mixed ages, i.e. inheritance of an older core ablated simultaneously with a younger rim, or experienced a Pb-loss during a hydrothermal/metamorphic event. 11 grains required two separate integrations due to ablation of an older core and younger rim, and each of these grains now represent two different ^{238}U/^{206}Pb ages. One grain age (31.9 Ma) in Laga 2 is reverse discordant. All ages were included into the analysis except two grains with common Pb contamination. Both samples of the lower Laga show similar age distributions with several peaks spanning a period from 29.6 Ma to 2590 Ma (Fig. 6B). The largest age population ranges from 223 to 323 Ma and shows a Permian peak at 278 Ma. A second prominent peak centers in the latest Eocene at 37.5 Ma and comprises a period of 29.6 to 45.6 Ma. Several subordinate peaks cover the time ranges of 390–536, 572–1080, 1414–1968, and 2363–2592. Mesozoic ages younger than 200 Ma occur only in Laga 1 (74.5, 167, and 172 Ma). Data is provided in the Appendix, Table A5.

4.4. Zircon fission-track ages

Zircon fission-track ages range from 6.0±2.4 Ma to 316±134 Ma (Appendix, Table A6). Resetting of fission-tracks can be excluded,

Table 1
Recalculated parameters of the framework composition for all samples of this study.

Data set 1

		Sample	Q_t	F	L+Ch	Q_m	F	L_t	L_m	L_{vh}	L_s	NCE	CE	CI	R_g	R_s	R_m
Fluvione section	Laga 1	F1	40	40	20	39	40	21	58	0	42	66	34	0	22	13	65
		F2	38	49	13	29	49	23	58	4	38	75	25	0	2	7	90
		F3	35	56	9	29	56	15	53	0	47	61	39	0	35	9	57
		F4	48	32	20	40	32	28	52	12	36	75	25	0	17	13	70
		F5	31	56	13	28	56	16	87	0	13	87	11	2	1	2	96
		F6	38	48	14	32	48	20	71	5	24	82	16	2	3	6	91
		F7	36	47	17	33	47	20	44	0	56	54	45	1	11	14	75
		F8	40	45	16	32	45	23	48	13	39	69	31	0	14	11	75
		F9	34	48	18	27	48	25	49	0	51	68	30	1	13	14	74
		F10	41	46	13	36	46	18	43	9	49	63	35	2	5	11	84
		F11	43	39	18	40	39	20	42	3	55	50	46	4	25	17	58
		F12	30	64	5	29	64	6	40	0	60	45	55	0	2	5	94
		F13	32	55	13	30	55	16	40	0	60	42	58	0	2	11	87
		F14	36	54	10	34	54	12	54	2	44	68	32	0	2	6	92
		F15	39	48	13	31	48	21	64	4	32	81	19	0	1	6	93
		F16	41	43	16	35	43	22	56	5	39	67	30	3	2	11	87
		AV_{L1}	38	48	14	33	48	19	54	4	43	66	33	1	10	10	81
		SD_{L1}	5	8	4	4	8	5	13	4	13	13	13	1	10	4	13
	Laga 2	F17	33	52	15	29	52	19	65	0	35	67	33	0	2	8	90
		F18	40	51	9	35	51	14	70	0	30	73	27	0	2	4	94
		F19	35	50	15	30	50	20	62	4	35	69	31	0	3	9	89
		F20	45	38	17	38	38	24	70	3	27	73	27	0	0	6	94
		F21	46	34	20	34	34	33	10	0	90	18	79	3	0	26	74
		F22	39	49	13	36	49	16	69	4	27	75	25	0	2	5	93
		F23	47	38	15	41	38	21	52	0	48	56	42	2	2	11	87
		F24	42	39	19	40	39	22	56	0	44	61	39	0	0	11	88
		F25	47	39	14	44	39	17	69	0	31	74	26	0	0	5	94
		F27	46	40	14	41	40	19	73	0	27	76	24	0	1	5	95
		F29	45	44	11	40	44	16	48	2	50	54	46	0	0	8	92
		AV_{L2}	42	43	15	37	43	20	59	1	40	63	36	0	1	9	90
		SD_{L2}	5	6	3	5	6	5	18	2	19	17	16	1	1	6	6
		AV_{L1+L2}	40	46	14	35	46	19	56	3	42	65	34	1	6	9	84
		SD_{L1+L2}	5	8	4	5	8	5	15	4	15	15	14	1	9	5	12

Data set 2

		Sample	Q_t	F	L+Ch	Q_m	F	L_t	L_m	L_{vh}	L_s	NCE	CE	CI
Fluvione section	Laga 1	L1FNS1	39	36	25	34	36	30	22	35	43	62	33	6
		L1FNS4	42	22	36	34	22	44	31	24	46	56	34	10
		L1FNS10	29	23	47	23	23	53	9	13	78	30	66	4
		L1FNS6	48	30	22	40	30	30	27	29	44	60	29	10
		AV_{L1}	39	28	33	33	28	39	22	25	53	52	40	8
		SD_{L1}	8	6	12	7	6	11	10	9	17	15	17	3
	Laga 2	L2FNS13	42	32	27	38	32	30	11	34	54	52	45	2
		L2FNS18	38	28	33	34	28	38	19	21	60	42	45	12
		L2FNS22	37	27	36	34	27	38	13	12	75	30	69	1
		AV_{L2}	39	29	32	35	29	36	15	22	63	42	53	5
		SD_{L2}	2	2	5	2	2	4	4	11	11	11	14	6
Vomano section	Laga 1	L1VNS46	44	31	24	39	31	29	16	27	56	55	45	0
		L1VNS42	45	33	21	39	33	28	34	32	34	74	26	0
		L1VNS25	35	31	34	32	31	37	21	16	64	42	57	1
		AV_{L1}	41	32	27	37	32	32	24	25	51	57	43	0
		SD_{L1}	6	1	7	4	1	5	9	8	15	16	16	1
	Laga 2	L2VNS31	44	28	28	38	28	33	18	21	62	56	44	0
		L2VNS33	43	28	29	38	28	34	26	17	57	46	41	13
		AV_{L2}	43	28	28	38	28	33	22	19	59	51	42	6
		SD_{L2}	1	0	1	0	0	0	6	3	3	7	2	9
		AV_{L1+L2}	40	29	30	35	29	35	21	23	56	51	44	5
		SD_{L1+L2}	5	4	7	5	4	7	8	8	13	13	14	5

because burial temperatures never exceeded 110°C (Bigi et al., 2009) and no indication of resetting was observed although two fission-track ages overlap, within error, with their depositional age. Thus, the age populations represent the pre-depositional cooling and ex-humation history of the source area. Three main age populations fit the age distributions of each sample, which are centered at 16, 34, and 138 Ma for base Laga 1 and at 17, 34, and 102 Ma for top Laga 2 (Fig. 7A, B and Table 3). Fig. 7C shows the fission-track ages of indi-vidual grains plotted against their ^{206}Pb/^{238}U ages. All grains have, within error, fission-track ages younger than their ^{238}U/^{206}Pb age.

5. Discussion

5.1. Provenance of the Laga Formation

5.1.1. Sandstone petrography and heavy mineral analysis

The high abundances of garnet, epidote, staurolite, and kyanite in the heavy mineral assemblage indicate greenschist- to amphibolite-facies metamorphic basement as major source. This is supported by the high amount of medium- to high-grade metamorphic rock fragments in the gross composition. The vast occurrence of carbonate

Table 2

Heavy mineral data for the Fluvione and Vomano sections, normed to 100%. Al = allanite; Ap = apatite; BlueA = blue amphibole; Chl = chloritoid; Cr-S = Cr-spinel; Ep = epidote; Gt = garnet; Ky = kyanite; Oth = others including monazite, brookite, xenotime; Ru = rutile; Sp = sphene; Stau = staurolite; To = tourmaline; undet = undetermined; Zo = zoisite; Zr = zircon.

		Sample	Zr	Ru	To	Sp	Ap	Gt	Ep	Zo	Al	Chl	Stau	Ky	BlueA	Cr-S	Oth	undet	Total
Fluvione section	Laga 1	L1FNS2	0.3	0.9	0.6	2.8	4.4	47.8	26.9	2.5	1.3	1.3	2.8	3.4	4.7	0.0	0.0	0.3	100
		L1FNS4	1.2	3.1	1.9	3.4	4.9	45.4	26.5	3.4	0.9	1.9	3.7	2.5	0.6	0.0	0.3	0.3	100
		L1FNS10	1.2	2.8	1.9	2.8	5.0	55.3	16.8	4.3	0.9	0.9	2.8	1.6	3.1	0.0	0.0	0.6	100
		L1FNS6	1.3	2.9	1.6	4.2	9.7	63.3	9.7	0.6	0.3	0.3	2.9	1.3	1.0	0.0	0.0	0.6	100
	Laga 2	L2FNS13	0.0	3.4	1.7	2.8	6.7	64.7	10.9	2.5	0.8	0.8	2.8	0.8	0.6	0.3	0.3	0.8	100
		L2FNS18	2.1	3.8	4.1	3.8	7.4	66.0	5.6	0.3	0.6	0.9	4.1	0.3	0.0	0.3	0.3	0.3	100
		L2FNS24	1.4	2.4	3.8	2.2	7.6	66.7	10.0	1.4	0.0	0.5	2.4	0.8	0.0	0.3	0.0	0.5	100
		AV$_{Fluvione}$	1.1	2.8	2.2	3.1	6.5	58.4	15.2	2.2	0.7	0.9	3.1	1.5	1.4	0.1	0.1	0.5	100
		SD$_{Fluvione}$	0.7	0.9	1.3	0.7	1.9	9.0	8.5	1.5	0.4	0.5	0.6	1.1	1.8	0.2	0.2	0.2	
Vomano section	Laga 1	L1VNS46	2.0	2.0	4.9	0.0	22.4	66.8	1.5	0.0	0.5	0.0	0.0	0.0	0.0	0.0	0.0	0.0	100
		L1VNS42	0.0	4.3	2.4	0.5	16.1	55.9	13.7	1.4	0.9	1.4	1.4	0.0	0.5	0.5	0.0	0.9	100
	Laga 2	L2VNS31	0.0	0.0	5.0	0.5	19.4	69.2	2.0	0.0	0.0	2.5	0.0	0.0	0.5	0.5	0.0	0.5	100
		L2VNS33	0.4	3.8	4.3	0.0	16.2	71.8	0.4	0.4	0.0	0.9	0.4	0.0	0.0	0.4	0.9	0.0	100
		AV$_{Vomano}$	0.6	2.5	4.1	0.2	18.5	65.9	4.4	0.5	0.4	1.2	0.5	0.0	0.2	0.3	0.2	0.4	**100**
		SD$_{Vomano}$	0.9	2.0	1.2	0.3	3.0	7.0	6.3	0.7	0.5	1.0	0.7	0.0	0.3	0.2	0.4	0.5	

clasts, especially dolostones, implies an additional carbonate source. Low amounts of Cr-spinel and serpentinites indicate a small contribution from mafic material.

To address possible sources of sedimentary recycling, the compositional data of the lower Laga is compared to the Chattian to Tortonian foredeep deposits (Macigno-Modino, Cervarola,
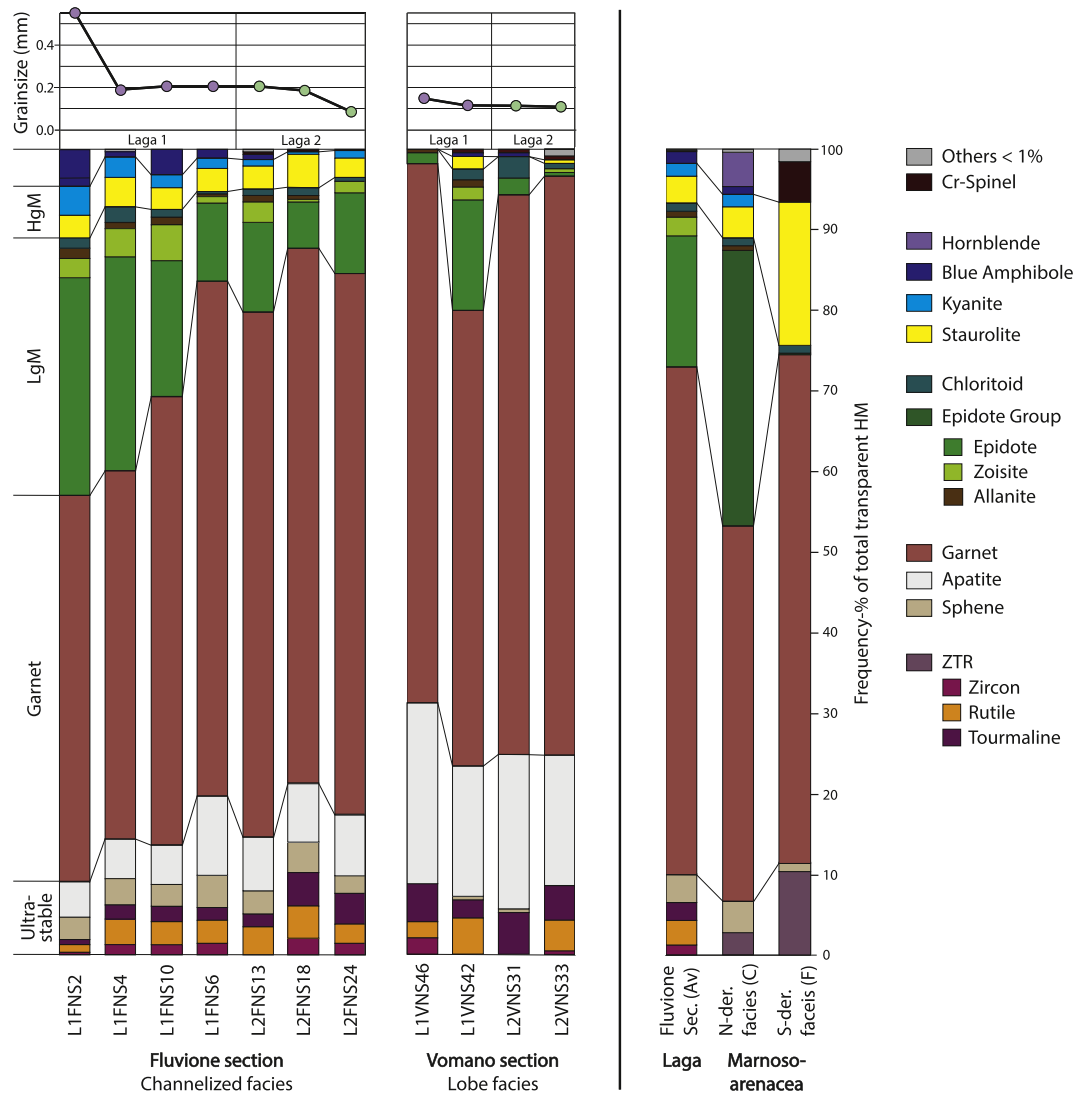
Fig. 5. Heavy mineral spectra of the Fluvione and Vomano sections with sample grain sizes. The composition of the Fluvione section is compared to the north-derived (petrofacies C, Alpine source) and south-derived (petrofacies F, Apenninic source) Serravallian to Tortonian Marnoso-arenacea Fm.
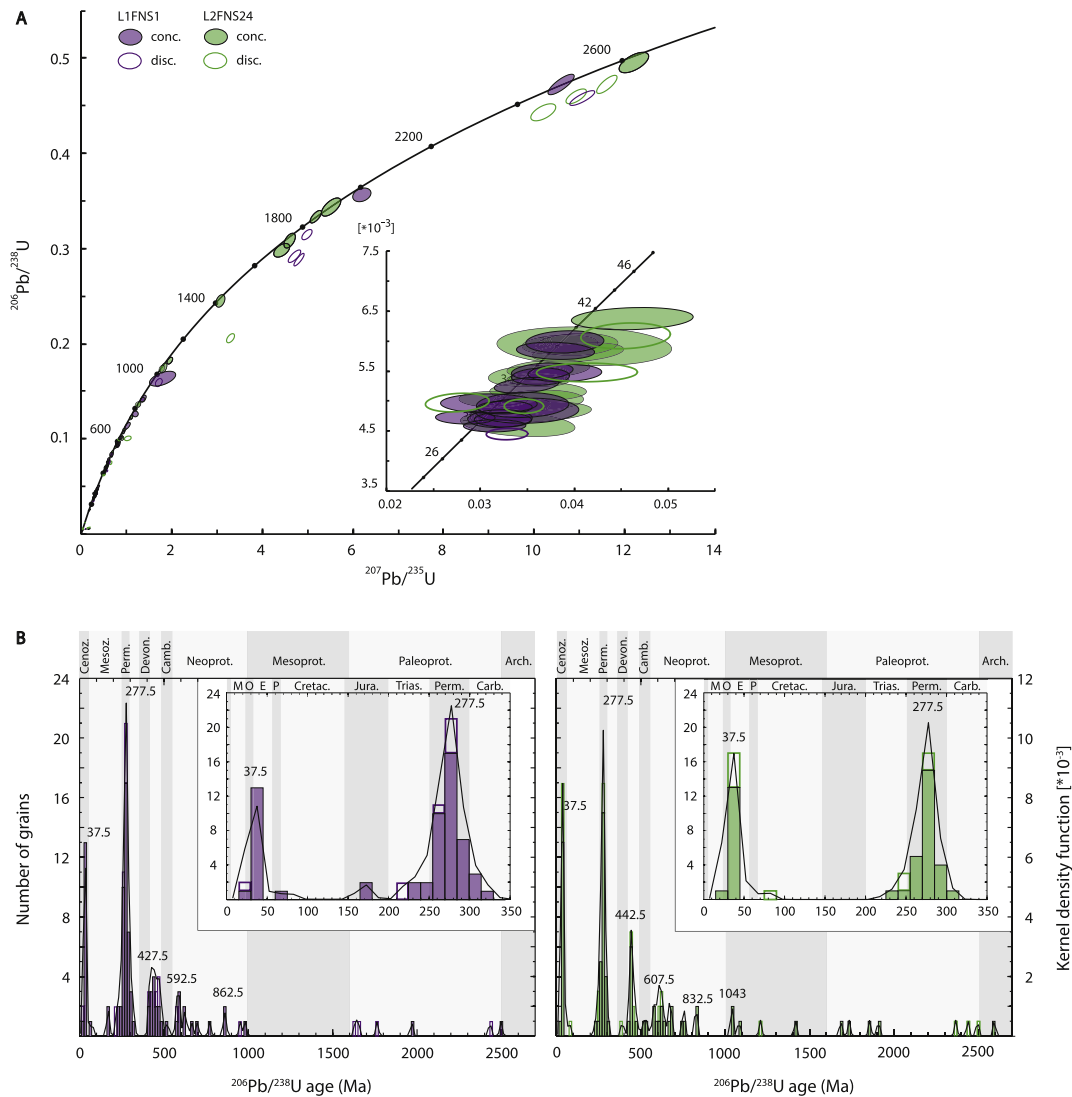
Fig. 6. Detrital zircon $^{238}U/^{206}Pb$ ages of base Laga 1 (sample L1FNS1) and top Laga 2 (sample L2FNS24). **A** Concordia plot with 2σ-standard deviation. Filled ellipses represent concordant ages, empty ellipses discordant ages. Inset shows a close up of the ages between 26 and 46 Ma. **B** Histograms and probability density functions (black, scale on right y-axis for both plots) with major peak ages (bin size = 15 Ma, bandwidth = 8). Filled boxes represent concordant ages, empty boxes discordant ages.

Marnoso-arenacea Fms), (sub-)Ligurian Flysch (Pietraforte, Ostia, Monte Gottero, Monghidoro, Petrignacola Fms), and to the epiligurian Bismantova Fm (Fig. 8 and Appendix, Tables A7 and A8). Petrographic dissimilarities are also visualized as Multidimensional Scaling maps (Vermeesch and Garzanti, 2015) (Appendix, Fig. A3). Given the relative large variations of the petrographic features of the lower Laga, it is necessary to define a threshold over which its compositional differences relative to other units can be considered significant. The composition of the lower Laga shows standard deviations of maximum 15% (SD_{L1+L2}, Table 1). We thus consider a difference >15% as significant for the petrographic composition. The relative differences between the compositional indices of all (sub-)Ligurian Flysch deposits and of the Laga Fm are larger than 15% (Fig. 8). The differences of the Chattian to Tortonian foredeep deposits and the epiligurian Bismantova Fm relative to the Laga Fm are, instead, for the most part smaller than 15%. Exceptions are the enrichment in metamorphic clasts of the Macigno and Modino Fm (≥+25%) and their depletion in sedimentary clasts (≥ −17%) (Fig. 8C). Moreover, the Cervarola Fm is significantly enriched (+24%) in the ultrastable minerals ZTR+Sphene (Fig. 8D). The Marnoso-arenacea Fm is characterized by several petrofacies that

correspond to northern and southern sources (Gandolfi et al., 1983; Gandolfi et al., 2007). Both petrofacies are enriched in sedimentary clasts (≥+14%) relative to the lower Laga, but their heavy mineral spectra are similar with a few exceptions (Figs. 5 and 8D): the south-derived petrofacies contain higher amounts of Cr-Spinel (+5.0%), less epidote (−18%) and no blue amphibole. The Langhian to Serravallian north-derived petrofacies are depleted in low-grade metamorphic minerals (≥ −9%) and blue amphibole. The Tortonian unit contains more epidote (+16%). The Bismantova Fm also shows a very similar heavy mineral spectrum as the Laga but is depleted in metamorphic clasts.

In case of recycling, the Laga Fm should yield a similar composition to its sedimentary source but in different proportions due to diagenetic and weathering effects. The composition should yield a higher quartz content, abundant siliciclastic rock fragments, an enrichment of ultrastable heavy minerals, and rounded rather than angular grains (Hubert, 1962; Folk, 1974; Pettijohn et al., 1987; Zuffa, 1987). Nevertheless, the effects of recycling on the detrital composition could be limited, or negligible, if recycling occurred penecontemporaneously within the basin itself due to remobilization in a tectonically active setting. Hence, except for the Bismantova Fm and the Tortonian
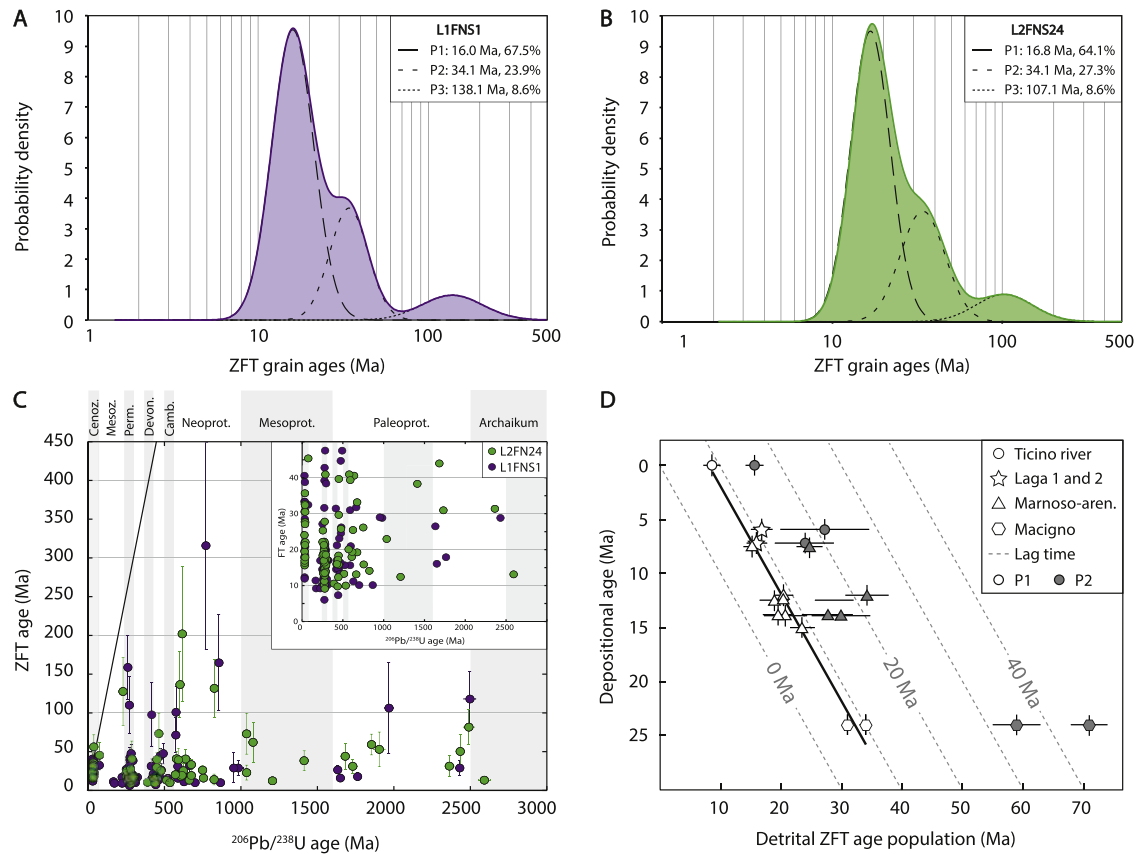
Fig. 7. A, B) Probability-density plot of detrital zircon fission-track ages with main age populations for Laga 1 (left) and Laga 2 (right). **C)** Zircon fission-track ages vs. ^{238}U/^{206}Pb ages. Black line represents equal fission-track and U-Pb ages. Error bars are 1σ for fission-track ages and 2σ for ^{238}U/^{206}Pb ages. Inlet shows a close-up of data with fission-track ages between 0 and 50 Ma. **D)** Comparison of the lower Laga detrital zircon fission-track age populations (P1, P2) with the Ticino river, the Marnoso-arenacea Fm (Bernet et al., 2001) and the Macigno Fm (Dunkl et al., 2001). Empty symbols represent the youngest age populations (P1), filled symbols ages of the second populations (P2). Error bars show 1σ-standard deviations for ZFT populations and 1 Ma uncertainties for depositional ages. Contour lines show constant lag times. The black line indicates the average lag time of 7.4 ± 1.3 Ma for the mid-Miocene to present exhumation periods in the Alpine hinterland (Bernet et al., 2009).

north-derived Marnoso-arenacea Fm, which show similar petrographic compositions to the lower Laga, recycling of Apenninic turbidite and (sub-)Ligurian Flysch deposits can be ruled out.

This conclusion is consistent with structural and stratigraphic observations that indicate that the Ligurian front along the northern Apennines was already close to its modern position during the Messinian (Fig. 2). This is constrained by piggyback basins sitting mainly on top of Ligurian units in a position close to and along the modern Apenninic front, where they were filled by Messinian evaporitic sediments (Rossi et al., 2002; Brogi and Liotta, 2008). Such an advanced position for the Messinian Ligurian front implies that the Cenozoic terrigenous deposits in the northern Apennines were already largely overridden by the Ligurian nappe. Thermochronometric data indicate that the western northern Apennines, which are at present still extensively covered by the Ligurian nappe (Fig. 1), started to exhume most likely around 4 Ma ago (Malusà and Balestrieri, 2012).

Table 3
Detrital zircon fission-track age populations with 1σ- standard deviation and percentage of data representing each peak (Frac. (%)), calculated using Binomfit (Brandon, 2002). Lag time and exhumation rates are calculated using the youngest age population (P1).

	L1FNS1	L2FNS24
P1 ± 1σ (Ma); Frac. (%)	16.0 ± 0.9 (67.5)	16.8 ± 1.1 (64.1)
P2 ± 1σ (Ma); Frac. (%)	34.1 ± 1.8 (23.9)	34.0 ± 2.1 (27.3)
P3 ± 1σ (Ma); Frac. (%)	138.1 ± 4.1 (8.6)	101.7 ± 4.1 (8.6)
Depositional age (Ma)	7.37	5.6
P1 lag time (Ma)	8.6	11.2
Exhum. rate (mma^{-1})	0.87	0.67

This precludes recycling of material from this region at 6 Ma. The eastern northern Apennines, which currently expose the Chattian to Tortonian terrigenous units (Fig. 1), started to exhume between 6 and 4 (Zattin et al., 2002; Thomson et al., 2010). These units could have been sources of recycled material for the Laga Basin only if they were already at the surface by the early Messinian. This would require erosion of a few km-thick Ligurian nappe (Reutter et al., 1983; Zattin et al., 2002; Thomson et al., 2010) over less than 1 Ma, if erosion started around 6 Ma. Yet, given its external position, the Marnoso-Arenacea Fm could have been only partly or not at all overridden by the Ligurian nappe in the Messinian. It is thus a possible source for the Laga Basin, as further discussed in Section 5.1.4.

The sole source of metamorphic rock fragments in modern river- and beach sands draining the Northern and Central Apennines is the Alpi Apuane metamorphic complex (Garzanti et al., 2002). Yet, this complex was covered by Tuscan and Ligurian nappes until the Pliocene and must therefore be excluded as source region (Bernini and Papani, 2002, and references therein). In the Alps, instead, ortho- and paragneisses of the Austroalpine, Lower Penninic, and Middle Penninic units carrying abundant staurolite, garnet, and kyanite are widely exposed since the middle Cenozoic, while dolomite is characteristic for the Southern Alps. Blue amphibole is present in the Western Alps as well as, for example, in the Misox and Zermatt-Saas zones, which lie close to the Lepontine dome (Bocquet, 1974; Oberhänsli, 1986). Metabasaltic rocks, greenschist-facies metagranites, and amphibolite lenses interbedded with paragneisses are commonly found in the Alpine realm and represent possible sources for epidote. Ophiolitic rocks are present in the Central Alps as for instance the Val
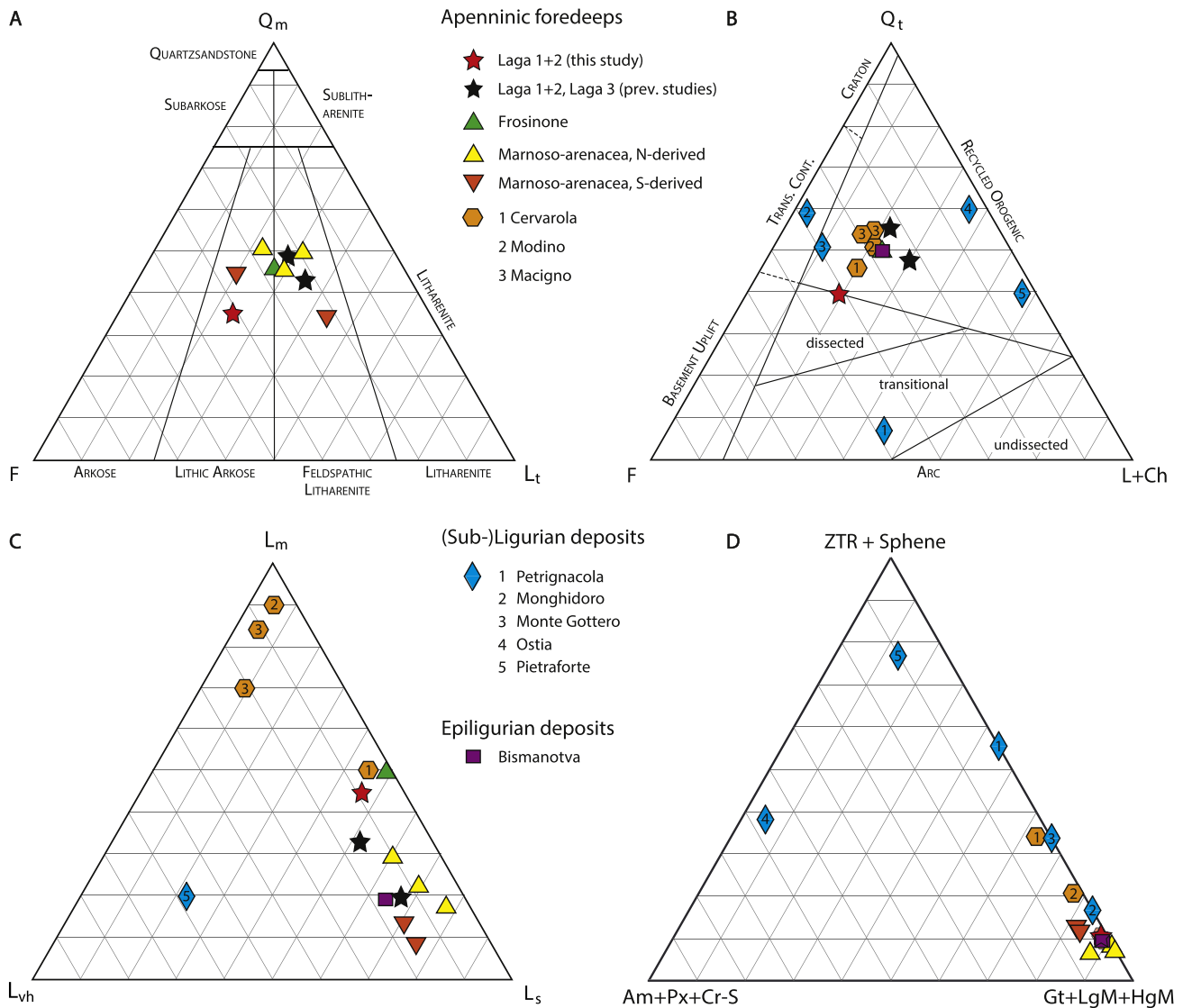
Fig. 8. A-C) Ternary diagrams for the lower Laga Fm, pre-Messinian Apenninic foredeep deposits, and selected (sub)-Ligurian Flysch and epiligurian deposits (see Fig. 1 for locations). Categories after Folk (1974) and Dickinson (1985) for Fig. 8A and B, respectively. **D)** Heavy minerals ternary diagram. A high content in ZTR+Sp would indicate recycled sediments, whereas high contents in amphibole (Amph), pyroxene (Px), and Cr-spinel (Cr-S) indicate contributions of ophiolites. Sediments plotting close to the garnet (Gt)+high- and low-grade minerals (HgM, LgM) corner are derived from a metamorphic source.

Malenco units east of the Bergell plutonic complex. The sedimentary composition of the lower Laga thus suggests a major Alpine provenance located in the Alpine realm, while recycling of the Oligocene-to-Middle Miocene Apenninic turbidite deposits can be excluded.

5.1.2. Zircon fission-track and $^{238}U/^{206}Pb$ ages

Three dominant age populations characterize the detrital zircon fission-track ages of the lower Laga. The oldest peak (P3) with grain ages >66 Ma is broad and corresponds to rocks unaffected by Cenozoic metamorphism but which may have experienced Cretaceous metamorphism. Today, such rocks are exposed in the Austroalpine cover nappes of the Eastern Alps, in the Southern Alps, in the southern Western Alps, and in the Apennines (Fig. 1). The second age population P2, centered at 34 Ma, can be related to the Cenozoic metamorphic overprint currently recorded in the Western and Central Alps and to the Oligocene Periadriatic magmatism (Hunziker et al., 1989, 1992; Hurford et al., 1989; Seward and Mancktelow, 1994; Bernet et al., 2001; Malusà et al., 2005; Bigot-Cormier et al., 2006). The youngest age population is derived from a source area yielding present-day bedrock zircon fission-track ages similar to the estimated lag time of the age population (Bernet et al.,

2001). The lag time is the difference between the time of closure of the fission-track system and the depositional age of the detrital sample, if sedimentary transport time is neglected (Garver et al., 1999). The youngest peaks P1, centered at 16 Ma for base Laga 1 and at 16.8 Ma for top Laga 2, yield lag times of ~9 and ~11 Ma, respectively (Table 3). They must thus be derived from an area with present-day bedrock ages in the range of 8–15 Ma, if steady-state exhumation is assumed. In the Apennines, such young zircon fission-track ages are restricted to the Alpi Apuane complex (Fellin et al., 2007) and to the Tortonian Marnoso-arenacea Fm, which contains an age population centered at 15 Ma (Bernet et al., 2001). The other Chattian to Serravallian Apenninic foredeep deposits yield ages older than 20 Ma (Bernet et al., 2001, 2009; Dunkl et al., 2001). In the Alpine realm, among the areas draining south-wards, fission-track ages younger than 15 Ma are currently observed in the Western and Central Alps and in the Western Tauern window.

The $^{238}U/^{206}Pb$ ages vary from 28 Ma to 2610 Ma and cover the main magmatic-metamorphic events observed in Alpine crystalline basement nappes. The small Precambrian age populations, varying from ~900 to 2610 Ma, correspond to several megacycles of crustal growth, supercontinent assimilation, and break up observed in

European basement rocks (Gebauer et al., 1989; Schaltegger and Gebauer, 1999; Linnemann et al., 2008). The late Neoproterozoic to early Cambrian populations can be related to the Cadomian orogenic events at the Gondwana active margin, while the Ordovician to Silurian peak can be associated with crustal extension coupled to the opening of the Rheic ocean and initial rifting of the Paleotethys (von Raumer et al., 2003, 2013; von Raumer and Stampfli, 2008;). The Devonian and Carboniferous zircon ages represent early Variscan subduction and the following continent collision (Schaltegger and Gebauer, 1999; Marotta and Spalla, 2007; Spalla et al., 2014). The few grains with Triassic-Permian, Jurassic (~177 Ma), and late Cretaceous (~75 Ma) ages can be assigned, respectively, to magmatic activities coupled to post-Variscan extension during the break-up of Pangaea, to the subsequent opening of the Alpine Tethys, and to andesitic volcanism during plate convergence mainly recorded in the Southern Alps (Gebauer, 1993; Waibel, 1993; Marotta and Spalla, 2007; Beltrán-Triviño et al., 2013). Finally, the Cenozoic ages (29–43 Ma) can be associated to the Periadriatic magmatic activity (29–43 Ma; Mayer et al., 2003; Schaltegger et al., 2009, and references therein; Schoene et al., 2012; Gianola et al., 2014) and to the Veneto Volcanic Province in NE Italy (30.5–51.1 Ma; Visonà et al., 2007). However, the Veneto Volcanic Province is mainly characterized by mafic alkaline lavas with zircon megacrysts showing U-Pb ages between 42 and 51.1 Ma (Visonà et al., 2007). Since ages in this range are absent in the Laga Fm, a contribution from this source seems unlikely. Moreover, the province was a possible source for the Venetian-Friulian Basin, which was disconnected from the Messinian Apenninic foreland (Stefani et al., 2007). Thus, while the Oligocene ages can refer to any of the Alpine magmatic/volcanic provinces, the Eocene ages can only be derived from the Adamello complex and related volcanic products.

5.1.3. Primary source area: the Alps

Zircon fission-track data of Oligocene to Miocene sediments from both the pro- and retroside of the Alps as well as from modern rivers draining the Alpine hinterland reveal an average lag time of ~7.4 ± 1.3 Ma for the youngest peak (Bernet et al., 2009, and references therein), which is similar within error to the lag times of ~9 and ~11 Ma observed in the lower Laga (Fig. 7D). Assuming exhumational steady-state, a geothermal gradient of 30°C km^{-1}, a closure temperature of 240°C (Brandon et al., 1998), and a surface temperature of 15°C, the lag times of the lower Laga correspond to an average exhumation rate of ~0.8 mma^{-1}. This value is in good agreement with the average long-term exhumation rate of 0.7 ± 0.1 mma^{-1} of the Alps (Bernet et al., 2009; Campani et al., 2010). In the Late Miocene, structural and stratigraphic data reveal that the Southern Alps were propagating southwards and uplifting by the activation of basement-rooted thrusts and the re-activation of major structures, such as the South Giudicarie system (Schönborn, 1992; Castellarin and Cantelli, 2000). Thermochronometric data indicate that the Adamello complex was uplifting and rapidly exhuming between 10 and 6 Ma (Reverman et al., 2012). Moreover, the abundance of dolostone lithics in the Laga is consistent with large contributions from the Southern Alps. Hence, these observations are all consistent with the Central and Southern Alps as major source areas for the lower Laga turbiditic deposits.

5.1.4. Reworking of the Marnoso-arenacea

The Central Alps were also the source of detritus for the Marnoso-arenacea Fm, whose N-derived facies have a compositional signature similar to the lower Laga. The recycling of the Burdigalian to Serravallian inner Marnoso-arenacea (Ricci Lucchi, 1986) can be ruled out based on the thermochronologic data. They indicate that: (1) before the Messinian, the inner stage deposits of the Marnoso-arenacea had already been overridden by the Ligurian nappe north and west of the Laga Basin (Zattin et al., 2002), and (2) its youngest age populations are older than those of the Laga arenites (Fig. 7D). Thus, an Apenninic source for the lower Laga could have been only unlithified deposits

related to the outer stage of Marnoso-arenacea Fm (Castellarin et al., 1978; Castellarin et al., 1982). Yet, several structural, stratigraphic, and sedimentary lines of evidence are inconsistent with recycling of this unit via subaerial exposure to weathering and erosion (Chiocchini and Cipriani, 1992). Firstly, the highly immature textural features of the lower Laga are indicators of first-cycle detritus rather than reworking, as for instance the low content of sedimentary noncarbonate clasts, the angular shape of the grains, the grain-supported texture, and the high organic content. Secondly, the occurrence of a continuous record of the outer stage Marnoso-arenacea sequence (Roveri et al., 2002, and references therein) is also inconsistent with the recycling hypothesis. Finally, evidence of large-scale erosion and subaerial exposure of the Marnoso-arenacea Basin is only associated with the later stage of the Messinian sea level drop during deposition of the upper Laga Fm (Roveri et al., 2001). Although these observations exclude recycling by subaerial exposure, they do not rule out intrabasinal reworking. Sediment remobilization could have occurred soon after the deposition due to the intense tectonic activity that caused the progressive shift of the Marnoso-arenacea Basin to a wedge-top position and eventually its closure. This process of sediment cannibalization would result in provenance signatures undistinguishable from those of detritus transported directly from the Alps to the foredeep. Precursors of a possible transfer system involving the outer stage deposits of the Marnoso-arenacea are the conglomerates and the coarse, immature sands that typify the "mixed deltaic/turbidite systems" constituting the main depositional systems of this portion of the Marnoso-arenacea Fm (Mutti et al., 2002).

5.2. Influence of sedimentary transport on sandstone composition

Heavy mineral assemblages of sandstones are affected by three main processes, namely dissolution causing partial or complete loss of certain minerals during weathering and burial diagenesis, abrasion during transport, and sorting controlled by hydrodynamic conditions (Morton and Hallsworth, 1999). Particle sorting is particularly effective within turbidite systems like the Laga complex where the transport mode changes along the basin from a high-velocity flow with both bed and suspended load to a low-velocity flow with suspension load (Milli et al., 2007; Marini et al., 2015). We sampled both the proximal channelized and the distal lobe facies of the lower Laga turbidites to directly study physical sorting along the sediment route. The depletion of heavy minerals in the Vomano section compared to the Fluvione section is evidence of sorting, since heavy minerals are preferentially enriched in the bedload, whereas light minerals like quartz and feldspar are transported to the distal facies in suspension (e.g., Garzanti and Andò, 2007). Furthermore, the relative higher abundance of platy, elongated, and small heavy minerals with lower densities (tourmaline, biotite, and apatite) and the low concentration of rounded ultradense minerals like sphene and zircons in the lobe facies directly mirror different hydraulic transport behavior of the minerals ("concept of settling equivalences" of Reid and Frostick, 1994), which depends on grain density, size, and shape (Morton and Hallsworth, 1999). The observed depletion in total heavy mineral diversity of the Vomano facies is thus interpreted to be caused solely by hydraulic processes rather than reflecting a provenance signal or diagenetic effects. Hence, despite the limited number of samples, we can conclude that samples from distal parts of turbidite systems may show an incomplete signal of the hinterland lithology, especially if they are derived from relatively thin beds. Furthermore, not only the heavy mineral diversity but also the total yield is depleted by hydraulic sorting which inhibits zircon fission-track and U-Pb dating.

5.3. Sediment- dispersal pattern in the early Messinian Adriatic foreland

The turbidite facies association of the lower Laga is characterized by immature and coarse-grained sands, channelized facies and amalgamated beds in the proximal sector of the basin coupled with fine-

grained sands and large lobes in the distal sector. The notable qualitative differences in the heavy mineral assemblages of the proximal and distal zones indicate severe sediment sorting processes along the short distance of the Laga Basin, although a more extensive data set would be needed for a definitive conclusion. The proximal facies are sand-rich deposits prevalently related to hyperpycnal flows that typically form during floods at the mouth of particle-laden rivers especially in tectonically active mountain ranges and during submarine slides of instable slope sediments (e.g., Mulder et al., 2003; Mutti et al., 2003, and references therein). Such a high-velocity transport mode can funnel sediments along submarine channels and transport coarse sand with no or little sorting effects along their pathway for several hundreds of kilometers (Brunner et al., 1999; Dadson et al., 2005). Thus, the sedimentological features of the lower Laga do not restrict the possible source areas to the Apennines. If the physiography of the Adriatic foreland was such that massive amounts of sediments delivered along the front of the Alps could have been funneled along channels located either at the front or on the top of the Apenninic wedge, then the Alpine detritus could have travelled for about 300 km all the way to the Laga Basin (Fig. 2).

The Tortonian, outer stage facies of the Marnoso-arenacea share some common features with the lower Laga as they also consist of immature sand-rich, coarse-grained turbidite deposited in a basin that eventually became confined by thrusts until its closure (Mutti et al., 2002; Roveri et al., 2002; Marini et al., 2015). These observations imply that the Marnoso-arenacea foredeep turned into a wedge-top basin during its outer stage and that the Alpine-derived detritus filling this basin crossed the Adriatic foreland and overrode the Apenninic wedge. Thus, the topographic gradient in the Adriatic foreland must have been downslope from the Alps to the outer wedge-top of the Northern Apennines and all the way south to the foredeep of the Central Apennines, where the Frosinone Fm was deposited, already during the Tortonian. In the early Messinian, the Laga Basin started to be filled through entry points located to the north by sediments derived directly from the Alps along a route bypassing the Pesaro-Ancona high, which was starved of terrigenous sediments and which separated the basin from the northern Apenninic foreland and from the Alps. It is unclear whether this high was a topographic barrier high enough to impede the transit of hyperpycnal flows from the north to the Laga Basin, whether it was bypassed acting simply as a transfer zone of no-deposition, or whether the sediments were routed along a more internal passage. Additionally, sediments shortly stored in the outer Marnoso-arenacea Basin could have been reworked down into the Laga Basin. At the beginning of the deposition of Laga 2, the entry points to the Laga Basin shifted from N to NW along the western shoulder of the basin without changes of the main sediment source. Alpine clastic detritus was also deposited in the early Messinian satellite basins, which were additionally supplied by locally sourced Apenninic detritus. Thus, it is very likely that the Alpine detritus filled the northern Adriatic foreland, drowning locally its incipient thrusts and branching southwards along a system of elongated, tectonically controlled wedge-top depozones. Once channeled on the wedge-top, the Alpine detritus found its way into several directions: partly to the northern satellite basins, the majority into the Laga Basin, and finally all the way to the southern satellite basins (Fig. 2). Some of the wedge-top channels feeding the Laga from the west might also have been ephemeral minor basins. The presence of multiple entry points is consistent with the interfingering and/or mixing of distally and locally derived detritus that characterizes the satellite basins. Mixing could also have occurred in the northern sector of the Laga Basin. Thus, the early Messinian change in the physiography of the Apenninic foreland basin has affected only the routing system of the sediments but not the major sediment source which remained the Alpine realm (Garzanti and Malusà, 2008). Conclusively, the early Messinian Adriatic foreland was still starved of Apenninic detritus, while Alpine detritus overfilled it to north and overspilled onto the Apenninic foredeep. Thus, erosion of the Apenninic

orogen was likely still modest. This implies a limited extension and height of its surface topography and an additional control of the Apenninic foredeep geometry besides topographic loading (Royden et al., 1987).

6. Conclusion

The combination of heavy mineral analysis, sandstone petrography, and detrital zircon U-Pb and fission-track dating identifies the Central and Southern Alps as major sources for the early Messinian turbidites of the Laga Basin. Recycling of Apenninic Chattian to Serravallian arenites is ruled out based on their compositional and textural features, detrital age signals and burial histories. The Central Alps provided metamorphic detritus and young fission-track ages of ~16 Ma, while the Southern Alps, including the Adamello batholith, were the sources of dolostone lithics and Cenozoic U-Pb ages. Detritus derived from the Adamello complex in the Adriatic foredeep is here documented for the first time by the presence of a main ~43 Ma old detrital zircon population.

The Laga Basin was the outermost depozone of the central Apenninic foreland whose sediment-dispersal system was connected to and fed by the Alps most likely through wedge-top basins and channels that acted as transfer zones. The early Messinian satellite basins north and south of the Laga are evidences of such a transport route. Intrabasinal reworking of the outer stage of the Marnoso-arenacea may have contributed to the sediment supply of the Laga and satellite basins.

No compositional difference was observed between the pre- (Laga 1) and syn-evaporitic (Laga 2) sedimentary successions. Hence, the observed shift in paleocurrent at the transition between these sequences rather reflects a stronger confinement of the basin topography due to thrust activity than a provenance signal (i.e., growth of the Acquasanta anticline). The sediment transport pathway might have shifted to a more internal position with the sedimentation of Laga 2, but the main source area was not affected by the onset of the Messinian salinity crisis.

Notable qualitative differences in the heavy mineral assemblages of the proximal channelized and distal zones of the basin suggest severe sediment sorting processes during turbidite transport within the basin. Because the distal facies shows a much more reduced heavy mineral spectrum, and therefore an incomplete provenance signal, the proximal facies of turbiditic sediments should be preferred in provenance studies.

Supplementary data to this article can be found online at https://doi.org/10.1016/j.sedgeo.2017.09.016.

References

Amendola, U., Perri, F., Critelli, S., Monaco, P., Cirilli, S., Trecci, T., Rettori, R., 2016. Composition and provenance of the Macigno Formation (Late Oligocene-Early Miocene) in the Trasimeno Lake area (Northern Apennines). Mar. Pet. Geol. 69, 146–167.

Argnani, A., Ricci Lucchi, F., 2001. Tertiary siliciclastic turbidite systems of the Northern Apennines. In: Vai, G.B., Martini, I.P. (Eds.), Anatomy of an Orogen: the Apennines and Adjacent Mediterranean Basins. Springer, Netherlands, pp. 327–350.

Argnani, A., Fontana, D., Stefani, C., Zuffa, G.G., 2006. Palaeogeography of the Upper Cretaceous-Eocene carbonate turbidites of the Northern Apennines from provenance studies. In: Moratti, G., Chalouan, A. (Eds.), Tectonics of the Western Mediterranean and North Africa. Geological Society, London, Special Publication Vol. 262 (1), pp. 259–275.

Balestrieri, M.L., Abbate, E., Bigazzi, G., 1996. Insights on the thermal evolution of the Ligurian Apennines (Italy) through fission-track analysis. J. Geol. Soc. 153 (3), 419–425.

Barbieri, C., Bertotti, G., Di Giulio, A., Fantoni, R., Zoetemeijer, R., 2004. Flexural response of the Venetian foreland to the Southalpine tectonics along the TRANSALP profile. Terra Nova 16, 273–280.

Barchi, M., Marroni, M., Barsella, M., Bizzarri, R., Botti, F., Meneghini, F., Pandolfi, L., Passeri, L., Pazzaglia, F., 2007. Note illustrative del Foglio 310 – Passignano sul Trasimeno. Carta Geologica d'Italia, scale 1: 50.000. Servizio Geologico d' Italia.

Bartolini, C., 1999. An overview of Pliocene to present-day uplift and denudation rates in the Northern Apennine. Geol. Soc. Lond., Spec. Publ. 162 (1), 119–125.

Beltrán-Triviño, A., Winkler, W., Quadt, A., 2013. Tracing Alpine sediment sources through laser ablation U–Pb dating and Hf isotopes of detrital zircons. Sedimentology 60 (1), 197–224.

Benini, A., De Nardo, M.T., Severi, P., Borsetti, A.M., Negri, A., Vaiani, S.C., 2009. Note illustrative del Foglio 238 – Passignano sul Trasimeno. Carta Geologica d'Italia, scale 1: 50.000. Servizio Geologico d' Italia.

Berger, A., Thomsen, T.B., Ovtcharova, M., Kapferer, N., Mercolli, I., 2012. Dating emplacement and evolution of the orogenic magmatism in the internal Western Alps: 1. The Miagliano Pluton. Swiss J. Geosci. 105 (1), 49–65.

Bernet, M., Zattin, M., Garver, J.I., Brandon, M.T., Vance, J.A., 2001. Steady-state exhumation of the European Alps. Geology 29 (1), 35–38.

Bernet, M., Brandon, M., Garver, J., Balestieri, M.L., Ventura, B., Zattin, M., 2009. Exhuming the Alps through time: clues from detrital zircon fission-track thermochronology. Basin Res. 21 (6), 781–798.

Bernini, M., Papani, G., 2002. La distensione della fossa tettonica della Lunigiana nord-occidentale (con Carta Geologica alla scala 1:50,000). Boll. Soc. Geol. Ital. 121 (3), 313–341.

Bigi, G., Castellarin, A., Coli, M., Dal Piaz, G.V., Sartori, R., Scandone, P., 1990. Structural model of Italy Sheet N. 1. 1:500'000. Consiglio Naz. Ricerche. Progetto Finalizzato Geodinamica. SELCA, Florence, Italy.

Bigi, G., Coli, M., Cosentino, D., Dal Piaz, G.V., Parotto, M., Sartori, R., Scandone, P., 1992a. Structural model of Italy Sheet N. 3. 1:500'000. Consiglio Naz. Ricerche. Progetto Finalizzato Geodinamica. SELCA, Florence, Italy.

Bigi, G., Coli, M., Cosentino, D., Parotto, M., Praturlon, A., Sartori, R., Scandone, P., Turco, E., 1992b. Structural model of Italy Sheet N. 4. 1:500'000. Consiglio Naz. Ricerche. Progetto Finalizzato Geodinamica. SELCA, Florence, Italy.

Bigi, S., Costa Pisani, P., Milli, S., Moscatelli, M., 2003. The control exerted by pre-thrusting normal faults on the Early Messinian foredeep evolution, structural styles and short-ening in the Central Apennines (Lazio-Abruzzo area, Italy). Studi Geologici Camerti, Volume Speciale 17–37.

Bigi, S., Milli, S., Corrado, S., Casero, P., Aldega, L., Botti, F., Moscatelli, M., Stanzione, O., Falcini, F., Marini, M., Cannata, D., 2009. Stratigraphy, structural setting and burial history of the Messinian Laga basin in the context of Apennine foreland basin system. Journal of Mediterranean Earth Sciences 1, 61–84.

Bigi, S., Casero, P., Ciotoli, G., 2011. Seismic interpretation of the Laga basin; constraints on the structural setting and kinematics of the Central Apennines. J. Geol. Soc. 168 (1), 179–190.

Bigot-Cormier, F., Sosson, M., Poupeau, G., Stéphan, J.-F., Labrin, E., 2006. The denudation history of the Argentera Alpine External Crystalline Massif (Western Alps, France-Italy): an overview from the analysis of fission tracks in apatites and zircons. Geodin. Acta 19 (6), 455–473.

Boccaletti, M., Ciaranfi, N., Cosentino, D., Deiana, G., Gelati, R., Lentini, F., Massari, F., Moratti, G., Pescatore, T., Ricci Lucchi, F., Tortorici, L., 1990. Palinspastic restoration and paleogeographic reconstruction of the peri-Tyrrhenian area during the Neogene. Palaeogeogr. Palaeoclimatol. Palaeoecol. 77 (1), 41–50.

Bocquet, J., 1974. Blue amphiboles of the Western Alps. Chemistry and physical characters. Schweiz. Mineral. Petrogr. Mitt. 54, 425–448.

Borsi, S., Del Moro, A., Sassi, F., Zirpoli, G., 1979. On the age of the Vedrette di Ries (Rieserferner) massif and its geodynamic significance. Geol. Rundsch. 68 (1), 41–60.

Bortolotti, V., Principi, G., Treves, B., 2001. Ophiolites, Ligurides and the tectonic evolution from spreading to convergence of a Mesozoic Western Tethys segment. In: Vai, G.B., Martini, I.P. (Eds.), Anatomy of an Orogen: The Apennines and adjacent Mediterranean basins. Kluwer Academic Publishers, Netherlands, pp. 151–164.

Brandon, M.T., 2002. Decomposition of mixed grain age distributions using Binomfit. On Track 24 (8), 13–18.

Brandon, M.T., Roden-Tice, M.K., Garver, J.I., 1998. Late Cenozoic exhumation of the Cascadia accretionary wedge in the Olympic Mountains, northwest Washington State. Geol. Soc. Am. Bull. 110 (8), 985–1009.

Brogi, A., Liotta, D., 2008. Highly extended terrains, lateral segmentation of the substra-tum and basin development: the Middle-Late Miocene Radicondoli Basin (inner northern Apennines, Italy). Tectonics 27 (TC5002), 1–20.

Brunner, C.A., Normark, W.R., Zuffa, G.G., Serra, F., 1999. Deep-sea sedimentary record of the late Wisconsin cataclysmic floods from the Columbia River. Geology 27 (5), 463–466.

Bürgi, A., Klötzli, U., 1990. New Data on the Evolutionary History Of The Ivrea Zone (Northern Italy). 56(130). Bulletin der Vereinigung Schweizerischer Petroleumgeologen und Petroleumingenieure, pp. 49–70.

Calamita, F., Centamore, E., Chiocchini, U., Deiana, G., Micarelli, A., Potetti, M., Romano, A., 1979. Analisi dell'evoluzione tettono-sedimentaria dei Bacini Minori torbiditici del Miocene medio-superiore nell'Appennino umbro-marchigiano e laziale-abruzzese: il Bacino di Camerino. Studi Geol. Camerti 5, 67–82.

Calamita, F., Centamore, E., Deiana, G., Ridolfi, M., 1995. Caratterizzazione geologico-strutturale dell'area marchigianoabruzzese esterna (Appennino centrale). Studi Geologici Camerti, Volume Speciale 1, 171–182.

Campani, M., Herman, F., Mancktelow, N., 2010. Two- and three-dimensional thermal modeling of a low-angle detachment: exhumation history of the Simplon Fault Zone, central Alps. J. Geophys. Res. Solid Earth 115 (B10420), 1–25.

Canavari, M., 1910. I ciottoli erratici nel calcare marnoso da cemento di Fabriano. Società Toscana di Scienze Naturali 42–46.

Cantalamessa, G., Centamore, E., Chiocchini, U., Micarelli, A., Potetti, M., Di Lorito, L., 1986. Il Miocene delle Marche. In: Centamore, E., Deiana, G. (Eds.), La Geologia delle Marche. Studi Geologici Camerti. Volume Speciale. 73° Congresso Società Geologica Italiana, pp. 35–55.

Capuano, N., D'Antonio, G., 1992. Studio sedimentologico-composizionale della sucessione tardo-miocenica della dorsale costiera Gabicce-Pesaro. Giorn. Geol. 54 (1), 107–123.

Caricchi, C., Aldega, L., Corrado, S., 2014. Reconstruction of maximum burial along the Northern Apennines thrust wedge (Italy) by indicators of thermal exposure and modeling. Geol. Soc. Am. Bull. 127 (3–4), 428–442.

Carmignani, L., Conti, P., Cornamusini, G., Meccheri, M., 2004. The internal Northern Apennines, the Northern Tyrrhenian Sea and the Sardinia-Corsica block. Geology of Italy, Special Volume, Italian Geological Society, IGC Vol. 32 pp. 59–77.

Carminati, E., Fabbi, S., Santantonio, M., 2014. Slab bending, syn-subduction normal faulting, and out-of-sequence thrusting in the Central Apennines. Tectonics 33, 530–551.

Castellarin, A., Cantelli, L., 2000. Neo-Alpine evolution of the Southern Eastern Alps. J. Geodyn. 30 (1), 251–274.

Castellarin, A., Colacicchi, R., Praturlon, A., 1978. Fasi distensive, trascorrenze e sovraseorrimenti lungo la "linea Ancona-Anzio" dal Lias al Pliocene. Geol. Romana 17, 161–189.

Castellarin, A., Colacicchi, R., Praturlon, A., Cantelli, C., 1982. The Jurassic-Lower Pliocene history of the Ancona-Anzio line (central Italy). Mem. Soc. Geol. Ital. 24, 325–336.

Centamore, E., Rossi, D., 2009. Neogene-Quaternary tectonics and sedimentation in the Central Apennines. Ital. J. Geosci. 128 (1), 73–88.

Centamore, E., Chiocchini, U., Cipriani, N., Deiana, G., Micarelli, A., 1978. Analisi dell'avoluzione tettonica-sedimentaria dei "Bacini Minori" torbiditici del Miocene Medio-Superiore nell'Appennino Umbro-Marchigiano e Laziale-Abruzzese: risultati degli studi in corso. Mem. Soc. Geol. Ital. 18, 135–170.

Centamore, E., Cantalamessa, G., Micarelli, A., Potetti, M., Berti, D., Bigi, S., Morelli, C., Ridolfi, M., 1991a. Stratigrafia e analisi di facies dei depositi del Miocene e del Pliocene inferiore dell'avanfossa marchigiano-abruzzese e delle zone limitrofe. Studi Geologici Camerti, Volume Speciale 2, 125–131.

Centamore, E., Pambianchi, G., Deiana, G., Calamita, F., Dramis, F., Gentili, B., Nanni, T., 1991b. L'ambiente fisico delle Marche: geologia, geomorfologia, idrogeologia. Regione Marche, Giunta Regionale, S.E.L.C.A., Firenze.

Centamore, E., Cantalamessa, G., Micarelli, A., Potetti, M., Ridolfi, M., Cristallini, C., Morelli, C., 1993. Contributo alla conoscenza dei depositi terrigeni neogenici di avanfossa del teramano (Abruzzo settentrionale). Boll. Soc. Geol. Ital. 112 (1), 63–81.

Centamore, E., Fumanti, F., Nisio, S., 2002. The Central-Northern Apennine geological evolution from Triassic to Neogene time. Boll. Soc. Geol. Ital. Vol. Spec. 1, 181–197.

Centamore, E., Di Manna, P., Rossi, D., 2007. Kinematic evolution of the Volsci Range: a new overview. Boll. Soc. Geol. Ital. 126 (2), 159–172.

Chayes, F., 1956. Petrographic modal analysis: an elementary statistical appraisal. Wiley, New York.

Chiocchini, U., Cipriani, N., 1984. Petrografia delle arenarie torbiditiche del bacino di Monte Vicino (Marche settentrionali). Boll. Soc. Geol. Ital. 103 (3), 579–589.

Chiocchini, U., Cipriani, N., 1986. Caratteri petrografici delle arenarie torbiditche mioceniche dei Bacini Minori. Studi geologici Camerti, Volume Speciale "La geologia delle Marche", pp. 57–60.

Chiocchini, U., Cipriani, N., 1989. The composition and provenance of the Tortonian and Messinian turbidites in the context of the structural evolution of the Central Apennines along the "Ancona-Anzio" line. Sediment. Geol. 63 (1–2), 83–91.

Chiocchini, U., Cipriani, N., 1992. Provenance and evolution of Miocene turbidite sedimen-tation in the Central Apennines, Italy. Sediment. Geol. 77 (3–4), 185–195.

Chiocchini, U., Cipriani, N., Giardini, G., 1981. Petrologia delle arenarie dei Bacini Minori torbiditici di Camerino e di San Donato-Cantia (Marche). Boll. Soc. Geol. Ital. 100 (2), 213–223.

Chiocchini, U., Cipriani, N., Di Giacomo, G., Giacchetta, D., Macri, F., 1987. Petrografia delle arenarie torbiditiche messiniane del bacino della Laga. Giorn. Geol. 3, 59–71.

Cibin, U., Spadafora, E., Zuffa, G.G., Castellarin, A., 2001. Continental collision history from arenites of episutural basins in the Northern Apennines, Italy. Geol. Soc. Am. Bull. 113 (1), 4–19.

Cipollari, P., Cosentino, D., 1995. Miocene unconformities in the Central Apennines: geodynamic significance and sedimentary basin evolution. Tectonophysics 252, 375–389.

Cita Sironi, M.B., Abbate, E., Balini, M., Conti, M.A., Falorni, P., Germani, D., Gropelli, G., Manetti, P., Petti, F.M., 2006. Catalogo delle formazioni - Unità tradizionali, Quaderni serie III, Vol 7, fasciolo VII, Carta Geologica d'Italia, scale 1: 50'000. Servizio Geologico d' Italia.

Corda, L., Morelli, C., 1996. Compositional evolution of the Laga and Cellino sandstones (Messinian-lower Pliocene, Adriatic foredeep). Boll. Soc. Geol. Ital. 115 (2), 423–437.

Cosentino, D., Cipollari, P., Di Donato, V., Sgrosso, I., Sgrosso, M., 2002. The Volsci Range in the kinematic evolution of the northern and southern Apennine orogenic system. Boll. Soc. Geol. Ital. Vol. Spec. 1, 209–218.

Cosentino, D., Cipollari, P., Pipponzi, G., 2003. The central Apennine orogenic system: Stratigraphical constraints and timing of the forelandward migration. Studi Geologici Camerti, Nuova Serie 87–101.

Cosentino, D., Cipollari, P., Marsili, P., Scrocca, D., 2010. Geology of the central Apennines: a regional review. In: Beltrando, M., Peccerillo, A., Mattei, M., Conticelli, S., Doglioni, C. (Eds.), The geology of Italy: tectonics and life along plate margins. Journal of the Virtual Explorer Vol. 36 (paper 12).

Cosentino, D., Buchwaldt, R., Sampalmieri, G., Iadanza, A., Cipollari, P., Schildgen, T.F., Hinnov, L.A., Ramezani, J., Bowring, S.A., 2013. Refining the Mediterranean "Messinian gap" with high-precision U-Pb zircon geochronology, central and northern Italy. Geology 41 (3), 323–326.

Coward, M.P., De Donatis, M., Mazzoli, S., Paltrinieri, W., Wezel, F., 1999. Frontal part of the northern Apennines fold and thrust belt in the Romagna-Marche area (Italy): shallow and deep structural styles. Tectonics 18 (3), 559–574.

Critelli, S., Ingersoll, R.V., 1995. Interpretation of neovolcanic versus palaeovolcanic sand grains: an example from Miocene deep-marine sandstone of the Topanga Group (southern California). Sedimentology 42 (5), 783–804.

Critelli, S., Le Pera, E., 1994. Detrital modes and provenance of Miocene sandstones and modern sands of the southern Apennines thrust-top basins (Italy). J. Sediment. Res. 64 (4), 824–835.

Critelli, S., Le Pera, E., Galluzzo, F., Milli, S., Moscatelli, M., Perrotta, S., Santantonio, M., 2007. Interpreting siliciclastic-carbonate detrital modes in foreland basin systems: an example from Upper Miocene arenites of the central Apennines, Italy. Geol. Soc. Am. Spec. Pap. 420, 107–133.

Critelli, S., Mongelli, G., Perri, F., Martin-Algarra, A., Martin-Martin, M., Perrone, V., Dominici, R., Sonnino, M., Zaghloul, M.N., 2008. Sedimentary evolution of the Middle Triassic-Lower Jurassic continental redbeds from Western-Central Mediterranean Alpine Chains based on geochemical, mineralogical and petrographical tools. J. Geol. 116, 375–386.

Dadson, S., Hovius, N., Pegg, S., Dade, W.B., Horng, M.J., Chen, H., 2005. Hyperpycnial river flows from an active mountain belt. J. Geophys. Res. Earth Surf. 110 (F4), 1–13.

De Celles, P.G., Giles, K.A., 1996. Foreland basin systems. Basin Res. 8 (2), 105–123.

Delfrati, L., Falorni, P., Gropelli, G., Petti, F.M., 2002. Catalogo delle formazioni - Unità tradizionali, Quaderni serie III, Vol 7, fasciolo III, Carta Geologica d'Italia, scale 1: 50'000. Servizio Geologico d' Italia.

Di Giulio, A., 1999. Mass transfer from the Alps to the Apennines: volumetric constraints in the provenance study of the Macigno–Modino source–basin system, Chattian–Aquitanian, northwestern Italy. Sediment. Geol. 124 (1), 69–80.

Dickinson, W.R., 1970. Interpreting detrital modes of graywacke and arkose. J. Sediment. Petrol. 40 (2), 695–707.

Dickinson, W.R., 1985. Interpreting provenance relations from detrital modes of sandstones. In: Zuffa, G.G. (Ed.), Provenance of Arenites. NATO Advanced Study Institute Series Vol. 148. D. Reidel, Dordrecht, Netherlands, pp. 333–361.

Dickson, J.A.D., 1966. Carbonate identification and genesis as revealed by staining. J. Sediment. Petrol. 36 (2), 491–505.

Dunkl, I., Di Giulio, A., Kuhlemann, J., 2001. Combination of single-grain fission-track chronology and morphological analysis of detrital zircon crystals in provenance studies: sources of the Macigno Formation (Apennines, Italy). J. Sediment. Res. 71 (4), 516–525.

Dunkl, I., Frisch, W., Grundmann, G., 2003. Zircon fission track thermochronology of the southeastern part of the Tauern Window and the adjacent Austroalpine margin, Eastern Alps. Eclogae Geol. Helv. 96 (2), 209–217.

von Eynatten, H., 2003. Petrography and chemistry of sandstones from the Swiss Molasse Basin: an archive of the Oligocene to Miocene evolution of the Central Alps. Sedimentology 50 (4), 703–724.

Fabbri, A., Curzi, P., 1979. The Messinian of the Tyrrhenian Sea: seismic evidence and dynamic implications. Giorn. Geol. 2 (43), 215–248.

Fellin, M.G., Reiners, P.W., Brandon, M.T., Wüthrich, E., Balestrieri, M.L., Molli, G., 2007. Thermochronologic evidence for the exhumational history of the Alpi Apuane metamorphic core complex, northern Apennines, Italy. Tectonics 26 (TC6015), 1–22.

Folk, R.L., 1974. Petrology of Sedimentary Rocks. Hemphill Publishing Company, Austin, Texas.

Fontana, D., 1991. Detrital carbonate grains as provenance indicatos in the Upper Cretaceous Pietraforte Formation (northern Apennines). Sedimentology 38, 1085–1095.

Frank, W., Kralik, M., Scharbert, S.T., Thöni, M., 1987. Geochronological data from the Eastern Alps. In: Flügel, H., Faupl, P. (Eds.), Geodynamics of the Eastern Alps. Deuticke, Vienna, pp. 272–281.

Fügenschuh, B., Schmid, S.M., 2003. Late stages of deformation and exhumation of an orogen constrained by fission-track data: a case study in the Western Alps. Geol. Soc. Am. Bull. 115 (11), 1425–1440.

Fügenschuh, B., Seward, D., Mancktelow, N., 1997. Exhumation in a convergent orogen: the western Tauern window. Terra Nova 9 (5–6), 213–217.

Funiciello, R., Giordano, G., Bozzano, F., Capelli, G., Cesi, C., Cipollari, P., Cosentino, D., Esposito, A., Eulilli, V., Gliozzi, E., Lanzini, M., Mattei, M., Porreca, M., Mazza, R., 2008. Note illustrative del Foglio 374 – Roma. Carta Geologica d'Italia, scale 1: 50.000. Servizio Geologico d' Italia.

Gandolfi, G., Paganelli, L., Zuffa, G.G., 1983. Petrology and dispersal pattern in the Marnoso-arenacea Formation (Miocene, Northern Apennines). J. Sediment. Petrol. 53 (2), 493–507.

Gandolfi, G., Paganelli, L., Cavazza, W., 2007. Heavy-mineral associations as tracers of limited compositional mixing during turbiditic sedimentation of the Marnoso-arenacea Formation (Miocene, Northern Apennines, Italy). In: Mange, M.A., Wright, D.T. (Eds.), Heavy minerals in use. Developments in Sedimentology Vol. 58. Elsevier, pp. 621–645.

Garver, J.I., Brandon, M.T., Roden-Tice, M., Kamp, P.J.J., 1999. Exhumation history of orogenic highlands determined by detrital fission-track thermochronology. Geol. Soc. Lond. Spec. Publ. 154 (1), 283–304.

Garzanti, E., Andò, S., 2007. Heavy mineral concentration in modern sands: implications for provenance interpretation. In: Mange, M.A., Wright, D.T. (Eds.), Heavy minerals in use. Developments in Sedimentology Vol. 58. Elsevier, pp. 517–545.

Garzanti, E., Malusà, M.G., 2008. The Oligocene Alps: domal unroofing and drainage development during early orogenic growth. Earth Planet. Sci. Lett. 268 (3), 487–500.

Garzanti, E., Canclini, S., Foggia, F.M., Petrella, N., 2002. Unraveling magmatic and orogenic provenance in modern sand: the back-arc side of the Apennine thrust belt, Italy. J. Sediment. Res. 72 (1), 2–17.

Garzanti, E., Vezzoli, G., Andò, S., France-Lanord, C., Singh, S.K., Foster, G., 2004. Sand petrology and focused erosion in collision orogens: the Brahmaputra case. Earth Planet. Sci. Lett. 220 (1), 157–174.

Garzanti, E., Doglioni, C., Vezzoli, G., Andò, S., 2007. Orogenic belts and orogenic sediment provenance. J. Geol. 115 (3), 315–334.

Gebauer, D., 1993. The pre-Alpine evolution of the continental crust of the Central Alps – an overview. In: von Raumer, J.F., Neubauer, F. (Eds.), Pre-mesozoic geology in the Alps. Springer, Berlin Heidelberg, pp. 93–117.

Gebauer, D., Williams, I.S., Compston, W., Grünenfelder, M., 1989. The development of the Central European continental crust since the Early Archaean based on conventional and ion-microprobe dating of up to 3.84 by old detrital zircons. Tectonophysics 157 (1–3), 81–96.

Ghielmi, M., Minervini, M., Nini, C., Rogledi, S., Rossi, M., 2013. Late Miocene-Middle Pleistocene sequences in the Po Plain – Northern Adriatic Sea (Italy): the stratigraphic record of modification phases affecting a complex foreland basin. Mar. Pet. Geol. 42, 50–81.

Gianola, O., Schmidt, M.W., von Quadt, A., Peytcheva, I., Luraschi, P., Reusser, E., 2014. Continuity in geochemistry and time of the Tertiary Bergell intrusion (Central Alps). Swiss J. Geosci. 107 (2–3), 197–222.

Guillong, M., von Quadt, A., Sakata, S., Peytcheva, I., Bachmann, O., 2014. LA-ICP-MS Pb–U dating of young zircons from the Kos–Nisyros volcanic centre, SE Aegean arc. J. Anal. At. Spectrom. 29 (6), 963–970.

Handy, M.R., Schmid, S.M., Bousquet, R., Kissling, E., Bernoulli, D., 2010. Reconciling plate-tectonic reconstructions of Alpine Tethys with the geological-geophysical record of spreading and subduction in the Alps. Earth Sci. Rev. 102, 121–158.

Haughton, P.D.W., Todd, S.P., Morton, A.C., 1991. Sedimentary provenance studies. Geol. Soc. Lond. Spec. Publ. 57 (1), 1–11.

Hilgen, J.F., Krijgsman, W., Langereis, C.G., Lourens, L.J., Santarelli, A., Zachariasse, W.J., 1995. Extending the astronomical (polarity) time scale into the Miocene. Earth Planet. Sci. Lett. 136 (3–4), 495–510.

Houghton, H.F., 1980. Refined techniques for staining plagioclase and alkali feldspars in thin section. J. Sediment. Petrol. 50 (2), 629–631.

Hubert, J.F., 1962. A zircon-tourmaline-rutile maturity index and the interdependence of the composition of heavy mineral assemblages with the gross composition and texture of sandstones. J. Sediment. Petrol. 32 (3), 440–450.

Hunziker, J.C., Desmons, J., Martinotti, G., 1989. Alpine thermal evolution in the central and the western Alps. Geol. Soc. Lond. Spec. Publ. 45 (1), 353–367.

Hunziker, J.C., Desmons, J., Hurford, A.J., 1992. Thirty-two years of geochronological work in the Central and Western Alps: a review on seven maps. Mémoires de Géologie Vol. 13. Université de Lausanne.

Hurford, A.J., 1986. Cooling and uplift patterns in the Lepontine Alps South Central Switzerland and and age of vertical movement on the Insubric fault line. Contrib. Mineral. Petrol. 92 (4), 413–427.

Hurford, A.J., Green, P.F., 1983. The zeta age calibration of fission-track dating. Chem. Geol. 41, 285–317.

Hurford, A.J., Flisch, M., Jäger, E., 1989. Unravelling the thermo-tectonic evolution of the Alps: a contribution from fission track analysis and mica dating. Geol. Soc. Lond. Spec. Publ. 45 (1), 369–398.

Ingersoll, R.V., 1990. Actualistic sandstone petrofacies: discriminating modern and ancient source rocks. Geology 18 (8), 733–736.

Ingersoll, R.V., Bullard, T.F., Ford, R.L., Grimm, J.P., Pickle, J.D., Sares, S.W., 1984. The effect of grain size on detrital modes: a test of the Gazzi-Dickinson point-counting method. J. Sediment. Petrol. 54 (1), 103–116.

Jackson, S.E., Pearson, N.J., Griffin, W.L., Belousova, E.A., 2004. The application of laser ablation-inductively coupled plasma-mass spectrometry to in situ U-Pb zircon geochronology. Chem. Geol. 211 (1), 47–69.

Kapferer, N., Mercolli, I., Berger, A., Ovtcharova, M., Fügenschuh, B., 2012. Dating emplacement and evolution of the orogenic magmatism in the internal Western Alps: 2. The Biella Volcanic Suite. Swiss J. Geosci. 105 (1), 67–84.

Krijgsman, W., Hilgen, F.J., Raffi, I., Sierro, F.J., Wilson, D.S., 1999. Chronology, causes and progression of the Messinian salinity crisis. Nature 400, 652–655.

Le Pera, E., Critelli, S., 2009a. Petrologia delle Areniti. In: Micarelli, A., Cantalamessa, G. (Eds.), Explanatory Notes of the Geological Map of Italy 1:50'000, 314 Sheet Montegiorgio. Servizio Geologico d'Italia, CARG, Italy, pp. 54–61.

Le Pera, E., Critelli, S., 2009b. Petrografia e Petrologia delle Areniti. In: Cello, G. (Ed.), Explanatory Notes of the Geological Map of Italy 1:50'000, 302 Sheet Macerata. Servizio Geologico d'Italia, CARG, Italy, pp. 71–74.

Lindholm, R.C., Finkelmann, R.B., 1972. Calcite staining: semiquantitative determination of ferrous ion. J. Sediment. Petrol. 42 (1), 239–242.

Linnemann, U., Romer, R., Pin, C., Aleksandrowski, P., Bula, Z., Geisler, T., Kachlik, V., Krzeminska, e., Mazur, S., Motuza, G., Murphy, J.B., Nance, R.D., Pisarevsky, S., Schulz, B., Ulrich, J., Wiszniewska, J., Zaba, J., Zeh, A., 2008. Precambrian. In: McCann, T. (Ed.), The geology of Central Europe. Precambrian and Paleozoic vol. 1. Geological Society, London, pp. 21–101.

Ludwig, K.R., 2001. Isoplot 4.1: A Geochronological Toolkit for Microsoft Excel. Special Publication Vol. 4. Berkeley Geochronology Center, Berkley.

Maino, M., Decarlis, A., Felletti, F., Seno, S., 2013. Tectono-sedimentary evolution of the Tertiary Piedmont Basin (NW Italy) within the Oligo–Miocene central Mediterranean geodynamics. Tectonics 32 (3), 593–619.

Malinverno, A., Ryan, W.B.F., 1986. Extension in the Tyrrhenian Sea and shortening in the Apennines as result of arc migration driven by sinking of the lithosphere. Tectonics 5 (2), 227–245.

Malusà, M.G., Balestrieri, M.L., 2012. Burial and exhumation across the Alps-Apennines junction zone constrained by fission-track analysis on modern river sands. Terra Nova 24, 221–226.

Malusà, M.G., Polino, R., Zattin, M., Bigazzi, G., Martin, S., Piana, F., 2005. Miocene to Present differential exhumation in the Western Alps: insights from fission track thermochronology. Tectonics 24 (TC3004), 1–23.

Manzi, V., Lugli, S., Lucchi, F.R., Roveri, M., 2005. Deep-water clastic evaporites deposition in the Messinian Adriatic foredeep (northern Apennines, Italy): did the Mediterranean ever dry out? Sedimentology 52 (4), 875–902.

Marini, M., Milli, S., Moscatelli, M., 2011. Facies and architecture of the Lower Messinian turbidite lobe complexes from the Laga Basin (central Apennines, Italy). Journal of Mediterranean Earth Sciences 3, 45–72.

Marini, M., Milli, S., Ravnås, R., Moscatelli, M., 2015. A comparative study of confined vs. semi-confined turbidite lobes from the Lower Messinian Laga Basin (Central Apennines, Italy): implications for assessment of reservoir architecture. Mar. Pet. Geol. 63, 142–165.

Marotta, A.M., Spalla, M.I., 2007. Permian-Triassic high thermal regime in the Alps: result of late Variscan collapse or continental rifting? Validation by numerical modeling. Tectonics 26 (TC4016), 1–27.

Martens, J.H.C., 1932. Piperine as an immersion medium in sedimentary petrography. Am. Mineral. 17 (5), 198–199.

Martini, I.P., Sagri, M., 1993. Tectono-sedimentary characteristics of Late Miocene – Quaternary extensional basins of the Northern Apennines. Earth Sci. Rev. 34, 197–233.

Mauffret, A., Contrucci, I., 1999. Crustal structure of the North Tyrrhenian Sea: first result of the multichannel seismic LISA cruise. In: Durand, B., Jolivet, L., Horvath, F., Séranne, M. (Eds.), The Mediterranean Basins: Tertiary Extension within the Alpine Orogen. Geological Society, London, Special Publication Vol. 156 (1), pp. 169–193.

Mayer, A., Cortiana, G., Dal Piaz, G., Deloule, E., De Pieri, R., Jobstraibizer, P., 2003. U-Pb single zircon ages of the Adamello batholith, Southern Alps. Mem. Soc. Geol. Ital. 55, 151–167.

Mezzadri, G., 1964. Petrografia delle 'Arenarie di Ostia'. Rendiconti Società Mineralogica Italiana 20, 193–220.

Milli, S., Moscatelli, M., 2000. Facies analysis and physical stratigraphy of the Messinian turbiditic complex in the Valle del Salto and Val di Varri (Central Apennines). Giorn. Geol. 62, 57–77.

Milli, S., Moscatelli, M., Stanzione, O., Falcini, F., 2007. Sedimentology and physical stratigraphy of the Messinian turbidite deposits of the Laga Basin (central Apennines, Italy). Boll. Soc. Geol. Ital. 126 (2), 255–281.

Milli, S., Cannata, D., Marini, M., Moscatelli, M., 2013. Facies and geometries of Lower Messinian Laga Basin turbidite deposits (central Apennines, Italy). Excursion Guidebook, XI GeoSed Post-Congress Field Trip. Journal of Mediterranean Earth Sciences Vol. 5, pp. 179–225.

Morelli, C., 1994. Ricostruzione dell'evoluzine tettonico-sedimentaria de bacini di avanfossa marchigiano-abbruzzesi durante il Messiniano ed il Pliocene inferiore. (PhD Thesis). SAPIENZA Università di Roma.

Morton, A.C., Hallsworth, C.R., 1999. Processes controlling the composition of heavy mineral assemblages in sandstones. Sediment. Geol. 124 (1), 3–29.

Morton, A.C., Hallsworth, C.R., 2007. Stability of detrital heavy minerals during burial diagenesis. In: Mange, M.A., Wright, D.T. (Eds.), Heavy minerals in use. Developments in Sedimentology Vol. 58. Elsevier, pp. 215–245.

Moscatelli, M., 2003. La sedimentazione torbiditica e le sue relazioni con quella fluvio-deltizia nel sistema d'avanfossa alto-miocenico dell'Appennino centro-meridionale. (PhD thesis). SAPIENZA Università di Roma.

Mulder, T., Syvitski, J.P.M., Migeon, S., Faugères, J., Savoye, B., 2003. Marine hyperpycnal flows: initiation, behaviour and related deposits. A review. Mar. Pet. Geol. 20 (6), 861–882.

Müller, W., Mancktelow, N.S., Meier, M., 2000. Rb–Sr microchrons of synkinematic mica in mylonites: an example from the DAV fault of the Eastern Alps. Earth Planet. Sci. Lett. 180 (3), 385–397.

Mutti, E., Normark, W.R., 1987. Comparing examples of modern and ancient turbidite systems: problems and concepts. In: Leggett, J.K., Zuffa, G.G. (Eds.), Marine Clastic Sedimentology: Concepts and Case Studies. Graham & Trotman, London, pp. 1–38.

Mutti, E., Ricci Lucchi, F., Roveri, M., 2002. Revisiting turbidites of the Marnoso-arenacea Formation and their basin-margin equivalents: problems with classic models. Excursion Guidebook, 64th EAGE Conference and Exhibition. Parma University and ENI - AGIP Division.

Mutti, E., Tinterri, R., Benevelli, G., di Biase, D., Cavanna, G., 2003. Deltaic, mixed and turbidite sedimentation of ancient foreland basins. Mar. Pet. Geol. 20 (6), 733–755.

Naeser, N.D., Zeitler, P.K., Naeser, C.W., Cerveny, P.F., 1987. Provenance studies by fission-track dating of zircon-etching and counting procedures. International Journal of Radiation Applications and Instrumentation. Part D. Nuclear Tracks and Radiation Measurements 13 (2), 121–126.

Oberhänsli, R., 1986. Blue amphiboles in metamorphosed Mesozoic mafic rocks from the Central Alps. Geol. Soc. Am. Mem. 164, 239–248.

Oberli, F., Meier, M., Berger, A., Rosenberg, C.L., Gieré, R., 2004. U-Th-Pb and ^{230}Th/^{238}U disequilibrium isotope systematics: precise accessory mineral chronology and melt evolution tracing in the Alpine Bergell intrusion. Geochim. Cosmochim. Acta 68 (11), 2543–2560.

Ori, G.G., Roveri, M., Vannoni, F., 1986. Plio-Pleistocene sedimentation in the Apenninic-Adriatic foredeep (Central Adriatic Sea, Itlay). In: Allen, P.A., Homewood, P. (Eds.), Foreland basins. International Association of Sedimentologists Special Publication Vol. 8. Blackwell Scientific Publications, Oxford, pp. 183–198.

Patacca, E., Sartori, R., Scandone, P., 1990. Tyrrhenian Basin and Apenninic arcs: kinematic relations since Late Tortonian times. Mem. Soc. Geol. Ital. 45, 425–451.

Paton, C., Woodhead, J.D., Hellstrom, J.C., Hergt, J.M., Greig, A., Maas, R., 2010. Improved laser ablation U-Pb zircon geochronology through robust downhole fractionation correction. Geochem. Geophys. Geosyst. 11 (3), 1–36.

Paton, C., Hellstrom, J., Paul, B., Woodhead, J., Hergt, J., 2011. Iolite: freeware for the visualisation and processing of mass spectrometric data. J. Anal. At. Spectrom. 26 (12), 2508–2518.

Petrus, J.A., Kamber, B.S., 2012. VizualAge: a novel approach to laser ablation ICP-MS U–Pb geochronology data reduction. Geostand. Geoanal. Res. 36 (3), 247–270.

Pettijohn, F.J., Potter, P., Siever, R., 1987. Sand and Sandstone. Springer, New York.

Pialli, G., Plesi, G., Damiani, A.V., Brozzetti, F., Boscherini, A., Bucefalo Palliani, R., Cardinali, M., Checcucci, R., Daniele, G., Galli, M., Luchetti, L., Motti, A., Nocchi, M., Ponziani, F., Rettori, R., 2000. Note illustrative del Foglio 289 – Città di Castello. Carta Geologica d'Italia, scale 1: 50.000. Servizio Geologico d' Italia.

Pieri, M., Groppi, G., 1981. Subsurface geological structure of the Po plain, Italy. CNR. 414. Program Final Geodinamica, p. 13.

Plesi, G., Arcaleni, A., Bartoccini, P., Boscherini, A., Botti, F., Checucci, R., Damiani, A.V., Daniele, G., Del Gaia, F., Felicioni, G., Galli, M., Luchetti, L., Motti, A., Palandri, S., Ponziani, F., Preziosi, E., Rettori, R., Sabatini, S., Simone, G., Tosti, D., Tuscano, F., Uffreduzzi, T., 2010. Note illustrative del Foglio 299 – Umbertide, Carta Geologica d'Italia, scale 1: 50.000. Servizio Geologico d'Italia.

von Raumer, J.F., Stampfli, G.M., 2008. The birth of the Rheic Ocean - Early Palaeozoic subsidence patterns and subsequent tectonic plate scenarios. Tectonophysics 461 (1), 9–20.

von Raumer, J.F., Stampfli, G.M., Bussy, F., 2003. Gondwana-derived microcontinents - the constituents of the Variscan and Alpine collisional orogens. Tectonophysics 365 (1), 7–22.

von Raumer, J.F., Bussy, F., Schaltegger, U., Schulz, B., Stampfli, G.M., 2013. Pre-Mesozoic Alpine basements – their place in the European Paleozoic framework. Geol. Soc. Am. Bull. 125 (1–2), 89–108.

Reid, I., Frostick, L.E., 1994. Fluvial sediment transport and deposition. In: Pye, K. (Ed.), Sediment Transport and Depositional Processes. Blackwell Scientific Publications, Oxford, pp. 89–155.

Reutter, K.J., Teichmuller, M., Teichmuller, R., Zanzucchi, G., 1983. The coalification pattern in ther northern Apennines and its paleogeothermic and tectonic significance. Geol. Rundsch. 72 (3), 861–893.

Reverman, R.L., Fellin, M.G., Herman, F., Willett, S.D., Fitoussi, C., 2012. Climatically versus tectonically forced erosion in the Alps: thermochronometric constraints from the Adamello Complex, Southern Alps, Italy. Earth Planet. Sci. Lett. 339, 127–138.

Ricci Lucchi, F., 1975. Miocene paleogeography and basin analysis in the Periadriatic Apennines. In: Squyres, C.H. (Ed.), Geology of Italy. Petroleum Exploration Society of Libya vol. 2, pp. 129–236.

Ricci Lucchi, F., 1986. The Oligocene to recent foreland basins of the northern Apennines. In: Allen, P.A., Homewood, P. (Eds.), Foreland Basins. International Association of Sedimentologists Special Publication Vol. 8. Blackwell Scientific Publications, Oxford, pp. 105–139.

Rossi, M., Rogledi, S., Barbacini, G., Casadei, D., Iaccarino, S., Papani, G., 2002. Tectono-stratigraphic architecture of Messinian piggyback basins of Northern Apennines: the Emilia folds in the Reggio-Modena area and comparison with the Lombardia and Romagna sectors. Boll. Soc. Geol. Ital. vol. spec. 1, 437–447.

Roveri, M., Bassetti, M.A., Ricci Lucchi, F., 2001. The Mediterranean Messinian salinity crisis: an Apennine foredeep perspective. Sediment. Geol. 140 (3), 201–214.

Roveri, M., Ricci Lucchi, F., Lucente, C.C., Manzi, V., Mutti, E., 2002. Stratigraphy, facies and basin fill history of the Marnoso-arenacea Formation. In: Mutti, E., Ricci Lucchi, F., Roveri, M. (Eds.), Revisiting Turbidites of the Marnoso-arenacea Formation and Their Basin-margin Equivalents: Problems with Classic Models, Part III. Excursion Guidebook, 64th EAGE Conference and Exhibition. Parma University and ENI - AGIP Division.

Roveri, M., Manzi, V., Ricci Lucchi, F., Rogledi, S., 2003. Sedimentary and tectonic evolution of the Vena del Gesso basin (Northern Apennines, Italy): implications for the onset of the Messinian salinity crisis. Geol. Soc. Am. Bull. 115 (4), 387–405.

Roveri, M., Landuzzi, M.A., Lugli, S., Manzi, V., Ricci Lucchi, F., Vai, G.B., 2004. The record of Messinian events in the Northern Apennines fordeep basins. 32nd International Geological Congress, Florence.

Roveri, M., Boscolo Gallo, A., Massimo, R., Gennari, R., Iaccarino, S.M., Lugli, S., Manzi, V., Negri, A., Rizzini, F., Taviani, M., 2005. The Adriatic foreland record of Messinian events (central Adriatic Sea, Italy). GeoActa 4, 139–158.

Roveri, M., Lugli, S., Manzi, V., Gennari, R., Schreiber, B.C., 2014. High-resolution strontium isotope stratigraphy of the Messinian deep Mediterranean basins: implications for marginal to central basins correlation. Mar. Geol. 349, 113–125.

Royden, L., Patacca, E., Scandone, P., 1987. Segmentation and configuration of subducted lithosphere in Italy: an important control on thrust-belt and foredeep-basin evolution. Geology 15, 714–717.

Savelli, D., Wezel, F.C., 1978. Schema geologico del Messiniano nel pesarese. Boll. Soc. Geol. Ital. 97 (1–2), 165–188.

Schaltegger, U., Gebauer, D., 1999. Pre-Alpine geochronology of the Central, Western and Southern Alps. Schweiz. Mineral. Petrogr. Mitt. 79, 79–87.

Schaltegger, U., Brack, P., Ovtcharova, M., Peytcheva, I., Schoene, B., Stracke, A., Marocchi, M., Bargossi, G.M., 2009. Zircon and titanite recording 1.5 million years of magma accretion, crystallization and initial cooling in a composite pluton (southern Adamello batholith, northern Italy). Earth Planet. Sci. Lett. 286 (1), 208–218.

Schmid, S.M., Fügenschuh, B., Kissling, E., Schuster, R., 2004. Tectonic map and overall architecture of the Alpine orogen. Eclogae Geol. Helv. 97 (1), 93–117.

Schoene, B., Schaltegger, U., Brack, P., Latkoczy, C., Stracke, A., Günther, D., 2012. Rates of magma differentiation and emplacement in a ballooning pluton recorded by U–Pb TIMS-TEA, Adamello batholith, Italy. Earth Planet. Sci. Lett. 355, 162–173.

Schönborn, G., 1992. Kinematics of a transverse zone in the Southern Alps, Italy. In: McClay, K.R. (Ed.), Thrust Tectonics. Springer, Netherlands, pp. 299–310.

Schwartz, S., Lardeaux, J.M., Tricart, P., Guillot, S., Labrin, E., 2007. Diachronous exhumation of HP–LT metamorphic rocks from south-western Alps: evidence from fission-track analysis. Terra Nova 19 (2), 133–140.

Scisciani, V., Montefalcone, R., 2006. Coexistence of thin and thick-skinned tectonics: an example from the Central Apennines, Italy. Geol. Soc. Am. Spec. Pap. 414, 33–54.

Scisciani, V., Calamita, F., Tavarnelli, E., Rusciadelli, G., Ori, G., Paltrinieri, W., 2001. Foreland-dipping normal faults in the inner edges of syn-orogenic basins: a case from the Central Apennines, Italy. Tectonophysics 330 (3), 211–224.

Seward, D., Mancktelow, N.S., 1994. Neogene kinematics of the central and western Alps: evidence from fission-track dating. Geology 22 (9), 803–806.

Spalla, M.I., Zanoni, D., Marotta, A.M., Rebay, G., Roda, M., Zucali, M., Gosso, G., 2014. The transition from Variscan collision to continental break-up in the Alps: insights from

the comparison between natural data and numerical model predictions. Geol. Soc. Lond., Spec. Publ. 405 (1), 363–400.

Spiegel, C., Kuhlemann, J., Dunkl, I., Frisch, W., 2001. Paleogeography and catchment evolution in a mobile orogenic belt: the Central Alps in Oligocene-Miocene times. Tectonophysics 341 (1), 33–47.

Spiegel, C., Siebel, W., Kuhlemann, J., Frisch, W., 2004. Toward a comprehensive provenance analysis: a multi-method approach and its implications for the evolution of the Central Alps. Geol. Soc. Am. Spec. Pap. 378, 37–50.

Stefani, C., Fellin, M.G., Zattin, M., Zuffa, G.G., Dalmonte, C., Mancin, N., Zanferrari, A., 2007. Provenance and paleogeographic evolution in a multi-source foreland: the Cenozoic Venetian–Friulian Basin (NE Italy). J. Sediment. Res. 77 (11), 867–887.

Stipp, M., Fügenschuh, B., Gromet, L., Stünitz, H., Schmid, S.M., 2004. Contemporaneous plutonism and strike-slip faulting: a case study from the Tonale fault zone north of the Adamello pluton (Italian Alps). Tectonics 23 (TC3004), 1–23.

Thinon, I., Guennoc, P., Serrano, O., Maillard, A., Lasseur, E., Réhault, J.P., 2016. Seismic markers of the Messinian Salinity Crisis in an intermediate-depth basin: data for understanding the Neogene evolution of the Corsica basin (northern Tyrrhenian Sea). Mar. Pet. Geol. 77, 1274–1296.

Thomson, S.N., Brandon, M.T., Reiners, P.W., Zattin, M., Isaacson, P.J., Balestrieri, M.L., 2010. Thermochronologic evidence for orogen-parallel variability in wedge kinematics during extending convergent orogenesis of the northern Apennines, Italy. Geol. Soc. Am. Bull. 122 (7–8), 1160–1179.

Thöni, M., 1999. A review of geochronological data from the Eastern Alps. Schweiz. Mineral. Petrogr. Mitt. 79 (1), 209–230.

Valloni, R., Zuffa, G.G., 1984. Provenance changes for arenaceous formations of the northern Apennines, Italy. Geol. Soc. Am. Bull. 95 (9), 1035–1039.

Valloni, R., Cipriani, N., Morelli, C., 2002. Petrostratigraphic record of the Apennine foredeep basins, Italy. Boll. Soc. Geol. Ital. 121 (1), 455–465.

Van der Plas, L., 1962. Preliminary note on the granulometric analysis of sedimentary rocks. Sedimentology 1 (2), 145–157.

Vermeesch, P., 2004. How many grains are needed for a provenance study? Earth Planet. Sci. Lett. 224 (3), 441–451.

Vermeesch, P., 2006. Tectonic discrimination diagrams revisited. Geochem. Geophys. Geosyst. 7 (6), 1–55.

Vermeesch, P., 2013. Multi-sample comparison of detrital age distributions. Chem. Geol. 341, 140–146.

Vermeesch, P., Garzanti, E., 2015. Making geological sense of 'Big Data' in sedimentary provenance analysis. Chem. Geol. 409, 20–27.

Viola, G., Mancktelow, N.S., Seward, D., 2001. Late Oligocene-Meogene evolution of Europe-Adria collision: new structural and geochronological evidence from the Giudicarie fault system (Italian Eastern Alps). Tectonics 20 (6), 999–1020.

Visonà, D., Caironi, V., Carraro, A., Dallai, L., Fioretti, A., Fanning, M., 2007. Zircon megacrysts from basalts of the Venetian Volcanic Province (NE Italy): U–Pb ages, oxygen isotopes and REE data. Lithos 94 (1), 168–180.

Waibel, A., 1993. Nature and plate-tectonic significance of orogenic magmatism in the European Alps: a review. Schweiz. Mineral. Petrogr. Mitt. 73 (3), 391–405.

Wildi, W., 1985. Heavy mineral distribution and dispersal pattern in Penninic and Ligurian flysch basins (Alps, northern Apennines). Giorn. Geol. 47 (1–2), 77–99.

Wolff, R., Dunkl, I., Kiesselbach, G., Wemmer, K., Siegesmund, S., 2012. Thermochronological constraints on the multiphase exhumation history of the Ivrea-Verbano Zone of the Southern Alps. Tectonophysics 579, 104–117.

Zattin, M., Zuffa, G.G., 2004. Unravelling the source rocks of Late Eocene-Miocene orogenic wedge and foredeep arenites of the northern Apennines and southern Alps. Boll. Soc. Geol. Ital. 123 (1), 67–76.

Zattin, M., Picotti, V., Zuffa, G.G., 2002. Fission-track reconstruction of the front of the Northern Apennine thrust wedge and overlying Ligurian unit. Am. J. Sci. 302 (4), 346–379.

Zuffa, G.G., 1980. Hybrid arenites: their composition and classification. J. Sediment. Petrol. 50 (1), 21–29.

Zuffa, G.G., 1985. Optical analyses of arenites: influence of methodology on compositional results. In: Zuffa, G.G. (Ed.), Provenance of Arenites. NATO Advanced Study Institute Series Vol. 148. Springer, Netherelands, pp. 165–189.

Zuffa, G.G., 1987. Unravelling hinterland and offshore palaeogeography from deep-water arenites. In: Legget, J.K., Zuffa, G.G. (Eds.), Marine Clastic Sedimentology: Concepts and Case Studies. Graham & Trotman, London, pp. 39–61.